JAC: Jena Atomic Calculator

— User Guide, Compendium & Theoretical Background —

http://www.atomic-theory.uni-jena.de/

Stephan Fritzsche

Helmholtz-Institut Jena &

Theoretisch-Physikalisches Institut, Friedrich-Schiller-Universität Jena, Fröbelstieg 3, D-07743 Jena, Germany

(Email: s.fritzsche@gsi.de, phone: +49-3641-947606)

Friday 20$^{\text{th}}$ March, 2020

Atomic representations

- Configuration-based expansions
- Restricted active spaces (layer-by-layer)
- CI+perturbation theory; Gamov states
- Approximate Green functions, ...

Processes & properties

- Transition probabilities
- Excitation, ionization & recombination
- Auger, DR, Rayleigh-Compton, multi-γ
- Hyperfine & Zeeman splitting; plasma
- Isotope shifts, Lande & form factors

Atomic cascades

- Average singe-configuration approach
- Multiple-configuration approach
- Incorporation of shake-up & shake-off
- Ion & electron distributions, ...

Symbolic Racah algebra

- Wigner symbols, special values
- Symmetries & recursions
- Symbolic sum rule evaluation
- Spherical harmonics & tensors

Interactive High-Level Language

JAC

Jena Atomic Calculator

A Julia implementation for atomic computations.

Open-source applications in physics, science and technology.

Atomic responses

- Field-induced processes & ionization
- High-harmonic generation
- Particle-impact processes
- Charge exchange

Time evolution

- Liouville equation for statistical tensors & atomic density matrices
- Atoms in intense light pulses
- Angle & polarization-dep. observables

Atomic descriptors

- Feature transform. & machine learning
- Bi-spectra of electronic densities
- Subshell & coupling descriptors
- Atomic fragments & effective charges

Semi-empirical estimates

- Weak-field ionization rates
- Asymptotic behaviour & formulas
- Stopping powers
- Plasma Stark broadening, ...

Contents

1. Overview about JAC. Structure of this User Guide

1.1. Goals of the JAC toolbox

Purpose of the JAC module:

- The Jena Atomic Calculator (JAC) provides tools for performing atomic (structure) calculations at various degrees of complexity and sophistication. This toolbox has been designed to calculate not only atomic level structures and properties [g-factors, hyperfine and isotope-shift parameters, etc.] or transition amplitudes between bound-state levels [dipole operator, Schiff moment, parity non-conservation, etc.] but, in particular, also (atomic) transition probabilities, Auger rates, photoionization cross sections, radiative and dielectronic recombination rates as well as cross sections and parameters for many other (elementary) processes.
- JAC also facilitates interactive computations, the simulation of atomic cascades and atomic responses, the time-evolution of statistical tensors as well as various semi-empirical estimates of atomic properties. It provides a diverse and wide-ranging, yet consistent set of methods which can be applied in different fields of atomic physics and elsewhere.
- In addition, the JAC module has been designed to readily support the display of level energies, electron and photon spectra, radial orbitals and several others entities.
- To find (the details about) individual features of the JAC program, see the index or search for keywords/phrases in this text.
- In practice, the design of JAC has been based on an analysis of typical user requirements and a hierarchical structure of the code.
- Since the theoretical background and data, implemented in JAC, have been extracted from quite many sources, we also hope to develop JAC as a repository of previous experience with electronic structure calculations of atoms in different environments, and that is to be further refined, expanded and developed here.
- The source code, an extensive documentation as well as a number of tutorials and examples are available from our Web site https://www.github.com/sfritzsche/JAC.jl.

- In order to support all these goals, several types of computation are distinguished within the Jac toolbox.
- With the design and development of Jac, we aim to identify (emerging) problems from AMO science and to provide a powerful toolbox that supports rapid scientific progress for the AMO community.
- When compared to astro and particle physics, and even if compared to quantum chemistry, the AMO community has placed less emphasis in developing and maintaining robust und user-friendly software tools for frequent applications.
- Although various (highly) specialized atomic codes have been developed over the fice past decades, they are often accessible only to a small group of researches or no longer maintained at all.
- Since many methods in dealing computationally with quantum many-particle physics have first been applied to atoms an ions, Jac aims to retain this knowledge and effort to make it usable by future AMO scientists.

Types of computations:

- Atomic computations, based on explicitly specified electron configurations: A typical computation, that is based on explicitly specified electron configurations, refers to the level energies, atomic states and to either one (or several) atomic properties for levels from a given multiplet or to the rates and cross sections of just one selected atomic process. For further details, see the supported amplitudes, properties and processes in Sections 6–8 below.
- Restricted active-space computations (RAS): A RAS computation refers to systematically-enlarged calculations of atomic states and level energies due to a specified (and usually restricted) active space of orbitals as well as due to the number and/or kind of virtual excitations to be included. Such RAS computations are internally performed *stepwise* in JAC by utilizing the self-consistent field (orbitals) from some prior step. This type has not yet been properly implemented so far.
- Interactive computations: In an interactive computation, the functions/methods of the JAC program are applied interactively, either directly within the REPL or by just a short JULIA script, in order to compute energies, expansion coefficients, transition matrices, rates, cross sections, etc. An interactive computation typically first prepares and generates (instances of) of different data structures of JAC, such as orbitals, (configuration-state) bases, multiplets, and later applies these computed data to obtain the desired information. More generally, all methods from JAC and its submodules can be utilized also interactively, although some specialized methods are often available and may facilitate the computations. Like for other JULIA functions, the functions and methods provided by JAC can be seen as (high-level) language elements in order to perform atomic computations at various degrees of sophistication.
- Atomic cascade computations: A cascade computation typically refers to three or more charge states of an atom, and which are connected to each other by different atomic processes, such as photoionization, dielectronic recombination, Auger decay, radiative transitions, etc. Different (cascade) approaches have been predefined in order to deal with atomic cascades. The particular atomic processes that are to be taken into account for the inidividual steps of the cascade need to be specified explicitly; these cascade computations have been only partly implemented so far.
- Atomic responses: Atomic response computations will support simulations of how atoms *respond* to an incident (beam of) light pulses and particles, such as field-induced ionization processes, high-harmonic generation and others. For these responses, the detailed atomic structure has often not been considered in much detail in the past, though it will become relevant as more elaborate and accurate measurements are carried out. These response computations have not yet been implemented so far.
- Time evolution of statistical tensors in (intense) light pusles: A time evolution of statistical tensors always proceeds within a pre-specified set of sublevels $\{\,|\alpha \mathcal{J} M\rangle\,\}$, i.e. subspace of the many-electron Hilbert space; all further (decay) processes that lead the system *out of this*

subspace must be treated by loss rates. Although such a time evolution can deal with pulses of different shape, strength and duration, it is assumed that they are *weak enough* not to substantially disturb the level structure and level sequence of the atoms in their neutral or ionic stage, i.e. that every sublevel can still be characterized by its (total) energy and symmetry. This time-evolution has not yet been implemented in detail so far. No attempt is made in JAC to solve the time-dependent (many-electron) Schrödinger equation explicitly.

➢ Semi-empirical estimates of atomic properties, cross sections, asymptotic behaviour, etc.: A semi-empirical 'estimate' of atomic data refers to some simple model computation or to the evaluation of fit functions in order to provide such atomic data, that cannot be generated so easily by *ab-initio* computations. These semi-empirical estimates are typically built on — more or less — sophisticated models and external parameter optimizations, although only a very few of such estimates have been implemented so far.

1.2. Notations

Atomic shells & subshells:

➢ Atomic shell model: This model, in which electrons fill a (more or less) regular list of atomic shells or make transitions (quantum jumps) between different shells, is key and guidance for calculating the electronic structure of atoms, ions and molecules, and most of their properties.

➢ Electron configuration: Describes the occupation of shells within the atomic shell model, for instance, $1s^2\,2s^2\,2p^6\,3s^2$. In JAC, closed-shell configurations can often be abbreviated, for instance, by [Ne] $3s^2$.

➢ Shells and subshells: Shells and subshells are the building blocks for the atomic shell model. In the relativistic theory, each non-relativistic $n\ell$-shell (apart from the ns-shells) splits into two relativistic subshells due to $j = \ell \pm 1/2$. In JAC, the shell and subshell notations are therefore used in order to denote the electron configurations, configuration state functions (CSF) and the orbitals of equivalent electrons. In JAC, there are special data struct's available to easily deal and communicate the (sub-) shell specification of levels and wave functions.

➢ Relativistic angular-momentum quantum number: $\kappa = \pm(j + 1/2)$ for $\ell = j \pm 1/2$ carries information about both, the total angular momentum j and the parity $(-1)^\ell$ of the (single-electron) wavefunction.

Atomic level notations:

➢ Bound (many-electron) levels and states: $|\alpha\mathbb{J}\rangle \equiv |\alpha J^P\rangle$; $|\alpha\mathbb{J}M\rangle \equiv |\alpha J^P M\rangle$.

Here, the multi-index α refers to all additional quantum numbers that are needed for a unique specification of some many-electron level or state. — For instance, we shall often use below $|\alpha_i\mathbb{J}_i\rangle$ and $|\alpha_f\mathbb{J}_f\rangle$ in order to denote the initial and final-ionic bound states of some atomic amplitude and process.

➢ (Many-electron) resonances or scattering states with a single free electron: $|(\alpha\mathbb{J},\, \varepsilon\kappa)\, \mathbb{J}_t\rangle \equiv |(\alpha J^P,\, \varepsilon\kappa)\, J_t^{P_t}\rangle$

describes a many-electron scattering wave with a single free electron in the partial wave $|\epsilon\kappa\rangle$, and where $\mathbb{J}_t$ denotes the overall symmetry of the many-electron scattering state (level).

Atomic multipoles:

➢ The multipole components (fields) of the radiation field occur at many different places in atomic theory due to the electron-photon interaction, though often within slightly different contexts. We here use the standard notations for the E1 (electric-dipole), M1 (magnetic-dipole), E2 (electric-quadrupole), etc. components and refer to them briefly as *multipoles* $\mathbb{M}$ of the radiation field.

➢ These multipoles or multipole components of the radiation field frequently occurs also in terms of *multipole transition operators* $\mathbb{O}^{(\mathbb{M})}$ and *multipole moment operators* $\mathbb{Q}^{(\mathbb{M})}$ as well as in summations $\sum_{\mathbb{M}} \ldots$ over such operators and/or the associated transition amplitudes (matrix elements).

➢ A multipole $\mathbb{M}$ is internally characterized by its multipolarity L and its (boolean) character *electric* `(= true/false)`.

Frequent technical terms used in the manual:

➢ Amplitude: Transition amplitudes are the many-electron matrix elements upon which atomic structure and collision theory is usually built on.

➢ Basis: In Jac, a basis refers to a many-electron basis that is specified in terms of a CSF list and the radial orbitals of all (equivalent) electrons. Each CSF is specified uniquely by a proper set of quantum numbers; here, the (so-called) seniority scheme is applied for the unique classification of the CSF and the evaluation of all matrix elements.

- Channel: Sublines of a given line that need to be distinguished due to the symmetry properties of the multipoles or partial waves in the decomposition of the many-electron levels or matrix elements.
- Grid: In JAC, all radial orbital functions are always represented on a grid. Only their grid representation is applied in the evaluation of all (single- and many-electron) matrix elements. Predefined grids refer to a 'exponential grid', suitable for bound-state computations, as well as a log-lin grid, which increases exponentially in the inner part and linearly in the outer part. The latter grid is suitable for collision processes and for dealing with the electron continuum.
- Lines and transitions: A line referts to an atomic transition that is characterized in terms of a well-defined initial and final level; it frequenty occurs in the computation of different properties, such as cross sections or rates, angular distribution parameters. Typically, a line contains various channels (sublines), for instance, due to occurance of multipoles or partial waves in the decomposition of the many-electron matrix elements
- Multiplet: Atomic levels are naturally *grouped together* into (so-called) mutiplets; most often, this term just stands for all fine-structure levels of one or several given configurations. More generally, multiplets may refer to any group of levels, for instance, to groups levels with the same total angular momentum J and/or parity P, or fine-structure levels of closely related configurations, etc.
- Orbital: In atomic physics, an orbital typically refers to a one-electron function in an radial-spherical representation. Often, only the radial function(s) are meant. In the relativistic theory, of course, one needs to distinghuish between the large and small components of the orbital, following Dirac's theory.
- Pathway: In contrast to an (atomic) line, that is characterized by an initial- and a final-level (and the corresponding multiplets), a pathway describe a sequence of three or more levels, and which often correspond to different atomic processes. These levels are usually referred to as initial, (one or several) intermediate and final level. Pathways occur naturally in dielectronic recombination as well as in various excitation-ionization of excitation-autoioization processes.
- Settings: In JAC, the control of most, if not all, computations is made by `Settings` that are associated to particular amplitudes, properties and processes. These settings are used to specify all details about the requested computation and enable one, for instance, to select individual levels or lines as well as various physical and technical parameters, such as the multipoles, gauges, etc.

1.3. A quick overview about amplitudes, level properties and processes handled in JAC

In Jac (partly) implemented amplitudes:

➢ Selected many-electron (reduced) amplitudes that are accessible within the JAC program. Further details about the call of these amplitudes can be found below in this manual or interactively by `?<module>.amplitude`.

Amplitude	Call within JAC	Brief explanation
$\langle \alpha \mathbb{J} \Vert \mathbb{T}^{(1)} \Vert \beta \mathbb{J}' \rangle$, $\langle \alpha \mathbb{J} \Vert \mathbb{T}^{(2)} \Vert \beta \mathbb{J}' \rangle$	Hfs.amplitude	Amplitude for the hyperfine interaction with the magnetic-dipole and electric-quadrupole field of the nucleus.
$\langle \alpha \mathbb{J} \Vert \mathbb{N}^{(1)} \Vert \beta \mathbb{J}' \rangle$	LandeZeeman.amplitude	Amplitude for the interaction with an external magnetic field.
$\langle \alpha_f \mathbb{J}_f \Vert \mathbb{O}^{(\mathbb{M}, \text{emission})} \Vert \alpha_i \mathbb{J}_i \rangle$	Radiative.amplitude	Transition amplitude for the emission of a multipole ($\mathbb{M}$) photon.
$\langle \alpha_f \mathbb{J}_f \Vert \mathbb{O}^{(\mathbb{M}, \text{absorption})} \Vert \alpha_i \mathbb{J}_i \rangle$	Radiative.amplitude	Transition amplitude for the absorption of a multipole ($\mathbb{M}$) photon.
$\langle (\alpha_f \mathbb{J}_f, \varepsilon\, \kappa)\, \mathbb{J}_t \Vert \mathbb{O}^{(\mathbb{M}, \text{photoionization})} \Vert \alpha_i \mathbb{J}_i \rangle$	PhotoIonization.amplitude	Photoionization amplitude for the absorption of a multipole ($\mathbb{M}$) photon and the release of an electron into the partial wave $\vert \varepsilon\, \kappa \rangle$.
$\langle \alpha_f \mathbb{J}_f \Vert \mathbb{O}^{(\mathbb{M}, \text{recombination})} \Vert (\alpha_i \mathbb{J}_i, \varepsilon\kappa) \mathbb{J}_t \rangle$	PhotoRecombination.amplitude	Photorecombination amplitude for the emission of a multipole ($\mathbb{M}$) photon and the capture of an electron that comes *in* the partial wave $\vert \varepsilon\, \kappa \rangle$.
$\langle (\alpha_f \mathbb{J}_f,\, \varepsilon\, \kappa)\, \mathbb{J}_t \Vert \mathbb{V}^{(\text{Auger})} \Vert \alpha_i\, \mathbb{J}_i \rangle$	Auger.amplitude	Auger transition amplitude due to the electron-electron interaction and the release of an electron into the partial wave $\vert \varepsilon\, \kappa \rangle$.
$\langle \alpha_f \mathbb{J}_f \Vert \sum \exp i\, \mathbf{q} \cdot \mathbf{r}_i \Vert \alpha_i \mathbb{J}_i \rangle$	FormFactor.amplitude	Amplitude for a momentrum transfer $\mathbf{q}$ with an external particle of photon field.
$\langle \alpha_f \mathbb{J}_f \Vert \mathbb{H}^{(\text{weak}-\text{charge})} \Vert \alpha_i \mathbb{J}_i \rangle$	PNC.weakChargeAmplitude	Amplitude for the nuclear-spin independent Hamiltonian of the (P-odd, T-even) internaction.
$\langle \alpha_f \mathbb{J}_f \Vert \mathbb{H}^{(\text{Schiff}-\text{moment})} \Vert \alpha_i \mathbb{J}_i \rangle$	PNC.schiffMomentAmplitude	Amplitude for the nuclear Schiff moment of the (P-odd, T-odd) internaction.
$\langle \alpha_f \mathbb{J}_f \Vert \mathbb{H}^{(\text{scalar}-\text{pseudo}-\text{scalar})} \Vert \alpha_i \mathbb{J}_i \rangle$	PNC.scalarPseudoScalarAmplitude	Amplitude for the scalar-pseudo-scalar (P-odd, T-odd) internaction.

In Jac (partly) implemented atomic level properties:

➢ In JAC implemented or partly-implememted atomic properties. For these properties, different parameters (observables) can generally be obtained by performing an `Atomic.Computation(..., properties=[id1, id2, ...])`, if one or more of the given identifiers are specified. For each of these properties, moreover, the corresponding (default) `Settings` can be overwritten by the user in order to control the detailed computations.

Property	id	Brief explanation.
$\|\alpha\mathbb{J}\rangle \longrightarrow \|\alpha(J)\,\mathbb{F}\rangle$	HFS	Hyperfine splitting of an atomic level into hyperfine (sub-) levels with total angular momentum $F = \|I - J\|$, ..., $I + J - 1$, $I + J$; hyperfine A and B coefficients; hyperfine energies and interaction constants; representation of atomic hyperfine levels in a IJF -coupled basis.
$\|\alpha\mathbb{J}\rangle \longrightarrow \|\alpha\,\mathbb{J}M\rangle$	LandeJ	Zeeman splitting of an atomic level into Zeeman (sub-) levels; Lande $g_J \equiv g(\alpha\mathbb{J})$ and $g_F \equiv g(\alpha\mathbb{F})$ factors for the atomic and hyperfine levels.
$K^{(\mathrm{MS})}$, F	Isotope	Isotope shift of an atomic level for two isotopes with mass numbers A, A': $\Delta E^{AA'} = E(\alpha\mathbb{J};\, A) - E(\alpha\mathbb{J};\, A')$; mass-shift parameter $K^{(\mathrm{MS})}$ and field-shift parameter F.
α-variations	AlphaX	Differential sensitivity of an atomic level $\|\beta\mathbb{J}\rangle$ with regard to variation of the fine-structure constant; $\Delta E(\delta\alpha;\, \beta\mathbb{J})$, $\Delta q(\delta\alpha;\, \beta\mathbb{J})$, $K(\beta\mathbb{J})$.
$F(q;\, \alpha\,\mathbb{J})$	FormF	Standard and modified atomic form factor of an atomic level $\|\alpha\mathbb{J}\rangle$ with a spherical-symmetric charge distribution.
$\omega(\alpha\mathbb{J}) + a(\alpha\mathbb{J}) = 1$	Yields	Fluorescence & Auger decay yields of an atomic level, or averaged over an electron configuration.
$\alpha^{(\mathbb{M})}(\omega)$		Static and dynamic (ac, multipolar) polarizibilities.
$E(\alpha\mathbb{J};$ plasma model$)$	Plasma	Plasma shift of an atomic level as obtained for different but still rather simple plasma models.
$\|\alpha_i\mathbb{J}_i\rangle \longrightarrow \|\alpha_f\mathbb{J}_f\rangle + \hbar\omega$	EinsteinX [a]	Photon emission from an atom or ion; Einstein A and B coefficients and oscillator strength between levels $\|\alpha_i\mathbb{J}_i\rangle \rightarrow \|\alpha_f\mathbb{J}_f\rangle$ that belong to a single multiplet (representation).

[a] Although the Einstein coefficients are not the property of a single level, we here still support a quick computation of these coefficients by means of the `Einstein` module for pairs of levels that are represented within a single CSF basis.

In Jac (partly) implemented atomic processes:

➢ In JAC implemented or partly-implememted atomic processes. For *one* process at a time, different parameters (observables) can generally be obtained by performing an `Atomic.Computation(..., process=id)`, if the corresponding identifier is specified. For this selected property, moreover, the corresponding (default) `Settings` can be overwritten by the user in order to control the detailed computations.

Process	id	Brief explanation
$A^* \longrightarrow A^{(*)} + \hbar\omega$	RadiativeX	Photon emission from an atom or ion; transition probabilities; oscillator strengths; angular distributions.
$A + \hbar\omega \longrightarrow A^*$	PhotoExc	Photoexcitation of an atom or ion; alignment parameters; statistical tensors.
$A + \hbar\omega \longrightarrow A^{+*} + e_p^-$	PhotoIon	Photoionization of an atom or ion; cross sections; angular parameters; statistical tensors.
$A^{q+} + e^- \longrightarrow A^{(q-1)+} + \hbar\omega$	Rec	Photorecombination of an atom or ion; recombination cross sections; angular parameters.
$A^{q+*} \longrightarrow A^{(q+1)+(*)} + e_a^-$	AugerX	Auger emission (autoionization) of an atom or ion; rates; angular and polarization parameters.
$A^{q+} + e^- \rightarrow A^{(q-1)+*} \rightarrow A^{(q-1)+(*)} + \hbar\omega$	Dierec	Dielectronic recombination (DR) of an atom or ion; resonance strengths.
$A + \hbar\omega_i \longrightarrow A^* \longrightarrow A^{(*)} + \hbar\omega_f$	PhotoExcFluor	Photoexcitation of an atom or ion with subsequent fluorescence emission.
$A + \hbar\omega \longrightarrow A^* \longrightarrow A^{(*)} + e_a^-$	PhotoExcAuto	Photoexcitation & autoionization of an atom or ion.
$A + \hbar\omega_i \longrightarrow A^{(*)} + \hbar\omega_f$	Compton	Rayleigh or Compton scattering of photons at an atom or ion; angle-differential and total cross sections.
$A + n\,\hbar\omega \longrightarrow A^*$ or $A^* \longrightarrow A^* + n\,\hbar\omega$	MultiPhoton	Multi-photon (de-) excitation of an atom or ion, including two-photon decay, etc.
$A + Z_p \longrightarrow A^* + Z_p$	CoulExc	Coulomb excitation of an atom or ion by fast, heavy ions; energy-differential, partial and total Coulomb excitation cross sections.
$A + \hbar\omega \rightarrow A^* + e_p^- \rightarrow A^{(*)} + e_p^- + \hbar\omega'$	PhotoIonFluor	Photoionization of an atom or ion with subsequent fluoescence emission.
$A + \hbar\omega \rightarrow A^* + e_p^- \rightarrow A^{(*)} + e_p^- + e_a^-$	PhotoIonAuto	Photoionization of an atom or ion with subsequent autoionization.
$A^{q+} + e^- \rightarrow A^{(q-1)+*} \rightarrow A^{(q-1)+(*)} + \hbar\omega \rightarrow A^{(q-1)+} + \hbar\omega + \hbar\omega'$	DierecFluor	Dielectronic recombination of an atom or ion with subsequent fluorescence.

Process	id	Brief explanation
$e_s^- + A \longrightarrow A^* + e_s^{-'}$	Eimex	Electron-impact excitation of an atom or ion; collision strength.
$A + e_s^- \rightarrow A^* + e_s^{-'} \rightarrow A^{+(*)} + e_s^{-'} + e_a^-$	EimexAuto	Electron-impact excitation and subsequent autoionization of an atom or ion.
$A^{q+*} \longrightarrow A^{(q+1)+(*)} + (e_a^- + \hbar\omega)$	RadAuger	Radiative-Auger (autoionization) of an atom or ion.
$A + n\,\hbar\omega \longrightarrow A^{(*)} + e_p^-$	MultiIon	Multi-photon ionization of an atom or ion.
$A + n\,\hbar\omega \longrightarrow A^{(*)} + e_{p_1}^- + e_{p_1}^-$	MultiDoubleIon	Multi-photon double ionization of an atom or ion.
$A^{q+}[\text{nucleus}^*] \longrightarrow A^{(q+1)+*} + e_c^-$	Conversion	Internal conversion, i.e. electron emission due to nuclear de-excitation.

1.4. Short comparison of JAC with other existing codes

We here compile some (incomplete) information about other existing atomic structure codes for the computation of level energies, transition rates, cross sections, etc. We remind to some of their special features and briefly summarize how these codes differ from the implementation of the Jac toolbox.

CATS (Cowan: 'Theory of Atomic Spectra', 1980):

- Cats relies on a semi-relativistic self-consistent potential and by using either a nonlocal Hartree-Fock (HF) or local Hartree-Fock-Slater (HFS) approach in order to deal with the exchange interaction.
- Level energies & ASF: Since the late 1960s, Cowan's HFX code has set some standard for many experimentalists and has, together with his well-known textbook, helped many (atomic) physicist to understand and make use of atomic structure theory. While these earlier developments are highly appreciated (and are still utilized for various applications), Cats has several severe limitations in the layout and implementation of the code, which are hard to *overcome*. The same applies also for the computation of various atomic properties, such at transition probabilities, photo-excitation and ionization cross sections and Auger rates.
- Cowan's code has been found a mature tool for identifying new lines, especially if additional information is available from experimental observations to support empirical adjustments.

➢ Display of data & spectra: Several tools and facility-programs have been developed for Cats in order to display the computed data and to compare them with each other and with experiment. The success of some of these tools has or will motivate us for developing some graphical interfaces for the display of (radial) orbitals, line spectra, etc. also for thte Jac toolbox.

➢ Selected advantages of Jac: Jac provides methods to display, for instance, radial functions and line spectra; cf. `JAC.display()`.

MCDFME (Desclaux *et al.*, 1975; Indelicato 200 and later):

➢ McdfMe code: The Multi-configuration Dirac-Fock and General-Matrix-Element code by Desclaux and Indelicato includes one-electron one-loop corrections (self-energy and vacuum polarization) and two-loop one-electron corrections (two-loop self-energy, mixed self-energy as well as vacuum polarization diagrams, Källen-Sabry potential contributions).

➢ McdfMe code: This code also includes vacuum-polarization due to the electronic potential, retardation beyond the Breit interaction and the effect from the electron-electron interaction on the self-energy evaluated within the so-called Welton method. From the comparison with the model operator approach by Shabaev and co-workers, a relative difference of $\leq$ 0.01 % was found for $Z = 18$.

GRASP (Grant *et al.*, 1980; Jönsson *et al.*, 2013; Fischer *et al.*, 2018):

➢ Level energies & ASF: Grasp has originally been devoloped since the late 1960s in order to provide level energies and eigenvectors for quite general open-shell atoms. Much emphasize during the last two decades was placed upon the systematic improvement of these energies and representations. While we also provide such level energies and atomic state functions by the Jac toolbox, we *do not* intent to facilitate such extensive wave function expansions. Instead, approximate level energies and ASF are mainly considered as the *technical preposition* for describing further atomic properties and processes. With the restricted-active space (RAS) computations, however, we shall provide in Jac useful features for a (more or less) systematic improvement of such *ab-initio* computations.

➢ Transition probabilities & oscillator strength: Apart from the level energies, Grasp has been extensively applied in order to compute and tabulate transition probabilities for many atoms, ions and isoeletronic sequences throughout the periodic table of elements. With Jac, we provide analogue or even simpler tools for such computations. Moreover, (the many-electron amplitudes that arise from) the coupling of the radiation field provides the natural *building blocks* for a large number of other atomic processes, cf. section 8 on atomic processes below.

➢ Selected advantages of Jac:

- Jac supports larger flexibility in handling the output data and, in particular, does not know practically-relevant limitations with regard to the length of filenames (in contrast, for instance, to 24 letters in grasp2K).

- SCF fields can be generated in JAC at different levels of complexity, including several (local) mean-field potentials as well as, in the future, the average-level and extended average-level schemes.
- JAC enables one to handle a much larger number of atomic properties and processes as well as atomic cascades and several other types of computation.
- The use of the JULIA language clearly facilitates the coding and maintenance of the JAC code, when compared to previous Fortran codes.

RMATRX (Berrington *et al.*, 1995):

➢ The Belfast Rmatrix code is readily available and used by a small group of users, and with an updated version from 2020.

RATIP (Fritzsche, 2001, 2012):

➢ Relativistic CI (RELCI): While RATIP has always used the SCF computations and orbitals from the GRASP code, it also supports relativistic CI computations. For several years, it helped define a new standard for performing the angular intergration (angular coefficients; cf. Gaigalas *et al.*, 2002). These angular coefficients are also utilized in JAC by an interface to the Fortran modules of RATIP.

➢ Atomic properties and processes: RATIP was (one of) the first codes that made use of GRASP's systematically improved wave functions in order to compute a good number of atomic properties and processes, such as relaxed-orbital transition probabilities (REOS; Fritzsche and Froese Fischer 1999), Auger rates, photoionization cross sections and angular parameters, radiative and dielectronic recombination rates, electron-impact excitation cross sections, and several others. The experience with RATIP has been found central for the development of JAC and has find its continuation here.

HULLAC (Bar-Shalom *et al.*, 2001):

➢ HULLAC has been developed as an integrated code for calculating atomic structure and cross sections for collisional and radiative atomic processes, based on the relativistic configuration interaction method.

➢ HULLAC: The Hebrew University Lawrence Livermore Atomic Code (HULLAC, Bar-Shalom *et al.* 2001) is a computional platform for atomic structures and cross sections that help modelling emission spectra as well as atomic processes in plasma; this code is based on a parametric potential method and has been applied to many medium and heavy elements.

➢ HULLAC: This code applies fully relativistic orbitals to calculate atomic energy levels and radiative transition probabilities. These orbitals are obtained as solution of the Dirac equation with a local and parametrized central-field potential $U(r)$ to represent the nucleus and the

spherically averaged interaction with all other electrons in the atom. The central-field potential is optimized such that energy levels of the ground state and a few excited states agree with the NIST (or related) tables. Although such a semi-empirical optimization procedure requires less computational resources, it hampers a systematic improvement of the results.

LADW (Bar-Shalom *et al.*, 2001):

➢ LADW, the Los Alamos Distorted-Wave code, has been developed by Sampson and co-workers; it has been further utilized and partly incorporated into the LASER code.

ELSEPA (Salvat *et al.*, 2005):

➢ ELSEPA facilitates the computation of differential cross sections, total cross sections and transport cross sections for (single) elastic scattering of electrons and positrons by neutral atoms, positive ions as well as randomly oriented molecules. Moreover, this code help compute scattering amplitudes and spin polarization functions for projectiles with kinetic energies $E_{\rm kin} \lesssim 5$ MeV by means of a conventional relativistic Dirac partial-wave analysis.

➢ For high kinetic energies, however, the convergence of the partial-wave series becomes slow and is then replaced by some approximate factorization method. ELSEPA has been found useful to explore the sensitivity of DCS for different choices of the (static) interaction potential.

GEANT4 (Amako *et al.*, 2005):

➢ GEANT4 is an object-oriented toolkit for analyzing and simulating the passage of particeles through matter that provides a variety of semi-empirical models to describe the underlying electromagnetic and hadronic interactions. GEANT4 combines theorical models with experimental data or parameterizations of such data.

➢ GEANT4 is especially based on a number of separate packages to deal with the electromagnetic interactions of (either) electrons, muons, positrons, photons, hadrons and ions as well as for specific energy range of the processes considered.

➢ Implemented processes: The electromagnetic packages of this code include: multiple scattering, ionization, Bremsstrahlung, positron annihilation, photoelectric effect, Compton and Rayleigh scattering, pair production, synchrotron and transition radiation, Cherenkov effect, refraction, reflection, absorption, scintillation, fluorescence as well as Auger electron emission (Amako *et al.*, 2005). Less attention has been placed however on the electronic structure of atoms and ions.

BSR (Zatsarinny 2006):

- ➢ Bsr code: The B-spline R-matrix (BSR) method and the accompanying code was developed by Zatsarinny and coworkers; this code computes photoionization and electron-impact excitation amplitudes. From these many-electron amplitudes, the cross sections and other experimentally observable parameters can be obtained. Apart from these amplitudes, the Bsr code also support simple bound-state computations for the energies and oscillator strengths.
- ➢ The Bsr code solves the close-coupling equations in coordinate space and, thus, is complementary to the usual convergent close-coupling (CCC) computations for electron-ion collisions in momentum space. The Bsr code applies a finite-element (B-spline) rather than a finite-difference approach in order to compute the Hamiltonian matrix elements in the inner region.
- ➢ The Bsr code supports the use of non-orthogonal sets of one-electron orbitals in order to account for the term-dependence of the valence orbitals. This enables one to apply an economical and flexible construction of both, bound-state wave functions and scattering states and, hence, the treatment of electron-impact single-ionization as well as photon-driven double ionization processes. Still, setting up the Hamiltonian matrix can be (very) expensive for complex targets, and the large number of resonances may require to deal with many thousands of collision energies separately; this makes it difficult to include details from the asymptotic region.
- ➢ The (published) Bsr code is a serial non-relativistic version that can be applied also for (semi-relativistic) Breit-Pauli computations. A relativistic DBSR as well as MPI-parallelized versions exists and has been applied by a small group of people.

FAC (Gu 2008):

- ➢ Fac is a well-known relativistic atomic structure code based on the fit of free parameters in order to define the atomic potentials and is mainly based on the (standard) Dirac-Fock-Slater method.
- ➢ Level energies & wave functions: The simplified and more object-oriented treatment of wave functions in the Fac code, when compared with Grasp, has stimulated the development of the Jac program. While Jac will enable the user to perform also systematic improvements on the underlying computational models, the support of rather simple approximations is crucial and need to be supported, for example, for dealing with cascades and time-evolutions.

tRecX (Scrinzi 2010):

➢ tRecX code: This code provides a general framework for solving initial-value problems of the form

$$\frac{\partial}{\partial t}\,\Psi \;=\; \mathbb{D}[\Psi,\,t] \,+\, \Phi(t)$$

for any number of spatial dimensions and for different coordinate systems. While the main emphasis was placed on *linear* evolution operators $\mathbb{D}$, non-linear operators can be used as well.

AUTOSTRUCTURE (Badnell, 2011):

➢ Autostructure is a rather general atomic code for the description of free-bound electron and photon collision processes, based on the original Superstructure code bei Eissner and coworkers.

➢ Autostructure supports efficient computations of dielectronic recombination cross sections and rates, especially if large numbers of highly-excited states are involed in the radiative stabilization of an atom or ion.

➢ The code applies the Breit-Pauli distorted wave method for the electron-impact excitation of atomic ions in order to support problems that are impractical or even impossible for more sophisticated methods.

➢ Autostructure mainly computes (Maxwell-averaged) effective collision strengths at temperatures of broad ionic abundance, rather then the detailed collision strength at all the energies.

LASER (Fontes *et al.*, 2015):

➢ Laser, i.e. the Los Alamos suite of relativistic atomic physics code, comprises various codes for fundamental atomic structure calculations as well as for various processes, such as photoexcitation, electron-impact excitation and ionization, photoionization and autoionization, within a consistent framework. It may help develop atomic physics models in either configuration- average and fine-structure modes, and by including a proper self-consistency. This suite has been developed for more than 20 years.

➢ Applications of the code: The Laser code has been applied to the collisional-radiative modeling of of plasmas, for line identifications in plasma spectroscopy and for testing relativistic atomic and quantum electro-dynamics (QED) theories. The code has been applied also for feasibility studies of the collisional-radiative modeling of non-LTE (optically thin) gold plasmas for and to questions from inertial confinement fusion.

➢ Approximations: Laser mainly employs the semi-relativistic theory, similar and often by directly applying Cowan's atomic structure code (Cats). The bound-electron wavefunctions are obtained from the semi-relativistic approach in Cats, while the continuum-electron

wavefuctions are obtained as solutions of the Schrödinger equation from some specialized routines. Typically, the bound and continuum radial wave functions are single-component type wavefunctions associated with the Schrdinger equation, rather than the four-component spinors associated with the Dirac equation.

➢ Features: Cross sections and other properties can be calculated for five fundamental processes: photo-excitation, photo-ionization, electron-impact excitation and ionization and autoionization. The code supports the IPCRESS (Independent of Platform and Can be Read by Existing Software Subroutines) random-access binary file format that is used to store large amounts of data, and which can be ported to any platform.

QEDMOD (Shabaev *et al.*, 2015):

➢ Self energy, $\mathbb{h}^{(\mathrm{QED})}$: Computes a model QED operator $\mathbb{h}^{(\mathrm{QED})}$ that accounts for the Lamb shift in accurate atomic-structure calculations. However, there are various difficulties with QEDMOD which make a direct application of the code and its combination with GRASP or JAC rather cumbersome.

➢ Effective QED Hamiltonian: The QEDMOD code provides one-electron matrix elements that, in principle could be directly added to any CI matrix and, hence, to the computation of level energies and multiplets. For the vacuum polarization, it includes automatically both, the Uehling and Wichmann-Kroll terms.

➢ Selected advantages of JAC: A simlified version of the effective QED Hamiltonian from QEDMOD has been implemented also in JAC.

QUANTICS (Worth, 2019):

➢ QUANTICS toolbox: For small molecules, this code help solve the time-independent Schrödinger equation as well as the (time-dependent) Liouville-von Neumann equationy by propagating density matrices. The package comprises various auxiliary programs to set-up calculations and to analyse different outputs.

➢ QUANTICS is a community code of the UK Collaborative Computational Project for Quantum Dynamics (CCPQ) and of the European E-CAM project, an e-infrastructure for software development by the Centre European de Calcul Atomique et Molculaire (CECAM).

1.5. To-do's, next steps & desired features of the JAC program

Encouragement for external users and developers:

- While we (will further) develop JAC for those applications, which are requested frequently by the users, here I shall compile a number of desired features which will make JAC even more powerful and/or easy to use. For these *additional features*, I wish to encourage collaboration with external developers. We welcome in particular all help from outside if the overall style of the program is maintained, and if some prior consensus exist how to add and implement additional features.
- New code developments may concern incremental improvements or also multiple approaches for algorithms and modules in order to provide well-defined alternatives, for instance, if some particular approach does not work properly.
- Emphasis will be placed first usually on those applications that receive enough attention by the community.

1.5.a. To-do lists

Urgent to-do's:

- Visualize a (given) continuum orbital and its normalization as obtained at sufficiently large r-values.
- Use of JAC on remote clusters: Work out some prototype example how 'job scripts' (similar to those from examples) can be exportet and handled at remote cluster computers and how to re-import the results later on.
- Documenter.jl: How to establish a documentation of JAC.

Short-term to-do's:

- Implement ... `Jac.modify("level energies: interactive", multiplet::Multiplet)`
- Implement ... `Jac.display("level energies: HFS", multiplets::HFSMultiplet[..])`
- Implement ... `Jac.display("level energies", multiplets::Multiplet[..])`
- Implement ... `Jac.display("configuration list: from basis", basis::Basis)`

Medium-term to-do's:

- Implement ... `Jac.apply("restrictions: CSF list", csfs::CsfR[..], basis::Basis)` ... to apply a number of restrictions interactively to a list of CSF. The procedure proceeds in three steps: (i) by taking and applying a restriction to a given CSF list; (ii) showing the number of CSF to be deleted from the given list; (iii) making this restrictions explicit. The user is requested to enter one restriction after the other, and until the reduction process is terminated by the user. A csfList::CsfR[] is returned; ..... Here we might adopt the form of restrictions from the RATIP program.
- Implement ... `Jac.apply("biorthogonal transformation", mplta::Multiplet, mpltb::Multiplet, grid::Radial.Grid)`
- Atoms in plasma environments: Implement 2-3 plasma models in order to deal with atoms in a few (averaged but) different plasma environments. This usually works via some effective `Jac.InteractionStrength.XL_BreitXL_plasma_ionSphere(L::Int64, a::Orbital, b::Orbital, c::Orbital, d::Orbital, lambda::Float64)` that depends on some particular model and plasma parameters; cf. Saha and Fritzsche, PRE (2004). This will likely require also the set-up of a corresponding Hamiltonian matrix: `Jac.compute("matrix: plasma, ion-sphere model", settings::Plama.Settings, basis::Basis)`.
- Interpolation: We might need (from time to time) a proper interpolation of functions from one grid to another, for instance, for using GRASP-type orbitals that have been generated on a different grid. Implement some function `Jac.interpolate("function: for new radial grid, trapez rule", from::Tuple(rOld::Float64[..],gridOld::Jac.Radial.Grid), to::Tuple(rNew::Float64[..],gridNew::Jac.Radial.Grid) )`.

1.5.b. Discussion about (further) implementations

Issues that need to be discussed:

- Further documentation of the code: How can the internal *doc-strings* be readily combined with the JAC websites ??
- Parallelization and performance of the code: How can one make the code parallel without that the user need to know and provide much information about the cluster that is used for the computations.
- Modern input forms in scientific computing: Which modern formats do exist ?? Which simple graphical (applet) features exist ? tomel.jl ??

1.5.c. Desired medium- and long-term features of the JAC program

Plotting and visualization:

- Implement ... `Jac.plot("radial orbitals", orbitals::Orbital[..])`
- Implement ... `Jac.plot("spectrum: oscillator strength over energy, emission", lines::RadiativeLine[..]; widths=value::Float64)` and `Jac.plot("spectrum: oscillator strength over energy, absorption", lines::RadiativeLine[..]; widths=value::Float64)`
- Implement ... `Jac.plot("spectrum: transition rates over energy, Gaussian", lines::RadiativeLine[..]; widths=value::Float64)` and `Jac.plot("spectrum: transition rates over energy, Lorentzian", lines::RadiativeLine[..]; widths=value::Float64)`
- Visualize the convergence of energies or other results as function of the size of the computation and/or model space.
- Visualize the level structure of a given multiplet, for instance, by displaying the level energies in different colors for different (leading) configurations or groups of such configurations.
- Visualize the level structure of a given multiplet together with further level or transition properties, such as lifetimes, HFS parameters, isotope parameters, etc.

Excitation and decay cascades:

- ➢ Analyze (and report) the fine-structure level population following the decay of an inner-shell hole state.
- ➢ Compute and extract the Fano parameters and line-shapes for a given set of autoionizing resonances.
- ➢ For a given cascade (data), evaluate the ion yields, electron spectra, (fine-structure) level population, fluorescence spectra, etc.

More physics in Jac ?

- ➢ Atomic spectra: Evaluate and display the photoabsorption spectra from calculated photoexcitation and photoionization cross sections.
- ➢ Computation of approximate single-electron properties:
  - Subshell-dependent differential and total photoionization cross sections; cf. Eichler and Meyerhof (1995, Eqs. 9.34 and 9.47).
  - Non-relativistic total K-shell or subshell radiative recombination cross sections by using the Stobbe cross section; cf. Eichler & Meyerhof (1995, Eqs. 9.49, 9.50)
  - Dirac energy (subshell); Dirac r^k expectation values; Dirac-matrices; `Dirac.Omega(subshell,theta,phi)`.
  - Coulomb-Greens functions for some given hydrogenic orbital.
- ➢ Collisional-radiative models: Such collisonal-radiative models have been frequently applied to describe the evolution of plasma and to derive information for plasma diagnostics. JAC provides many, if not all, the rates and cross sections to built-up such models for selected (plasma) environments.
- ➢ Electron-momentum distributions: Provide the expectation values $\langle p^k \rangle$, $k = -2, ..., 4$ of the single-electron radial momentals, i.e. the radial orbitals in momentum space. These expectation values are frequently applied in crystallography and in studying Compton profiles; cf. Koga and Thakkar (1996), Eq. (10-11). In the first instance, these expectation values could be readily provided as semi-empirical values by following the work above.

1.6. Remarks on the implementation of JAC

Why Julia ?

➢ Here, we just recall a few remarks from the literature as well as some own experience why JULIA have been found helpful for developing the JAC program. Some of these arguments are directly taken from the work of Bezanson *et al.* (2017, 2018).

➢ JULIA is a language for scientific computing that offers many of the features of productivity languages, namely rapid development cycles; exploratory programming without having to worry about types or memory management; reflective and meta-programming; and language extensibility via multiple dispatch (Bezanson *et al.*, 2018).

➢ Productivity *vs.* performance: JULIA is often said to stand for the combination of productivity and performance through a careful language design and carefully chosen technologies; it never forces the user to resort to C or Fortran for fast computations. — JULIA's design allows for gradual learning of modern concepts in scientific computing; from a manner familiar to many users and towards well-structured and high-performance code.

➢ JULIA's productivity features include: dynamic typing, automatic memory management, rich type annotations, and multiple dispatch. JULIA also supports some control of the memory layout and just-in-time compilation in order to eliminate much of the overhead of these features above (Bezanson *et al.*, 2018).

➢ Julia promises scientific programmers the ease of a productivity language at the speed of a performance language (Bezanson *et al.*, 2018).

➢ High-level languages: Most traditional high-level languages are hampered by the overhead from the interpretor, and which typically results into more run-time processing of what is strictly necessary. One of these hindrances is (missing) type information, and which then results in the request for supporting vectorization. JULIA is a 'verb'-based language in contrast to most object-oriented 'noun'-based language, in which the generic functions play a more important role than the datatypes.

➢ Language design: Julia includes a number of (modern) features that are common to many productivity languages, namely dynamic types, optional type annotations, reflection, dynamic code loading, and garbage collection (Bezanson *et al.*, 2018).

➢ Multiple dispatch: This concept refers to the dynamically selected implementation and to running the right code at the right time. This is achieved by overloading by means of multiple-argument function, a very powerful abstraction. Multiple dispatch makes it easier to structure the programs close to the underlying science.

➢ Multiple dispatch is perhaps the most prominent feature of JULIA's design and is crucial for the performance of the language and its ability to inline code efficiently. Another promise of multiple dispatch is that it can be used to extend existing behavior with new features.

- Multiple dispatch: At run-time, a function call is dispatched to the most specific method applicable to the types of its arguments. JULIAs type annotations can also be attached to datatype declarations so that they can be checked whenever typed fields are assigned to. Multiple dispatch also help the programmers to extend the core languages functionalities to their particular needs.
- Multiple dispatch also reduces the needs for argument checking at the begin of a function. The overloading of functions by multiple dispatch is also called ad-hoc polymophism. Instead of encapsulating methods inside classes, JULIA's multiple dispatch is a paradigm in wich methods are defined on combinations of data types (classes). JULIA shows that this is remarkably well-suited for numerical computing.
- JULIA's type system: JULIA's expressive type system allows optional type annotations; this type system supports an agressive code specializiation against run-time types. To a large extent, however, JULIA code can be used without any mentioning of types (in contrast to C and Fortran); this is achieved by data-flow interference. — User's own types are also first class in JULIA, that is there is no meaningful distinction between built-in and user-defined types. There are mutable and (default: immutable) composite types.
- Optimization in JULIA: The JULIA compiler is built on three strategies that are performed on a high-level intermediate representation, while all native code generation is later delegated to the LLVM compiler infrastructure. These optimization strategies are: (1) method inlining which devirtualizes multi-dispatched calls and inline the call target; (2) object unboxing to avoid heap allocation; and (3) method specialization where code is special cased to its actual argument types (Bezanson *et al.*, 2018).
- Performance: There are helpful macros, such as `@timing function_call(parameters)` or `@benchmark function_call(parameters)` to analyze the performance of the program and to find (and resolve) bottlenecks.
- Data types: JULIA distinguishes between concrete data types, that can be instantiated, and abstract types, that can (only) be extended by subtypes to built up an hierarchy of such types.
- In JULIA, users are always encouraged to make their programs, whenever possible, type stable. Much of the efficiency of a JULIA code relies on being type stable and on devirtualization and inlining.
- LAPACK: All of LAPACK is available in JULIA, not just the most common functions. LAPACK wrappers are fully implemented by `ccall` and can be called directly from the Julia promt.

Requests in building large software packages:

- These and further requests have been summarized by Post and Kendall (2004).
- Physical models: In general, better physics is more important than better computer science. It is recommended to use modern but well-proven computer-science techniques, and a 'physics code' should not be a computer-science research project. Instead, one should use best

engineering practices to improve quality rather than processes. Emphasis should be given to improvements of the physics capabilities. Do not use the latest computer-science features; let the new ideas mature first. Better physics is the most important product of the code.

- Code development and evolution: The scale of code-development can become truly immense; a good overview/quantitative database about (previously) successful software projects in some given field is typically required for good estimation for resources and schedules. It is easy to loose motivation on a project that last years and which has few incremental deliveries. Continues replacement of code modules is recommended as better tools and techniques are developed. Every code development typically proceeds in steps: First develop a core capability (with a small team) and let this small core be tested by users and, if successful, add further capabilities (so-called incremental delivery).
- Success criteria: One of the important success criteria is the costumer focus. — What do the user really need ?
- Code specification: Some flexibility in the requirement specification phase is essential because it is difficult to predict when (or if) a new algorithm/approach will be available. There is a need to pursue multiple approaches for algorithms and modules near to the critical path. If one approach is not feasible, another one can be used.
- External users and developers: The validation of physics models is a critical issue for all extended software packages and need to be done with regard to authoritative reference data.
- Documentation should be intended to cover all needs of the beginner through to the expert user who wishes to expand the capabilities of JAC.

2. Dirac's hydrogenic atom

2.1. Energies and wave functions

Notations & application in Jac:

- In Jac, non-relativistic hydrogenic orbitals can be easily generated by a call to `JAC.HydrogenicIon.radialOrbital()`.
- Jac also provides approximate radial (relativistic bound-state) orbitals by just applying the kinetic-balance condition to the corresponding non-relativistic radial orbital and by re-normalizing it afterwards.

Dirac's (one-electron) energies:

- Relativistic bound-state energy spectrum: For electrons with principal quantum number n and angular-momentum quantum number κ, the relativistic bound-state energy spectrum is given by

$$\varepsilon_{n\kappa} \;=\; mc^2\, W_{n\kappa} \;=\; \frac{mc^2}{\left[1 + \left(\frac{\alpha Z}{n' + s}\right)\right]}$$

  where α is the fine-structure constant, $n' = n - |\kappa| = 0,\, 1,\, 2,\, ...$ is the number of nodes, and $s = \sqrt{\kappa^2 - (\alpha Z)^2}$, respectively.

- Since $W_{n\kappa} < 1$, it can be expanded in terms of (αZ) and written as

$$W_{n\kappa} \;=\; 1 - \frac{1}{2}\frac{(\alpha Z)^2}{n^2} - \frac{1}{2}\frac{(\alpha Z)^4}{n^3}\left(\frac{1}{j + 1/2} - \frac{3}{4\,n}\right) - \;...$$

  where the second term, multiplied with mc^2, represents the nonrelativistic binding energy of a hydrogenic atom.

➢ For a given (principal) shell n, the eigenvalues are the same for equal values of j but are different for equal values of ℓ. For a given value of ℓ, the spin-orbit splitting between states with $j = \ell + 1/2$ and $j = \ell - 1/2$ gives rise to the fine-structure in the spectrum of hydrogen-like atoms. The equation above shows that the relativistic corrections to the one-electron energies decreases rapidly with n. The relativistic correction to the non-relativistic energy is therefore important, especially for highly-charged ions with rather large Z.

Non-relativistic radial orbitals:

➢ Radial orbital functions $P(r)$: These functions in the non-relativistic orbital $\psi(r,\vartheta,\varphi) = \frac{P(r)}{r} Y_{\ell m}(\vartheta,\varphi)$ is known to obey the *radial* Schrödinger equation and belongs to either the discrete part of the spectrum with the (negative) energies $E_n = -\frac{Z^2}{2n^2}$ a.u. < 0 (bound states), or to the contineous part for all energies $E > 0$ (the so-called *free-electron* or *continuum* states).

➢ Radial orbital functions $P(r)$: An analytic solution of the radial functions $P(r)$ in terms of the confluent hypergeometric function $F(\alpha,\beta;x)$ are known for both, the bound-states

$$P_{n\ell}(r) = r^{l+1} \frac{1}{(2\ell+1)!} \sqrt{\frac{(n+\ell)!}{(n-\ell-1)!\,2n}} \left(\frac{2Z}{n}\right)^{3/2+\ell} e^{\left(-\frac{Zr}{n}\right)} F\left(-(n-\ell-1),\, 2\ell+2;\, \frac{2Zr}{n}\right)$$

as well as for the *continuum* ($E > 0$) with $k = \sqrt{2E}$ and $n' = Z/k$

$$P_{E\ell}(r) = \frac{2\sqrt{Z}}{\sqrt{1-e^{-2\pi n'}}} \left[\prod_{s=1}^{\ell} \sqrt{s^2+n'^2}\right] \frac{(2kr)^l}{(2\ell+1)!} e^{-ikr} F(in'+\ell+1,\, 2\ell+2,\, 2ikr).$$

Relativistic radial orbitals:

➢ Radial orbital functions $P(r)$, $Q(r)$: Analogue to the non-relativistic case, the solution $\psi(\mathbf{r})$ of the Dirac equation can be separated for a spherical potential into a radial and angular part

$$\psi_{\kappa m}(r,\vartheta,\varphi) = \frac{1}{r} \begin{pmatrix} P(r)\,\Omega_{\kappa m}(\vartheta,\varphi) \\ i\,Q(r)\,\Omega_{-\kappa m}(\vartheta,\varphi) \end{pmatrix},$$

where $\Omega_{\kappa m}(\vartheta,\varphi)$ denotes a standard Dirac spin-orbital function, and where $\kappa = \pm(j+1/2)$ for $\ell = j \pm 1/2$ is called the *relativistic* angular-momentum quantum number.

➢ Relativistic angular-momentum quantum number: Owing to the definition of $\kappa = \pm 1, \pm 2, \ldots$, this relativistic quantum number carries information about both, the total angular momentum j and the parity $(-1)^\ell$ of the orbital function.

➢ Large & small component: The radial part of a relativistic wavefunctions is given by the two functions $P(r)$ and $Q(r)$, and which are often called the *large* and *small* components.

➢ Dirac spin-orbital: As usual, the Dirac spin-orbitals can be written in terms of the spin-1/2 Pauli spinors $\chi_\pm$ and the spherical harmonics by

$$\Omega_{\kappa m}(\vartheta,\varphi) \;=\; \sum_{m_\ell} \langle \ell\, m_l,\; 1/2, m - m_\ell \,|\, jm\rangle \; Y_{\ell m_\ell}(\vartheta,\varphi)\; \chi_{m-m_\ell}\,.$$

$$Q(r) \;=\; \frac{1}{2m\,c}\left(\frac{d}{dr} \;+\; \frac{\kappa}{r}\right) P(r)\,.$$

2.2. Coulomb-Green function

Relativistic radial Coulomb-Greens function:

➢ Radial Green function of the Dirac equation: Following Yerokhin and Shabaev (1999, appendix D), the radial Green function of the Dirac equation for electrons with the angular-momentum symmetry κ can be written in the form:

$$G_\kappa(\omega, r_1, r_2) \;=\; -\,\frac{1}{W_\kappa(\omega)}\,\Big[\boldsymbol{\phi}^\infty_\kappa(\omega, r_1)\;\boldsymbol{\phi}^{0^T}_\kappa(\omega, r_2)\,\Theta(r_1 \,-\, r_2) \;+\; \boldsymbol{\phi}^0_\kappa(\omega, r_1)\;\boldsymbol{\phi}^{\infty^T}_\kappa(\omega, r_2)\,\Theta(r_2 \,-\, r_1)\Big]$$

where $\boldsymbol{\phi}^0_\kappa(\omega, r)$ and $\boldsymbol{\phi}^\infty_\kappa(\omega, r)$ are solutions of the radial Dirac equation, bounded at the origin and at the infinity, and where $W_\kappa(\omega)$ is the Wronskian.

➢ The functions $\boldsymbol{\phi}^0_\kappa(\omega, r)$ and $\boldsymbol{\phi}^\infty_\kappa(\omega, r)$ can be calculated in terms of the Whittaker functions of the first and second kind, although special care has to be taken.

2.3. Matrix elements with Dirac orbitals

2.3.a. Matrix elements with radial orbitals

Matrix elements with non-relativistic radial orbitals:

➢ Special non-relativistic r^k expectation values: The following expectation values are displayed by Marxer (1991)

$$\langle r^{-1} \rangle = \frac{Z}{a_o\, n^2}$$

$$\langle r^{-6} \rangle = \left[\frac{Z}{a_o}\right]^6 \frac{35n^4 - n^2\,[30\ell\,(\ell+1) - 25] + 3(\ell-1)\,\ell\,(\ell+1)\,(\ell+2)}{8n^7\,(\ell-3/2)\,(\ell-1)\,(\ell-1/2)\,\ell\,(\ell+1/2)\,(\ell+1)\,(\ell+3/2)\,(\ell+2)\,(\ell+5/2)}$$

$$\langle r^{-k-2} \rangle = \left[\frac{Z}{a_o}\right]^{k+2} \frac{1}{n^{k+3}\,\ell^{k+1}}\,\mathcal{P}_{k,\ell}\left(\frac{n}{\ell}\right), \qquad \mathcal{P}_{k,\ell}(x) = \frac{(2\ell)^{k+1}\,(2\ell-k)!)}{(2\ell+1)!}\,{}_3F_2(-k, k+1, \ell+1-\ell\,x;\ 1, 2\ell+2;\ 1)$$

➢ Pasternack-Kramers rekursion relation: For $k \le 0$, the r^{-k} expectation values of any $(n\ell)$ level fullfill the relation (Marxer 1991)

$$\langle r^{-k-2} \rangle = \frac{4}{(2\ell+1)^2 - k^2}\left[\left(\frac{2k-1}{k}\right)\frac{Z}{a_o}\langle r^{-k-1}\rangle - \left(\frac{k-1}{k}\right)\frac{Z^2}{n^2\,a_o^2}\langle r^{-k}\rangle\right]$$

$$\langle r^{k} \rangle = \frac{(2\ell+k+2)!}{(2\ell-k-1)!}\left[\frac{n\,a_o}{2Z}\right]^{2k+3}\langle r^{-k-3}\rangle$$

From this relation, explicit formulas for low principal quantum number n can be computed rather easily.

Matrix elements with relativistic Dirac wavefunctions:

➢ An analytical expression of the matrix elements with operators $r^k\,e^{-sr}$ can be found (also) for Dirac's relativistic wavefunctions. In order to derive such expressions, it is typically more convenient first to re-write the standard representation of the hydrogenic functions in terms of a series expansion in r as it was suggested originally by Rose (1961).

➢ An expression for the corresponding matrix element is given by:

$$\begin{aligned}
\left\langle n\,\kappa \left| r^k\, e^{-\,\sigma\, r} \right| n'\,\kappa' \right\rangle &= \int_0^\infty dr\; e^{-\,\sigma r}\; \left(P_{n\kappa}(r)\, P_{n'\kappa'}(r) + Q_{n\kappa}(r)\, Q_{n'\kappa'}(r)\right) \\
&= N_{n\kappa}\, N_{n'\kappa'} \sum_{\nu=0}^{n-|\kappa|} \sum_{\nu'=0}^{n'-|\kappa'|} \left(c^{+}_{n\kappa,\nu}\, c^{+}_{n'\kappa',\nu'} \;+\; c^{-}_{n\kappa,\nu}\, c^{-}_{n'\kappa',\nu'}\right) \frac{q^{s+\nu-1}\, q'^{\,s'+\nu'-1}}{(q+q'+\sigma)^{1+\nu+\nu'+s+s'+k}}\, \Gamma(\nu+\nu'+k+s+s'+1)\,, \\
c^{\pm}_{n\kappa,\nu} &= \left(1 \pm \sqrt{1-q^2}\right)^{1/2} \frac{((-n+|\kappa|)_\nu\; 2^\nu)}{\nu!\;(2s+1)_\nu}\; \left[(\nu - n + |\kappa|) \pm (\alpha Z/q - \kappa)\right]
\end{aligned}$$

with $(a)_\nu$ being the Pochhammer symbol and where the parameters $q,\ s$ and the normalization factor $N_{n\kappa}$ were defined above.

2.3.b. Matrix elements including the angular part of Dirac orbitals

Matrix elements of spherical tensors:

➢ Matrix elements of the $\mathbb{C}^K$ tensors: Gaidamauskas *et al.* (2011) use the following definition:

$$\left\langle \kappa_a \left\| \mathbb{C}^{(K)} \right\| \kappa_b \right\rangle = (-1)^{j_a\,+\,1/2}\; [j_a,\, j_b]^{1/2} \begin{pmatrix} j_a & K & j_b \\ 1/2 & 0 & -1/2 \end{pmatrix} \delta_{\ell_a+\ell_b+1,\,\mathrm{even}}$$

2.4. Frequently applied expansions and identities in atomic theory

2.4.a. Partial-wave expansions of free electrons

Partial-wave expansion:

➢ Partial-wave components of a plane-wave electron: The computation of partial (and total) ionization cross sections often requires an integration over all possible angles $\Omega_p = (\vartheta_p, \varphi_p)$ of the photoelectrons, emitted in 4π. In practice, this integration over Ω_p can be carried out rather easily by making use of the *decomposition* of the free-electron wavefunction $|\mathbf{p}\, m_s\rangle$ into *partial-wave* components.

➢ In practice, however, this expansion generally depends on the choice of the quantization axis.

➢ If the quantization axis is taken along $\mathbf{e}_z$, this expansion is given by

$$|\mathbf{p}\, m_s\rangle \;=\; \sum_{\kappa\, m} i^{\ell}\, e^{-i\,\Delta_\kappa}\, \langle l m_\ell,\, 1/2\, m_s \,|\, jm\rangle\; Y^*_{\ell m_\ell}(\vartheta_p, \varphi_p)\; |\varepsilon\kappa m\rangle \;,$$

and where the summation runs over all partial waves, $\kappa = \pm 1, \pm 2, \ldots$ as well as $m = -j, \ldots, j$. In this expansion, moreover, Δ_κ is the Coulomb phase shift, and the (nonrelativistic orbital angular momentum) quantum number ℓ just distinguishes the parity of the partial waves.

2.4.b. Expansions including spherical harmonis

Expansions including the spherical harmonics:

➢ Expansion of a plane-wave in terms of spherical Bessel functions:

$$e^{i\,\mathbf{k}\cdot\mathbf{r}} \;=\; 4\pi \sum_{\ell m} i^{\ell}\, j_\ell(kr)\, Y^*_{\ell m}(\hat{k})\, Y^*_{\ell m}(\hat{r}) \;.$$

➢ Multipole expansion of the (transverse-gauge) plane-wave vector potential:

$$\mathbf{A}^{\,(\mathrm{transverse})}(\mathbf{r}, \omega) \;=\; 4\pi \sum_{LM\, p=0,1} i^{L-p} \left(\mathbf{Y}^{(p)}_{LM}(\hat{k}) \cdot \boldsymbol{\epsilon} \right)\; \mathbf{a}^{(p)}_{LM}(\mathbf{r}),$$

where the vector functions $\mathbf{a}^{(p)}_{LM}(\mathbf{r})$ are referred to as multipole potentials, and where only terms with $p = 0$ (magnetic) and $p = 1$ (electric) contribute, since $\mathbf{Y}^{(-1)}_{LM}(\hat{k})$ is orthogonal to $\boldsymbol{\epsilon}$.

2.4.c. Useful idendities

Useful idendities:

➢ Derivative of the spherical Bessel functions:

$$j_{n-1}(z) \;=\; \frac{n+1}{z}\, j_n(z) \;+\; j_n'(z), \qquad\qquad j_{n+1}(z) \;=\; \frac{n}{z}\, j_n(z) \;-\; j_n'(z)$$

2.5. Frequently occuring radial integrals

Notation & applications in Jac:

➢ In Jac, all these radial integrals can be directly computed by a call to some function from the `RadialIntegrals` module.

Functions $Y^k(r;\,ab)$ and $Z^k(r;\,ab)$:

➢ Nonrelativistic functions $Y^k(r;\,ab)$ and $Z^k(r;\,ab)$: These two function naturally arises from the derivative of the (two-electron) Slater integrals and appear very frequently in all atomic structure calculations. For radial orbitals with quantum numbers $a = (n_a, \kappa_a)$, $b = ...$, these functions are given by

$$Y^k(r;\,ab) \;=\; r\int_0^\infty ds\,\frac{r_<^k}{r_>^{k+1}}\,P_a(s)\,P_b(s) \;=\; \int_0^r ds\,\left(\frac{s}{r}\right)^k\,P_a(s)\,P_b(s) \;+\; \int_r^\infty ds\,\left(\frac{r}{s}\right)^{k+1}\,P_a(s)\,P_b(s)$$

$$Z^k(r;\,ab) \;=\; \int_0^r ds\,\left(\frac{s}{r}\right)^k\,P_a(s)\,P_b(s).$$

Indeed, the fast and accurate calculation of $Y^k(r;\,ab)$ depends on $Z^k(r;\,ab)$, i.e. the first part in the definition above.

➢ Solutions of the $Y^k(r;\,ab)$ and $Z^k(r;\,ab)$ functions: It was orginally suggested by Hartree that the $Y^k(r;\,ab)$ and $Z^k(r;\,ab)$ integrals can be determined by simultaneously solving a pair of differential equations with boundary conditions

$$\frac{d}{dr}\,Z^k(r;\,ab) \;=\; P_a(r)\,P_b(r) \;-\; \frac{k}{r}\,Z^k(r;\,ab), \qquad\qquad Z^k(0;\,ab) \;=\; 0$$

$$\frac{d}{dr}\,Y^k(r;\,ab) \;=\; \frac{1}{r}\,\left[\,(k+1)\,Y^k(r;\,ab) \;-\; (2k+1)\,Z^k(r;\,ab)\,\right], \qquad\qquad Y^k(r\to\infty;\,ab) \;=\; Z^k(r\to\infty;\,ab)$$

Grant's radial integrals for the coupling of the radiation field:

➢ Grant (1988) defines the following radial integrals that frequently occur in the coupling of the radiation field

$$I^o_L(q;\, ab) \;=\; \int_0^\infty dr\; j_L(qr)\;\left[P_a\, Q_b\right] \;=\; \int_0^\infty dr\; j_L(qr)\;\left[P_a(r)\, Q_b(r)\right]$$

$$I^\pm_L(q;\, ab) \;=\; \int_0^\infty dr\; j_L(qr)\;\left[P_a\, Q_b \;\pm\; Q_a\, P_b\right]$$

$$J_L(q;\, ab) \;=\; \int_0^\infty dr\; j_L(qr)\;\left[P_a\, P_b \;+\; Q_a\, Q_b\right]$$

➢ These integrals are useful also if the spherical Bessel function occurs in the integrant as $j_L(qr)/qr$, and where the following recursion relations can be used:

$$\frac{j_L(x)}{x} \;=\; \frac{1}{2L+1}\;\left[\, j_{L-1}(x) \;+\; j_{L+1}(x)\,\right].$$

Further radial integrals for different one-electron spherical tensor operators:

➢ In the treatment of the electron nucleus (hyperfine) interaction and the interaction with an external magnetic field, some radial integrals occur frequently:

$$I_L^{[r]}(ab) \equiv [r^L]_{ab} = \int_0^\infty dr\, r^L\, [P_a\, Q_b + Q_a\, P_b]$$

$$J_L^{<r>}(ab) = \langle r^L \rangle_{ab} \equiv \int_0^\infty dr\, r^L\, [P_a\, P_b + Q_a\, Q_b]$$

➢ Vinti-Integral: In the treatment of the (relativistic) mass shift, the (so-called) Vinti-Integrals occur

$$R^{(\text{Vinti})}(a,b) = \int_0^\infty dr\, P_a \left[\frac{d}{dr} - \frac{\kappa_a(\kappa_a+1) - \kappa_b(\kappa_b+1)}{2r}\right] P_b + \int_0^\infty dr\, Q_a \left[\frac{d}{dr} - \frac{-\kappa_a(-\kappa_a+1) + \kappa_b(-\kappa_b+1)}{2r}\right] Q_b\,.$$

2.6. B-splines

Properties of B-splines:

➢ A B-spline (basis spline) is a spline function with a minimal support and which can be used to express all spline function of any given as a finite linear combination.

➢ In physics, B-splines are often utilized for curve-fitting and in order to fit derivatives to experimental data.

➢ Knot sequence: A sequence of (radial) grid points $\{t_1, t_2, ..., t_m\}$ with $t_1 \le t_2 \le ... \le t_m$.

➢ Set of B-splines: Set of piecewise polynomial functions of order k, the so-called B-splines:

$$\left\{B_1^{(k)}(x),\, B_2^{(k)}(x),\, ...,\, B_n^{(k)}(x)\right\}, \qquad B_i^{(1)}(x) = \begin{cases} 1 & \text{for } t_i \le x \le t_{i+1} \\ 0 & \text{otherwise,} \end{cases} \qquad i = 1, 2, ..., m-1\,.$$

➢ Recursion relation for the generation of B-splines:

$$B_i^{(k)}(x) \;=\; \frac{x \,-\, t_i}{t_{i+k-1} \,-\, t_i}\, B_i^{(k-1)}(x) \;+\; \frac{t_{i+k} \,-\, x}{t_{i+k} \,-\, t_{i+1}}\, B_{i+1}^{(k-1)}(x) \qquad\qquad i \;=\; 1, 2, \ldots, m-k$$

The number of B-splines $n = m - k\ (k < m)$ is determined by the order k and the number of knots m. For B-splines of a given order, it is therefore sufficient to use the notation $B_i^{(k)}(x)$

➢ Each B-spline is non-negative and is non-zero only for: $B_i(x) > 0$ for $t_i < x < t_{i+k}$ and $B_i(x) = 0$ for $x < t_i,\ x > t_{i+k}$. — Essentially, the B-spline $B_i(x)$ starts at t_i and ends at t_{i+k} with only positive values in between.

Application of B-splines:

➢ Application of B splines for constructing single- and many-electron basis sets are nowadays widely employed in computational atomic and molecular physics.

➢ B-splines: For a B-spline representation of single-electron orbitals, only the low-lying orbitals will usually contribute significantly to the many-electron wave function. More generally, the configuration mixing between two configuration states is inversely proportional to the energy interval between them. It is therefore said sometimes that a B-spline representation of the single-electron orbitals provide an effective and natural way in order to adopt the basis to the problem of interest.

➢ B-splines in relativistic theory: In contrast to the nonrelativistic theory, the use of B-splines in relativistic computations is often accompanied by the occurrence of spurious states (Shabaev *et al.*, 2004). In a Coulomb potential, spurious states appear especially for $\kappa > 0$ as the lowest bound states but with rather nonphysical energies.

2.7. Generation of continuum orbitals

Simple approximations in Jac:

➢ For a first estimate of continuum processes, we have implemented a number of (rather) simple approximations/methods for the continuum orbitals that occur frequently at various places in the program. In Jac, the particular method can be selected by (re-) defining the global variable `JAC_CONT_SOLUTION` by a proper call to `Jac.define("method: continuum; ...)`.

➢ Approximations implemented in Jac:

(a) spherical Bessel functions;

(b) non-relativistic Coulomb waves for the large component of the continuum orbital, together with the kinetic-balance condition to obtain a small component;

(c) asymptotically correct, relativistic Coulomb orbital;

(d) Galerkin method to solve for continuum orbitals within a B-spline basis and for a given atomic potential.

➢ In Jac, spherical Bessel orbitals are generated if the global constant `JAC_CONT_SOLUTION = ContBessel`; cf. `JAC.define()` and section 2.7.a.

➢ In Jac, a free nonrelativstic Coulomb orbitals are generated if the global constant is `JAC_CONT_SOLUTION = NonrelativisticCoulomb`; cf. `JAC.define()` and section 2.7.b. Not available at present.

➢ In Jac, asymptotically-correct relativistic Coulomb orbitals are generated for a potential with a Coulombic tail, if the global constant `JAC_CONT_SOLUTION = AsymptoticCoulomb`; cf. `JAC.define()` and section 2.7.c.

➢ In Jac, a B-spline representation of the relativistic orbital $\varepsilon\kappa$ in a given local potential are generated if the global constant `JAC_CONT_SOLUTION = BsplineGalerkin`; cf. `JAC.define()` and section 2.7.d.

➢ In Jac, different normalization methods can be selected for all continuum orbitals; a pure-sine normalization for `JAC_CONT_NORMALIZATION = PureSine`, an asymptotic Coulomb normalization for `JAC_CONT_NORMALIZATION = CoulombSine`, or a WKB-type normalization for multiply and highly-charged ions for `JAC_CONT_NORMALIZATION = OngRussek`; cf. `JAC.define()`.

➢ At present, no attempt has yet been made to incorporate the exchange interaction of the continuum and bound-state orbitals.

2.7.a. Spherical Bessel orbitals

Implementation and numerical details:

➢ Generating equation and solutions: The spherical Bessel functions $j_\ell(|\mathbf{k}|\,r)$ obey the (non-relativistic) *free* radial Schrödinger equation for positive energies $\varepsilon > 0$, and the corresponding wave number $k = \sqrt{2\,\varepsilon}$, $\rho = kr$ and for well-defined orbital angular momentum ℓ

$$R_{\varepsilon\ell}(r) \;=\; \frac{P_{\varepsilon\ell}}{r} \;=\; N\, j_\ell(|\mathbf{k}|\,r) \;=\; N\, j_\ell(\sqrt{2\,\varepsilon}\,r) \qquad\Longleftrightarrow\qquad j_\ell''(\rho) \,+\, 2\,\frac{j_\ell'(\rho)}{\rho} \,+\, \left(1 \,-\, \frac{\ell(\ell+1)}{\rho^2}\right) j_\ell(\rho) \;=\; 0\,.$$

➢ While the large component of such a continuum (Bessel) orbital $|\varepsilon\kappa\rangle$ are represented by the Bessel function $P = N\,r\;\; j_\ell(|\mathbf{k}|\,r)$ above, the small components are here obtained from the kinetic-balance condition.

2.7.b. Non-relativistic Coulomb orbitals

Implementation and numerical details:

➢ The non-relativstic Coulomb orbitals $|\varepsilon\ell\rangle$ are known analytically for $\varepsilon > 0$ and can be utilized to represent the large components of a relativistic orbital with this (given kinetic) energy, while the small components are here obtained again from the kinetic-balance condition.

➢ Non-relativistic free Coulomb waves: The free solutions with $\varepsilon > 0$ to the radial Schrödinger equation with a central-field potential $V(r)$ with Coulombic tail satisfy the boundary condition:

$$P_{\varepsilon\ell}(0) \;=\; 0; \qquad P_{\varepsilon\ell}(r\to\infty) \;\simeq\; \sqrt{\frac{2}{\pi\,k}}\,\sin\left(kr \,+\, \frac{\bar{Z}}{k}\,\ln(2k\,r) \,-\, \frac{\ell\,\pi}{2} \,+\, \sigma_\ell^{(\mathrm{Coulomb})} \,+\, \delta_\ell\right),$$

where $k^2 = 2\,\varepsilon$, $\bar{Z} = Z - N$ is the effective charge as seen by the free electron at large distance and $\sigma_\ell^{(\mathrm{Coulomb})} = \arg\,\Gamma(\ell + 1 - i\,\bar{Z}/k)$ is the (well-known) Coulomb phase. Note that this solution is normalized on the energy scale.

➢ See section 2.1 for a representation of a non-relativistic Coulomb orbital with positive energy $\varepsilon > 0$. This approach does not yet work properly since there is no hypergeometric function with complex arguments available in Julia.

2.7.c. Asymptotically-correct relativistic Coulomb orbitals

Implementation and numerical details:

➢ Relativistic free-Coulomb waves: The free solutions to the radial Dirac equation in a spherical potential with Coulombinc tail satisfy the boundary conditions (Åberg and Howat, 1982; Eqs. (19.29-30))

$$P_{\varepsilon\kappa}(0) \;=\; Q_{\varepsilon\kappa}(0) \;=\; 0$$

$$P_{\varepsilon\kappa}(r\to\infty) \;\simeq\; \sqrt{\frac{\varepsilon \,+\, 2c^2}{\pi\, c^2\, k}}\, \cos\,[\theta_\kappa(\varepsilon) \,+\, \delta_\kappa(\varepsilon)]\,, \qquad\qquad Q_{\varepsilon\kappa}(r\to\infty) \;\simeq\; -\sqrt{\frac{\varepsilon}{\pi\, c^2\, k}}\, \sin\,[\theta_\kappa(\varepsilon) \,+\, \delta_\kappa(\varepsilon)]$$

$$\theta_\kappa(\varepsilon) \;=\; k\,r \,+\, y\,\ln(2k\,r) \,-\, \arg\Gamma(\bar\gamma \,+\, i\,y) \,-\, \frac{1}{2}\,\pi\,\bar\gamma \,+\, \eta, \qquad\qquad k^2 \;=\; 2\,\varepsilon \,+\, \frac{\varepsilon}{c^2}$$

$$\bar\gamma \;=\; +\left(\kappa^2 \,-\, \frac{\bar Z^2}{c^2}\right)^{1/2}, \qquad\qquad y \;=\; \frac{\bar Z\,(\varepsilon \,+\, c^2)}{c^2\, k} \qquad\qquad \exp(2i\,\eta) \;=\; -\,\frac{\kappa \,-\, i\,y\,/\,(\varepsilon \,+\, c^2)}{\bar\gamma \,+\, i\,y}\,.$$

➢ The phase-shift δ_κ is the non-Coulombic phase shift and is set to $\delta_\kappa \,=\, 0$ for a pure Coulombic potential.

2.7.d. Continuum orbitals in an atomic potential: Galerkin method

Implementation and numerical details:

➢ One advantages of using B-splines is that solutions of the Schrödinger or Dirac equation can be found for any energy $\varepsilon \,>\, 0$ by properly adopting $r_{\max}$.

➢ While both the Schrödinger and Dirac equations have formally a solution for any positive energy $\varepsilon \,>\, 0$, a diagonalization in a B-spline representation provides only a discrete set of solutions due to the boundary condition $P(r_{\max}) \,=\, Q(r_{\max}) \,=\, 0$, and where $r_{\max}$ here denotes the size of the *numerical box*.

➢ Galerkin method: This method determines an approximate solution of the generalized eigenvalue equations

$$\sum_i \langle B_i \,|\, (\mathbb{H} - \varepsilon) \,|\, B_j \rangle \; c_j \;=\; \sum_i A_{ij}\, c_j \;=\; 0, \qquad\qquad A_{ij} \;=\; \langle B_i \,|\, (\mathbb{H} - \varepsilon) \,|\, B_j \rangle \;=\; H_{ij} \;-\; \varepsilon\, S_{ij}.$$

➢ Galerkin method: A possible approximation to this generalized eigenvalue problem is to compute the smallest eigenvalue of $\mathbf{A} \cdot \mathbf{c} \;=\; \lambda\, \mathbf{c}$, a more accurate solution follows from a minimization of $|\, A\, \psi\,|^2$ under the contraint $|\, \psi\,|^2 \;=\; 1$. This variational problem is mathematically equivalent to find the smallest eigenvalue of the matrix $A^+\, A$: $\mathbf{A}^+\, \mathbf{A} \cdot \mathbf{c} \;=\; a\, \mathbf{c}$. — The eigenvector of the smallest eigenvalue $a_i \;>\; 0$ is then the requested (approximate) solution of the eigenvalue problem above.

2.7.e. Normalization and phase of continuum orbitals

Pure sine behaviour at large r:

➢ Pure sine behaviour: The free radial Schrödinger equation without an external potential always satisfies the asymptotic pure sine behaviour $\sim\; \sin(kr \;+\; \varphi)$. A very similar asymptotic form $\sim\; \sin(kr \;-\; \ell\, \pi/2 \;+\; \varphi)$ also applies for all partial-wave solutions $\ell \;\geq\; 0$ and positive energy $\varepsilon \;>\; 0$ for the standard radial Schödinger equation with just a centrifugal potential $\sim\; 1/r^2$.

➢ Normalization for a pure sine behaviour: For this normalization, the large component is assumed to be given with $k \;=\; \sqrt{2\, \varepsilon}$ by

$$P(r \;\approx\; r_{\max}) \;\;=\;\; \sqrt{\frac{2}{\pi\, k}} \begin{cases} \sin\,(kr \;+\; \varphi) & \text{for} \quad \ell = 0 \\ \sin\,(kr \;-\; \frac{\ell\, \pi}{2} \;+\; \varphi) & \text{for} \quad \ell > 0\,. \end{cases}$$

With this behaviour, the normalization constant N and the phase φ can be obtained by means of the logarithmic derivative P/P' .

Asymptotic Coulomb behaviour at large r:

➢ Normalization for an asymptotic Coulomb behaviour: For this normalization, the large and small components are assumed to be described for all r-values by the asymptotic behaviour as shown in subsection 2.7.c. With this assumption, the normalization constant N and the phase φ can again be obtained by means of the logarithmic derivative P'/P .

➢ Instead of the logarithmic derivative P'/P , one can of course also apply the ratio Q/P ; this option is currently hard-coded in Jac but need to be further tested.

Normalization for multiply-charged ions due to Ong and Russek (1973):

➢ This normalization scheme has not yet been implemented and tested so far.

➢ Normalization on energy scale: Continuum orbital functions are often normalized on an energy scale, $\langle \varepsilon\kappa \,|\, \varepsilon'\kappa' \rangle = \delta(\varepsilon - \varepsilon') = \delta(E - E')$, and where E, E' are the free-electron energies *inclusive* the rest mass energy, i.e. $E > mc^2$.

➢ WKB ansatz for the large component $P_{\varepsilon\kappa}(r)$: If $V(r)$ is an atomic central-field potential of the ionic core and if we make use of the ansatz below for the large component in the Dirac equation, a second-order ODE can be derived for the function $\phi(r)$, cf. Ong and Russek (1978)

$$P_{\varepsilon\kappa}(r) \;=\; A \sqrt{\frac{E - V(r) \,+\, c^2}{c\,(d\phi/dr)}}\, \cos\phi(r),$$

$$-\left(\frac{d\phi}{dr}\right)^2 \;+\; \frac{(E-V)^2 - c^4}{c^2} \;-\; \frac{\kappa(\kappa+1)}{r^2} \;+\; \left(\frac{d\phi}{dr}\right)^{1/2} \frac{d^2}{dr^2}\left(\frac{d\phi}{dr}\right)^{-1/2} \;-\; (E - V + c^2)^{1/2}\, \frac{d^2}{dr^2}\,(E - V + c^2)^{-1/2} \;+\; \frac{\kappa}{r}\,\frac{dV/dr}{E - V + c^2} \;=\; 0\,.$$

➢ WKB approximation: If the last three terms are neglected in the equation above, an approximate solution to this ODE is given by

$$\left(\frac{d\phi}{dr}\right)^2 \;\approx\; \frac{(E-V)^2 - c^4}{c^2} \;-\; \frac{\kappa\,(\kappa+1)}{r^2}, \qquad\qquad P_{\varepsilon\kappa}(r) \;\approx\; \frac{A\,\sqrt{E - V + c^2}}{\left[(E-V)^2 - c^4 - c^2\,\kappa\,(\kappa+1)/r^2\right]^{1/4}}\, \cos\phi(r)\,.$$

➢ Normalization and phase of the WKB solution at some finite value r_o: Following Ong and Russek (1978, Eq. 12), one can introduce an auxiliary potential $U(r)$, from which the normalization constant $A(r_o)$ and the phase $\phi(r_o)$ at some finite radius r_o is obtained by

$$U(r) \;=\; \frac{c}{2}\,\frac{(E-V)\frac{dV}{dr} - c^2\,\kappa\,(\kappa+1)/\,r^3}{\left[(E-V)^2 - c^4 - c^2\,\kappa\,(\kappa+1)/\,r^2\right]^{3/2}}\; P_{\varepsilon\kappa}(r) \;-\; c\,\frac{\frac{dP_{\varepsilon\kappa}}{dr} \,+\, \frac{dV/dr}{2(E-V+2c^2)}\; P_{\varepsilon\kappa}(r)}{\left[(E-V)^2 - c^4 - c^2\kappa\,(\kappa+1)/r^2\right]^{1/2}}$$

$$A(r_o) \;=\; \sqrt{\frac{\left[(E-V)^2 - c^4 - c^2\,\kappa\,(\kappa+1)/\,r^2\right]^{1/2}}{E - V + c^2}\,\left(P_{\varepsilon\kappa}^2 + U^2\right)\,|_{\,r\,=\,r_o}}\,, \qquad\qquad \phi(r_0) \;=\; \mathrm{atan2}\,(U, P_{\varepsilon\kappa})\,|_{\,r\,=\,r_o}\,.$$

➢ Normalization and phase of the asymptotic wave function $P_{\varepsilon\kappa}(r)$: The normalization of $A(r_o)$ can be used to normalize also the large (and small) component $P_{\varepsilon\kappa}(r)$. For $V(r_o) \approx 0$ and $\phi(r) \approx kr + \delta_\kappa(\varepsilon)$ and if C is the normalization constant so that $CP_{\varepsilon\kappa}$ has the correct asymptotic amplitude, one finally obtains

$$C = \frac{1}{A}\sqrt{\frac{(E+c^2)\,c\,d\phi/dr}{\pi\,c^2\,k\,(E-V+c^2)}} \approx \frac{1}{A\sqrt{\pi\,c}}, \qquad \delta_\kappa(\varepsilon) \approx \phi(r) - kr.$$

2.8. Nuclear models and potentials

2.8.a. Uniform nuclear model

Uniform charge distribution and potential:

➢ Uniform nuclear-charge distribution: For a nucleus with radius R, charge Z and mass number A, the nuclear charge distribution and potential is given for $r \le r$ by

$$\rho^{(\text{uniform})}(r) = \frac{3\,Z}{4\pi\,R^3}, \qquad \phi^{(\text{uniform})}(r) = \begin{cases} \frac{Z\,e}{2\,R}\left[3 - \left(\frac{r}{R}\right)^2\right] & \text{if } r \le R \\ \frac{Z\,e}{R} & \text{if } r > R \end{cases}$$

$$R = R_n\sqrt{\frac{1 + (5s^2/2\,R_n^2)}{1 + (3s^2/4\,R_n^2)}}, \qquad R_n = 1.07\times10^{-15}\,A^{1/3}\ \text{m}, \qquad s = 2.0\times10^{-15}\ \text{m}.$$

➢ Form factor for nuclei with uniform nuclear-charge distribution:

$$F^{(\text{uniform})}(q;\,R) \equiv 4\pi\int_0^\infty dr\,r^2\,\frac{\sin(q\,r)}{q\,r}\,\rho^{(\text{uniform})}(r) = \frac{3\,Z}{(q\,R)^3}\,[\sin(q\,R) - q\,R\,\cos(q\,R)]\,.$$

2.8.b. Helm's uniform-uniform nuclear model

Uniform-uniform charge distribution and potential:

➢ Helm's uniform-uniform nuclear-charge distribution: An alternative realistic nuclear-charge distribution can be expressed as convolution of two uniform distributions $\rho_1^{(\text{uniform})}$, $\rho_2^{(\text{uniform})}$ with nuclear radii $R_1 > R_2$ and normalization constant N (Salvat *et al.*, 2005)

$$\rho^{(\text{Helm})} = Z\,N \int d^3\mathbf{r}'\, \rho_1^{(\text{uniform})}(\mathbf{r}')\, \rho_2^{(\text{uniform})}(\mathbf{r} - \mathbf{r}')$$

$$\phi^{(\text{Helm})} = \begin{cases} N & \text{if } r \le R_1 - R_2 \\ N\, \frac{[(r+R_1)^2 - R_2^2 + 2r\,R_1]\,[(r-R_1)^2 - R_2^2]^2 \quad + \quad [(r+R_2)^2 - R_1^2 + 2r\,R_2]\,[(r-R_2)^2 - R_1^2]^2}{32\,r^3\,R - 2^3} & \text{if } R_1 - R_2 \le r \le R_1 + R_2 \\ 0 & \text{if } r \quad R_1 - R_2 \end{cases}$$

➢ The normalization constant N of Helm's uniform-uniform nuclear-charge distribution and the corresponding electrostatic potential $\phi^{(\text{Helm})}$ need to be determined numerically.

2.8.c. Helm's nuclear-depression model

Distribution and potential for central nuclear depression:

➢ Central depression of the nuclear density: In (super-) heavy nuclei with $Z \gtrsim 100$, a central depression of the nuclear density is caused by the Coulomb repulsion of the Z protons, i.e. the nuclear charge distribution slighgtly rise from the centre towards the surface region. Although this nuclear suppression is further affected by the (detailed) nuclear shell structure, it leads to an estimated decrease of up to 7.5 % of the nuclear matter density at the center of the nucleus (Friedrich *et al.*, 1986).

➢ Helm model: A quantitative relation between the nuclear electromagnetic form factor and the nuclear charge distribution has been established by means of the folding (Helm) model. In this Helm model, the nuclear charge density is described by means of a convolution of a square-well distribution $\rho^{(\text{square-well})} = \rho_o\,\Theta(R_d - r)$, with diffraction radius R_d, and a Gaussian distribution $\rho^{(\text{Gaussian})} = \rho(r, \sigma)$.

➢ Nuclear charge disribution:

$$\rho^{(\text{Helm})} = \rho^{(\text{square-well})}\,\rho^{(\text{Gaussian})} = (1 + w\,r^2)\,\rho^{(\text{homogeneous})}\,\exp\left(-\frac{r^2}{2\,\sigma^2}\right)$$

➢ Modified Helm model: Since the rise of the nuclear density near to the origin is proportional to r^2, a modified modified Helm model has been suggested by Friedrich *et al.* (1986) in terms of the weight w whose value follows from the normalization $\int dr\, \rho^{(\text{Helm})} = 1$. With this weight parameter, the nuclear charge distribution is often written as:

$$\rho^{(\text{modified Helm})} = \frac{(1 + w\, r^2)}{1 + w\, \langle r^2 \rangle^{(\text{homogeneous})}}\, \rho^{(\text{homogeneous})}\, \exp\left(-\frac{r^2}{2\,\sigma^2}\right) .$$

2.8.d. Fermi nuclear model

Fermi charge distribution and potential:

➢ Fermi model: For a nucleus with *root-mean-square* (rms) radius $R = \sqrt{\langle r^2 \rangle}$

$$\rho(r, R) = \frac{N}{1 + \exp[(r - c)/a]}, \qquad \int dr\, r^2\, \rho(r, R) = 1$$

where the thickness parameter a is often chosen as $a = 2.3/4\, \ln 3$.

➢ Fermi nuclear-charge distribution: For a nucleus with *half-density* density R_n, the Fermi distribution is uniform in the center and falls off smoothly at the surface of the nucleus from 0.9 to 0.1 of the central density within a skin of thickness t

$$\rho^{(\text{Fermi})} = \frac{\rho_o}{\exp[(r - R_n)/z] + 1}, \qquad z = \frac{t}{(4\, \ln 3)} = 0.546 \times 10^{-15}\, \text{m}$$

➢ The normalization constant ρ_o of the Fermi nuclear-charge distribution and the corresponding electrostatic potential $\phi^{(\text{Fermi})}$ need to be determined numerically.

➢ With high accuracy, the parameters N and c can be obtained from the analytical formulas

$$N = \frac{3}{4\pi\, c^3}\left(1 + \frac{\pi^2\, a^2}{c^2}\right)^{-1}, \qquad c = \sqrt{\frac{5}{3}\, \langle r^2 \rangle - \frac{7}{3}\, \pi^2\, a^2}\, .$$

Nuclear potential:

➢ Potential of extended nucleus:

$$\mathbb{V}^{(\mathrm{nuc})}(r;R) \;=\; -4\pi\,\alpha\,Z\int_0^\infty dr'\,r'^2\,\frac{\rho(r',R)}{r_>} \;=\; -\frac{4\pi\,\alpha\,Z}{r}\int_0^r dr'\,r'^2\,\rho(r',R) \;-\; 4\pi\,\alpha\,Z\int_r^\infty dr'\,r'\,\rho(r',R), \qquad r_> \;=\; \max(r,r').$$

3. Many-electron atomic interactions, state functions, density operators and statistical tensors

3.1. Electron-electron interaction

Background & notations:

➢ In the (non-relativistic) limit of a rather slow motion of the electrons, each electron pair just interact by the instantaneous Coulomb repulsion

$$\frac{1}{r_{12}} \equiv \frac{1}{|\mathbf{r}_1 - \mathbf{r}_2|}.$$

Already this quite simple (interaction) operator results mathematically in various complications and is generally the major source of electron-electron correlations in all many-electron computations.

➢ For moving charges, Maxwell's theory also predicts both, current-current and retarded interactions, to which we briefly refer as Breit interactions in atomic physics. — These relativistic contributions to the electron-electron interactions must be added to the electro-static Coulomb repulsion.

➢ An effective (relativistic) operator for the electron-electron interaction can be formally derived from QED in perturbation theory with regard to the number of virtually exchanged photons (Sapirstein 1987, Grant und Quiney 1988), while the same expressions can be obtained also from heuristic arguments as given, for example, by Bethe and Salpeter (1957) und Johnson (1995).

➢ In practice, the computation of the electron-electron interaction usually requires the largest effort in all electronic-structure codes and, therefore, deserves special consideration. In atomic physics, a considerable simplification is usually achieved if all electron-electron interaction operators are represented as spherical tensors.

➢ For two electrons in orbitals a, b and with energies ε_a, ε_b, the interaction energy can be written as difference of a direct and exchange matrix element of the potential

$$\mathbb{V}^{(\mathrm{tr})} \;=\; -\frac{1}{2\pi}\int \frac{d^3k}{k^2-\omega^2}\; e^{i\,\mathbf{k}\cdot(\mathbf{r}_1-\mathbf{r}_2)} \sum_{i,j=1}^{3}\left[\delta_{ij} \;-\; \frac{k_i\,k_j}{k^2}\right]\,\alpha_{1i}\,\alpha_{2j}$$

where α_{1i} is the i-th component of the $\boldsymbol{\alpha}$ matrix (vector) of the electron at position $\mathbf{r}_1$ and

$$\omega \;=\; \begin{cases} 0 & \text{direct matrix element} \\ \frac{|\epsilon_a-\epsilon_b|}{c} & \text{exchange matrix element} \end{cases}$$

refers to the momentum of the exchanged photon.

➢ The exchange matrix elements of the potential $\mathbb{V}^{(\mathrm{tr})}$ is generally complex; while the *real* part describes an energy shift due to this transverse interaction, the *imaginary* part represents a rate for the decay $a \to b$ for $\epsilon_a > \epsilon_b$ or $b \to a$ *vice versa*.

➢ Frequency-independent Breit interaction: For $\omega \to 0$, the transversal Breit interaction gives rise to the frequency-independent Breit interaction

$$b^{o}_{12} \;=\; -\frac{1}{2\,r_{12}}\left[\boldsymbol{\alpha}_1\cdot\boldsymbol{\alpha}_2 \;+\; \frac{(\boldsymbol{\alpha}_1\cdot\mathbf{r}_{12})\,(\boldsymbol{\alpha}_2\cdot\mathbf{r}_{12})}{r_{12}^2}\right],$$

which neglects all contributions $\sim \alpha^4 Z^3$ (as well as of higher order in αZ).

➢ Typically, the explicit energy-dependence of the transverse interaction [upon the energy difference of the two electrons] gives rather tiny corrections, so that, in practice, often no difference is made between the transversal and zero-frequency Breit interaction.

➢ Gaunt interaction: The first term of the zero-frequency Breit interaction (operator) is known also as Gaunt interaction (Gaunt 1929). This term describes the current-current interaction due to the motion of the electrons and contributes about 90 % of the total Breit interaction for closed-shell atoms.

➢ For many elements of the periodic table, the corrections due to the Breit interaction are usually small, when compared with the dominant Coulomb repulsion. This applies especially for the Breit contributions to the electron-electron correlation.

➢ For describing most processes, it is sufficient, if at all, to include the Breit interaction perturbatively in lowest order. Formally, however, both terms

$$v_{12} \;=\; \frac{1}{r_{12}} \;+\; b_{12} \qquad \Longleftrightarrow \qquad \mathbb{V}^{(\mathrm{e-e})} \;=\; \mathbb{V}^{(\mathrm{Coulomb})} \;+\; \mathbb{V}^{(\mathrm{Breit})}$$

are equivalent, and they should be treated simply together for all (super-) heavy elements.

➢ In JAC, only the frequency-independent Breit interaction is currently implemented.

Effective interaction strength $X^{(L)}(abcd)$ of scalar electron-electron interactions:

➢ All operators of the (scalar) electron-electron interaction can be generally represented as spherical tensors in the form:

$$g_{12} \equiv g(\mathbf{r}_1, \mathbf{r}_2) = \sum_L g_L(r_1, r_2) \left(\mathbb{T}^{(L)}(\vartheta_1, \varphi_1) \cdot \mathbb{T}^{(L)}(\vartheta_2, \varphi_2) \right)$$

$$\langle n_a \kappa_a m_a(1)\, n_b \kappa_b m_b(2) \,|\, \mathfrak{g}_{12} \,|\, n_c \kappa_c m_c(1)\, n_d \kappa_d m_d(2) \rangle = \sum_{L\,M} (-1)^{L-M+j_a-m_a+j_b-m_b} \begin{pmatrix} j_a & L & j_c \\ -m_a & M & m_c \end{pmatrix} \begin{pmatrix} j_b & L & j_d \\ -m_b & -M & m_d \end{pmatrix} X^{(L)}(abcd),$$

leading to a simple factorization of the two-electron matrix elements, and where the magnetic quantum numbers (i.e. the angular dependence) of the matrix elements only occurs in the phase and the Wigner $3-j$ symbols.

➢ Effective interaction strength $X^{(L)}(abcd)$ of order L: The strengths $X^{(L)}(abcd)$ describe the physical interaction and are specific for every operator. They are often used as the building blocks in order to handle the electron-electron interactions efficiently in electronic structure computations.

Effective interaction strength $X^{(L,\,\text{Coulomb})}(abcd)$ of the Coulomb repulsion:

➢ Coulomb repulsion: The decomposition of the Coulomb operator is given by:

$$\frac{1}{r_{12}} = \sum_{L=0}^{\infty} U_L(r,s)\, P_L(\cos(\vartheta)) = \sum_{L=0}^{\infty} U_L(r,s) \left(\mathbb{C}^{(L)}(\vartheta_1, \varphi_1) \cdot \mathbb{C}^{(L)}(\vartheta_2, \varphi_2) \right), \qquad U_L(r,s) = \begin{cases} \frac{r^L}{s^{L+1}} & r < s \\ \frac{s^L}{r^{L+1}} & r > s\,. \end{cases}$$

In this expansion, $P_L(x)$ denotes a Legendre-polynomial and $\vartheta = \mathbf{r} \cdot \mathbf{s}/rs$ the angle between the two electron coordinates.

➢ Effective interaction strength of the Coulomb repulsion:

$$X^{(L,\,\mathrm{Coulomb})}(abcd) \;=\; \delta(j_a,j_c,L)\;\delta(j_b,j_d,L)\;\Pi^{e}(\kappa_a,\kappa_c,L)\;\Pi^{e}(\kappa_b,\kappa_d,L)\;(-1)^{L}\;\left\langle\kappa_a\,\middle\|\,\mathbb{C}^{(L)}\,\middle\|\,\kappa_c\right\rangle\left\langle\kappa_b\,\middle\|\,\mathbb{C}^{(L)}\,\middle\|\,\kappa_d\right\rangle\;\;R^{L}(abcd)\,,$$

$$\delta(j_a,j_b,j_c) \;=\; \begin{cases} 1 & |j_a-j_b|\;\le\;j_c\;\le\;|j_a+j_b| \quad \text{and cyclic interchanged} \\ 0 & \text{otherwise}\,, \end{cases}$$

and where $\Pi^{e}(\kappa,\kappa',L)$ represent the angular momentum and parity selection rules.

Effective interaction strength $X^{(L,\,\mathrm{Breit})}(abcd)$ of the Breit interaction:

➢ Effective interaction strength of the zero-frequency Breit: For the zero-frequency interaction, we find

$$X^{(L,\,\mathrm{Breit})}(abcd) \;=\; (-1)^{L}\;\left\langle\kappa_a\,\middle\|\,\mathbb{C}^{(L)}\,\middle\|\,\kappa_c\right\rangle\left\langle\kappa_b\,\middle\|\,\mathbb{C}^{(L)}\,\middle\|\,\kappa_d\right\rangle\;\left[\Pi^{o}(\kappa_a,\kappa_c,L-1)\;\Pi^{o}(\kappa_b,\kappa_d,L+1)\;\sum_{\mu=1}^{8}\;s_{\mu}^{L}(abcd)\;S_{\mu}^{L}(abcd)\;+\right.$$

$$\left.+\;\sum_{\nu\,=\,L-1}^{L+1}\;\Pi^{o}(\kappa_a,\kappa_c,\nu)\;\Pi^{o}(\kappa_b,\kappa_d,\nu)\;\sum_{\mu=1}^{4}t_{\mu}^{\nu,L}(abcd)\;T_{\mu}^{\nu}(abcd)\right]\,.$$

$$\Pi^{o}(\kappa_a,\kappa_b,L) \;=\; \begin{cases} 1 & \text{if}\quad l_a+l_b+L\quad\text{odd} \\ 0 & \text{otherwise.} \end{cases}$$

➢ The constant coefficients s_{μ}^{L} and $t_{\mu}^{\nu,L}$ just depend on the angular quantum numbers $\{\kappa_a,\,\kappa_b,\,\kappa_c,\,\kappa_d,\,\nu,\,L\}$ and are diplayed, for example, by Grant (1988; tables 3 and 4, and where we here use $t_{\mu}^{\nu,L}\equiv r_{\mu}^{\nu,L}$).

Table 3.1.: Definition of the integrales $S_\mu^\nu(abcd)$ und $T_\mu^\nu(abcd)$

$S_1^\nu(abcd)$	$= S^\nu\,[ac\,\|\|\,bd]$	$S_2^\nu(abcd)$	$= S^\nu\,[bd\,\|\|\,ac]$	$T_1^\nu(abcd)$	$= T^\nu\,[ac\,\|\|\,bd]$
$S_3^\nu(abcd)$	$= S^\nu\,[ca\,\|\|\,db]$	$S_4^\nu(abcd)$	$= S^\nu\,[db\,\|\|\,ca]$	$T_2^\nu(abcd)$	$= T^\nu\,[ca\,\|\|\,db]$
$S_5^\nu(abcd)$	$= S^\nu\,[ac\,\|\|\,db]$	$S_6^\nu(abcd)$	$= S^\nu\,[db\,\|\|\,ac]$	$T_3^\nu(abcd)$	$= T^\nu\,[ac\,\|\|\,db]$
$S_7^\nu(abcd)$	$= S^\nu\,[ca\,\|\|\,bd]$	$S_8^\nu(abcd)$	$= S^\nu\,[bd\,\|\|\,ca]$	$T_4^\nu(abcd)$	$= T^\nu\,[ca\,\|\|\,bd]$

➢ The radial integrals $S_\mu^\nu(abcd)$ and $T_\mu^\nu(abcd)$ are different (linear) combinations of the two integrals [cf. table 3.1]

$$S^\nu\,[ac\,|\,bd] = \int_0^\infty dr \int_0^\infty ds\; P_a(r)\,Q_c(r)\,\frac{1}{2}\,[\,W_{\nu-1,\,\nu+1,\,\nu}(r,s;\,\omega_{ac}) \;+\; W_{\nu-1,\,\nu+1,\,\nu}(r,s;\,\omega_{bd})\,]\;P_b(s)\,Q_d(s)$$

$$T^\nu\,[ac\,|\,bd] = \int_0^\infty dr \int_0^\infty ds\; P_a(r)\,Q_c(r)\,\frac{1}{2}\,[\,V_\nu(r,s;\,\omega_{ac}) \;+\; V_\nu(r,s;\,\omega_{bd})\,]\;P_b(s)\,Q_d(s)$$

$$V_\nu(r,s;\,\omega) = \begin{cases} -(2\nu+1)\;j_\nu(\omega r)\;n_\nu(\omega s) & r<s \\ -(2\nu+1)\;j_\nu(\omega s)\;n_\nu(\omega r) & r>s \end{cases}$$

$$W_{\nu-1,\,\nu+1,\,\nu}(r,s;\,\omega) = \begin{cases} -(2\nu+1)\;j_{\nu-1}(\omega r)\;n_{\nu+1}(\omega s) + \left(\frac{2\nu+1}{\omega}\right)^2 \frac{r^{\nu-1}}{s^{\nu+2}} & r<s \\ -(2\nu+1)\;\omega\;j_{\nu-1}(\omega s)\;n_{\nu+1}(\omega r) & r>s \end{cases}.$$

➢ In these expressions, $j_\nu(\omega r)$ and $n_\nu(\omega r)$ denote the spherical Bessel functions, and $\omega_{ac} = |\,\epsilon_a - \epsilon_c\,|$ the difference of the corresponding single-particle energies.

3.2. Atomic potentials

Parametrized many-electron densities:

➢ Thomas-Fermi-Moliere (TFM) electron density: A useful analytical model for the spherical symmetric electron density follows from a simple parametrization of the Thomas-Fermi (TF) screening function $\chi^{(\mathrm{TFM})}(r)$ and its substitution into the Poisson equation (Salvat *et al.*, 2005)

$$\chi^{(\mathrm{TFM})}(r) = \sum_{i=1}^{3} A_i \, \exp\left(\frac{a_i \, r}{b}\right), \qquad A_1 = 0.1, \quad A_2 = 0.55, \quad A_3 = 0.35, \qquad a_1 = 6, \quad a_2 = 1.2, \quad a_3 = 0.3$$

$$b = \frac{(3\pi)^{2/3}}{2^{7/3}} \, \frac{\hbar^2}{m \, e^2 \, Z^{1/3}} = \frac{0.88534 \, a_o}{Z^{1/3}}$$

$$\rho^{(\mathrm{TFM,\,electrons})}(r) = \frac{Z}{4\pi \, r} \sum_{i=1}^{3} A_i \, a_i^2 \, \exp\left(a_i \, r\right).$$

➢ Thomas-Fermi-Dirac (TFD) electron density: The TFD theory also accounts for the exchange term of the electron gas and leads again to a differential equation that need to be solved numerically for each individual atom or ion. A parametrized form for an approximated TFD screening function $\chi^{(\mathrm{TFD})}$ has been suggested in the literature but results in a rather lengthy and cumbersome expansion.

3.2.a. In JAC implemented potentials

Atomic potentials:

➢ Core-Hartree potential:

$$V^{(\mathrm{core-Hartree})}(r) = \int_0^\infty dr' \, \frac{\rho_c(r')}{r_>}, \qquad r_> = \max(r, r'), \qquad \rho_c(r) = \sum_a \left(P_a^2(r) + Q_a^2(r)\right),$$

and where the summation runs over all *core* orbitals of electron configurations. This potential is applied if just a single valence electron occurs (alkali atoms). In JAC, this potential can be obtained for a given level from `Jac.computePotentialCoreHartree(grid::Radial.Grid, level::Level)`.

➢ Dirac-Fock-Slater potential:

$$V^{(\mathrm{DFS})}(r) \;=\; \int_0^\infty dr' \,\frac{\rho_t(r')}{r_>} \;-\; \left(\frac{3}{4\pi^2\, r^2}\,\rho_t(r)\right)^{1/3}, \qquad r_> \;=\; \max(r,r'), \qquad \rho_t(r) \;=\; \sum_a \left(P_a^2(r) \;+\; Q_a^2(r)\right),$$

and where the summation runs over *all* orbitals (electrons). In JAC, this potential can be obtained for a given level from `Jac.computePotentialDFS(grid::Radial.Grid, level::Level)`.

➢ Hartree potential:

$$V^{(\mathrm{Hartree})}(r) \;=\; -\sum_a \,\bar{q}_a\; r\; Y^0_{aa}(r)$$

where $\bar{q}_a$ is the generalized occupation number, and where the summation runs over all orbitals here. In JAC, this potential can be obtained for a given level from `Jac.computePotentialHartree(grid::Radial.Grid, level::Level)`.

➢ Hartree-Slater potential:

$$V^{(\mathrm{HS})}(r) \;=\; -\sum_a \,\bar{q}_a\; Y^0_{aa}(r) \;+\; \frac{3}{2}\,\left(\frac{3}{4\pi^2\, r^2}\,\rho(r)\right)^{1/3}\,\frac{r}{2} \qquad \rho(r) \;=\; \sum_a \bar{q}_a\,\left(P_a^2(r) \;+\; Q_a^2(r)\right),$$

and where the summation runs over *all* orbitals. In JAC, this potential can be obtained for a given level from `Jac.computePotentialDFS(grid::Radial.Grid, level::Level)`.

➢ Kohn-Sham potential:

$$V^{(\mathrm{Kohn-Sham})}(r) \;=\; \int_0^\infty dr' \,\frac{\rho_t(r')}{r_>} \;-\; \frac{2}{3\,r}\,\left(\frac{81}{32\,\pi^2}\,r\,\rho_t(r)\right)^{1/3}, \qquad r_> \;=\; \max(r,r'), \qquad \rho_t(r) \;=\; \sum_a \left(P_a^2(r) \;+\; Q_a^2(r)\right),$$

and where the summation runs over *all* orbitals (electrons). In JAC, this potential can be obtained for a given level from `Jac.computePotentialKohnSham(grid::Radial.Grid, level::Level)`.

3.2.b. Further atomic potentials, not yet considered in JAC

Atomic potentials:

➢ Modified Dirac-Fock potential: For a closed-shell N-electron atom, a modified Dirac-Fock potential has been defined for the (outgoing) electron by Derevianko *et al.* (1999) as

$$V(r) \;=\; \sum_b (2\,j_b \,+\, 1)\,\frac{Y_0(r,\,bb)}{r} \;-\; V^{\,(\mathrm{exchange})}(r), \qquad\qquad V^{\,(\mathrm{exchange})}(r) \;=\; \frac{V^{\,(\mathrm{direct})}(r)}{N}\,.$$

In this potential, the function $Y_0(r,\,bb)/r$ is the Hartree screening potential for an electron in subshell b, and all generated orbitals are orthonormal to each other if the bound electrons are generated self-consistently in this potential. All continuum orbitals can then be generated in the same potential.

➢ Tietz (1954) potential:

$$V^{\,(\mathrm{Tietz})}(r) \;=\; -\,\frac{\alpha\,Z}{r}\,\phi(x), \qquad \phi(x) \;=\; \frac{1}{(1\,+\,(\pi/8)^{2/3}\,x\,)^2}, \qquad x \;=\; \frac{r\,Z^{1/3}}{\mu}, \qquad \mu \;=\; \left(\frac{3\pi}{4}\right)^{2/3} \approx\; 0.8853.$$

➢ Modified-Tietz potential: (Neuffer and Commins, 1977)

$$V^{\,(\mathrm{modified-Tietz})}(r) \;=\; -\,\frac{\alpha}{r}\left(1\,+\,\frac{(Z-1)}{(1+t\,r)^2}\,e^{-\gamma\,r}\right)$$

where γ and t are parameters adjusted to fit the low-lying spectra of the atoms under consideration. Johnson *et al.* (1985) tabulate these parameters for rhubidium, cesium, gold and thallium.

3.3. Construction of symmetry-adapted CSF basis

Excitation schemes for the constructing a many-electron CSF basis:

➢ Several (de-) excitation schemes for the construction of non-relativistic configuration lists are defined within JAC in order to facilitate the set-up of (lists of) CSF bases with selectec total symmetry $\mathbb{J}$. These bases are required specially for the computation of cascades and/or approximate many-electron Green functions.

➢ In JAC, various excitation schemes are distinguished by the (abstract) `scheme::Basics.AbstractExcitationScheme`, and which is used for the construction of systematically enlarged basis sets, the computation of approximate Green functions as well as for the generation of atomic cascades.

➢ (De-) excitation of a single electron from a given set of (non-relativistic) configurations `(DeExciteSingleElectron)`: This schemes includes all excitations and de-excitations of a single electron from a given list of (nonrelativistic bound-electron) configurations. Here, of course, the number of electrons of the newly generated configurations is the *same* as given by the configuration, while up to *one* free electron occur in each CSF for representing N-electron scattering levels.

Example: $1s^2 2s^2 2p^6 \longrightarrow \left\{ \begin{array}{l} 1s 2s^2 2p^6 \, (ns + np + nd + \, ...) \\ 1s^2 2s 2p^6 \, (ns + np + nd + \, ...) \\ 1s^2 2s^2 2p^5 \, (ns + np + nd + \, ...) \end{array} \right\}$

➢ (De-) excitation of two electrons from a given set of (non-relativistic) configurations `(DeExciteTwoElectrons)`: Similar as above, this schemes includes all excitations and de-excitations of up to *two* electrons from the given list of (bound-electron) configurations and, hence, allows up to *two* free electrons for representing the N-electron scattering levels.

Example: $1s^2 2s^2 2p^6 \longrightarrow \left\{ \begin{array}{l} 1s 2s^2 2p^6 \, (ns + np + nd + \, ...) \, + \, 2s^2 2p^6 \, nl \, n'l' \\ 1s^2 2s 2p^6 \, (ns + np + nd + \, ...) \, + \, 1s^2 2p^6 \, nl \, n'l' \\ 1s 2s 2p^6 \, nl \, n'l' \\ ... \end{array} \right\}$

➢ Add a single electron to a given set of configurations `(AddSingleElectronWithoutHoles)`: This scheme generates all configurations with one additonal electron to the given set of configurations but without any replacement from the occupied orbitals.

Example: $1s^2 2s^2 2p^6 \longrightarrow \left\{ \, 1s^2 2s^2 2p^6 \, (ns + np + nd + \, ...) \, \right\}$

3.4. Atomic estimates of quantum-electrodynamic (QED) corrections

3.4.a. QED model operators & model potentials

Background & notations:

➢ Various proposals have been made in the literature to incorporate the (radiative) quantum-electrodynamic corrections by different model potentials into correlated many-electron methods, such as the MCDHF, many-body perturbation or coupled-cluster theories.

➢ Effective single-electron QED Hamiltonian: To a good approximation, these QED corrections can be incorporated into the (many-electron) representation $\{c_r(\alpha\mathbb{J})\}$ of some level $|\alpha\mathbb{J}\rangle$ by means of a local single-electron QED Hamiltonian. This Hamiltonian can be separated into two parts

$$\mathbb{h}^{(\mathrm{QED})} \;=\; \mathbb{h}^{(\mathrm{SE})} + \mathbb{h}^{(\mathrm{VP})},$$

the self-energy (SE) and vacuum-polarization (VP) Hamiltonians, and which are often written in terms of (effective) potentials.

➢ Vacuum-polarization: The vacuum-polarization is given by a *local* potential and can be further splitted into an Uehling and a Wichmann-Kroll potential; this local potential is rather straightforward to calculate and has already been applied in many applications in the past.

➢ Self-energy Hamiltonian $\mathbb{h}^{(\mathrm{SE})}$: Such a Hamiltonian can be generally represented as sum of a local and non-local potential. These potentials are typically based on *ab initio* calculations of the diagonal and nondiagonal matrix elements of the one-loop QED operator with H-like wave functions (Shabaev *et al.*, 2013).

➢ Shabaev and coworkers (2013) have shown that the QED corrections can be systematically incorporated into an effective Hamiltonian that acts in the space of Slater determinants, if these determinants are built from one-electron positive-energy states only and if the total (many-electron binding) energies of the system are smaller than the pair-creation energy. This effective QED Hamiltonian can then be added to the Dirac-Coulomb-Breit Hamiltonian.

➢ Beyond QED model Hamiltonians: Explicit calculations of radiative corrections are extremely sophisticated and time-consuming for many-electron systems, if the standard QED perturbation theory is to be applied. Until the present, such detailed QED computations can be carried out only for highly-charged, few-electron ions and by still making use of an effective screening potential (instead of the complete perturbation expansion for all electron-electron pairs).

Vacuum polarization potentials:

➢ Uehling potential: This potential is the dominant part of the VP and can be obtained from the direct numerical integration of the well-known formula

$$V^{\,(\mathrm{Uehling})}(r) \;=\; -\alpha\,Z\,\frac{2\,\alpha}{3\,\pi}\int_0^\infty dr'\,4\pi\,r'\,\rho(r')\int_1^\infty dt\,\left(1+\frac{1}{2\,t^2}\right)\frac{\sqrt{t^2-1}}{t^2}\,\frac{e^{-2m\,|r-r'|\,t}-e^{-2m\,(r+r')\,t}}{4m\,r\,t},$$

and where $Z\,\rho(r)$ denotes the density of the nuclear charge distribution, if normalized to $\int dV\,\rho(r) = 1$.

➢ Approximate Uehling potential: The Uehling potential can be calculated also by an approximate formula for a point-like nucleus (Flambaum and Ginges, 2005)

$$V^{\,(\text{simplified Uehling})}(r) \;=\; \frac{2\,\alpha}{3\,\pi}\,V_{\mathrm{nuc}}(r)\int_1^\infty dt\,\left(1+\frac{1}{2\,t^2}\right)\frac{\sqrt{t^2-1}}{t^2}\,e^{-2m\,r\,t}.$$

➢ Wichmann-Kroll potential: A detailed evaluation of the Wichmann-Kroll potential is (much) more sophisticated but can be estimated again to a rather good accuracy by the approximate formula for a point-like nucleus and with the classical radius r_c (Flambaum and Ginges, 2005)

$$V^{\,(\text{simplified WK})}(r) \;=\; -\,\frac{2\,\alpha}{3\,\pi}\,V(r)\,\frac{0.092\,Z^2\,\alpha^2}{1+(1.62\,r/r_c)^4}.$$

➢ The Wichmann-Kroll correction is generally small and gives a $\sim$ 1 % contribution to the VP shifts only for $Z \gtrsim 80$ (Flaumbaum and Ginges, 2005).

Local self-energy potentials:

➢ Shabaev *et al.* (2013) suggest a local but independent part of the self-energy potential for each symmetry block κ of the one-electron orbitals of the form

$$V_\kappa^{(\text{local SE})}(r) \;=\; A_\kappa \,\exp\left(-\frac{2\pi\, r}{\lambda_C}\right) \;=\; A_\kappa \,\exp\left(-\frac{r}{\alpha}\right),$$

where the constants A_κ are chosen to reproduce the SE shift for the lowest (one-electron, H-like) energy of each given κ symmetry, and where $\lambda_C = h/m\,c$ is the Compton wavelength of the electron.

➢ These local contributions can also be cast be into the form

$$V^{(\text{local SE})}(r) \;=\; \sum_\kappa A_\kappa\, P_\kappa \,\exp\left(-\frac{2\pi\, r}{\lambda_c}\right), \qquad\qquad \langle a\,|P_\kappa|\,b\rangle \;=\; \delta_{\kappa,\kappa_a}\,\delta_{\kappa,\kappa_b}\,.$$

➢ Self-energy interaction strength: Following the discussion with Volotka (2019), a (single-electron) local self-energy interaction strength for the (local) potential above can be written

$$\left\langle a \,\middle\|\, \mathbb{h}^{(\text{local SE})} \,\middle\|\, a\right\rangle \;=\; \left[\frac{\left\langle n_g\kappa \,\middle\|\, \mathbb{h}^{(\text{local SE})} \,\middle\|\, n_g\kappa\right\rangle}{\left\langle n_g\kappa \,\middle\|\, \exp\left(-\frac{r}{\alpha}\right) \,\middle\|\, n_g\kappa\right\rangle}\right]_{\text{hydrogenic}} \left\langle a \,\middle\|\, \exp\left(-\frac{r}{\alpha}\right) \,\middle\|\, a\right\rangle, \qquad \left\langle a \,\middle\|\, \mathbb{h}^{(\text{local SE})} \,\middle\|\, b\right\rangle \;=\; 0 \quad \text{for} \quad a \neq b,$$

where $|n_g\kappa\rangle = \{1s_{1/2},\, 2p_{1/2},\, 2p_{3/2},\, 3d_{3/2},\, ...\}$ refers to the lowest hydrogenic orbitals of symmetry κ and nuclear charge Z. For a non-diagonal self-energy potential, the representation of the one-electron matrix elements will be more difficult and are presently not considered in Jac.

➢ Self-energy interaction strength: Shabaev *et al.* (2013) have tabulated values for $\left\langle n_g\kappa \,\middle\|\, \mathbb{h}^{(\text{local SE})} \,\middle\|\, n_g\kappa\right\rangle_{\text{hydrogenic}}$ for selected nuclear charges, which can be readily applied in order to compute the self-energy interactions strengths for general many-electron atoms and ions.

Radiative potentials:

➢ Radiative potential: Flambaum and Ginges (2005) suggest an approximate expression for a (so-called) radiative potential which can be utilized in order to estimate the radiative corrections in strong Coulomb fields to the energies and electric-dipole transition amplitudes in atomic (many-electron) computation. This (alternative) potential is said to give good QED estimates with an accuracy of just a few percent but has been mainly tested and applied to (neutral) cesium only.

➢ Radiative potential: Flambaum and Ginges (2005) decompose this radiative potential into five terms which are explained either above or below:

$$V^{\,(\text{total QED})} \;=\; V^{\,(\text{simplified Uehling})} \,+\, V^{\,(\text{magnetic form})} \,+\, V^{\,(\text{electric form})} \,+\, V^{\,(\text{low frequency})} \,+\, V^{\,(\text{simplified WK})}.$$

➢ Magnetic form-factor potential: For the magnetic form-factor contribution, Flambaum and Ginges (2005) give

$$V^{\,(\text{magnetic form})} \;=\; \frac{\alpha}{4\,\pi\,m}\; i\,\boldsymbol{\gamma}\cdot\boldsymbol{\nabla}\left[\,V(r)\,\left(\int_1^\infty dt\;\frac{\exp\left(-\,2m\,r\,t\right)}{t^2\,\sqrt{t^2\,-\,1}}\;-\;1\right)\right],$$

and where $\boldsymbol{\gamma} \,=\, (\gamma_1, \gamma_2, \gamma_3)$ is the vector of gamma matrices.

➢ Low-frequency potential to the electric form-factor: Flambaum and Ginges (2005) suggest the (low-frequency) expression

$$V^{\,(\text{low frequency})} \;=\; -\,\frac{B(Z)}{e}\;Z^4\,\alpha^5\,mc^2\,\exp\left(\frac{Z\,r}{a_o}\right), \qquad\qquad B(Z) \;=\; 0.074 \,+\, 0.35\,Z\,\alpha,$$

with the Bohr radius a_o and where the function $B(Z)$ has been fitted in order to reproduce the radiative energy shifts for p-levels of selected heavy elements. This term should be used with some care however.

➢ Electric form-factor potential (including high-frequency contributions): Flambaum and Ginges (2005) display a final expression for the electric form-factor contribution

$$V^{\,(\text{electric form})}(r) \;=\; -\,A(Z,r)\,\frac{\alpha}{\pi}\,V(r)\,\int_1^\infty dt\;\frac{\exp\left(-\,2m\,r\,t\right)}{\sqrt{t^2\,-\,1}}\,\left[\left(1\,-\,\frac{1}{2\,t^2}\right)\,\left[\ln(t^2\,-\,1)\,+\,4\,\ln(1/Z\alpha\,+\,0.5)\right]\,-\,\frac{3}{2}\,+\,\frac{1}{t^2}\right].$$

Here, the function $A(Z,r) = (1.071 - 1.976\,x^2 - 2.128\,x^3 + 0.169\,x^4)\,m\,r\,/\,(m\,r + 0.07\,Z^2\,\alpha^2)$, has been suggested with $x = (Z-80)\,\alpha$. The detailed form of $A(Z,r)$ was found by fitting the radiative shifts for the high Coulomb s levels from the literature. This term should be used with good care again.

➢ Note that this local potential by Flambaum and Ginges (2005) was optimized for weakly bound valence states of heavy neutral atoms and may be less accurate for strongly bound ionic or even core-hole states.

3.4.b. In JAC implemented QED estimates

Models & applications:

➢ In Jac, the radiative QED corrections can be incorporated into the computation and representation of the wave functions if `AsfSettings(..)` is initialized with `qedModel = QedPetersburg()` or `qedModel = QedSydney()`. This singleton datat types tell Jac how the estimates for the vacuum polarization and the (local) self-energy contributions are incorporated into the Hamiltonian matrix, cf. below.

➢ In Jac, use `qedModel = NoneQed()` in `AsfSettings(..)` if no QED estimates are to be included; this is also the default.

Implementation:

➢ QedPetersburg model: Here, we simply add to all matrix elements $\langle a \,\|\, \mathbb{h}^{(1-\text{particle})} \,\|\, b\rangle$ in the many-electron Hamiltonian matrix the (single-electron) matrix elements

$$\langle a \,\|\, \mathbb{h}^{(\text{QED})} \,\|\, b\rangle \;=\; \langle a \,\|\, \mathbb{h}^{(\text{local SE})} \,\|\, b\rangle \;+\; \langle a \,\|\, \mathbb{h}^{(\text{simplified Uehling})} \,\|\, b\rangle\,.$$

➢ QedSydney model: Analogues, here we add to all matrix elements $\langle a \,\|\, \mathbb{h}^{(1-\text{particle})} \,\|\, b\rangle$ in the many-electron Hamiltonian matrix the (single-electron) matrix elements

$$\langle a \,\|\, \mathbb{h}^{(\text{QED})} \,\|\, b\rangle \;=\; \langle a \,\|\, \mathbb{h}^{(\text{magnetic form})} \,\|\, b\rangle \;+\; \langle a \,\|\, \mathbb{h}^{(\text{electric form})} \,\|\, b\rangle \;+\; \langle a \,\|\, \mathbb{h}^{(\text{low frequency})} \,\|\, b\rangle \;+\; \langle a \,\|\, \mathbb{h}^{(\text{simplified Uehling})} \,\|\, b\rangle\,.$$

➢ Effective QED operator With the definitions from above, the total QED operator for a many-electron atom includes of course a summation over all atomic electrons:

$$\mathbb{H}^{(\mathrm{QED})} = \mathbb{H}^{(\mathrm{SE})} + \mathbb{H}^{(\mathrm{VP})} = \sum_j \mathbb{h}_j^{(\mathrm{QED})} = \sum_j \left(\mathbb{h}_j^{(\mathrm{SE})} + \mathbb{h}_j^{(\mathrm{VP})} \right),$$

where the $\mathbb{h}_j^{(\mathrm{SE})}$ and $\mathbb{h}_j^{(\mathrm{VP})}$ refers to the one-electron operators for electron j.

3.5. Unitary $jjJ - LSJ$ transformation of atomic states

3.5.a. Transformation matrices from jjJ- to LSJ-coupling

Atomic coupling schemes:

➢ Coupling schemes: Atomic and ionic levels are usually identified and labeled by means of quantum numbers of an appropriate coupling scheme. However, these quantum numbers are well-conserved only for a pure coupling of symmetry-adapted many-electron state, and which is realized only (rather) approximately in Nature.

➢ LSJ- and jjJcoupling are nowadays the two most frequently applied coupling schemes in atomic theory.

➢ As usual in quantum mechanics, the transformation from one to another orthononal basis (i.e. the representation of atomic levels in a particular coupling scheme) is simply given by a unitary matrix, although it is generally not easy to evaluate this transformation matrix for arbitrary shell structures of atoms and ions.

➢ LSJ-notation: In atomic spectroscopy, the standard LSJ-notation of the levels is frequently applied for classifying the low-lying level structures of atoms or ions.

➢ Labeling of levels: Atomic energy levels are often labeled by means of their leading LSJ-coupled CSF in a wave function expansion. However, special care need to be taken, if the same CSF occurs largest in the expansion of two levels, since then, the classification is no longer unique.

➢ The lack of providing a fast and proper spectroscopic notation in relativistic computations may hamper the spectroscopic level classification of medium and heavy elements as well as the interpretation and analysis of inner-shell processes.

$jjJ - LSJ$ transformation of subshell states:

➢ Unique subshell order: Since each non-relativistic $n\ell$-shell (apart from the ns shells) split into two relativistic subshells with $j = \ell \pm 1/2$, the order of these subshell is relevant for the transformation of the many-electron basis and is always fixed in JAC to $n\ell_{\,j=\ell-1/2},\ n\ell_{\,j=\ell+1/2}$. For the np- and nd-shells, for example, we always assume the sequence $np_{1/2}$, $np_{3/2}$ and $nd_{3/2}$, $nd_{5/2}$ in all formulas below.

➢ Non-relativistic subshell states: In the transformation of the non-relativistic shell states $\left|n\ell^N\,\alpha\nu\,LS\right\rangle$, we generally have to consider the product of two (relativistic) subshell states $\left|n\kappa^{\bar{N}}\,\bar{\nu}J,\ n\kappa^{\stackrel{+}{N}}\,\stackrel{+}{\nu}J\right\rangle$, and with $\bar{N} + \stackrel{+}{N} = N$. Here, the $+$ and $-$ on top of the quantum numbers just refer to the relativistic subshells with $j = \ell \pm 1/2$.

➢ The transformation between the (sub-) shell states in jjJ- and LSJ-coupling can be expressed with real Fourier coefficients as

$$\left|(n\kappa^{\bar{N}}\,\bar{\nu}J,\ n\kappa^{\stackrel{+}{N}}\,\stackrel{+}{\nu}J)\,J\right\rangle \;=\; \sum_{\alpha\nu\,LS} \left|n\ell^N\,\alpha\nu\,LSJ\right\rangle \left\langle n\ell^N\,\alpha\nu\,LSJ\,|\,(n\kappa^{\bar{N}}\,\bar{\nu}J,\ n\kappa^{\stackrel{+}{N}}\,\stackrel{+}{\nu}J)\,J\right\rangle, \qquad N \equiv \bar{N} + \stackrel{+}{N}$$

$$\left\langle n\ell^N\,\alpha\nu\,LSJ\,|\,(n\kappa^{\bar{N}}\,\bar{\nu}J,\ n\kappa^{\stackrel{+}{N}}\,\stackrel{+}{\nu}J)\,J\right\rangle \;=\; \left\langle (n\kappa^{\bar{N}}\,\bar{\nu}J,\ n\kappa^{\stackrel{+}{N}}\,\stackrel{+}{\nu}J)\,J\,|\,n\ell^N\,\alpha\nu\,LSJ\right\rangle.$$

➢ The evaluation of the (unitary) transformation does generally not involve the radial (orbital) functions but depends only on the spin-angular functions.

➢ Although the notation of the non-relativistic and relativistic (sub-) shell states is quite similar in jjJ- and LSJ-coupling, these states generally belong to different irreducible representations of the SO_3 rotation group. This can be seen already from the splitting of each non-relativistic shell into two subshells as outlined above.

Transformation of atomic states:

➢ LSJ-coupled, non-relativistic CSF:

$$\left|\gamma^{\,(\mathrm{NR})}\,LSJ\right\rangle \;=\; \left|\left(\left(\,.\,\left(\left((n_1\ell_1^{N_1}\,\alpha_1\nu_1\,L_1S_1),\,(n_2\ell_2^{N_2}\,\alpha_2\nu_2\,L_2S_2)\right)\,L_{12}S_{12},\,(n_3\ell_3^{N_3}\,\alpha_3\nu_3\,L_3S_3)\right)\,L_{123}S_{123},\,...\right)\,LS\right)\,J\right\rangle$$

➢ jjJ-coupled, relativistic CSF:

$$\left|\gamma^{(\mathrm{R})}\, J\right\rangle \;=\; \left|\left(.\left(\left(\left((n_1\kappa_1^{-})^{\bar{N}_1}\,\nu_1^{-}J_1),\,(n_1\kappa_1^{+})^{\bar{N}_1}\,\nu_1^{+}J_1)\right)\,X_1^{+},\,(n_2\kappa_2^{-})^{\bar{N}_2}\,\nu_2^{-}J_2)\right)\,X_2^{-},\,(n_2\kappa_2^{+})^{\bar{N}_2}\,\nu_2^{+}J_2)\right)\,X_2^{+},\,...\right)\,J\right\rangle$$

➢ To determine the explicit transformation matrix for going from one to another (many-electron) basis, of course, all these quantum numbers above play an important role in practice. For the sake of simplicity, however, it is sufficient to just re-call that the jj-coupled CSF basis spans a (finite) part $\mathcal{H}^{(\mathrm{finite})}$ of the N-electron Hilbert space and that the matrix $\left(\left\langle\gamma^{(\mathrm{NR})}\,LSJ\,|\,\gamma^{(\mathrm{R})}\,J\right\rangle\right)$ just represent the (usual) Fourier coefficients for the expansion of an atomic state with respect to the basis $\{\left|\gamma^{(\mathrm{NR})}\,LSJ\right\rangle\}$ in $\mathcal{H}^{(\mathrm{finite})}$.

➢ Representation of atomic state functions:

$$|\psi_\alpha\rangle \;=\; \sum_r c_r^{(\mathrm{R})}(\alpha)\left|\gamma_r^{(\mathrm{R})}\,\mathbb{J}\right\rangle \;=\; \sum_t c_t^{(\mathrm{NR})}(\alpha)\left|\gamma_t^{(\mathrm{NR})}(L_t,,S_t)\,\mathbb{J}\right\rangle$$

➢ Formal construction of the $jjJ \;\rightarrow\; LSJ$ transformation matrix: If we denote the basis states of the (standard) product basis of the (subshell) states in jjJ- and LSJ-coupling by the $|\mathrm{standard-jjJ}\rangle$ and $|\mathrm{standard-LSJ}\rangle$, the transformation of a relativistic CSF can be formally written as

$$\begin{aligned}
\left|\gamma_r^{(\mathrm{R})}\,\mathbb{J}\right\rangle \;&=\; \sum_{\mathrm{standard-jjJ}} |\mathrm{standard-jjJ}\rangle\,\left\langle\mathrm{standard-jjJ}\,|\,\gamma_r^{(\mathrm{R})}\,\mathbb{J}\right\rangle \\
&=\; \sum_{\substack{\mathrm{standard-jjJ}\\ \mathrm{standard-LSJ}\\ \mathrm{atomic-LSJ}}} \left|\gamma_t^{(\mathrm{NR})}(L_t,\,S_t)\,JP\right\rangle\,\left\langle\gamma_t^{(\mathrm{NR})}(L_t,\,S_t)\,JP\,|\,\mathrm{standard-LSJ}\right\rangle\langle\mathrm{standard-LSJ}\,|\,\mathrm{standard-jjJ}\rangle\left\langle\mathrm{standard-jjJ}\,|\,\gamma_r^{(\mathrm{R})}\,\mathbb{J}\right\rangle \\
&=\; \sum_{Q_p,Q_r} \left|\gamma_t^{(\mathrm{NR})}(L_t,\,S_t)\,\mathbb{J}\right\rangle\;\times\;[\mathrm{LSJ-recoupling}]\;\times\;[\mathrm{product\ of\ LSJ-jjJ\ matrix\ elements}]\;\times\;[\mathrm{jjJ-recoupling}]
\end{aligned}$$

Here, a summation over $\mathrm{standard-jjJ},\ \mathrm{standard-LSJ},\ ...$ implies a summation over all quantum numbers that are not bound due to given values at the left-hand-side of the expression. In the last line, in particular, the summation runs over the (product basis) quantum numbers $Q_p = [(\alpha_1\nu_1\,L_1S_1),\,(\alpha_2\nu_2\,L_2S_2),\,...]$ as well as over the (re-coupling) quantum numbers as defined by the [LSJ-recoupling] and [jjJ-recoupling] recoupling coefficients, $Q_p = [J_1, J_2, J_{12},\, J_3, J_{123},\, ...,\, T_1, T_2, T_{12},\, T_3, T_{123},\, ...]$ with $\delta_{J_1,T_1}\,\delta_{J_2,T_2}\,\delta_{J_{12},T_{12}}\,...$.

➢ Re-coupling from the LSJ-product to the $(L_t, S_t)\,J$-coupled basis:

$$\left\langle \gamma_t^{(\mathrm{NR})}(L_t S_t)\,\mathbb{J}\,|\,\mathrm{standard-LS}\right\rangle \;\equiv\; [\mathrm{LSJ-recoupling}]$$

$$= \;\langle(.\,(.((L_1,L_2)\,L_{12},\;L_3)\,L_{123},\;...)\;L_t,\;(.((S_1,S_2)\,S_{12},\;S_3)\,S_{123},\;...)\;S_t\,)\;J\,|\,(.\,((\,(L_1,S_1)\,T_1,\;(L_2,S_2)\,T_2)\,T_{12},\;(L_3,S_3)\,T_3\,)\;T_{123},\;...)\;J\rangle$$

➢ Re-coupling from the jjJ-product to the jXJ-coupled basis:

$$\left\langle \mathrm{standard-jj}\,|\,\gamma_r^{(\mathrm{R})}\,\mathbb{J}\right\rangle \;\equiv\; [\mathrm{jjJ-recoupling}]$$

$$= \;\left\langle\left(.\left(\left((\overset{-}{J}_1,\overset{+}{J}_1)\,J_1,\;(\overset{-}{J}_2,\overset{+}{J}_2)\,J_2\right)\;J_{12},\;(\overset{-}{J}_3,\overset{+}{J}_3)\,J_3\right),\;J_{123},\;...\right)\;J\,|\,\left(.\left(\left((\overset{-}{J}_1,\overset{+}{J}_1)\,\overset{+}{X}_1,\;\overset{-}{J}_2\right)\,\overset{-}{X}_2,\;\overset{+}{J}_2\right)\,\overset{+}{X}_2,\;\overset{-}{J}_3\right)\,\overset{-}{X}_3,\;...\right)\;J\right\rangle$$

➢ In practice, the summation over such large sets of quantum numbers is often replaced by a (simpler or even single) summation over the allowed and predefined sets of quantum numbers.

3.5.b. Re-coupling coefficients

Zero open shell:

➢ CSF with *no* open shell are the same in the jjJ- and LSJ-coupling scheme,

$$\left|\gamma_r^{(\mathrm{R,\,closed})}\,\mathbb{J}=0^+\right\rangle \;\equiv\; \left|\gamma_r^{(\mathrm{NR,\,closed})}\,\mathbb{J}=0^+\right\rangle$$

and can be simply replaced with their (expansion) coefficients in the expansion of the wave function.

Single open shell:

➢ Re-coupling from the LSJ-product to the $(L_t, S_t)J$-coupled basis:

$$[\mathrm{LSJ-recoupling}] \;=\; \langle(L_1,S_1)\,J\,|\,(L_1,S_1)\,J\rangle \;=\; 1\,.$$

➢ Re-coupling from the jjJ-product to the jXJ-coupled basis:

$$[\text{jjJ} - \text{recoupling}] \;=\; \left\langle (\bar{J}_1, \overset{+}{J}_1)\, J \,|\, (\bar{J}_1, \overset{+}{J}_1)\, J \right\rangle \;=\; 1\,.$$

Two open shells:

➢ Re-coupling from the LSJ-product to the $(L_t, S_t)J$-coupled basis:

$$[\text{LSJ} - \text{recoupling}] \;=\; \langle ((L_1, L_2)\, L_{12},\, (S_1, S_2)\, S_{12})\, J \,|\, ((L_1, S_1)\, T_1,\, (L_2, S_2)\, T_2)\, J \rangle$$

$$= \sqrt{[T_1,\, T_2,\, L_{12},\, S_{12}]} \begin{Bmatrix} L_1 & S_1 & T_1 \\ L_2 & S_2 & T_2 \\ L_{12} & S_{12} & J \end{Bmatrix}, \qquad Q_r \;=\; [T_1, T_2].$$

➢ Re-coupling from the jjJ-product to the jXJ-coupled basis:

$$[\text{jjJ} - \text{recoupling}] \;=\; \left\langle \left((\bar{J}_1, \overset{+}{J}_1)\, J_1,\, (\bar{J}_2, \overset{+}{J}_2)\, J_2 \right) J \,|\, \left(((\bar{J}_1, \overset{+}{J}_1)\, \overset{+}{X}_1,\, \bar{J}_2),\, \bar{X}_2,\, \overset{+}{J}_2 \right) J \right\rangle$$

$$= (-1)^{\bar{J}_2 + \overset{+}{J}_2 + J_1 + J}\; \delta(\bar{J}_1, \overset{+}{J}_1, J_1)\; \delta_{J_1 \overset{+}{X}_1} \sqrt{[J_2, \bar{X}_2]} \begin{Bmatrix} J_1 & \bar{J}_2 & \bar{X}_2 \\ \overset{+}{J}_2 & J & J_2 \end{Bmatrix}, \qquad Q_r \;=\; [J_1, J_2].$$

➢ The summation over Q_r also implies all further quantum numbers that are needed in order to distinguish different subshell states in jjJ and to LSJ product basis, respectively. In JAC, this summation is performed by (1) applying the standard coupling $L \oplus S = T_{\text{low}}, ..., T_{\text{up}}$ and (2) by a summation over the corresponding subshell states from a internally (defined) list. An explicit summation over J_1, J_2 can be omitted because of orthogonality, and which gives rise to the Kronecker factors δ_{T_1,J_1}, δ_{T_2,J_2} .

Three open shells:

➢ Re-coupling from the LSJ-product to the $(L_t, S_t)J$-coupled basis:

$$[\text{LSJ}-\text{recoupling}] = \langle(((L_1, L_2)\, L_{12},\, L_3)\, L_{123},\, ((S_1, S_2)\, S_{12},\, S_3)\, S_{123})\, J \,|\, (((L_1, S_1)\, T_1,\, (L_2, S_2)\, T_2)\; T_{12},\, (L_3, S_3)\, T_3)\, J\rangle$$

$$= \ldots, \qquad Q_r = [T_1, T_2, T_{12}, T_3].$$

➢ Re-coupling from the jjJ-product to the jXJ-coupled basis:

$$[\text{jjJ}-\text{recoupling}] = \left\langle \left((\overset{-}{J}_1, \overset{+}{J}_1)\, J_1,\, (\overset{-}{J}_2, \overset{+}{J}_2)\, J_2)\, J_{12} (\overset{-}{J}_3, \overset{+}{J}_3)\, J_3 \right) J \,\middle|\, \left(((((\overset{-}{J}_1, \overset{+}{J}_1)\, \overset{+}{X}_1,\, \overset{-}{J}_2)\, \overset{-}{X}_2,\, \overset{+}{J}_2)\, \overset{+}{X}_2,\, \overset{-}{J}_3)\, \overset{-}{X}_3,\, \overset{+}{J}_3 \right) J \right\rangle$$

$$= \ldots, \qquad Q_r = [J_1, J_2, J_{12}, J_3].$$

➢ The summation over Q_r also implies all further quantum numbers that are needed in order to distinguish different subshell states in jjJ and to LSJ product basis, respectively. In JAC, this summation is performed by (1) applying the standard coupling $L \oplus S = T_{\text{low}}, \ldots, T_{\text{up}}$ and (2) by a summation over the corresponding subshell states from a internally (defined) list. An explicit summation over J_1, J_2, J_3 can be omitted because of orthogonality, and which gives rise to the Kronecker factors δ_{T_1,J_1}, δ_{T_2,J_2}, δ_{T_3,J_3}

3.5.c. In JAC implemented $jjJ - LSJ$ transformation

Transformation, notations & application:

➢ Representation $c_s^{(\mathrm{NR})}(\alpha)$ of atomic states.

$$|\psi_\alpha\rangle \;=\; \sum_t c_t^{(\mathrm{NR})}(\alpha)\,\Big|\gamma_t^{(\mathrm{NR})} LS\,J\Big\rangle \;=\; \sum_r c_r^{(\mathrm{R})}(\alpha)\,\big|\gamma_r^{(\mathrm{R})}\,J\big\rangle$$

➢ Unique label: $\big(\ldots\,\big((n_1\ell_1)^{N_1}\ {}^{2S_1+1}L_1;\,(n_2\ell_2)^{N_2}\ {}^{2S_2+1}L_2\big)\ {}^{2S_{12}+1}L_{12},\,(n_3\ell_3)^{N_3}\ {}^{2S_3+1}L_3\ldots\big)\ {}^{2S+1}L_J$
Such a label is assigned to each selected level, for instance, by printing
$[(n_1\ell_1)^{N_1}\ {}^{2S_1+1}L_1]\ {}^{2S_1+1}L_1:\ \ [(n_2\ell_2)^{N_2}\ {}^{2S_2+1}L_2]\ {}^{2S_{12}+1}L_{12}:\ \ [(n_3\ell_3)^{N_3}\ {}^{2S_3+1}L_3]\ {}^{2S_{123}+1}L_{123}:\ \ \ldots$

➢ In JAC, a $jjJ - LSJ$ transformation is performed for all selected levels if `jjLS = LSjjSettings(true, ...)` is set in `AsfSettings()`.

➢ In JAC, the LSJ-coupled expansion of selected levels is printed by default after the diagonalization of the (many-electron) Hamiltonian matrix.

➢ Apart from the LSJ assignment to atomic levels, JAC can rather easily support also the full transformation of the wave functions, if required for (nonrelativistic) computations. This is achieved by setting the cut-off parameter to *zero* in `LSjjSettings(...)`.

➢ A proper LSJ spectroscopic notation has been found useful in order to explain the excitation and decay properties of individual levels, at least qualitatively.

➢ The $jjJ - LSJ$ transformation of the (jjJ-coupled) CSF is supported for all shell structures with (up to) two open shells, including open s-, p-, d-shells. Further work is required to fully implement also transformation of open f-shells.

Implementation of $jjJ - LSJ$ transformation:

➢ Internally, a $jj - LS$ transformation of selected levels from a given mutliplet is carried out by the following steps:

1) Generation of a non-relativistic shell list for the given multiplet, based on a proper relativistic subshell list. The program terminates with an error message if the relativistic subshells of the given multiplet are ordered in *non-standard order*, for example, ..., $2p_{3/2}$, $2p_{1/2}$, ... or similar.

2) Extract all non-relativistic configurations that contribute to the given multiplet and generate a corresponding set of nonrelativistic CSF states; define an instance of a nonrelativistic basis.

3) Expand (in turn) each relativistic CSF into the non-relativistic basis and add their contributions to the (nonrelativistic) eigenvectors. This expansion is made independently of CSF with zero-, one-, two-, ... open (nonrelativistic) shells.

4) Check and print the LSJ expansion of all selected levels in a neat format with respect to the (nonrelativistic) configurations as well as CSF.

```
"""
‘struct  LS_jj_qn‘  ... defines a struct for the generalized quantum numbers (qn) of a LS_jj matrix element.
    + NN          ::Int64    ... occupation w = NN
    + QQ          ::Int64    ... subshell total quasispin 2*Q = nu
    + LL          ::Int64    ... subshell total angular momentum 2*L
    + SS          ::Int64    ... subshell total angular momentum 2*S
    + JJ          ::Int64    ... subshell total angular momentum 2*J
    + Nm          ::Int64    ... subshell Nm
    + Qm          ::Int64    ... subshell quantum number 2*Qm = nu^-
    + Jm          ::Int64    ... subshell quantum number 2*Jm
    + Qp          ::Int64    ... subshell quantum number 2*Qp = nu^+
    + Jp          ::Int64    ... subshell quantum number 2*Jp
"""
```

3.6. Atomic interaction amplitudes

Concept of interaction amplitudes:

➢ Hamiltonian matrix: The (scalar) Hamiltonian matrix elements in section **??** below describe the interaction energy between two ASF $|\alpha \mathbb{J} M\rangle$ and $|\alpha' \mathbb{J}' M'\rangle$, and these Hamiltonian matrix elements are perhaps the most simplest (many-electron) interaction amplitudes in atomic structure theory: $\langle \psi_\alpha \,|\, \mathbb{H} \,|\, \psi_{\alpha'} \rangle \;=\; \langle \alpha\, \mathbb{J} M \,\|\, \mathbb{H} \,\|\, \alpha' \mathbb{J}' M' \rangle \;=\; \sum_{rs}\, c_r^*(\alpha)\, H_{rs}\, c_s(\alpha')\, \delta_{JJ'}\, \delta_{MM'}\, \delta_{PP'}$.

➢ In relativistic atomic structure theory, in particular, $E_\alpha \;=\; \big\langle \alpha\, \mathbb{J} \,\big\|\, \mathbb{H}^{(\mathrm{DCB})} \,\big\|\, \alpha \mathbb{J} \big\rangle \;\approx\; \big\langle \alpha\, \mathbb{J} \,\big\|\, \mathbb{H}^{(\mathrm{DC})} \,\big\|\, \alpha \mathbb{J} \big\rangle$ is the total energy of a given level $|\alpha \mathbb{J}\rangle$.

➢ Many-electron interaction amplitudes: Using time-dependent perturbation theory and Fermi's Golden rule, most atomic level and transition properties can be expressed rather similarly as matrix elements of a (so-called) transition or *interaction* operator $\mathbb{T}$:

$$\langle \psi_\alpha \,|\, \mathbb{T} \,|\, \psi_\beta \rangle \;\;=\;\; \sum_{rs}\, c_r^*(\alpha)\, T_{rs}\, c_s(\beta)\,.$$

➢ Reduced matrix elements: More often than not, the transition operator $\mathbb{T}$ can be expressed in terms of spherical tensor operators of rank K, and, perhaps, with magnetic projections $Q \;=\; -K, -K+1, ..., K$, respectively. These spherical tensor operators transform under rotations like the spherical harmonics $Y_{KQ}(\vartheta, \varphi)$: $\mathbb{T} \;=\; \sum_{KQ}\, a(K,Q)\, \mathbb{T}^{(K)}_Q$. – Instead of the complete matrix elements, that include the magnetic projections M of the given atomic or configuration states as well as of the tensor operators, one often makes then use of the reduced matrix elements by applying the Wigner-Eckart theorem:

$$T^{(K)}_{Q,\,rs} \;\equiv\; \Big\langle \alpha_r\, \mathbb{J}_r M_r \,\Big|\, \mathbb{T}^{(K)}_Q \,\Big|\, \alpha_s\, \mathbb{J}_s M_s \Big\rangle \;=\; \langle J_r M_r,\, KQ \,|\, J_s M_s \rangle\; \big\langle \alpha_r\, \mathbb{J}_r \,\big\|\, \mathbb{T}^{(K)} \,\big\|\, \alpha_s\, \mathbb{J}_s \big\rangle \;.$$

➢ Although these reduced transition amplitudes are frequently utilized in the literature, for instance in order to discuss and analyze various atomic processes, not many codes make explicit use of these amplitudes as the *natural* building blocks for describing the level structure and properties of (open-shell) atoms and ions. – More often than not, a prior decomposition of these transition amplitudes into various types of one- and two-particle (reduced) matrix elements or even directly into radial integrals is made well before any implementation or coding is considered. This prior decompositon has seriously hampered the modelling of complex processes and is still the reason, why most atomic structure codes support the computation of just a few properties, cross sections and rates.

➢ Indeed, the different techniques, which are employed in the decomposition of the many-electron amplitudes, as well as the large number of definitions (and notations) of angular- or radial-type integrals in the literature has hampered not only the comparison of different codes

during the last decades but made it difficult also to (re-) use these entities for other properties than those considered by the original program developers.

➢ In JAC, we attempt to overcome this situation and to make consequent use of the many-electron amplitudes $\left\langle \alpha_r \, \mathbb{J}_r M_r \left| \, \mathbb{T}^{(K)}_Q \, \right| \alpha_s \, \mathbb{J}_s M_s \right\rangle$ and/or $\left\langle \alpha_r \, \mathbb{J}_r \left\| \, \mathbb{T}^{(K)} \, \right\| \alpha_s \, \mathbb{J}_s \right\rangle$ as the central building blocks for describing the interaction among the electrons as well as with external particles and fields.

➢ The concept of these interaction amplitudes has helped to simplify and maintain the code. — Moreover, it (will hopefully) enable us to exploit the many-electron interaction and transition amplitudes also in second- and higher-order processes, once an appropriate (intermediate) basis $\{\psi_\nu(PJM) \equiv |\alpha_\nu \, \mathbb{J}_\nu M_\nu\rangle \,, \;\; \nu = 1, ..., n_\nu\}$ has been constructed for modelling some given process.

Reduced matrix elements of spherical tensor operators for two CSF:

➢ For two CSF of well-defined symmetry, the reduced matrix elements of spherical tensor operators take always the form

$$\left\langle \gamma_r P_r J_r \left\| \, \mathbb{T}^{(K)} \, \right\| \gamma_s P_s J_s \right\rangle \;=\; \sum_t u(a_t b_t; K)\, X(a_t b_t; K), \qquad \mathbb{T}^{(K)} = \sum_j \mathbb{t}^{(K)}(j; \, ...) \qquad \text{... one part. operators}$$

$$\left\langle \gamma_r P_r J_r \left\| \, \mathbb{T}^{(K)} \, \right\| \gamma_s P_s J_s \right\rangle \;=\; \sum_t v(L_t; \; a_t b_t c_t d_t; K)\, X^{L_t}(a_t b_t c_t d_t; K), \qquad \mathbb{T}^{(K)} = \sum_{i<j} \mathbb{T}^{(K)}(i, j; \, ...) \quad \text{... symmetric two part. operators,}$$

and where $X(a_t b_t; K)$ and $X^{L_t}(a_t b_t c_t d_t; K)$ are one- and two-particle (effective) interaction strengths, cf. section 3.1. These interaction strengths are specific to the particular transition or interaction operator under consideration, and special care has to be taken that the same phase convention applies, if different interaction amplitudes are to be combined with each other.

➢ In practice, there are two steps in the computation of the transition amplitudes above for any pair of CSF, which need to be performed separately: The (pure) angular coefficients are usually calculated by means of some proper program, for instance ANCO (Gaigalas *et al.*, 2001), for either a pair or a whole set of CSF, and all the non-vanishing coefficients are then returned together to the calling routine. For these coefficients, the associated one- or two-particle interaction strengths are evaluated and summed up to form the requested matrix element T_{rs} of the transition matrix.

➢ To decrease the computational effort, these (one- and two-particle) interaction strength are often also *stored* and *re-utilized* in various applications, a feature which has not yet been considered in JAC.

➢ A similar decomposition of the many-electron matrix elements (amplitudes) as for the Hamiltonian matrix elements into a sum of *angular coefficient* × *interaction strength* can be made for every physically relevant (interaction) amplitude, independent of the particular rank of

the corresponding interaction operator. Since most atomic processes can be traced back to just a (very) few of such interaction or transition amplitudes, we made use of them as the *building blocks* in the design and implementation of the JAC tools.

Electron-electron interaction:

➢ The interaction among the electrons is described by the scalar operator that occurs in the Dirac-Coulomb-Breit Hamiltonian; cf. section 3.1

$$\mathbb{V}^{(\mathrm{e-e})} \;=\; \mathbb{V}^{(\mathrm{Coulomb})} + \mathbb{V}^{(\mathrm{Breit})} \;=\; \sum_{i<j} \left(\frac{1}{r_{ij}} + b_{ij} \right) .$$

➢ The Dirac-Coulomb-Breit Hamiltonian gives rise to the (reduced) interaction amplitudes

$$\left\langle \gamma_r P_r J_r \left\| \mathbb{V}^{(\mathrm{e-e})} \right\| \gamma_s P_s J_s \right\rangle \;=\; \left\langle \gamma_r P_r J_r \left\| \mathbb{V}^{(\mathrm{Coulomb})} \right\| \gamma_s P_s J_s \right\rangle \;+\; \left\langle \gamma_r P_r J_r \left\| \mathbb{V}^{(\mathrm{Breit})} \right\| \gamma_s P_s J_s \right\rangle .$$

For scalar operators, the full and reduced matrix elements coincide with each other and need not to be distinguished, since the Clebsch-Gordan coefficient in the Wigner-Eckert theorem then simply evaluates to $\langle J_r M_r, 00 \,|\, J_s M_s \rangle \;=\; \delta_{J_r J_s}\, \delta_{M_r M_s}$ for $K = Q = 0$.

➢ Since the Coulomb and Breit interaction operators are both scalar operators and since they contribute *additively* to the total electron-electron interaction, the same (pure) angular coefficients $v(L_t;\, a_t b_t\; c_t d_t; K = 0)$ occur in the decompsition of the amplitudes above, although different angular and parity selection rules apply for the various interaction strengths themselve, cf. section 3.1. In the computation of these amplitudes, the Breit interaction can therefore be added quite easily to the (usual) instantaneous Coulomb repulsion, if this appears appropriate for some particular process:

$$X^{(L)}(abcd) \;=\; X^{(\mathrm{L,\,Coulomb})}(abcd) \;+\; X^{(\mathrm{L,\,Breit})}(abcd) .$$

➢ The electron-electron interaction amplitudes above are indeed utilized (and calculated) in many components of the JAC tools.

Electron-photon interaction:

➢ The (relativistic) interaction of an electron with the radiation field is central for describing all photo-excition, ionization, emission and capture processes.

➢ The electron-photon interaction is described by the one-particle operator: $\mathcal{R}_\lambda(\mathbf{k}) \;=\; \sum_i \boldsymbol{\alpha}_i \cdot \mathcal{A}_{\lambda,i}(\mathbf{k})$; cf. chapter 5 below.

Electron-nucleus (hyperfine) interactions:

- For a nuclear spin $I > 0$, the hyperfine interaction describes the interplay of each atomic electron with the electric and magnetic (multipole) fields of the nucleus, apart from the dominant (electric-monopole) field of the nuclues due to its nuclear charge Ze.
- The two dominant contributions to the hyperfine interaction arise from the nuclear magnetic-dipole field $\mathbf{A} = \frac{\boldsymbol{\mu}\times\mathbf{r}}{r^3}$ and the electric-quadrupole field $\Phi(r) = \sum_{ij} \frac{r_i\, r_j}{2r^5} Q_{ij}$, while all higher magnetic and electric multipole fields, that may in principle occur for nuclei with spin $I > 1$, are typically negligible.

3.7. Atomic density operators and matrices

3.7.a. Single-electron reduced density matrix

First-order reduced density matrix:

➢ First-order reduced density matrix: This single-electron density matrix is known also as generalized density function and is given in terms of the N-electron wave function $\Psi(\mathbf{q}_1, ..., \mathbf{q}_N)$ by

$$\rho^{(1)}(\mathbf{q}_1, \mathbf{q}'_1) \;=\; N \int d\mathbf{q}_2 \;...\; d\mathbf{q}_N \; \Psi(\mathbf{q}_1, ..., \mathbf{q}_N) \; \Psi^*(\mathbf{q}'_1, ..., \mathbf{q}'_N)$$

From this first-order reduced density matrix, the (spin-less) electron density is simply obtained by the summation over all spin projections for $\mathbf{q}_1 = \mathbf{q}'_1$, and is usually normalized to number of electron of the sytem

$$\rho(\mathbf{r}_1) \;=\; \sum_{\sigma_1} \rho^{(1)}(\mathbf{q}_1, \mathbf{q}'_1), \qquad\qquad \int d\mathbf{r}\, \rho(\mathbf{r}) \;=\; \int dr\, d\vartheta\, d\varphi\, r^2\, \sin\vartheta\, \rho(\mathbf{r}) \;=\; N\,.$$

3.7.b. Atomic density matrix formalism

Motivation

➢ Density matrix formalism: In this formalism, the state of a physical system is characterized by means of statistical operators ρ which describe a single system or an ensemble of equally prepared collision systems in either a pure quantum state or in a mixture of different states with any given degree of coherence.

➢ The great benefit of using the (atomic) density matrix theory is that it enables one to "accompany" such an ensemble through one or several steps of excitation, decay and/or collision process, and without loss of quantum-mechanical information.

➢ Transition operators R of the density-matrix elements If one starts from a well-specified initial state of the system, as described by the operator ρ_i, all information about the atomic interactions, that govern the process, simply resides in the (so-called) *transition operators* R, and the final state operator just follows from the well-known relation: $\rho_f \;=\; R\,\rho_i\,R^+$.

- Building blocks: The electron-photon, electron-electron interaction and electron-nucleus interaction amplitudes from above are the building blocks to form the (scattering or) transition matrix for all atomic processes of interest and, hence, the density matrices of the system at the various steps of some particular excitation or decay process.
- For scattering states with a single electron in the continuum, these interaction amplitudes can be readily calculated by means of the Jac tools.
- Apart from the efficient computation of these building blocks, one also requires a simple book-keeping of these amplitudes in order to set-up the (atomic) density matrices at the various steps. To facilitate this handling and the book-keeping of these amplitudes, they are typically provided in Jac by some (amplitude) array, and together with all quantum numbers that are needed for their unique classification.
- The prior computation of the many-electron amplitudes enables one to start directly from the amplitudes (for one or several elementary processes) and to combine them into an appropriate form, in order to support the prediction of different atomic properties and parameters.
- Set-up of the density matrix: In practice, the computation of all interaction amplitudes is performed within three steps: (i) the generation of all necessary bound-state wave functions, (ii) the evaluation of the transition amplitudes between bound states and scattering states in the continuum, and (iii) the set-up and handling of the density matrices, i.e. by applying the formulas from chapter 8.

Density operator of an atom in level $|\alpha\mathbb{J}\rangle$:

➢ Mixed states of a level $|\alpha\mathbb{J}\rangle$: For an atom in a well-defined and isolated level $(\alpha\mathbb{J})$, a general mixed state with regard to its magnetic subspace (i.e. its projections M) can always be written as

$$\hat{\rho} \;=\; \sum_{MM'} c_{MM'}\; |\alpha\,\mathbb{J}M\rangle\,\langle\alpha\,\mathbb{J}M'|\,.$$

➢ Statistical tensor: Often, it is most convenient to represent the intermediate state of the ions in terms of its so-called statistical tensors

$$\rho_{kq}(\alpha\mathbb{J}) \;=\; \sum_{MM'} (-1)^{J-M'}\; \langle JM,\, J\,(-M')\,|\,kq\rangle\; \langle\alpha\,JM\,|\,\rho\,|\,\alpha\,\mathbb{J}M'\rangle\;.$$

and which are non-zero only for $0 \le k \le 2\,J$ and $-k \le q \le k$. These statistical tensors transform like the spherical harmonics.

➢ Although both, the (reduced, mixed) density matrix and the statistical tensors of some level $(\alpha\mathbb{J})$ are mathematically equivalent, the latter form can be transformed more easily and analogue to the spherical harmonics of rank k under a rotation of the coordinates.

➢ (Initial) polarization state of an atom: The polarization state of the initial atom can be characterized by the statistical tensors $\rho_{kq}^{\mathbf{n}_t}(\alpha_i\mathbb{J}_i)$, if defined with regard to the axis of the (target) polarization $\mathbf{n}_t = (\vartheta_t, \varphi_t)$. While the odd-rank tensors $k = 1, 3, \ldots$ are known to characterize the orientation of the target atom, the even-rank tensors $k = 2, 4, \ldots$ describe its alignment. The maximal rank of these tensors is limited by the condition $k \le 2\,J$.

3.8. Parity- and time-violating atomic interactions

3.8.a. Interactions beyond the standard model

Standard electro-weak model:

➢ The success of the standard electro-weak model of elementary particles is indeed extraordinary. It has been tested by many physical processes that cover more than ten orders of magnitude in momentum transfer. The standard model also correctly predicted the existence of new particles, such as the neutral Z boson.

- The standard model is sometimes understood also as a low-energy manifestation of a more complete theory that, perhaps, unifies the four forces. Many well-motivated extensions to the standard model have been proposed, such as supersymmetric, technicolour and left-right symmetric models, and they often predictr physical phenomena quite different from those of the standard model.
- CP symmetry: This symmetry refers to the combined symmetry of charge conjugation C and parity P.
- Violation of CP symmetry: The violation of CP symmetry was first discovered in 1964 in decays of the neutral K mesons, and this violation is taken into account by the standard electro-weak model by just a single complex phase in the quark-mixing matrix (the so-called Kobayashi-Maskawa mechanism).
- Various extensions of the standard model, such as supersymmetry, predict considerably larger EDM of the particles. Any observation of these EDM would therefore lead unambiguously to a hint of *new physics*.
- In addition, the standard model of particle physics is sometimes said to violate time-reversal (T) invariance, but again only through just a single phase in the Cabibbo-Kobayashi-Maskawa matrix, that mixes the quark flavors.
- For a rather long time, K mesons remained the only system in which CP-violation wwere observed explicitly. In 2001, however, the BaBar and Belle collaborations detected CP violation also for neutral B mesons, although this is still consistent with the predictions of the standard model.
- CPT symmetry: The (mathematical) structure of most gauge theories suggest that the combined symmetry of charge conjugation C, parity change P and time-reversal violation T has to be conserved.
- If CPT is *conserved*, as suggested by gauge theories, then CP-violation must be strictly accompanied by T (time-reversal) violation. Until the present, however, there has been no (undisputed) direct observation of T violation and its detection is of fundamental interest by itself. A direct detection of T-violation may shed further light also on the origin of CP-violation.
- Permanent electric dipole moment (EDM) The measurement of a per of neutrons, atoms, or molecule would show explicit evidence of T-violation.
- New physics: theories in physics beyond the standard model predict new sources of T-violation and these sources may lead to EDM that are many orders of magnitude larger than those from the standard model. This may allow EDM measurements by means of current experiments. Already the parameter space of quite popular extensions of the standard model, such as such as supersymmetry, multi-Higgs models, and left-right symmetric models, are strongly restricted by current measurements.
- Schiff theorem: If an external electric field acts upon a neutral atom, that consists out of non-relativistic point-like charged particles with some EDM and that only interact via electrostatic forces with each other, the field is screened exactly at each particle. This screening

arises due to the polarization of the atomic electrons by the external field. Therefore, an external electric field cannot induce an atomic EDM. As shown by Schiff, however, this schielding is incomplete if magnetic or finite-size effects are taken into account, and this may give rise in principle to an atomic EDM.

High-precision measurements on fundamental symmetries of atoms:

- Atomic high-precision experiments: High-precision measurements on the (violation of fundamental) symmetries in atoms are suitable to test the standard model of elementary particles and to search for new physics beyond it. Such precision experiments in atomic physics complement measurements in high-energy physics.
- Indeed, atomic experiments have played an important role in the verification of the standard model for more than 30 years ago already. While the first evidence for neutral-weak currents, i.e. the existence of the neutral Z boson, was discovered in neutrino scattering, a parity violation was first established in atomic experiments, and before it was later observed also in high-energy electron scattering.
- Today, atomic physics plays a major role in the search for *new* physics beyond the standard model.
- PNC measurements for cesium: For example, the cesium measurement on parity non-conservation in atomic physics have been found in excellent agreement with the standard model.
- Atomic PNC measurements: Instead of more and more accurate PNC measurements and computations, it appears useful today to perform such measurements for different isotopes of the same atom, since the ratio of the PNC signals for two different isotopes is rather insensitive to the details of the electron structure. For such measurements, the largest uncertainty to the PNC amplitudes arise from the unknown neutron distribution of the isotopes (Roberts *et al.*, 2014).

3.8.b. Parity-violating (P-odd, T-even) interactions

Motivation:

- Parity non-conservation (PNC) effects: These effects arise in atoms largely due to the exchange of Z^0-bosons between the atomic electrons and the nucleus.
- The exchange of Z^0 bosons is formally described by the Weinberg-Salam theory and leads to (observable) phenomena, such as circular dichroism and optical rotation, and which have been investigated in order to detect P-violation in cesium, thallium, bismut and plumbum.
- There is also another contribution to atomic parity violation due to the exchange of Z^0 bosons between each pair of electrons; however, this effect is negligibly small for heavy atoms and well suppressed by a factor $10^{-3} \ldots 10^{-4}$. This contribution is usually neglected in most PNC studies.
- PNC effects in atoms can be caused also by nuclear moments, i.e. by parity-violating electromagnetic form factors that occur in addition to the usual nuclear magnetic-dipole and electric-quadrupole moments (form factors).
- Rare-earth atoms: Several PNC experiments in rare-earth atoms have been suggested for close-lying levels of opposite parity in order to enhance the PNC effects. Moreover, rare-earth often have various stable isotopes and, hence, the dependence on atomic theory can be removed by taking ratios of the measured PNC contributions for different isotopes.
- Enhancement of PNC signals: Several physical factors can contribute to an enhancement (or suppression) of the measured parity-violating signal for selected atomic transitions: (i) The PNC amplitude is expected to scale slightly faster than Z^3 with the nuclear charge of the ions and make heavy elements even more favorable; and (ii) the existence of close-lying levels of different parity. For the alkaline-earth elements, there are often levels with a splitting $\sim$ 10 cm^{-1} which need to be compared to the well-studied $6s - 7s$ PNC transition in Cs with a splitting $\sim$ 104 cm^{-1} (Roberts *et al.*, 2014).

Nuclear-spin independent P-odd electron-nucleus interactions:

- Nuclear-spin independent Hamiltonian: For non-relativistic nucleons, the nuclear-spin independent Hamiltonian for the P-odd electron-nucleus interaction is given by the effective single-electron operator

$$\mathbb{H}^{(\mathrm{weak-charge})} \;=\; -\frac{G}{\sqrt{2}}\,\gamma_5\;\left[Z\,C_{1p}\,\rho_p(r)\;+\;N\,C_{1n}\,\rho_n(r)\right]\,,$$

where Z and N are the number of protons and neutrons, and where the proton and neutron densities are normalized to unity, $\int dr\;\rho_p(r) = 1 = \int dr\;\rho_n(r)$.

➢ If the proton and neutron densities coincide, $\rho_p = \rho_n \equiv \rho$, the nuclear-spin independent Hamiltonian simplifies and can be described in terms of a nuclear weak-charge Q_W,

$$\mathbb{H}^{(\text{weak}-\text{charge})} = -\frac{G}{2\sqrt{2}}\,\gamma_5\,Q_W\,\rho\,.$$

➢ Nuclear weak charge Q_W: This charge is very close to the neutron number and is in lowest order in the electro-weak interaction given by

$$Q_W = -N + Z\,(1 - 4\sin^2\theta_W) \approx -N\,.$$

This value for Q_W is modified however by radiative corrections.

➢ The nuclear-spin independent electron-neutron interaction is a scalar that mixes levels (states) with the same total electron angular momentum but different parity.

➢ For heavy atoms, the nuclear-spin independent interaction due to the nuclear weak-charge gives the dominat contribution to parity violation, when compared to other mechanisms.

Nuclear-spin dependent P-odd electron-nucleus interactions:

➢ P-odd interactions that depend on the nuclear spin I: There are different interactions that depend on the nuclear spin I due to:
i) the neutral weak current; ii) hyperfine-induced neutral currents; or iii) the nuclear anapole moment.

➢ Spin-dependent electron-nucleus interactions: The dominating contribution in heavy atoms comes from the nuclear anapole moment (κ_a), while smaller contributions still arise from the Z_0 exchange due to spin-dependent electron-nucleus weak interactions (κ_z) as well as the interaction of the weak charge (κ_Q) with the magnetic hyperfine interaction (Roberts *et al.*, 2014).

➢ Interaction with the nuclear anapole: The anapole moment gives typically the dominant nuclear-spin dependent P-odd electron-nucleus interaction. The nuclear anapole moment arises from P-odd interactions inside the nucleus. These interactions manifest themselve in atoms through a slightly modified electro-magnetic interaction of the nucleus with atomic electrons.

➢ The anapole moment κ_a increases with the atomic mass number, $\kappa_a \propto A^{2/3}$ and, thus, dominates in heavy atoms, when compared to other nuclear-spin dependent mechanisms listed above.

➢ Hamiltonian for the electron-anapole (-moment) interaction: For an external nucleon with orbital angular momentum ℓ, the Hamiltonian is given by (Dzuba *et al.*, 2009)

$$\mathbb{H}^{(\mathrm{anapole})} = \frac{G}{\sqrt{2}}\,\kappa_a\,\frac{K}{I(I+1)}\,\alpha\cdot\mathbf{I}\,\rho(r), \qquad K = (I+1/2)\,(-1)^{I+1/2-\ell}.$$

Anapole moment:

➢ Anapole moment: The anapole moment arises from P-odd, T-even nuclear moments (i.e. parity-violating nuclear forces) and usually requires less accurate atomic structure calculations. This may simplify the search for favorable conditions and atomic systems.

➢ The notion of the anapole moment was introduced by Zel'dovich just after the discovery of parity violation.

➢ However, an nuclear anapole moment was unambiguously detected only 30 years later. In 1997, a group at Boulder measured a nuclear anapole moment in ^{133}Cs to an accuracy of 14 % in an atomic experiment. This is considered as the first observation of an electromagnetic moment that violates fundamental discrete symmetries (Ginges and Flambaum, 2003).

➢ A P-odd, T-even anapole moment of the nucleus arises due to the presence of a parity violating weak interaction between nucleons.

➢ The anapole moment is directed along the nuclear spin **I**: $\langle \mathbf{a} \rangle = -\pi \langle r^2 \mathbf{j} \rangle = a\, \mathbf{I}/I$. Since the current vector **j** changes its sign under reflection of coordinates, but not the spin **I**, an anapole moment need to violate parity but not time-reversal symmetry.

3.8.c. Time-reversal violating (P-odd, T-odd) interactions

Motivation:

➢ Time-reversal symmetry: Many physical systems and processes are asymmetric under time-reversal. In classical mechanics, for example, a velocity reverses its direction under time reversal, $v \rightarrow -v$, while an acceleration does not. This time-reversal asymmetry is often associated with some energy dissipation and, hence, with the second law of thermodynamics. Without dissipation, the laws of mechanics are usually considered to be invariant with regard to time-reversal.

➢ In nuclei, P-odd and T-odd nuclear moments can arise due to an intrinsic EDM of the nucleons, or due to P-odd and T-odd nuclear forces. The P-odd and T-odd nuclear forces induce larger nuclear moments than a single nucleon EDM.

➢ Various P-odd and T-odd interactions can be considered, especially for heavy atoms and ions. These interaction include the tensor-pseudotensor electron-nucleon (e-N) interaction, the scalar-pseudoscalar (e-N) interaction, the nuclear Schiff moment and the interaction of the electron EDM with the internal nuclear magnetic field of the atom.

➢ An atomic EDM can be induced if the nucleus possesses P-odd and T-odd nuclear moments.

P-odd & T-odd Hamiltonians due to electron-nucleus interactions:

➢ The expressions for $\mathbb{H}^{(\text{scalar}-\text{pseudoscalar})}$ and $\mathbb{H}^{(\text{weak charge})}$ as well as $\mathbb{H}^{(\text{I}-\text{independent})}$ are quite similar.

➢ These electron-nucleus interactions mixes atomic states of opposite parity and induces a static electric-dipole moments in atoms.

P-odd & T-odd nuclear moments:

➢ The operators $\mathbb{H}^{(\text{scalar}-\text{pseudoscalar})}$ and $\mathbb{H}^{(\text{tensor})}$ have both electronic and nuclear components. While these Hamiltonians are overall scalar, the electronic and nuclear operators can be of any (equal) rank. To obtain any non-zero matrix element, therefore, the triangle rule for coupling of angular momenta imposes restrictions on the angular momenta of the electron and nuclear states.

➢ Nuclear moments that violate parity and time-reversal invariance: electric dipole, magnetic quadrupole, electric octupole. For an nuclear electric-dipole moment, the Hamiltonian must be of the form $\mathbb{H}^{(\text{Schiff moment})}$ in order to mix electron states of opposite parity.

➢ Nuclear electric-dipole (Schiff) moments: If $\mathbf{S}$ is nuclear Schiff moment, the associated P-odd and T-odd Hamiltonian is given by

$$\mathbb{H}^{(\text{Schiff}-\text{moment})} \;=\; -e\,\phi^{(\text{Schiff}-\text{moment})} \;=\; -4\pi e\,\mathbf{S}\cdot\nabla\,\delta(r).$$

Here $\phi^{(\text{Schiff}-\text{moment})}$ is the electrostatic potential of the nucleus that corresponds to a P-odd and T-odd charge distribution.

➢ Nuclear magnetic-quadrupole moments (MQM): A general expression for the nuclear MQM can be constructed in terms of the total angular momentum of the system I,

$$M_{ij} \;=\; -e\,\frac{3}{2}\,\frac{M}{I(2I-1)}\,\left[I_iI_j+I_jI_i-\frac{2}{3}\,I(I+1)\delta_{ij}\right].$$

The quantity M is conventionally referred to as the nuclear MQM and is defined as the maximum projection of M_{ij} upon the nuclear axis, $M = M_{zz}$. The magnetic quadrupole moment violates parity and time-reversal invariance.

3.8.d. Time-reversal violating atomic electric-dipole moments

Motivation:

➢ A non-zero electric-dipole moment (EDM) of atoms require P-odd and T-odd interactions, either among the nucleons or the electrons and the nucleus.

➢ Therefore, the null measurements of EDM in atoms place severe restrictions upon new sources of CP-violation that often arise in models beyond the standard model, such as supersymmetry.

➢ The nuclear EDM exceeds the EDM of single nucleons by one to two orders of magnitude. P-odd and T-odd nuclear forces generate all P-odd and T-odd nuclear moments, such as the Schiff and MQM moments. These nuclear moments can be 10-to-100 times larger than those generated by the presence of a nucleon EDM.

➢ In the standard model, an atomic EDM is suppressed by many orders when compared to predictions from (so-called) *new* theories. Therefore, the detection of an EDM would be unambiguous evidence of new physics, even if it contributes only weakly to a very small signal in atomic parity violation.

➢ An atomic EDM can arise from various P-odd and T-odd mechanisms (Ginges and Flambaum, 2004): i) an intrinsic EDM of an electron; (ii) a P-odd and T-odd electron-nucleon interaction; (iii) an intrinsic EDM of an external nucleon; (iv) a P-odd and T-odd nucleon-nucleon interaction.

➢ Until the present, no permanent EDMs in neutrons, atoms or molecules have been detected.

➢ The best limits on the electron electric dipole moment is presently derived from measurements of atomic EDM.

Physics of the atomic EDM:

➢ An atomic EDM is associated with an atomic level $|\alpha\mathbb{J}\rangle$ and arises due to the admixture of levels (states) $|\nu\mathbb{J}_\nu\rangle$ with opposite-parity wave functions. This atomic EDM has the form

$$\mathbb{d}^{(\text{atomic EDM})} \;=\; 2\sum_{\nu}\frac{\langle\alpha\mathbb{J}\,|\mathbb{D}|\,\nu\mathbb{J}_\nu\rangle\,\langle\nu\mathbb{J}_\nu\,|\mathbb{H}^{(\text{PT})}|\,\alpha\mathbb{J}\rangle}{E_\alpha\,-\,E_\nu} \;=\; d^{(\text{atomic EDM})}\,\frac{\mathbf{F}}{F}\,,$$

where $\mathbb{D}$ is the electric dipole operator, $\mathbb{H}^{(\text{PT})}$ the P-odd and T-odd operator that mixes $|\alpha\mathbb{J}\rangle$ with the set of wave functions $|\alpha_\nu\mathbb{J}_\nu\rangle$, and F is the total angular momentum of the atom corresponding to the state $|\alpha\mathbb{J}\rangle$.

➢ A typical EDM experiment is performed in parallel electric and magnetic fields and can be described by the Hamiltonian

$$\mathbb{H}^{(\text{em field})} \;=\; -\mu\cdot\mathbf{B}\,-\,\mathbf{d}\cdot\mathbf{E}.$$

➢ A linear Stark shift is measured by observing the change in frequency when the electric field is reversed, since it is sensitive to the P-odd and T-odd term $\mathbf{E}\cdot\mathbf{B}$.

➢ Interaction Hamiltonian of the electron EDM with an internal atomic electric field $\mathbf{E}^{\text{int}}$: The Hamiltonian for interaction of the electron EDM with internal atomic electric field $\mathbf{E}^{\text{int}}$ can be written as (Dzuba and Flambaum, 2009)

$$\mathbb{H}^{\text{eEDM}-\text{electric}} \;=\; -\,d_e\sum_{i=1}^{N}(\gamma_o\,-\,1)_i\,\mathbf{\Sigma}_i\cdot\mathbf{E}^{\text{int}},\qquad\qquad \mathbf{\Sigma}_i\;=\;\begin{pmatrix}\boldsymbol{\sigma_i} & 0\\ 0 & \boldsymbol{\sigma_i}\end{pmatrix}.$$

➢ Atomic EDM: An atomic EDM can be caused by the interaction of the electron EDM (if it exists) with either the internal electric field of the atom or the scalar-pseudoscalar electron-nucleon (T-odd, P-odd) interaction; an EDM of atoms in their ground state is then given by

$$\mathbf{d}_{\text{atom}} \;=\; 2\sum_{\nu}\frac{\langle 0\,|\mathbb{D}|\,\nu\rangle\,\langle\nu\,|\mathbb{H}^{\text{eEDM}-..}|\,0\rangle}{E_o\,-\,E_\nu}$$

where $|0\rangle$ is the atomic ground state, $\mathbb{D} = -e \sum_i \mathbf{r}_i$ is the electric-dipole operator and $\mathbb{H}^{\mathrm{eEDM}-\cdot\cdot}$ the (P-odd, T-odd) interaction operator. Here, the summation need formally to be performed over the complete many-electron spectrum of the intermediate levels ν with total energies E_ν .

➢ Measurements of EDMs in paramagnetic atoms, i.e. for a total electron angular momentum $J \neq 0$, are most sensitive to leptonic sources of P- and T-violation, and especially the electron EDM.

➢ In contrast, measurements of EDM in diamagnetic systems with zero total electron angular momentum are most sensitive to P-odd and T-odd mechanisms in the hadronic sector.

3.9. Elements from atomic spectroscopy

3.9.a. Line profiles

Line profiles in atomic spectroscopy:

➢ Experimental photon energy distribution: In order to fit the observed spectra to Fano's formula, the experimental photon energy distribution (window function) need usually to be taken into account. This experimental window function can often be represented by Gaussian with a full-width-at-half maximum (FWHM) according to the experimental energy spread. Therefore, the Fano profile has to be convoluted with a Gaussian. Analogue convolutions are known from the Voigt line profiles in the emission spectroscopy of hot gases which also includes the convolution of a Lorentzian with a Gaussian line curve.

➢ Convolution of a Lorentzian and a Gaussian line profile: The Voigt profile arises from the convolution of a Lorentzian and a Gaussian line profile with the Lorentzian and Gaussian FWHM Δ_L and Δ_G

$$L(E) \;=\; \frac{2\,A}{\pi}\;\frac{\Delta_L}{4(E-E_r)^2\;+\;\Delta_L^2}, \qquad G(E) \;=\; \frac{2}{\Delta_G}\sqrt{\frac{\ln 2}{\pi}}\;\exp\left[-\frac{4(\ln 2)\,E^2}{\Delta_G^2}\right], \qquad \int dE\,L(E) \;=\; A, \qquad \int dE\,G(E) \;=\; 1$$

$$V(E) \;=\; \int_{-\infty}^{\infty} dE'\,L(E')\,G(E'-E) \;=\; A\frac{4\sqrt{\ln 2}}{\pi^{3/2}\Delta_G}\int_{-\infty}^{\infty} dE'\;\frac{\Delta_L}{4(E'-E_r)^2\;+\;\Delta_L^2}\exp\left[-\frac{4(\ln 2)\,(E-E')^2}{\Delta_G^2}\right].$$

➢ Convolution of a Lorentzian and a Gaussian line profile: The convolution of a Lorentzian profile with a Gaussian function generally results in a Faddeeva function that can be utilized for a fast and accurate evaluation of the convolution, e.g., in peak fitting routines (Schippers 2018). With the following definitions, the Voigt profile can be expressed in terms of the Fadeeva function as

$$t \;=\; \frac{2\sqrt{\ln 2}(E'-E)}{\Delta_G}, \qquad x \;=\; \frac{2\sqrt{\ln 2}(E_r-E)}{\Delta_G}, \qquad y \;=\; \frac{\Delta_L\sqrt{\ln 2}}{\Delta_G}, \qquad z \;=\; x+iy$$

$$V(E) \;=\; A\frac{2\sqrt{\ln 2}}{\Delta_G\sqrt{\pi}}\,\frac{1}{\pi}\int_{-\infty}^{\infty} dt\;\frac{y\,e^{-t^2}}{(t-x)^2+y^2}dt \;=\; A\frac{2\sqrt{\ln 2}}{\Delta_G\sqrt{\pi}}\;\Re[w(z)]$$

➢ Faddeeva function $w(z)$: The Faddeeva function is a scaled complex error function which, for $\Im z = y > 0$, is defined as (Schippers 2018)

$$w(z) = e^{-z^2}\,\mathrm{erfc}(-iz) = \frac{i}{\pi}\int_{-\infty}^{\infty} dt\,\frac{e^{-t^2}}{z-t}, \qquad \Re[w(z)] = \frac{1}{\pi}\int_{-\infty}^{\infty} dt\,\frac{y e^{-t^2}}{(t-x)^2+y^2}, \qquad \Im[w(z)] = \frac{-1}{\pi}\int_{-\infty}^{\infty} dt\,\frac{(t-x)e^{-t^2}}{(t-x)^2+y^2}.$$

$\Re[w(x+iy)]$ and $\Im[w(x+iy)]$ can be displayed as functions of the scaled energy x for different ratios y of Lorentzian and Gaussian widths.

➢ Convolution of a Fano and a Gaussian line profile: One can re-define the Fano line profile slightly differently from above with a positive amplitude $a > 0$ and with the same definition of t, x and y as above. This definition of the Fano profile is consistent with the theoretical treatment of the atomic photoabsorption cross section. For the convolution of a Fano and a Gaussian line profile, this gives rise to (Schippers 2018):

$$F(E) = \frac{2a}{q^2\Delta_L\pi}\left[\frac{(q+\epsilon)^2}{1+\epsilon^2}-1\right], \qquad \lim_{q\to\infty} F(E) \to L(E)\,.$$

$$C(E) = \int_{-\infty}^{\infty} dE'\,F(E')\,G(E'-E) = \frac{2a}{q^2\Delta_L\pi}\left[\frac{1}{\sqrt{\pi}}\int_{-\infty}^{\infty} dt\,\frac{[qy+(t-x)]^2 e^{-t^2}}{(t-x)^2+y^2}dt - 1\right], = \frac{a}{q^2}\frac{2\sqrt{\ln 2}}{\Delta_G\sqrt{\pi}}\left\{(q^2-1)\,\Re(w) - 2q\,\Im(w)\right\}.$$

3.9.b. Atomic target distributions

Target distributions:

➢ Gaussian target distribution: A localized but macroscopic target can be described by a Gaussian probability distribution that is centred with width σ around the impact parameter $\mathbf{b}_0$ with regard to the beam axis. Then the probability distribution is given by

$$f(\mathbf{b};\mathbf{b}_0) = \frac{1}{2\pi\sigma^2}\,e^{-\frac{(\mathbf{b}-\mathbf{b}_0)^2}{2\sigma^2}} = \frac{1}{2\pi\sigma^2}\,e^{-\frac{b^2+b_0^2-2\,b\,b_0\,\cos\phi_b}{2\sigma^2}}.$$

3.9.c. Miscellaneous

Experimental features & conditions:

➢ Resonant behaviour: A resonance generally refers to a drastic change in the intensity of some signal, while the energy (or some other other parameter) changes only little. In quantum physics, resonances in the intensity pattern are often accompanied by some – more or less strong – interference of different quantum amplitudes.

➢ Energy calibration of photon-ion merged-beams measurements: Since the ions move opposite to the photon beam, the (photon) energy need to be Doppler corrected within the framework of the ion. If $E^{\,(\mathrm{lab})}$ is the photon energy in the laboratory and $\theta \simeq 180^o$ the angle between the beams, the Doppler-shifted energy is:

$$E^{\,(\mathrm{merged-beam})} \;=\; \frac{E^{\,(\mathrm{lab})}}{\gamma\,(1\,+\,\cos\,\theta)}, \qquad\qquad \gamma \;=\; \frac{1}{\sqrt{1\,-\,\beta^2}}, \qquad\qquad v \;=\; \beta\,c.$$

➢ Energy calibration of photon-ion merged-beams measurements: The ion velocity v can be derived from the acceleration voltage $U^{\,(\mathrm{acceleration})}$ via the kinetic energy $E^{\,(\mathrm{kin})}$ of the ions as well as their mass $M^{\,(\mathrm{ion})}$ and their Lorentz factor γ as (Müller *et al.*, 2018)

$$E^{\,(\mathrm{kin})} \;=\; qe\,U^{\,(\mathrm{acceleration})} \;=\; (\gamma\,-\,1)\,M^{\,(\mathrm{ion})} \qquad\longrightarrow\qquad \beta \;=\; \sqrt{1\,-\,\frac{1}{(1+x)^2}}, \qquad x \;=\; \frac{qe\,U^{\,(\mathrm{acceleration})}}{M^{\,(\mathrm{ion})}\,c^2}$$

$$E^{\,(\mathrm{merged-beam})} \;=\; \frac{E^{\,(\mathrm{lab})}}{(1\,+\,x)\,+\,\sqrt{2x\,+\,x^2}\,\cos\theta} \qquad\longrightarrow\qquad E^{\,(\mathrm{lab})}\,\Big[(1\,+\,x)\,+\,\sqrt{x}\,\sqrt{2\,+\,x}\Big] \qquad \text{for} \quad \theta \approx 180^o\,.$$

➢ Madelung ordering *versus* Coulomb ordering of shells: While the Coulomb order of (sub-) shells follow from the hydrogenic solutions $n\ell$, $\ell \,=\, 0, .., n-1$, $n \,=\, 1, 2, \ldots$, the Madelung order describes the shell order as it is filled by the elements from the periodic table

$1s,\ 2s,\ 2p,\ 3s,\ 3p,\ 4s,\ 3d,\ 4p,\ 5s,\ 4d,\ 5p,\ 6s,\ 4f,\ 5d,\ 6p,\ 7s,\ 5f,\ 6d,\ \ldots.$

Rate coefficients $\alpha(T)$:

➢ Rate coefficients $\alpha(T)$: The rate coefficient of a capture or transfer process [in cm^3/s] is generally temperature-dependent and obtained by averaging the energy-dependent cross section $\sigma_{fi}(E)$ over a Maxwellian velocity distribution (Babb *et al.*, 2017)

$$\alpha(T) \;=\; \left(\frac{8}{m\,pi}\right)^{1/2} \left(\frac{1}{k_B\,T}\right)^{3/2} \int_0^\infty dE\; E\;\sigma_{fi}(E)\;\exp\left(-\frac{E}{k_B\,T}\right), \qquad\qquad k_B \;=\; 1.380\times 10^{-23}\;\mathrm{J\,K^{-1}}.$$

Here, m refers to the (reduced) electron mass-

➢ Quasi-rate $R(E)$: An effective energy-dependent rate of a capture or transfer process from state $i \to f$ can be obtained from the relationship (Babb *et al.*, 2017)

$$R_{fi}(E) \;=\; v\;\sigma_{fi}(E) \;=\; \sqrt{2\,E/m}\;\;\sigma_{fi}(E) \qquad\qquad [\mathrm{in\ cm^3\ s^{-1}}]$$

and can be used for estimating the rate coefficients $\alpha(T)$ of the given process if the energy E of the incident particles is converted into a temperature T.

4. Atomic representations

Methods, characterization & applications. An overview:

- Post-HF methods: Moller-Plesset (Rayleigh-Schrödinger) perturbation theory, configuration interaction (CI) expansions, coupled cluster (CC) theory, convergent close-coupling.
- Various *ab-initio* many-electron methods have been developed during the last decades to accurately describe the level structure and properties of atoms and ions with a relatively simple shell structure, such as the configurations interaction (CI), many-body perturbation theory (MBPT), coupled-cluster (CC) theory, correlation potential (CP) or multiconfigurational Dirac-Fock (MCDF) methods. These *ab-initio* methods are frequently applied for atoms and ions with just a (very) few valence electrons above a closed-shell core but cannot be applied so easily to systems with more than, say, four valence electrons.
- Weak or dynamic correlations: These correlation can be captured in a systematic fashion by various post-HF methods. More often than not, these weak correlations are built upon a single Slater determinant, although a multi-reference formulation also exist for most of these methods. In single-reference methods, however, very large expansions are often needed in order to retrieve the strong (static) correlation.
- Size-consistency of (molecular) wave functions: For two noninteracting subsystems, the total wavefunction should be separable and the total energy additive. While the coupled-cluster method is always size-consistent because of its exponential wavefunction ansatz, a typical configuration-interaction wave function with k virtual excitations is usually not size-consistent for $N > k$ electrons in the system.
- An independent optimization of the wave functions for level groups of different total symmetry $\mathbb{J}$ still ensures that parts of the electron relaxation of the electron density is taken into account. Of course, an independent variation finally also results in a set of orbitals which, for a given level group, are not orthogonal to the orbitals of any other group.
- In the study of transition probabilities and other atomic processes, this relaxation of the electron density causes technical problems but, otherwise, often yields results that are in better agreement with experiments.
- Atomic resonances: Since inner-shell hole states lay — by its very nature — high up embedded within the continuum of the next higher charge state, these atomic states have to be treated as resonances. From scattering theory, several (formal) approaches, such as the K-matrix

, exist in order to treat the interaction among different resonances or decay channels properly. Up to the present, it remains open whether and to which extent such sophisticated scattering approaches can be properly implemented into many-electron structure codes and how well they are suitable also for open-shell systems.

➢ Description of scattering states: The size of the CSF expansions often increases very rapidly if the atomic bound-state density is *coupled* to the electron continuum, since the presence of one (or more) electrons in the continuum automatically leads to extra open shells. Such an *additional* increase of the CSF expansion and, hence, of the computations practically occurs in the study of all ionization, autoionization and scattering processes.

➢ Less attention was paid overall the years to the calculation of atomic properties other than line strength, hyperfine structures or isotopes shifts. With the Jac tools, we here wish to provide a simple access to the computation of (relativistic) atomic transition, ionization and capture properties, including the description of scattering states with one or more electrons in the continuum, and along with many other features of these tools.

➢ CSF basis: In practice, the definition of a physically appropriate basis turns out to be less simple. In particular, the difficulties in calculating *open-shell* atoms and ions have long been underrated. The first (successful) structure calculations of a few simple atoms and ions in the sixties and seventies quickly led to the popular fallacy, that it would take only a bit more effort and computational power in order to theoretically predict the structure and properties of atoms in rather arbitrary configurations.

➢ We know much better now: Many atomic properties have been found to depend rather sensitive on the *correlated* motion of the electrons and, thus, on the shell structures of the atoms and ions. Although much larger computations are feasible today, most open-shell atoms are yet not well understood. In fact, the *real* challenge when dealing with open-shell structures concerns the very rapidly growing wave function expansions, if one or several open shells are already involved within the reference configuration(s).

➢ Many-particle states close to the particle emission threshold: These states often display unusual properties, such as halo and Borromean structures, clusterization phenomena, or cusps in various observables. This behaviour arises due to the strong coupling of (quasi-) bound states to the continuum.

➢ Complex eigenvalue Schrödinger equation (CESE) method: The SE with a complex or non-hermitian potential has been studied at various places, especially in order to describe resonance states.

Elements from atomic representation theory:

➢ Atomic state function (ASF): Similar to the well-known – non-relativistic and symmetry-adapted – Hartree-Fock (HF) method, in which the state of an atom or ion is approximated by a single (symmetry-adapted) Slater determinant, an atomic state function is written in

the CI or multi-configuration Dirac-Hartree-Fock (MCDHF) method as linear combination of configuration state functions (CSF) with well adapted symmetry

$$|\alpha\ \mathbb{J}M\rangle \ \equiv\ \psi_\alpha(\mathbb{J}M) \ =\ \sum_{r=1}^{n_c} c_r(\alpha)\ |\gamma_r\, PJM\rangle\ .$$

In this ansatz, n_c is the number of CSF, $\mathbb{J} \equiv J^P$ the total angular momentum and parity of the state, and α refers to all (further) quantum numbers that are needed to specify the state uniquely. Moreover, $\{c_r(\alpha)\}$ denotes the representation of the atomic state in the given basis.

➢ Secular equation: For a given CSF basis, the representation of an atomic state above (i.e. the mixing coefficients $\mathbf{c}(\alpha) \equiv (c_1(\alpha), c_2(\alpha), \ldots, c_{n_c}(\alpha))$ is obtained by solving the secular equation

$$\det\left(\mathbf{H} - E_\alpha^{(n_c)}\,\mathbf{I}\right) \ =\ 0\,, \qquad\qquad \mathbf{H} \ =\ (H_{rs}) \ =\ \left(\left\langle\gamma_r\, PJM\,|\,\mathbb{H}\,|\,\gamma_s\,\bar{P}\bar{J}\bar{M}\right\rangle\ \delta_{P\bar{P}}\,\delta_{J\bar{J}}\,\delta_{M\bar{M}}\right)$$

and where $E_\alpha^{(n_c)}\,(PJ)$ denotes the eigenvalue.

➢ Hamiltonian matrix: This matrix is block-diagonal in the total parity and angular momentum of the atom, and this is independent of the particular choice of the electron-electron interaction in the Hamiltonian.

➢ Hamiltonian matrix: Since the Hamiltonian matrix is real and symmetric, all atomic states are orthogonal for $E_\alpha \neq E_\beta$ or can be chosen in this way for $E_\alpha = E_\beta$. In practice, an efficient decomposition of the many-electron matrix elements H_{rs} in the Hamiltonian matrix above is central to every implementation of the CI or related method.

➢ Hamiltonian matrix: Owing to the symmetry of the Hamiltonian, the computational effort of the MCDHF method can be reduced by a rather large factor (> 10), if the various (total) angular momenta and parities $\mathbb{J} = J^P$ of the atomic states of interest are considered independently.

➢ Hamiltonian matrix: Formally, the number of basis states and, hence, the size of the Hamiltonian matrix grows exponentially with the number of electrons as well as the size of the active space; cf. section 4.1.c.

➢ Choice of atomic Hamiltonian: The decision about the atomic Hamiltonian operator, that is utilized in a particular CI or MCDHF computation, is often made on the basis of (1) the nuclear charge, (2) the charge state of the atom or ion, (3) its particular shell structure as well as (4) the atomic property under consideration. Further relativistic and radiative corrections to the (total energies of the) atomic levels can be added in various (effective) approximations.

➢ Spin-angular integrals: For symmetry-adapted CSF, the integration over the spin-angular variables of all N electrons can be performed algebraically and enables one to write the Hamiltonian matrix elements always in the form (Grant, 1989)

$$H_{rs} \;=\; \sum_t u_{rs}(a_t b_t)\;\langle a_t \,\|\, \mathbb{h}_{\rm D} \,\|\, b_t\rangle \;+\; \sum_t v_{rs}^{(L_t)}(a_t b_t c_t d_t)\, X^{(L_t)}(a_t b_t c_t d_t)\,.$$

In this expansion, $u_{rs}(ab)$ and $v_{rs}^{(L_t)}(abcd)$ are one- and two-particle (scalar) angular coefficients, while the $X^{(L)}(abcd)$ describe the effective interaction strengths of (formally) the four electrons a, b, c, d that are involved in the interaction. As usual, we here abbreviate the one-particle quantum numbers $a = (n_a, \kappa_a)$, $b = (n_b, \kappa_b)$, ... to have a compact notation for the subshells of equivalent electrons.

➢ Reduced one-electron matrix elements of the Dirac Hamiltonian: As usual, the reduced matrix elements of the (one-electron) Dirac Hamiltonian,

$$\langle a \,\|\, \mathbb{h}_{\rm D} \,\|\, b\rangle \;=\; \delta_{\kappa_a \kappa_b} \int_0^\infty dr\, \left[c\, Q_a \left(\frac{d}{dr} + \frac{\kappa_a}{r} \right) P_b \;+\; c\, P_a \left(-\frac{d}{dr} + \frac{\kappa_a}{r} \right) Q_b \;-\; 2\, c^2\, Q_a\, Q_b \;+\; V_{\rm nuc}(r)\, (P_a P_b \;+\; Q_a Q_b) \right] ,$$

describe the kinetic and potential energy of an electron in subshell a and can be expressed in terms of the *large* and *small* (radial) components, $P_a(r)$ and $Q_a(r)$, of the corresponding one-electron orbital functions.

➢ These reduced matrix elements can be considered as the one-particle *analogua* to the effective interaction strength $X^{(L)}(abcd)$ as discussed above in section 3.1 for the electron-electron interaction.

➢ Restricted active spaces: In most standard all-electron implementations of the CI method and beyond, the electrons are often divided into (closed) core-shell and valence electrons, and with virtual excitations only included for the valence electrons within a restricted active orbital space.

4.1. In JAC implemented atomic representations

4.1.a. Mean-field basis (Atomic)

Use:

- Using JAC: Generate an `Atomic.Representation(.., MeanFieldBasis(meanFieldSettings))` for a given set of reference configurations and given settings; cf. `? MeanFieldSettings` or `MeanFieldSettings()`.
- Using JAC, see also the functions: `Basics.generate()`.

4.1.b. Configuration interaction (CI) expansions (Atomic)

Use:

- Using JAC: Generate an `Atomic.Representation(.., CiExpansion(orbitals, excitations, ciSettings))` for a given set of reference configurations as well as given orbitals, excitation and settings; cf. `? CiSettings` or `CiSettings()`. The dictionary of (fixed) orbitals can be generated, for instance, by a `MeanFieldBasis` expansion from Section 4.1.a.
- Using JAC: The virtual excitations to be included with regard to the reference configurations can be defined by `RasStep(seFrom=.., seTo=.., deFrom=.., deTo=, .., frozen=..)`, where all optional parameters refer to shell lists in order to specify single excitations (se) from → to, double excitations (de) from → to as well as the list of frozen shells.
- Using JAC, see also the functions: `Basics.generate()`.

4.1.c. Restricted active space (RAS) expansions `(Atomic)`

Use & notations:

- Restricted active space (RAS) method: This method includes the *correlated* motion of the bound electrons in a (much) more systematic fashion; it is based either one mean-field DHF or MCDHF solutions of the one-electron orbitals *and* a retricted active space that is formed by a subset of occupied and virtual orbitals. The idea of the RAS method is to account for an excitation of the *active* electrons from the outer shells (into a number of predefined *unoccupied* orbitals), while some 'electronic core' remains often fixed in the set-up of the RAS self-consistent field (RAS-SCF) computations.
- Using Jac: Generate an `Atomic.Representation(.., RasExpansion(LevelSymmetry(..), NoElectrons, steps, rasSettings))` for a given set of reference configurations as well as a specified level symmetry, number of electrons, the requested (list of excitation) steps and settings; cf. `? RasSettings` or `RasSettings()`.
- Using Jac: The individual steps of the RAS computations are defined by `RasStep(seFrom=.., seTo=.., deFrom=.., deTo=, .., frozen=..)`, where all optional parameters refer to shell lists in order to specify single excitations (se) from → to, double excitations (de) from → to as well as the list of frozen shells.
- Using Jac, see also the functions: `Basics.generate()`.
- Classes of virtual excitations: It is often useful to divide the virtual excitations of the active electrons into different *classes*, namely single (S), double (D), triple (T), ... excitations, in dependence of how many electrons are *to be replaced* with regard to the set of reference configurations. While single and double excitations are typically treated quite equally, because of Brillouin's theorem for the Dirac-Hartree-Fock approximation, the triple and higher excitations are typically less important and, if considered at all, areincorporated only for/within the valence shells.
- Implementation of the (RAS-SCF) method: The RAS and SCF parts are often implemented by means of a two-step cycle to (1) re-optimize the self-consistent field and (2) to enlarge the (layers of) shells in the representation of the atomic state vectors.

4.1.d. Approximate many-electron Green function for atomic levels (GreenFunction)

Formal representation & notations:

➢ Formal quantum notation: $[\,\{E_{\nu_1},\,|\psi_{\nu_1}(\beta_1 \mathbb{J}_1)\rangle\}\,,\,\{E_{\nu_2},\,|\psi_{\nu_2}(\beta_2 \mathbb{J}_2)\rangle\}\,,\,...\,] \quad \longrightarrow \quad \mathbb{G}(E) = \sum\!\!\!\!\!\!\int_{\nu_1\,\nu_2\,...} \frac{|\psi_{\nu_i}(\beta_i \mathbb{J}_i)\rangle\langle\psi_{\nu_i}(\beta_i \mathbb{J}_i)|}{E - E_{\nu_i}}$.

➢ Spectral (many-electron) Green function representation for the levels of one or several (given) configurations: Such a representation refers to just one or several lists of many-electron levels $\left\{E_{\nu_i},\,|\psi_{\nu_i}(\beta_i \mathbb{J}_i)\rangle\,,\,\nu_i = 1,...,\nu_i^{(\max)}\right\}$, $\mathbb{J}_i \in \mathbb{J}^{(\max)}$ from a list of total symmetries $\mathbb{J}^{(\max)} = [\mathbb{J}_1,\,Jsym_2,\,...]$ *and* with up to $n = n^{(\max)}$ electrons within the continuum, i.e. with $n = 0,\,...,n^{(\max)}$ free (unbound) electrons.

➢ Classification of Green functions: Each Green function is classified by the (maximum) number of free electrons and a pre-specified *(de-) excitation scheme* that is to be applied in order to generate from a list of given configurations all those (nonrelativistic) configurations that are to be considered in the many-electron (CSF) basis of the Green function representation.

➢ Classification of the many-electron Green functions: In Jac, the major classification of Green function representations is based on the number of free electrons in the continuum. The many-electron basis must hereby include both, bound-type CSF as well as CSF with up to the maximum number of free electrons, and this CSF basis should be constructed in a systematic manner. At present, we restrict ourselves to Green function representations with at least $N-1$ bound electrons and, hence, just up to a single electron in the continuum.

➢ Green function channel: A channel refers to the set of atomic levels $\{E_{\nu_i},\,|\psi_{\nu_i}(\beta_i \mathbb{J}_i)\rangle\}$, all with same total symmetry $\mathbb{J}_i$. Each Green function representation typically contains several (Green function) channels.

➢ Atomic levels in a Green function representation: The levels in such a many-electron representation formally belong to both, the bound-state spectrum of the atom $(E_{\nu_i} < 0)$ as well as to the continuum spectrum (scattering states) with 1, 2, ... electrons in the continuum. All these levels are constructed from a single set of one-electron orbitals, and which has to be properly chosen to represent reasonably well the bound-state levels of the given configurations.

➢ 'Infinities' in Green function representations: Already a single-electron Green function generally implies three *infinities* due to the electron's spatial degrees of freedom, and which are often treated numerically by restricting the principal quantum number $n^{(\max)}$ and the angular momentum quantum numbers $j^{(\max)}$, $m_j^{(\max)}$. An N-fold multiple of such infinities arise for N-electron Green functions and make their approximation a real challenge. In Jac, approximation many-electron Green functions are restricted by:

- orbitals with a principal quantum number $n^{(\max)}$ which applies for to all κ symmetry blocks;
- a specified list of orbital angular momenta $[\ell_1,\,\ell_2,\,...]$ for the virtual excitations and the generation of all non-relativistic configurations;
- the coupling of the N orbitals to total symmetries $\mathbb{J}_1,\,\mathbb{J}_2,\,...$.
  Each of these total symmetries represent a many-electron continuum, and in which the Hamiltonian is still diagonal.

Use:

- Approximate many-electron Green functions play an essential role in studying all second- and higher-order perturbation processes as well as for various dynamic processes in atomic systems. For many-electron atoms and ions, however, the construction of proper Green function approximations is still rare in the literature because of their complexity and the required computational resources. More often than not, Green functions have mainly been used in the past in order to describe either single-electron or quasi-single-electron atoms.
- Using Jac: Generate an `Atomic.Representation(.., GreenExpansion(approach::Atomic.AbstractGreenApproach, scheme::Basics.AbstractExcitationScheme, levelSymmetries, NoElectrons, greenSettings))` for a given set of reference configurations as well as a specified (Green function) approach, excitation scheme, (list of) level symmetries, number of electrons and settings; cf. `? GreenSettings` or `GreenSettings()`.
- Using Jac: The `approach::Atomic.AbstractGreenApproach` determines how and to which extent correlations among the bound and continuum electrons are taken into account into the Green function representation.
- Using Jac: The `scheme::Basics.AbstractExcitationScheme` determines how and to which extent excitations from the reference configurations into the specified *active* set of orbitals are included into the representation.
- In Jac, further details about the requested Green function can be specified by the maximum principle quantum number $n^{(\max)}$ and a list of orbital angular momenta $[\ell_1, \ell_2, ...]$ that are allowed within the given (de-) excitation scheme in order to generate the many-electron (CSF) basis. These parameters have to be specified in `GreenSettings(..)`.
- In Jac, the output of a Green (function) expansion is a list of `GreenChannel`'s, i.e. a list of multiplets that are suitable for numerical computations and/or summation over many-electron levels..
- Using Jac, see also the functions: `Basics.generate()`.
- Using Jac: Perform an `Atomic.Computation(.., properties=[Green, ..], configs=[..], greenSettings= GreenFunction.Settings(..), ..)` or call directly functions from the module `GreenFunction`.
- Green function approaches: Several approaches are distinguished in Jac in order to determine how the set of many-electron levels $\{E_{\nu_i}, |\psi_{\nu_i}(\beta_i \mathcal{J}_i)\rangle\}$ are to be generated and how much of the electron-electron interaction is to be taken into accout in order to represent *both*, the bound and continuum spectra of the atom or ion:

(a) Diagonal CSF basis without configuration interaction (`SingleCSFwithoutCI`): This is a fast though very rough approximation, in which each CSF with total symmetry $\mathbb{J}_i(\beta_i\,\mathbb{J}_i)$ also just represents a single level $|\psi_{\nu_i}\rangle$ of the spectrum. This approximation fully omits all configuration interactions within the CSF basis (of a fixed $\mathbb{J}_i$ symmetry).

(b) Configuration interaction only between bound-state orbitals (`CoreSpaceCI`): This approach diagonalizes (in turn) the Hamiltonian matrices of symmetry $(\beta_i\mathbb{J}_i)$ by including the electron-electron interaction only between bound-state orbitals, while their interaction with and among the free electrons are neglected.

(c) Damped configuration-interaction approach (`DampedCI`): This approach again diagonalizes the Hamiltonian matrices of symmetry $(\beta_i\mathbb{J}_i)$ by including the electron-electron interaction for all pairs of electrons but *damped* by some exponentional factor $e^{-\tau\,r}$. The use of such a *damping function* in the Slater integrals (and, possibly the Breit integrals – although this has not been realized so far) ensures that the bound-bound, bound-free and free-free interactions are treated equally without that a *continuation* of the continuum orbitals for $r \to \infty$ need to be considered in the numerical evaluation of the radial integrals.

➢ (De-) Excitation schemes of electrons for the representation of approximate Green functions: Since many-electron Green functions are very complex entities with many 'infinities' involved already within their formal definition, further control about the generation of such Green function approximations is obtained by specifying a proper (de-) excitation scheme of the electrons with regard to the given configurations:

(i) (De-) excitation of a single electron from a given set of (nonrelativistic) configurations (`DeExciteSingleElectron`): Cf. section 3.3

(*) Further (de-) excitation schemes will be implemented as the needs arises in selected applications.

Green functions for scattering processes:

➢ Green functions for the study of scattering processes: Formally, most scattering processes can be analyzed by solving the Schrödinger equation for some given many-electron Hamiltonian $\mathbb{H}$, the collision energy E and by including the proper scattering boundary conditions

$$\mathbb{H}\,\big|\Psi^+\big\rangle \;=\; E\;\big|\Psi^+\big\rangle\,.$$

➢ Lippman-Schwinger representation: A formal solution to the Schrödinger equation above is given by the Lippman-Schwinger equation which provides an integral form of the scattering wave function $|\Psi^+\rangle$ in terms of the initial state $|\Psi_o\rangle$ and the many-electron Green function $\mathbb{G}^+(E)$ (cf. Tong *et al.*, 2009)

$$\big|\Psi^+\big\rangle \;=\; |\Psi_o\rangle + \frac{1}{E\,-\,\mathbb{H}\,+\,i\eta}\,\mathbb{V}\;|\Psi_o\rangle \,+\, \ldots \;=\; |\Psi_o\rangle \,+\, \mathbb{G}^+(E)\,\mathbb{V}\;|\Psi_o\rangle \,+\, \ldots\,.$$

Here, $\eta > 0$ is a small positive infinitesimal which ensures that the boundary conditions of an outgoing wave are properly taken into account, and where a (radiative) loss rate can be incorporated into the representation of $|\Psi^+\rangle$ by means of a complex energy E.

➢ Green function with optical potential: The Green function of the scattering system with total scattering energy E can be formally written as

$$\mathbb{G}^+(E) \;=\; \sum_\nu \frac{|\psi_\nu\rangle\,\langle\psi_\nu|}{E \,-\, E_\nu \,+\, i\eta}\,,$$

and where the summation runs over all (generalized) eigenfunctions of the Hamiltonian $\mathbb{H}$. This Green function can be utilized also for many scattering and dynamical processes if just a proper (sub-) set of many-electron levels $\{E_\nu,\, |\psi_\nu\}\rangle$ is taken into account.

➢ Optical potential: If a proper optical potential is added to the (inner-) atomic potential, the outgoing wave is formally absorbed due to the occurance of complex single-electron energies. Tong *et al.* (2009) suggest an energy-dependent optical potential of the form

$$V^{\,(\mathrm{optical})}(r;\,\varepsilon) \;=\; \begin{cases} 0 & \text{for} \quad r \,<\, r_c \\ V_o\,\left(\frac{r\,-\,r_c}{r_{\max}\,-\,r_c}\right) & \text{for} \quad r \,\geq\, r_c \end{cases}\,, \qquad \frac{\varepsilon^{1/2}}{r \,-\, r_c} \,<\, V_o \,<\, \varepsilon^{1/2}\,(r_{\max} \,-\, r_c),$$

and where the optical potential becomes *nonzero* at r_c. However, little experience exists so far how the parameters r_c, $r_{\max}$, ε need to be chosen in order to obtain a realistic representation of the Green function, and how useful such an approximation is in different physical contexts.

➢ Diagonalization of the Hamiltonian matrix with an optical potential: For an optical potential, the Hamiltonian matrix is no longer hermitian but symmetric complex, and it generally includes both diagonal and off-diagonal matrix elements due to the electron-electron interaction. From the diagonalization of the Hamiltonian matrix in a CSF basis with well-defined total symmetry $\mathbb{J}_i$, one then obtains the eigenenergies $\{E_\nu\}$ and (atomic) eigenvectors $\{E_{\nu_i},\, |\psi_{\nu_i}\rangle\}$, but which need to be calculated just once.

4.2. In JAC partly-implemented atomic representations

4.2.a. Multi-configuration Dirac-Hartree-Fock (MCDHF) expansions `(Atomic)`

Use & notations:

➢ Multi-configuration Dirac-Hartree-Fock (MCDHF) method: This method has been found a versatile tool for calculating the level structure and approximate wave functions for atoms and ions of all elements across the periodic table. In contrast to the CI method above, both the radial (one-electron) functions as well as the expansion coefficients $\{c_r(\alpha),\ r = 1, \ldots, n_c\}$ are optimized simultaneously on the basis of the Dirac-Coulomb Hamiltonian.

➢ Using Jac: Generate an `Atomic.Representation(.., McdhfExpansion(ciSettings))` for a given set of reference configurations and given settings; cf. `? McdhfSettings` or `McdhfSettings()`.

➢ Using Jac, see also the functions: `Basics.generate()`.

➢ Steps for practical MCDHF computations: In the MCDHF method and in Jac as well, the atomic bound states are typically generated by a series of steps:

- Definition of the nuclear parameters as well as the angular structure (and extent) of the CSF basis $\{|\gamma\, PJM\rangle\}$ in the MCDHF ansatz;
- Algebraic evaluation and computation of the spin-angular integrals (the so-called angular coefficients), based on standard techniques from Racah's algebra;
- Generation or collection of proper radial start orbitals and self-consistent field (SCF) calculations, based on the Dirac-Coulomb Hamiltonian;
- Configuration interaction (CI) calculations in order to incorporate further relativistic contributions into the Hamiltonian matrix and/or to enlarge the CSF basis beyond the given SCF model.

Often, these four steps are repeated at several stages by systematically enlarging the one-electron (active) orbital space.

➢ Radiative corrections: There are two dominant corrections for all medium and heavy elements which arise from QED; cf. section 3.4. When compared to missing correlation contributions, these QED corrections are relevant only if the inner-shell electrons of these elements are involved in some (atomic) property or process, and they are often negligible otherwise, at least as the present level of computational accuracy.

➢ Other MCDHF codes: During the last decades, a number of codes have became available, which implement the MCDHF method for free atoms and ions and which provide the approximate energies and wave functions for atomic bound states. For example, GRASP2K and later versions of the former Oxford package (Jönsson *et al.* 2013, 2018) now facilitate large-scale computations and supports wave function expansion of up to or beyond a million CSF as required for many open-shell atoms.

4.2.b. Combined configuration interaction & perturbation theory (CI-PT) expansions (. . .)

Formal representation:

➢ Combined CI-PT method: While the diagonalization of the many-electron Hamiltonian matrix is perhaps the simplest way to take electronic correlations into account, only very few core excitations can typically be included by the CI method. In practice, further correlations between the valence and core electrons can be calculated and incorporated into the CI matrix by means of many-body perturbation theory (MBPT). Of course, no correlations between the core and valence electrons are included if excitations from the core are prohibited.

➢ CI-PT method: In this method, most of the weakly-correlated many-electron basis states (usually with rather high excitation energy) are not directly included into the diagonalization of the CI matrix but are treated instead perturbatively (Dzuba *et al.*, 2017). This approach significantly reduces the size of the CI matrix and, hence, removes one of the major limitations of this method for any larger number of valence electrons.

➢ Partioning of CI spaces: In the CI-PT method, all CSF $\{|\gamma_r \mathbb{J} M\rangle\,,\ r = 1, ..., N_c\}$ as many-electron basis are assumed to be ordered in energy and divided into the (CI) model space P with $r = 1, ..., N_p$ CSF and a complementary space Q with $N_q = N_c - N_p$ CSF, and for $r = N_p + 1, ..., N_c$. The CI matrix $(H_{rs} \equiv \langle \gamma_r \mathbb{J}_r M_r \,|\, H \,|\, \gamma_r \mathbb{J}_s M_s \rangle\,, \quad r, s = 1, ..., N_p\,)$ is diagonalized only within the P space, while all off-diagonal matrix elements from the Q space are neglected.

➢ Effective CI matrix: For the coupling between the P and Q spaces, all off-diagonal matrix elements $(H_{rs},\ r = 1, ..., N_p,\ s = N_p + 1, ..., N_c\,)$ as well as all diagonal matrix elements $(H_{ss},\ s = N_p + 1, ..., N_c\, 9$ are taken into account explicitly in terms of an effective CI matrix with modified matrix elements:

$$H_{rs} \;\longrightarrow\; H_{rs} + \sum_k \frac{\langle r \,|\, H \,|\, k \rangle\ \langle k \,|\, H \,|\, s \rangle}{(E - E_k)}, \qquad\qquad N_p < k \le N_p + N_Q.$$

In these matrix elements, E formally refers to the (exact) energy from the many-electron SE. Owing to the overall symmetry of the Hamiltonian, this effective CI matrix can be computed and solved independently for each level symmetry $\mathbb{J}$ of interest.

➢ Iteration of the effective CI matrix: Since the exact energy E is not known, it need to be initially replaced by some proper approximation $E \rightarrow E^{)0}$ and, hence, the set-up and diagonalization of the effective CI matrix need to be solved iteratively, using the CI energy $E^{(t)}$, $t = 0$, ... from the previous iteration. If more than one level of symmetry $\mathbb{J}$ is required, this iteration of the effective CI matrix need to be done separately because of the different energies $E^{(t)}(\alpha\mathbb{J}) \rightarrow E(\alpha\mathbb{J})$, making the approach much less efficient. Moreover, the use of different energies $E(\alpha\mathbb{J})$ in the effective CI matrix results in ASF that are not quite orthogonal to each other.

Use & notations:

➢ Using JAC: Perform an `Atomic.Computation(.., properties=[Green, ..], configs=[..], greenSettings= GreenFunction.Settings(..), ..)` or call directly functions from the module `GreenFunction`.

➢ In JAC, we provide ... .

➢ The CI-PT method can be easily applied if: (i) only a few low-lying levels are required with a large projection within the chosen P space already, (ii) all many-electron CSF are ordered in terms of their energy and (iii) if there is a reasonable *energy gap* between the CSF included directly into the CI matrix and those treated perturbatively. In practice, these conditions mean that the perturbative summation over the high-energy CSF must overall result in a rather small correction; the method fails if these conditions are not fulfilled.

➢ Parallelization: Since the summation over the high-energy CSF is very time-consuming but need to be performed independently for each matrix element, the CI-PT method is very suitable for parallel computations.

Applications:

➢ Such a combined CI and perturbation theory (CI-PT) treatment has been applied especially for (super-) heavy elements and multiply-charged ions with open p-, d- and f-shells. Because of the particular shell structure, many of these multiply- and highly-charged ions have optical transitions near to their ground level and might be sensitive to physics beyond the standard model. This refers to possible variations of the fine-structure constant or violations of the (local) Lorenz invariance and Einstein equivalence principle as well as to potential interactions with dark matter.

➢ Two multiply-charged ions have been considered in the search for time variations of the fine-structure constant; these are Ir^{17+} ions with a $4f^{13}\,5s$ and Ho^{14+} ions with a $4f^{6}\,5s$ ground configuration.

➢ Dzuba *et al.* (2017) apply the V^{N-M} approximation in order to generate the initial Dirac-Hartree-Fock basis for the CI-PT procedure. In this approximation, only the core-shell electrons are included into the Dirac-Hartree-Fock, while all valence-shell are treated a *virtual* at

this step of the computation. However, the set-up of the CI matrices then follows the standard procedure by using the orbitals from the Dirac-Hartree-Fock orbitals from the single-electron basis.

➢ Owing to the effective completeness of B-splines, Dzuba and Johnson (1998) showed for the low-lying levels of barium that a combined CI-MBPT method may significantly improve the convergence and numerical accuracy of many-electron computations.

4.2.c. Fast configuration interaction & perturbation theory (FCI-PT) expansions (...)

Formal representation:

➢ Fast CI: Dzuba *et al.* (2019) suggest a further modification to the CI-PT method from above which is termed fast configuration interaction (fast CI). In this modification, the denominator in the perturbative sum of the CI-PT method is approximated by $|E - E_k| \approx |E - E_c|$, where E_c denotes some mean configuration energy of the basis state $|k\rangle$. This approximation enables one to re-write the summation as

$$\sum_k \frac{\langle r \,|\, H \,|\, k\rangle \;\langle k \,|\, H \,|\, s\rangle}{(E \;-\; E_k)} \;\approx\; \sum_{\text{configurations}} \frac{1}{E \;-\; E_c} \sum_{k_c} \langle r \,|\, H \,|\, k_c\rangle \;\langle k_c \,|\, H \,|\, s\rangle \,, \qquad\qquad N_p \;<\; k \;\leq\; N_p + N_Q \,.$$

➢ While, at the first glance, this seem to make not much difference to the CI-PT method, it can considerably accelerate the computation of the second summation $\sum_{k_c} \langle r \,|\, H \,|\, k_c\rangle \;\langle k_c \,|\, H \,|\, s\rangle$. Such a simplification is possible for the evaluation of the many-electron matrix elements, since all the matrix elements can be traced back to a rather small number of radial integrals *times* some angular coefficients which only depend on the configuration but not on the detailed coupling of the basis states. Moreover, the mean configuration energy can also be expressed in terms of simple radial matrix elements or computed numerically just from the trace of the corresponding submatrix.

➢ A similar reduction in computation time might be obtained however by a careful arrangement of the many-electron basis states $|k\rangle$ and by the re-use of angular coefficients and radial integrals.

Use & notations:

➢ Using Jac: Perform an `Atomic.Computation(.., properties=[Green, ..], configs=[..], greenSettings= GreenFunction.Settings(..), ..)` or call directly functions from the module `GreenFunction`.

➢ In Jac, we provide ... .

➢ Because of the rapid increase in the computational costs, a reasonable active space can be applied in (standard) CI expansions only for a moderate number of (active) valance electrons, often not more that for 3-4 valence electrons above of closed shells otherwise.

4.3. Further atomic representations, not yet considered in JAC

4.3.a. Complex-scaling method

Formal representation:

➢ Complex scaling: This scaling method is based on the global rotation of all radial coordinates ϑ, $r \longrightarrow r\,e^{i\vartheta}$. This rotation generally transforms hermitian into non-hermetian Hamiltonians whose (bound) eigenstates then describe both, bound and resonant states of the quantum system. The resonant states have complex energies whose imaginary part describe the width (lifetime) of the resonances (with regard to autoionization).

Use & notations:

➢ Boundary conditions become irrelevant: Since a complex-scaled function vanishes for $r \rightarrow \infty$, a representation of the resonances can be obtained by diagonalizing the rotated Hamiltonian within a square-integrable basis, and without taking special care of the boundary conditions.

➢ Rotation of the Hamiltonian: A rotation of the radial coordinates by an angle ϑ is possible only, if the potential is (so-called) *dilatation-analytic*. While this is the case for any reasonable atomic Hamiltonian, this property is not necesseraly fulfilled for pseudo- or polarization potentials, which can either be nonanalytical or even diverge within the complex plane for small values of ϑ (Fossez *et al.*, 2015).

➢ Exterior complex scaling: The (so-called) infinite-range exterior complex scaling method provides an efficient tool for modelling an absorbing boundary in (time-dependent) many-electron calculations, such as many-electron atoms in an intense laser pulse. The exterior complex scaling is based on the transformation: $r \rightarrow z(r) = R + r\,e^{i\,\vartheta}$.

4.3.b. Berggren expansion method

Formal representation:

➢ Berggren expansion method (BEM): In this single-particle method, (complex-energy) resonance states are described by a particular completeness relation for bound, decaying and scattering states, first introduced by Berggren in 1968. Because of the quasi-localized nature of the single-particle states, the BEM method does not require a precise treatment of the boundary conditions at infinity.

➢ Completeness relation of Berggren ensembles: A (single-particle) Berggren ensemble satisfies for each partial wave κ the relation

$$\sum_{n\,\in\,b,d} |u_{n\kappa}\rangle \langle u_{n\kappa}| \;+\; \int_{\mathcal{L}_\kappa^+} |u_{\varepsilon\kappa}\rangle \langle u_{\varepsilon\kappa}| \;=\; 1\,.$$

Here, $|u_{n\kappa}\rangle$ are the radial wave functions of the bound (b) and decaying (d) states, while $|u_{\varepsilon\kappa}\rangle$ represent scattering states, and $\mathcal{L}_\kappa^+$ denotes the contour that encompasses the decaying states in the fourth quadrant of the complex ϵ-plane.

➢ Coupled-channel formalism: A Berggren ensemble represents a single-particle spectrum in the vincinity of some resonance and can be combined quite easily with the coupled-channel method in order to describe (resonant) behaviour in nuclei, atoms and molecules.

Use & notations:

➢ Berggren ensemble: This ensemble refers to the single-particle spectrum of a Hamiltonian with complex eigenvalues; it generally contains bound (b), decaying (d), and scattering (s) single-particle states along the contour $\mathcal{L}_\kappa^+$ for each partial wave κ.

➢ Slater determinants built from a Berggren ensemble: The Berggren single-particle states can be also utilized to construct a many-particle basis, in which the (many-particle) Hamiltonian is diagonalized. This scheme has so far been applied especially in in nuclear-structure theory in order to describe the beaviour of valence nucleons outside of a closed core. Since the contour of the Berggren ensemble is discretized, the same applies also to the many-body basis that is spanned from this ensemble.

➢ Gamow shell model (GSM): This model is an extension of the traditional nuclear shell model with complex-energy single-particle states. In this model, a single-particle Berggren basis is generated in a finite-depth potential, independent for each partial wave κ, and then comprises Gamow (or resonant) discrete states as well as the nonresonant scattering continuum.

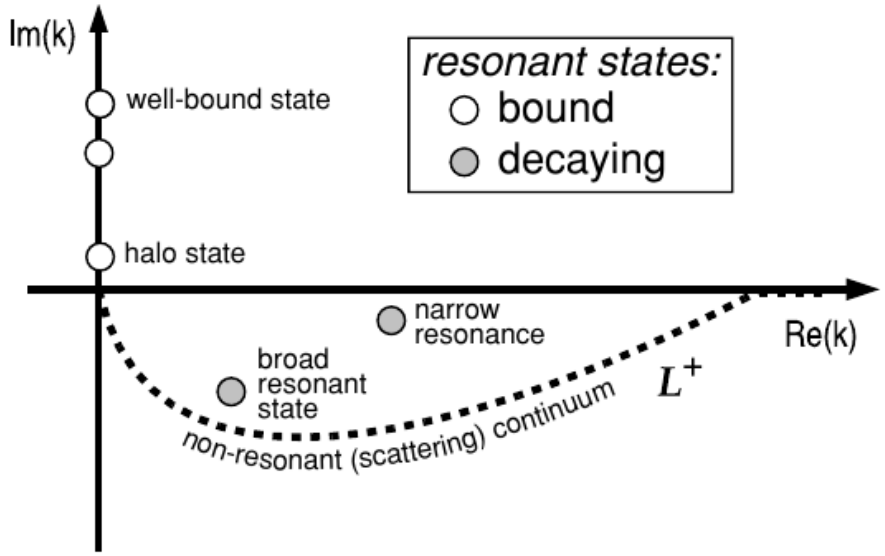

Figure 4.1.: Illustration of the Berggren ensemble in the complex k-plane. While the bound states are all located on the positive imaginary axis, the weakly bound halo states lay close to the origin and the positive-energy resonant states in the fourth quadrant. All states with a small imaginary part can be interpreted as resonances. The complex-k shells on the contour $\mathcal{L}^+$ represent the nonresonant scattering continuum. From Rotureau *et al.* (2009).

➢ Complex-energy Gamow shell model (GSM): The structure and represenation of weakly bound and unbound nuclear states close to particle drip lines has attracted much recent interest in nuclear physics. A proper treatment of these states goes beyond the traditional shell model, wich makes only use of localized states, but requires to allow particle emission. The GSM enables one to describe resonant and nonresonant many-body states on equal footing (Jaganathen *et al.*, 2017).

Applications:

➢ Fossez *et al.* (2015) applied the Berggren expansion method to parts of the unbound spectrum of dipolar molecules and achieved both, a much higher accuracy for the representation of the weakly-bound as well as the unbound resonance states.

➢ Structure of light nuclei: Light nuclei have been traditional applied to test microscopic nuclear structure models. The work by Lane (1955)

and Kurath (1956) on p-shell nuclei have become a cornerstone of nuclear structure theory and provided great guidance to analyzing the wealth of spectroscopic data on energy levels, electromagnetic transitions, nuclear moments, and various particle decays during the past decades (Jaganathen *et al.* 2017).

4.3.c. Convergent close-coupling (CCC) method

Formal representation:

- Coupled-channel equations: For scattering problems, the convergent close-coupling method refers to a reformulation of the SE in terms of an infinite set of coupled-channel equations. This reformulation assumes a complete set of target states.
- The Convergent Close-Coupling (CCC) method has been worked out originally in order to compute accurate cross sections for the scattering of light projectiles on (quasi-) one- and two-electron targets. In the original representation of this method, the scattering wavefunctions are often given in momentum space and are based on the Lippmann-Schwinger equation.
- Advantages of the CCC method: This method enables one to treat the many-particle continuum systematically by means of square-integrable functions. In particulyr, the CCC starts from an expansion of the target into a complete set of orthogonal L^2 functions to span the Hilbert space.

Use & notations:

- Difficulties with the CCC method The continuum channels at *intermediate* energies are particular important and need to be well represented in their coupling to other channels.
- Convergence: Convergence in the scattering amplitudes can (and need to be) shown as the size of the square-integrable functions increases.

4.3.d. Density-matrix renormalization group (DMRG) method

Formal representation:

- *Ab-initio* DMRG method: This method can be described either in terms of the renormalization group and renormalized operators, and as it was formulated originally, *or* by means of matrix product states and matrix product operators (MPS & MPO), a more recent language. These two languages use different vocabularies and appear to be quite different in their formulation (Chan *et al.*, 2016).
- Use of MPS & MPO language: The power of this language consists in new perspectives and algorithms, rather than in just re-writing the original renormalization group operator (RGO) language. For example, the algebra of the MPS & MPO language provides various new operations beyond the scalar computation of expectation values, and which can be utilized for instance to describe time evolutions.
- Matrix product state (MPS): For a given quantum many-particle system, the MPS generally refer to some low-rank decomposition of the full interaction matrix. In atomic physics and quantum chemistry, this matrix is known also as the (full) configuration-interaction matrix or tensor.
- In atomic physics and elsewhere, the DMRG method provides a nonperturbative scheme that is useful to replace the (full) configuration interaction method in restricted active spaces.
- The DMRG method has attracted increasing interest in quantum chemistry during the past two decades.

Use & notations:

- Matrix product ansatz: The power of the DMRG method mainly arise from the matrix product ansatz which enables one to expresses the low entanglement nature of one- or few-dimensional low-energy quantum eigenstates, including the ground-state (Chan *et al.*, 2016).
- Dimension of MPS: The (virtual) dimension of the MPS designates the rank of the decomposition and, hence, the dimension of many-body Hilbert subspace that is taken into account. In the DMRG method, this dimension can be increased systematically until numerical convergence is reached (Wouters and van Neck, 2014).
- Left- and right-bases: To support a simple translation from the renormalization-group operators to the MPS & MPO language (and back, if requested), emphasis must be places to the relation between the left- and right-bases *and* the tensors in the MPS & MPO language. Moreover, these relations need to be worked out for (i) the renormalized wavefunctions, (ii) the representation of the Hamiltonian, (iii) the minimization of energies as well as (iv) for the evaluation of expectation values within these two schemes.
- Difficulties in 2D and 3D: The DMRG has difficulties with achieving good accuracy for two- and three-dimensional systems since the need of computational resources increase more or less exponentially with system size. From a detailed comparison of 1D and 2D lattices, it was recognized that this behaviour is closely related to scaling of entanglement in many-body states as decribed, for instance, by the area laws (Schollwöck 2011).

Matrix product states:

➢ Matrix product states (MPS): These product states refer to a particular wavefunction representation that help define the variational space of the DMRG. For an orthonormal Fock-space basis $\{|n_1\, n_2\, \cdots\, n_K\rangle\}$ of K orbitals (including spin labels), an atomic wave function is written in occupation representation as

$$|\psi\rangle \;=\; \sum_{n_1\, n_2\, \cdots\, n_K} \psi^{n_1\, n_2\, \cdots\, n_K} \;\; |n_1\, n_2\, \cdots\, n_K\rangle\,.$$

For a fixed particle number N, moreover, we have the condition

$$\psi^{n_1\, n_2\, \cdots\, n_K} \;=\; \begin{cases} \psi^{n_1\, n_2\, \cdots\, n_K} & \sum_{k=1}^{K}\, n_k \;=\; N \\ 0 & \text{else}\,. \end{cases}$$

➢ MPS amplitudes: For any state of the atom or ion, the wavefunction amplitude can be written

$$\psi^{n_1\, n_2\, \cdots\, n_K} \;=\; \sum_{\{\alpha_k\}} A^{n_1}_{\alpha_1}[1]\; A^{n_2}_{\alpha_1\, \alpha_2}[2]\; \cdots\; A^{n_K}_{\alpha_{K-1}}[K]$$

as a product of $M \times M$ matrices $A^{n_k}[k]$, of equal dimension, apart from the $1 \times M$ leftmost and $M \times 1$ rightmost matrices. This particular construction of the MPS ensures that the matrix product always results in the *scalar* amplitude $\psi^{n_1\, n_2\, \cdots\, n_K}$. In a non-relativistic formulation, moreover, the dimension of these matrices is $2 \times M \times M$ if the spin-index of the (spin-) orbitals is taken into account.

➢ MPS bond dimension M: The number of renormalized states gives rise to the dimension M of the matrices and makes the representation of the state with increasing M more flexible. For bound-state systems, it can be assumed that the matrices $A^{n_k}[k]$ are all real.

➢ Graphical representation of MPS: A general wavefunction amplitude can always be represented graphically as a tensor with K legs, while the MPS as a whole is just represented by a connected set of 2-index and 3-index tensors, each associated with a certain site. In addition, graphical rules can be derived to contract the tensors in various ways.

➢ DMRG sweep algorithm: The MPS & MPO language also suggests a new formulation of the *ab-initio* DMRG sweep algorithm itself (Chan *et al.*, 2016).

Applications:

- The entanglement perspective of the DMRG method made it possible to extent its application towards new fields, such as matrix product operator representations, the time-evolution of atoms and molecules, infinite systems, systems at finite temperatures as well as towards higher-dimensions. In addition, the language of matrix product and tensor network states is nowadays quite widely applied to reason about the structure of many-particle quantum states (Chan *et al.*, 2016).
- Earlier *ab-initio* DMRG applications in quantum chemistry have mainly focused upon level and excitation energies as well as reduced density matrices, which can be computed stepwise by running through all orbitals.
- 1D spin chains: The DMRG method has been found a versatile tool especially for simulating the static and dynamical behaviour of strongly correlated 1D quantum lattice systems (Schollwöck 2011). The use of MPS, in particular, has lead to a much deeper understanding of the DMRG method itself including both, its great potential and limitations.
- For such 1D spin chains, the accuracy of DMRG simulations has been found limited only by machine precision, rather independent of the particular choice of Hamiltonian.
- Application of 1D spin chains: 1D and 2D strongly-correlated systems have applications in condensed matter physics, such as for studying spin chains and ladders, high-temperature superconductance of frustrated magnets in low spatial dimensions and at several places elsewhere. These spin chains have found interest also in exploring ultra-cold gases in optical lattices.
- Applications in nuclear physics: The DMRG method (may) enable configuration interaction studies of weakly bound and unbound strongly-interacting complex systems, which cannot be treated by any direct diagonalization because of the prohibitively large Fock space (Rotureau *et al.* 2009). Any theoretical description of such states requires a rigorous treatment of the many-body correlations in the presence of decay channels and a scattering continuum.
- Applications to nonequilibrium systems: While most of the previous DMRG studies were focused on equilibrium properties in strongly-correlated closed quantum systems with a hermitian density matrix, nonequilibrium systems with non-hermitian and non-symmetric density matrices can also be treated, though with rather mixed success.

4.4. Other representations, related to JAC

4.4.a. Density funtional theory (DFT)

Formal representation:

- ➢ Hohenberg-Kohn theorem: Hohenberg and Kohn showed that all ground-state properties of atoms, molecules, etc. are uniquely determined by the electron density alone. In particular, there exist a unique universal functional of the electron density that can be utilized in order to obtain the ground state energy and density.
- ➢ Kohn-Sham theorem: The universal functional of the electron density can be re-written as a sum of kinetic energies of noninteracting (so-called Kohn-Sham) particles *and* some exchange-correlation functional. This representation enables one to represent the electron density by means of a single (Kohn-Sham) Slater determinant, even if the exact form of the exchange-correlation functional remains unknown.
- ➢ Hohenberg-Kohn theorem: This theorem tells that the energy of any (finite quantum) system can be written as a functional of the electron density, the well-known basis of Density Function Theory (DFT). Various approximate density functionals have been developed and explored with regard to different physical and chemical properties. For instance, concepts from DFT have been applied in order to obtain chemical reactivity indices and to characterize the chemical reactions of molecular systems in terms of perturbations (distortions) of the electron density.
- ➢ Approximate exchange-correlation functionals: Many approximate semi-empirical exchange-correlation functionals have been proposed in the literature with different strengths and complexity.
- ➢ Strength and weaknesses of DFT: Since the exact exchange-correlation functional remains unknown, not all correlation can usally be retrieved by the DFT method. Indeed, DFT has been found good in capturing dynamic correlations, i.e. if the main physics can be described by means of the single Slater determinant, but if often fails for strong correlations for which multireference methods are then required.

Applications:

- ➢ Today, the simple Kohn-Sham representation of DFT is the basis for its great success for different – and partly very complex – systems, such as clusters, biomolecules and nanostructures.

4.4.b. Relativistic coupled-cluster (RCC) theory

Formal representation:

➢ All-order techniques: One of the most popular all-order technique is the CC approach in which correlation contributions are classified due to the number of excited particles rather than by the order of the perturbation.

➢ All-order techniques: From many-body and coupled-cluster (CC) computations, one knows that only certain classes of correlation diagrams need to be incorporated to all orders in order to obtain very accurate results.

Applications:

➢ In practice, most CC computations include just single and pair correlations to all orders but neglect triple and higher correlations, though selected triple and quadrupole excitations might be included (Dzuba and Johnson, 1998).

4.4.c. Transformation of atomic into qubit Hamiltonians

Formal representation:

➢

Quantum hardware and algorithms for atomic physics:

➢ Atomic computations & quantum computing: Quantum computing may affect atomic computations due to: (1) Runnig atomic computations on quantum hardware and (2) Transformation of atomic Hamiltonians into qubit Hamiltonians and quantum circuits [cf. McClean *et al.* (2019) and the code OpenFermium].

➢ Qubit transformation of atomic Hamiltonians: Once the problem has been recast in the second quantized, it need to be mapped upon qubits. While electrons are indistinguishable fermions, qubit representations have to be distinguishable in order to support useful computations.

- Qubit transformation: Several transformations, such as the Jordan-Wigner (JW), Bravyi-Kitaev (BK), and Bravyi-Kitaev super fast (BKSF) transformations, are known today to support the mapping of indistinguishable fermions to distinguishable qubits. These transformations also take the antisymmetry (particle statistics) of the electronic wave functions into account. In particular, the Jordan-Wigner transformation directly returns an equivalent 'qubit operator' for the atomic Hamiltonian.
- Quantum computational supremacy: Fault-tolerant quantum computing can speed-up significantly the solutions of various NP-hard problems, such as the factorization of prime numbers, search algorithms, linear-algebra and various others. While, until to the present, most realizations of multi-qubit realizations are fragile and suffer from noise and sub-universal behaviour, newly emerging quantum processors are expected to be developed and to be powerful enough in order to outperform classical computers for selected tasks, known also as quantum computational supremacy (Killoran *et al.*, 2019).
- Quantum computing is known as a rapidly growing discipline that aims for the discovery of exponentially faster quantum algorithms that are than the best-known classical algorithms. However, one first need to know and control the required resources in order to realize such algorithms.
- Resources of quantum computing: In pure-state quantum computations, entanglement is often considered as a necessary resource in order to achieve an exponential speed-up in the computations. Although this seems not to be true for mixed-state quantum computations, until the present, it is largely unclear which entities help quantify the resource in such a computational model. Moreover, there is no simple relationship known between different resources for mixed-state quantum computations.
- Application of quantum simulations: Modern simulations make use of approximate quantum optimization algorithms, quantum annealing or the sampling from computationally expensive probability distributions. Similar techniques may be applied also to tackle problems in quantum chemistry, machine learning or even at stock markets.

Continuous variable (CV) model of quantum computing:

- Continuous variable (CV) model of quantum computing: In the CV model, the basic (information-processing) unit is an infinite-dimensional bosonic mode as it can be realized and manipulated with light. While such a CV model of quantum computing retains the major features from the standard qubit model, it promises simpler implementations for various bosonic systems, such as photons, electromagnetic fields, trapped atoms, harmonic oscillators or Bose-Einstein condensates. More general, a CV model of quantum computing may facilitate quantum computations and simulations for all those systems where continuous quantum operators are naturally occur, such as position and momentum.
- Systems based on continuous variables (CV): Many quantum systems have (also) spatial degree of freedoms and, hence, are intrinsically continuous. With these systems, an infinite-dimensional Hilbert space is associated, and any representation in such a space is very different

from a discrete qubit representation. Indeed, the CV model of quantum computing got its name from the continuous spectra of the quantum operators associated with spatial degrees of freedoms and which offers a paradigm for quantum computations.

➢ Qubits *versus* continuous variables (CV): It can be shown that every qubit-based computation can be realized also by means of CV representations. This makes the CV model of quantum computing a powerful extension of the familiar qubit model.

➢ Systems based on continuous variables (CV): Perhaps, the most simple CV system is the 1D bosonic harmonic oscillator which can be defined either by its (canonical) mode operators a and a^+ with $[a, a^+] = \mathbb{1}$ *or*, equivalently, by its the – position and momentum – (quadrature) operators

$$\hat{x} \;=\; \sqrt{\frac{\hbar}{2}}\,\left(a \,+\, a^+\right), \qquad\qquad \hat{p} \;=\; -i\,\sqrt{\frac{\hbar}{2}}\,\left(a \,-\, a^+\right), \qquad\qquad [\hat{x},\,\hat{p}] \;=\; i\hbar\,\mathbb{1}\,.$$

In a optical fibre or waveguide, for instance, a fixed harmonic oscillator mode can be considered (drawn) as a single 'wire' in a quantum circuit, and these modes are the fundamental units of CV quantum computers.

Software tools for qubit transformations:

➢ OpenFermion: This is an open-source software library in Python for simulation of fermionic and bosonic models. It aims to provide a (preliminary) interface for translating the atomic or quantum chemistry specification of problems into a (qubit) representation, suitable for quantum hardware. The goal is to specify a quantum circuit for solving or studying electronic structure problems, and without that the user need to have *domain expertise* in quantum information theory.

➢ OpenFermion: This toolbox provides some preliminary functionality for developing (new) quantum algorithms for solving electronic-structure problems. Until the present, however, efficient algorithms for atomic physics and quantum chemistry are still a challenge and their implementation on quantum hardware remains a rather formidable task. This toolbox also aims to facilitate the comunication between quantum-chemistry and quantum-information community.

➢ Strawberry Fields: This Python package refers to an open-source software architecture for photonic quantum computing. It is based on the new quantum programming language Blackbird and is especially designed for dealing with CV models of quantum computing. This package makes us of different circuit decompositions from quantum photonics, such as the Williamson, Bloch-Messiah or Clements decompositions (Killoran *et al.*, 2019). Strawberry Fields can be utilized either as Python package or as a browser-based interface for the set-up of quantum circuits.

➢ Decompositions of Strawberry Fields: Several decompositions are realized, including: (a) the Williamson decomposition to decompose arbitrary Gaussian states into some symplectic transformation that can be applied on thermals states, (b) the Bloch-Messiah decomposition for modelling interferometers and single-mode squeezing as well as (c) the Clements decomposition for representing multi-mode linear interferometers in terms of arrays of beamsplitters and rotations of fixed depth.

4.4.d. qumodes

Formal representation:

➢ Representation of qumodes: In a CV model and with the vacuum state $|0\rangle$, each qumode can be written in terms of the quadrature states

$$|\psi\rangle \;=\; \int dx\; \psi(x)\; |x\rangle\,, \qquad\qquad \hat{x}\;|x\rangle \;=\; x\;|x\rangle\,, \qquad\qquad x\;\in\;\mathbb{R}$$

$$|\psi\rangle \;=\; \exp(-i\,\mathbb{H}\,t)\,|0\rangle\,,$$

and where $\mathbb{H}$ is a bosonic Hamiltonian, i.e. a function of the mode operators a, a^+ and of the time t; the quadrature states are a sub-class of the so-called Gaussian states of qumodes.

➢ Gaussian states: For these states, the Hamiltonian $\mathbb{H}$ is at most quadratic in a, a^+ . Gaussian single-qumode states can be parametrized by two complex variables, a displacement parameter $\alpha \in \mathbb{C}$ and a squeezing parameter $z \in \mathbb{C}$.

5. Atomic interactions with the radiation field

5.1. Wave equations & optical fields

5.1.a. Homogeneous wave equation

General solutions:

➢ Monochromatic plane-wave light: Monochromatic plane-wave light is uniquely determined by either the electric ($\mathbf{E}$) or magnetic ($\mathbf{B}$) field. Without restriction, we here consider a plane-wave along $\mathbf{k} \,||\, \mathbf{e}_z$.

➢ Waves that propagate along the wave vector $\pm\,\mathbf{k}$: We consider the homogenous wave equation (for $\psi \;=\; \{\mathbf{E},\, \mathbf{B},\, \Phi,\, \mathbf{A},\, ...\}$) with the known solution (proof by substitution and by means of the chain rule), whose wave fronts propagate along $\pm\,\mathbf{k}$

$$\Box\,\psi(\mathbf{r},t) \;=\; 0 \qquad\qquad \psi(\mathbf{r},t) \;=\; \psi_+(\mathbf{k}\cdot\mathbf{r} \,+\, \omega t) \;+\; \psi_-\underbrace{(\mathbf{k}\cdot\mathbf{r} \,-\, \omega t)}_{\textbf{phase}}$$

for arbitary functions $\psi_\pm(\mathbf{k}\cdot\mathbf{r} \,\pm\, \omega t)$, and if they fullfill the dispersion relation $\omega \;=\; (\pm)\, c\, k$.

➢ (Complex) monochromatic plane waves: If we restrict ourselves to periodic (harmonic) solutions, two obvious solutions are

$$\psi(\mathbf{r},t) \;=\; A_-\, e^{i\,(\mathbf{k}\cdot\mathbf{r}\,-\,\omega t)} \qquad \text{or} \qquad \psi(\mathbf{r},t) \;=\; A_+\, e^{i\,(\mathbf{k}\cdot\mathbf{r}\,+\,\omega t)}$$

$$\psi \;=\; \text{const.} \qquad \text{for} \qquad t = t_o \qquad \Longleftrightarrow \qquad \mathbf{k}\cdot\mathbf{r} \;=\; \text{const.}$$

Here, the vector $\mathbf{k}$ is called the wave or propagation vector and ω the frequency of the plane waves.

5.1.b. Plane-wave radiation

Plane-wave solutions:

➢ Plane waves: Plane waves always propagate into the direction of the wave vector and can be written as

$$\mathbf{E}(\mathbf{r},t) \;=\; \mathbf{E}_o\, e^{i\,(\mathbf{k}\cdot\mathbf{r}\,-\,\omega t)}, \qquad\qquad \mathbf{B}(\mathbf{r},t) \;=\; \mathbf{B}_o\, e^{i\,(\tilde{\mathbf{k}}\cdot\mathbf{r}\,-\,\tilde{\omega} t)}$$

However, since the em field must satisfy not only the homogenous wave equation $\Box\,\psi \;=\; 0$ but also Maxwell's equations for the coupling of the $\mathbf{E}$ - und $\mathbf{B}$ fields

$$\mathbf{rot}\,\mathbf{E} \;=\; -\,\frac{\partial\,\mathbf{B}}{\partial t} \qquad\Longleftrightarrow\qquad i\,(\mathbf{k}\times\mathbf{E}_o\,)\,e^{i\,(\mathbf{k}\cdot\mathbf{r}\,-\,\omega t)} \;=\; i\,\tilde{\omega}\,\mathbf{B}_o\,e^{i\,(\tilde{\mathbf{k}}\cdot\mathbf{r}\,-\,\tilde{\omega} t)}, \qquad \omega \;=\; \tilde{\omega}\,; \qquad \mathbf{k} \;=\; \tilde{\mathbf{k}}\,; \qquad \mathbf{k}\times\mathbf{E}_o \;=\; \omega\,\mathbf{B}_o\,.$$

Of course, this Maxwell equation need to be fulfilled for all times and places.

➢ If we use of the three other Maxwell equations, we furthermore obtain:

$$\mathbf{div}\,\mathbf{E} \;=\; 0 \qquad\Longrightarrow\qquad \mathbf{k}\cdot\mathbf{E}_o \;=\; 0$$

$$\mathbf{div}\,\mathbf{B} \;=\; 0 \qquad\Longrightarrow\qquad \mathbf{k}\cdot\mathbf{B}_o \;=\; 0$$

$$\mathbf{rot}\,\mathbf{B} \;=\; \frac{1}{c^2}\,\frac{\partial\,\mathbf{E}}{\partial t} \qquad\Longrightarrow\qquad \mathbf{k}\times\mathbf{B}_o \;=\; -\,\frac{\omega}{c^2}\,\mathbf{E}_o \qquad\Longrightarrow\qquad (\mathbf{k}\times\mathbf{B}_o)^2 \;=\; k^2\,B_o^2 \;=\; \frac{\omega^2}{c^4}\,E_o^2 \qquad\Longrightarrow\qquad E_o^2 \;=\; c^2\,B_o^2.$$

Therefore, the three vectors $\mathbf{E}_o$, $\mathbf{B}_o$, $\mathbf{k}$ form (up to any even permutation) an orthogonal and right-handed system, i.e. the vectors $\mathbf{E}$ and $\mathbf{B}$ are perpendicular on $\mathbf{k}$ for plane waves.

➢ Vector potential:

$$\mathbf{A}(\mathbf{r},t) \;=\; \mathbf{A}_{\pm}\,e^{i\,(\mathbf{k}\cdot\mathbf{r}\,\pm\,\omega t)} \;=\; \sum_{\lambda}\,A_{o,\lambda}\,\mathbf{e}_{\lambda}\,e^{i\,(\mathbf{k}\cdot\mathbf{r}\,\pm\,\omega t)}$$

➢ Equation of a plane: For plane waves, all spatial points $\mathbf{r}$ with $\mathbf{k}\cdot\mathbf{r} \;=\; \text{const.}$ have the same value at any time $t \;=\; t_o\,.$

➢ Wave crest: The wave crest of a plane wave is $A_{\pm}\,e^{i\,(\mathbf{k}\cdot\mathbf{r}\,\pm\,\omega t)}$ and propagates into the direction $\pm\,\mathbf{k}\,.$

Conserved properties of plane waves with $\mathbf{k} \,||\, \mathbf{e}_z$:

➢ (Linear) momentum:

$$p_k \;=\; -i\,\partial_k, \qquad\qquad p_{x,y}\,\mathbf{A}(\mathbf{r},t) \;=\; 0, \qquad\qquad p_z\,\mathbf{A}(\mathbf{r},t) \;=\; k_z.$$

➢ Orbital angular momentum:

$$\ell_z \;=\; -i\,(x\,\partial_y \,-\, y\,\partial_x) \;=\; -i\,\frac{\partial}{\partial\,\varphi}, \qquad\qquad \ell_z\,\mathbf{A} \;=\; 0.$$

➢ Spin (of photons):

$$s_z \;=\; -i \begin{pmatrix} 0 & 1 & 0 \\ -1 & 0 & 0 \\ 0 & 0 & 0 \end{pmatrix}, \qquad\qquad s_z\,\mathbf{A} \;=\; \lambda\,\mathbf{A}.$$

➢ Total angular momentum:

$$j_z \;=\; \ell_z \,+\, s_z, \qquad\qquad j_z\,\mathbf{A} \;=\; \lambda\,\mathbf{A}.$$

➢ For plane waves, the (four) good quantum numbers refer to $\mathbf{p} \;=\; (p_x,\, p_y,\, p_z)$ and λ_c.

5.1.c. Polarization of plane waves in classical electrodynamics

Polarization of plane-waves beams:

➢ Apart from the (well-defined) frequency of plane-wave photons, each photon has generally a spin angular momentum $\hbar$ that can be (partly) aligned in parallel or antiparallel to the direction of propagation. A full alignment of all photon spins gives then rise to a circularly-polarized light beam.

➢ A beam with a circularly-polarized planar wavefront has an azimuthal component of the Poynting vector that is proportional to the radial intensity gradient, even if it has no orbital angular momentum. This gives rise to a finite value, if integrated over the total cross-section of the beam.

➢ Polarization of the electric field: Polarization is an additional property of (em) waves that describes the orientation of their oscillations; by convention, the polarization $-1 \leq p \leq 1$ refers to the electric field. The polarization of light is associated with the spin-angular momentum (density) of the em wave.

➢ The polarisation is said to be linear if $p = 0$, and is left- or right-circular for $p = -1$ and $p = +1$, respectively. For all other values of $-1 < p < 1$, the wave is said to be elliptically polarized. Sometimes, one also refers to the chirality or handedness of the waves in order to denote the left- or right-circular polarization of the light beam.

➢ Vector potential of a circularly-polarized plane wave:

$$\mathbf{A}(\mathbf{r},t) \;=\; \mathbf{e}_\lambda\, e^{i\,(kz\,-\,\omega t)}; \qquad\qquad \mathbf{e}_\lambda \;=\; (\mathbf{e}_x \,+\, i\,\lambda\,\mathbf{e}_y) \qquad\qquad \begin{cases} \lambda \;=\; +1 & \text{left circular} \\ \lambda \;=\; -1 & \text{right circular} \end{cases}$$

➢ Spin angular momentum (SAM): The circular polarization of light is usually associated with a well-defined SAM.

➢ Complex spherical unit vectors $\mathbf{e}_\pm$:

$$\mathbf{e}_\pm \;=\; \frac{1}{\sqrt{2}}\,(\mathbf{e}_x \,\pm\, i\mathbf{e}_y) \qquad\qquad \Longleftrightarrow \qquad\qquad \begin{aligned} \mathbf{e}_x \;&=\; \tfrac{1}{\sqrt{2}}\,(\mathbf{e}_+ \,+\, \mathbf{e}_-) \\ \mathbf{e}_y \;&=\; \tfrac{-i}{\sqrt{2}}\,(\mathbf{e}_+ \,-\, \mathbf{e}_-)\,. \end{aligned}$$

➢ Complex electric field $\mathbf{E}^{(c)} \;=\; (E_x^{(c)},\, E_y^{(c)}, 0)$: Although a complex notation of em fields is often very convinient, the transverse, real electric field is given by

$$\left.\begin{aligned} E_x^{(c)} \;&=\; |E_x^{(c)}|\, e^{i\,\gamma} \\ E_y^{(c)} \;&=\; |E_y^{(c)}|\, e^{i\,(\gamma+\delta)} \end{aligned}\right\} \qquad \mathbf{E}^{(c)} \;=\; \Re\left[(E_x^{(c)}\,\mathbf{e}_x \,+\, E_y^{(c)}\,\mathbf{e}_y)\, e^{i\,(k\,z\,-\,\omega t)}\right] \;=\; E_x\,\mathbf{e}_x \,+\, E_y\,\mathbf{e}_y$$

$$E_x \;=\; |E_x^{(c)}|\,\cos(k\,z \,-\, \omega t \,+\, \gamma), \qquad\qquad E_y \;=\; |E_y^{(c)}|\,\cos(k\,z \,-\, \omega t \,+\, \gamma \,+\, \underbrace{\delta}_{!!}) \quad \text{... real.}$$

➢ Relative phase δ to distinguish different polarization: This relative phase δ refers to the complex field amplitudes $E_x^{(c)}$ and $E_y^{(c)}$

➢ Linear polarization along the angle α: For $\delta = n\pi$ $(n \in \mathbb{N})$

$$\mathbf{E}^{(c)} = \left(|E_x^{(c)}|\,\mathbf{e}_x \pm |E_y^{(c)}|\,\mathbf{e}_y\right)\,\cos(k\,z - \omega t + \gamma) = |\mathbf{E}^{(c)}|\,\mathbf{e}_\alpha\,\cos(k\,z - \omega t + \gamma)$$

$$|\mathbf{E}^{(c)}| = \sqrt{|E_x^{(c)}|^2 + |E_y^{(c)}|^2}, \qquad \tan\alpha = \pm\frac{|E_y^{(c)}|}{|E_x^{(c)}|} \qquad \ldots \begin{cases} (+) & n = \text{gerade} \\ (-) & n = \text{ungerade} \end{cases}$$

$$\mathbf{e}_\alpha = \cos\alpha\,\mathbf{e}_x + \sin\alpha\,\mathbf{e}_y$$

The angle α denotes the (polarization-) direction of $\mathbf{E}$ with regard to the x-axis.

➢ General monochromatic plane wave: Any plane wave can always be written as superposition of two components

5.2. Representation and parametrization of photons in atomic theory

5.2.a. Stokes parametrization and density matrix of a photon

Stokes parameters:

➢ Stokes parameters: These parameters provide a simple and alternative characterization for the polarization of plane waves and are given in terms of three real parameters that describe the polarization state of (transversal) electromagnetic radiation.

➢ Stokes parameters P_1, P_2, P_3 : The first two Stokes parameters quantify the *relative* asymmetries between intensities I_χ of light that is linearly polarized under different angles χ with regard to the the reaction plane: $P_1 = (I_o - I_{90})/(I_o + I_{90})$ and $P_2 = (I_{45} - I_{135}/(I_{45} + I_{135})$. The parameter P_3 reflects the degree of circular polarization of the emitted photons.

➢ The Stokes parameters were defined by George Gabriel Stokes in 1852 as a mathematically convenient alternative to the more common description of incoherent or partly polarized radiation in terms of its total intensity I, the degree of polarization P, and the orientation of the (so-called) polarization ellipse.

➢ Degree of polarization: The polarization state of the photon is said to be *pure* if they obey the Stokes parameters obey the restriction $\sum_{i=1}^{3} P_i^2 = 1$.

Table 5.1.: Stokes parametrization of photons for selected polarization of photons with $\mathbf{k} \,||\, \mathbf{e}_z$.

Selected photon polarization	P_1	P_2	P_3
unpolarized	0	0	0
polarized along x-axis	1	0	0
polarized along y-axis	-1	0	0
right-circularly polarized	0	0	1
left-circularly polarized	0	0	-1

➢ Degree of linear polarization: The parameter $P_\ell = \sqrt{P_1^2 + P_2^2}$ is called the degree of linear polarization.

➢ Stokes parameters $P_3 = P_c$: Photons with $\lambda = +1$ are called right-circularly polarized photons, and photons with $\lambda = -1$ are called left-circularly polarized photons.

➢ Note that the notation in optics is often opposite to that used in quantum electrodynamics for historical reasons.

Alternative representation of polarized photons:

➢ Instead of the Stokes parameters P_1 and P_2, it is often convenient for the analysis of different experimental situations to use the degree of linear polarization P_ℓ and the direction of the principal axis of the polarization ellipse φ_0.

➢ Polarization ellipse: If, in the chosen coordinate frame, the x-axis is directed along the principal axis of a polarized photon beam ($\varphi_0 = 0°$), the Stokes parameter P_1 takes the largest value $|P_1| = P_\ell$, while the Stokes parameter P_2 vanishes. This easily shows that the Stokes parameters P_1 and P_2 depend on the choice of the x-axis even if the z-axis is fixed along the beam, while the degree of linear polarization P_ℓ remains invariant.

➢ Polarization ellipse: It is often convenient to introduce the angle φ_0 by the relations

$$\cos 2\,\varphi_0 = \frac{P_1}{P_\ell}, \qquad \sin 2\,\varphi_0 = \frac{P_2}{P_\ell}$$

➢ Probability for measuring a linearly polarized photon along φ in the xy-plane: For a density matrix with given P_ℓ, φ_0 Balashov *et al.* (2001) shows the probability distribution

$$W(\varphi) = \frac{1}{2}(1 + P_\ell \cos 2(\varphi - \varphi_0))$$

for measuring linearly-polarized photon along φ in the xy-plane.

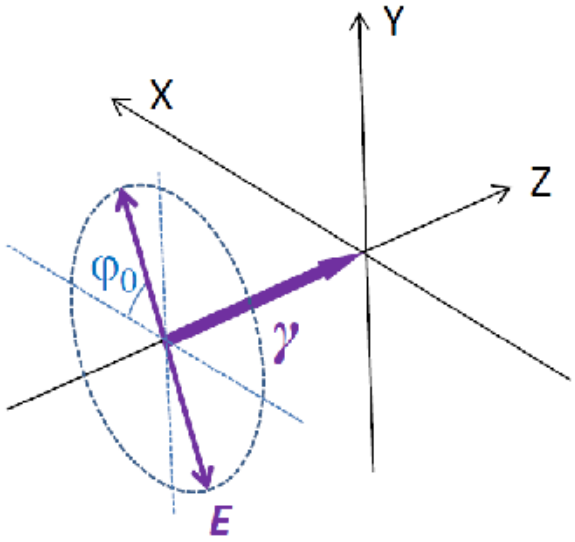

Figure 5.1.: Laboratory coordinate system.

➢ Angle of the polarization vector: The angle φ_0 indicates the *principal axis* of the *polarization ellipse* of the photon beam. It describes the direction of the axis (with regard to the x-axis) which the intensity of the transmitted photon beam is the largest, while it is lowest intensity perpendicular to this direction.

Photon density matrix:

➢ Photon density matrix in helicity representation: Most naturally, the spin state of an incident photon is expressed within its helicity representation

$$\rho_\gamma \;=\; \sum_{\lambda\,\lambda'} c_{\lambda\lambda'}\,|\mathbf{k}\,\lambda\rangle\,\langle\mathbf{k}\,\lambda'|\,,$$

where the helicity λ is the spin projection of the photon upon the direction of its propagation, i.e. along the momemtum or wave vector $\mathbf{k}$.

➢ Since for a photon (with intrinsic spin $s \equiv 1$) the helicity just takes the values $\lambda = \pm 1$, only three real parameters are required to describe the spin state of the photons. These parameters in the photon density matrix are closely connected to the Stokes parameters of light (Rose, 1961)

$$(c_{\lambda\lambda'}) \;=\; \langle\mathbf{k}\,\lambda\,|\,\rho_\gamma\,|\,\mathbf{k}\,\lambda'\rangle \;=\; \frac{1}{2}\begin{pmatrix} 1+P_3 & P_1 - iP_2 \\ P_1 + iP_2 & 1-P_3 \end{pmatrix}.$$

Note that this definition differs from those in Balashov *et al.* (2005) by a factor -1 for the P_1 and P_2 parameters because of the different convention of the spherical unit vectors $\mathbf{e}_\pm$.

5.2.b. Pure polarization states of photons

Linearly-polarized plane-wave photons with $\mathbf{k} \,||\, \mathbf{e}_z$:

➢ In this section, we consider pure polarization states of an incoming photon, i.e. light with a photon density matrix $P_1^2 + P_2^2 + P_3^2 = 1$, and which is thus equivalent to a density-matrix with $\rho^2 = \rho$.

➢ With this restriction in mind, any polarized state of a transvere photon can be described by the linear combination

$$|\mathbf{e}\rangle \;=\; g_+\,\mathbf{e}_+ \,+\, g_-\,\mathbf{e}_-\,,$$

where $\mathbf{e}_\lambda \quad (\lambda = \pm)$ are the unit polarization vectors within the circular basis, and with $\quad |g_+|^2 \,+\, |g_-|^2 \,=\, 1\,.$

➢ The state of a linearly-polarized photon along some given direction φ_0 in the $x-y$ plane can be written in the form

$$|\mathbf{e}_{\varphi_0}\rangle \;=\; -\frac{1}{\sqrt{2}}\,\left(e^{-i\,\varphi_0}\,\mathbf{e}_+ \;-\; e^{i\,\varphi_0}\,\mathbf{e}_-\right)\,.$$

➢ Pure linearly-polarized light with $P_\ell \,=\, 1$: $\quad |g_+| \,=\, |g_-|\,.$

Elliptically-polarized plane-wave photons with $\mathbf{k}\,||\,\mathbf{e}_z$:

➢ Photon density matrix in terms of the $g_\pm$ coefficients: With these notations, an arbitrarely polarized pure state of a (transversal) photon can be expressed in terms of the $g_\pm$ coefficients by either a $2\,\times\,2$ matrix or by means of the corresponding Stokes parameters:

$$\langle \mathrm{k}\lambda\,|\rho|\,\mathrm{k}\lambda'\rangle \;=\; \begin{pmatrix} |g_+|^2 & g_+\,g_-^* \\ g_+^*\,g_- & |g_-|^2 \end{pmatrix}\,, \qquad P_1 \;=\; -2\,\Re\left(g_+\,g_-^*\right), \qquad P_2 \;=\; 2\,\Im\left(g_+\,g_-^*\right), \qquad P_3 \;=\; |g_+|^2 \,-\, |g_-|^2\,.$$

➢ Polarization ellipse: The linear polarization can be characterized also by P_ℓ and φ_0 with

$$P_\ell \;=\; 2\,\left|g_+\,g_-^*\right| \;=\; 2\,|g_+|\;|g_-|\cos 2\,\varphi_0 \;=\; -\frac{\Re\left(g_+\,g_-^*\right)}{|g_+\,g_-^*|}\,, \qquad \sin 2\varphi_0 \;=\; -\frac{\Im\left(g_+\,g_-^*\right)}{|g_+\,g_-^*|}.$$

These simple relations can be used to also find the $g_\pm$-coefficients for given paramters P_ℓ and φ_0 .

➢ Fully-polarized light with $P_\ell \,\neq\, 1$:

$$\text{for } |g_+| \,>\, |g_-|: \qquad |g_+| \;=\; \frac{1}{2}\,\left(\sqrt{1+P_\ell}\,+\,\sqrt{1-P_\ell}\right), \qquad |g_-| \;=\; \frac{1}{2}\,\left(\sqrt{1+P_\ell}\,-\,\sqrt{1-P_\ell}\right)$$

$$\text{for } |g_+| \,<\, |g_{-1}|: \qquad |g_+| \;=\; \frac{1}{2}\,\left(\sqrt{1+P_\ell}\,-\,\sqrt{1-P_\ell}\right), \qquad |g_-| \;=\; \frac{1}{2}\,\left(\sqrt{1+P_\ell}\,+\,\sqrt{1-P_\ell}\right)$$

➢ The relative phase of the coefficients: $g_+ \,=\, |g_+|\,e^{i\,\xi_+}$; $\quad g_- \,=\, |g_-|\,e^{i\,\xi_-}$ can be found from the equation: $\quad \xi_- \,-\, \xi_+ \,=\, 2\,\varphi_0 \,+\, \pi\,.$

➢ Polarization vectors $\boldsymbol{\epsilon}_1$, $\boldsymbol{\epsilon}_2$ of elliptical-polarized plane-wave radiation: An alternative representation of the polarization vector is given by:

$$\boldsymbol{\epsilon}_j \;=\; \left(\mathbf{e}_x\,\cos\left(\frac{\xi_j}{2}\right) \,+\, i\,\mathbf{e}_y\,\sin\left(\frac{\xi_j}{2}\right)\,\exp\left(\frac{i\,\eta_j}{2}\right)\right), \qquad \boldsymbol{\epsilon}_j^* \;=\; \left(\mathbf{e}_x\,\cos\left(\frac{\xi_j}{2}\right) \,-\, i\,\mathbf{e}_y\,\sin\left(\frac{\xi_j}{2}\right)\,\exp\left(\frac{-\,i\,\eta_j}{2}\right)\right), \qquad j \;=\; 1,2.$$

➢ Two elliptically-polarized beams with the same angular momentum but opposite helicity: The easist way to describe such a superposition is $\xi_1 = \xi_2 = \pi/2, \quad \eta_1 = \eta_2 = 0$, and this leads to

$$\boldsymbol{\epsilon}_1 = \boldsymbol{\epsilon}_2 \equiv \boldsymbol{\epsilon}, \qquad \boldsymbol{\epsilon}_1^* = \boldsymbol{\epsilon}_2^* \equiv \boldsymbol{\epsilon}^*, \qquad \boldsymbol{\epsilon}\cdot\boldsymbol{\epsilon}^* = 1, \qquad \boldsymbol{\epsilon}\cdot\boldsymbol{\epsilon} = \boldsymbol{\epsilon}^*\cdot\boldsymbol{\epsilon}^* = 0\,.$$

➢ Two elliptically-polarized beams with the same helicity and opposite angular momentum: These beams are descroibed by $\xi_1 = -\xi_2 = \pi/2, \quad \eta_1 = \eta_2 = 0$, and the two polarization vectors then fulfill

$$\boldsymbol{\epsilon}_1 = \boldsymbol{\epsilon}_2^* \equiv \boldsymbol{\epsilon}, \qquad \boldsymbol{\epsilon}_1^* = \boldsymbol{\epsilon}_2 \equiv \boldsymbol{\epsilon}^*, \qquad \boldsymbol{\epsilon}\cdot\boldsymbol{\epsilon}^* = 1, \qquad \boldsymbol{\epsilon}\cdot\boldsymbol{\epsilon} = \boldsymbol{\epsilon}^*\cdot\boldsymbol{\epsilon}^* = 0\,.$$

Beams of fully-polarized light with $\mathbf{k} \nparallel \mathbf{e}_z$:

➢ Sequences of completely polarized light pulses: In experiments, one often considers a sequence of (fully polarized) photon pulses, which propagate however into different directions.

➢ Hierarchy of angles in defining the em pulses: For such a sequence of pulses, all angles are defined with respect to a fixed laboratory frame $\Sigma = (x, y, z)$, and where we assume all coordinate systems to be properly 'right-handed'.

➢ In the (primed) coordinates Σ' as associated with some given pulse, the polarization cofficients are assumed to be:

$$g_+ = 1, \qquad g_- = 0 \qquad \text{(for 'helicity : } +1')$$

$$g_+ = 0, \qquad g_- = 1 \qquad \text{(for 'helicity : } -1')$$

$$g_+ = -\frac{1}{\sqrt{2}}\, e^{-i\,\phi_0}, \qquad g_- = \frac{1}{\sqrt{2}}\, e^{i\,\phi_0} \qquad \text{(for 'linear' and given } \phi_0).$$

➢ First pulse: The wave vector of the first pulse always defines the z-axis and its linear polarization (ϕ_0) the x-axis of the fixed frame Σ, i.e. the first pulse defines the $x-z$ scattering plane. For a circularly polarized pulse, the x-axis is defined indirectly due to the definition of subsequent pulses (see below); it need not to be defined explicitly if there is only a single, circularly-polarized pulse.

➢ Parameters of the first pulse:

$$\phi_1 = 0; \qquad \theta_1 = 0; \qquad (\phi_1 = 0 \qquad \text{for circularly polarized light})$$

5.3. Multipole decomposition of the radiation field

5.3.a. Elements from the theory of multipole transitions

Transition amplitudes:

➢ Johnson (2008) provide a systematic decomposition of the transition amplitudes into multipole components.

➢ Transition amplitudes due to a transverse-gauge vector potential $\mathbf{A}^{\,(\text{transverse})}(\mathbf{r},\omega)$: For a single-electron atom, the transition amplitude from state $a = |n_a\kappa_a m_a\rangle \longrightarrow b = |n_b\kappa_b m_b\rangle$ due to the interaction with a plane-wave radiation field with the transverse-gauge vector potential $\mathbf{A}^{\,(\text{transverse})}(\mathbf{r},\omega) = \boldsymbol{\epsilon}\, e^{i\,\mathbf{k}\cdot\mathbf{r}}$, with $\boldsymbol{\epsilon}\cdot\mathbf{e}_z = 0$ is

$$T_{ba} = \int d^3\mathbf{r}\;\; \psi_b^*\, \boldsymbol{\alpha}\cdot\mathbf{A}^{\,(\text{transverse})}(\mathbf{r},\omega)\;\psi_a .$$

Multipole potentials:

➢ Plane-wave multipole potentials $\mathbf{a}_{LM}^{(p)}(\mathbf{r})$: In the multipole expansion of the plane-wave vector potential, the multipole potentials satisfy both, the Helmholtz equation and transversality condition

$$\boldsymbol{\nabla}^2\,\mathbf{a}_{LM}^{(p)} + k^2\,\mathbf{a}_{LM}^{(p)} = 0, \qquad\qquad \boldsymbol{\nabla}\cdot\mathbf{a}_{LM}^{(p)} = 0 \qquad\qquad p = 0,\,1\,.$$

➢ The multipole potentials $\mathbf{a}_{LM}^{(p)}$ with $p = 0$ are the magnetic multipole potentials and with $p = 1$ the electric multipole potentials.

➢ Electron-multipole interaction operator: The interaction operator $\boldsymbol{\alpha}\cdot\mathbf{a}_{LM}^{(p)}$ is an irreducible tensor operator of rank L and parity $(-1)^{L+1-p}$.

➢ The multipole expansion of the (transverse-gauge) plane-wave vector potential still contains all information about the polarization and propagation direction of the photons.

➢ Representation of the multipole potentials: Using the well-known idendities of the spherical Bessel functions, the multipole potentials $\mathbf{a}_{LM}^{(p)}$ can be expressed as (Johnson, 2007)

$$\mathbf{a}_{LM}^{(0)}(\mathbf{r}) \;=\; j_L(kr)\,\mathbf{Y}_{LM}^{(0)}(\mathbf{r}), \qquad\qquad \mathbf{a}_{LM}^{(1)}(\mathbf{r}) \;=\; \left[j_L'(kr) \;+\; \frac{j_L(kr)}{kr}\right]\mathbf{Y}_{LM}^{(1)}(\mathbf{r}) \;+\; \sqrt{L(L+1)}\,\frac{j_L(kr)}{kr}\,\mathbf{Y}_{LM}^{(-1)}(\mathbf{r}).$$

5.3.b. Single-electron (reduced) multipole-transition matrix elements

Johnson's single-electron reduced multipole-transition matrix elements:

➢ Transverse (velocity) gauge: Johnson (2007, section 6.3) derives the reduced multipole-transition matrix elements for $\mathbb{M} = (L,p)$ and $q = \omega/c$ as:

$$\left\langle a \left\| \mathbb{t}^{(\mathbb{M},\,\text{magnetic})}(\omega) \right\| b \right\rangle \;=\; \left\langle -\kappa_a \left\| \mathbb{C}^{(L)} \right\| \kappa_b \right\rangle \int_0^\infty dr\;\frac{\kappa_a \;+\; \kappa_b}{L+1}\,j_L(qr)\;[P_a\,Q_b \;+\; Q_a\,P_b]$$

$$\left\langle a \left\| \mathbb{t}^{(\mathbb{M},\,\text{electric})}(\omega) \right\| b \right\rangle \;=\; \left\langle \kappa_a \left\| \mathbb{C}^{(L)} \right\| \kappa_b \right\rangle \int_0^\infty dr\;\left\{-\frac{\kappa_a \;-\; \kappa_b}{L+1}\left[j_L'(qr) \;+\; \frac{j_L(qr)}{qr}\right][P_a\,Q_b \;+\; Q_a\,P_b] \;+\; L\,\frac{j_L(qr)}{qr}\;[P_a\,Q_b \;-\; Q_a\,P_b]\right\}.$$

➢ Length gauge: While the reduced multipole-transition matrix elements are the same in length gauge, Johnson (2007, section 6.3) derives the reduced multipole-transition matrix elements in length gauge as:

$$\left\langle a \left\| \mathbb{t}^{(\mathbb{M},\,\text{electric})}(\omega) \right\| b \right\rangle$$
$$= \left\langle \kappa_a \left\| \mathbb{C}^{(L)} \right\| \kappa_b \right\rangle \int_0^\infty dr\;\left\{j_L(qr)\;[P_a\,P_b \;+\; Q_a\,Q_b] \;+\; j_{L+1}(qr)\left[\frac{\kappa_a \;-\; \kappa_b}{L+1}\;[P_a\,Q_b \;+\; Q_a\,P_b] \;+\; [P_a\,Q_b \;-\; Q_a\,P_b]\right]\right\}.$$

Johnson's frequency-dependent multipole-moment operators:

➢ Multipole-moment matrix elements: Following Johnson (2007), the reduced multipole-moment matrix elements can be calculate for the reduced multipole-transition matrix elements

$$\left\langle a \left\| \mathfrak{q}^{(\mathbb{M})}(\omega) \right\| b \right\rangle = \frac{(2L+1)!!}{q^L} \left\langle a \left\| \mathbb{t}^{(\mathbb{M})}(\omega) \right\| b \right\rangle .$$

5.3.c. Many-electron (reduced) multipole emission and absorption amplitudes

JAC's (standard) multipole amplitudes for photon absorption and emission:

➢ Mutipole (absorption) amplitude $|\alpha_i \mathbb{J}_i\rangle + \hbar\omega(\mathbb{M}, \lambda) \rightarrow |\alpha_f \mathbb{J}_f\rangle$: For the absorption of a photon with energy ω, well-defined multipolarity (angular momentum) L and helicity $\lambda = \pm 1$, we always use the notation

$$\left\langle \alpha_f \mathbb{J}_f \left\| \mathbb{O}^{(\mathbb{M},\,\text{absorption})}(\omega) \right\| \alpha_i \mathbb{J}_i \right\rangle .$$

➢ Photon emission: from an atom or ion $|\alpha_i \mathbb{J}_i\rangle \longrightarrow |\alpha_f \mathbb{J}_f\rangle + \hbar\omega(\mathbb{M})$.

➢ Care has to be taken about the many-electron multipole amplitudes which appear in many expressions. While we need formally to distinguish between the absorption a_L^{λ} and emission operators $a_L^{\lambda+}$ operators, all (one- and many-electron) multipole-transition matrix elements are always evaluated *in absorption*.

➢ For any photon emission process, this would then require to 'interchange' the sequence *final-state — operator — initial-state* explicitly. This is a (very) high price however in such a large software project, since such an interchange affects the intuitive description of many processes in terms of initial-intermediate-final levels as well as still possibly other subsequent (final) states/levels.

5.4. Electromagnetic light pulses

5.4.a. High-intensity pulses

Matter in intense fields:

➢ The exposure of atoms and matter to high-intensity laser fields is known to give rise to high-harmonic generation, above-threshold ionization and well as laser-induced dissociation and plasma formation, and which are all fundamentally different from processes in the weak-field regime.

➢ These phenomena are often outside of what is described by (standard) atomic-structure methods since the external field, that acts upon the electrons in typical strong-field experiments, is then comparable to the Coulomb potential of the nucleus.

➢ Pump-probe experiments: In these experiments, two short pulses are typically required. While the pump pulse starts the reaction, the probe pulse investigates the state of the system after a defined time delay. These measurements is repeated several times with increasing time delays in order to finally obtain a molecular movie.

➢ If the level structure of the atoms is not affected by the (moderately intense) laser pulses, the time-dependent density matrix may allow to model the (time-dependent) level occupuation and coherences of an atoms and, eventually, all the photoexcitation and ionization processes.

➢ Two-color absorption in strong laser fields: The simultaneous absorption of a single high-frequency photon in a strong optical laser field generally leads to equally spaced sideband peaks in the photoelectron spectra due to the (additional) absorption or emission of several laser photons. This (XUV + IR) two-color absorption has been first observed in high-order harmonic generation by overlapping high harmonics with the fundamental laser frequency. With a femtosecond XUV pulse from a FEL, the two-color absorption in strong laser fields can be explored without the contributions from neighboured harmonics (Gramajo *et al.*, 2017).

➢ Two-color absorption in strong laser fields: Two different interaction regimes can be distinguished for the interaction of atoms with a combined and overlapping XUV and IR pulses owing to their relative pulse duration: (i) If the XUV pulse duration $\tau^{(\mathrm{XUV})} \gtrsim \tau^{(\mathrm{IR})}$ is longer than the IR pulse, the intensity of the sideband peaks in the photelectron spectrum directly reflect the intensity of the IR laser; (ii) for $\tau^{(\mathrm{XUV})} \ll \tau^{(\mathrm{IR})}$, in constrast, the photelectron spectrum acts as as *streak camera* and reflects the shape and duration of an IR laser pulse. Moreover, variations of the polarization state of the XUV and/or IR laser fields gives generally rise to dichroic effects in the photoelectron spectrum (Gramajo *et al.*, 2017).

5.4.b. Pulse shapes and optical cycles

Pulse shaping in physics and science:

➢ Pulse shaping is frequently used in physics, science and technology. Pulse shaping generally refers to the the process of changing the waveform of a (transmitted) pulse, for instance, in order to make a transmitted signal better suited for a particular communication channel. In telecommunication, for example, pulse shaping is essential in order to ensure that the signal fit to a given frequency band.

➢ In femtosecond physics and chemistry, pulse shaping describes a technology for generating nearly arbitrary pulses with user defined, ultrafast optical waveforms, and by controlling its phase, amplitude, and polarization. Here, the most widely applied technique is Fourier transform pulse shaping.

Frequently applied pulse shapes for time-dependent atomic computations:

➢ In pump- and/or pump-probe experiments, all (symmetric) light pulses are typically defined in terms of a central frequency ω and a (delay) time T_d for the arrival of the pulse center with regard to same reference time $t_0 = 0$. Moreover, the shape function is always normalized to $\max[f_s(t)] = \max[f(t)/f_o] = 1$ and, hence, the intensity of the em field must be captured properly by the constant f_o.

➢ In JAC, the following (symmetric) shapes of the em pulses have been pre-defined: `"sin^2"`, `"sin^2: plateau"`, `"sin^2: cycles"` and `"gaussian"` facilitate the description of experimentally specified pulses. Further pulses shapes might be added if the need arises from the side of experiment.

➢ It is important to ensure that the pulse-shape function $f_s(t)$ (envelope) just contains an integer number of optical cycles. Therefore, one often starts with an $\sin^2$ envelope. For example, an envelope function $\sin^2$ 10T pulse refers to a pulse with 10 optical cycles.

➢ Laser pulse: In time-resolved computations, the laser-atom interaction can be described either by a smooth or a square pulse with envelope (Gharibnejab *et al.*, (2020)

$$\boldsymbol{\mathcal{E}}(t) = \begin{cases} \mathcal{E}_o \, \sin^2\left(\frac{\pi t}{T}\right) \, \mathbf{e}_z & 0 \le t < T \\ 0 & \text{otherwise} \end{cases} , \qquad \boldsymbol{\mathcal{E}}(t) = \begin{cases} \mathcal{E}_o \, \mathbf{e}_z & 0 \le t < T \\ 0 & \text{otherwise} \end{cases}$$

➢ Vector potential of laser pulses in velocity gauges: For a smooth or square pulse and $\phi^{(\mathrm{CEP})} = 0$, the vector potential in the interval

$0 \leq t < T$ is (Gharibnejab *et al.*, 2020)

$$A(t) = c\,\mathcal{E}_o \left(\frac{\sin^2(a^+ t/2)}{2\,a^+} - \frac{\sin^2(a^- t/2)}{2\,a^-} - \frac{\sin^2(\omega\, t/2)}{\omega} \right), \qquad a^+ = \frac{2\pi}{T} + \omega, \qquad a^- = \frac{2\pi}{T} - \omega \qquad \text{smooth pulse}$$

$$A(t) = -c \int_0^t d\tau\, \mathcal{E}(\tau) = -2c\,\mathcal{E}_o \frac{\sin^2(\omega\, t/2)}{\omega} \qquad \text{square pulse}$$

➢ In time-dependent studies, various findings abuot the relative timing and the convergence of numerical results with regard to the step size are independent of the particular type of the laser pulse, i.e. are similar for smooth and square pulse.

➢ Length *versus* velocity gauge: In length gauge, the interaction with the external electro-magnetic field is local and gives rise to a straightforward time evolution due to the given Hamiltonian. In the velocity gauge, in contrast, the Hamiltonian is hermitian and the interaction is *non-local*. In realistic problems, therefore, the choice of the gauge can make significant differences in dependence of the given wavelength. This dependence is also a direct consequence which (high) angular momenta are relevant for the coupling of the radiation field to the electrons.

5.4.c. Maximum pulse intensity

Vector potential:

➢ Amplitude of the vector potential: This amplitude need to be derived from the (maximum) intensity of a laser pulses that is typically given in W/cm^2. In general, this relation between intensity and amplitude is non-trivial since the relationship between intensity and the electric field depends also slightly on the polarization of the pulse. A simple relation only occurs for a linearly-polarized laser beam.

➢ Average intensity of a pulse: If only the average intensity is given, the conversion factor depends also on the particular pulse-shape function. In practice, however, experimentalists rarely know the intensity accurately and, hence, a simplified normalization procedure can normally be used.

➢ Vector potential of a single pulse: The interaction of the electrons with the electric field of the incident pulse of frequency ω, duration T, carrier envelope phase ϕ and with linear polarization along $\mathbf{e}_p$ is often described in terms of the vector potential

$$\mathbf{A}(t) = A_o \sin^2\left(\frac{\pi\, t}{T}\right) \sin(\omega\, t + \phi)\, \mathbf{e}_p, \qquad A_o = \frac{1}{\omega}\sqrt{\frac{I}{I_o}},$$

and where $I_o = 3.5 \cdot 10^{16}$ W/cm^2.

Intensity and pulse geometry:

➢ The atomic unit of electric field is $m_e^2\, e^5/\hbar^4 = 5.1422 \cdot 10^9$ V/cm. From this we have: $E_0\,[a.u.] = 5.34 \cdot 10^{-9}\,\sqrt{I\,[W/cm^2]}$.

5.4.d. Bichromatic laser fields

Bichromatic laser fields:

➢ Bichromatic laser fields: Of some special interests in light-atom interaction studies are fields with two components of commensurate frequencies; for instance, the fundamental component ω and one of its low harmonics $2\,\omega$ or $3\,\omega$. Moreover, these two components are in general out of phase by some angle ϕ.

➢ Linearly-polarized bichromatic fields: For such a field, the electric field can be written in a quite general form as

$$E(t) \;=\; F(t)\,\left[\cos\left(\omega\,t \,+\, \phi_1^{(\mathrm{cep})}\right) \,+\, \eta\,\cos\left(2\,\omega\,t \,+\, \phi_2^{(\mathrm{cep})}\right)\right]$$

with frequencies ω of the fundamental radiation and $2\,\omega$ due to the second harmonic. Here, the same envelope function $F(t)$ is applied for both, the fundamental and the second harmonic, while the ratio of the corresponding amplitudes is specified by the real parameter $\eta\;(\eta > 0)$. The carrier-envelope phases (CEP) are here denoted by $\phi_1^{(\mathrm{cep})}$ and $\phi_2^{(\mathrm{cep})}$, respectively.

➢ Time-dependent electric field in two-color experiments: In two-color experiments, the field is often approximated by (DiFraia *et al.*, 2019)

$$\mathcal{E}(t) \;=\; \sqrt{I_\omega(t)}\,\cos\,\omega\,t \,+\, \sqrt{I_{2\,\omega}(t)}\,\cos\,(2\,\omega\,t \,-\, \phi), \qquad\qquad \boldsymbol{\mathcal{E}}(t) \;=\; \mathcal{E}(t)\,\mathbf{e}_z,$$

and where $I_\omega(t)$, $I_{2\,\omega}(t)$ are the envelopes of the two pulses and ϕ the relative phase between the $\omega - 2\,\omega$ pulses. In this definition, the larger ϕ as more the $2\,\omega$ pulse is delayed.

5.5. Elements from modern optics

Singular optics:

➢ Singular optics: This field of modern optics makes use of wavefront dislocations and phase singularities.

➢ Singular optics: The subject of singular optics are light fields with an intricate knot structure in their field line, fields with optical vortices and (so-called) C-lines as well as light fields with spirals, umbilics, ribbons and Möbius strips in their polarization. These light fields give rise to many different phenomena if they are coupled with space-dependent birefringent elements.

6. Atomic amplitudes

6.1. In JAC implemented amplitudes

6.1.a. Dipole amplitudes (MultipoleMoment)

Amplitude, notations & application:

- Formal quantum notation: $\langle \alpha_f \mathbb{J}_f \,\|\, \mathbb{D} \,\|\, \alpha_i \mathbb{J}_i \rangle \;=\; \langle \alpha_f \mathbb{J}_f \,\|\, \sum_i \mathbf{r}_i \,\|\, \alpha_i \mathbb{J}_i \rangle \quad \text{for} \quad P_f \neq P_i$
- Note that the full dipole operator is often defined by: $\mathbb{D}' \;=\; -\,|e|\,\mathbb{D}\,.$
- Using JAC: Call `MultipoleMoment.dipoleAmplitude(level`$_f$`::Level, level`$_i$`::Level)` or `(level`$_f$`::Level, level`$_i$`::Level; display=true)`, if the value of the amplitude needs to be printed to screen.

6.1.b. Electro-magnetic multipole transition amplitudes (MultipoleMoment, Radiative)

Amplitude, notations & application:

- Formal quantum notation:

$$\left\langle \alpha_f \mathbb{J}_f \left\| \mathbb{O}^{(\mathbb{M},\,\text{emission})}(\omega) \right\| \alpha_i \mathbb{J}_i \right\rangle \;=\; \left\langle \alpha_i \mathbb{J}_i \left\| \sum_{k=1}^{N} \boldsymbol{\alpha}_k \, a^{p}_{k,\,L} \right\| \alpha_f \mathbb{J}_f \right\rangle^{*} \;\equiv\; \left\langle \alpha_i \mathbb{J}_i \left\| \mathbb{O}^{(\mathbb{M},\,absorption)}(\omega) \right\| \alpha_f \mathbb{J}_f \right\rangle^{*}$$

$$\left\langle \alpha_f \mathbb{J}_f \left\| \mathbb{T}^{(\mathbb{M},\,\text{absorption})}(\omega) \right\| \alpha_i \mathbb{J}_i \right\rangle$$

which retains the right order of the initial and final levels with regard to absorption or emission and which and can be obtained from `Jac.Radiative.amplitude()`; cf. section 5.3.c.

➢ Using Jac: Call `Radiative.amplitude("absorption", Mp::Multipole, gauge::EmGauge, omega::Float64, level`$_f$`::Level, level`$_i$`::Level)` or `("absorption", Mp::Multipole, gauge::EmGauge, omega::Float64, level`$_f$`::Level, level`$_i$`::Level; display=true)`, if the value of the amplitude needs to be printed to screen.

➢ Using Jac: Call `MultipoleMoment.transitionAmplitude(Mp::Multipole, gauge::EmGauge, omega::Float64, level`$_f$`::Level, level`$_i$`::Level)` or `(Mp::Multipole, gauge::EmGauge, omega::Float64, level`$_f$`::Level, level`$_i$`::Level; display=true)`, if the value of the amplitude needs to be printed to screen.

Further remarks:

➢ A multipole $\mathbb{M} \equiv (L,p) \equiv (L, \text{electric/magnetic}) =$ E1, M1, E2, ... hereby contains all information about its multipolarity (angular momentum) L and type *magnetic* $(p=0)$ or *electric* $(p=1)$, respectively.

➢ In the module `Radiative`, the multipole-transition amplitudes can be calculated in one of the gauge = {`Coulomb, Babushkin, Magnetic`} as appropriate for electric- and magnetic-multipole transitions.

➢ Johnson's multipole-transition operators: Following Johnson (2007), the electron-photon interaction with the multipole fields ($\mathbb{M}$) can be expressed in terms of a dimensionless multipole-transition operator $\mathbb{T}^{(\mathbb{M})}_M(\omega) = \sum_j \mathbb{t}^{(\mathbb{M})}_M(\mathbf{r}_j;\omega)$, an irreducible tensor operator, whose reduced (single-electron) matrix elements are given in Section 5.3.b. The amplitudes to these operators always describe the absorption of a photon with a given multipolarity.

➢ Johnson's (2007) multipole-transition amplitudes can be calculated in one of the gauge = {`Velocity, Length, Magnetic`} as appropriate for electric- and magnetic-multipole transitions.

6.1.c. Electro-magnetic multipole-moment amplitudes (`MultipoleMoment`)

Amplitude, notations & application:

➢ Formal quantum notation:

$$\left\langle \alpha_f \mathbb{J}_f \left\| \mathbb{Q}^{(\mathbb{M})}(\omega) \right\| \alpha_i \mathbb{J}_i \right\rangle$$

➢ Using JAC: Call `MultipoleMoment.amplitude(Mp::Multipole, gauge::EmGauge, omega::Float64, level_f::Level, level_i::Level)` or `(Mp::Multipole, gauge::EmGauge, omega::Float64, level_f::Level, level_i::Level; display=true)`, if the value of the amplitude needs to be printed to screen.

Further remarks:

➢ Johnson's multipole-moment operator: Johnson (2007) also defines a frequency-dependent (irreducible tensor) multipole-moment operator

$$\mathbb{Q}_M^{(\mathbb{M})}(\omega) \;=\; \sum_j \mathfrak{q}_M^{(\mathbb{M})}(\mathbf{r}_j;\,\omega) \;\equiv\; \frac{(2L+1)!!}{(\omega/c)^L} \sum_j \mathbb{t}_M^{(\mathbb{M})}(\mathbf{r}_j;\,\omega)$$

➢ These amplitudes are calculated by a call to (Johnson's) multipole-transition amplitudes from above [cf. section 6.1.b] but by taking the frequency-dependence into account.

➢ Electric multipole-moment amplitudes can be calculated in one of the gauge = {`Velocity, Length, Magnetic`} as appropriate for electric- and magnetic-multipole transitions.

6.1.d. Momentum transfer amplitudes (`FormFactor`)

Amplitude, notations & application:

➢ Formal quantum notation: $\left\langle \alpha_f \mathbb{J}_f \left\| \sum_j \exp\left(i\,\mathbf{q}\cdot\mathbf{r}_j\right) \right\| \alpha_i \mathbb{J}_i \right\rangle$ = selection rules

➢ Using JAC: Call `FormFactor.amplitude(level_f::Level, level_i::Level, ...)` or `(level_f::Level, level_i::Level, ...; display=true)`, if the value of the amplitude needs to be printed to screen.

Further remarks:

➢ The (single-electron) momentum transfer amplitude help describe inelastic scattering processs and is closely related also to the (so-called) generalized oscillator strength.

➢ The (one-electron) momentum-transfer operator $\mathbb{T}^{(1)}(\mathbf{q}) = \sum_{j=1}^{N} \exp(i\,\mathbf{q}\cdot\mathbf{r}_j)$ can be utilized in order to express the standard form factor for an atom in a given sublevel $|\alpha\,\mathcal{J}M\rangle$ in terms of an (many-electron) expectation value; cf. 7.1.d.

6.2. In JAC partly-implemented amplitudes

6.2.a. Parity non-conservation amplitudes (ParityNonConservation)

Amplitude, notations & application:

➢ Formal quantum notation: $\langle \alpha_f \mathcal{J}_f \,\|\, \mathbb{H}^{(\mathrm{weak-charge})} \,\|\, \alpha_i \mathcal{J}_i \rangle$

➢ Using JAC: Call `ParityNonConservation.weakChargeAmplitude(level`$_f$`::Level, level`$_i$`::Level, model::Nuclear.Model)` or `(level`$_f$`::Level, level`$_i$`::Level, model::Nuclear.Model; display=true)`, if the value of the amplitude needs to be printed to screen.

Further remarks:

➢ Parity non-conservation (PNC) effects arises in atoms mainly because of the exchange of Z^0-bosons between atomic electrons and the nucleus. Various observables due to this parity non-conserving interactions can be described in terms of a nuclear-spin independent Hamiltonian $\mathbb{H}^{(\mathrm{weak-charge})}$, an effective single-electron operator, if non-relativistic nucleons can be assumed, cf. section 3.8.b.

➢ Especially, if the proton and neutron densities coincide, $\rho_p = \rho_n = \rho$, the general nuclear-spin independent Hamiltonian simplifies and can be described in terms of a single nuclear- weak charge Q_W,

$$\mathbb{H}^{(\mathrm{weak-charge})} = -\frac{G}{2\sqrt{2}}\, Q_W \sum_j \gamma_{5,j}\, \rho(r_j)\,,$$

where $G = 2.22{\cdot}10^{-14}$ a.u. is the Fermi constant, $\rho(r)$ is the normalized nuclear density with $\int dV\,\rho(\mathbf{r}) = 1$, and $Q_W \approx -N + Z\,(1 - 4\,\sin^2\,\theta_W)$ is the nuclear weak charge with θ_W being the Weinberg angle.

6.2.b. Schiff-moment amplitudes (ParityNonConservation)

Amplitude, notations & application:

➢ Formal quantum notation: $\left\langle \alpha_f \mathbb{J}_f \right\| \mathbb{H}^{(\text{Schiff}-\text{moment})} \left\| \alpha_i \mathbb{J}_i \right\rangle = \left\langle \alpha_f \mathbb{J}_f \right\| \mathbb{H}^{(\text{Schiff}-\text{moment})} \left\| \alpha_i \mathbb{J}_i \right\rangle \delta_{J_f,J_i} \quad P_f \neq P_i$

➢ Using Jac: Call `ParityNonConservation.schiffMomentAmplitude(level`$_f$`::Level, level`$_i$`::Level, model::Nuclear.Model)` or `(level`$_f$`::Level, level`$_i$`::Level, model::Nuclear.Model; display=true)`, if the value of the amplitude needs to be printed to screen.

Further remarks:

➢ Nuclear electric-dipole (Schiff) moments: If $\mathbf{S}$ is the P-odd and T-odd nuclear Schiff moment, the associated P-odd and T-odd Hamiltonian is given by (Dzuba *et al.*, 2009)

$$\mathbb{H}^{(\text{Schiff}-\text{moment})} = -e\,\phi^{(\text{Schiff}-\text{moment})} = -4\pi e\,\mathbf{S}\cdot\nabla\,\delta(r) = -\frac{3\,S^{(\text{SM})}\,(\mathbf{I}/I)\cdot\mathbf{r}}{R}\,\rho(r)$$

where $S^{(\text{SM})}\,(\mathbf{I}/I)$ is the Schiff-moment vector, i.e. the product of the coupling constant $S^{(\text{SM})}$ and the nuclear spin $\mathbf{I}$, and $R = \int_0^\infty dr\; r^4\;\rho(r)$. Moreover, $\phi^{(\text{Schiff}-\text{moment})}$ is the electrostatic potential of the nucleus corresponding to a P-odd and T-odd charge distribution; cf. section 3.8.c.

6.3. Further amplitudes, not yet considered in JAC

6.3.a. Anapole-moment amplitudes (ParityNonConservation)

Amplitude, notations & application:

➢ Formal quantum notation: $\left\langle \alpha_f \mathbb{J}_f \left\| \mathbb{H}^{(\text{anapole}-\text{moment})} \right\| \alpha_i \mathbb{J}_i \right\rangle$

Further remarks:

➢ A P-odd, T-even anapole moment of the nucleus was first introduced by Zel'dovich and arises due to the presence of a parity-violating weak interaction between nucleons, cf. section 3.8.b. The anapole moment is directed along the nuclear spin **I**, gives typically the dominant nuclear-spin dependent electron-nucleus interaction and manifests itself in terms of a slightly modified electro-magnetic interaction between the nucleus and the atomic electrons.

➢ Hamiltonian for the interaction of the electrons with the nuclear anapole moment: This Hamiltonian has the form (Dzuba *et al.*, 2009)

$$\mathbb{H}^{(\text{anapole}-\text{moment})} = \frac{G}{\sqrt{2}} (I + 1/2) (-1)^{I+1/2-\ell_N} \kappa_{\text{AM}} \sum_j \frac{\mathbf{I} \cdot \boldsymbol{\alpha}_j}{I(I+1)} \rho(r_j),$$

where $G = 2.22 \cdot 10^{-14}$ a.u. is the Fermi constant, I is the nuclear spin, ℓ_N the orbital angular momentum of the outermost nucleon and κ_{AM} is a dimensionless coupling constants for ...

6.3.b. Scalar-pseudo-scalar amplitudes

Amplitude, notations & application:

➢ Formal quantum notation: $\left\langle \alpha_f \mathbb{J}_f \left\| \mathbb{H}^{(\text{scalar}-\text{pseudo}-\text{scalar})} \right\| \alpha_i \mathbb{J}_i \right\rangle$

Further remarks:

➢ Hamiltonian for the P-odd, T-odd scalar-pseudo-scalar interaction: In coordinate represetation, this Hamiltonian can be written as (Dzuba *et al.*, 2009)

$$\mathbb{H}^{(\text{scalar}-\text{pseudo}-\text{scalar})} = -\frac{G}{\sqrt{2}}\,\frac{1}{2m_p\,c}\,C_s\sum_j\left[\gamma_0\,\frac{d\,\rho(r)}{dr}\right]_j$$

where G is the Fermi constant, m_p is the nucleon mass, C_s is a (isotope and) nuclear-state dependent constant, and where $\left[\gamma_0\,\frac{d\,\rho(r)}{dr}\right]$ is a scalar term that arises from the scalar product of the ∇-vector with an particularly averaged spin-vector of the nucleus.

6.3.c. Tensor-pseudo-tensor amplitudes

Amplitude, notations & application:

➢ Formal quantum notation: $\left\langle \alpha_f \mathbb{J}_f \,\middle\|\, \mathbb{H}^{(\text{tensor}-\text{pseudo}-\text{tensor})} \,\middle\|\, \alpha_i \mathbb{J}_i \right\rangle$

Further remarks:

➢ Hamiltonian for the P-odd, T-odd tensor-pseudo-tensor interaction: In coordinate representation, this Hamiltonian can be written as (Dzuba *et al.*, 2009)

$$\mathbb{H}^{(\text{tensor}-\text{pseudo}-\text{tensor})} = i\,\sqrt{2}\,G\,C_t\sum_j\left[\gamma\,\rho(r)\right]_j$$

where G is the Fermi constant, C_t is a (isotope and) nuclear-state dependent constant, and where $[\gamma\,\rho(r)]$ is a scalar term that arises from the scalar product of the γ-vector with an averaged spin-vector of the nucleus.

➢ Total P-odd, T-odd electron-nucleus interaction Hamiltonian: $\mathbb{H}^{(\text{P}-\text{odd, T}-\text{odd electron}-\text{nucleus})} = \mathbb{H}^{(\text{tensor}-\text{pseudo}-\text{tensor})} + \mathbb{H}^{(\text{tensor}-\text{pseudo}-\text{tensor})}$

6.3.d. Nuclear magnetic-quadrupole-moment amplitudes due to internal B-field

Amplitude, notations & application:

➢ Formal quantum notation: $\left\langle \alpha_f \mathbb{J}_f \right\| \mathbb{H}^{(\text{nuclear}-\text{MQM})} \left\| \alpha_i \mathbb{J}_i \right\rangle$

Further remarks:

➢ This interaction (Hamiltonian) arise from the interaction of the electron EDM d_e with the electro-magnetic fields of the nucleus as seen by the electron. If the treatment is restricted to second order, only the interaction of the electron EDM with the magnetic field $\mathbf{B}$, which is created by the nuclear magnetic-dipole moment, need to be taken into account.

➢ Nuclear-MQM Hamiltonian: In coordinate representation, this Hamiltonian can be written as (Dzuba *et al.*, 2009)

$$\mathbb{H}^{(\text{nuclear}-\text{MQM})} \;=\; -\,i\,d_e\,\boldsymbol{\gamma}\cdot\boldsymbol{B} \;=\; -\,i\,d_e\sum_j \boldsymbol{\gamma}_j\cdot\left[\boldsymbol{\nabla}_j\times\frac{\mathbf{M}\times\mathbf{r}_j}{r^3_{>,j}} \;+\; ...\right]$$

6.4. Composed many-electron amplitudes, not yet considered in JAC

6.4.a. Parity-violating (non-diagonal, second-order) amplitudes

Amplitude, notations & application:

➢ Parity violation: The (effective) parity-violating interaction is caused by the exchange of Z_o bosons between the atomic electrons and the nucleus. The parity-violating interaction typically results in non-vanishing off-diagonal electric-dipole matrix element between two atomic states of the same parity; cf. section 3.8.b.

6.4.b. Charge-parity-violating (diagonal, second-order) amplitudes

Amplitude, notations & application:

➢ Charge-parity violation: An intrinsic electron electric dipole moment d_e leads to CP-violation in atoms and also induces an atomic electric dipole moment. cf. section 3.8.d.

6.4.c. Electric-dipole moment enhancement factor

Amplitude, notations & application:

➢ An intrinsic electric-dipole moment (EDM) of the electron can enhanced the EDM of the atom. In heavy atoms, in particular, an induced atomic EDM can be strongly enhanced, when compared to the electron EDM itself.

➢ A typical goal is to find the atomic EDM $d_{\rm atom} = |\mathbf{d}_{\rm atom}| \equiv d_{\rm atom}\,|\mathbf{F}/F|$, where $\mathbf{F} = \mathbf{I} + \mathbf{J}$ is the total angular momentum of an atomic (hyperfine) level.

➢ The value of the atomic EDM, compared to the electron EDM, is expressed by means of an enhancement factor $K = d_{\rm atom}/d_e$, and which increases with nuclear charge Z faster than Z^3.

7. Atomic properties

7.1. In JAC implemented level properties

7.1.a. Transition probabilities for a single multiplet (Einstein)

Properties, notations & application:

- Photon emission: from an atom or ion $A^* \longrightarrow A^{(*)} + \hbar\omega$
- Formal quantum notation: $|\alpha_i \mathbb{J}_i\rangle \longrightarrow |\alpha_f \mathbb{J}_f\rangle + \hbar\omega$
- Using JAC: Perform an `Atomic.Computation(.., properties=[EinsteinX, ..], configs=[..], einsteinSettings= Einstein.Settings(..), ..)` or call directly functions from the module `Einstein`.
- In the JAC program, the transition probabilities, oscillator strength (in emission) and radiative lifetimes are calculated and tabulated by default for all selected transitions from a given single multiplet (i.e. list of configurations). Apart from the multipoles, the user can also specify an overall shift in the photon energies as well as a minimum and maximum transition energy, for which transitions are taken into account.
- In the `Einstein` module, the emission (transition) amplitudes $\left\langle \alpha_f \mathbb{J}_f \left\| \mathbb{O}^{(\mathbb{M},\,\text{emission})} \right\| \alpha_i \mathbb{J}_i \right\rangle$ or absorption amplitudes $\left\langle \alpha_f \mathbb{J}_f \left\| \mathbb{O}^{(\mathbb{M},\,\text{absorption})} \right\| \alpha_i \mathbb{J}_i \right\rangle$ can be obtained directly by call of the function `Jac.Einstein.amplitude()`.

Further remarks:

- Einstein A and B coefficients and oscillator strength for levels $|\alpha\mathbb{J}\rangle$ from a single multiplet are frequently needed for various applications and in different contexts.

- Although these coefficients are *no* (single) level property, the `Einstein` module still supports the computation of these coefficients for levels from a single multiplet, and which is generated by a single CSF basis.
- Although the `Einstein` module does not allow to include relaxation effects, this module helps obtain either a quick estimate of the Einstein coefficients between levels from just a few configurations or to deal with cascade computations.
- JAC's standard multipole amplitudes for photon emission: Although all (one- and many-electron) matrix elements are always evaluated *in absorption* within the JAC toolbox, we keep the intuitive description of the matrix elements as *final-state – operator – initial-state*, cf. section 5.3.c.

7.1.b. Hyperfine parameters and hyperfine representations (`Hfs`)

Properties, notations & application:

- Hyperfine splitting of an atomic level into hyperfine (sub-) levels: $|\alpha\mathbb{J}\rangle \longrightarrow |\alpha(J)\,\mathbb{F}\rangle\,, \qquad F = |I-J|, ..., I+J-1, I+J$.
- Formal quantum notation: $|\alpha\mathbb{J}\rangle \longrightarrow |\alpha\,\mathbb{F}\rangle \equiv |(I,\,\alpha'\mathbb{J})\,\mathbb{F}\rangle \equiv |\alpha(I\mathbb{J})\,\mathbb{F}\rangle \equiv |\alpha(IJP)\,\mathbb{F}\rangle$ or
  $|\alpha\mathbb{J}M_J\rangle \longrightarrow |\alpha\,\mathbb{F}M\rangle \equiv |(I,\,\alpha'\mathbb{J})\,\mathbb{F}M\rangle \equiv |\alpha(I\mathbb{J})\,\mathbb{F}M\rangle \equiv |\alpha(IJP)\,\mathbb{F}M\rangle$.
- Using JAC: Perform an `Atomic.Computation(.., properties=[HFS, ..], configs=[..], hfsSettings=Hfs.Settings(..), ..)` or call directly functions from the module `Hfs`. The Boolean values `calcT1` and `calcT2` in `Hfs.Settings` determine which parts of the hyperfine Hamiltonian are taken into account into the computations.
- In the JAC program, the hyperfine A and B coefficients as well as the (electric) hyperfine amplitudes $\langle\alpha\mathbb{J}\,\|\,\mathbb{T}^{(1)}\|\,\alpha\mathbb{J}\rangle$, $\langle\alpha\mathbb{J}\,\|\,\mathbb{T}^{(2)}\|\,\alpha\mathbb{J}\rangle$ are calculated and tabulated by default for all selected levels together with the energy shifts ΔE_F of the hyperfine levels with regard to the (electronic) level energy $E_{\alpha\,\mathbb{J}}$.
- In JAC, the hyperfine amplitudes $\langle\beta_r\mathbb{J}_r\,\|\,\mathbb{T}^{(1)}\,\|\,\beta_s\mathbb{J}_s\rangle$ and $\langle\beta_r\mathbb{J}_r\,\|\,\mathbb{T}^{(2)}\,\|\,\beta_s\mathbb{J}_s\rangle$ can be obtained from the function `Jac.Hfs.amplitude()`.
- In JAC, moreover, an explicit representation of a hyperfine multiplet is obtained by diagonalizing the Hamiltonian $\mathbb{H} = \mathbb{H}^{(\mathrm{DCB})} + \mathbb{H}^{(\mathrm{hfs})}$ within the atomic hyperfine IJF-coupled basis if `calcIJFexpansion=true` is set in `Hfs.Settings`.
- In JAC, all the (hyperfine) level energies $E_{\alpha\,\mathbb{F}}$ and the energies relative to the lowest (hyperfine) level are tabulated if `printDeltaEF=true` in `Hfs.Settings`.

➢ In JAC, all (diagonal and nondiagonal) hyperfine amplitudes are calculated and tabulated explicitly if `calcNondiagonal=true` in `Hfs.Settings`.

Further remarks:

➢ For a nucleus with *non-zero* spin $I > 0$, a hyperfine splitting of (all) atomic levels generally occurs since each atomic electron also interacts with the electric and magnetic (multipole) fields of the nucleus. This is sometimes described also as the interaction of the magnetic moments of the electrons and nucleus.

➢ In atomic physics, this interaction is better known as 'hyperfine interaction' whose two dominant contributions arise from the nuclear magnetic-dipole field $\mathbf{A} = \frac{\boldsymbol{\mu}\times\mathbf{r}}{r^3}$ and the electric-quadrupole field $\Phi(r) = \sum_{ij} \frac{r_i\, r_j}{2\, r^5}\, Q_{ij}$, respectively. In these expressions, $\boldsymbol{\mu}$ is the nuclear magnetic moment operator and Q_{ij}, $i, j = 1..3$ are the Cartesian components of the nuclear quadrupole operator.

➢ Apart from the hyperfine parameters $A(\alpha\, \mathbb{J})$ and $B(\alpha\, \mathbb{J})$, we also provide in JAC a representation of the atomic hyperfine levels that can be utilized, for instance, to compute hyperfine quenched transitions probabilities.

Hyperfine interaction Hamiltonian:

➢ Relativistic hyperfine interaction Hamiltonian: For many-electron systems, this Hamiltonian can be written as

$$H^{\,(\mathrm{hfs})} \;=\; \sum_{K} \mathbb{W}^{(K)} \cdot \mathbb{T}^{(K)}$$

where $\mathbb{W}^{(K)}$ and $\mathbb{T}^{(K)}$ represent the spherical tensor operators of rank K that occur in the nucleonic and electronic sectors, respectively.

➢ Reduced nuclear matrix elements: These matrix elements are determined geometrically by

$$\langle I \,\|\, \mathbb{W}^{(1)} \,\|\, I \rangle \;=\; \mu_I \sqrt{\frac{I+1}{I}}, \qquad\qquad \langle I \,\|\, \mathbb{W}^{(2)} \,\|\, I \rangle \;=\; \frac{Q}{2} \sqrt{\frac{(I+1)\,(2I+3)}{I\,(2I-1)}}\,,$$

while, in contrast, the corresponding electronic amplitudes require detailed atomic structure calculations.

➢ Values of nuclear magnetic dipole and electric quadrupole moments can be found in the compilation by Stone (2005).

➢ Electronic tensor operators: For an N-electron atom or ion, these tensor operators are given by (Andersson and Jönsson, 2008)

$$\mathbb{T}^{(1)} = \sum_j^N \mathbb{t}^{(1)}(j) = \sum_j^N -i\sqrt{2}\,\alpha\,\frac{(\alpha_j\,\mathbb{C}^{(1)}(j))^{(1)}}{r_j^2} \qquad \text{interaction with the magnetic} - \text{dipole field}$$

$$\mathbb{T}^{(2)} = \sum_j^N \mathbb{t}^{(2)}(j) = \sum_j^N -\frac{\mathbb{C}^{(2)}(j)}{r_j^3} \qquad \text{interaction with the electric} - \text{quadrupole field,}$$

and where α is the fine-structure constant, α_j the vector of Dirac matrices of the j-th electron, and the $\mathbb{C}^{(K)}$ are (normalized) spherical tensors as before.

Atomic (hyperfine) IJF-coupled basis:

➢ This (geometrically fixed) basis is obtained by the standard coupling of the nuclear states $|IM_I\rangle$ and the ASF $|\alpha\,\mathbb{J}M_J\rangle$

$$|\alpha(I,J)\,\mathbb{F}M\rangle \equiv |(I,\,\alpha'\,\mathbb{J})\,\mathbb{F}M\rangle = \sum_{M_I\,M_J} |IM_I\rangle\,|\alpha'\,\mathbb{J}M_J\rangle\,\langle IM_I,\,JM_J\,|\,FM\rangle\,.$$

➢ The atomic (hyperfine) IJF-coupled basis, also called the IJF-coupled ASF basis, is applied internally to represent all hyperfine levels, see below.

Atomic hyperfine amplitudes and levels:

➢ Atomic hyperfine levels: For the combined system 'nucleus+electrons', the atomic hyperfine states (magnetic sub-levels) can be formed as linear combination

$$|\alpha\,\mathbb{F}M\rangle = \sum_{r=1} \tilde{c}_r(\alpha)\,|(I,\,\beta_r\,\mathbb{J}_r)\,\mathbb{F}M\rangle$$

of hyperfine (basis) states $|(I,\,\beta_r\mathbb{J}_r)\,\mathbb{F}M\rangle$ of the same total angular momentum F and (the same electronic) parity P, and where $\{\tilde{c}_r(\alpha)\}$ denotes the representation of these states in the atomic hyperfine-coupled basis (Johnson, 2010).

➢ Analogue as for the ASF $|\alpha\mathbb{J}\rangle$ in the standard MCDF ansatz, the representation $\{\tilde{c}_r(\alpha)\}$ of an atomic hyperfine state is obtained by diagonalizing the Hamiltonian $\mathbb{H} = \mathbb{H}^{(\mathrm{DFB})} + \mathbb{H}^{(\mathrm{hfs})}$ of the combined system 'nucleus+electrons' in either the IJF-coupled CSF or ASF basis.

➢ In the IJF-coupled ASF basis, we can make use of $\mathbb{H}^{(\mathrm{DFB})}\,|(I,\,\beta_r\,\mathbb{J}_r)\,\mathbb{F}M\rangle = E(\beta_r\,\mathbb{J}_r)\,|(I,\,\beta_r\,\mathbb{J}_r)\,\mathbb{F}M\rangle \equiv E_{\beta_r\,\mathbb{J}_r}\,|(I,\,\beta_r\,\mathbb{J}_r)\,\mathbb{F}M\rangle$.

➢ For the hyperfine part of the Hamiltonian, the (reduced) matrix elements can be written after some standard angular momentum algebra as

$$\begin{aligned}\left\langle (I,\,\beta_r\mathbb{J}_r)\,\mathbb{F}M \,\middle|\, H^{(\mathrm{hfs})} \,\middle|\, (I,\,\beta_s\mathbb{J}_s)\,\mathbb{F}'M' \right\rangle &= \delta_{MM'}\,\left\langle (I,\,\beta_r\mathbb{J}_r)\,\mathbb{F} \,\middle|\, H^{(\mathrm{hfs})} \,\middle|\, (I,\,\beta_s\mathbb{J}_s)\,\mathbb{F}' \right\rangle \\ &= \delta_{MM'}\;\delta_{\mathbb{F}\mathbb{F}'}\;(-1)^{I+J_r+F}\sum_K \begin{Bmatrix} I & J_r & F \\ J_s & I & K \end{Bmatrix} \left\langle \beta_r\mathbb{J}_r \,\middle\|\, \mathbb{T}^{(K)} \,\middle\|\, \beta_s\mathbb{J}_s \right\rangle \left\langle I \,\middle\|\, \mathbb{W}^{(K)} \,\middle\|\, I \right\rangle ,\end{aligned}$$

with $\delta_{\mathbb{F}\mathbb{F}'} = \delta_{PP'}\,\delta_{FF'}$, and if all nuclear excitations are ignored right from the beginning.

➢ Hyperfine amplitudes: These amplitudes refer to the (reduced) electronic matrix elements $\left\langle \beta_r\mathbb{J}_r \,\middle\|\, \mathbb{T}^{(K)} \,\middle\|\, \beta_s\mathbb{J}_s \right\rangle$. In the JAC program, we compute the hyperfine amplitudes for both, the magnetic-dipole and the electric-quadrupole operators of the electron-nucleus interaction.

➢ These hyperfine amplitudes are utilized to set-up and diagonalize the Hamiltonian matrix within the atomic IJF-coupled basis for $\mathbb{H} = \mathbb{H}^{(\mathrm{DCB})} + \mathbb{H}^{(\mathrm{hfs})}$ in order to determine the representation $\{\tilde{c}_r(\alpha)\}$ of the atomic hyperfine states.

Hyperfine energies and interaction constants:

➢ Hyperfine interaction constants: Usually the hyperfine splitting is considered independently for each atomic level $|\alpha\mathbb{J}\rangle$ and without the need to specify all the hyperfine level energies $E_{\alpha\mathbb{F}}$ explicitly. Instead, the energy splitting of an atomic level $|\alpha\mathbb{J}\rangle$ into hyperfine levels $|\alpha\mathbb{F}\rangle$ can be expressed conveniently in terms of the (hyperfine interaction) constants

$$A(\alpha\,\mathbb{J}) = \frac{\mu_I}{I}\,\frac{1}{\sqrt{J(J+1)}}\,\left\langle \alpha\,\mathbb{J} \left\|\mathbb{T}^{(1)}\right\| \alpha\,\mathbb{J} \right\rangle , \qquad B(\alpha\,\mathbb{J}) = 2Q\sqrt{\frac{J(2J-1)}{(J+1)(2J+3)}}\,\left\langle \alpha\,\mathbb{J} \left\|\mathbb{T}^{(2)}\right\| \alpha\,\mathbb{J} \right\rangle$$

➢ Hyperfine energy splitting: With these constants, the hyperfine energy shifts with regard to the electronic level energy $E(\alpha\mathbb{J})$ is given by

$$\Delta\,E_F = \frac{A(\alpha\,\mathbb{J})\,C}{2} + B(\alpha\,\mathbb{J})\,\frac{3/4\,C(C+1) - I(I+1)\,J(J+1)}{2I\,(2I-1)\,J\,(2J-1)}, \qquad C = F(F+1) - J(J+1) - I(I+1).$$

7.1.c. Isotope-shift parameters (IsotopeShift)

Properties, notations & application:

- Isotope shift of an atomic level for two isotopes A, A' with nuclear masses $M < M'$: $E(\alpha\mathbb{J}; A) \longrightarrow E(\alpha\mathbb{J}; A')$.
- Formal quantum notation: $\Delta E(\alpha\mathbb{J}; A, A') / h = \frac{M'-M}{M\,M'} K^{(\mathrm{MS})} + F\,\delta\langle r^2\rangle$.
- Using Jac: Perform an `Atomic.Computation(.., properties=[Isotope, ..], configs=[..], isotopeSettings= IsotopeShift.Settings(..), ..)` with `calcNMS=true, calcNMS=true` or `calcF=true` and/or call directly functions from the module `IsotopeShift` in order to include the various contribution of the recoil Hamiltonian.
- In Jac, we calculate and tabulate by default the (relativistic) mass-shift parameters $K^{(\mathrm{MS})}$, $K^{(\mathrm{NMS})}$, $K^{(\mathrm{SMS})}$ and the field-shift parameter F for all selected levels.

Further remarks

- Owing to the conservation of the total momentum, the (total non-relativistic) mass shift is a sum of two parts, the (so-called) normal mass shift (NMS) and the specific mass shift (SMS):

$$\mathbb{H}^{(\mathrm{MS,\,nr})} = \mathbb{H}^{(\mathrm{NMS,\,nr})} + \mathbb{H}^{(\mathrm{SMS,\,nr})} = \frac{1}{2\,M}\sum_j \mathbf{p}_j^2 + \frac{1}{2\,M}\sum_{i\neq j} \mathbf{p}_i\cdot\mathbf{p}_j$$

  While the normal mass shift operator is obviously a one-particle operator, the specific mass shift is a two-particle operator. The sum of these two parts is known also as the total recoil operator within the nonrelativistic theory.

Relativistic recoil (Hamilton) operator:

➢ Recoil Hamiltonian: Within the lowest-order relativistic approximation ($\sim v^2/c^2$) and in first order of m/M for a nucleus with mass M, the recoil corrections are given by means of the (recoil) Hamiltonian (Tupitsyn *et al.*, 2003):

$$\mathbb{H}^{(\mathrm{recoil})}(M) \;=\; \frac{1}{2\,M}\sum_{ij}\left[\mathbf{p}_i\cdot\mathbf{p}_j \;-\; \frac{\alpha\,Z}{r_i}\left(\boldsymbol{\alpha}_i \;+\; \frac{(\boldsymbol{\alpha}_i\cdot\mathbf{r}_i)\,\mathbf{r}_i}{r_i^2}\right)\cdot\mathbf{p}_j\right]$$

➢ The expectation value of $\mathbb{H}^{(\mathrm{recoil})}(M)$ with regard to the relativistic wave function from $\mathbb{H}^{(\mathrm{DCB})}$ gives the recoil correction to the energy of the atomic energy $|\alpha\mathbb{J}\rangle$ in first order of m/M .

➢ Decomposition of the relativistic recoil Hamiltonian: Similar as in the non-relativistic theory, the (relativistic) recoil operator above can be written as (Tupitsyn *et al.*, 2003; Gaidamauskas *et al.*, 2011)

$$\begin{aligned}
\mathbb{H}^{(\mathrm{recoil})}(M) \;&=\; \mathbb{H}^{(\mathrm{NMS,\,relativistic})} \;+\; \mathbb{H}^{(\mathrm{SMS,\,relativistic})} \\
&=\; \frac{1}{2\,M}\sum_{i}\left[\mathbf{p}_i^2 \;-\; \frac{\alpha\,Z}{r_i}\left(\boldsymbol{\alpha}_i \;+\; \frac{(\boldsymbol{\alpha}_i\cdot\mathbf{r}_i)\,\mathbf{r}_i}{r_i^2}\right)\cdot\mathbf{p}_i\right] \;+\; \frac{1}{2\,M}\sum_{i\neq j}\left[\mathbf{p}_i\cdot\mathbf{p}_j \;-\; \frac{\alpha\,Z}{r_i}\left(\boldsymbol{\alpha}_i \;+\; \frac{(\boldsymbol{\alpha}_i\cdot\mathbf{r}_i)\,\mathbf{r}_i}{r_i^2}\right)\cdot\mathbf{p}_j\right] \\
&=\; \frac{1}{2\,M}\sum_{i}\left[\mathbf{p}_i^2 \;-\; \frac{\alpha\,Z}{r_i}\,\boldsymbol{\alpha}_i\cdot\mathbf{p}_i \;-\; \frac{\alpha\,Z}{r_i}\,(\boldsymbol{\alpha}_i\cdot\mathbb{C}_i^{(1)})\,\mathbb{C}_i^{(1)}\cdot\mathbf{p}_i\right] \;+\; \frac{1}{2\,M}\sum_{i\neq j}\left[\mathbf{p}_i\cdot\mathbf{p}_j \;-\; \frac{\alpha\,Z}{r_i}\,\boldsymbol{\alpha}_i\cdot\mathbf{p}_j \;-\; \frac{\alpha\,Z}{r_i}\,(\boldsymbol{\alpha}_i\cdot\mathbb{C}_i^{(1)})\,\mathbb{C}_i^{(1)}\cdot\mathbf{p}_j\right] \\
&=\; \mathbb{H}^{(\mathrm{NMS})} \;+\; \mathbb{H}^{(\mathrm{SMS,\,A})} \;+\; \mathbb{H}^{(\mathrm{SMS,\,B})} \;+\; \mathbb{H}^{(\mathrm{SMS,\,C})}
\end{aligned}$$

➢ The relativistic correction to the recoil effect is typically strongly overestimated if the nonrelativistic recoil operator is applied just together with relativistic wave functions.

➢ The full relativistic theory of the nuclear recoil effect can be formulated only within the framework of quantum electrodynamics. Such a theory was first formulated by Shabaev (1985), where the complete $\alpha\,Z$ -dependence of the recoil corrections to an energy level $|\alpha\,\mathbb{J}\rangle$ was derived in first order of m/M .

Reduced one-electron matrix elements of the recoil (Hamilton) operator:

➢ Recoil Hamiltonian: While the normal mass-shift Hamiltonian is a one-particle operator, the specific mass-sift is a (symmetric) two-particle operator

$$\mathbb{H}^{(\mathrm{NMS})} \;=\; \sum_j \mathbb{h}^{(\mathrm{NMS})}(\mathbf{r}_j), \qquad\qquad \mathbb{H}^{(\mathrm{SMS,\,k})} \;=\; \sum_{i\neq j} \mathbb{h}^{(\mathrm{SMS,\,k})}(\mathbf{r}_i,\mathbf{r}_j) \;=\; \sum_{i\neq j} g(r_i,k)\, g(r_j,k)\, \left(\mathbb{T}_i^{(1)}\cdot\mathbb{T}_j^{(1)}\right), \qquad k \;=\; A,B,C$$

The particular tensorial structure of the two-particle specific mass-shift Hamiltonian ensures that the reduced (one-electron) matrix elements can be expressed in terms of the first-rank effective interaction strength $X^{(1;\,\mathrm{SMS,\,k})}$ that are specified below for $k = A, B, C$.

➢ Reduced one-electron matrix element for the normal mass-shift: With the definition of the angular coefficients in Grasp, this one-electron matrix element is given with $P' = \frac{\partial P}{\partial r}$ (Gaidamauskas *et al.*, 2011)

$$\left\langle a \left\| \mathbb{h}^{(\mathrm{NMS})} \right\| b \right\rangle \;=\; \delta_{\kappa_a,\kappa_b}\, \frac{1}{2M} \int_0^\infty dr\; \left(P'_a\, P'_b \;+\; Q'_a\, Q'_b \;+\; \frac{\ell_b\,(\ell_b+1)\, P_a\, P_b \;+\; (2j_b-1)\, 2j_b\, Q_a\, Q_b}{r^2} \right.$$

$$\left. -\; (2\alpha Z)\, \frac{Q_a\, P'_b \;+\; Q_b\, P'_a}{r} \;-\; (\alpha Z) \left(\frac{\kappa_b - 1}{r^2}\right) (Q_a\, P_b \;+\; Q_b\, P_a) \right)$$

Parametrization of the isotope shift:

➢ Mass shift of two isotopes: Within lowest order of m/M , the (isotope) mass shift for an atomic level $|\alpha\, \mathbb{J}\rangle$ is determined by the difference of the expectation values of $\mathbb{H}^{(\mathrm{recoil})}(M)$ for two different isotopes:

$$\Delta\, E^{(\mathrm{MS})}\,(M,M') \;=\; \left\langle \alpha\, \mathbb{J} \right| \mathbb{H}^{(\mathrm{recoil})}(M) \;-\; \mathbb{H}^{(\mathrm{recoil})}(M') \left| \alpha\, \mathbb{J} \right\rangle \;=\; \frac{M' \;-\; M}{M\, M'}\; K^{(\mathrm{MS})}$$

$$\frac{K^{(\mathrm{MS})}}{M} \;=\; \left\langle \alpha\, \mathbb{J} \right| \mathbb{H}^{(\mathrm{recoil})}\,(M) \left| \alpha\, \mathbb{J} \right\rangle \;=\; \left\langle \alpha\, \mathbb{J} \right\| \mathbb{H}^{(\mathrm{recoil})}(M) \left\| \alpha\, \mathbb{J} \right\rangle,$$

and where the Wigner-Eckardt theorem is used here in a special form that is consistent with Grasp and that is utilized for the implementation of corresponding angular coefficients.

➢ The conversion factor between the mass-shift parameters $K^{(MS)}$ in the frequently applied units is:
$K^{(MS)}/[\text{GHz u}] = 3609.4824\, K^{(MS)}/[\text{a.u.}]$.

➢ Field shift of two isotopes: is caused by their different nuclear charge distributions and can be parametrized by:

$$\Delta E^{(FS)}(M, M') = -\left\langle \alpha\, \mathbb{J} \left| \sum_{j=1}^{N} \left(\mathbb{V}^{(nuc)}(r_j; R') - \mathbb{V}^{(nuc)}(r_j; R) \right) \right| \alpha\, \mathbb{J} \right\rangle = \left\langle \alpha \mathbb{J} \left\| \sum_{j=1}^{N} \delta\, \mathbb{V}^{(nuc)}(r_j;\, R', R) \right\| \right\rangle = -F\, \delta \left\langle r^2 \right\rangle$$

$$F = \frac{\left\langle \alpha\, \mathbb{J} \left| \sum_j \left(\mathbb{V}^{(nuc)}(r_j; R') - \mathbb{V}^{(nuc)}(r_j; R) \right) \right| \alpha\, \mathbb{J} \right\rangle}{R' - R}$$

where $\delta \langle r^2 \rangle = R' - R$ is the difference of the *root-mean-square* (rms) charge radii of the two isotopes with masses M', M .

7.1.d. Atomic form factors (FormFactor)

Properties, notations & application:

➢ Form factor $F(q;\, \alpha\, \mathbb{J})$ of an atom in level $|\alpha \mathbb{J}\rangle$ with an (assumed) spherical-symmetric charge distribution:.

➢ Formal quantum notation: $F^{(standard)}(q;\, \alpha\, \mathbb{J})$, $F^{(modified)}(q;\, \alpha\, \mathbb{J})$.

➢ Using Jac: Perform an `Atomic.Computation(.., properties=[FormF, ..], configs=[..], formSettings= FormFactor.Settings(..), ..)` or call directly functions from the module `FormFactor`.

➢ In Jac, the standard and modified form factors are calculated and tabulated by default for all selected levels in `FormFactor.Settings` and for all specified q-values [in a.u.]; the default values of the momentum transfer are $q = 0.1,\, 1.0,\, 10.0$ a.u.

➢ Atomic form factor: In atomic physics, the form factors are generally taken as a fast approximation to the (scattering) amplitude in forward direction at $\vartheta \simeq 0$ if an incident quantum wave is scattered by an isolated atom with spherical-symmetric charge distribution.

➢ In practice, of course, the definition of the atomic form factor depends on both, the particular scattering (elastic or inelastic) as well as the type of incident radiation, such as photons, electrons or neutrons. As usual, we here restrict ourselves to the atomic form factor for the elastic (x-ray) scattering of photons.

➢ Momentum transfer: Most easily, the atomic form factor can be written as function of the momentum transfer $q = |\mathbf{q}|$, that is closely related also to the scattering angle: $\hbar q = 2k \sin(\vartheta/2) = \frac{2}{\lambda} \sin(\vartheta/2)$.

➢ Momentum-transfer variable: Instead of the momentum transfer q, some tabulations of x-ray scattering amplitude make use also of the (so-called) momentum-transfer variable $x = [\sin(\vartheta/2)] / \lambda\,[\mathrm{A}]$ with $\lambda\,[\mathrm{A}] = 12.398520/E\,[\mathrm{keV}]$.

➢ Application of form factors: The elastic scattering of photons by atoms, ions or molecules has been found important in many fields of physics, such as crystallography, plasma physics and astrophysics. For high-photon energies well above the K-shell threshold energy of the atom or ion, both the standard form factor (FF) or the modified form factor (MFF) approximations are widely applied and were found moderately successful in estimating the scattering cross sections. However, both form factor approximations typically fail for small photon energies.

Definition of atomic form factors:

➢ Standard atomic form factor: For an atom in level $|\alpha\, \mathbb{J}\rangle$ with a spherically-symmetric charge distribution $\rho(r)$, the standard atomic form factor is given by

$$F^{\,(\mathrm{standard})}(q;\, \alpha\, \mathbb{J}) \;=\; 4\pi \int dr\; r^2\; \rho(r)\; \frac{\sin(qr)}{q\, r} \;=\; \frac{1}{2J+1} \sum_{M} \big\langle \alpha\, \mathbb{J}M \,\big|\, \mathbb{T}^{\,(1-\mathrm{particle})}(\mathbf{q}) \,\big|\, \alpha\, \mathbb{J}M \big\rangle\,.$$

It is equal to the Fourier transform of the charge density $\rho(r)$, if the charge density is just normalized to the number of bound electrons: $4\pi \int dr\, r^2 \rho(r) = N$. The second equivalence still need to be worked out in detail since $\mathbb{T}^{\,(1-\mathrm{particle})}(\mathbf{q})$ is a general (symmetric) one-particle operator but without definite rank.

➢ As seen from above, this standard form factor can be expressed also as (averaged many-electron) expectation value of the single-electron) momentum-transfer operator $\mathbb{T}^{\,(1-\mathrm{particle})}(\mathbf{q}) = \sum_{j=1}^{N} \exp(i\, \mathbf{q} \cdot \mathbf{r}_j\,)$ for a given sublevel $|\alpha\, \mathbb{J}M = 0\rangle$.

➢ Modified atomic form factor: For an atom or ion with a spherically-symmetric charge distribution, a modified atomic form factor can be defined via the charge distributions of the individual (sub-) shells of the element

$$F^{\,(\mathrm{modified})}(q; \alpha\, \mathbb{J}) \;=\; 4\pi \sum_{i=1}^{N} \int dr\; r^2\; \rho_i(r)\; \frac{\sin(qr)}{q\, r}\; \frac{mc^2}{\varepsilon_i' \,-\, V(r)},$$

and where $\rho_i(r)$ is the charge density of the i-th electron, $\varepsilon_i' = \varepsilon_i + mc^2$ its energy (including the rest mass), and $V(r)$ the (full atomic) potential of the i-th electron as seen at position r. Here, the summation is taken over all electrons, and the charge distribution must fullfill again the constraint that $4\pi \sum_i \int dr\, r^2 \rho_i(r) = N$ is equal to the number of bound electrons.

➢ Generalized atomic form factor: A generalized form factor can be defined for any pair of states; it is often calculated for the ground state $|\alpha_o\, \mathbb{J}_o M_o\rangle$ and some excited state $|\alpha_e\, \mathbb{J}_e M_e\rangle$ by:

$$F^{\,(\text{generalized})}(q;\, \alpha_e\, \mathbb{J}_e M_e; \alpha_o\, \mathbb{J}_o M_o) \;=\; \big\langle \alpha_e \mathbb{J}_e M_e \,\big|\, \mathbb{T}^{(1)}(\mathbf{q}) \,\big|\, \alpha_o\, \mathbb{J}_o M_o \big\rangle \;.$$

This generalized atomic form factor help describe also inelastic scattering processs and is closely related to the generalized oscillator strength, cf. Section 8.3.o.

7.1.e. Energy shifts in plasma environments (PlasmaShift)

Properties, notations & application:

➢ Plasma shift of an atomic level: $E(\alpha\mathbb{J}) \;\longrightarrow\; E(\alpha\mathbb{J};\, \text{plasma model and parameters})$.

➢ Formal quantum notation: $\Delta\, E^{\,(\text{plasma})}(\alpha\mathbb{J}) \;=\; E(\alpha\mathbb{J};\, \text{plasma model and parameters}) \;-\; E(\alpha\mathbb{J};\, \text{unperturbed})$.

➢ Spectral line shifts: The interaction between the plasma and the bound electrons of an ion embedded into the plasma alters the ionic structure and transition properties. Therefore, a plasma environment generally results in spectral line shifts, line broadening and changes in the line shapes, when compared with the free ion.

➢ For realistic plasma conditions, the number of bound states of the ions often becomes finite and the electrons less tightly bound by the nucleus, if the plasma coupling parameter increases.

➢ Using Jac: Perform an `Atomic.Computation(.., properties=[Plasma, ..], configs=[..], plasmaSettings= PlasmaShift.Settings(..), ..)` or call directly functions from the module `PlasmaShift`.

➢ In Jac, the plasma (energy) shifts are calculated and tabulated by default for a Debye-Hückel plasma model with screening parameter $\lambda = 0.25$. Hereby, the Debye-Hückel interaction is incorporated only in first-order perturbation theory within the CI matrix.

High-density plasma:

➢ Relativistic corrections to the plasma screening may become necessary for a detailed analysis of atomic spectra, especially if lines of multiply-charged ions are used in some spectral analysis.

➢ Collisional-radiative model: The effects of the plasma-environment can be further taken into account also by kinetic *or* collisional-radiative models, and where the energy shifts are often introduced by semi-empirically formulas, such as the formula by Stewart and Pyatt.

➢ Application of simple plasma models: Apart from plasma diagnostics, a proper treatment of a (plasma) screening potential has been found useful also in other areas of physics, such as nuclear and elementary particle physics, solid state physics, or even the design of nanostructures.

➢ Strongly-coupled plasma: For a strongly-coupled *dense* plasma, the (averaged) electrostatic energy between neighbouring particles in the plasma exceeds their thermal energy. The coupling parameter $\Gamma = q^2/4\pi\epsilon_0 R_0\, kT > 1$ is used in order to characterize such a strongly-coupled plasma. This coupling parameter Γ simply describes the ratio of the electrostatic and the thermal energy of the plasma particles, and where $R_o = (3/4\,\pi n_e)^{1/3}$.

➢ Laser-induced plasma with $\Gamma \gg 1$: Strongly-coupled plasma obeys generally classical statistics and has been observed for a large number of experimental and astrophysical conditions. In the laboratory, for instance, laser-induced plasma with $\Gamma \gg 1$ has been investigated in high-compression fusion experiments. Such a laser-produced plasma provides a very typical example of a high-density, strongly-coupled plasma with electronic densities well beyond $10^{24}\,\mathrm{cm}^{-3}$.

➢ Theoretical (plasma) models for hot and dense plasma are necessary to simulate its properties, such as the equation of state, radiative transfer coefficients or the conduction coefficients in plasma. These properties are relevant for inertial confinement fusion and astrophysics.

➢ Average-atom (AA) model: The AA model has been utilized to describe the electronic structure of hot and dense plasmas. This model was developed in order to describe bound electrons in terms of the (atomic) shell model, and to deal with the free electrons within the Thomas-Fermi statistical model.

➢ Plasma models: Plasma screening effects have been investigated extensively by employing various analytical models, such as the ion sphere, Debye-Hückel, Stewart-Pyatt as well as Ecker-Kröll models.

Frequently applied plasma models in atomic structure calculations:

➢ Debye-Hückel model: This model has been commonly used in order to incorporate plasma effects into atomic structure calculations. However, the validity of this model remains rather questionable because it is valid only when the *correlation* time of the ion is much longer than the lifetime of excited atomic states. Therefore, this perturbative approach is at best valid for weakly-coupled plasmas and should not be applied for modeling of high-density plasmas.

➢ Coulomb interaction in the Debye-Hückel model: In this model, the (pairwise) Coulomb interaction among the charged particles is modified

(screened) for an ion with nuclear charge Z to

$$V^{(\mathrm{DH})}(r,\,\lambda) \;=\; -\sum_{i}^{N}\frac{Ze^{-\lambda\,r_i}}{r_i} + \sum_{i>j}^{N}\frac{e^{-\lambda\,r_{ij}}}{r_{ij}} \;=\; \sum_{i}^{N} V^{(\mathrm{e-n,\,DH})}(r_i,\,\lambda) \;+\; \sum_{i>j}^{N} V^{(\mathrm{e-e,\,DH})}(r_{ij},\,\lambda).$$

Here, N is the number of bound electrons in the ion, r_i is the distance of the i-th electron from the nucleus, and r_{ij} the distance between the electrons i and j.

➢ Plasma screening parameter λ: This parameter is the inverse of the Debye shielding length for a certain plasma environment and can be readily expressed in terms of the electron density n_e and the temperature T_e of the plasma by:

$$\lambda \;=\; \left[\frac{4\pi\,n_e}{k\,T_e}\right]^{\frac{1}{2}}.$$

➢ Debye-Hückel model: To obtain the modified two-particle integrals due the plasma screening, we can write

$$V^{(\mathrm{e-e,\,DH})}(r_{ij},\lambda) \;=\; -\lambda\,\sum_{l=0}^{\infty}(2l+1)\;j_l(i\lambda\,r_<)\;h_l^1(i\lambda\,r_>)\,P_l(cos\theta)$$

in terms of the *larger* ($r_> = \max(r_i, r_j)$) and *smaller* radii ($r_< = \min(r_i, r_j)$) of the one-particle radii r_i and r_j, respectively, and where j_l denotes a spherical Bessel function and h_l^1 a Hankel function of the first kind.

➢ Nonrelativistic functions $Y^k(r;\,ab)$ and $Z^k(r;\,ab)$ for a Debye-Hückel potential: Jiao *et al.* (2019) reformulated the frequently-applied $Z^k(r;\,ab)$ and $Y^k(r;\,ab)$ for atoms and ions in a Debye-Hückel potential, i.e. for weakly-coupled plasmas. In this reformulation, use is made of the Gegenbauer expansion in order to decompose the screened interelectronic Coulomb potential.

➢ Electron-electron interaction in a Debye-Hückel plasma: For atoms in a screened Debye-Hückel plasma, the Coulomb operator $\mathbb{V}^{(\mathrm{Coulomb})}$ has to be replaced by (Jiao *et al.*, 2019)

$$\mathbb{V}^{(\mathrm{e-e,\,DH})} \;=\; \frac{e^{-\lambda\,r_{12}}}{r_{12}} \;=\; \sum_{k=0}^{\infty}(2k+1)\;\frac{I_{k+\frac{1}{2}}(\lambda\,r_<)}{\sqrt{r_<}}\;\frac{K_{k+\frac{1}{2}}(\lambda\,r_>)}{\sqrt{r_>}}\;P_k(\cos\vartheta_{12}),$$

where λ is the screening parameter and I_α and K_α are the modified (but not spherial) Bessel functions of the first and second kind.

➢ Solutions of the $Y^k(r;\, ab)$ and $Z^k(r;\, ab)$ functions: For atoms in a screened Debye-Hückel potential, the pair of differential equations can be written (Jiao *et al.*, 2019)

$$\frac{d}{dr}\, Z^k(r;\, \lambda, ab) \;=\; \left[\frac{k+1}{r} \,-\, \lambda\, \frac{K_{k+3/2}(\lambda\, r)}{K_{k+\frac{1}{2}}(\lambda\, r)}\right]\, Z^k(r;\, \lambda, ab) \quad + \quad (2k+1)\; I_{k+\frac{1}{2}}(\lambda\, r)\; K_{k+\frac{1}{2}}(\lambda\, r)\; P_a(r)\; P_b(r),$$

$$\frac{d}{dr}\, Y^k(r;\, \lambda, ab) \;=\; \left[\frac{k+1}{r} \,-\, \lambda\, \frac{K_{k+3/2}(\lambda\, r)}{K_{k+\frac{1}{2}}(\lambda\, r)}\right]\, Y^k(r;\, \lambda, ab) \quad - \quad \lambda\, \left[\frac{I_{k+3/2}(\lambda\, r)}{I_{k+\frac{1}{2}}(\lambda\, r)} \,+\, \frac{K_{k+3/2}(\lambda\, r)}{K_{k+\frac{1}{2}}(\lambda\, r)}\right]\, Z^k(r;\, \lambda, ab)$$

and with the same boundary conditions $Z^k(0;\, \lambda, ab) \,=\, 0, \quad Y^k(r \to \infty;\, ab) \,=\, Z^k(r \to \infty;\, ab)$ for all finite λ. It is therefore convenient to calculate $Z^k(r;\, \lambda, ab)$ by an outward integration from $r \,=\, 0$ and then to obtain $Y^k(r;\, \lambda, ab$ by an inward integration from $r \,\approx\, \infty$.

➢ Debye-Hückel model: While the Debye-Hückel screening of the electron-nucleus interaction usually destabilizes the binding of the electron, the screening of the electron-electron repulsion counteracts this trend.

➢ Saha and Fritzsche (2006) demonstrated for beryllium-like ions that the Debye-Hückel screening (if applicable) should be incorporated into both, the electron-nucleus and electron-electron interaction in order to obtain reliable results for the plasma shifts.

➢ Ion-sphere model: In this model, the ion is typically enclosed in a spherically symmetric cell that contains the exact number of electrons in order to ensure neutrality. In the ion-sphere model, one needs to define an electron-density distribution that either obeys self-consistency equations or need to make some simple hypothesis, such as an uniform density within the cell.

Plasma in oscillating electric fields:

➢ Plasma in oscillating electric fields: The collective movement of plasma particles, such as the electron plasma waves (Langmuir oscillations) or ion plasma waves, is mainly determined by the plasma creation and/or heating device but lead also to quite significant fields (Peyrusse 1977).

Free-electron distributions in plasma:

➢ In a plasma, the free-electron (radial) density $n_e(r)$ can follow different distributions:

➢ Maxwell-Boltzmann distribution: The Maxwell-Boltzmann statistics has been often applied to describe the free-electron distribution but is not well justified for high-density or low-temperature plasma.

➢ Fermi-Dirac distribution: This distribution is preferable if the free electrons are degenerate

$$n_e(r) \;=\; \frac{4}{\sqrt{\pi}} \int_{r_o}^{\infty} dr \, \frac{\sqrt{r}}{e^{r\,-\,r_o\,-\,\mu/k\,T_e} \;+\; 1} \;=\; 2\,\lambda_{\rm th}^{-3}\,\mathcal{F}_{1/2}\left(-\frac{V(r)}{k\,T_e} \;+\; \frac{\mu}{k\,T_e}; \; -\frac{V(r)}{k\,T_e}\right) .$$

Here μ is the chemical potential of the plasma, $\mathcal{F}_{1/2}(x,y)$ the incomplete Fermi-Dirac integral and $\lambda_{\rm th} = \sqrt{2\pi \,/\, k\,T_e}$ the thermal de-Broglie thermal wavelength.

➢ Uniform electron-gas distribution: This distribution considers a sphere of radius $R_o = (3/4\pi n_e)^{1/3}$ around the ion with N_b bound electrons, in which the ionic charge is completely neutralized by the additional $N_f = Z - N_b$ *free* electrons. Although all electrons inside of the sphere will strongly interact with the embedded ion, the free electrons are here assumed to be distributed uniformly. With this assumption in mind, the electrostatic potential for the bound electrons with radial coordinate r is given by

$$V^{\,(\rm IS)}(\mathbf{r};\mathbf{R}_0) \;=\; \begin{cases} -\frac{Z}{\mathbf{r}} \;+\; \frac{Z-N_b}{2R_0}\left[3 - \left(\frac{\mathbf{r}}{\mathbf{R}_0}\right)^2\right] & \text{for} \quad \mathbf{r} \le \mathbf{R}_0 \\ 0 & \text{for} \quad \mathbf{r} > \mathbf{R}_0 \,. \end{cases}$$

In this potential above, the first term describes the interaction of the bound electron with the nucleus, while the second (repulsive) term arises from the plasma background and always causes a shift of all the level energies towards the continuum.

➢ Collision-induced localization: The plasma environment typically leads to a broadening of the momentum distribution of free electrons and partly also to its localization. Indeed, random collisions of the continuum electron with particles from the plasma environment may

results in a loss of coherence of the outgoing, photoionized electrons when leaving the parent ions. Such a collision-induced localization resembles the Anderson localization of randomly scattered electrons in solids as well as the dynamical localization of Rydberg electrons in plasma.

➢ Collision-induced localization: The collision-induced energy and momentum broadening of stationary states can reduce also the lifetime of the bound states. At a given plasma temperature, the momentum broadening increases with the plasma density or, in other words, the electron localization is more pronounced in a dense plasma.

Gordon-Kim theory:

➢ In the Gordon-Kim theory (1972), the total energy of the system consists out of the direct Coulomb potential energy, the exchange Coulomb potential energy, the kinetic energy as well as the correlation energy. The direct Coulomb potential energy is calculated by integrating the Coulomb potential for the (approximated) electron density, while the other contributions to the total energy were calculated by using a temperature-dependent local density functional (LDA) approach.

7.1.f. Level-dependent fluorescence and Auger yields (DecayYield)

Properties, notations & application:

➢ Fluorescence *versus* Auger decay of an (excited) atomic level: $A^{q+*} \longrightarrow \begin{bmatrix} A^{q+(*)} + \hbar\omega \\ A^{(q+1)+(*)} + e_a^- \\ \dots \end{bmatrix}$.

The corresponding level-specific or configuration-averaged fluorescence and Auger yields just describe the fraction of atoms in a particular level or configuration that decay either by fluorescence *or* Auger electron emission.

➢ Formal quantum notation: $|\alpha \mathbb{J}\rangle \longrightarrow \begin{bmatrix} \{\, |\alpha_r \mathbb{J}_r\rangle + \hbar\omega\,(\{\mathbb{M}\})\,\} \\ \{\, |\alpha_a \mathbb{J}_a\rangle + |\varepsilon\,\kappa\rangle\,\} \\ \dots \end{bmatrix}$.

- Using JAC: Perform an `Atomic.Computation(.., properties=[Yields, ..], configs=[..], yieldSettings= DecayYield.Settings(..), ..)` or call directly functions from the module `DecayYield`.
- In JAC, we calculate and tabulate by default the fluorescence yields $\omega_r(\alpha\mathbb{J})$ and Auger yields $\omega_a(\alpha\mathbb{J})$ for all selected levels.
- In JAC, the computation of all fluorescence and Auger yields is always traced back to single-step cascade computations. Therefore, the same (cascade) approaches { `AverageSCA, SCA, ...` } can be applied as in cascade computations, cf. section 9.1. The particular approach, that is to be applied in the given computation above, need to be specified however as `String` in the `DecayYield.Settings("AverageSCA", ...)`.
- In JAC, the explicit settings of the underlying `Cascade.Computation` can be overwritten in the function `Cascade.determineSteps()`; no attempt has been made so far to support such control features directly by means of the `DecayYield.Settings(...)`.
- Fluorescence yields $\omega_r(\alpha\mathbb{J})$: This yield typically represents the probability of an inner-shell (core) hole to be filled under photon emission, in contrast and competition with other nonradiative processes.
- Auger yields $\omega_a(\alpha\mathbb{J})$: This yield describes the (complementary) probability for an inner-shell hole level to decay by electron emission, hence: $\omega_r(\alpha\mathbb{J}) + \omega_a(\alpha\mathbb{J}) = 1$. The Auger yield is sometimes further partitioned into an Auger and Coster-Kronig yield: $\omega_a(\alpha\mathbb{J}) = \omega^{(\mathrm{Auger})}(\alpha\mathbb{J}) + \omega^{(\mathrm{Coster-Kronig})}(\alpha\mathbb{J})$.
- If not explicitly overwritten within the code [cf. the module `Cascade`], only the electric-dipole (E1) transitions and the Coulomb interaction $\mathbb{V}^{(\mathrm{Coulomb})}$ are taken into account in the evaluation of all Auger and radiative transition amplitudes and rates.
- More often than not, the fluorescence and Auger yields are computed and analyzed for either K- or L-shell (holes) states, and for which usually no distinction need to be made for the different fine-structure levels $(\alpha\mathbb{J})$ that arise only due to the couplings of the valence shells.
- Typically, it is completely sufficient to include only electric-dipole decay channels, although other multipoles could be incorporated explicitly in the computations, as far this is supported by the underlying cascade approach, or invoked explicitly within the code.

7.2. In JAC partly-implemented level properties

7.2.a. Radial electron density distribution & natural orbitals (ElectronDensity)

Properties, notations & application:

➢ Radial electron density distribution: The electron density can also be obtained from the N-electron wave function as expectation value of the $\delta(\mathbf{r})$ operator

$$\rho(\mathbf{r}) \;=\; N \int d\mathbf{q}_1\, d\mathbf{q}_2\, ...\, d\mathbf{q}_N\; \Psi(\mathbf{q}_1,\, ...,\, \mathbf{q}_N)\; \delta^{\,(\mathrm{N-electron})}(\mathbf{r})\; \Psi^*(\mathbf{q}'_1,\, ...,\, \mathbf{q}'_N).$$

➢ Many-electron $\delta^{\,(\mathrm{N-electron})}(\mathbf{r})$ operator: This operator probes whether all electrons are at a given position $(\mathbf{r}_1, \mathbf{r}_2,\, ...,\, \mathbf{r}_N$ in space and can be written in terms of the single-electron operators

$$\delta(\mathbf{r} \,-\, \mathbf{r}_j) \;=\; \frac{1}{r^2\, \sin\vartheta}\, \delta(r \,-\, r_j)\, \delta(\vartheta \,-\, \vartheta_j)\, \delta(\varphi \,-\, \varphi_i) \;=\; \frac{1}{r^2}\, \delta(r \,-\, r_j) \sum_{\ell m} Y_{\ell m}(\vartheta, \varphi)\, Y^*_{\ell m}(\vartheta_j, \varphi_j)$$

$$\delta(\mathbf{r})^{\,(\mathrm{N-electron})} \;=\; \sum_{j=1}^{N} \delta(\mathbf{r} \,-\, \mathbf{r}_j) \;=\; \frac{1}{r^2} \sum_{j=1}^{N} \delta(r \,-\, r_j) \sum_{\ell m} Y_{\ell m}(\vartheta, \varphi)\, Y^*_{\ell m}(\vartheta_j, \varphi_j).$$

➢ Radial electron-density distribution for single configurations: This distribution represents the probability to find an electron in the interval $[r,\, r \,+\, dr]$ from the nucleus, averaged over all directions:

$$D(r) \;\equiv\; r^2\, \rho(r) \;=\; \sum_a q_a\, \left(P_a^2(r) \,+\, Q_a^2(r)\right), \qquad\qquad \int_0^\infty dr\; D(r) \;=\; \int_0^\infty dr\; r^2\, \rho(r) \;=\; \sum_a q_a \;=\; N.$$

➢ Radial electron-density distribution for MCDHF wave functions: In general, this representation can be written for a given level $|\alpha \mathbb{J}\rangle$ in terms of the CSF mixing coefficients as (Borgoo *et al.*, 2010)

$$D(r) \;\equiv\; r^2\, \rho(r,\, \alpha\mathbb{J}) \;=\; \sum_{ij} c_i^*\, D_{ij}(r)\, c_j \;=\; \sum_{ij} c_i^* \left[\sum_{\kappa,\, nn'} u_{ij}(n\kappa, n'\kappa)\; I_\rho(n'\kappa, n\kappa)\right] c_j \;=\; \sum_{\kappa,\, nn'} \rho^{(\kappa)}_{n'n}\; I_\rho(n'\kappa, n\kappa)$$

$$\rho^{(\kappa)}_{n'n} \;=\; \sum_{ij} c_i^*\; u_{ij}(n\kappa, n'\kappa)\; c_j,$$

and where $u_{ij}(n\kappa, n'\kappa)$ are the angular coeffients for a zero-rank one-electron operator, $I_\rho(n'\kappa, n\kappa) = (P_{n'\kappa}\, P_{n\kappa} + Q_{n'\kappa}\, Q_{n\kappa})$ radial functions, and where the summation over ij runs over all CSF in the wave function expansion.

➢ Natural orbitals: These orbitals are defined as the one-electron orbital functions that diagonalize the block-diagonal (first-order) density matrix $\mathbf{C}^+ \boldsymbol{\rho}^{(\kappa)}_{n'n} \mathbf{C} = \tilde{\boldsymbol{\rho}}$. The natural orbitals are then obtained as linear combination (Borgoo *et al.*, 2010):

$$\tilde{R}_{n\ell}(r) = C^{(\kappa)}_{n',n}\, R_{n'\kappa}(r),$$

and the eigenvalue $\tilde{\boldsymbol{\rho}}_{nn} = \tilde{q}_{n\kappa}$ is interpreted as the occupation numbers of the natural orbital $(n\kappa)$.

7.2.b. Scattering amplitudes and scattering factors (FormFactor)

Properties, notations & application:

➢ Scattering amplitude $S(q;\, \alpha\, \mathbb{J})$ of an atomic level with supposed spherical-symmetric charge distribution:.

➢ Formal quantum notation: .

Anomalous scattering factors:

➢ Coherent Rayleigh scattering factor: This scattering factor characterizes the (complex) scattering amplitude in forward direction and is obtained by:

$$\frac{1}{2} \sum_{\varepsilon_i, \varepsilon_f} M(\varepsilon_i, \mathbf{k}_i,\, \varepsilon_f, \mathbf{k}_f = \mathbf{k}_i),$$

i.e. as average over the polarization (states) of the incident photon and by a summation over the polarization of the scattered photon.

➢ Using the modified form factor for describing the scattering in forward-scattering angle $\vartheta \approx 0$, the real $g'(\omega)$ and imaginary $g''(\omega)$ anomalous scattering factors can be approximately defined in terms of the photoionization cross sections and oscillator strength (Zhou *et al.*, 1990). This formally requires a summation over the complete spectrum of the atom, although the major contributions arise from just a few resonances.

➢ Anomalous scattering factor: The real $g'(\omega)$ and imaginary $g''(\omega)$ anomalous scattering factors are frequently employed in order to express the coherent (Rayleigh) scattering factor $G(\omega)$ for incident photons with energy $\hbar\omega$.

➢ Coherent Rayleigh scattering factor: For incident photons with energies $\hbar\omega$, the coherent (Rayleigh) scattering factor in forward direction has been written as (Zhou *et al.*, 1990)

$$G(\omega) \;=\; F(0) \;+\; g'(\omega) \;+\; i\, g''(\omega),$$

where $F(0) = N$ is the atomic form factor. Therefore, the (Rayleigh) scattering amplitude and scattering factor can be expressed also in terms of the standard (atomic) form factor (FF) or the modified form factor (MFF).

Incoherent scattering function $S(\mathbf{q})$:

➢ Incoherent scattering function:

➢ Incoherent scattering function: This scattering function can be expressed in terms of the generalized atomic form factor

$$S(\mathbf{q}; \alpha_o \mathbb{J}_o M_o) \;=\; \sum_{e \neq o} |F^{\,(\text{generalized})}\,(q;\; \alpha_e \mathbb{J}_e M_e; \alpha_o \mathbb{J}_o M_o)|^2 \;=\; \big\langle \alpha_o \mathbb{J}_o \,\big|\, \mathbb{T}^{(2)}(\mathbf{q}) \,\big|\, \alpha_o \mathbb{J}_o \big\rangle \;-\; |F^{\,(\text{standard})}(q; \alpha_o \mathbb{J}_o)|^2 \,.$$

but where the summation over e includes all discrete levels as well as an integration over the continuum. In the second equivalence, the two-electron momentum-transfer operator $\mathbb{T}^{(2)}(\mathbf{q}) = \sum_{m,n=1}^{N} \exp[i\,\mathbf{q}\cdot(\mathbf{r}_m - \mathbf{r}_n)]$ occurs, but then just requires to compute the expectation value of this operator with regard for the ground state $|\alpha_o \mathbb{J}_o M_o\rangle$.

7.2.c. Lande g_J factors and Zeeman splitting of fine-structure levels (`LandeZeeman`)

Properties, notations & application (not yet fully implemented):

➢ Zeeman splitting of an atomic level into Zeeman (sub-) levels: $|\alpha \mathbb{J}\rangle \;\longrightarrow\; |\alpha\, \mathbb{J} M\rangle\,, \qquad M \;=\; -J,\, ...,\, J-1,\, +J$.

➢ Formal quantum notation: $|\alpha \mathbb{J} M\rangle$.

➢ Using Jac: Perform an `Atomic.Computation(.., properties=[LandeJ, ..], configs=[..], zeemanSettings= LandeZeeman.Settings(..), ..)` with `calcLandeJ=true` or call directly functions from the module `LandeZeeman`.

➢ In JAC, we calculate and tabulate by default the Lande $g_J \equiv g(\alpha \mathbb{J})$ factors for the selected fine-structure levels.

➢ In the JAC program, the Zeeman amplitudes $\langle \beta_r \mathbb{J}_r \| \mathbb{N}^{(1)} \| \beta_s \mathbb{J}_s \rangle$ and $\langle \beta_r \mathbb{J}_r \| \Delta \mathbb{N}^{(1)} \| \beta_s \mathbb{J}_s \rangle$ can be obtained from the function `Jac.LandeZeeman.amplitude()`.

Further remarks:

➢ The Zeeman effect describes the (level) splitting of an atomic level $|\alpha \mathbb{J}\rangle$ into its sub-levels $|\alpha \mathbb{J} M\rangle$ in the presence of a static magnetic field.

➢ The various components $|\alpha\, \mathbb{J} M\rangle$ of a Zeeman-splitted line usually have different intensities, and with some of them possibly even forbidden within the dipole approximation.

➢ The energy splitting of the Zeeman sub-levels depends of course on the magnetic field strength. — Therefore, the Zeeman effect has be applied for measuring magnetic field strengths, e.g. in astrophysics at the surface of the Sun or in laboratory plasmas.

Zeeman Hamiltonian $\mathbb{H}^{(\mathrm{mag})}$:

➢ If the z-axis is chosen along the magnetic field $\mathbf{B} \,||\, \mathbf{e}_z$ and if we neglect diamagnetic contributions, the magnetic (Zeeman) Hamiltonian can be written in terms of spherical tensors (Andersson and Jönsson, 2008)

$$\mathbb{H}^{(\mathrm{mag})} \;=\; \left(\mathbb{N}_0^{(1)} \,+\, \Delta\, \mathbb{N}_0^{(1,\,\mathrm{QED})} \right)\, B$$

$$\mathbb{N}^{(1)} \;=\; \sum_j^N \mathbb{n}^{(1)}(j) \;=\; \sum_j^N -i\, \frac{\sqrt{2}}{2\,\alpha}\, r_j \;\; \left(\boldsymbol{\alpha}_j\, \mathbb{C}^{(1)}(j) \right)^{(1)}$$

$$\Delta\, \mathbb{N}^{(1)} \;=\; \sum_j^N \Delta\, \mathbb{n}^{(1)}(j) \;=\; \sum_j^N \frac{g_s \,-\, 2}{2}\, \beta_j \;\boldsymbol{\Sigma}_j, \qquad\qquad \boldsymbol{\Sigma} \;=\; \begin{pmatrix} \boldsymbol{\sigma} & 0 \\ 0 & \boldsymbol{\sigma} \end{pmatrix},$$

and where the second term in the magnetic Hamiltonian above is (so-called) Schwinger's QED correction. Here, $g_s \;=\; 2.00232$ is the g-factor of the electron, including some leading QED corrections.

➢ Total Hamiltonian: For a moderate magnetic $\mathcal{B}$-field, one considers the total Hamiltonian $\mathbb{H}^{(\mathrm{DC})} + \mathbb{H}^{(\mathrm{mag})}$ whose matrix is diaognal in P, M but no longer in the total angular momentum quantum number J. In practice, one usually starts from a given ASF basis, in which

$\mathbb{H}^{(\mathrm{DC})}$ is already diagonal, and then diagonalized the total Hamiltonian matrix in very moderate basis of atomic state functions. For a non-zero nuclear spin, however, the hyperfine and Zeeman splitting is often comparable and the Hamiltonian $\mathbb{H}^{(\mathrm{DC})} + \mathbb{H}^{(\mathrm{mag})} + \mathbb{H}^{(\mathrm{hfs})}$ need then to be diagogonalized in some given ASF basis. In this case, only the parity and M_F are diagonal, i.e. good quantum numbers.

Lande factor $g_J \equiv g(\alpha\mathbb{J})$ and Zeeman splitting of an electronic level $|\alpha\,\mathbb{J}\rangle$:

➢ Zeeman splitting of an atomic level $|\alpha\mathbb{J}\rangle$: If the energy splitting due to the magnetic field is small, when compared with the fine-structure splitting, it can be expressed in first-order perturbation theory by

$$\begin{aligned}\Delta E^{(\mathrm{mag})}(\alpha\mathbb{J}M) &= E(\alpha\mathbb{J}M) - E(\alpha\mathbb{J}, M=0)\\ &= \left\langle \alpha\,\mathbb{J}M \left| \mathbb{N}_0^{(1)} + \Delta\,\mathbb{N}_0^{(1,\mathrm{QED})} \right| \alpha\,\mathbb{J}M \right\rangle = (-1)^{J-M} \begin{pmatrix} J & 1 & J \\ -M & 0 & M \end{pmatrix} \sqrt{2J+1}\, \left\langle \alpha\,\mathbb{J} \left\| \mathbb{N}^{(1)} + \Delta\,\mathbb{N}^{(1,\mathrm{QED})} \right\| \alpha\,\mathbb{J} \right\rangle B\\ &= \frac{M}{\sqrt{J\,(J+1)}} \left\langle \alpha\,\mathbb{J} \left\| \mathbb{N}^{(1)} + \Delta\,\mathbb{N}^{(1,\mathrm{QED})} \right\| \alpha\,\mathbb{J} \right\rangle B\end{aligned}$$

and with regard to the unperturbed energy $E(\alpha\mathbb{J}, M=0) = E(\alpha\mathbb{J}, B=0)$.

➢ Lande g_J factor of an atomic level $|\alpha\mathbb{J}\rangle$: Usually, the dependence on the M quantum number is factored out and the energy splitting is expressed for a single level $|\alpha\mathbb{J}\rangle$ in terms of its Lande factor $g_J \equiv g(\alpha\mathbb{J})$

$$\Delta E^{(\mathrm{mag})}(\alpha\mathbb{J}M) = g(\alpha\mathbb{J})\, M\, \frac{B}{2}, \qquad g(\alpha\mathbb{J}) \equiv g_{\mathbb{J}} = 2\, \frac{\left\langle \alpha\,\mathbb{J} \left\| \mathbb{N}^{(1)} + \Delta\,\mathbb{N}^{(1,\mathrm{QED})} \right\| \alpha\,\mathbb{J} \right\rangle}{\sqrt{J\,(J+1)}}$$

7.2.d. Lande g_F factors and Zeeman splitting of hyperfine levels (LandeZeeman)

Properties, notations & application (not yet fully implemented):

➢ Zeeman splitting of an atomic hyperfine level into Zeeman (sub-) levels: $|\alpha(J)\mathbb{F}\rangle \longrightarrow |\alpha\,(J)\mathbb{F}M\rangle$, $M = -F, ..., F-1, +F$.

➢ Formal quantum notation: $|\alpha(J)\mathbb{F}M\rangle$.

➢ Using JAC: Perform an `Atomic.Computation(.., properties=[LandeJ, ..], configs=[..], zeemanSettings= LandeZeeman.Settings(..), ..)` with `calcLandeF=true` or call directly functions from the module `LandeZeeman`.

➢ In JAC, we calculate and tabulate by default the Lande $g_F \equiv g(\alpha\mathbb{F})$ factors for the selected hyperfine-structure levels.

Further remarks:

➢ The Lande g-factor (also kown as g value or dimensionless magnetic moment) is a dimensionless entity that characterizes the gyromagnetic ratio of an atomic or hyperfine level. The Lande g-factor is basically a proportionality constant how efficient a particle, spin or quantum state with given total angular momentum s contributes to the splitting in an external magnetic fiel B.

Lande factor $g_F \equiv g(\alpha\mathbb{F})$ of an hyperfine level $|\alpha\,\mathbb{F}\rangle$:

➢ Zeeman splitting of an hyperfine level $|\alpha\mathbb{F}\rangle$: If the energy splitting due to the magnetic field is small, when compared with the hyperfine-splitting, it can be expressed in first-order perturbation theory in terms of the reduced electronic Zeeman amplitudes by

$$\begin{aligned}
\Delta E^{(\mathrm{mag})}(\alpha\mathbb{F}M) &= E(\alpha\mathbb{F}M) - E(\alpha\mathbb{F}, M=0) \\
&= \Big\langle (I,\alpha\mathbb{J})\,FM \Big| \mathbb{N}_0^{(1)} + \Delta\mathbb{N}_0^{(1,\mathrm{QED})} \Big| (I,\alpha\mathbb{J})\,FM \Big\rangle \\
&= M\,\frac{F(F+1)+J(J+1)-I(I+1)}{2\,F(F+1)}\,\frac{\Big\langle \alpha\mathbb{J}\Big\| \mathbb{N}_0^{(1)} + \Delta\mathbb{N}_0^{(1,\mathrm{QED})} \Big\| \alpha\mathbb{J}\Big\rangle}{\sqrt{J(J+1)}} \\
&= M\,\frac{F(F+1)+J(J+1)-I(I+1)}{2\,F(F+1)}\,g(\alpha\mathbb{J})\,\frac{B}{2}\,,
\end{aligned}$$

and expressed with regard to the unperturbed hyperfine energy $E(\alpha\mathbb{F}, M=0) = E(\alpha\mathbb{F}, B=0)$.

➢ Lande factor $g_F \equiv g(\alpha\mathbb{F})$ and Zeeman energy splitting of an hyperfine level $|\alpha\mathbb{F}\rangle$:

$$g(\alpha\mathbb{F}) = \frac{F(F+1)+J(J+1)-I(I+1)}{2\,F(F+1)}\,g(\alpha\mathbb{J}) \qquad \Longrightarrow \qquad \Delta E^{(\mathrm{mag})}(\alpha\mathbb{F}M) = g(\alpha\mathbb{F})\,M\,\frac{B}{2}$$

7.2.e. Sensitivity of level energies with regard to variations of α (AlphaVariation)

Properties, notations & application (not yet fully implemented):

➢ Differential sensitivity parameter $\Delta q\,(\delta\alpha;\ \beta\mathbb{J})$ of an atomic level: For an atomic level $|\beta\mathbb{J}\rangle$, the level energy depends of course on the fine-structure constant α. Therefore, an energy shift arises for any variation $\delta\alpha = \alpha - \alpha_o$ of the fine-structure constant and for a non-zero differential sensitivity parameter $\Delta q\,(\delta\alpha;\ \beta\mathbb{J})$:

$$\Delta E(\delta\alpha;\ \beta\mathbb{J}) \;=\; \Delta q\,(\delta\alpha;\ \beta\mathbb{J})\ \left[\left(\frac{\alpha}{\alpha_o}\right)^2 - 1\right],$$

and where α_o is the (current) reference value of the fine-structure constant.

➢ Formal quantum notation: $\Delta E(\delta\alpha;\ \beta\mathbb{J})$, $\Delta q\,(\delta\alpha;\ \beta\mathbb{J})$, $K(\beta\mathbb{J})$.

➢ Using Jac: Perform an `Atomic.Computation(.., properties=[AlphaVar, ..], configs=[..], alphaSettings= AlphaVariation.Settings(..), ..)` or call directly functions from the module `AlphaVariation`.

➢ In Jac, we calculate and tabulate by default the differential sensitivity parameter $\Delta q\,(\delta\alpha;\ \beta\mathbb{J})$ and the enhancement factor $K(\beta\mathbb{J})$ for all selected levels.

Further remarks:

➢ Fine-structure constant α: The dimensionless constant α becomes dynamical, i.e. explicitly time-dependent, in a number of (quantum-field) theories that go beyond the standard model and general relativity.

➢ Search for variations of fundamental constants: This search is closely related to several, so-far still unexplained phenomena of the Universe, such as the nature of dark matter.

➢ From the individual level-dependent sensitivity parameters $\Delta q\,(\delta\alpha;\ \beta\mathbb{J})$ and enhancement factors $K(\beta\mathbb{J})$, the analogue values for any atomic transition can be simply obtained by taking the sum of the corresponding level parameters.

➢ Experimentally, a variation of α are currently measured by monitoring for two ions the ratio of (two) clock frequencies with quite different values of K.

➢ Current limits on the time variation of α: Currently, the best laboratoy limit of $\dot{\alpha}$ was obtained from a comparison of the frequency ratio Al^+ / Hg^+ over the course of *one* year. This ratio is sensitive to variations in α because these two optical transitions have quite different sensitivity coefficients with regard to time-variations in the 'current' value of the fine-structure constant α_o (Berengut *et al.*, 2012)

$$q \;=\; \frac{d\omega}{dx}\,|_{x\,=\,0}, \qquad\qquad x \;=\; \frac{\alpha^2}{\alpha_o^2} \;-\; 1,$$

➢ Limits on the time variation of α: Various proposals have been made in the literature to limit the time variations of α more tightly, provided that the frequency ratio can be measured with similar accuracy as for Al^+ / Hg^+ clock transitions. This is possible for clock transitions with a much higher sensitivity q, as expected for the optical transitions of the Tl^+ clock, for multiply-charged Te, Po, and Ce ions as well as for the ^{229}Th nuclear clock, which all have a rather large sensitivity to the variation of α.

Enhancement and sensitivity of atomic levels with regard to variations of $\delta\alpha$:

➢ Enhancement of energy shifts due to $\delta\alpha$ variations: The sensitivy of an atomic level energy $E(\beta\mathbb{J};\,\alpha)$ on $\delta\alpha$ can be re-written also in terms of the dimensionless enhancement factor $K \;=\; 2\,\Delta q/\,\Delta E$ as:

$$\frac{E(\beta\mathbb{J};\,\alpha) \;-\; E(\beta\mathbb{J};\,\alpha_o)}{E(\beta\mathbb{J};\,\alpha_o)} \;=\; K\,\frac{\alpha \;-\; \alpha_o}{\alpha_o} \;=\; K\,\frac{\delta\alpha}{\alpha_o}$$

➢ The reasons for $\delta\alpha$ variations can be of different type, such as temporal, spatial, slow drift, or of oscillatory nature, and it can depend on the gravity-potential or others reasons. The theoretical reasoning about such changes is typically outside of atomic theory.

7.3. Further properties, not yet considered in JAC

7.3.a. Photoemission in external magnetic fields (MagneticFieldInduced)

Properties & notations:

➢ Magnetic-field induced transitions (MIT): These induced transitions occur when an external magnetic field mixes levels with different total angular momenta $\mathbb{J}$.

Magnetic-field-induced transitions:

➢ Transition rates for magnetic-field and hyperfine-induced transitions: These transition rates are calculated as a sum over (reduced, unperturbed and single-photon) emission amplitudes between fine- or hyperfine-structure levels, respectively, and weighted by the representation of the corresponding expansion coefficients. Special care has to be taken if the radiative widths of the (hyperfine) levels becomes comparable with the level splitting which, at least in principle, then requires a common treatment of both, the hyperfine and magnetic-field interactions. The corresponding changes in the line intensities is also known as radiation damping in the literature.

➢ Li *et al.* (2020) provide a GRASP module for calculating magnetic-field and hyperfine-induced transitions, including a number of graphical procedures in order to analyze the observed spectra and to disentangle various features due to the splitting of the fine and hyperfine levels. This module computes the Zeeman energy splittings of fine- and hyperfine structure substates in an external magnetic field together with the associated expansion coefficients. In these simulations, it is typically assumed that each hyperfine line has a Gaussian-Doppler profile with a given full-width-half-maximum (FWHM) due to the resolution in the observes spectra. If there are more than one isotope in the source cloud, the spectra from different isotopes should be scaled due to their relative abundance.

➢ Hyperfine and magnetic-field induced transitions have been investigated for different atomic systems both, theoretically and experimentally. In plasma diagnostics, these transitions may help in the determination of electron densities, isotope compositions as well as magnetic fields. A proper implementation of these induced transitions also help analyze spectra from electron-beam ion trap (EBIT) sources as well as the spectra of magnetic stars.

➢ High-resolution spectra from (magnetic) stars: In many high-resolution astrophysical spectra, the observed lines are broadened due to the unresolved or partly-resolved hyperfine or isotope structure of the elements. These unresolved structure can be even enhanced for magnetic stars, for which the emitted radiation is affected by the magnetic field (Andersson *et al.*, 2006).

Amplitudes and rates:

➢ Magnetic-field induced transitions (MIT): In an external magnetic field, the direction of the $\boldsymbol{\mathcal{B}}$-field is typically chosen as quantization axis. For this choice, only states with the same parity and some magnetic quantum number M but from different J will mix with each other

$$|\alpha PM;\, \mathcal{B}\rangle \;\equiv\; |\psi_\alpha(PM)\rangle \;=\; \sum_{\beta=1} c_\beta(\alpha;\, \mathcal{B})\; |\beta\, \mathbb{J}M,\, \mathcal{B}=0\rangle\,, \qquad\qquad c_r(\alpha;\, \mathcal{B}) \;=\; \frac{\left\langle \beta\;\mathbb{J}M;\, \mathcal{B}=0 \,\middle|\, H^{(\mathcal{B}-\text{field})} \,\middle|\, \alpha\;PM;\, \mathcal{B}\right\rangle}{E(\beta\mathbb{J}M;\mathcal{B}=0)\;-\;E(\alpha PM;\mathcal{B})}$$

and where the mixing coefficients $c_r(\alpha;\, \mathcal{B})$ are here given in first-order perturbation approximation.

➢ Oscillator strength for transitions between hyperfine levels: If the (off-diaognal) hyperfine interaction is negligible between neighboured fine-structure levels $|\alpha\mathbb{J}\rangle$, the absorption oscillator strengths for the electric-dipole transitions between two hyperfine levels $|\alpha_i(IJ_i)\,\mathbb{F}_i\rangle \to |\alpha_f(IJ_f)\,\mathbb{F}_f\rangle$ can be expressed in terms of the transition energy $\Delta E = (E(\alpha_i(IJ_i)\,\mathbb{F}_i) - E(\alpha_f(IJ_f)\,\mathbb{F}_f))$ and the associated fine-structure amplitudes and with

$$\begin{aligned} gf(\alpha_i(IJ_i)\,\mathbb{F}_i \;\to\; \alpha_f(IJ_f)\,\mathbb{F}_f) \;&=\; \frac{2}{3}\,\Delta E\;\left|\left\langle \alpha_f(IJ_f)\,\mathbb{F}_f \,\middle|\, \mathbb{O}^{(\text{E1, absorption})} \,\middle|\, \alpha_i(IJ_i)\,\mathbb{F}_i\right\rangle\right|^2 \\ &=\; \frac{2}{3}\,\Delta E\,(2F_i+1)\,(2F_f+1)\,\begin{Bmatrix} J_i & I & F_i \\ F_f & 1 & J_f \end{Bmatrix}\;\left|\left\langle \alpha_i\mathbb{J}_i \,\middle|\, \mathbb{O}^{(\text{E1, absorption})} \,\middle|\, \alpha_f\mathbb{J}_f\right\rangle\right|^2. \end{aligned}$$

In this case, the distribution of the oscillator strength among the hyperfine-resolved transitions is just determined geometrically by the Wigner 6–j symbol, i.e. due to the $(IJ)\,F$ coupling of the nuclear spin and the total electronic angular momentum.

➢ Oscillator strength for transitions between hyperfine levels: If, more generally, the hyperfine coupling between neighboured fine-structure levels $\{|\alpha\mathbb{J}\rangle\}$ is not negligible, the expansion coeffients $c(\alpha J,\, \mathcal{B})$ of the hyperfine levels in the given ASF basis need to be taken into account. Then, the absorption oscillator strength for the electric-dipole transitions between two hyperfine levels $|\alpha_i(IJ_i)\,\mathbb{F}_i\rangle \to |\alpha_f(IJ_f)\,\mathbb{F}_f\rangle$ can

still be written in terms of the associated fine-structure E1 transition amplitudes (Andersson *et al.*, 2006)

$$gf(\alpha_i\mathbb{F}_i \rightarrow \alpha_f\mathbb{F}_f; \mathcal{B}) = \frac{2}{3}\Delta E \left| \sum_{\beta_i J_i}\sum_{\beta_f J_f} c_{\beta_i}(\alpha_i J_i)\, c_{\beta_f}(\alpha_f J_f) \left\langle \beta_i(IJ_i)\,\mathbb{F}_i \right| \mathbb{O}^{(\mathrm{E1,\,absorption})} \left| \beta_f(I,J_f)\,\mathbb{F}_f \right\rangle \right|^2$$

$$= \frac{2}{3}\Delta E\,(2F_i+1)\,(2F_f+1) \left| \sum_{\beta_i J_i}\sum_{\beta_f J_f} c_{\beta_i}(\alpha_i J_i)\, c_{\beta_f}(\alpha_f J_f) \begin{Bmatrix} J_i & I & F_i \\ F_f & 1 & J_f \end{Bmatrix} \left\langle \beta_i\mathbb{J}_i \right| \mathbb{O}^{(\mathrm{E1,\,absorption})} \left| \beta_f\mathbb{J}_f \right\rangle \right|^2 .$$

Here, the summation runs over all fine-structure levels in the representation of the inital and final hyperfine levels. Moreover, interferences occurs if different terms in this summation are of similar size, and this may lead to a sizeable redistribution of the oscillator strengths from the different fine-structure transitions that can be formed between selected fine-structure levels in the ASF representations above.

7.3.b. Multipole polarizibilities (`MultipolePolarizibility`)

Properties & notations:

- ➢ General multipole polarizibility of an atomic level: .
- ➢ Dynamic polarizibility of an atomic level: .

Multipole polarizibilities:

- ➢ Frequency-dependent (multipole) polarizibilities are important in various fields of physics.
- ➢ The ac Stark shift of a clock transition, for example, is determined by the frequency-dependent electric-dipole polarizibilities of the clock states. The (so-called) magic wavelengths of a clock transition can be determined by finding the frequencies where the ac electric-dipole polarizabilities of the two clocks states are the same.
- ➢ Dynamic multipole (ac 2^L-pole) polarizibility: of a level $|0\rangle$ is (Porsev *et al.*, 2018)

$$\alpha^{(\mathbb{M})}(\omega,\, \beta_o\mathbb{J}_o) = \frac{L+1}{L}\,\frac{2L+1}{[(2L+1)!!]^2}\,(\alpha\,\omega)^{2L-2} \sum_{\nu} \frac{(E_\nu - E_o) \left| \left\langle \alpha_\nu\mathbb{J}_\nu \right| \mathbb{T}^{(\mathbb{M})} \left| \beta_o\mathbb{J}_o \right\rangle \right|^2}{(E_\nu - E_o)^2 - \omega^2}$$

where $\mathbb{T}^{(\mathbb{M})}$ is the corresponding multipole operator for E1, M1, ... transitions.

Dynamic electric-dipole polarizibility:

➢ The (dynamic) electric-dipole polarizibility is defined as (Derivianko *et al.*, 1999)

$$\alpha^{(\mathrm{E1})}(i\,\omega,\,\beta_o\mathbb{J}_o) \;=\; \frac{2}{3}\sum_{\nu}\frac{E_\nu\,-\,E_o}{(E_\nu\,-\,E_o)^2\,+\,\omega^2}\;\;|\langle\alpha\_\nu\mathbb{J}_\nu\,|\,\mathbf{R}\,|\,\beta_o\mathbb{J}_o\rangle|^2$$

and which includes for $\alpha^{(\mathrm{E1})}(\omega\,\equiv\,0)$ the static electric-dipole polarizibility.

➢ Dynamic (dipole) polarizability $\alpha(\omega)$: The dynamic polarizibility describes the response of an atoms and nanoobjects to an (external) electromagnetic disturbance as long as this field is weaker than the (internal) atomic field: $E \ll E^{(\mathrm{atomic})} = m^2\,e^5/\hbar^4 \approx 5.14\cdot 10^9$ V/cm, and if the wavelength of the field is much larger than the size of the object (Astapenko 2013).

➢ Mathematically, the dynamic polarizability $\alpha(\omega)$ can be expressed by a second-rank tensor (α_{ij}) that connects the induced dipole moment $\mathbf{d}$ of the atom with the strength of the external electric field $\mathbf{E}$ at the frequency ω

$$d_i \;=\; \sum_j \alpha_{ij}\,E_j(\omega)\,.$$

➢ For spherically symmetrical systems, this tensor simplifies to a scalar

$$\alpha_{ij}(\omega) \;=\; \alpha(\omega)\,\delta_{ij} \qquad\longrightarrow\qquad \mathbf{d}(\omega) \;=\; \alpha(\omega)\,\mathbf{E}.$$

➢ Static polarizibility of level $|\beta \mathbb{J} M\rangle$: In a dc electric field $\mathbf{E} = E\,\mathbf{e}_z$, the static polarizibility is defined as (Porsev *et al.* 1999)

$$\Delta E(\beta \mathbb{J} M) = -\frac{1}{2}\,\alpha(\beta \mathbb{J} M)\,E^2 = -\frac{1}{2}\left(\alpha^{(0)}(\beta \mathbb{J}) + \frac{3\,M^2 - J(J+1)}{J\,(2J-1)}\,\alpha^{(0)}(\beta \mathbb{J})\right) E^2$$

$$\alpha(\beta \mathbb{J} M) = -2 \sum_{\nu} \frac{|\,\langle \beta_\nu \mathbb{J}_\nu M_\nu \,|\, \mathbb{D}_z \,|\, \beta \mathbb{J} M\rangle\,|^2}{E_\beta - E_\nu}$$

$$\alpha^{(0)}(\beta \mathbb{J}) = \frac{-2}{3\,(2J+1)} \sum_{\nu} \frac{|\,\langle \beta_\nu \mathbb{J}_\nu \,|\, \mathbb{D} \,|\, \beta \mathbb{J}\rangle\,|^2}{E_\beta - E_\nu}$$

$$\alpha^{(2)}(\beta \mathbb{J}) = \left(\frac{40\,J\,(2J-1)}{3\,(2J+3)\,(2J+1)\,(J+1)}\right)^{1/2} \sum_{\nu} (-1)^{J+J_\nu+1} \begin{Bmatrix} J & 1 & J_\nu \\ 1 & J & 2 \end{Bmatrix} \frac{|\,\langle \beta_\nu \mathbb{J}_\nu \,|\, \mathbb{D} \,|\, \beta \mathbb{J}\rangle\,|^2}{E_\beta - E_\nu}$$

➢ Clausius-Mossotti relation: For a system embedded into a medium, the dynamic polarizability of atoms also defines the dielectric permittivity $\varepsilon(\omega)$ of the medium with number density n_a of atoms, and if the medium is assumed to just concists out of a single type of atoms

$$\frac{\varepsilon(\omega) - 1}{\varepsilon(\omega) + 2} = \pi\, n_a\, \alpha(\omega)$$

➢ Measurement of the dynamic polarizibility: Experimentally, the dynamic polarizability $\alpha(\omega) = \alpha(\omega,\, \beta_o \mathbb{J}_o)$ can be determined by measuring the refraction index of the substance $n(\omega) = \sqrt{\varepsilon(\omega)}$.

➢ Quadratic Stark effect: The dynamic polarizability also defines the energy shift ΔE_n of an atomic level in an external electric field. In second-order perturbation theory and for a spherically-symmetric state $|\beta_o \mathbb{J}_o\rangle$, this level shift can be written for

$$\Delta E_n^{(2)}(\beta_o \mathbb{J}_o) = -\frac{1}{2}\,\alpha_n(\omega,\, \beta_o \mathbb{J}_o)\,E^2$$

➢ Linear Stark effect: If the frequency of the external field coincides with the eigenfrequency of an atom, $\omega \approx \omega^{(atom)}$, the energy shift is found to be linear in electric field intensity.

➢ Static polarizibility $\alpha(0)$: For a static external field, the polarizibility $\alpha(\omega = 0)$ just describes the level shift in a constant electric field that arises in addition to the interatomic interaction potential of the atoms at long distances (van-der-Waals interaction). This static polarizability also describes the polarization potential of a neutral atom with for slow particles with charge e_o at long distance as well as the scattering cross section for the elastic scattering at such a charged particle

$$V^{\,(\mathrm{pol})} \;=\; -\,e_o^2\,\frac{\alpha(0)}{2\,r^4}, \qquad\qquad \sigma^{\,(\mathrm{elastic-scattering})} \;=\; 2\,\pi\,e_o\,\sqrt{\frac{\alpha(0)}{2\,E}}\,.$$

In deriving this cross section, one assumes a semi-classical motion of the incident particle with energy E along a well-defined trajectory with impact parameter b, and over which one need to average.

➢ Atomic dipole moment: Because of its spherical symmetry, the dipole moment of a atom is *zero* without an external field (Schiff theorem); therefore, the induced dipole moment is a direct measure for the disturbance of an atom by a field and for low-enough field strengths, the response of an atom to electromagnetic field can be simply characterized by its polarizability.

➢ Dynamic polarizibility $\alpha(\omega)$: The dynamic polarizability of an atom in level $|\beta_o \mathbb{J}_o\rangle$ can be expressed in terms of the transition frequencies and osciallator strength related to this level

$$\alpha(\omega,\,\beta_o\mathbb{J}_o) \;=\; \frac{e^2}{m}\sum_n \frac{f_{no}}{\omega_{no}^2 \,-\, \omega^2 \,-\, i\,\omega\,\delta_{no}} \qquad\Longrightarrow\qquad \alpha_0 \;\equiv\; \alpha(\omega=0) \;=\; \frac{e^2}{m}\sum_n \frac{f_{no}}{\omega_{no}^2}\,.$$

This expressions shows that the dynamic polarizability of an atom is generally a complex value with the dimension of a volume. While the imaginary part of the dynamic polarizibility describes damping (constants) of the transition oscillators, i.e. the absorption of radiation, the real part defines the refraction of an electromagnetic wave in a medium. Moreover, the summation includes both, the discrete as well as the continuous (parts of the) energy spectrum.

➢ Static polarizibility $\alpha(0)$: This is a real and positive value which may take rather large numerical values, if there are transitions with high oscillator strength and low eigenfrequency in the atomic spectrum as, for instance. for the alkaline-earth atoms.

Scalar and tensor polarizibility:

➢ The scalar polarizability of a level $\alpha\mathbb{J}$ in a light field at frequency ω can be expressed as the sum over intermediate states that are allowed by the electric-dipole selection rules (Safronova *et al.*, 2018)

$$\alpha_0(\omega) \;=\; \frac{2}{3\,(2J+1)}\sum_k \frac{(E_\nu \,-\, E_o)\;\langle \alpha_\nu \mathbb{J}_\nu \,\|\mathbb{D}\|\, \beta_o \mathbb{J}_o\rangle}{(E_\nu \,-\, E_o)^2 \,-\, \omega^2}\,,$$

and where the frequency ω of the incident light is assumed to be off resonance by at least several linewidths with regard to any of the intermediate levels $\{|\alpha_\nu \mathbb{J}_\nu\rangle\}$.

➢ The expression for the tensor polarizability has a similar structure.

Electric-dipole and magnetic-dipole susceptibitilities:

➢ Susceptibility: The susceptibility $\chi^{(\text{electric, magnetic})}$ is generally a (dimensionless) proportionality constant that characterizes the induced polarization of a medium in response to an applied electric or magnetic field. The greater the susceptibility, the greater the response of the material to an applied field.

➢ Electric susceptibility $\chi_e \equiv \chi^{(\text{electric})}$: A proportionality constant or tensor which relates the induced dielectric polarization density $\mathbf{P}$ to the applied field and which is very closely related to the atomic or molecular polarizibility α:

$$\mathbf{P} = \varepsilon_o \chi_e \mathbf{E}, \qquad \mathbf{p} = \varepsilon_o \alpha \mathbf{E}_{\text{local}}$$

Here $\mathbf{p}$ refers to the induced atomic or molecular electric-dipole moment. Analogue expressions also exit for the magnetic susceptibility $\chi^{(\text{magnetic})}$, the magnetic field $\mathbf{B}$ and the magnetization $\mathbf{M}$ as well as for the magnetic-dipole moment $\mathbf{m}$.

7.3.c. Dispersion coefficients

Remarks & notations:

➢ Lennard-Jones model: This model refers to a mathematically simple potential for describing the interaction between a pair of neutral atoms or molecules. It was proposed first in 1924 by John Lennard-Jones.

➢ The long-range interactions between atoms and molecules play a prominent role especially in the low-energy and low-temperature collision experiments.

➢ Dispersion coefficients C_n: The interaction of atoms at large interatomic distances, for instance for cold gases in a cold traps, is usually described in terms of dispersion (van der Waals) coefficients C_n.

➢ Alkaline-earth dimers: For two alkaline-earth atoms in their ground state, the long-range potential as function of the internuclear distance R can be written as (Porsev and Derivianko, 2006)

$$V(R) \;=\; -\,\frac{C_6}{R^6} \,-\, \frac{C_8}{R^8} \,-\, \frac{C_{10}}{R^{10}} \,-\, ...$$

Atomic computation of dispersion coefficients:

➢ Atom-wall coefficient, C_3: For an atom in a spherically-symmetric ground state $|\psi_o\rangle \;=\; |\beta_o\, \mathbb{J}_o M_o\rangle$, the dispersion coefficient C_3 of the Lennar-Jones interaction between an atom and a perfectly conducting wall is given by (Derivianko *et al.*, 1999)

$$C_3 \;=\; \frac{1}{4\pi} \int_0^\infty d\omega \;\alpha^{(\mathrm{E1})}(i\,\omega;\; \beta_o \mathbb{J}_o M_o) \;=\; \frac{1}{12}\; \langle \beta_o \mathbb{J}_o M_o \,|\, \mathbf{R}\cdot\mathbf{R} \,|\, \beta_o \mathbb{J}_o M_o\rangle \,, \qquad\qquad \mathbf{R} \;=\; \sum_{i=1}^{N} \mathbf{r}_i \,.$$

➢ Van-der-Waals coefficient, C_6: For an atom in a spherically-symmetric ground state $|\psi_o\rangle \;\equiv\; |\beta_o\, \mathbb{J}_o M_o\rangle$, the dispersion coefficient C_6 of the Lennar-Jones interaction can be expressed as integral over the dynamic electric-dipole polarizibility (Derivianko *et al.*, 1999)

$$C_6 \;=\; \frac{3}{\pi} \int_0^\infty d\omega\, [\alpha^{(\mathrm{E1})}(i\,\omega;\; \beta_o \mathbb{J}_o M_o)]^2 \,.$$

➢ Since the van-der-Waals coefficients C_6 contains the dipole matrix element to the fourth power, these dipole amplitudes must usually be calculated with high accuracy.

➢ Long-range interaction of two atoms: For two atoms a and b in spherical-symmetric ground states, $|\psi_a\rangle \;=\; |\beta_a\, \mathbb{J}_a M_a\rangle$ and $|\psi_b\rangle \;=\; |\beta_b\, \mathbb{J}_b M_b\rangle$, the long-range interaction can be written as (Porsev and Derivianko, 2006)

$$V(R) \;=\; -\sum_{n=3} \frac{C_{2n}^{ab}}{R^{2n}}, \qquad C_{2n}^{ab} \;=\; \frac{(2n\,-\,2)!}{2\pi} \sum_{k=1}^{n-2} \frac{1}{(2k)!\;(2k')!} \int_0^\infty d\,\omega\; \alpha_k^{(\mathrm{E1})}(i\omega;\; \psi_a)\; \alpha_{k'}^{(\mathrm{E1})}(i\omega;\; \psi_b), \qquad k' \;=\; n \,-\, k \,-\, 1,$$

and where $\alpha_k^{(\mathrm{E1})}(i\omega;\; \psi_c)$ is the 2^k -pole dynamic (electric-dipole) polarizibility of each atom c in its given state $|\alpha_c\, \mathbb{J}_c M_c\rangle$.

➢ Dispersion coefficients $C_n^{(AB)}$ of mixtures: For mixed interactions of atomic pairs (AB) , a simple rule is often applied:

$$C_n^{(AB)} \;=\; \sqrt{C_n^{(A)}\, C_n^{(B)}} \,.$$

➢ Van-der-Waals coefficients C_{12} and C_{14} : The high-order dispersion coefficients, i.e. the van der Waals coefficients C_{12} and C_{14} are usually not so easily available for most systems of interest. They can be approximated from the low-order dispersion coefficients C_{12} and C_6, C_8, C_{10} by using certain dimensionless ratios of such coefficients as discussed for instance by Douketis *et al.* (1982).

7.3.d. Stark shifts and ionization rates in static electric fields

Remarks & notations:

➢ LoSurdo-Stark effect: refers to the shifting and broadening of atomic and molecular states under the influence of an external electric field. (Dynamic) Stark shift: The dynamic Stark shift is caused by the interaction of an atom with the electro-magnetic field.

➢ Such a dynamic (time-dependent) Stark shift can be induced by a laser pulses but also by a single-photon wave packet.

➢ Keldish adiabacity parameter γ_K : Different strong-field ionization mechanisms can be distinguished for different laser frequencies ω_L , (electric) field strength $E_o = |\mathbf{E}_o|$ as well as atomic ionization potentials I_p . They are often distinguished by the Keldish adiabacity parameter, $\gamma_K = \omega \sqrt{2\, I_p}/E_o$.

➢ Multiphoton regime, $\gamma_K \gg 1$: This regime is realized at high frequency and low or moderate field strength and gives rise to a a power law for the ionization rate, $\Gamma \propto E_o^n$.

➢ Tunnel regime, $\gamma_K \ll 1$: This regime occurs at low laser frequency and high-field strength and gives rise to an exponential dependence of Γ on E_o . In the tunnel regime, the ionization is often considered as a quasi-static process due to the low frequency, and the total ionization yield is obtained as integral over the time-dependent field strength:

$$A = 1 - \exp\left[1 - \int_{-\infty}^{\infty} dt\, \Gamma\left(E_o(t)\right)\right] .$$

➢ In the tunnel regime, atomic structure computation can provide reliable predictions for both, the Stark shifts in an (quasi-static) electric field as well as for the ionization rates.

➢ Ammosov-Delone-Krainov (ADK) formula: This formula for the ionization rate has often been used for many-electron atoms and has been extended also towards molecules.

➢ Quasi-static regime: For $\gamma_K \ll 1$, one often further distinghuishes between the (tunnel ionization and the above-barrier ionization due to the (semi-classical) field strength $E^{(\text{above}-\text{barrier})} = I_p^2/4$. From a simplified classical viewpoint, the electron can leave the atom without

tunneling for $E_o > E^{(\text{above}-\text{barrier})}$ due to the suppression of the (atomic) Coulomb potential. In practice, however, this *barrier* is not sharp since an outgoing (scattered) electron is still partly reflected even for a classical suppressed barrier.

➢ (Quasi-) Static ionization rates: Within the tunneling regime, a variety of semiempirical expressions exist for the static ionization rates $\Gamma(E_o)$. Many of them are based on Landau's seminal formula for the ionization rate of the hydrogen atom in its ground state, such as the ADK rule.

7.3.e. Dressed atomic (Floquet) states and quasi-energies in slowly varying laser fields

Remarks & notations:

➢ Dressed atomic states: In a laser pulse of moderately varying intensity, the dressed states follow adiabatically the temporal evolution of the intensity during the passage of the pulse. The slow variation of the intensity then results into fairly slow changes in the (coefficients of the) superposition of the dressed states when compared with the optical period of the laser.

➢ Quasi-stationary wave function of dressed states: For sufficiently slow variations of the laser intensity, each dressed state can be written in the Floquet form, i.e. by means of a space-independent complex exponential *multiplied* by a time-harmonic function that oscillates with the same (optical) period as the incident field.

➢ Floquet equations: If the incident field is expanded in terms of a Fourier series, the time-dependent Schrödinger equation can be decomposed and re-written as a system of time-independent equations, the (so-called) Floquet equations. For multiphoton ionization, this system should be solved together with the radiation (Siegert) boundary conditions.

➢ The Floquet ansatz generally enables one to adopt the (time-independent) dressed-state approach to pulses with a sufficiently slowly varying field intensity, and where the time-dependence in captured by slow changes in the coefficients of the superposition.

➢ The (complex) eigenvalues of the Floquet equations provide both, the quasienergies of the dressed states and the resonance poles of the scattering amplitudes for laser-assisted scattering.

➢ The Floquet approximation is typically adequate for infrared laser pulses as well as for atoms in either the ground or some Rydberg level. It has been found inappropriate for UV laser frequencies and for low-lying excited levels because of avoided crossings between the dressed levels and large non-ponderomotive ac Stark shifts at suchhigh frequencies.

➢ The computation of the widths of quasi-energies often requires to go beyond first-order perturbation theory.

➢ Quasi-dressed states of atoms in a constant dc-field of constant intensity and frequency:quad The dressed states of atoms in a field of constant intensity and frequency refer to particular quasi-stationary solutions of the time-dependent Schrödinger equation.

➢ In atomic physics and if the laser pulses are neither ultra-intense nor ultra-short, these pulses can be modeled as a rapidly oscillating electric field but with a well-defined and slowly varying envelope (field amplitude). For such quasi-constant dc-fields, the behaviour of atoms can be described in terms of superpositions of dressed bound states that decay under the emission of photoelectrons.

Neutral atoms in direct-current (dc) fields:

➢ Complex-eigenvalue Schrödinger equation: The system "neutral atom + dc field" defines a rather complicated many-electron problem. Because of the (additional) time-dependent field, the discrete spectrum of the atom changes into a resonance spectrum whose states are obtained as solutions of a complex-eigenvalue Schrödinger equation

$$(H - z_o)\psi = 0, \qquad H = H^{(\mathrm{atom})} + \sum_i \mathbf{F}\cdot\mathbf{r}_i, \qquad z_o = E_o + \Delta(F) - \frac{i}{2}\Gamma(F)\,.$$

➢ Solution of the complex eigenvalue equation: This equation can be solved in terms of square-integrable function spaces, if the transformation $\rho = r\,e^{i\,\theta}$ is applied.

➢ This coordinate rotation for ρ has been applied to the Hamiltonian operators for the computation of the LoSurdo-Stark ground-state resonance of hydrogen atoms, and the solution was achieved by direct diagonalization of the non-Hermitian Hamiltonian on a large square-integrable basis set. However, such a direct diagonalization of the the non-Hermitian Hamiltonian matrix is quite unrealistic for the decaying states of many-electron atoms and molecules.

7.3.f. Fano profiles of continuum-embedded resonances

Remarks & notations:

➢ In physics, a Fano resonance generally refers to a resonant scattering process (phenomenon), and which gives rise to an asymmetric line-shape due to the interference between a constant background and a resonant scattering amplitude. Fano-type resonances can be found across many areas of physics and engineering because resonant scattering is a general wave phenomenon.

➢ In atomic physics, the background amplitude often arise from the direct (ionization) amplitude to the continuum, while the resonant amplitude arise from the (indirect) coupling of the atom to a discrete, localized state that is embedded into the continuum.

7.3.g. Light shifts of atomic levels

Remarks & notations:

➢ Light shifts for clock levels: The frequency of an atomic clock can be affected by (i) the thermal bath of blackbody radiation (BBR), (ii) the electric-quadrupole coupling of the ions to the trapping field and with other residual electro-magnetic fields, (iii) by ambient magnetic fields as well as (iv) through various Stark shifts (Yudin *et al.*, 2014).

➢ In highly-charged ions, the gross energy intervals nominally grow $\propto \tilde{Z}^2 \equiv (Z-N)^2$ as $\tilde{Z}$ increases. This leads to a substantial suppression of the ac-Stark and BBR shifts that are $\propto 1/\tilde{Z}^4$. Moreover, the quadrupolar moments of the bound-state electronic density scale with $1/\tilde{Z}^2$ and, this also reduces the quadrupolar shifts.

➢ Blackbody radiation (BBR) shift: For a time-independent environment, the BBR shift is given at temperature T in terms of the polarizibility α_o by (Berengut *et al.*, 2012)

$$\delta E \;=\; -\frac{1}{2}\,(831.9\ \mathrm{V/m})^2\,\left[\frac{T\,[K]}{300}\right]^4\,\alpha_o\,(1\,+\,\eta)$$

and where η refers to some dynamic correction due to the frequency distribution of the atom.

7.3.h. Frequency-dependent ac Stark shifts of atomic levels

Perturbative treatment of ac-Stark shifts $E_n(\omega)$:

➢ Atoms and ions in intense laser field: A perturbative description of the ac Stark shift of atoms in fields with intensity $I > 10^{13}\ \mathrm{W/cm^2}$) has been a subject of continuing concern.

➢ Although, perturbation theory is often considered inadequate for the analysis of multiphoton ionization experiments with atoms and ions, little is known about the breakdown of perturbation theoryt (Pan *et al.*, 1988). Nevertheless, a perturbative treatment of the many-electron atom in intense fields is still of interest for various scenarios and intensities.

7.3.i. Black-body radiation shifts

Remarks & notations:

➢ From radiation studies it is known that object emit radiation whose wavelength depends on its temperature.

➢ Black-body radiation shifts: More generally, the interaction with an environment at non-zero absolute temperature causes a level shift in the atom.

7.3.j. Hyperpolarizibility

Remarks & notations:

➢ The hyperpolarizability of atoms refers to a nonlinear-optical property of matter and is closely related to the second-order electric susceptibility (per unit volume).

➢ Any accurate calculation of static hyperpolarizabilities is still a great challenge for atomic theory, and this even applies to simple atoms, such as lithium with only three electrons. As reported in the literature, both the choice of the basis set (grid) as well as the electronic correlations can have a large effects upon the (accuracy of the) computed hyperpolarizabilities

➢ Hyperpolarizibility of closed-shell atoms: For a neutral, closed-shell atom in its ground state $|\beta\,{}^1S_0\rangle$, the energy (level) shift in the presence of a homogeneous static electric field of strength F is given by (Kassimi and Thakkar, 1994)

$$E(F;\,\beta\mathbb{J}) \;-\; E_o \;\;=\;\; -\,\alpha\,\frac{F^2}{2!} \;-\; \gamma_2\,\frac{F^4}{4!} \;-\; \gamma_4\,\frac{F^6}{6!} \;-\; \gamma_6\,\frac{F^8}{8!} \;-\; ....,$$

where α is the (static) dipole polarizibility and $\gamma_k,\;\; k \;=\; 2, 4, ...$ the hyperpolarizibility parameters of the atom.

➢ Induced dipole moment μ: In the same field static field F, the dipole moment is then given by

$$\mu(F;\,\beta\mathbb{J}) \;\;=\;\; \alpha\,F \;+\; \gamma_2\,\frac{F^3}{3!} \;+\; \gamma_4\,\frac{F^5}{5!} \;+\; \ldots\,.$$

➢ Finite-field procedure: In the computational procedure, the polarizabilities and hyperpolarizabilities are obtained from energy and/or dipole moment calculations of the atom in the presence of an electric fields of various strengths, and by using truncations of the given expansion above.

7.3.k. Electron localization function (ELF)

Remarks & notations:

➢ Electron localization function (ELF): Becke and Edgecombe (1990) derived a simple *localization function* in order to reveal the atomic shell structure as well as the core, binding and lone electron pairs in simple molecules. This localization function is an orbital-independent measure and based on the Hartree-Fock pair probability. Such a concept of localized electron groups is quite different from the delocalized Hartree-Fock orbitals; it supports a descriptive chemistry and may thus help identify, for instance, σ- and π-electrons systems.

➢ Localization *versus* Hartree-Fock theory: The canonical HF orbitals can be transformed unitarely due to different precriptions and by leaving the total HF energy unchanged. However, these transformations are generally not unique and can even result in qualitatively different 'bondings' of the electrons. In fact, Hartree-Fock theory is defined by its single-electron density matrices, which are invariant with regard to unitary orbital transformations. Therefore, any meaningful definition of electron localization must be sought in the density matrix itself and not in the orbitals (Becke and Edgecombe, 1990).

➢ Electron localization function (ELF): The ELF depends on the total electronic density, its gradient as well as the kinetic energy density. For all noble gases, this function completely reveals their expected shell structure. The ELF is closely related also to density-functional theory which asserts the total electronic density as the fundamental variable of many-electron theory. Moreover, since the probability density ρ_σ is *nonnegative*, it can be shown that D_σ must vanish for one-electron systems as well as in multi-electron systems that is dominated by a single, localized spin orbital.

➢ Electron localization function (ELF): Becke and Edgecombe (1990) propose a localization function in terms of the modified (spin) density D_σ and an analogue density D_σ^o of a uniform electron gas with a spin density equal to the local value of $\rho_\sigma(\mathbf{r})$

$$\text{ELF} \;=\; \left[1 \,+\, \left(\frac{D_\sigma}{D_\sigma^o}\right)^2\right]^{-1}, \qquad\qquad D_\sigma^o \;=\; \frac{3}{5}\,(6\pi^2)^{2/3}\,\rho_\sigma^{5/3}, \qquad\qquad 0 \;\leq\; \text{ELF} \;\leq\; 1$$

Of course, the ratio $D_\sigma \,/\, D_\sigma^o$ is a dimension-less localization index that is calibrated with regard to the uniform-density electron gas. Here, the upper limit $\text{ELF} \,=\, 1$ correspond to a perfect localization, while a value $\text{ELF} \,=\, 1/2$ refers to a electron-gas like pair probability.

➢ Electron localization function (ELF): In (quantum) chemistry, the ELF has been found a valuable alternative in the description and interpretation of chemical bindings.

7.4. Other topics closely related to atomic properties

7.4.a. Laser cooling, precision spectroscopy and quantum control

Quantum logic spectroscopy:

- Quantum logic spectroscopy: Quantum logic is typically implemented by the laser-induced coupling of the internal and external degrees of freedom of two ions, namely the spectroscopy and the logic ion. By making use of appropriate laser pulses, the information about the internal state of the spectroscopic ion can then be transferred from the spectroscopic to the logic ion.
- Such a quantum-logical transfer scheme can be realized with two ions in a linear Paul trap.
- Quantum-logic techniques: Many limitations of precision spectroscopy can be overcome if simple quantum-logic techniques are used and if the spectroscopic and logic ion is controlled together. In this technique, especially, the readily-controllable logic ion provides sympathetic cooling, internal state preparation and detection of the ion with an interesting spectroscopic transition.
- Simply speaking, the logic ion can be viewed as both, a remote control and a sensitive quantum sensor for the internal and external state of the spectroscopy ion.
- Quantum logic can also be used to laser-cool molecules to near their rotational and vibrational ground state by avoiding spontaneous emission of photons from the molecule.

Laser cooling and precision spectroscopy:

- Laser-cooling techniques: The recent development of laser-cooling techniques made cold and ultra-cold atomic samples available for optical spectroscopy. This development nowadays allowed for long interrogation times and significantly reduced Doppler shifts and gave eventually rise to an unprecedented uncertainty in atomic clocks, exceeding one part in 10^{-15}.
- In 1995, a controlled-NOT (CNOT) gate between a trapped atomic ion and its motional mode in the trap was first experimentally realized. Since then, the coherent control over the internal and external degrees of freedom in an atomic system has been demonstrated.
- In quantum information processing with trapped ions, precision spectroscopy has lead to new applications, such as teleportation, error-correction as well as the implementation of the Deutsch-Jozsa and semi-classical Fourier transformation algorithms.
- Internal *vs.* motional degrees of freedom: Laser spectroscopy helped develop methods to simultaneously control both, the internal electronic and motional degrees of freedom of individual atoms, molecules and singly-charged ions in traps with high accuracy.

- Most laser spectroscopy with clouds of trapped ions have explored a rather small class of atoms and atomic ions, including hydrogen, the alkali and alkaline-earth atoms and ions as well as few other species (Schmöger *et al.*, 2015). These atoms and ions have electronic transitions that are suited for laser cooling and that help localize the atoms for precision spectroscopy.
- Coulomb crystals: A signature for trapped and well-localized ions is the formation of Coulomb crystals, i.e. spatially ordered ensembles of mutually repelling ions that are confined in a common external trapping potential.
- Coulomb crystals form when the thermal kinetic energy becomes (much) smaller than the ion-ion electrostatic energy.
- Sympathetic cooling: If atoms and ions do not have a direct cooling transition, sympathetic cooling by use of co-trapped ions has been found a successful strategy in the past for singly and doubly charged atoms and molecules.

7.4.b. Atomic clocks

Search and application of atomic clocks:

- An atomic clock is typically based on an electron transition of either microwave, optical or ultraviolet frequency, and which serves as frequency standard for its time-keeping element.
- Atomic clocks are the most accurate time and frequency standards; they are frequnetly applid as primary standards for international time distribution services, to control the wave frequency of television broadcasts as well as the global navigation satellite systems such as GPS.
- While earlier atomic clocks were based on masers at room temperature, modern clocks are operated near to absolute zero temperature by probing an atomic fountains in a microwave-filled cavity. The NIST-F1 atomic clock, for example, one of the national primary time and frequency standards of the United States.
- Recent developments in the set-up and control of optical atomic clocks has improved their precision by a factor of 1000 in less than two decades.
- One particular goal in developing atomic clocks is to establish a clock with a high sensitivity to the variation of the fundamental fine-structure constant α .
- Applications of atomic clocks: Various applications of atomic clocks are now in reach or have already been realized by the improved precision and the high stability of thse clocks. These applications include: (1) the study of many-body physics and quantum simulations; (2) relativistic geodesy; (3) very long baseline interferometry; (4) searches for the variation of the fundamental constants; (5) searches for dark matter candidates; (6) tests of the Lorentz invariance and several others.

➢ These and further ideas and applications, such as the use of atomic clocks for gravitational wave detection, will require even more precise clocks in the future.

➢ The accuracy and stability of optical atomic clocks has been advanced significantly over the past ten years. The systematic uncertainty of the Sr optical lattice clock has been reduced to 2.1×10^{-18} in (so-called) fractional frequency units. A similar small (systematic) uncertainty of 3.2×10^{-18} was reported also for a single-trapped ion atomic clock, based on an electric-octupole transition in Yb^+.

➢ Application of atomic clocks: Atomic clocks with even improved accuracy will find their application in many fields of science and technology, such as in relativistic geodesy, (very) long baseline interferometry, gravitational wave detection tests of the Lorentz invariance, the search for variations of the fundamental constants or the re-definition of the second. Further improvement of clock precision is needed for several of these applications.

➢ Shifts of atomic clock transitions for HCI: Taken from Berengut *et al.* (2012).

Contribution to the shift	Scaling
Second-order Stark shift	$\sim /(Z^{(\mathrm{eff})})^4$
Blackbody shift	$\sim /(Z^{(\mathrm{eff})})^4$
Second-order Zeeman shift	suppressed due to large energy denominators.
Electric-quadrupole shift	$\sim /(Z^{(\mathrm{eff})})^2$
Fine structure	$\sim Z^2\ (Z^{(\mathrm{eff})})^2/(Z_{\mathrm{ion}}+1)$
Hyperfine A coefficient	$\sim Z\ (Z^{(\mathrm{eff})})^2/(Z_{\mathrm{ion}}+1)$

Types of optical atomic clocks:

➢ There are currently two types of optical atomic clocks under development: (i) based on neutral atoms in optical lattices or (ii) based on a single trapped ion. For both types, a similar uncertainty have been reached, namely: 2.1×10^{18} for a Sr neutral atom clock (Nicholson *et al.*, 2015) and 3.2×10^{18} for a Yb^+ trapped ion clock (Huntemann *et al.*, 2016), that have been operated on a particular electric-octupole (E3) transition.

➢ Proposals for a Yb atomic clock: The $4f^{14}\,6s^2\ {}^1S_0 - 4f^{14}\,6s\,6p\ {}^3P_0$ transition in neutral Yb can be induced by hyperfine mixing in isotopes with nuclear spin $I \neq 0$ and has served already as some frequency standard. However, neutral Yb has still another and very

interesting $4f^{14}\,6s\,6p\ {}^3P_0 - 4f^{13}\,6s^2\,5d\ (J = 2)$ electric-quadrupole (E2) transition at an easily accessible wavelength of 1695 nm, which might be suitable as well for the development of another frequency standard in this atom (Safronova *et al.*, 2018).

➢ ^{229m}Th clock: Thorium has one exceptional nuclear state that is known for the last 40 years and that has a very low energy of presumably below 10 eV. The currently assumed excitation energy of this isomeric state is 7.8 ± 0.5 eV, or correspondingly 159 ± 11 nm or ~ 1900 THz. This isomeric state conceptually allows for a direct laser excitation of the nucleus by using solid-state laser technology. This state has therefore been proposed for the development of a nuclear clock of extremely high stability owing to the expected high resilience against external influences and its radiative lifetime in the range of minutes to hours (von der Wense *et al.*, 2017).

7.4.c. Atomic partition functions

Motivation:

➢ The atomic partition function $U(T)$ includes a summation over all bound levels of the atom and is defined as

$$U(T) \;=\; \sum_j g_j \,\exp\left(-\frac{E_i}{kt}\right) .$$

7.4.d. Quantum similarity measures & similarity indices for pairs of atoms and ions

Quantum similarity measures:

➢ Quantum similarity measures (QSM): A number of such similarity measures has been worked out formally in the early 1980s by Carbo and coworkers (1980, 2004). These measures and indices for pairs of atoms or molecules are mainly based on the (overlap of the) electron density distribution of two quantum systems. When applied to isolated atoms, these measures can help analyze the chemical periodicity in the periodic table of elements.

➢ Quantum similarity measure: For two quantum systems with (spinless, electron) densities $\rho^{(A)}(\mathbf{r})$, $\rho^{(B)}(\mathbf{r})$ and a separation operator $\Omega(\mathbf{r}_1, \mathbf{r}_2)$, Carbo *et al.* (1980) define such a similarity measure by

$$Z^{(A,B)}(\Omega) \;=\; \int d\mathbf{r}_1\, d\mathbf{r}_2\, \rho^{(A)}(\mathbf{r}_1)\, \Omega(\mathbf{r}_1, \mathbf{r}_2)\, \rho^{(B)}(\mathbf{r}_2).$$

Often, the separation operator $\Omega(\mathbf{r}_1, \mathbf{r}_2) = \delta(\mathbf{r}_1 - \mathbf{r}_2)$ is chosen which *reduces* the double integration to a 'overlap' integral of the two electron densities. For $\Omega(\mathbf{r}_1, \mathbf{r}_2) = \frac{1}{|\mathbf{r}_1 - \mathbf{r}_2|}$, in contrast, a Coulomb-interaction integral is obtained.

➢ Quantum similarity index: A *normalized* similarity measure, known as similarity index, is obtained by

$$I^{(A,B)}(\Omega) \;=\; \frac{Z^{(A,B)}(\Omega)}{\sqrt{Z^{(A,A)}(\Omega)}\,\sqrt{Z^{(B,B)}(\Omega)}}, \qquad\qquad 0 \;\le\; I^{(A,B)}(\Omega) \;\le\; 1.$$

Both, the quantum similarity measure and similarity index can be evaluated quite easily by using proper densities of ions, atoms or molecules.

➢ Quantum similarity measures: These measures can be used also to provide compact information about (pairs of) molecules with regard to their shape and extent of the electron density. These measures might be used also as atomic and molecular descriptors in predicting molecular structures and reactivities. Various modifications have been suggested for the quantum similarity measures from above by using different separation operators or reactivity-motivated densities.

7.4.e. Atom-atom and atom-ion interaction potentials

Motivation:

➢ Interatomic forces and potentials: Accurate interatomic potentials are of fundamental importance for understanding and modelling the static and dynamic properties of gases, liquids or even solids.

➢ In particular, a good knowledge of the interatomic forces in (closed-shell) molecules has been found a key for understanding the behavior of various systems, such as the geometry and stability of molecular solids, the properties of liquids and their phase transitions as well as collisions between molecules in gases or in molecular beams.

- While the theory of interatomic forces has been developed over the last four decades, fast and reasonably reliable predictions are still often not easily available, especially if a whole range of intermolecular separations need to be considered.
- While the scattering of charged particles has already a rather long history, collisions of ions and neutral particles at ultracold temperatures has emerged only recently as an exciting (new) field in AMO physics.
- Ion-atom interactions at cold temperatures: At cold temperatures of just a few Kelvin or even lower, ion-atom interactions are often affected by (i) rapid energy variations in the potentials as induced by long-range polarization contributions, (ii) the generally large number of contributing partial waves and (iii) a rather sensitive dependence of the interatomic interactions upon the details of the short-range potential. Further difficulties may arise from (iv) other weak interactions, such as hyperfine interactions and other.
- The standard numerical methods for dealing with intermolecular forces are often not only inefficient in addressing these difficulties but they sometimes even miss important physics, such as extremely narrow resonances.
- Intermolecular interaction: The (inter-molecular) interaction energies are often partitioned into the SCF parts of the individual atoms and the correlation energy of the molecule as a whole. For atoms, the SCF computation can be carried out quite easily, while the correlation energies need to be obtained semi-empirically by means of standard long range multipolar expansion (Douketis *et al.*, 1982).
- Ion transport coefficients in a gaseous environment: These coefficients can often be derived from the ion-neutral interaction potentials and such computations are now routine for atomic ion-atom systems.
- The (attractive) interatomic interaction is dominated by correlation or dispersion effects at large internuclear distances R, where perturbation theory gives rise to a series expansion R^{-2n}, $n \geq 3$. However, this perturbation series is known to be asymptotically divergent and is best truncated at its smallest term, following the work of Dalgarno and Lewis.
- Because of these difficulties, many accurate interatomic potentials have been determined experimentally by combining data from beam scattering experiments, virial and transport coefficient measurements as well as liquid and solid state properties. In practise, however, the interatomic potentials are still best probed in the intermediate regions.

Gordon-Kim (1972) theory for atom-atom interactions:

- Gordon and Kim (1972) developed a model to calculate the interactions between closed-shell atoms, ions and molecules. In this model, the electron density of the system is taken as the sum of the two separate densities, and the non-Coulombic part of the interaction potential is calculated from this density by using energy expressions from the free-electron gas.
- Assumptions of the Gordon-Kim theory: Three basic assumptions were made by Gordon and Kim (1972):

i) No rearrangement or distortion of the separate atomic densities occurs when the two atoms are brought together and, hence, the total electron density is just the sum of the two (spherically symmetric) atomic densities. This assumption neglects of course the rearrangement of the electron density and therefore restricts the theory to systems with a strong chemical bond, including covalent chemical bonds and to interatomic distances that are smaller than about half of the equilibrium separation.

ii) The interatomic interaction can be evaluated from the combined atomic density, including the Coulomb interactions between all charges.

iii) Gordon and Kim applied originally Hartree-Fock wave-functions in order to obtain the electron densities of the separate atoms, although other, and perhaps more accurate, wave functions should work as well.

- Total interaction of the two (atomic) charge distributions: The total energy includes the contributions from the kinetic, exchange and correlation energies as well as the (direct) Coulomb interactions energy. Below, we briefly summarize how these contributions can be calculated by juar using atomic wave functions.
- Apart from the Coulomb interaction of the two (atomic) charge distributions, the kinetic, exchange and correlation energy contributions to the total interaction energy are obtained from the electron density and the free-electron gas approximation.
- The regions around the nuclei (in which the density varies rather rapidly) do overall not contribute much to the interaction energy, even if they strongly affect the total energy. These contributions to the total energy cancel out if the atomic energies are substracted. Only the outer regions of the atoms, in which the atomic densities overlap, contribute significantly to the interaction energy. For these reasons, the uniform electron gas model should be reasonably accurate (Gordon and Kim, 1972).
- The rather simple Gordon-Kim potential have been used, for example, in the treatment of ionic compounds such as alkali-halide and alkaline-earth-dihalide molecules in order to predict (surprisingly) accurate molecular properties (Kim and Gordon, 1974). In this work, Gordon and Kim made the following two basic assumptions in addition to those assumptions already made for their pair potentials: (a) the systems are made of free ions; (b) the interactions of ions are pairwise additive, i.e. the total interaction is the sum of all the pair interactions, neglecting the many-body interactions.

Perturbative methods:

- Different regions of the molecular potential curves have been investigated by different theoretical methods. Perturbation theory has been applied, in particular, to describe the long-range attraction, and where the first- and second-order perturbation energies are often approximated by just the first few terms in a multipole-series expansion of the Coulomb interaction between the molecules.
- Failure of perturbation theory: However, the perturbation method fails to desribe the potential at short and intermediate distances since it: (i) does not include exchange interactions between the electrons, (ii) diverges for strong interatomic interactions, and (iii) because a multipole expansion generally fails when the electron distributions overlap each other.

➢ At intermediate distances, i.e. in the region of the minimum of the intermolecular potential, only SCF computations typically predict the potentials reasonably well if the molecule does not form strong chemical bonds.

7.4.f. Dispersive interactions in liquid and solids

Dispersive interactions in molecular-dynamics and Monte-Carlo simulations:

➢ Dispersive interactions: Dispersive forces and interactions in media often refer to contributions to the intermolecular interactions that arise from the polarization of one the atoms in the (fluctuating) instantaneous multipole field of other atoms. Therefore, dispersive interactions exist between each pair, triple, etc. of atoms or ions.

➢ Application of dispersive interactions: Apart from inert-gas or crystallized solids of various organic molecules, the dispersive interactions are small, though not negligible. Reasonable estimates of the magnitude of the dispersion interaction are therefore necessary for many solid-state studies, such as the cohesion of matter, the behaviour of ionic crystals, for molecular liquids, the adsorption on surfaces or in porous media (Pellenq and Nicholson, 1998).

➢ In Monte-Carlo and molecular-dynamics simulations, for example, a reasonable accurate potential energy function is required and need to be based on quantum-mechanical estimates, even if the dynamics of the particles is described classically.

➢ For dense-phase and solid-state systems, full quantum mechanical calculations of the interaction energy are generally not feasible and, hence, require to describe the interactions by means of inter-molecular or inter-ionic potentials; cf. section 7.4.e.

➢ Expressions for the dispersion coefficients can be derived from perturbation theory; however, the theory of inter-molecular interaction also shows clearly that the dispersive interactions in media are generally not pair-additive. Apart from the two-particle interactions, the three-body terms are known to play a significant role in the thermodynamics of condensed phases.

Two-body dispersive interactions:

➢ Long-range dispersive interactions: If we consider two interacting neutral atoms, time-dependent perturbation theory gives rise to a long-range dispersive interaction due to charge fluctuations of the interacting species.

➢ Multipole expansion: For two spherically symmetric atoms or molecules A and B, that are separated by a distance R, a multipole expansion

is given by (Pellenq and Nicholson, 1998)

$$V^{\,(\text{dispersion, AB})}(R) \;=\; -\left[\frac{C_6}{R_6} + \frac{C_8}{R_8} + \frac{C_{10}}{R_{10}} + ...\right].$$

➢ In this expansion, the dispersion coefficient C_6 describes the interaction between two instantaneous dipoles, C_8 the interaction between a quadrupole and a dipole and C_{10} both, the interaction between an octopole and a dipole as well as between two quadrupoles.

Three-body dispersive interactions:

➢ In the multipole expansion, the terms with triplets of species A, B and C are obtained from perturbation theory at the third and fourth orders. For such a triplet, the total dispersion energy is however non-additive:

$$V^{\,(\text{dispersion})} \;=\; V^{\,(\text{dispersion, AB})} + V^{\,(\text{dispersion, BC})} + V^{\,(\text{dispersion, CA})} + V^{\,(\text{dispersion, ABC})} + ...$$

where $V^{\,(\text{dispersion, ABC})}$ represents a sum of several terms describing the three-body interaction.

7.4.g. Transport coefficients for ion mobility and diffusion in gases

Transport coefficients in gases:

➢ Ion-mobility spectrometry (IMS): The IMS is an analytical technique that is used to separate and identify ionized molecules in the gas phase, based on their mobility within a carrier buffer gas.

➢ IMS has been heavily employed for military or security purposes, such as detecting drugs and explosives, but also for the analysis of both small and large biomolecules.

➢ Ion mobility K: The ion mobility is defined as the proportionality factor between the drift velocity v_d of the ions and the applied electric field E : $v_d = K\,E$. These ion mobilities are usually reported as reduced (ion) mobilities for a standard gas density n_0 , i.e. for standard temperature $T = 273$ K and pressure $p_o = 1013$ hPa.

➢ Ion mobilities also help in analysis of collision broadening in ion cyclotron resonance, the study of ion-molecule reactions as a function of electric field strength in flow-drift tubes, and especially the use of mobility data to test or determine ion-neutral interaction potentials.

➢ Since the reduced ion mobility just refers to the standard density, it is still temperature dependent $K_o = K \frac{n}{n_o} == K \frac{T_o}{T} \frac{p}{p_o}$.

➢ Kinetic theory of ion mobility in neutral gases: Viehland and Mason (1978) present the first rigorous kinetic theory of ion mobility in neutral gases which is valid for electric fields of arbitrary strength and without restriction to the ion-neutral mass ratio or interaction potential. The results have proved useful in a number of applications: the calculation of low-field ion mobilities in high-temperature gases, if measurements as function of electric field strength were made before in low-temperature gases.

7.4.h. Polarizibility and optical absorbance of nanoparticles

Optical properties of nanoparticles:

➢ Noble-metal nanoparticles with a size, that is comparable to the wavelength of the incident light, show characteristic colors owing to the strong absorption and scattering of light in the visible region.

➢ Localized surface plasmon resonance (LSPR). The LSPR are often explained as collective oscillation of free electrons in the nanoparticle that are induced by the electro-magnetic waves. Therefore, the color of the absorbed light can be tuned by the size, shape, materials as well as the surrounding environment of the nanoparticles, and with applications in chemistry, physics and biomedical fields.

➢ Nanoparticles with a size below 10 nm have an extremely high surface-to-volume ratios and, thus, substantially different optical properties when compared to large nanoparticles or the bulk material. These optical properties also depend on the atomistic structure.

Methods for calculating the polarizibility of nanoparticles:

➢ The polarizability of a discretized medium is in general proportional to its volume.

➢ Polarizability of the i-th atom α_i : In a given nanoparticle, the polarizability of the i-th atom α_i can be approximated by multiplying the polarizability of the free atom $\alpha^{(\text{free})}$ with the relative volume (ratio), i.e. by dividing the effective volume $V^{(\text{eff})}$ by the volume of the free atom $V^{(\text{free})}$,

$$\alpha_i = \frac{V^{(\text{eff})}}{V^{(\text{free})}} \alpha^{(\text{free})} = \frac{V^{(\text{eff})}}{V^{(\text{free})}} \frac{e^2}{m} \sum_n \frac{f_n}{\omega_n^2 - \omega^2 - i\,\omega\,\delta}$$

where ω_n is the n-th absorption frequency, f_n its oscillator strength and where the frequency shift δ depends on the coordination factor within the nanoparticle.

➢ Optical absorbance of nanoparticles: The optical absorbance of the nanoparticle is obtained from the total polarizability by

$$\sigma^{(\text{absorption})} = \frac{4\pi\,\omega}{c}\,\Im\left\{\alpha^{(\text{total})}(\omega)\right\} = \frac{4\pi\,\omega}{c}\,\Im\left\{\sum_i^N \alpha_i^{(\text{SCF})}(\omega)\right\}$$

7.4.i. Laser-produced plasma

Properties & applications of laser-produced plasma (LPP):

➢ Laser-produced plasmas (LPP) have attracted recent interest because of their use in developing laboratory ion sources and pulsed light sources at short wavelengths.

➢ In LPP, hot electrons can subsequently ionize the much cooler atoms, forming an x-ray-emitting, high-temperature plasma spark at the surface of the solid (Murnane *et al.*, 1991).

➢ The emitted x-rays from such a laser-produced plasma are generally incoherent but have a high brightness because of the small size, short lifetime and the high temperature of the radiating plasma.

➢ LPP have been proposed as source of both, x-rays and multiply-charged ions. Whereas x-ray sources aim for a high radiation loss from the plasma due to the generation of highly stripped atoms, such higher charge states of ions are mainly produced by a high plasma temperature and a low radiation level (loss).

➢ To determine the properties of a LPP, such as temperature, density or its radiation emission, one needs a proper model for the coupling of the laser light with the heavy element (solid-state) target.

➢ LPP will find applications in extreme ultraviolet (EUV) lithography, EUV metrology as well as in the modification of surfaces.

➢ LPP sources have been developed for x-rays in the water window, though with limited conversion efficiency and/or brightness so far. These plasmas can be used for novel microscope designs as well as for cell tomography.

➢ Scaling laws for LPP: Scaling laws predict that brighter and more efficient x-ray sources will be obtained if (more) intense laser pulses are employed. These sources can then be used for time-resolved x-ray scattering studies and for the development of x-ray lasers.

➢ Scaling laws for LPP: Simple arguments can be used to derive scaling laws predict the response of the LPP if the laser parameters are varied. If any hydrodynamic expansion is neglected during the interaction with the laser pulse, we can equate the incident heating flux to the cooling flux that occurs due to classical thermal conduction.

➢ Scaling laws can be used also to predict the radiation output from a LPP. For a short pulse of about 100 fs, the heat can penetrate for about 50 nm, and the hot radiating region can be considered as optically thin (Murnane *et al.*, 1991). Therefore, the Planck mean-free path X of the radiation is much longer than the characteristic length L, and the plasma radiates as a diluted black body with power $P_r = A\,\sigma\,T^4\,L\,/\,\lambda$, and where σ is the Stefan-Boltzmann constant and A the radiating area.

Ultrafast x-ray pulses from laser-produced plasma:

➢ A high-temperature plasma is created when an intense laser pulse is focused onto the surface of a solid (Murnane *et al.*, 1991). From such a plasma, an ultrafast pulse of x-ray radiation is emitted when the laser pulse length is less than about a picosecond.

➢ X-ray pulses with a duration of a picosecond or less have been observed, more than an order of magnitude shorter than those produced by any other x-ray source.

➢ A direct comparison of fast x-ray pulses from LPP with other x-ray sources is difficult; in general, however, LPP yield x-rays with much higher peak power but lower average power than synchrotrons and other high-average power sources such as rotating anode tubes.

Ionization models for LPP:

➢ Collisional-radiative (CR) ionization model: A CR model can be applied to LPP with temperatures above a few tens of eV. At these temperatures, the average ionization stage A^{q+} of a given element is dominated by the electron plasma temperature due to electron and photon-impact excitation and ionization processes.

➢ Indeed, two main types of excitation and ionization processes occur in LPP: collisional and radiative processes, and where the corresponding de-excitation and recombination refer to the same types of processes. The ionization-recombination equations for both processes are:

$$A^{(q-1)+} + e^- \longleftrightarrow A^{q+} + e_1^- + e_2^-, \qquad A^{(q-1)+} + \hbar\,\omega \longleftrightarrow A^{q+} + e_p^-.$$

➢ Ionization-recombination equation: In these ionization-recombination equations, one often only considers collisions with (free) electrons since these collisions are much more efficient than those with heavier particles. Obviously, these equations also neglect autoionization and its (inverse) dielectronic recombination.

Deflagration models for LPP:

➢ Deflagration from the dictionary: Deflagration refers to an explosion in which the speed of burning is lower than the speed of sound in the surroundings or, in other words, a deflagration is a fire in which a flame travels rapidly, but at subsonic speed, through a gas.

➢ The radiative deflagration (model) describes the rapid interaction of the incident laser radiation with a very thin layer near to the target surface. In this layer, the electron density reaches a cut-off $n^{(\mathrm{cut-off})} = 10^{21} / \lambda^2\,[\mu\,\mathrm{m}]$. This rapid interaction also leads to a hot plasma that expands into the vacuum and which *vice versa,* results in a shock wave into the solid owing to momentum conservation.

➢ The properties of the hot plasma in the (thin) interaction layer can then be determined mainly from the power density in the focal zone and the wavelength of the incident radiation.

7.4.j. Plasma diagnostics

Interpretation of line spectra:

➢ More often than not, any detailed interpretation of the line spectra from laboratory plasmas and astrophysical sources has been found a great challenge since it requires one to go often beyond a local thermodynamical equilibrium (LTE) approach. If no equlibrium is reached, the spatially-dependent photon emission and absorption need to be taken into account in the solution of the rate equations throughout the emitting medium.

➢ Laboratory *versus* astrophysical plasma: Laboratory plasmas can differ from astrophysical sources in various ways:

- Laboratory plasmas can be short-lived so that they do not reach statistical equilibrium.
- Even if often much larger densities occur in laboratory plasma, when compared to typical astrophysical sources, still not all lines are optically thick and, in partiular, the re-bound and free-free transitions (continuum radiation) are usually optically thin.
- In laboratory plasma, most atomic levels are often collisionally rather than radiatively dominated.
- The (large) density of laboratory plasma can dramatically affect the line profiles, and this should be taken into account in the radiative-transfer calculations.

➢ However, in order to determine the relevant physical parameters that describe both, the astrophysical and laboratory plasmas, i.e. its electron temperature, density distribution, ion and element abundances, etc., we need to compare the observed data to a theoretical model spectra.

- In general, any collision between particles cause energy exchange and changes in the state distribution changes.
- Non-local thermodynamic equilibrium (NLTE): NLTE exists in a wide variety of astrophysical and laboratory-created plasmas. Examples of NLTE astronomical plasmas are the stellar corona, interstellar nebulae and some other low-density ionized plasmas. In the laboratory, NLTE exists in laser-produced plasmas, tokamaks and Z-pinch based experiments.
- X-ray satellites, such as Chandra and Xmm-Newton have provided large amounts of high-resolution spectra from astronomical objects, and with many of them in NLTE.

Diagnostics of astrophysical plasma:

- Hot plasmas are present in the universe in a variety of astrophysical objects, from stellar coronae to the birth of stars and up to the intergalactic medium in clusters of galaxies. The high-quality data, that have been obtained during the last few decades from space observatories, like Einstein, Rosat, Asca, and Sax, eneabled one to study in great detail the physical condition of several astrophysical plasmas.
- Solar corona plasma: The solar corona plasma is low-density plasma and is believed to be dominated by the spontaneous decay and radiative recombination. For these two processes, the corresponding decay rates are much higher than the collisional decay and three-body recombination and, hence, the plasma is not in a local thermodynamic equilibrium and cannot be described by Saha or Boltzmann equations.
- Static stellar atmospheres: In the standard models of static stellar atmospheres, the atomic (or ionic) populations, the radiation field, the temperature and density are calculated self-consistently by means of rate equations and radiative transfer equations but owing to certain constraints, such as statistical equilibrium, radiative equilibrium or a hydrostatic equilibrium.

Diagnostics of laboratory plasma:

- For ITER, various concepts have been developed to reduce the peak heat at the plasma-facing components of the tokamak. Indeed, much of the current experimental and theoretical work in fusion research focus on the question of how the heat from the plasma need to be transferred to the walls of the main and divertor chambers.
- Heat transfer process: To analyse this heat transfer and to enroll the relative importance of the primary atomic processes, simple quasi-analytic models and refined rate coefficients and cross sections have been utilized. Important heat transfer processes refer to the radiation losses through bremsstrahlung, impurity radiation losses from the plasma edge, the charge exchange and radiation losses from hydrogen in outer layer as well as to radiation losses due to impurities in the divertor plasma.

- In large fusion devices such as ITER, most of the heating power strikes the divertor plate and results in a high peak-heat loads of all plasma-facing components.
- The ITER divertor has been designed in order to enhance the charge exchange processes, hydrogen and impurity line radiation, ionization, or elastic collisions between the recycling gas and the plasma in the diverted plasma and, hence, to spread out the heat and momentum transfer over the device.

Diagnostics of tungsten plasma:

- Atomic physics has been crucial for understanding the plasma-energy balance and for diagnostic development. In particular, tungsten is nowadays very frequently used on present-day tokamaks in preparation for ITER.
- Tungsten has become of high importance since it will be a major constituent of ITER plasmas. Tungsten will be applied as plasma-facing component that is able to withstand high heat loads and with a lower tritium retention than other possible materials.
- ITER Core Imaging x-ray Spectrometer (CIXS): The CIXS has been designed to measure the ion temperature and the motion of ITERs plasma core, based especially on the x-ray emission of neon-like W^{64+} ions (Beiersdorfer *et al.*, 2015). The emission from tungsten will be measured by extreme ultraviolet (EUV) and optical spectrometers in order to determine its concentration in the plasma and to the assess power loss and the sputtering rate of tungsten.

Diagnostics of lanthanide ions:

- The radiative properties of the lanthanide ions have numerous applications in solid-state laser materials, photonics and the lighting industry. Radiative transitions of lanthanide ions were observed in doped crystals and in solution with small shifts relative to those of the free ions.
- Suzuki *et al.* (2018) have systematically observed extreme ultraviolet (EUV) spectra from the highly-charged ions of nine lanthanide elements with nuclear change $Z = 60..70$ in optically thin plasmas as produced in the Large Helical Device (LHD). The wavelengths of the main peaks in the quasi-continuum features were found to agree well previously measured singlet transitions of Pd-like ions as well as with the discrete spectral lines from Cu-like and Ag-like ions.
- The bright emission spectra from highly-charged ions of lanthanide elements ($Z = 57-71$) are known to appear in the extreme ultraviolet (EUV) or soft x-ray wavelength range due to $n = 4-4$ transitions of lanthanide ions in the wavelength range of 5-12 nm. These emission spectra are typically strongly affected by relativistic effects and multi-electron correlations. Likely, these emission spectra will play an important role in application to the next generation light sources for EUV lithography.

➢ Observationos with the Hubble Space Telescope: In astrophysics, observationos with the Hubble Space Telescope of spectra of chemically peculiar stars have proven the presence of lanthanide ions up to doubly-charged stages. More recently, the shortly delayed observation of gravitational waves and the emission of electromagnetic waves during a neutron-star merger have renewed the interest for radiative properties of higher-charged lanthanide ions.

7.4.k. Radial distribution functions for plasma and liquid models

General remarks:

➢ Distribution functions for plasma: The radial distribution function for a plasma is often required and need to be calculated. In these computations, quantum effects have to be taken into account for small inter-particle separations, either by using a modified path-integral technique or, equivalently, by a summation over states, together with the assumption that the charged particles interact via a shielded Coulomb potential.

➢ General expressions for the radial distribution function in an electron-ion plasma outside of an thermal equilibrium have been obtained in the literature in first-order of the plasma parameters.

➢ Distribution functions for fluids: Tadial distribution function and static structure factors have been computed at several places in the literature. The radial distribution function can be utilized to characterize a fluid, for instance in terms of the pronounced maxima at some inter-particle distance, and followed by successive minima and maxima with reduced amplitudes.

Quantal hypernetted-chain approximation:

➢ Hypernetted-chain equation: In statistical mechanics, the hypernetted-chain equation arises as a closure relation in order to solve the Ornstein-Zernike equation, i.e. a relation between the direct and total correlation functions. The hypernetted-chain equation is commonly applied in fluid theory in order to obtain, e.g. expressions for the radial distribution function.

➢ The hypernetted-chain approximation is an integral-equation method from statistical physics that arises from the theory of liquids.

➢ A quantal version of the hypernetted-chain equation (QHNC) was derived in the literature by using the density-functional method, and extended to treat a liquid metal and a plasma as an ion-electron mixture.

7.4.I. Average-atom model for warm-dense matter

Warm-dense matter:

- Warm-dense matter (WDM): This term generally refers to some state of matter under plasma conditions, and which can range from condensed matter to weakly-coupled plasmas with typical temperatures from a few to a few hundred eV as well as with densities from a few hundredths to about a hundred times of the solid density.
- In modeling WDM, great challenges arise from the partial ionization of the plasma, the degeneracy of the electron states, the bound-state level shifts, the pressure ionization in plasma as well as the strong coupling of the ion-ion pairs that must be taken into account self-consistently.
- Equation of state: A good understanding of the properties and behaviour of WDM, such as the equation of state, its radiation opacity, or transport properties, has been found important, for modeling for example astrophysical objects or inertial confinement fusion experiments (Hou *et al.*, 2015).
- Electronic structure of impurities: Studies on the electronic structure of impurities within an electron gas have been performed in the literature as function of their density and temperature. For these investigations, one need to know the dependence of screening effects on the plasma parameters.
- Friedel oscillations: At low temperatures and metallic densities, especially, the electron density often exhibits Friedel oscillations as known also from solid-state physics.
- Hou *et al.* (2015) combined the average-atom model with the hypernetted chain approximation (to a so-called AAHNC approximation) in order to describe the electronic and ionic structure in the WDM regime.

Average-atom model:

- Average-atom (AA) model: This model divides the plasma into separate neutral Wigner-Seitz cells with a nucleus of charge Z and Z free electrons. Various versions of the AA model have been implemented in plasma physics for describing warm- and hot-dense plasma.
- In the AA model, each ion or atom is described within a finite (ion) sphere and by using a central-field approximation for the bound electrons. For heavy atoms and ions, a (radial) Dirac equation can be applied but where the potential $V(r)$ need again to be calculated self-consistently.

➢ Electron density in the AA model: For an isolated atom or ion, the electron density is calculated in the AA model in order to include the level broadening of the energy levels within a plasma environment. This density is applied also for studying the temperature and density effects upon the electron distributions within a statistical way.

➢ Radial potential in the AA model: (Hou *et al.*, 2015)

$$V(r) = -\frac{Z}{r} + \int d^3r' \frac{\rho_b(r')}{|\mathbf{r} - \mathbf{r}'|} + V_{\rm xc}[\rho_b(r) + \rho_{e,0}] - V_{\rm xc}(\rho_{e,0}) - \frac{\rho_{e,0}}{\beta} \int d^3r' C_{ee}(|\mathbf{r} - \mathbf{r}'|) h_{ie}(r') - \frac{\rho_{i,0}}{\beta} \int d^3r' C_{ie}(|\mathbf{r} - \mathbf{r}'|) h_{ii}(r')$$

where the first four terms constitute the contributions from a single ion: electron-nucleus interaction, the electro-static repulsion with the other bound electrons as well as the exchange and correlation potential, which are often evaluated by using some local density approximation. The last two terms in this expression represent the interaction of the ion with the surrounding free electrons and with the other ions. Here, $\rho_{e,0} = \rho(r_b)$ is the uniform electron density.

Spectral emission from plasma in a non-local thermodynamic equilibirum (NLTE):

➢ In a non-local thermodynamic equilibirum (NLTE), in which the levels of each configuration are in LTE among each other, the population N_a of a given configuation follows as solution of a system of rate equations

$$\frac{\partial N_a}{\partial t} = -N_a \sum_b R_{ab} + \sum_b R_{ba} N_b,$$

where R_{ab} is a global transition rate that connects the configurations a and b.

➢ Many collisional-radiative models, that are applied for a realistic modelling of NLTE line emission, often account for individual levels explicitly for spectroscopic reasons, while the levels of other configurations are lumped together. These superlevels have no spectroscopic meaning but are included to describe the population kinetics.

7.4.m. Equation-of-state relations for astro physics and condensed matter

Equation-of-state:

➢ Equation-of-state relations: More often than not, the equation-of-state refers to the pressure-density or pressure-temperature relation for matter under (more or less) extreme conditions.

➢ When the atomic density is rather low, we can deal with isolated atoms that are in equilibrium with the surrounding free electrons, while the statistical or Thomas-Fermi-Dirac model has been found useful for a very high density.

Liberman's self-consistent model:

➢ Liberman (1979) describes a model for condensed matter in which the ions surrounding a particular atom are replaced by a positive charge distribution which is constant outside of a sphere containing the atom and zero inside. This models enables one to separate the quantities that pertain to the atom from those of the electron gas (in which it is imbedded) and hence to derive the desired equation-of-state data.

➢ The model assumes that there are sufficient electrons in the system in order to give overall electrical neutrality together with the (required) electrical neutrality inside the sphere.

➢ Instead of a polyhedral cell, which are surrounded by other identical cells, a nearly equivalent spherical cell is assumed in Liberman's model, and surrounded by a uniform electron gas. The density of this electron gas is the same as the mean density of ionic charges. Therefore, the electron gas outside will not alter the charge distribution inside the cell, if its density is correctly chosen, nor will the atom affect the electron gas.

7.4.n. Radiation damage of DNA by electron impact

Radiation damage of DNA:

➢ Radiation damage: This term often refers to the damage of biological material on rather short time scales, i.e. reactions and processes that occur within ns or even less following the interaction of a high energy quantum with a living cell. These initial events may ultimately lead to the collapse of such cells. In practice, they result in the death of the individual cells within hours or days but may affect the matter also on much longer time scales.

➢ Low-energy electrons (LEE) that interact with the DNA: The absorption of high-energetic photons by biological matter often leads to low-energy electrons (LEE) that interact with the DNA. These LEE can cause specific resonant processes and may lead eventually either to single- or double-strand breaks in DNA materials, to the damage of its molecular components and possibly even to biological apoptosis (Bacarelli *et al.*, 2011).

➢ Several theoretical and computational approaches have been developed for studying the molecular processes that occur in the various steps of the energy deposition by LEE.

➢ In contrast, an alteration of the genetic expression of DNA may cause the onset of some diseases.

Electron-molecule dynamics:

➢ To understand the electron-impact of bio-molecules, a quite sizeable computational machinery need to be developed. The multiple inelastic scattering of these electrons will result in a re-distribution in the energy content and may lead to a fragmentation as well as the excitation of various vibrational modes.

7.4.o. Exotic atoms and ions

Muonic atoms and ions:

➢ Muonic atom: When a muon is captured by the nucleus, it generally forms a hydrogen-like muonic ion, although it is typically still surrounded by other atomic electrons.

➢ Measurements of the transition energies in muonic atoms help determine nuclear parameters, such as charge radii, quadrupole moments and magnetic hyperfine constants. One of the most precise measurements of the nuclear root-mean-square radius by means of muonic atoms refer to the radius of ^{208}Pb at the 0.2 % level.

➢ Muonic hydrogen: In muonic hydrogen, the electron is replaced by a muon μ with a 200 times larger mass. This large mass results orbits that are 200 times closer to the nuclues, when compared to the electron in regular hydrogen.

➢ Because of the finite extent of the proton, muons in their s-state have therefore some enhanced probability to be inside the proton, and where it sees also a slightly reduced electric charge of the proton. Therefore, the muon is less bound as larger the proton is.

7.4.p. Spectroscopy of (super-) heavy elements

Super-heavy nuclei:

➢ Radioactive isotopes: All nuclei with $Z > 98$ have typically rather short lifetimes from fractions of seconds to, say, hundreds of days. For the super-heavy nuclei ($Z > 104$), in contrast, an island of stability has been hypothetically proposed several decades ago, mainly based on quite limited nuclear structure computations at that time. In particular, the double-magic flerium nucleus with $Z = 114$ and $N = 184$

is expected to be more stable (than other super-heavy nuclei), because both protons and neutrons form closed shells. Such a weakly-stable island may include also the elements Ubn, Ubh as well as some other isotopes. — In practice, however, no (nearly-) stable super-heavy nuclei are nowadays expected anymore.

➢ Magic numbers: For spherical, super-heavy nuclei, the magic neutron number $N = 184$ is supposed quite generally, while several magic proton numbers $Z = 114, 120, 126$ are still discussed in the literature. Further magic number from the literature are: $Z = 122$ and $N = 172, 178, 182, 194$, respectively.

➢ Neutron-poor isotopes: Up to the present, all synthesized superheavy nuclei ($Z > 104$) are neutron-poor, i.e. with significantly less neutrons than expected for reasonably stable nuclei. For example, the heaviest synthesized flerium isotope ^{292}Fl still miss 6 neutrons to the (expected) *magic neutron number* $N = 184$. In general, a larger neutron number help compensate the strong Coulomb repulsion among the protons.

Laser spectroscopy of (super-) heavy elements:

➢ Laser spectroscopy for (super-) heavy elements: While laser spectroscopy offers great precision $\sim \mu$eV, it usually requires prior knowledge about the level structure and transitions of the elements that need to be synthesized by nuclear fusion reactions at large accelerator facilities.

➢ Isotope shifts of superheavy elements ($Z > 104$): Until the present, isotope shifts have been measured for the (heavy) elements Pu, Am, Cm and No, while no experimental data are available near to flerium or other super-heavy isotopes.

8. Atomic processes

8.1. In JAC implemented processes

8.1.a. Photoemission. Transition probabilities (PhotoEmission)

Process, notations & application:

- Photoemission: from an atom or ion $A^* \longrightarrow A^{(*)} + \hbar\omega$
- Formal quantum notation: $|\alpha_i \mathbb{J}_i\rangle \longrightarrow |\alpha_f \mathbb{J}_f\rangle + \hbar\omega$
- JAC's standard multipole amplitudes for photon emission: Although all (one- and many-electron) electron-photon interaction matrix elements are always evaluated in *absorption* within JAC, we wish and need to retain the intuitive description of matrix elements as typically applied in quantum mechanics: $\langle \text{final}-\text{state}\,|\,\text{operator}\,|\,\text{initial}-\text{state}\rangle$. In JAC, we therefore introduce an explicit and independent notation for a *standard (reduced) emission as well as absorption multipole matrix element*

$$\langle \alpha_f \mathbb{J}_f \,\|\, \mathbb{O}^{(\mathbb{M},\,\text{emission})} \,\|\, \alpha_i \mathbb{J}_i \rangle \;=\; \left\langle \alpha_i \mathbb{J}_i \left\| \sum_{k=1}^{N} \boldsymbol{\alpha}_k \, a^{p}_{k,\,L} \right\| \alpha_f \mathbb{J}_f \right\rangle^{*} \;\equiv\; \langle \alpha_i \mathbb{J}_i \,\|\, \mathbb{O}^{(\mathbb{M},\,absorption)} \,\|\, \alpha_f \mathbb{J}_f \rangle^{*}$$

  which retains the right order and can be obtained from `Jac.PhotoEmission.amplitude()`; cf. section 5.3.c. A multipole $\mathbb{M} \equiv (L, p) =$ E1, M1, E2, ... hereby contains all information about its multipolarity (angular momentum) L and type *magnetic* $(p = 0)$ or *electric* $(p = 1)$.

- Using JAC: Perform an `Atomic.Computation(.., process=Jac.Radiative, processSettings=PhotoEmission.Settings(..), ..)` or call directly functions from the module `PhotoEmission`.

➢ In JAC, the transition probabilities and radiative lifetimes are tabulated by default for all selected transitions $i \to f$.

➢ In JAC, the anisotropy (structure) parameters $f_k(\alpha_i \mathbb{J}_i, \alpha_f \mathbb{J}_f)$ are calculated and tabulated if the flag `calcAnisotropy = true` is set in `PhotoEmission.Settings`.

Transition probabilities and oscillator strengths:

➢ With the notation of the (standard reduced) emission multipole matrix element from above, the transition probability and oscillator strengths are given by

$$W_{i\to f} = \frac{8\pi\,\alpha\,\omega}{2J_i+1} \sum_{\mathbb{M}} \left| \left\langle \alpha_f \mathbb{J}_f \right\| \mathbb{O}^{(\mathbb{M},\,\text{emission})} \left\| \alpha_i \mathbb{J}_i \right\rangle \right|^2 , \qquad f_{i\to f} = \frac{2\,\omega}{3\,(2J_i+1)} \sum_{\mathbb{M}} \left| \left\langle \alpha_f \mathbb{J}_f \right\| \mathbb{O}^{(\mathbb{M},\,\text{emission})} \left\| \alpha_i \mathbb{J}_i \right\rangle \right|^2 ,$$

and where the sum over $\mathbb{M}$ = E1, M1, E2, ... runs over all requested multipoles in a given computation.

Angular distribution and anisotropy parameters of the fluorescence radiation:

➢ The fluorescence (radiation) from an excited atom is characterized not only by its frequency $\hbar\omega$ but also by the angular distribution and polarization of the emitted radiation. Both of these properties of the emitted photons depend on the sublevel occupation of the excited atom or ion and, hence, on its reduced statistical tensors $\mathcal{A}_{kq}(\alpha_i \mathbb{J}_i)$ which are associated with the prior excitation process.

➢ Angular distribution for the photoexcitation of initially unpolarized but aligned atoms: For initially unpolarized but aligned atoms, the angular distribution of the (characteristic) fluorescence radiation is given in perturbation theory by:

$$W(\vartheta) = \frac{W_o}{4\pi} \left(1 + \sum_{k=2,4,..} f_k(\alpha_i \mathbb{J}_i, \alpha_f \mathbb{J}_f)\, \mathcal{A}_{k0}(\alpha_i \mathbb{J}_i)\, P_k(cos\vartheta) \right) ,$$

where W_o is the total decay rate and ϑ the angle of the photons with regard to the alignment axis (quantization axis).

➢ Anisotropy (structure) parameters $f_k(\alpha_i \mathbb{J}_i, \alpha_f \mathbb{J}_f)$: In the angular distribution above, the anisotropy (or structure) parameters $f_k(\alpha_i \mathbb{J}_i, \alpha_f \mathbb{J}_f)$ are independent of the particular excitation process of the level $|\alpha_i \mathbb{J}_i\rangle$ and merely reflects the electronic structure of

the ion in the two levels involved in the fluorescence

$$f_k(\alpha_i \mathbb{J}_i, \alpha_f \mathbb{J}_f) = \left[\sum_{\mathbb{M}} \left| \left\langle \alpha_i \mathbb{J}_i \right\| \mathbb{O}^{(\mathbb{M},\,\text{emission})} \left\| \alpha_f \mathbb{J}_f \right\rangle \right|^2 \right]^{-1} \frac{\sqrt{2J_i+1}}{2} \sum_{\mathbb{M}\,\mathbb{M}'} i^{L'+p'-L-p} (-1)^{J_f+J_i+1+k} [L, L']^{1/2} \langle L1,\ L'-1 \,|\, k0 \rangle$$

$$\times \left(1+(-1)^{L+p+L'+p'-k}\right) \begin{Bmatrix} L & L' & k \\ J_i & J_i & J_f \end{Bmatrix} \left\langle \alpha_f \mathbb{J}_f \right\| \mathbb{O}^{(\mathbb{M},\,\text{emission})} \left\| \alpha_i \mathbb{J}_i \right\rangle \left\langle \alpha_f \mathbb{J}_f \right\| \mathbb{O}^{(\mathbb{M}',\,\text{emission})} \left\| \alpha_i \mathbb{J}_i \right\rangle^* ,$$

➢ Of course, there is usually one multipole term that dominates the radiative decay (fluorescence) for any given pair of initial and final-bound states.

Semi-empirical calculations of transition probabilities:

➢ Semi-empirical calculations of transition probabilities are often performed by using Cowan's code and, especially, the components RCN/RCN2/RCG/RCE. In a first step, Hartree-Fock calculations of radial integrals are carried out, including relativistic corrections (HFR) to generate all required atomic orbitals and average energies of configurations. The diagonalization of the Hamiltonian matrix then leads to approximate energy values and eigenvectors of levels in intermediate coupling.

➢ When, in addition, also experimental energies are available, RCE is run to perform an iterative least-squares fit with the aim to minimize the differences between the calculated and experimental energies, and where the radial integrals are applied as fitting parameters. The mean error of such a fit is defined by $\Delta E = \sqrt{\sum_i \left(E_i^{(\text{exp})} - E_i^{(\text{calc})}\right)^2 / (N_i - N_p)}$ where N_i is the number of experimentally known energies and N_p the number of free parameters.

Unresolved transition arrays (UTA):

➢ Unresolved transition arrays: The UTA approach has become the method of choice in order to calculate the radiative properties of high-Z elements. Within this approach, a group of lines (i.e. a so-called array) which belongs to the same pair of electron configurations are treated globally by a Gaussian distributions whose width and position are given by analytical formulae.

➢ The UTA approach is computationally efficient and accurate for plasma conditions where the line broadening is such, that individual line profiles merge. This approach has been further extended to a group of arrays in the so-called super-transition array method (STA) where set of arrays are treated globally.

- Resolved transition arrays (RTA): The RTA method was proposed to overcome the shortcoming of the UTA method that just a few transitions often dominate the spectral emission distribution of the array. This RTA method improves on the UTA approach by resolving the transition array into individual lines by using random lines but without performing an explicit atomic structure calculation.
- UTA method: For a group of lines with known transition energies E_i and corresponding the oscillator strengths g_i, the UTA is obtained by calculating the first two moments for the array of N transitions:

$$\mu^{(1)} = \frac{\sum_i^N g_i E_i}{\sum_i g_i}, \qquad \mu^{(2)} = \frac{\sum_i^N g_i E_i^2}{\sum_i g_i},$$

- These two moments can be utilized together with the variance $\sigma^2 = \mu^{(2)} - \left(\mu^{(1)}\right)^2$ in order to define the spectral distribution of the UTA

$$f(\mathcal{E}) = \frac{1}{\sigma\sqrt{\pi}} \exp\left[-\frac{(\mathcal{E} - \mu^1)^2}{2\,\sigma^2}\right].$$

- By avoiding the explicit calculation of the properties of each line, that belongs to a given array, the UTA method enables one to account for a large number of transitions for a rather low computational cost.
- Overall, however, the use of such UTA appears quite tedious, and the application of the formulasas derived by Bauche-Arnould and coworkers (1985, 1988) might lose its importance as more powerful computers become available.

Two-electron one-photon transitions (TEOP):

- Two-electron one-photon transitions were postulated almost 100 years ago and are well-known from the optical region.
- In the early 1970s, Wölfli *et al.*. reported results for nickel and iron, for which high-energetic satellites arose due to two-electron one-photon transition. In these experiments, two vacancies in the K-shell were simultaneously filled by two L-shell electrons under the emission of a single photon.
- Since the interaction with the electro-magnetic field is governed by an one-electron operator, the contribution of two-electron one-photon (TEOP) transitions can usually be ignored in comparison to other, E1 allowed one-electron transitions.

Fractional occupation number (FON) approach:

➢ Fractional occupation number (FON) approach: The FON approach involves the prescription of a single, fictitious configuration with FONs for each (n, κ) subshell in order to represent an entire set of physical configurations within a given model. This fictitious configuration is used to first generate a single set of bound wave functions. Second, integer occupation numbers are then combined with the (averaged) wave functions in order to describe all the physical configurations that are enumerated in a particular model (Sampson *et al.*, 2009).

8.1.b. Photoexcitation or photoabsorption (PhotoExcitation)

Process, notations & application:

➢ Photoexcitation of an atom or ion: $A + \hbar\omega \longrightarrow A^*$

➢ Formal quantum notation: $|\alpha_i \mathbb{J}_i\rangle + \hbar\omega\,(\mathbf{k}, \lambda) \longrightarrow |\alpha_f \mathbb{J}_f\rangle$

➢ Using JAC: Perform an `Atomic.Computation(.., process=Jac.PhotoExc, processSettings=PhotoExcitation.Settings(..), ..)` or call directly functions from the module `PhotoExcitation`.

➢ In JAC, the photoexcitation cross sections are calculated by default for resonant and completely linearly-polarized plane-wave radiation.

➢ In JAC, the photoexcitation cross sections are calculated also for plane-wave radiation with given Stokes parameters (P_1, P_2, P_3) if the flag `calcStokes = true` are set in `PhotoExcitation.Settings` and if the Stokes parameters are given explicitly by `PhotoExcitation.Settings.stokes`.

➢ In JAC, the statistical tensors $\rho_{kq}(\alpha_f \mathbb{J}_f)$ and the alignment parameters $\mathcal{A}_{kq}(\alpha_f \mathbb{J}_f)$ are calculated and tabulated for unpolarized atoms and plane-wave photons with given Stokes parameters, if the flag `calcTensors = true` is set in `PhotoExcitation.Settings` and if the Stokes parameters are given explicitly by `PhotoExcitation.Settings.stokes`.

Photoexcitation cross sections:

➢ Total photoabsorption cross section: For initially unpolarized atoms and incident photons with given (photon) density matrix $\langle \mathbf{k}\lambda \,|\, \rho_\gamma \,|\, \mathbf{k}\lambda' \rangle$, the total photoabsorption cross section can be most easily defined in the limit of a *zero* linewidth as

$$\sigma(\alpha_i \mathbb{J}_i \to \alpha_f \mathbb{J}_f;\, \omega) \;=\; \frac{4\pi^2 \alpha}{\omega\,(2J_i+1)} \sum_{M_i M_f,\, \lambda\lambda'} \langle \mathbf{k}\lambda \,|\, \rho_\gamma \,|\, \mathbf{k}\lambda' \rangle \, \big\langle \alpha_f \, \mathbb{J}_f M_f \,\big|\, \mathbb{T}^{\,(\text{absorption})}(\mathbf{k},\lambda) \,\big|\, \alpha_i \, \mathbb{J}_i M_i \big\rangle$$
$$\times \, \big\langle \alpha_f \, \mathbb{J}_f M_f \,\big|\, \mathbb{T}^{\,(\text{absorption})}(\mathbf{k},\lambda') \,\big|\, \alpha_i \, \mathbb{J}_i M_i \big\rangle^{*} \; \delta(\omega + E_i - E_f) \,,$$

and where $\mathbb{T}^{\,(\text{absorption})}(\mathbf{k},\lambda)$ formally describes the electron-photon interaction operator for absorbing a photon $\hbar\omega\,(\mathbf{k},\lambda)$.

➢ In order to allow for a finite natural width Γ_f of the excited level, we need to replace the $\delta(\omega + E_i - E_f)$ function in the above expression by a (Lorentzian) spectral distribution

$$\sigma(\alpha_i \mathbb{J}_i \to \alpha_f \mathbb{J}_f;\, \omega) \;=\; \frac{4\pi^2 \alpha}{\omega\,(2J_i+1)} \sum_{M_i M_f,\, \lambda\lambda'} \langle \mathbf{k}\lambda \,|\, \rho_\gamma \,|\, \mathbf{k}\lambda' \rangle \, \big\langle \alpha_f \, \mathbb{J}_f M_f \,\big|\, \mathbb{T}^{\,(\text{absorption})}(\mathbf{k},\lambda) \,\big|\, \alpha_i \, \mathbb{J}_i M_i \big\rangle$$
$$\times \, \big\langle \alpha_f \, \mathbb{J}_f M_f \,\big|\, \mathbb{T}^{\,(\text{absorption})}(\mathbf{k},\lambda') \,\big|\, \alpha_i \, \mathbb{J}_i M_i \big\rangle^{*} \quad \frac{1}{\pi} \, \frac{\Gamma_f/2}{(\omega + E_i - E_f)^{\,2} + \Gamma_f^2/4} .$$

➢ Photoexcitation cross sections for initially unpolarized atoms: For incident plane-wave photons with (photon) density matrix $(c_{\lambda\lambda'}) = \frac{1}{2} \begin{pmatrix} 1+P_3 & P_1 - iP_2 \\ P_1 + iP_2 & 1-P_3 \end{pmatrix}$, which are resonant to the given transition $|\alpha_i \mathbb{J}_i\rangle \to |\alpha_f \mathbb{J}_f\rangle$, the total photoexcitation cross section is

$$\sigma(\alpha_i \mathbb{J}_i \to \alpha_f \mathbb{J}_f;\, \omega) \;=\; \frac{2\pi^3 \alpha}{\omega\,(2J_i+1)} \sum_{\mathbb{M},\,\lambda} c_{\lambda\lambda} \, \big| \big\langle \alpha_f \, \mathbb{J}_f \,\big\|\, \mathbb{O}^{\,(\mathbb{M},\,\text{absorption})}(\lambda) \,\big\|\, \alpha_i \, \mathbb{J}_i \big\rangle \big|^2 \;\times\; \begin{cases} \delta(E_i + \omega - E_f) \\ \frac{1}{\pi} \, \frac{\Gamma_f/2}{(E_i + \omega - E_f)^2 + \Gamma_f^2/4} \end{cases} .$$

➢ Photoexcitation cross sections for initially unpolarized atoms and linear-polarized, circularly-polarized or unpolarized incident photons: For resonant and unpolarized or completely linearly-polarized or circularly-polarized plane-wave photons, especially, the total photoexcita-

tion cross section is given by

$$\sigma(\alpha_i \mathbb{J}_i \rightarrow \alpha_f \mathbb{J}_f;\, \omega) \;=\; \frac{8\pi^3 \alpha}{\omega\,(2J_i+1)} \sum_{\mathbb{M}} \left| \left\langle \alpha_f\, \mathbb{J}_f \right\| \mathbb{O}^{(\mathbb{M},\,\text{absorption})}(\lambda) \left\| \,\alpha_i\, \mathbb{J}_i \right\rangle \right|^2 \times \begin{cases} \delta(E_i \,+\, \omega \,-\, E_f) \\ \frac{1}{\pi}\, \frac{\Gamma_f/2}{(E_i+\omega-E_f)^2+\Gamma_f^2/4} \end{cases}$$

Final-level statistical tensors and alignment parameters:

➢ Statistical tensors: Instead of the (final-level) density matrix, it is often more convenient to describe the population of the magnetic sublevels in terms of (so-called) statistical tensors of the atom or ion

$$\rho_{kq}(\alpha_f \mathbb{J}_f) \;=\; \sum_{M_f M_f'} (-1)^{J_f - M_f'} \left\langle J_f M_f,\, J_f\,(-M_f') \,|\, kq \right\rangle \left\langle \alpha_f\, \mathbb{J}_f M_f \,|\, \rho \,|\, \alpha_f\, \mathbb{J}_f M_f' \right\rangle .$$

and which are non-zero only for $0 \,\le\, k \,\le\, 2\,J_f$ and $-k \,\le\, q \,\le\, k$.

➢ Reduced statistical tensors or alignment parameters: The reduced statistical tensors of the excited levels or so-called alignment parameters are defined by

$$\mathcal{A}_{kq}(\alpha_f \mathbb{J}_f) \;=\; \frac{\rho_{kq}(\alpha_f \mathbb{J}_f)}{\rho_{00}(\alpha_f \mathbb{J}_f)} .$$

➢ Statistical tensors for the photoexcitation of initially unpolarized atoms and incident plane-wave radiation: For incident plane-wave photons with (photon) density matrix $(c_{\lambda\,\lambda'}) \;=\; \frac{1}{2} \begin{pmatrix} 1+P_3 & P_1 - iP_2 \\ P_1 + iP_2 & 1-P_3 \end{pmatrix}$, which are resonant to the given transition $|\alpha_i \mathbb{J}_i\rangle \rightarrow |\alpha_f \mathbb{J}_f\rangle$, the reduced statistical tensors can be written as

$$\rho_{kq}(\alpha_f \mathbb{J}_f) \;=\; \ldots$$

➢ Statistical tensors for the photoexcitation of initially unpolarized atoms by incident plane-wave radiation with well-defined helicity λ: For

incident plane-wave photons with helicity λ, the reduced statistical tensors can be written as (Surzhykov *et al.*, 2015)

$$\rho_{kq}(\alpha_f \mathbb{J}_f) = \delta_{q0}\, C \sum_{\mathbb{M}\,\mathbb{M}'} i^{\,L+L'}\, [L,\, L]^{1/2}\, (i\,\lambda)^p\, (-i\,\lambda)^{p'}\, (-1)^{\,L'+J_f+J_i+k}\, \langle L\lambda,\, L'\, -\lambda \,|\, kq\rangle \begin{Bmatrix} L & L' & k \\ J_f & J_f & J_i \end{Bmatrix}$$

$$\times \left\langle \alpha_f \mathbb{J}_f \left\| \mathbb{O}^{(\mathbb{M},\,\text{absorption})} \right\| \alpha_i \mathbb{J}_i \right\rangle \left\langle \alpha_f \mathbb{J}_f \left\| \mathbb{O}^{(\mathbb{M}',\,\text{absorption})} \right\| \alpha_i \mathbb{J}_i \right\rangle^* .$$

Photoabsorption and line-shape function:

➢ Absorption coefficient $\alpha(\omega)$: For a beam of light that propagates in x-direction, the absorption coefficient is phenomenologically defined in terms of changes of the spectral intensity $I(\omega)$, cf. Hilborn (2002)

$$\frac{1}{I(\omega)}\, \frac{d\, I(\omega)}{dx} = -\,\alpha(\omega)\,.$$

The spectral intensity $I(\omega)$ is spectroscopically a time-averaged quantity over, at least, several optical cycles.

➢ Line-shape function $g(\omega)$: In most practical applications, the frequency dependence of the absorption and emission processes (coefficient) is important butis often approximated simply by means of a normalized line-shape function $g(\omega)$ with $\int_{-\infty}^{\infty} d\omega\; g(\omega) = 1$, and where negative frequencies have no special physical meaning. Here, the use of $-\infty$ as the lower limit in the normalization integral greatly simplifies the normalization calculation. — For atoms in motion or in collision, the line-shape function $g(\omega)$ describes the appropriate ensemble-averaged line shape. The line-shape function $g(\omega)$ has the dimensions of 1/angular frequency and, hence, the explicit functional form of $g(\omega)$ and $\tilde{g}(\lambda)$ is not equivalent.

➢ Absorption cross section $\sigma^{\,(\text{absorption})}(\omega)$: If we assume $\alpha(\omega)$ to be proportional to the number N_o of atoms per unit volume in the lower level $|\beta_o \mathbb{J}_o\rangle$, which the beam intercepts, the absorption cross section is given by:

$$\alpha(\omega) = N_o\, \sigma^{\,(\text{absorption})}(\omega).$$

➢ Relation between absorption cross section and Einstein's A and B coefficients: (Hilborn 2002)

$$\sigma^{(\text{absorption})}(\omega) = \frac{g_f}{4\,g_i}\,\lambda_{fi}^2\,g(\omega)\,A_{fi}, \qquad \sigma_o^{(\text{absorption})}(\omega) = \frac{g_f}{4\,g_i}\,\lambda_{fi}^2\,A_{fi}$$

$$\sigma^{(\text{absorption})}(\omega) = \frac{\hbar\,\omega}{c}\,B_{12}^{\omega}\,g(\omega), \qquad \sigma_o^{(\text{absorption})} = \frac{\hbar\,\omega_{21}}{c}\,B_{12}^{\omega}\,.$$

➢ Relation between line strength and Einstein A coefficient for a spontaneous $i \rightarrow f$ emission:

$$S_{if} = \frac{3\,\epsilon_o\,h\,c^3}{2\,\omega_{if}^3}\,g_i\,A_{if}\,.$$

➢ Weighted oscillator strength: From the principle of detailed balance and in order to avoid confusion about the absorption or emission viewpoint, one often reports the weighted oscillator strength $g\,f = g_1\,f_{12}^{(\text{absorption})} \equiv -g_2\,f_{21}^{(\text{emission})}$.

➢ Rabi frequency for on-resonance excitations: At resonance $\omega = \omega_{fi}$ of the incident (linearly-polarized) light field and for two non-degenerate levels (i, f), the Rabi frequency can be expressed in terms of the electric field amplitude of the (and the transition dipole moment μ_{fi} by

$$\Omega_R = \frac{\mu_{fi}\,E}{\hbar}, \qquad \mu_{fi} = \left\langle \alpha_f \mathbb{J}_f M = 0 \left| \mathbb{O}^{(\mathbb{M},\,\text{absorption})} \right| \alpha_i \mathbb{J}_i M = 0 \right\rangle$$

For degenerate upper and lower levels, there are generally several Rabi frequencies for each combination $\left\langle \alpha_f \mathbb{J}_f M_f \left| \mathbb{O}^{(\mathbb{M},\,\text{absorption})} \right| \alpha_i \mathbb{J}_i M_i \right\rangle$, and this gives usually rise to a rather complicated dynamical behaviour (Hilborn 2002).

Photoexcitation by plane-wave photons:

➢ Vector potential for a plane-wave light field: As usual, the electron-photon interaction operator $R = \sum_q \boldsymbol{\alpha}_q\,\mathbf{A}^{(\text{plane-wave})}(\mathbf{r}_q)$ is given in terms of the Dirac matrices $\boldsymbol{\alpha}_q$ of the q^{th} particle and the vector potential $\mathbf{A}^{(\text{plane-wave})}(\mathbf{r}_q)$. For an incident plane-wave radiation with wave vector $\mathbf{k}$, polarization vector $\mathbf{e}_{\mathbf{k}\,\lambda}$ and with helicity $\lambda = \pm 1$, the vector potential can be written in Coulomb gauge as

$$\mathbf{A}^{(\text{plane-wave})}(\mathbf{r}) = \mathbf{e}_{\mathbf{k}\,\lambda}\,e^{i\,\mathbf{k}\cdot\mathbf{r}}\,.$$

➢ Multipole operators of the electron-photon interaction: For the analysis of atomic photo-excitation and ionization processes, it is generally convenient to expand the vector potential $\mathbf{A}^{(\mathrm{plane-wave})}(\mathbf{r})$ in terms of its electric and magnetic multipole fields. If the (plane-wave) field propagates along $\mathbf{n}_\mathbf{k} = \mathbf{k}/k = (\theta_k, \phi_k, 0) \nparallel \mathbf{e}_z$, this expansion is given by:

$$\mathbf{e}_{\mathbf{k}\,\lambda}\, e^{i\,\mathbf{k}\cdot\mathbf{r}} \;=\; \sqrt{2\,\pi}\, \sum_{LM}\, \sum_{p=0,1}\, i^L\, [L]^{1/2}\, (i\lambda)^p\, D^L_{M\,\lambda}(\varphi_k, \theta_k, 0)\, \mathbf{a}^{(p)}_{LM}(\mathbf{r}).$$

Here, $[L] = 2L+1$, $D^L_{M\lambda}$ is the Wigner rotation matrix, while $\mathbf{a}^{(p)}_{LM}(\mathbf{r})$ refers to magnetic ($p = 0$) and electric ($p = 1$) multipole components of the vector potential; these components are constructed as irreducible tensors of rank L and, eventually, enable one to evaluate the transition amplitude $M^{(\mathrm{plane-wave})}_{fi}$ analytically.

➢ Transition amplitudes of the multipole fields: Using the expansion for the plane-wave vector potential from above and by making use of the Wigner-Eckart theorem, the transition amplitudes of the multipole fields can be written in terms of (many-electron) *reduced* matrix elements as

$$M^{(\mathrm{plane-wave})}_{fi} \;=\; \sqrt{2\,\pi}\, \sum_{LM}\, \sum_{p=0,1}\, i^L\, \frac{[L]^{1/2}}{[J_f]^{1/2}}\, (i\lambda)^p\, D^L_{M\lambda}(\theta_k, \varphi_k, 0)\; \langle J_i M_i\, LM \mid J_f M_f\rangle\; \langle \alpha_f J_f \parallel H_\gamma(pL) \parallel \alpha_i J_i\rangle\;,$$

$$\langle \alpha_f J_f \,\|H_\gamma(pL)\|\, \alpha_i J_i\rangle \;\equiv\; \left\langle \alpha_f \mathbb{J}_f \left\| \sum_q \boldsymbol{\alpha}_q\, \mathbf{a}^{(p)}_L(\mathbf{r}_q) \right\| \alpha_i \mathbb{J}_i \right\rangle .$$

These (reduced) matrix element does *neither* depend on the projections of the angular momenta of an atom and photon *nor* the particular choice of the quantization axis *nor* the propagation direction $\mathbf{n}_\mathbf{k}$. They solely reflect the electronic structure of an atom and its coupling to a particular multipole component (pL) of the radiation field.

Photoexcitation by twisted light:

➢ Photoexcitation by twisted light:

$$\hbar\,\omega^{(\mathrm{twist})} \;+\; A \quad\longrightarrow\quad A^*$$

➢ Photoinduced processes with twisted light: Since the helical phase structure of twisted beams causes a non-uniform intensity profile and a rather complex energy flow, many photo-induced atomic processes are modified in twisted light. This applies to both, the photo-excitation

and ionization as well as to Rayleigh, Raman and Compton scattering processes. For example, the use of twisted (vortex light) may help reduce the light shift of bound-state transitions and, hence, in the control of electric dipole-forbidden (atomic) clock transitions.

➢ Photoexcitation by twisted light: For the different multipole components of the radiation field, the ratio of partial photoexcitation cross sections is quite sensitive with regard to the topological charge ℓ and the parameters of the incident light. In particular, this (photoexcitation) cross section ratio differs significantly from the exitation by a plane wave.

➢ Photoexcitation of macroscopic targets: For macroscopic targets, the sublevel-dependent photoexcitation cross sections $\sigma_{m_f}^{(\text{twist})} = f(\vartheta_k)$ as well as the cross section ratio with regard to incoming plane-wave radiation $\sigma^{(\text{twist})}/\sigma^{(\text{plane})}$ have been calculated.

➢ Finite, localized targets: For finite, localized targets, the sublevel-dependent photoexcitation cross sections as well as alignment and polarization parameters all depend on the impact parameter of the target with regard to the beam axis,

$$\sigma_{m_f}^{(\text{twist})} = f(\vartheta_k, \quad ..., \mathbf{b}, m), \qquad \frac{\sigma^{(\text{twist})}}{\sigma^{(\text{plane})}} = f(\mathbf{b}, \text{ target size}), \qquad \mathcal{A}_2,\ P_1 = f(\mathbf{b}, \text{ target size}).$$

➢ The photoexcitation of atoms by a Bessel beam of twisted light has been investigated for low-Z hydrogen-like ions. Markgraf-Scholz *et al.* (2014) have calculated especially the *partial* (subshell) cross sections and the alignment of the excited states, if the beam interacts with macroscopic hydrogen target.

➢ Vector potential for twisted Bessel beams: For an incident Bessel beam, the vector potential $\mathbf{A}^{(\text{Bessel})}(\mathbf{r})$ is given by (Schulz *et al.*, 2019)

$$\mathbf{A}^{(\text{Bessel})}(\mathbf{r}) = \mathbf{A}^{(\text{Bessel})}_{\varkappa m k_z \lambda}(\mathbf{r}) = \int \frac{d^2\,\mathbf{k}_\perp}{(2\pi)^2}\ \mathbf{e}_{\mathbf{k}\,\lambda}\ e^{i\mathbf{k}\cdot\mathbf{r}}\ a_{\varkappa m}(\mathbf{k}_\perp)\ e^{-i\mathbf{k}_\perp\cdot\mathbf{b}}, \qquad a_{\varkappa m}(\mathbf{k}_\perp) = e^{im\varphi_k}\,\frac{2\pi}{k_\perp}\,\delta(k_\perp - \varkappa).$$

This vector potential represents *Bessel* photons with well-defined helicity λ, the longitudinal component k_z of the wave vector and the projection m of the total angular momentum (TAM) upon the light propagation axis (z-axis). These Bessel photons also have a well-defined (absolute) value of the transverse momentum $|\mathbf{k}_\perp)| = \varkappa$ and are, hence, monochromatic with $\omega = k/\alpha = \sqrt{k_z^2 + \varkappa^2}/\alpha$.

➢ Amplitude for twisted Bessel beams: The expression above expands the vector potential of *Bessel* photons in terms of (a coherent superposition of) plane waves $\mathbf{e}_{\mathbf{k}\lambda}\ e^{i\mathbf{k}\cdot\mathbf{r}}$ whose wave vectors $\mathbf{k}$ are uniformly distributed upon the surface of a cone with a polar opening angle $\theta_k = \arctan(\varkappa/k_z)$. Using the standard expansion of these plane waves in terms of multipoles and by inserting $\mathbf{A}^{(\text{Bessel})}_{\varkappa m k_z \lambda}(\mathbf{r})$, one finds after some algebra the amplitude for the $|\alpha_i J_i M_i\rangle + \gamma \rightarrow |\alpha_f J_f M_f\rangle$ transition induced by Bessel light

$$M_{fi}^{(\text{Bessel})} = \sqrt{\frac{1}{[J_f]}} \sum_{LM} \sum_{p=0,1} i^{L+M}\,[L]^{1/2}\,(i\lambda)^p\,d^L_{M\lambda}(\theta_k)\,J_{m-M}(\varkappa b)\,e^{i(m-M)\varphi_b}\,\langle J_i M_i\,LM\,|\,J_f M_f\rangle\,\langle \alpha_f J_f\,\|\,H_\gamma(pL)\,\|\,\alpha_i J_i\rangle\,.$$

Similar as for plane waves, $M_{fi}^{(\mathrm{Bessel})}$ is now written as a sum of reduced matrix elements $\langle \alpha_f \mathbb{J}_f \,\|\, H_\gamma(pL) \,\|\, \alpha_i \mathbb{J}_i \rangle$ that are weighted by some additional geometric (angular) factors. For Bessel photons, these weight factors depend on the opening angle θ_k and the TAM projection m of the beam as well as on the impact parameter of an atom b; they enter the amplitude above in particular through the small Wigner function $d^L_{M\lambda}(\theta_k)$ and the Bessel function $J_{m-M}(b\varkappa)$.

➢ Excitation rate for twisted Bessel beams: The total rate for the excitation of atoms by Bessel light is obtained as usual by taking the average (summation) over the magnetic quantum numbers of the initial and final states,

$$W_{fi}^{(\mathrm{Bessel})} \;=\; \frac{2\pi}{[J_i]\,\alpha^2} \sum_{M_i M_f} \Big| M_{fi}^{(\mathrm{Bessel})} \Big|^2 \;=\; \sum_{pL} W_{fi}^{(\mathrm{Bessel})}(pL) \;=\; \sum_{pL} \sum_{M} \big|\, d^L_{M\lambda}(\theta_k)\, J_{m-M}(b\varkappa) \,\big|^2 \; W_{fi}^{(\mathrm{plane-wave})}(pL).$$

➢ Excitation rate for twisted Bessel beams: Similar to $W_{fi}^{(\mathrm{plane-wave})}$, the rate $W_{fi}^{(\mathrm{Bessel})}$ is still a sum of partial rates of allowed multipole transitions (pL). Moreover, each partial rate $W_{fi}^{(\mathrm{Bessel})}(pL)$, is a product of its plane-wave counterpart *times* a geometrical term that describes the properties of the Bessel beam and the position of the target atom. This decomposition ensures that the relative contributions of the multipole channels (pL) to the total rate of the $|\alpha_i \mathbb{J}_i\rangle + \gamma \to |\alpha_f \mathbb{J}_f\rangle$ transition can be modified by changing the parameters of twisted light, such as θ_k, κ, ...

➢ Excitation rate for twisted Bessel beams & Gaussian target: Making use of the Gaussian target distribution above, the photoexcitation rate can be written as:

$$W_{fi}^{(\mathrm{Bessel})}(\mathbf{b}_0, \sigma) \;=\; \sum_{pL} \sum_{M} \big|\, d^L_{M\lambda}(\theta_k) \,\big|^2 \; \mathcal{J}_{m-M}(b_0)\, W_{fi}^{(\mathrm{pl})}(pL)$$

$$\mathcal{J}_{m-M}(b_0) \;=\; \int \frac{\mathrm{d}\mathbf{b}}{(2\pi)^2}\, f(\mathbf{b};\mathbf{b}_0)\, |J_{m-M}(\varkappa b)|^2 \;=\; \frac{1}{(2\pi)^2\sigma^2} \int_0^\infty \mathrm{d}b\, b\, I_0\left(\frac{b\, b_0}{\sigma^2}\right) |\, J_{m-M}(\varkappa b)\,|^2 \; e^{-\frac{b^2+b_0^2}{2\sigma^2}}$$

and where I_0 is the modified Bessel function of the first kind. Similar as before, the partial multipole rates in this rate expression are given by the product of the plane-wave counterparts $W_{fi}^{(\mathrm{plane-wave})}(pL)$ *times* a weight function that depends on the properties of twisted beam as well as the geometry and the distribution of the target but does not depend on the electronic structure of the atoms.

➢ Excitation rate for plane-wave *versus* twisted beams: While, for plane-wave radiation, the partial multipole rates are entirely determined by the electronic structure of the target atom, these partial multipole rates $W_{fi}^{(\mathrm{Bessel})}(pL)$ also depend on the (geometrical) properties of the radiation as well as the position of the atom with regard to the beam axis for twisted light. For instance, we can consider how the

(relative) strength of multipoles is affected by properties of the twisted light by taking the probability ratio (Schulz *et al.*, 2019)

$$\frac{W_{fi}^{(\mathrm{Bessel})}(p_1 L_1)}{W_{fi}^{(\mathrm{Bessel})}(p_2 L_2)} \;=\; \mathcal{R}_{L_1 L_2}\;(\varkappa b)\;\frac{W_{fi}^{(\mathrm{plane-wave})}(p_1 L_1)}{W_{fi}^{(\mathrm{plane-wave})}(p_2 L_2)}, \qquad \mathcal{R}_{L_1 L_2}\;(\varkappa b) \;=\; \frac{\sum_M \left|\, d^{L_1}_{M\lambda}(\theta_k)\, J_{m-M}(b\varkappa)\,\right|^2}{\sum_M \left|\, d^{L_2}_{M\lambda}(\theta_k)\, J_{m-M}(b\varkappa)\,\right|^2}\,.$$

In this factorization, the first term just describes the geometry of the electron-photon interaction which depends on the TAM projection m and the opening angle θ_k of the Bessel beam as well as on the position of the target atom.

➢ Excitation rate for Bessel beams & Gaussian target: For a Gaussian distributed target, located at the impact parameter b, the geometrical factor $\mathcal{R}_{L_1 L_2}\,(\varkappa b)$ has for a located atom to be modified by just the *averaged* geometrical factor

$$\langle \mathcal{R}_{L_1 L_2}\;(\varkappa b_0)\rangle \;=\; \frac{\sum_M \left| d^{L_1}_{M\lambda}(\theta_k)\right|^2 \mathcal{J}_{m-M}(b_0\,\kappa)}{\sum_M \left| d^{L_2}_{M\lambda}(\theta_k)\right|^2 \mathcal{J}_{m-M}(b_0\,\kappa)}\,,$$

With this *averaged* geometrical factor, we can analyze the role of different multipole transitions in atomic trap experiments.

➢ Geometrical contribution to multipole excitations: For plane-waves, the geometrical factor is $\mathcal{R}^{\,(plane-wave)} = 1$ for all ratios of the partial multipole rates. For the interaction of atoms with a Bessel beam, in contrast, the geometrical factor $\mathcal{R}_{L_1=2,\,L_2=1}\,(\varkappa b)$ can be much larger, and especially for $m > 1$ and small impact parameters $kb \to 0$. This enhancement is observed for all (non-zero) opening angles θ_k and can be explained based on the *selection rules* for a transition $|\alpha_i \mathbb{J}_i M_i\rangle + \gamma \to |\alpha_f \mathbb{J}_f M_f\rangle$ induced by twisted light. Generally, these modified selection rules strongly depend on the position of the target atom in the Bessel wave front. For the particular case of $b \to 0$, i.e. when atom is located at the beam axis, the magnetic quantum numbers M_i and M_f of the initial and final state are related to the TAM projection m of the Bessel beam by

$$M_f = m + M_i\,.$$

From this simple relation and the transition amplitudes for Bessel radiation it immediately follows that only multipoles with $L \geq |m|$ can contribute to the excitation. For $m = 2$ and small impact parameters, therefore, dipole transitions are strongly suppressed, and this then results in a drastic enhancement of $\mathcal{R}_{L_1=2,\,L_2=1}\,(\varkappa b)$.

8.1.c. Atomic photoionization (PhotoIonization)

Process, notations & application:

- Photoionization of an atom or ion: $A + \hbar\omega \longrightarrow A^{+*} + e_p^-$
- Formal quantum notation: $|\alpha_i \mathbb{J}_i\rangle + \hbar\omega\,(\mathbb{M}) \longrightarrow |\alpha_f \mathbb{J}_f\rangle + e_p^-(\mathbf{p}, m_s)$ or $|\alpha_i \mathbb{J}_i\rangle + \hbar\omega\,(\mathbb{M}) \longrightarrow |\alpha_f \mathbb{J}_f\rangle + e_p^-(\varepsilon\,\kappa)$
- Using Jac: Perform an `Atomic.Computation(.., process=Jac.Photo, processSettings=PhotoIonization.Settings(..), ..)` or call directly functions from the module `PhotoIonization`.
- In Jac, the total photoionization cross sections are calculated and tabulated by default, while the partial cross sections are printed only if the flag `calcPartialCs = true` is set in `PhotoIonization.Settings`.
- In Jac, the statistical tensors of the photoion are calculated and tabulated for the photoionization of unpolarized atoms by plane-wave photons with given Stokes parameters, if the flag `calcTensors` is set in `PhotoIonization.Settings` and if the Stokes parameters are given explicitly in `Ionization.Settings.stokes`.
- Using Jac: Perform an `Atomic.Computation(.., process=Jac.PhotoInPlasma, processSettings = PlasmaShift.PhotoSettings(..), ..)` or call directly functions from the modules `PhotoIonization` and `PlasmaShift`. Until the present, however, only a Debye-Hückel plasma model is supported in Jac, and where the Debye-Hückel screening of the electron-nucleus and electron-photon interaction is incorporated only in first-order perturbation theory into the CI matrix.
- In Jac, the reduced matrix elements above are the main *building blocks* to represent and discuss most photo-ionization properties as they arise from the interaction of atoms and ions with the radiation field.
- Quantization axis: While the magnetic quantum numbers of the ion and photo electron usually refer to the adopted *quantization axis* of the overall system (z-axis), the helicity λ of the photon is *always* defined with regard to the wave vector $\mathbf{k}$ of the photon, i.e. with regard to the direction of the incident photons.
- Electron-electron correlations: Interesting correlation effects with regard to exchange, interchannel coupling, relaxation and polarization occurs often in the vincinity of the photoionization threshold.
- Dichroism: A dichroism in the photoelectron emission is conventionally related to a change in the polarization of the incident light, and while the polarization state of the target is kept fixed.

Photoionization amplitude:

➢ Emission of an electron with well-defined asymptotic momentum $\mathbf{p}$ and spin projection m_s: If the atom undergoes the transition $|\alpha_i\, \mathbb{J}_i M_i\rangle \rightarrow |\alpha_f\, \mathbb{J}_f M_f\rangle$ during the photoionization process, the transition amplitude for the absorption of a photon with wave vector $\mathbf{k}$ and helicity $\lambda = \pm 1$ is given by:

$$\mathcal{M}\,(M_f, m_s, \lambda, M_i) \;=\; \left(\frac{4\pi^2\alpha}{\omega}\right)^{1/2} \left\langle \alpha_f\, \mathbb{J}_f M_f,\, \mathbf{p}\, m_s \left| \sum_{i=1}^{N} \alpha_i\, \mathbf{u}_\lambda\, e^{i\,\mathbf{k}\cdot\mathbf{r}_i} \right| \alpha_i\, \mathbb{J}_i M_i \right\rangle .$$

➢ The population of the magnetic sublevels $|\alpha_f\, \mathbb{J}_f M_f\rangle$ of the photoion depends (of course) on the spin projection λ of the incident photons as well as the magnetic quantum numbers M_f of the final state of the photoion, while one need to average over the initial sublevels and the spin projections of the emitted electron.

➢ (Reduced many-electron) photoionization amplitude: For a partial-wave decomposition of the outgoing photoelectron and with a multipole expansion of the electron-photon interaction, the reduced photoionization amplitude describes the contribution of individual multipole components of the radiation field to the formation of a scattering state $|(\alpha_f \mathbb{J}_f, \varepsilon\, \kappa)\, \mathbb{J}_t\rangle$ with well-defined total symmetry and free-electron energy ε

$$\left\langle (\alpha_f \mathbb{J}_f, \varepsilon\, \kappa)\, \mathbb{J}_t \,\middle\|\, \mathbb{O}^{(\mathbb{M},\,\text{photoionization})} \,\middle\|\, \alpha_i \mathbb{J}_i \right\rangle \;=\; i^{-\ell}\, \exp(i\,\Delta_\kappa)\, \left\langle (\alpha_f \mathbb{J}_f, \varepsilon\, \kappa)\, \mathbb{J}_t \,\middle\|\, \mathbb{O}^{(\mathbb{M},\,\text{absorption})} \,\middle\|\, \alpha_i \mathbb{J}_i \right\rangle$$

Here, the photoioniozation amplitude also accounts for the proper phase (or the asymptotic boundary condition) of the outgoing electron.

➢ In JAC, the reduced photoionization amplitudes above are the main *building blocks* to represent and discuss most photoionization properties as they arise from the interaction of atoms and ions with the radiation field.

Partial and total cross sections:

➢ Partial photoionization cross sections for the photoionization of an initially unpolarized atom: For the photoionization of an initially unpolarized atom from level $|\alpha_i \mathbb{J}_i\rangle \rightarrow |\alpha_f \mathbb{J}_f M_f\rangle$ by unpolarized plane-wave photons with wave vector $\mathbf{k} \,||\, \mathbf{e}_z$ (quantization axis), the

partial cross sections can be expressed as:

$$\begin{aligned}
\sigma(\alpha_i \mathbb{J}_i \to \alpha_f \mathbb{J}_f M_f) &= \frac{1}{2(2J_i+1)} \sum_{M_i\,\lambda\,m_s} \int d\Omega_p \; |\mathcal{M}\,(M_f, m_s, \lambda, M_i)|^2 \\
&= \frac{4\pi^2\alpha}{2\,\omega\,(2J_i+1)} \sum_{M_i\,\lambda} \sum_{\kappa m} \sum_{JJ'M} \langle J_f M_f\, jm \,|\, JM\rangle \; \langle J_f M_f\, jm \,|\, J'M\rangle \left\langle (\alpha_f \mathbb{J}_f, \varepsilon\kappa)\, \mathbb{J}M \left| \sum_{i=1}^{N} \alpha_i\, \mathbf{u}_\lambda\, e^{i\mathbf{k}\cdot\mathbf{r}_i} \right| \alpha_i \mathbb{J}_i M_i \right\rangle \\
&\qquad \times \left\langle (\alpha_f J_f, \varepsilon\kappa)\, \mathbb{J}'M \left| \sum_{i=1}^{N} \alpha_i\, \mathbf{u}_\lambda\, e^{i\mathbf{k}\cdot\mathbf{r}_i} \right| \alpha_i J_i M_i \right\rangle^* .
\end{aligned}$$

Here, the integration over all emission angles $\Omega_p = (\vartheta_p, \varphi_p)$ of the photoelectron results into a *incoherent* summation over the partial waves of the many-electron scattering states with different κ's of the electron.

➢ Partial photoionization cross sections for initially unpolarized atoms by unpolarized plane-wave photons: For unpolarized atoms and unpolarized incident plane-wave photons, the partial cross sections from above can be simplified and expressed as:

$$\begin{aligned}
\sigma(\alpha_i \mathbb{J}_i \to \alpha_f J_f M_f) &= \frac{8\pi^3\,\alpha}{2\omega\,(2J_i+1)} \sum_{t\lambda} \sum_{\kappa} \sum_{JJ'} \sum_{\mathbb{M}\,\mathbb{M}'} i^{L-L'}\,(i\lambda)^p\,(-i\lambda)^{p'}\,(-1)^{L+L'} \sqrt{(2L+1)(2L'+1)(2J+1)(2J'+1)} \\
&\qquad \times \langle L'\lambda\, J_f M_f \,|\, t, \lambda+M_f\rangle \; \langle L\lambda\, J_f M_f \,|\, t, \lambda+M_f\rangle \begin{Bmatrix} j & J' & J_f \\ J & J_i & L \\ J_f & L' & t \end{Bmatrix} \\
&\qquad \times \left\langle (\alpha_f \mathbb{J}_f, \varepsilon\kappa)\, \mathbb{J} \left\| \mathbb{O}^{(\mathbb{M},\,\text{photoionization})} \right\| \alpha_i \mathbb{J}_i \right\rangle \left\langle (\alpha_f \mathbb{J}_f, \varepsilon\kappa)\, \mathbb{J}' \left\| \mathbb{O}^{(\mathbb{M}',\,\text{photoionization})} \right\| \alpha_i \mathbb{J}_i \right\rangle^* .
\end{aligned}$$

➢ Total photoionization cross sections for initially unpolarized atoms by unpolarized plane-wave photons: For the photoionization of an initially unpolarized atom from level $|\alpha_i \mathbb{J}_i\rangle \to |\alpha_f \mathbb{J}_f\rangle$ by unpolarized plane-wave photons with wave vector $\mathbf{k} \,||\, \mathbf{e}_z$, the total cross sections

can be expressed as:

$$\sigma(\alpha_i \mathbb{J}_i \rightarrow \alpha_f \mathbb{J}_f) \;=\; \sum_{M_f} \sigma(\alpha_i \mathbb{J}_i \rightarrow \alpha_f \mathbb{J}_f M_f) \;=\; \frac{4\,\pi^2\,\alpha\,\omega}{2\,(2J_i+1)} \sum_{\kappa\,J} \sum_{\mathbb{M}} \left| \left\langle (\alpha_f \mathbb{J}_f,\, \varepsilon\kappa)\mathbb{J} \left\| \mathbb{O}^{(\mathbb{M},\,\text{photoionization})} \right\| \alpha_i \mathbb{J}_i \right\rangle \right|^2 .$$

Final-state density matrix 'photo-ion + photo-electron':

➢ The final-state density matrix of the overall system 'photo-ion + photo-electron' is not so useful in general and is needed only for entanglement studies and related topics. Here, we just summarize some formulas but further work is needed to find the proper expression for different properties of the incident light.

➢ Final-state density matrix of the 'photo-ion + photo-electron': After the absorption of the photon, we have a free electron with asymptotic linear momentum $\mathbf{p}$ and with spin projection m_s, while the photoion is left in a fine level $|\alpha_f \mathbb{J}_f\rangle$. Using a basis with well-defined (angular) momenta J_i and J_f of the initial as well as the residual ion and the asymptotic linear momentum $\mathbf{p}$ and spin projection m_s of the ejected electron, the final-state density matrix can be written as

$$\begin{aligned}
&\left\langle \alpha_f J_f M_f, \mathbf{p}\, m_s \,|\, \rho_f \,|\, \alpha_f J_f M'_f, \mathbf{p}\, m'_s \right\rangle \\
&\quad = \sum_{M_i M'_i\, \lambda\lambda'} \left\langle \alpha_f \mathbb{J}_f M_f, \mathbf{p}\, m_s \left| \hat{\mathcal{R}} \right| \alpha_i \mathbb{J}_i M_i, \mathbf{k}\lambda \right\rangle \left\langle \alpha_i \mathbb{J}_i M_i, \mathbf{k}\lambda \,|\, \rho_i \,|\, \alpha_i \mathbb{J}_i M'_i, \mathbf{k}\lambda' \right\rangle \left\langle \alpha_i \mathbb{J}_i M'_i, \mathbf{k}\lambda' \left| \hat{\mathcal{R}}^\dagger \right| \alpha_f J_f M'_f, \mathbf{p}\, m'_s \right\rangle \\
&\quad = \sum_{M_i M'_i\, \lambda\lambda'} c_{M_i M'_i}\; c_{\lambda\lambda'} \left\langle \alpha_f \mathbb{J}_f M_f, \mathbf{p}\, m_s \left| \alpha \cdot \mathbf{u}_\lambda\, e^{i\mathbf{k}\cdot\mathbf{r}} \right| \alpha_0 J_0 M_0 \right\rangle \left\langle \alpha_f \mathbb{J}_f M'_f, \mathbf{p}\, m'_s \left| \alpha \cdot \mathbf{u}_{\lambda'}\, e^{i\mathbf{k}\cdot\mathbf{r}} \right| \alpha_i \mathbb{J}_i M'_i \right\rangle^* ,
\end{aligned}$$

where $\left\langle \alpha_f \mathbb{J}_f M_f, \mathbf{p}\, m_s \left| \alpha \cdot \mathbf{u}_\lambda\, e^{i\mathbf{k}\cdot\mathbf{r}} \right| \alpha_i \mathbb{J}_i M_i \right\rangle$ represents the photoionization amplitude from above.

Angular distribution of photoelectrons:

➢ Measurement operator for angular distributions: If the detector is not sensitive to the spin state of the photoelectron and the residual photoion, a proper measurement (projection) operator is obtained if we sum over the electron spin projections m_s as well as the magnetic quantum numbers M_f of the ion. In the density matrix formalism, this projection operator for measuring the angular distribution of the

emitted photoelectrons therefore is:

$$P \;=\; \sum_{M_f m_s} |\alpha_f \mathbb{J}_f M_f,\, \mathbf{p}\, m_s\rangle \, \langle \alpha_f \mathbb{J}_f M_f,\, \mathbf{p}\, m_s| \,,$$

➢ With this measurement operator, the well-known angular distribution of the photoelectrons is just the normal trace of the final-state density matrix:

$$W(\vartheta) \;=\; \mathrm{Tr}\,(P\,\rho_f) \;=\; \sum_{M_f m_s} \langle \alpha_f \mathbb{J}_f M_f,\, \mathbf{p}\, m_s \,|\, \rho_f \,|\, \alpha_f \mathbb{J}_f M_f,\, \mathbf{p}\, m_s\rangle \,.$$

➢ Photoionization of closed-shell atoms: Derevianko *et al.* (1999) provide a detailed study of the photoionization cross sections and angular distributions of all rare-gas atoms up to xenon and by going beyond the typical dipole approximation. In particular, these authors include all corrections $\mathcal{O}(ka)$ and $\mathcal{O}(k^2a^2)$ where k is the modulus of the wave vector and a the radius of the ionized subshell. While, within the electric-dipole approximation, the photoelectron angular distribution for the photoionization by linearly or unpolarized light is characterized by a single (anisotropy) parameter β, the $\mathcal{O}(ka)$ corrections are characterized by two parameters γ and δ, and the $\mathcal{O}(k^2a^2)$ corrections by even three parameters λ, μ, ν with the constraint $\lambda + \mu + \nu = 0$ as well as a correction $\Delta\,\beta$ to the dipole parameter.

➢ Angle-differential photoionization cross section for closed-shell atoms: For the photoionization of an electron from an initially closedsubshell by linearly-polarized light, the angle-differential photoionization cross section is given by (Derevianko *et al.*, 1999)

$$\frac{d\sigma}{d\Omega}(\vartheta,\varphi) \;=\; \frac{\sigma_o}{4\pi}\,\big\{1 \,+\, (\beta \,+\, \Delta\,\beta)\,P_2(\cos\vartheta) \,+\, (\delta \,+\, \gamma\,\cos^2\vartheta)\,\sin\vartheta\,\cos\varphi \,+\, \lambda\,P_2(\cos\vartheta)\,\cos 2\varphi \,+\, \mu\,\cos 2\varphi \,+\, \nu\,(1\,+\,\cos 2\varphi)\,P_4(\cos\vartheta)\big\}$$

with $\lambda + \mu + \nu = 0$, and where (ϑ,φ) are the polar angles of the outgoing photoelectrons. This expansion applies, if the quantization axis is chosen along the polarization, $\mathbf{u} \,||\, \mathbf{e}_z$, and $\mathbf{e}_x \,||\, \mathbf{k}$ along the photon propagation. This expression also includes the standard angular distribution of photoelectron, $1 + \beta\,P_2(\cos\vartheta)$ in the electric-dipole approximation, where β results from the interference of (electric-dipole) amplitudes for different partial waves of the outgoing electron. Derevianko *et al.* (1999) discuss also briefly which interferences due to the various multipole components of the radiation field give rise to all other anisotropy parameters, while expressions are given only in one-electron notation as appropriate for hydrogenic and closed-shell systems. No attempt has been made to derive expressions for open-shell atoms. Derevianko *et al.* (1999) found the non-dipole angular parameters rather insensitive with regard to details of the chosen potential $V(r)$.

➢ Formulas of the (non-) dipole anisotropy parameters for closed-shell atoms: All dipole and non-dipole anisotropy parameters can be readily expressed in terms of the (reduced) multipole transition amplitudes. Derevianko *et al.* (1999) provide tables and graphs of the seven angular

distribution parameters, calculated within the relativistic independent-particle approximation (IPA). Results are shown for electron energies between 20-5000 eV for all subshells of the rare gas atoms He, Ne, Ar, Kr and Xe. For Ar and Kr, moreover, comparison is made for selected parameters with results from the random-phase approximation in order to illustrate the influence of electron correlations.

Reduced statistical tensors of the photoion:

➢ Statistical tensors of the photoion in level $|\alpha_f \mathbb{J}_f\rangle$ after the photoionization of unpolarized atoms by unpolarized plane-wave photons: If the incident light propagates along the x-axis (quantization axis, because of its typical use in experimental discussions) and if the photoelectron remains unobserved, the statistical tensors are given by Kämpfer *et al.* (2016)

$$\rho_{kq}(\alpha_f \mathbb{J}_f) = \frac{\pi}{2J_i+1}\,\delta_{q0} \sum_{\mathbb{M}\mathbb{M}'} \sum_{\kappa JJ'} \sum_{\lambda=\pm 1} i^{L+p-L'-p'}\,\lambda^{p+p'}\,[L,L',J,J']^{1/2}\,(-1)^{J+J'+J_f+J_i+j+1}\,\langle L\lambda, L'-\lambda \,|\, kq\rangle \begin{Bmatrix} J_f & j & J' \\ J & k & J_f \end{Bmatrix} \begin{Bmatrix} J' & J_i & L' \\ L & k & J \end{Bmatrix}$$

$$\times \left\langle (\alpha_f \mathbb{J}_f, \varepsilon\kappa)\mathbb{J} \left\| \mathbb{O}^{(\mathbb{M},\,\text{photoionization})} \right\| \alpha_i \mathbb{J}_i \right\rangle \left\langle (\alpha_f \mathbb{J}_f, \varepsilon\kappa)\mathbb{J}' \left\| \mathbb{O}^{(\mathbb{M}',\,\text{photoionization})} \right\| \alpha_i \mathbb{J}_i \right\rangle^{*} .$$

➢ Statistical tensors of the photoion in level $|\alpha_f \mathbb{J}_f\rangle$ after the photoionization of unpolarized atoms by plane-wave photons with given density matrix $(c_{\lambda\lambda'})$: If the incident plane-wave light with well-defined (photon) density matrix $(c_{\lambda\lambda'})$, i.e. with the given Stokes parameters (P_1, P_2, P_3) , propagates along the z-axis, the statistical tensors are given more generally by (Sharma *et al.*, 2010)

$$\rho_{kq}(\alpha_f \mathbb{J}_f) = \frac{\pi}{2J_i+1} \sum_{\mathbb{M}\mathbb{M}'} \sum_{\kappa JJ'} \sum_{\lambda\lambda'} \left[\delta_{\lambda\lambda'}(1+\lambda P_3) + (1-\delta_{\lambda\lambda'})\,(P_1 - i\lambda P_2)\right]\, i^{\,L-L'+p-p'}\,\lambda^p\,(\lambda')^{p'}\,[L,L',\,J,J']^{1/2}$$

$$\times (-1)^{(J+J'+J_f+J_i+j+1)}\,\langle L\lambda L'-\lambda' \,|\, kq\rangle \begin{Bmatrix} J_f & j & J' \\ J & k & J_f \end{Bmatrix} : \begin{Bmatrix} J' & J_i & L' \\ L & k & J \end{Bmatrix}$$

$$\times \left\langle (\alpha_f J_f,\, \varepsilon\kappa)J \left\| \mathbb{O}^{(\mathbb{M},\,\text{photoionization})} \right\| \alpha_i J_i \right\rangle \left\langle (\alpha_f J_f,\, \varepsilon\kappa)J' \left\| \mathbb{O}^{(\mathbb{M}',\,\text{photoionization})} \right\| \alpha_i J_i \right\rangle^{*} ,$$

➢ In Jac, the statistical tensors of the photoion are calculated and tabulated for the photoionization of unpolarized atoms by plane-wave photons with given Stokes parameters, if the proper information is given by the `PhotoIonization.Settings`.

Time-resolved photoionization:

➢ Time-resolved photoionization experiments: During the last two decades, experiments with subfemto-second resolution enabled one to study the electron dynamics of atoms. Examples refer to the observation of time-resolved autoionizing resonances, the decay of core vacancies or the (relative) delay time of emitted photoelectrons. All these relaxation processes usually occur within tens of attoseconds in dependence of the excitation energy and the electronic structure of the atomic targets. Following Heisenberg's uncertainty principle, of course, a natural trade-off exist between the temporal and spectral resolution, though resolution can be tune to either the time or frequency domain. In the time domain, such spectoscopic studies have largely benefitted from high-resolution frequency combs based on phase-stable femtosecond pulse trains.

➢ Time-resolved photoionization experiments: Isinger *et al.* (2017) used the high-order harmonic spectrum in order to analyze the interplay between high-resolution photoelectron spectroscopy and attosecond dynamics. This analysis enabled them to disentangle the direct $2s$ ionization of neon from ionization-excitation processes of two $2p$ electrons (shake-up processes) by utilizing a phase-stable interferences between attosecond pulses in the pulse train. The $2s - 2p$ time delay derived from this detailed analysis agrees well with theoretical predictions based on the Wigner time. Here, the observation of the shake processes also provided an explanation to the discrepancy with earlier observations by Schultze *et al.* (2010).

➢ Wigner (time) delay: The photoionization time delay or Wigner delay refers to the delay of the group velocity of the electronic wave packet as created by the absorption of xuv radiation. This Wigner delay can be obtained quite readily by taking the derivative of the scattering phase of the outgoing electron wave. — An additional time delay arises from the interaction of the laser probe field with the Coulomb potential, and this can be calculated accurately at high kinetic energies from either the asymptotic form of the wave function or by classical trajectories (Isinger *et al.*, 2017).

Photoeionization by twisted light:

➢ Photoionization by twisted light:

$$A \; + \; \hbar\,\omega^{(\mathrm{twist})} \quad \longrightarrow \quad A^{+} \; + \; e_{p}^{-}$$

8.1.d. Radiative recombination (PhotoRecombination)

Process, notations & application:

- Radiative recombination or photorecombination of an atom or ion: $A^{q+} + e^- \longrightarrow A^{(q-1)+} + \hbar\omega$
- Formal quantum notation: $|\alpha_i \mathbb{J}_i\rangle + |\varepsilon\kappa\rangle \longrightarrow |\alpha_f \mathbb{J}_f\rangle + \hbar\omega\,(\mathbb{M})$ or $|\alpha_i \mathbb{J}_i\rangle + |\mathbf{p}\, m_s\rangle \longrightarrow |\alpha_f \mathbb{J}_f\rangle + \hbar\omega\,(\mathbb{M})$
- Using JAC: Perform an `Atomic.Computation(.., process=Jac.Rec, processSettings=PhotoRecombination.Settings(..), ..)` or call directly functions from the module `PhotoRecombination`.
- In JAC, the total radiative recombination cross sections are calculated and tabulated by default for all selected recombination lines.
- In JAC, the (reduced) photorecombination amplitudes are the building blocks to obtain most of the properties below.
- In JAC, the anisotropy parameters $\beta_\nu^{(\mathrm{REC})}$, $\nu = 1, ..., 4$ are calculated and tabulated for all selected photorecombination lines if the flag `calcAnisotropy = true` is set in `PhotoRecombination.Settings`.
- In JAC, the statistical tensors for the recombination of unpolarized ions with unpolarized plane-wave electrons are calculated and tabulated if the flag `calcTensors = true` is set in `PhotoRecombination.Settings`.
- The photorecombination of ions is known also as radiative recombination (RR) or radiative electron capture (REC) in the literature.
- The radiative recombination (RR) can be viewed as the time-reversed photoionization process and occurs frequently in stellar and laboratory plasmas as well as in ion-trap and storage-ring experiments.
- If a highly-charged ion circulates in a storage ring, it may capture electrons from rest-gas atoms in the ring and will then be misbent by subsequent steering magnets. Therefore, the radiative recombination or electron capture typically results in a loss of the ion from the ring, and where the lifetime is usually proportional to the inverse of the product of the capture cross section and the target pressure.
- Magnetic sublevel population $|\alpha_f \mathbb{J}_f M_f\rangle$ of the recombined ion: The radiative recombination amplitude from above can be used also to describe the (magnetic) sublevel population of the recombined ion. In the framework of density matrix theory, this sublevel population of the ionic (or atomic) states is described most conviniently in terms of the *statistical tensors* $\rho_{kq}(\alpha_f \mathbb{J}_f)$ of the recombined ion in its final level $|\alpha_f \mathbb{J}_f\rangle$.
- *Quantization axis:* Similar as in the photoionization process, the particular expression for the statistical tensors depend on the choice of the *quantization axis* of the overall system (z-axis) as well as the geometry of the experiments.

Photorecombination amplitude:

➢ Photorecombination amplitude: In first-order perturbation theory, most radiative recombination properties can be traced back to the evaluation of the (reduced photon emission) matrix element

$$\left\langle \alpha_f \mathbb{J}_f \left\| \mathbb{O}^{(\mathbb{M},\,\text{recombination})} \right\| (\alpha_i \mathbb{J}_i, \varepsilon\kappa)\mathbb{J}_t \right\rangle \;=\; \left\langle (\alpha_i \mathbb{J}_i, \varepsilon\kappa)\mathbb{J}_t \left\| \mathbb{O}^{(\mathbb{M},\,\text{photoionization})} \right\| \alpha_f \mathbb{J}_f \right\rangle^*$$

which describes the capture of a free electron with energy ε and angular momentum κ under the (simultaneous) emission of a photon with multipolarity $\mathbb{M} = (L, p)$.

Final-state density matrix 'recombined ion + photon':

➢ Final-state density matrix 'recombined ion + photon': For an unpolarized ion with nuclear spin $I = 0$ and for unpolarized plane-wave electrons, this density matrix can be expressed as:

$$\left\langle \alpha_f \mathbb{J}_f M_f,\, \mathbf{k}\lambda \,|\, \rho_f \,|\, \alpha_f \mathbb{J}_f M'_f,\, \mathbf{k}\lambda' \right\rangle$$

$$= \frac{8\pi}{2(2J_i+1)} \sum_{\mathbb{M}\mathbb{M}'} \sum_{J\,J'} \sum_{\kappa\,\kappa'} \sum_{\nu\,\mu_1\,\mu_2\,s\,s'} D^{\nu}_{\mu_1\mu_2}(\mathbf{k} \to \mathbf{e}_z)\, i^{L'-L}\, (i\lambda')^{\pi'}\, (-i\lambda)^{\pi}\, (-1)^{1/2+J_i+J'+L+s+s'-M'_{J,f}}\, [\ell, \ell', L, L', j, j', J, J', s]^{1/2}$$

$$\times [s'] \begin{Bmatrix} j' & 1/2 & \ell' \\ \ell & s & j \end{Bmatrix} \begin{Bmatrix} j' & J_i & J' \\ J & s & j \end{Bmatrix} \begin{Bmatrix} J & L & J_f \\ \nu & s' & L' \end{Bmatrix} \begin{Bmatrix} J & J' & s \\ J_f & s & L' \end{Bmatrix} \langle \ell' 0\, \ell 0 \,|\, s0 \rangle \left\langle J_f M_f\, s' - M'_f \,|\, \nu\mu_1 \right\rangle$$

$$\times \left\langle s0\, s' M'_f \,|\, J_f M'_f \right\rangle \left\langle L'\lambda'\, L - \lambda \,|\, \nu\mu_2 \right\rangle \left\langle \alpha_f \mathbb{J}_f \left\| \mathbb{O}^{(\mathbb{M},\,\text{recombination})} \right\| (\alpha_i \mathbb{J}_i, \varepsilon\kappa)\mathbb{J} \right\rangle \left\langle \alpha_f \mathbb{J}_f \left\| \mathbb{O}^{(\mathbb{M}'',\,\text{recombination})} \right\| (\alpha_i \mathbb{J}_i, \varepsilon\kappa')\mathbb{J} \right\rangle^* .$$

and if a nuclear spin $I = 0$ is assumed.

➢ In Jac, no attempt has been made so far to implement the density matrix of the overall system 'recombined ion + photon' because of its little relevance for practical computations. However, this density matrix could be implemented quite easily by using the photorecombination amplitudes from above.

Total recombination cross sections:

➢ Total recombination cross section: If the density of states and the principle of detailed balance between the capture and the (photo-) ionization of an electron is taken into account, the total cross section reads as

$$\sigma(\alpha_i \mathbb{J}_i, \alpha_f \mathbb{J}_f) \;=\; \frac{8\alpha^3\,\pi^3\,\omega}{(2J_i+1)}\,\frac{1}{\beta^2\,\gamma^2}\left[\sum_{\mathbb{M}\,J\kappa}\left|\left\langle \alpha_f \mathbb{J}_f \,\middle\|\, \mathbb{O}^{(\mathbb{M},\,\text{recombination})} \,\middle\|\, (\alpha_i \mathbb{J}_i,\,\varepsilon\kappa)\mathbb{J}\right\rangle\right|^2\right],$$

where $\beta = v/c$ and $\gamma = \sqrt{1-\beta^2}$ arise from the Lorentz transformation in going from the projectile into the laboratory frame.

Angular distribution of emitted photons:

➢ Angular distribution of emitted photons: For initially unpolarized ions and unpolarized incident plane-wave electrons, the angular distribution of the emitted (RR) photons can be readily obtained from the final-state density matrix by taking the trace $\text{Tr}\,(P_{\mathbf{k}}\,\rho_f)$ with regard to the measurement (projection operator) of plane-wave photons:

$$W(\theta) \;=\; \frac{\sigma}{4\pi}\left(1 \,+\, \sum_{\nu=1} P_\nu(\cos\theta)\;\beta_\nu^{(\text{REC})}(\alpha_i \mathbb{J}_i, \alpha_f \mathbb{J}_f)\right).$$

➢ Anisotropy parameters of the emitted photons:

$$\begin{aligned}\beta_\nu^{(\text{REC})} \;=\; -\frac{1}{2}\sum_{JJ'\kappa\kappa'}\sum_{\mathbb{M}\mathbb{M}'} i^{L+p-L'-p'}\,(-1)^{J_i-1/2-J_f}\,[L,L',\ell,\ell',j,j',J,J']^{1/2}\;\langle \ell 0,\,\ell' 0\,|\,\nu 0\rangle\;\langle L1,\,L'-1\,|\,\nu 0\rangle\;\left(1+(-1)^{L+p+L'+p'-\nu}\right)\\ \times\begin{Bmatrix} J & J' & \nu \\ L' & L & J_f\end{Bmatrix}\begin{Bmatrix} J & J' & \nu \\ j' & j & J_i\end{Bmatrix}\begin{Bmatrix} j & j' & \nu \\ \ell' & \ell & 1/2\end{Bmatrix}\left\langle \alpha_f \mathbb{J}_f \,\middle\|\, \mathbb{O}^{(\mathbb{M},\,\text{recombination})} \,\middle\|\, (\alpha_i \mathbb{J}_i,\,\varepsilon\kappa)\mathbb{J}\right\rangle^*\\ \times\left\langle \alpha_f \mathbb{J}_f \,\middle\|\, \mathbb{O}^{(\mathbb{M}',\,\text{recombination})} \,\middle\|\, (\alpha_i \mathbb{J}_i,\,\varepsilon\kappa')\mathbb{J}'\right\rangle \quad\left[\sum_{J\kappa\,\mathbb{M}}\left|\left\langle \alpha_f \mathbb{J}_f \,\middle\|\, \mathbb{O}^{(\mathbb{M},\,\text{recombination})} \,\middle\|\, (\alpha_i \mathbb{J}_i,\,\varepsilon\kappa)\mathbb{J}\right\rangle\right|^2\right]^{-1}.\end{aligned}$$

(Reduced) Statistical tensors of the recombined ion in the level $|\alpha_f \mathbb{J}_f\rangle$:

➢ Statistical tensors $\rho_{k0}(\alpha_f \mathbb{J}_f)$ of the final ion following the recombination of unpolarized atoms with unpolarized plane-wave electrons: If the quantization axis is adopted along the incoming electron momentum $\mathbf{p} \,||\, \mathbf{e}_z$, the statistical tensors of the recombined ion in the level $|\alpha_f \mathbb{J}_f\rangle$ are given by

$$\rho_{k0}(\alpha_f \mathbb{J}_f) \;=\; \frac{32\,\pi^3}{2J_i\,+\,1} \sum_{\mathbb{M}} \sum_{JJ'\kappa\kappa'} [\ell,\ell',j,j',J,J']^{1/2}\,(-1)^{J_i+L-J_f+J-J'-1/2}\,\langle \ell 0,\, \ell' 0 \,|\, k0\rangle \begin{Bmatrix} j & j' & k \\ \ell' & \ell & 1/2 \end{Bmatrix} \begin{Bmatrix} j & j' & k \\ J' & J & J_i \end{Bmatrix} \begin{Bmatrix} J & J' & k \\ J_f & J_f & L \end{Bmatrix}$$

$$\left\langle \alpha_f \mathbb{J}_f \,\middle\|\, \mathbb{O}^{(\mathbb{M},\,\text{recombination})} \,\middle\|\, (\alpha_i \mathbb{J}_i, \varepsilon\kappa)\mathbb{J} \right\rangle^* \left\langle \alpha_f \mathbb{J}_f \,\middle\|\, \mathbb{O}^{(\mathbb{M},\,\text{recombination})} \,\middle\|\, (\alpha_i \mathbb{J}_i, \varepsilon\kappa')\mathbb{J}' \right\rangle$$

Here, the summation over $(\mathbb{M}\, J\kappa)$ includes all allowed combinations of the multipoles of the radiation field as well as the many-electron continua $|(\alpha_i \mathbb{J}_i, \varepsilon\kappa)\mathbb{J}\rangle$ of the initial ion.

➢ Reduced statistical tensors: Instead of using the statistical tensors $\rho_{k0}(\alpha_f \mathbb{J}_f)$, it is often more convenient to describe the sublevel population of the residual ions in terms of the (so-called) *reduced* tensors:

$$\mathcal{A}_{k0}(\alpha_f \mathbb{J}_f) \;=\; \frac{\rho_{k0}(\alpha_f \mathbb{J}_f)}{\rho_{00}(\alpha_f \mathbb{J}_f)}\,,$$

which are directly related to the population cross sections $\sigma(\alpha_i \mathbb{J}_i \to \alpha_f \mathbb{J}_f M_f)$ for the electron capture into an ionic sublevel $|\alpha_f \mathbb{J}_f M_f\rangle$.

Photorecombination of ions with twisted electrons:

➢ Angular distribution and the linear polarization of photons: Expressions have been derived for the angular distribution and the linear polarization of the emitted photons due to the capture of twisted electrons into the ground state of (hydrogen-like) ions. These expressions showed that the angular and polarization distributions are sensitive to both, the transverse momentum and the topological charge of the incident electron beam.

➢ Photorecombination with twisted electrons: For twisted electrons with well-defined values of the linear momentum p_z and with topological charge $m \;=\; 0, \pm 1, \pm 2$, i.e. with well-defined projection of the OAM upon the propagation direction, the initial-state wave function is

given by:

$$\psi_i^{(\mathrm{tw})}(\mathbf{r}) \;\equiv\; \psi_{\kappa\, m\, p_z}^{(\mathrm{tw})}(\mathbf{r}) \;=\; \int \frac{\mathrm{d}^2\mathbf{p}_\perp}{(2\pi)^2}\; a_{\kappa m}(\mathbf{p}_\perp)\; \mathrm{e}^{\mathrm{i}\,(\mathbf{p}_\perp\cdot\mathbf{r}_\perp\, +\, p_z\, z)},$$

where $a_{\kappa m}(\mathbf{p}_\perp)$ refer to the Fourier coefficients that include also the transverse momentum profile of the beam.

➢ Final bound-state wave functions:

$$\psi_f(\mathbf{r} \,-\, \mathbf{b}_\perp) \;=\; e^{-i\,\mathbf{p}\cdot\mathbf{b}_\perp}\; \psi_f(\mathbf{r})\;.$$

8.1.e. Auger and autoionization processes (AutoIonization)

Process, notations & application:

➢ Auger emission (autoionization) of an atom or ion: $A^{q+*} \;\longrightarrow\; A^{(q+1)+(*)} \,+\, e_a^-$

➢ Formal quantum notation: $|\alpha_i \mathbb{J}_i\rangle \;\longrightarrow\; |\alpha_f \mathbb{J}_f\rangle \,+\, |\varepsilon\kappa\rangle$

➢ Using Jac: Perform an `Atomic.Computation(.., process=Jac.Auger, processSettings=AutoIonization.Settings(..), ..)` or call directly functions from the module `Auger`.

➢ In Jac, the partikular kind of the Auger operator $\mathbb{V}^{(\mathrm{Auger})}$ can be specified by selecting `AutoIonization.Settings.operator = ("Coulomb", "Breit", "Coulomb+Breit", ...)`.

➢ In Jac, the Auger rates and (Auger) lifetimes are tabulated by default for all selected (Auger) transitions.

➢ In Jac, the intrinsic anisotropy parameters are calculated and tabulated if the flag `calcAnisotropy = true` is set in `AutoIonization.Settings`.

➢ Using Jac: Perform an `Atomic.Computation(.., process=Jac.AutoIonizationInPlasma, processSettings= PlasmaShift.AutoIonizationSettings(..), ..)` or call directly functions from the modules `AutoIonization` and `PlasmaShift`. Until the present, however, only a Debye-Hückel plasma model is supported and where the Debye-Hückel screening of the electron-nucleus and electron-photon interaction is incorporated only in first-order perturbation theory within the CI matrix.

- An autoionization of an (inner-shell) excited bound state can occur (only) if the initial level is energetically embedded into the *continuum* of the next higher charge state.
- Formally, an electron emission from such an embedded resonance (level) arise due to its coupling to one or several scattering states, which are degenerate with the initial state and which involve one (or more) *free* electrons.
- While the Coulomb repulsion in the Auger amplitude above is typically sufficient in order to describe the autoionization of light and medium elements, the Breit interaction has been found important for electron emission and capture processes of highly-charged ions.
- The restriction to the electron-electron interaction in the computation (evaluation) of the Auger amplitudes is quite standard in all presently available Auger codes, even if the orbital functions of the resonant scattering state $|\alpha_t \mathbb{J}_t\rangle$ and the final-ionic state $|\alpha_i \mathbb{J}_i\rangle$ are not quite orthogonal to each other.
- In Jac, we generally support the computation of nonradiative (Auger) rates, relative Auger intensities and intrinsic angular anisotropy parameters. To this end, first the (reduced) Auger amplitudes are calculated for all selected pairs of initial and final levels and, later, these amplitudes are combined into Auger rates, intrinsic anisotropy or spin-polarization parameters.
- Since the number of possible Auger transitions often increases very rapidly, especially if several inner-shell holes and/or valence electrons occur, Jac provides several additional control features for reducing the complexity: Apart from (1) the selection of particular Auger lines, these features include (2) the definition of an energy threshold (i.e. a minimum energy) of the free electron as well as (3) a maximum angular momentum (negative κ quantum number) for the partial waves of the outgoing electron. A proper use of (3) mainly affects the number of the scattering states, that are taken into account, and can be chosen independently of the formally allowed couplings of the free-electron.
- These control features are in line with the common experience that partial waves with high angular momenta do either not contribute at all (i.e. have *zero* Auger amplitudes in most computational models) or are simply negligible. In addition, Jac supports the use of an overall energy shift of all Auger transition energies which can be specified interactively.
- Often, the number of the possible scattering states $|(\alpha_f \mathbb{J}_f, \varepsilon\, \kappa)\, \alpha_t \mathbb{J}_t\rangle$ of a system increases rapidly since the free electrons may couple in quite different ways to the bound-state electrons from the final (Auger) ions.
- Reaction plane of the Auger emission: For a prior photo-absorption or particle impact, this reaction plane is usually defined by the directions of the incident photon (particle) beam and the emitted Auger electron.

Auger amplitudes:

➢ Auger amplitude: Following Åberg and Howat (1982), the Auger transition amplitude for the autoionization of an excited bound state $|\alpha_i\, \mathbb{J}_i M_i\rangle$ into the final scattering state $|\alpha_t\, \mathbb{J}_t M_t\rangle$, built from an ion in the final level $|\alpha_f\, \mathbb{J}_f\rangle$, can be expressed most generally as

$$\begin{aligned}\left\langle (\alpha_f \mathbb{J}_f,\, \varepsilon\, \kappa)\, \mathbb{J}_t M_t \,\middle|\, \mathbb{V}^{(\text{Auger})} \,\middle|\, \alpha_i\, \mathbb{J}_i M_i \right\rangle &= \left\langle (\alpha_f \mathbb{J}_f,\, \varepsilon\, \kappa)\, \mathbb{J}_t \,\middle\|\, \mathbb{V}^{(\text{Auger})} \,\middle\|\, \alpha_i\, \mathbb{J}_i \right\rangle \delta_{J_i,J_t}\, \delta_{M_i,M_t}\, \delta_{P_i,P_t} \\ &= \left\langle (\alpha_f \mathbb{J}_f,\, \varepsilon\, \kappa)\, \mathbb{J}_t \,\middle\|\, \mathbb{H} - E \,\middle\|\, \alpha_i\, \mathbb{J}_i \right\rangle \delta_{J_i,J_t}\, \delta_{M_i,M_t}\, \delta_{P_i,P_t} .\end{aligned}$$

This amplitude is independent of the projection M_i of the initial state owing to the rotational symmetry of free atoms and the scalar character of the Hamiltonian and/or interelectronic interactions.

➢ In an autoionization process, the final scattering states $|\alpha_t\, \mathbb{J}_t M_t\rangle \equiv |(\alpha_f \mathbb{J}_f,\, \varepsilon\, \kappa)\, \mathbb{J}_t M_t\rangle$ arise from the coupling of the final state $|\alpha_f\, \mathbb{J}_f M_f\rangle$ of the ion with well-defined symmetry with the partial-wave $|\varepsilon\, \kappa\, m_j\rangle$ of the outgoing electron with energy ε and (one-electron) angular momentum $\kappa = \kappa(j,l)$ as well as magnetic projection m_j .

➢ In Jac, as in most other tools for computing autoionization processes, a common set of *orthonormal* orbitals is often supposed for the representation of the initial $|\alpha_i \mathbb{J}_i\rangle$ and final (ionic) bound levels $|\alpha_f \mathbb{J}_f\rangle$ in the evaluation of the Auger amplitudes. In this case, the Auger transition operator $\mathbb{V}^{(\text{Auger})} \equiv \mathbb{H} - E \approx \mathbb{V}^{(\text{e-e})}$ simplifies to the electron-electron interaction operator, while the (reduced) Auger amplitude becomes

$$\left\langle (\alpha_f \mathbb{J}_f,\, \varepsilon\, \kappa)\, \mathbb{J}_t \,\middle\|\, \mathbb{V}^{(\text{Auger})} \,\middle\|\, \alpha_i\, \mathbb{J}_i \right\rangle \simeq \left\langle (\alpha_f \mathbb{J}_f,\, \varepsilon\, \kappa)\, \mathbb{J}_t \,\middle\|\, \mathbb{V}^{(\text{e-e})} \,\middle\|\, \alpha_i\, \mathbb{J}_i \right\rangle \delta_{J_i,J_t}\, \delta_{M_i,M_t}\, \delta_{P_i,P_t} .$$

➢ Within the framework of the Dirac-Coulomb-Breit Hamiltonian, the interelectronic interaction is the sum of the Coulomb repulsion and Breit interaction, $\mathbb{V}^{(\text{e-e})} = \mathbb{V}^{(\text{Coulomb})} + \mathbb{V}^{(\text{Breit})} \simeq \mathbb{V}^{(\text{Coulomb})}$, although it is often approximated by just the Coulomb part.

Auger rates:

➢ Auger rates: If the (continuum) interaction between the different Auger channels is neglected, the Auger rates are simply given by

$$A(i \to f) \;=\; 2\pi \sum_{\kappa} \left| \left\langle (\alpha_f \mathbb{J}_f,\, \varepsilon\, \kappa)\, \mathbb{J}_i \,\middle\|\, \mathbb{V}^{(\mathrm{Auger})} \,\middle\|\, \alpha_i\, \mathbb{J}_i \right\rangle \right|^2 ,$$

where the summation runs over all partial waves $|\varepsilon\, \kappa\rangle$ that fulfill the triangular rule $\delta(J_f,\, j,\, J_i)$ and where the Auger interaction operator $\mathbb{V}^{(\mathrm{Auger})}$ still need to be specified due to the (computational) framework and additional approximations that are made in practice.

➢ In Jac, the Auger rates and (Auger) lifetimes are tabulated by default for all selected (Auger) transitions.

Angular distribution of Auger electrons:

➢ Angular distribution of emitted electrons: If only the Auger electrons are detected from the autoionization of an (inner-shell) excited ion in the level $|\alpha_i \mathbb{J}_i\rangle$, and which is fully characterized by the reduced statistical tensors $\mathcal{A}_{kq}(\alpha_i \mathbb{J}_i)$, the angular distribution of the emitted electrons of the Auger transition $|\alpha_i \mathbb{J}_i\rangle \to |\alpha_f \mathbb{J}_f\rangle$ can be written in the general form (Balashov *et al.* 2000, equation 3.10)

$$W(\vartheta, \varphi;\, \alpha_i \mathbb{J}_i \to \alpha_f \mathbb{J}_f) \;=\; \frac{A(i \to f)}{4\pi} \left[1 \,+\, \sum_{k\,=\,2,\,4,\,\ldots}^{k_{\max}} \sqrt{\frac{4\pi}{2k+1}}\; \alpha_k(\alpha_i \mathbb{J}_i \to \alpha_f \mathbb{J}_f) \sum_{q\,=\,-k}^{k} \mathcal{A}_{kq}(\alpha_i \mathbb{J}_i)\; Y_{kq}(\vartheta, \varphi) \right] ,$$

and where $\alpha_k(\alpha_i \mathbb{J}_i \to \alpha_f \mathbb{J}_f)$ are the (so-called) intrinsic anisotropy parameters of the electron emission

$$\begin{aligned} \alpha_k(\alpha_i \mathbb{J}_i \to \alpha_f \mathbb{J}_f) \;=\; & \left[\sum_{\kappa} \left\langle (\alpha_f \mathbb{J}_f,\, \varepsilon\, \kappa)\, \mathbb{J}_i \,\middle\|\, \mathbb{V}^{(\mathrm{Auger})} \,\middle\|\, \alpha_i\, \mathbb{J}_i \right\rangle \right]^{-1} (-1)^{J_i + J_f + k - 1/2} \sqrt{2J_i + 1} \sum_{\kappa\kappa'} [\ell, \ell', j, j']^{1/2}\; \langle \ell 0,\, \ell' 0 \,|\, k 0 \rangle \\ & \times \begin{Bmatrix} J_i & j & J_f \\ j' & J_i & k \end{Bmatrix} \begin{Bmatrix} \ell & j & 1/2 \\ j' & \ell' & k \end{Bmatrix} \left\langle (\alpha_f \mathbb{J}_f,\, \varepsilon\, \kappa)\, \mathbb{J}_i \,\middle\|\, \mathbb{V}^{(\mathrm{Auger})} \,\middle\|\, \alpha_i\, \mathbb{J}_i \right\rangle \left\langle (\alpha_f \mathbb{J}_f,\, \varepsilon\, \kappa')\, \mathbb{J}_i \,\middle\|\, \mathbb{V}^{(\mathrm{Auger})} \,\middle\|\, \alpha_i\, \mathbb{J}_i \right\rangle^{*} \end{aligned}$$

➢ Here, the factor $A(i \to f)$ is the total probability of the Auger transition $|\alpha_i \mathbb{J}_i\rangle \to |\alpha_f \mathbb{J}_f\rangle$, integrated over the ejection angles. The anisotropy parameters $\alpha_k(\alpha_i \mathbb{J}_i \to \alpha_f \mathbb{J}_f)$ contain all information about the dynamics of the decay, while the tensors $\mathcal{A}_{kq}(\alpha_i \mathbb{J}_i)$ just describe the polarization properties of the initial level.

➢ Angular distribution of emitted Auger electrons averaged over several final levels: If several final levels cannot be resolved by the detector, the total angular distribution is an incoherent sum of the angular distributions of all unresolved final levels with total angular momenta J_f:

$$W(\vartheta, \varphi;\, \alpha_i \mathbb{J}_i \rightarrow \{\alpha_f \mathbb{J}_f\}) \;=\; \sum_{\alpha_f \mathbb{J}_f} W(\vartheta, \varphi;\, \alpha_i \mathbb{J}_i \rightarrow \alpha_f \mathbb{J}_f)\;.$$

In this case, the angular distribution can be expressed also by means of some average anisotropy parameter (within the electric-dipole approximation)

$$\bar{\beta}_2 \;=\; \frac{\sum_{\alpha_f \mathbb{J}_f} \beta_2(i \rightarrow f)\, A(i \rightarrow f)}{\sum_{\alpha_f \mathbb{J}_f} A(i \rightarrow f)}, \qquad\qquad \beta_2(i \rightarrow f) \;=\; \alpha_2(\alpha_i \mathbb{J}_i \rightarrow \alpha_f \mathbb{J}_f)\, A_{20}(\alpha_i \mathbb{J}_i).$$

Spin polarization of Auger electrons:

➢ The spin polarization of Auger electrons is usually described by an polarization vector $\mathbf{P}$. The three components of $\mathbf{P}$ can be expressed in terms of the statistical tensors of the initial level as well as the intrinsic anisotropy parameters of the considered Auger transition.

➢ Two coordinate systems, $S(XYZ)$ and $S'(X'Y'Z')$ are often employed in order to characterize the spin polarization of Auger electrons; cf. the figure below and Kabachnik *et al.* (2007).

Two-electron single Auger emission (TESA):

➢ Non-resonant three-electron Auger transitions have been suggested several decades ago, though clear evidence for such TESA transition were found in Ar only with very low intensity relative to the normal Auger lines.

➢ Theobserved TESA transitions usually start with the creation of a double vacancy, i.e. with two vacancies in an inner shell, and which are filled simultaneously by two outer-shell electrons, while the released energy is passed to a third emitted electron.

➢ Such inner-shell double vacancies are normally at energies above the minimum fourfold ionization energy and can easily be filled also by two separate successive two-electron Auger transitions involving four electrons in total.

8.1.f. Dielectronic recombination (Dielectronic)

Process, notations & application:

- Dielectronic recombination (DR) of an atom or ion: $A^{q+} + e^- \longrightarrow A^{(q-1)+*} \longrightarrow A^{(q-1)+(*)} + \hbar\omega$
- Formal quantum notation: $|\alpha_i \mathbb{J}_i\rangle + |\varepsilon\,\kappa\rangle \longrightarrow |\alpha_d \mathbb{J}_d\rangle \longrightarrow |\alpha_f \mathbb{J}_f\rangle + \hbar\omega\,(\mathbb{M})$ or
  $|\alpha_i \mathbb{J}_i\rangle + |\mathbf{p}_i\, m_i\rangle \longrightarrow |\alpha_d \mathbb{J}_d\rangle \longrightarrow |\alpha_f \mathbb{J}_f\rangle + \hbar\omega\,(\mathbb{M})$
- Using Jac: Perform an `Atomic.Computation(.., process=JAC.Dierec, processSettings=Dielectronic.Settings(..), ..)` or call directly functions from the module `Dielectronic`.
- In Jac, both the individual $S(i \to d \to f)$ and total resonance strengths $S(i \to d)$ are calculated and tabulated by default for all selected pathways.
- In Jac, the capture (Auger) and radiative amplitudes and rates are finally computed by the corresponding modules `Auger` and `PhotoEmission`.
- In most computations, the dielectronic recombination of a N-electron target ion in the (initial) level $|\alpha_i \mathbb{J}_i\rangle$ is typically handled as a two-step process, in which first an electron is captured resonantly from the continuum into a [$(N+1)$-electron] resonance level $|\alpha_d \mathbb{J}_d\rangle$, embedded into the continuum of the initial ion and with often two or more electrons in excited (one-electron) orbitals. In a second step, this excited level $|\alpha_d \mathbb{J}_d\rangle$ then either decays radiatively by the emission of photons to some (final) level $|\alpha_f \mathbb{J}_f\rangle$, below of the ionization threshold of the ion, or it returns by autoionization back into the charge stage of the initial target ion.
- Apart from the computation of accurate Auger rates, helpful calculation of DR spectra critically depends on the simple control (and handling) of all the — radiative and non-radiative — decay branches of the resonantly excited ion. In Jac, these branches are treated equally within the `Dielectronic` module.
- As seen from the (total) resonance strength below, the experimentally observed strength of the dielectronic recombination for a given resonance level $|\alpha_d \mathbb{J}_d\rangle$ is proportional to the capture rate $A_a(i \to d)$ as well as the (total) radiative rate.
- If, in particular, the intermediate level $|\alpha_d \mathbb{J}_d\rangle$ can autoionize only back to the ground state of the target ion, as for example for the $3s$ valence excitation of a sodium-like target ion, the total Auger rate is then — up to statistical factors — equal to the capture rate.
- In practice, the number of the possible scattering states $|(\alpha_i\, \mathbb{J}_i,\, \varepsilon\,\kappa),\, \mathbb{J}_d M_d\rangle$ of the recombined ion often increases very rapidly since, the free electrons may couple in many different ways to the bound-state electrons of the initial ion.

Strength of dielectronic recombination (DR) resonances:

➢ Partial resonance strength: If the interference between the radiative and dielectronic (nonradiative) capture of the electron is negligible in the field of the target, the dielectronic recombination of an ion from an initial, via the isolated resonance state and into the final (ground) state of the (recombined) atom, $i \to d = f$ can be characterized by a (so-called) resonance strength. This strength can be solely expressed in terms of the Auger and radiative rates of the resonant state d as well as its (half-) widths Γ_d by

$$S(i \to d \to f) \equiv \int_{-\infty}^{\infty} dE \; \sigma^{(\mathrm{DR})}(E) = \frac{2\,\pi^2\,\hbar}{k_i^2} \; \frac{A_a(i \to d)\, A_r(d \to f)}{\Gamma_d}.$$

In this expression, k_i is wave number of the incident electron, $A_a(i \to d)$ the rate for the electron capture (inverse Auger) from the initial into the excited resonance state, and $A_r(d \to f)$ the rate for the radiative stabilization into the state f. The resonance strength refers to the area *under* the energy-dependent differential DR cross sections and is typically given in units of: $[S] = \mathrm{cm}^2\,\mathrm{eV}$.

➢ In the resonance strength above, $A_a(i \to d)$ is the rate for the inverse Auger capture from the initial into the (doubly-excited) resonance level $|\alpha_d \mathbb{J}_d\rangle$, while $A_r(d \to f)$ refers to the rate for the radiative stabilization to the final level $|\alpha_f \mathbb{J}_f\rangle$ of the $N+1$-electron ion.

➢ Total width of the resonance level $|\alpha_d \mathbb{J}_d\rangle$: The total width Γ_d is determined by all possible decay channels of the resonance level $|\alpha_d \mathbb{J}_d\rangle$ and is given in first-order perturbation theory by

$$\Gamma_d = \hbar \left(\sum_j A_a(d \to j) + \sum_{f'} A_r(d \to f') \right),$$

i.e. by taking the sum over all the individual Auger and radiative rates (widths) of the intermediate level $|\alpha_d \mathbb{J}_d\rangle$.

➢ The Auger and inverse capture rates $A_a(i \to d) = g_i/g_d \; A_a(d \to i)$ are proportional to each other owing to the principle of kinetic balance, and with the g's being the statistical factors of the initial and intermediate resonance levels.

➢ The use of the individual resonance strength $S(i \to d \to f)$ is appropriate especially, if the energy-dependent DR cross section has a Lorentzian profile

$$\sigma^{(\mathrm{DR})}(E) = \frac{S}{\pi} \frac{\Gamma/2}{(E_r - E)^2 + \Gamma^2/4}$$

around the resonance energy $E_r = E_d - E_i$ as well as a natural width less or comparable to the energy spread of the electron beam. In general, this condition is well fulfilled for most $\Delta n \geq 1$ resonances (with an excitation of a bound electron from the shell $n_i \rightarrow n_f$, for which the total widths are small in most cases), but this condition can usually be utilized also for the $\Delta n = 0$ lines if the shape of the resonances is not to be analyzed in detail.

➢ Threshold behaviour: Owing to the energy of the incident electron [cf. the factor $1/k_i^2$ above], the resonance strength increases rapidly towards the threshold of the dielectronic recombination and makes the process sensitive to low kinetic energies of the incoming electrons.

➢ Total resonance strength: At storage rings, the radiative stabilization of the ions in the (intermediate) resonance level $|\alpha_d \mathbb{J}_d\rangle$ is often not observed explicitly and, hence, the radiative rate for the individual transition $d \rightarrow f$ in the resonance strength above has to be replaced by the total radiative rate of the (doubly-excited) resonance level $|\alpha_d \mathbb{J}_d\rangle$:

$$A_r(d \rightarrow f) \quad \longrightarrow \quad \sum_{f'} A_r(d \rightarrow f') \qquad \Longrightarrow \qquad S(i \rightarrow d \rightarrow f) \quad \longrightarrow \quad S(i \rightarrow d) = \sum_{f'} S(i \rightarrow d \rightarrow f')$$

➢ In Jac, both the individual $S(i \rightarrow d \rightarrow f)$ and total resonance strengthes $S(i \rightarrow d)$ are calculated and tabulated by default for all selected pathways.

8.1.g. Photoexcitation & fluorescence (PhotoExcitationFluores)

Process, notations & application:

➢ Photoexcitation of an atom or ion with subsequent fluorescence emission: $A + \hbar\omega_i \quad \longrightarrow \quad A^* \quad \longrightarrow \quad A^{(*)} + \hbar\omega_f$

➢ Formal quantum notation: $|\alpha_i \mathbb{J}_i\rangle + \hbar\omega\,(\mathbf{k} \,||\, \mathbf{e}_z,\, \lambda;\, \{\mathbb{M}\}) \quad \longrightarrow \quad |\alpha_e \mathbb{J}_e\rangle \quad \longrightarrow \quad |\alpha_f \mathbb{J}_f\rangle + \hbar\omega_f\,(\Omega;\, \mathbf{P})$

➢ Using Jac: Perform an `Atomic.Computation(.., process=PhotoExcFluor, processSettings=PhotoExcitationFluores.Settings(..), ..)` or call directly functions from the module `PhotoExcitationFluores`.

➢ In Jac, the reduced density matrix of a fluorescence photon can be calculated at a selected solid angle $\{\Omega = vartheta, \varphi)$ by calling the function `PhotoExcitationFluores.computePhotonDM`, and if the solid angle is specified explicitly.

➢ The photoexcitation and (subsequent) fluorescence emission from atoms and ions has been investigated in good detail in the literature for both, incident plane-wave radiation as well as for twisted Bessel and Laguerre-Gaussian beams.

➢ Since the properties of the photo-excited atoms can be calculated by the module `PhotoExcitation` and the properties of the radiative emission by the module `Radiative`, here we shall focus only upon properties that are specific to the overall photoexcitation & fluorescence process, such as the angular distribution or density matrix of the fluorescence photons.

➢ In JAC, the alignment parameters of the (intermediate) excited level $\mathcal{A}_{kq}(\alpha_e \mathbb{J}_e)$ can be calculated and tabulated by the module `PhotoExcitation`, while the structure functions $f_k(\alpha_e \mathbb{J}_e,\ \alpha_f \mathbb{J}_f)$ can be obtained by using the module `PhotoEmission`.

➢ In JAC, the statistical tensors $\rho_{kq}(\alpha_e \mathbb{J}_e)$ of the intermediate excited level can be calculated and tabulated by the module `PhotoExcitation`. These tensors are also required for describing the photoexcitation & fluorescence process.

Density matrix of the fluorescence photon $\hbar\,\omega_f(\Omega)$:

➢ (Reduced) density matrix of the fluorescence photons for the photoemission from an aligned or oriented atom: For photons emitted under the angle $\Omega = (\vartheta, \varphi)$ with regard to the propagation direction of the incident plane-wave radiation $\mathbf{k} \,||\, \mathbf{e}_z$, the (reduced) density matrix can be readily expressed in terms of the statistical tensors of the excited level $\rho_{kq}(\alpha_e \mathbb{J}_e)$ as

$$\begin{aligned} \left\langle \mathbf{k}_0\, \lambda \,\middle|\, \rho_{\omega_f} \,\middle|\, \mathbf{k}_0\, \lambda' \right\rangle &= 2\pi \sum_{k,\, qq'} \sum_{\mathbb{M}\,\mathbb{M}'} D^k_{-qq'}(\varphi, \vartheta, 0)\ \rho_{kq}(\alpha_e \mathbb{J}_e)\ i^{L'+p'-L-p}\ \lambda^p\ (\lambda')^{p'}\ \sqrt{2L+1}\,\sqrt{2L'+1}\ (-1)^{J_f+J_e+k+q+1} \\ &\times \left\langle L\lambda,\ L'(-\lambda') \,|\, k-q' \right\rangle \begin{Bmatrix} L & L' & k \\ J_e & J_e & J_f \end{Bmatrix} \left\langle \alpha_f\, \mathbb{J}_f \left\| \mathbb{O}^{(\mathbb{M},\,\mathrm{emission})}(\omega_f) \right\| \alpha_e\, \mathbb{J}_e \right\rangle \left\langle \alpha_f\, \mathbb{J}_f \left\| \mathbb{O}^{(\mathbb{M}',\,\mathrm{emission})}(\omega_f) \right\| \alpha_e\, \mathbb{J}_e \right\rangle^* \end{aligned}$$

➢ In JAC, the reduced density matrix of a fluorescence photon can be calculated at a selected solid angles $\{\Omega = (\vartheta, \varphi)$, see above.

Angular distribution and Stokes parameters of the fluorescence photon $\hbar\,\omega_f(\Omega;\, \mathbf{P})$:

➢ Angular distribution of the fluorescence light for the photoemission from a aligned or oriented atom: Most generally, the angular distribution can be obtained from the photon density matrix above by a summation over the two polarization states:

$$W(\vartheta, \varphi) = \sum_{\lambda} \left\langle \mathbf{k}_0\, \lambda \,\middle|\, \rho_{\omega_f} \,\middle|\, \mathbf{k}_0\, \lambda \right\rangle .$$

➢ Using the expressions from above, this angular distribution can be readily calculated for a set of angles $\{\Omega_1 = (\vartheta_1, \varphi_1),\ \Omega_2,\ ...\}$, see above.

➢ Angular distribution of the fluorescence light: For initially unpolarized atoms and unpolarized photons in the photo-excitation process, in particular, the angular distribution is given by the same formulas as for the photoemission (alone), i.e. in terms of the alignment parameters $\mathcal{A}_{k0}(\alpha_e \mathbb{J}_e)$ and the structure function of the (intermediate) excited level $|\alpha_e \mathbb{J}_e\rangle$:

$$W(\vartheta) \;=\; \frac{W_o}{4\pi}\left(1 + \sum_{k=2,4,..} f_k(\alpha_e \mathbb{J}_e, \alpha_f \mathbb{J}_f)\, \mathcal{A}_{k0}(\alpha_e \mathbb{J}_e)\, P_k(cos\vartheta)\right) .$$

8.1.h. Photoexcitation & autoionization (PhotoExcitationAutoion)

Process, notations & application:

➢ Photoexcitation & autoionization of an atom or ion: $A + \hbar\omega \;\longrightarrow\; A^* \;\longrightarrow\; A^{(*)} + e_a^-$

➢ Formal quantum notation: $|\alpha_i \mathbb{J}_i\rangle + \hbar\omega\,(\mathbf{k}\,||\,\mathbf{e}_z,\,\lambda;\,\{\mathbb{M}\}) \;\longrightarrow\; |\alpha_r \mathbb{J}_r\rangle \;\longrightarrow\; |\alpha_f \mathbb{J}_f\rangle + |\varepsilon\kappa\rangle$

➢ Using Jac: Perform an `Atomic.Computation(.., process=PhotoExcAuto, processSettings=PhotoExcitationAutoion.Settings(..), ..)` or call directly functions from the module `PhotoExcitationAutoion`.

➢ In Jac, the partial photoexcitation & autoionization cross sections $\sigma(i \to r \to f)$ are calculated and tabulated by assuming that the direct photoionization cross sections $\sigma^{(\text{photionization})}(i \to f)$ is negligible.

➢ The photoexcitation and (subsequent) autoionization of atoms and ions has been explored in good detail, either as the dominant (photo-) ionization process within the vincinity of certain (photoionization) resonances or simply as competitive process to atomic photoionization.

➢ Often, the photoexcitation & autoionization can be considered independently from the *direct* photoionization and then leads to partial and total photoexcitation & autoionization cross sections.

➢ If the direct photoionization is negligible, the photoexcitation & autoionization is the time-reversed process to the dielectronic recombination.

Fano profiles in photo-ionization cross sections:

➢ Fano's parametrization: For an isolated resonance $|\alpha_r \mathbb{J}_r\rangle$, the total photoionization cross section can be (formally) parametrized in the vincinity of this resonance by the energy-dependent cross section

$$\sigma(\mathcal{E}) \;=\; \sigma^{(\mathrm{EA})}\,\frac{(q\,+\,\mathcal{E})^2}{1\,+\,\mathcal{E}^2} \;+\; \sigma^{(\mathrm{D})}$$

where $\sigma^{(\mathrm{D})}$ is the direct photoionization cross section and $\sigma^{(\mathrm{EA})}$ the cross section due to the photoexcitation & autoionization of the resonance. Moreover, $\mathcal{E} = (E_\omega - E_r)/(\Gamma/2)$ indicates the detuning of the incident photon energy E_ω from the resonance energy E_r , in units of the half-width $(\Gamma/2)$ of the resonance.

➢ Fano q parameter: This parameter determines the overall profile of the cross section, ranging from a near-Lorentzian $(q \to \infty)$, to a window-like $(q \to 0)$, and up to a completely asymmetric resonance $(q \to \pm 1)$.

➢ In JAC, no attempt has been made so far to calculate the Fano profiles explicitly for selected resonances, although this is possible quite readily by combining proper calls to functions from the modules `PhotoIonization`, `PhotoExcitation` as well as `Auger`.

Total photoionization amplitude and cross sections across the resonance level $|\alpha_r \mathbb{J}_r\rangle$:

➢ The photoexcitation and (subsequent) autoionization of atoms and ions obviously contributes to the photoionization and, hence, to its amplitudes and cross sections.

➢ Total photoionization amplitudes across the resonance level $|\alpha_r \mathbb{J}_r\rangle$:

$$\mathcal{M}\,(\omega;\,(\alpha_f \mathbb{J}_f,\,\varepsilon\kappa)\,\mathbb{J}_t,\,\alpha_r \mathbb{J}_r,\,\alpha_i \mathbb{J}_i)$$

$$= \;\big\langle (\alpha_f \mathbb{J}_f,\,\varepsilon\kappa)\,\mathbb{J}_t \,\big\|\, \mathbb{O}^{(\mathbb{M},\,\mathrm{photoionzation})} \big\|\, \alpha_i \mathbb{J}_i \big\rangle \;+\; \frac{\big\langle (\alpha_f \mathbb{J}_f,\,\varepsilon\kappa)\,\mathbb{J}_t \,\big\|\, \mathbb{O}^{(\mathrm{Auger})} \,\big\|\, \alpha_r \mathbb{J}_r \big\rangle \,\big\langle \alpha_r \mathbb{J}_r \,\big\|\, \mathbb{O}^{(\mathbb{M},\,\mathrm{absorption})} \big\|\, \alpha_i \mathbb{J}_i \big\rangle}{E_i \,+\, \omega \,-\, E_r \,+\, i\,\Gamma_r/2}$$

In this notation of the resonant photoionization, we assume the photoelectron to escape by means of the partial wave $|\varepsilon\,\kappa\rangle$ with kinetic energy $\varepsilon = E_i + \omega - E_f$ and with well-defined angular momentum and parity.

➢ Apart from the *direct* photoionization amplitude (first term), the total photoionization amplitude also contains the photoexcitation & autoionization amplitudes (second term).

➢ From these amplitudes, the total photoionization cross section (intensity) is obtained as before by the summation over all the possible scattering states of the final system 'photoion + electron':

$$\sigma\,(\omega;\,\alpha_i \mathbb{J}_i,\,\alpha_f \mathbb{J}_f) \;=\; \frac{4\,\pi^2\,\alpha\,\omega}{3\,(2J_i+1)} \sum_{\alpha_r \mathbb{J}_r\,\kappa\,\mathbb{J}_t} |\,\mathcal{M}\,(\omega;\,(\alpha_f \mathbb{J}_f,\,\varepsilon\kappa)\,\mathbb{J}_t,\,\alpha_r \mathbb{J}_r,\,\alpha_i \mathbb{J}_i)\,|^2,$$

This includes both, the summation over all relevant resonances as well as the summation over the partial waves of the photoelectron and the total angular momenta and parities of the total scattering states $|\alpha_t \mathbb{J}_t\rangle$.

➢ In Jac, no attempt has yet been made to calculate and tabulate the resonant photoionization cross sections or angular anisotropy parameters, although this will be possible since all required many-electron matrix elements are internally quite readily available.

Angular distribution of resonantly emitted Auger electrons:

➢ Of course, the angular distribution of the emitted Auger electrons critically depend on the (properties of the) prior excitation process; in this `PhotoExcitationAutoion` module, we assume a photoexcitation of the atoms or ions for calculating subsequent properties of Auger electrons. We here also assume that the direct photoionization is negligible near to the considered resonance level $|\alpha_r \mathbb{J}_r\rangle$.

➢ If the resonantly-excited level $|\alpha_r \mathbb{J}_r\rangle$ is axially symmetric along the z-axis, $\mathcal{A}_{kq}(\alpha_r \mathbb{J}_r) \sim \delta_{q0}$, the angular distribution only depends on the angle ϑ between the symmetry (z-) axis and the linear momentum of the ejected electron. Then, the angular distribution simplifies to

$$W(\vartheta;\,\alpha_r \mathbb{J}_r \to \alpha_f \mathbb{J}_f) \;=\; \frac{A_a(r \to f)}{4\pi} \left[1 + \sum_{k\,=\,2,\,4\,,\ldots}^{k_{\max}} \alpha_k(\alpha_r \mathbb{J}_r \to \alpha_f \mathbb{J}_f)\;\mathcal{A}_{k0}(\alpha_r \mathbb{J}_r)\;P_k(\cos\vartheta)\right] .$$

➢ In Jac, no attempt has been made so far to tabulate the angular distribution $W(\vartheta;\,\alpha_i \mathbb{J}_i \to \alpha_f \mathbb{J}_f)$ explicitly for selected scenarios; cf. section 8.1.e.

➢ Photoexcitation of initially unpolarized atoms within the dipole approximation: For the photoexcitation of initially unpolarized atoms the Auger angular distribution further simplifies to

$$W(\vartheta;\,\alpha_r \mathbb{J}_r \to \alpha_f \mathbb{J}_f) \;=\; \frac{A_a(r \to f)}{4\pi}\;[1 + \beta_2(r \to f)\;P_2(\cos\vartheta)] \;\equiv\; \frac{A_a(r \to f)}{4\pi}\;[1 + \alpha_2(\alpha_r \mathbb{J}_r \to \alpha_f \mathbb{J}_f)\,\mathcal{A}_{20}(\alpha_r \mathbb{J}_r)\;P_2(\cos\vartheta)]\,.$$

In this case, the overall form of the angular distribution for the photoinduced Auger emission coincides with those for the (direct) photoelectron emission, although the asymmetry parameter β is now a product of two factors: $\beta_2(r \to f) = \alpha_2(\alpha_r \mathbb{J}_r \to \alpha_f \mathbb{J}_f)\;\mathcal{A}_{20}(\alpha_r \mathbb{J}_r)$. However, this factorization of the β_2 anisotropy parameter is only valid if the initial level is (sufficiently) well isolated.

➢ The angular distribution of the emitted Auger electrons is sensitive to the phase difference between the Auger amplitudes, in contrast to the total probability $A(i \to f)$. Since the coefficients are symmetric with regard to an interchange $\kappa \leftrightarrow \kappa'$ in the summation of the angular distribution, this distribution is invariant also with respect to the inversion: $\vartheta \to \pi - \vartheta$, $\varphi \to \varphi + \pi$, simply because it only contains the spherical harmonics of even rank.

Spin polarization of resonantly emitted Auger electrons:

➢ The spin polarization of Auger electrons is usually described by an polarization vector $\mathbf{P}$. The three components of $\mathbf{P}$ can be expressed in terms of the statistical tensors of the initial level as well as the intrinsic anisotropy parameters of the considered Auger transition.

➢ Two coordinate systems, $S(XYZ)$ and $S'(X'Y'Z')$ are often employed in order to characterize the spin polarization of Auger electrons; cf. the figure below and Kabachnik *et al.* (2007).

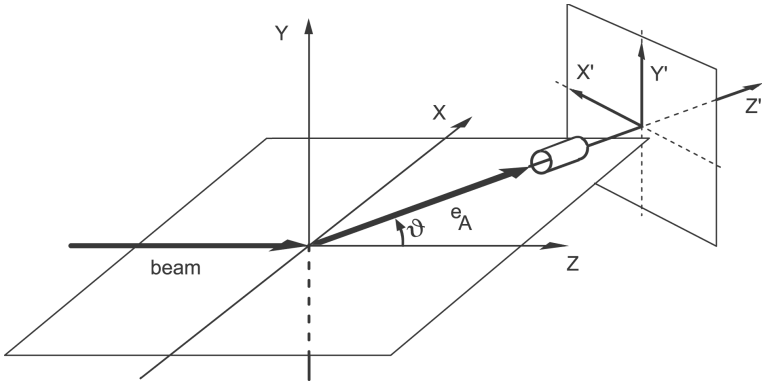

Figure 8.1.: The coordinate systems that are usually utilized for describing the Auger electron spin polarization. From Kabachnik *et al.* (2007).

➢ (Longitudinal) spin component of the emitted Auger electrons: If the initial level $|\alpha_i \mathbb{J}_i\rangle$ is produced by photoabsorption of unpolarized target atoms with monochromatic plane-wave photons, the (longitudinal) spin component of the emitted Auger electrons along their propagation direction can be written as:

$$P_{z'} \;=\; \frac{\mathcal{A}_{10}(\alpha_i \mathbb{J}_i)\; \delta_1 \;\cos\vartheta}{1 \;+\; \alpha_2(\alpha_i \mathbb{J}_i \to \alpha_f \mathbb{J}_f)\, \mathcal{A}_{20}(\alpha_i \mathbb{J}_i)\; P_2(\cos\vartheta)} \,.$$

➢ Transverse spin component: The transverse spin component within the $(x-z)$ reaction plane $P_{x'}$ and the transverse component perpendicular to the reaction plane $P_{y'}$ take the form

$$P_{x'} = \frac{\mathcal{A}_{10}(\alpha_i \mathbb{J}_i)\ \xi_1\ \sin\vartheta}{1 + \alpha_2(\alpha_i \mathbb{J}_i \to \alpha_f \mathbb{J}_f)\, \mathcal{A}_{20}(\alpha_i \mathbb{J}_i)\ P_2(\cos\vartheta)}, \qquad P_{y'} = P_y = \frac{\mathcal{A}_{20}(\alpha_i \mathbb{J}_i)\ \xi_2\ \sin 2\vartheta}{1 + \alpha_2(\alpha_i \mathbb{J}_i \to \alpha_f \mathbb{J}_f)\, \mathcal{A}_{20}(\alpha_i \mathbb{J}_i)\ P_2(\cos\vartheta)},$$

➢ For the photoionization by unpolarized or linearly polarized light, the photo ion is aligned along the beam direction or photon polarization direction, respectively. From these expressions above for the components of the spin-polarization vector, it follows then that the spin of the Auger electron can be oriented only perpendicular to the (reaction) plane that contains the alignment axis and the electron emission direction. This has been called dynamic polarization (Klar 1980, Kabachnik 1981).

➢ For the photoionization by circularly-polarized light, the photon ion is not only aligned but also oriented. In this case, the spin components of the Auger electrons in the reaction plane do not vanish. This is an example of an polarization transfer process (Klar 1980).

8.2. In JAC partly-implemented processes

8.2.a. Rayleigh & Compton scattering of light (RayleighCompton)

Process, notations & application:

➢ Rayleigh or Compton scattering of photons at an atom or ion: $A + \hbar\omega_i \longrightarrow A^{(*)} + \hbar\omega_f$ ... including $\omega_i = \omega_f$

➢ Formal quantum notation: $|\alpha_i \mathbb{J}_i M_i\rangle + \hbar\omega_i(\mathbf{k}_i, \lambda_i; \{\mathbb{M}_i\}) \longrightarrow |\alpha_f \mathbb{J}_f M_f\rangle + \hbar\omega_f(\mathbf{k}_f, \lambda_f; \{\mathbb{M}_f\})$

$\omega_i = \omega_f$ ... for elastic Rayleigh scattering

➢ Using JAC: Perform an `Atomic.Computation(.., process=Compton, processSettings=RayleighCompton.Settings(..), ..)` or call directly functions from the module `RayleighCompton`.

Motivation:

➢ The elastic scattering of light by the bound electrons of an atom or ion is commonly known as Rayleigh scattering and has been found a versatile tool in the past for studying the electronic structure of atoms and their (chemical) environment.

➢ The inelastic (Compton or Raman) scattering of light on atoms, ions or molecules is associated in contrast with an excitation of the target and has also been explored since the 1920s, both experimentally and theoretically.

➢ First theoretical investigations on the elastic scattering of photon by bound electrons date back to the mid-1930s. While initially rather simple approximations were applied, for instance based on atomic form factors, a more rigorous quantum-electrodynamical (QED) approach was developed later in terms of the relativistic second-order S-matrix amplitude.

➢ Rayleigh scattering: The Rayleigh scattering of incident light by the atomic electrons is the dominant elastic scattering mechanism for all photon energies below 2 MeV, while the nuclear Thomson, nuclear resonance and low-energy Delbrück (virtual pair) scattering is negligible for these photon energies.

➢ In JAC, the angular-differential cross sections for the elastic Rayleigh and inelastic Compton scattering are calculated and tabulated for all selected levels of $(i \rightarrow f)$ line.

Second-order scattering amplitude

➢ Compton scattering amplitude: In second-order perturbation theory, the elastic Rayleigh and inelastic Compton process can be described in terms of the two-photon transition amplitudes for a transition from substates $|\alpha_i \mathbb{J}_i M_i\rangle \rightarrow |\alpha_f \mathbb{J}_f M_f\rangle$ owing to the absorption and emission of photons with well-defined wave vectors $\mathbf{k}_{i,f}$ and polarization vectors $\boldsymbol{\epsilon}_{i,f}$. This amplitude is given in terms of the electron-photon interaction operator by (Jahrsetz *et al.*, 2015)

$$\mathcal{M}_{fi}^{(\text{Compton})}(\alpha_f \mathbb{J}_f M_f,\, \alpha_i \mathbb{J}_i M_i; \mathbf{k}_f, \boldsymbol{\epsilon}_f,\, \mathbf{k}_i, \boldsymbol{\epsilon}_i) \;=\; \sum_{\alpha_\nu \mathbb{J}_\nu M_\nu} \left[\frac{\left\langle \alpha_f \mathbb{J}_f M_f \left| \hat{R}^\dagger(\mathbf{k}_f, \boldsymbol{\epsilon}_f) \right| \alpha_\nu \mathbb{J}_\nu M_\nu \right\rangle \left\langle \alpha_\nu \mathbb{J}_\nu M_\nu \left| \hat{R}(\mathbf{k}_i, \boldsymbol{\epsilon}_i) \right| \alpha_i \mathbb{J}_i M_i \right\rangle}{E_i \,+\, \omega_i \,-\, E_\nu} \right.$$

$$\left. + \frac{\left\langle \alpha_f \mathbb{J}_f M_f \left| \hat{R}(\mathbf{k}_i, \boldsymbol{\epsilon}_i) \right| \alpha_\nu \mathbb{J}_\nu M_\nu \right\rangle \left\langle \alpha_\nu \mathbb{J}_\nu M_\nu \left| \hat{R}^\dagger(\mathbf{k}_f, \boldsymbol{\epsilon}_f) \right| \alpha_i \mathbb{J}_i M_i \right\rangle}{E_i \,-\, \omega_f \,-\, E_\nu} \right] .$$

Here, the energies of the photons involved are related by $\omega_f = \omega_i - E_f + E_i$ to each other and to the energies of the initial and final states of the atoms or ions.

➢ Owing to the time-ordering in (time-dependent) perturbation theory, there are obviously two contributions to this second-order amplitude for the *absorption-emission* and *emission-absorption* of the two photons involved.

➢ Although these second-order amplitudes can be readily written down, they are less useful for practical computations as they are based on different representations of the atomic and photon state(s); we therefore first need to perform a multipole expansion of the electron-photon interaction operators and to do all neccessary simplifications.

➢ Compton (scattering) amplitude for the scattering of photons with well-defined helicity and multipolarity:

$$\mathcal{M}_{fi}^{(\text{Compton})}(\alpha_f \mathbb{J}_f M_f,\, \alpha_i \mathbb{J}_i M_i;\, \mathbb{M}_f, \lambda_f,\, \mathbb{M}_i, \lambda_i) \;=\; \ldots \frac{\left\langle \alpha_f \mathbb{J}_f \left\| \mathbb{O}^{(\mathbb{M}_f,\, \text{emission})} \right\| \alpha_\nu \mathbb{J}_\nu \right\rangle \left\langle \alpha_\nu \mathbb{J}_\nu \left\| \mathbb{O}^{(\mathbb{M}_i,\, \text{absorption})} \right\| \alpha_i \mathbb{J}_i \right\rangle}{E_i \,+\, \omega_f \,-\, E_\nu} \;+\; \ldots$$

Angle-differential and total cross sections:

➢ Angle-differential cross section for the Compton scattering of unpolarized light by initially unpolarized atoms: For unpolarized incident plane-wave photons and if the polarization of the scattered photons as well as the magnetic sublevel population of the residual ions both remain unobserved, the angle-differential cross section is given by

$$\frac{d\sigma^{(\mathrm{Compton})}}{d\Omega}(\vartheta;\,\omega_i)$$

$$= \frac{1}{2}\frac{\omega_f}{\omega_i}\frac{1}{2J_i+1}\sum_{\lambda_i\,\lambda_i'\,\lambda_f\lambda_f'}\sum_{M_i,\,M_f} c_{\lambda_i\,\lambda_i'}\;\mathcal{M}_{fi}^{(\mathrm{Compton})}(\alpha_f\mathbb{J}_f M_f,\,\alpha_i\mathbb{J}_i M_i;\,\mathbb{M}_f,\lambda_f,\,\mathbb{M}_i,\lambda_i)\;\mathcal{M}_{fi}^{(\mathrm{Compton})}(\alpha_f\mathbb{J}_f M_f,\,\alpha_i\mathbb{J}_i M_i;\,\mathbb{M}_f,\lambda_f',\,\mathbb{M}_i,\lambda_i')$$

Unfortunately, there is no simple parametrization of this angle-differential cross section $\frac{d\sigma^{(\mathrm{Compton})}}{d\Omega}(\vartheta;\,\omega_i)$.

➢ The angle-differential Rayleigh cross sections can be obtained from the formulas above by using $|\alpha_f\mathbb{J}_f\rangle = |\alpha_i\mathbb{J}_i\rangle$ in the two-photon amplitudes and irreducible tensors.

➢ In Jac, the angle-differential Rayleigh and Compton scattering cross sections are calculated by default for all selected initial levels and $(i \to f)$ lines, if a proper spectrum is specified in `RayleighCompton.Settings.spectrum`.

8.2.b. Multi-photon excitation and decay (`MultiPhotonDeExcitation`)

Process, notations & application:

➢ Multi-photon excitation of an atom or ion: $A + n\,\hbar\omega \longrightarrow A^*$

➢ Multi-photon decay of an atom or ion: $A^* \longrightarrow A^* + n\,\hbar\omega$

➢ Formal quantum notation: $|\alpha_i\mathbb{J}_i\rangle + \hbar\omega_1(\mathbf{k}_1,\lambda_1;\,\{\mathbb{M}_1\}) + \hbar\omega_2(\mathbf{k}_2,\lambda_2;\,\{\mathbb{M}_2\}) + \ldots + \hbar\omega_n(\mathbf{k}_n,\lambda_n;\,\{\mathbb{M}_n\}) \longrightarrow |\alpha_f\mathbb{J}_f\rangle$ or

$$|\alpha_i\mathbb{J}_i\rangle \longrightarrow |\alpha_f\mathbb{J}_f\rangle + \hbar\omega_1(\mathbf{k}_1,\lambda_1;\,\{\mathbb{M}_1\}) + \hbar\omega_2(\mathbf{k}_2,\lambda_2;\,\{\mathbb{M}_2\}) + \ldots + \hbar\omega_n(\mathbf{k}_n,\lambda_n;\,\{\mathbb{M}_n\})$$

➢ Using Jac: Perform an `Atomic.Computation(.., process=MultiPhoton, processSettings=MultiPhotonDeExcitation.Settings(..), ..)` or call directly functions from the module `MultiPhotonDeExcitation`.

Motivation:

➢ The two-photon decay of few-electron ions $|\alpha_i\, \mathbb{J}_i\rangle \longrightarrow |\alpha_f\, \mathbb{J}_f\rangle + \hbar\omega_1 + \hbar\omega_2$ has often been considered, both experimentally and theoretically. For this two-photon decay, the total decay rate as well as the spectral (energy) distribution of the emittedvphotons have been explored.

➢ In Jac, only the inital and final levels are tabulated by default, together with their symmetry and total transition energy, while the proper flags must be set in `MultiPhotonDeExcitation.Settings` for all further cross section information.

Two-photon decay amplitude and total rate:

➢ Two-photon amplitude for the emission of photons with well-defined helicity and multipolarity:

$$\mathcal{M}_{fi}^{(2-\text{emission})}\,(\alpha_f \mathbb{J}_f M_f,\, \alpha_i \mathbb{J}_i M_i;\, \mathbb{M}_2, \lambda_2,\, \mathbb{M}_1, \lambda_1;\, \omega) \;=\; \frac{\big\langle \alpha_f \mathbb{J}_f \,\big\|\, \mathbb{O}^{(\mathbb{M}_2,\,\text{emission})} \,\big\|\, \alpha_\nu \mathbb{J}_\nu \big\rangle \,\big\langle \alpha_\nu \mathbb{J}_\nu \,\big\|\, \mathbb{O}^{(\mathbb{M}_1,\,\text{emission})} \,\big\|\, \alpha_i \mathbb{J}_i \big\rangle}{E_i \,-\, \omega \,-\, E_\nu}$$

➢ Two-photon energy-differential emission rate: For the transition of the atom from level $|\alpha_i \mathbb{J}_i\rangle \,\rightarrow\, |\alpha_f \mathbb{J}_f\rangle$ can be written as (Goldman and Drake, 1988; Surzhykov 2005)

$$\frac{dW}{d\omega_1}(\omega_1;\, \alpha_i\, \mathbb{J}_i \rightarrow \alpha_f\, \mathbb{J}_f) \;=\; \frac{4\pi}{2J_i \,+\, 1}\, \frac{\omega_1\, \omega_2}{(2\pi)^3\, c^2} \sum_{M_i\, M_f} \sum_{\lambda_1,\, \lambda_2} |\, \mathcal{M}_{fi}(\alpha_f \mathbb{J}_f M_f,\, \alpha_i \mathbb{J}_i M_i;\, \mathbb{M}_2, \lambda_2,\, \mathbb{M}_1, \lambda_1;\, \omega)\, |^2\, d\,\Omega_1\, d\,\Omega_2$$

$$= \frac{(4\pi)^5}{2J_i \,+\, 1}\, \frac{\omega_1\, \omega_2}{(2\pi)^3\, c^2} \sum_{\mathbb{M}_1,\, \mathbb{M}_2} \sum_{\mathbb{J}_\nu} \left\{ \frac{1}{2J_\nu \,+\, 1} \left(|S_{\mathbb{J}_\nu}^{(2-\text{emission})}(\omega_1;\, \mathbb{M}_2, \mathbb{M}_1;\, fi)|^2 \,+\, |S_{\mathbb{J}_\nu}^{(2-\text{emission})}(\omega_2;\, \mathbb{M}_1, \mathbb{M}_2;\, fi)|^2 \right) \right.$$

$$\left. + \,2 \sum_{\mathbb{J}'_\nu} (-1)^{J_\nu \,+\, J'_\nu \,+\, L_1 \,+\, L_2} \begin{Bmatrix} J_f & J'_\nu & L_1 \\ J_i & J_\nu & L_2 \end{Bmatrix} S_{\mathbb{J}_\nu}^{(2-\text{emission})}(\omega_2;\, \mathbb{M}_1, \mathbb{M}_2;\, fi)^*\; S_{\mathbb{J}_\nu}^{(2-\text{emission})}(\omega_1;\, \mathbb{M}_2, \mathbb{M}_1;\, fi) \right\}$$

Here, the summations over $\mathbb{J}_\nu$ and $\mathbb{J}'_\nu$ are restricted, and their allowed values can be quite easily read-off from the standard selection rules for the multipole matrix elements.

➢ Reduced two-photon (emission) amplitude:

$$S^{(2-\text{emission})}_{\mathbb{J}_\nu}(\omega;\, \mathbb{M}_2, \mathbb{M}_1;\, \alpha_f\, \mathbb{J}_f,\, \alpha_i\, \mathbb{J}_i) \;\equiv\; S^{(2-\text{emission})}_{\mathbb{J}_\nu}(\omega;\, \mathbb{M}_2, \mathbb{M}_1;\, fi)$$

$$= \sum_{\alpha_\nu} \frac{\left\langle \alpha_f \mathbb{J}_f \,\middle\|\, \mathcal{O}^{(\mathbb{M}_2,\,\text{emission})} \,\middle\|\, \alpha_\nu \mathbb{J}_\nu \right\rangle \left\langle \alpha_\nu \mathbb{J}_\nu \,\middle\|\, \mathcal{O}^{(\mathbb{M}_1,\,\text{emission})} \,\middle\|\, \alpha_i \mathbb{J}_i \right\rangle}{E_i \;-\; \omega \;-\; E_\nu}$$

$$= S^{(2-\text{absorption})}_{\mathbb{J}_\nu}(???\;\omega;\, \mathbb{M}_2, \mathbb{M}_1;\, fi\;???) \;=\; S^{(2-\text{Compton})}_{\mathbb{J}_\nu}(???\;\omega;\, \mathbb{M}_2, \mathbb{M}_1;\, fi\;???)$$

➢ In JAC, the two-photon energy-differential emission rate are calculated and tabulated if ...

Two-photon absorption amplitude and total rate:

➢ Two-photon absorption of monochromatic light of an atom or ion: $A \;+\; 2\,\hbar\,\omega \;\longrightarrow\; A^*$

➢ Formal quantum notation: $|\alpha_i \mathbb{J}_i\rangle \;+\; \hbar\,\omega\,(\mathbf{k}, \lambda_1;\, \{\mathbb{M}_1\}) \;+\; \hbar\,\omega\,(\mathbf{k}, \lambda_2;\, \{\mathbb{M}_2\}) \;\longrightarrow\; |\alpha_f \mathbb{J}_f\rangle \qquad E_f \;-\; E_i \;=\; 2\,\hbar\omega$

➢ Final-state density matrix following the absorption of two monochromatic photons: For a two-photon excitation (transition) $\alpha_i \mathbb{J}_i \to \alpha_f \mathbb{J}_f$ of an atom or ion by (two) monochromatic and equally-polarized photons, the final-state density matrix $\left\langle \alpha_f \mathbb{J}_f M_f \,|\, \rho_f \,|\, \alpha_f \mathbb{J}_f M'_f \right\rangle$ of the residual photoion can be expressed in terms of the intial-state density matrix $\langle \alpha_i \mathbb{J}_i M_i \,|\, \rho_i \,|\, \alpha_i \mathbb{J}_i M'_i \rangle$ of the atom, the photon density matrices

$c_{\lambda\lambda'}$ of the two photons as well as the two-photon transition amplitudes by

$$\langle \alpha_f \mathbb{J}_f M_f \,|\, \rho_f \,|\, \alpha_f \mathbb{J}_f M'_f \rangle$$

$$= \sum_{\lambda_1\lambda'_1,\,\lambda_2\lambda'_2} c_{\lambda_1\lambda'_1}\, c_{\lambda_2\lambda'_2}\, \langle \alpha_i \mathbb{J}_i M_i \,|\, \rho_i \,|\, \alpha_i \mathbb{J}_i M'_i \rangle\ \mathcal{M}(\mathbf{k},\lambda_2,\lambda_1;\ \alpha_i \mathbb{J}_i M_i \ \to\ \alpha_f \mathbb{J}_f M_f)\ \mathcal{M}(\mathbf{k},\lambda'_2,\lambda'_1;\ \alpha_i \mathbb{J}_i M_i \ \to\ \alpha_f \mathbb{J}_f M_f)$$

$$\mathcal{M}(\mathbf{k},\lambda_2,\lambda_1;\ \alpha_i \mathbb{J}_i M_i \ \to\ \alpha_f \mathbb{J}_f M_f)$$

$$= \sum_{\alpha_\nu \mathbb{J}_\nu M_\nu} \frac{\langle \alpha_f \mathbb{J}_f M_f \,|\, R(\mathbf{k},\mathbf{u}_{\lambda_2}) |\, \alpha_\nu \mathbb{J}_\nu M_\nu \rangle\, \langle \alpha_\nu \mathbb{J}_\nu M_\nu \,|\, R(\mathbf{k},\mathbf{u}_{\lambda_1}) |\, \alpha_i \mathbb{J}_i M_i \rangle}{E_i \,+\, \omega \,-\, E_\nu}$$

$$= 2\pi \sum_{Kq} \sum_{\mathbb{M}_1\,\mathbb{M}_2,\,\mathbb{J}_\nu} i^{L_1-p_1+L_2-p_2}\, (-\lambda_1)^{p_1}\, (-\lambda_2)^{p_2}\, (-1)^{J_f-M_f+K-q}\, \sqrt{[L_1,L_2]}\, [K] \begin{pmatrix} K & J_f & J_i \\ q & -M_f & M_i \end{pmatrix} \begin{pmatrix} L_2 & L_1 & K \\ \lambda_1 & \lambda_2 & -q \end{pmatrix}$$

$$\times \quad \begin{Bmatrix} J_i & J_f & K \\ L_2 & L_1 & J_\nu \end{Bmatrix} \sum_{\alpha_\nu} \frac{\langle \alpha_f \mathbb{J}_f \,\|\, \mathbb{O}^{(\mathbb{M}_2,\,\text{absorption})} \,\|\, \alpha_\nu \mathbb{J}_\nu \rangle\, \langle \alpha_\nu \mathbb{J}_\nu \,\|\, \mathbb{O}^{(\mathbb{M}_1,\,\text{absorption})} \,\|\, \alpha_i \mathbb{J}_i \rangle}{E_i \,+\, \omega - E_\nu} \,.$$

$$= 2\pi \sum_{Kq} \sum_{\mathbb{M}_1\,\mathbb{M}_2,\,\mathbb{J}_\nu} i^{L_1-p_1+L_2-p_2}\, (-\lambda_1)^{p_1}\, (-\lambda_2)^{p_2}\, (-1)^{J_f-M_f+K-q}\, \sqrt{[L_1,L_2]}\, [K] \begin{pmatrix} K & J_f & J_i \\ q & -M_f & M_i \end{pmatrix} \begin{pmatrix} L_2 & L_1 & K \\ \lambda_1 & \lambda_2 & -q \end{pmatrix}$$

$$\times \quad \mathcal{U}^{(K,\,\text{absorption})}(\alpha_f \mathbb{J}_f, \mathbb{M}_2, \mathbb{J}_\nu, \omega,\ \mathbb{M}_1, \alpha_i \mathbb{J}_i)$$

➢ Reduced two-photon absorption amplitude:

$$\mathcal{U}^{(K,\,\text{absorption})}(\alpha_f \mathbb{J}_f, \mathbb{M}_2, \mathbb{J}_\nu, \omega,\ \mathbb{M}_1, \alpha_i \mathbb{J}_i) \ = \ \begin{Bmatrix} J_i & J_f & K \\ L_2 & L_1 & J_\nu \end{Bmatrix} \sum_{\alpha_\nu} \frac{\langle \alpha_f \mathbb{J}_f \,\|\, \mathbb{O}^{(\mathbb{M}_2,\,\text{absorption})} \,\|\, \alpha_\nu \mathbb{J}_\nu \rangle\, \langle \alpha_\nu \mathbb{J}_\nu \,\|\, \mathbb{O}^{(\mathbb{M}_1,\,\text{absorption})} \,\|\, \alpha_i \mathbb{J}_i \rangle}{E_i \,+\, \omega - E_\nu}$$

In the reduced amplitude $\mathcal{U}^{(K)}(\alpha_f \mathbb{J}_f, \mathbb{M}_2, \mathbb{J}_\nu, \omega,\ \mathbb{M}_1, \alpha_i \mathbb{J}_i)$ above, the summation α_ν runs over all the atomic states of given symmetry $\mathbb{J}_\nu$, i.e. over all the ASf as provided by a given Green function channel of symmtry $\mathbb{J}$.

➢ Total two-photon absorption cross sections: For initially unpolarized atoms, the two-photon absorption cross section for the transition $\alpha_i \mathbb{J}_i \rightarrow \alpha_f \mathbb{J}_f$ and for the absorption of two arbitrary but equally-polarized photons with $c_{\lambda\lambda'} = c_{\lambda\lambda'}(P_1, P_2, P_3)$ is given by

$$\sigma^{(2\gamma\ \text{absorption})}(\alpha_i \mathbb{J}_i + 2\omega \rightarrow \alpha_f \mathbb{J}_f)$$

$$= \frac{8\pi^3\,\alpha^2}{\omega^2\ [J_i]} \sum_{M_i M_f} \langle \alpha_f \mathbb{J}_f M_f \,|\, \rho_f \,|\, \alpha_f \mathbb{J}_f M_f \rangle$$

$$= \frac{8\pi^3\,\alpha^2}{\omega^2\ [J_i]} \sum_{M_i M_f} \sum_{\lambda_1\lambda_1',\,\lambda_2\lambda_2'} c_{\lambda_1\lambda_1'}\, c_{\lambda_2\lambda_2'}\, \mathcal{M}(\mathbf{k}, \lambda_2, \lambda_1;\ \alpha_i \mathbb{J}_i M_i \rightarrow \alpha_f \mathbb{J}_f M_f)\ \mathcal{M}(\mathbf{k}, \lambda_2', \lambda_1';\ \alpha_i \mathbb{J}_i M_i \rightarrow \alpha_f \mathbb{J}_f M_f)$$

$$= \frac{32\pi^5\,\alpha^2}{\omega^2\ [J_i]} \sum_{\lambda_1\lambda_1',\,\lambda_2\lambda_2'} c_{\lambda_1\lambda_1'}\, c_{\lambda_2\lambda_2'} \sum_{Kq} \sum_{\mathbb{M}_1\,\mathbb{M}_2,\,\mathbb{J}_\nu} i^{L_1-p_1+L_2-p_2}\,(-\lambda_1)^{p_1}\,(-\lambda_2)^{p_2}\,(-1)^{K-q}\,\sqrt{[L_1, L_2]} \begin{pmatrix} L_1 & L_2 & K \\ \lambda_1 & \lambda_2 & -q \end{pmatrix}$$

$$\times \sum_{\mathbb{M}_1'\,\mathbb{M}_2',\,\mathbb{J}_\nu'} i^{L_1'-p_1'+L_2'-p_2'}\,(-\lambda_1')^{p_1'}\,(-\lambda_2')^{p_2'}\,(-1)^{K-q}\,\sqrt{[L_1', L_2']} \begin{pmatrix} L_1' & L_2' & K \\ \lambda_1' & \lambda_2' & -q \end{pmatrix}$$

$$\times \quad \mathcal{U}^{(K,\,\text{absorption})}(\alpha_f \mathbb{J}_f, \mathbb{M}_2, \mathbb{J}_\nu, \omega,\ \mathbb{M}_1, \alpha_i \mathbb{J}_i)\ \mathcal{U}^{(K,\,\text{absorption})}(\alpha_f \mathbb{J}_f, \mathbb{M}_2', \mathbb{J}_\nu', \omega,\ \mathbb{M}_1', \alpha_i \mathbb{J}_i)$$

➢ Two-photon absorption cross section for linearly-polarized photons: For linear-polarization $(P_1 = 1)$, the total two-photon amplitude contains a full summation over λ_1, λ_2, and the two-photon absorption cross section becomes

$$\sigma^{(2\gamma\ \text{absorption, linear})}(\alpha_i \mathbb{J}_i + 2\omega \rightarrow \alpha_f \mathbb{J}_f)$$

$$= \frac{8\,\pi^5\,\alpha^2}{\omega^2\ [J_i]} \sum_{Kq} \left| \sum_{\lambda_1\lambda_2} \sum_{\mathbb{M}_1\mathbb{M}_2\,\mathbb{J}_\nu} i^{L_1-p_1+L_2-p_2}\,(-\lambda_1)^{p_1}\,(-\lambda_2)^{p_2}\,[L_1, L_2]^{1/2} \begin{pmatrix} L_1 & L_2 & K \\ \lambda_1 & \lambda_2 & -q \end{pmatrix} \begin{pmatrix} J_i & J_f & K \\ L_2 & L_1 & J_\nu \end{pmatrix} \right.$$

$$\left. \times \quad \mathcal{U}^{(K,\,\text{absorption})}(\alpha_f \mathbb{J}_f, \mathbb{M}_2, \mathbb{J}_\nu, \omega,\ \mathbb{M}_1, \alpha_i \mathbb{J}_i) \right|^2$$

➢ Two-photon absorption cross section for right-circularly polarized photons: For right-circularly polarized light $(P_3 = 1)$, the two-photon absorption cross section is given by

$$\sigma^{(2\gamma\ \text{absorption},\,\circlearrowleft)}(\alpha_i \mathbb{J}_i + 2\omega \rightarrow \alpha_f \mathbb{J}_f)$$

$$= \frac{8\,\pi^5\,\alpha^2}{\omega^2\ [J_i]} \sum_{Kq} \left| \sum_{\mathbb{M}_1 \mathbb{M}_2\ \mathbb{J}_\nu} i^{L_1 - p_1 + L_2 - p_2}\ [L_1, L_2]^{1/2} \begin{pmatrix} L_1 & L_2 & K \\ 1 & 1 & -q \end{pmatrix} \begin{pmatrix} J_i & J_f & K \\ L_2 & L_1 & J_\nu \end{pmatrix} \mathcal{U}^{(K,\,\text{absorption})}(\alpha_f \mathbb{J}_f, \mathbb{M}_2, \mathbb{J}_\nu, \omega,\ \mathbb{M}_1, \alpha_i \mathbb{J}_i) \right|^2$$

➢ Two-photon absorption cross section for unpolarized photons: For unpolarized light $(P_1 = P_2 = P_3 = 0)$, the summation over λ_1, λ_2 occurs *outside* of the modulus (of the amplitude), and the two-photon absorption cross section becomes

$$\sigma^{(2\gamma\ \text{absorption},\,\circlearrowleft)}(\alpha_i \mathbb{J}_i + 2\omega \rightarrow \alpha_f \mathbb{J}_f)$$

$$= \frac{8\,\pi^5\,\alpha^2}{\omega^2\ [J_i]} \sum_{Kq} \sum_{\lambda_1 \lambda_2} \left| \sum_{\mathbb{M}_1 \mathbb{M}_2\ \mathbb{J}_\nu} i^{L_1 - p_1 + L_2 - p_2}\ (-\lambda_1)^{p_1}\ (-\lambda_2)^{p_2}\ [L_1, L_2]^{1/2} \begin{pmatrix} L_1 & L_2 & K \\ \lambda_1 & \lambda_2 & -q \end{pmatrix} \begin{pmatrix} J_i & J_f & K \\ L_2 & L_1 & J_\nu \end{pmatrix} \right.$$

$$\left. \times\ \mathcal{U}^{(K,\,\text{absorption})}(\alpha_f \mathbb{J}_f, \mathbb{M}_2, \mathbb{J}_\nu, \omega,\ \mathbb{M}_1, \alpha_i \mathbb{J}_i) \right|^2$$

8.2.c. Multi-photon ionization (`MultiPhotonIonization`)

Process, notations & application:

➢ Multi-photon ionization: of an atom or ion $A + n\,\hbar\,\omega \longrightarrow A^{(*)} + e_p^-$

➢ Formal quantum notation: $|\alpha_i \mathbb{J}_i\rangle + \hbar\,\omega_1(\mathbb{M}_1) + \hbar\,\omega_2(\mathbb{M}_2) + ... + \hbar\,\omega_n(\mathbb{M}_n) \longrightarrow |\alpha_f \mathbb{J}_f\rangle + |\varepsilon\,\kappa\rangle$

➢ If the photon energy is smaller than the ionization threshold of the atom, it can still be ionized due to its simultaneous interaction with several photons. However, the probability generally decreases rapidly with the number of photons N, that are required to overcome the ionization threshold.

➢ Multi-photon ionization is studied mainly by means of intense, pulsed lasers. The ionization probability is for moderate intensities proportional to the N-th power of the intensity, I^N, while this power law breaks down at high intensities due to the ac-Stark effect.

➢ In first strong-field laser experiments, a rather large probability was found for a multiple ionization of atoms, relative to single-ionization probability, and gave rise to various speculation about *collective modes* in the electronic motion of atoms and ions.

Two-photon ionization with monochromatic light:

➢ Formal quantum notation: $|\alpha_i \mathbb{J}_i\rangle \; + \; \hbar\,\omega(\mathbb{M}_1) \; + \; \hbar\,\omega(\mathbb{M}_2) \quad \longrightarrow \quad |\alpha_f \mathbb{J}_f\rangle \; + \; |\varepsilon\,\kappa\rangle\,;$ equally-polarized photons

➢ Final-state density matrix of the 'photo-ion + photo-electron': For the two-photon ionization with monochromatic and equally-polarized photons (typically from the same beam), the photoion is found in the final level $|\alpha_f \mathbb{J}_f\rangle$, while the *free* photoeelectron is emitted with asymptotic linear momentum $\mathbf{p}$ and spin projection m_s . In a basis of well-defined angular momenta $\mathbb{J}_i$, $\mathbb{J}_f$, the initial-state density matrix is $\langle \alpha_i \mathbb{J}_i M_i \,|\, \rho_i \,|\, \alpha_i \mathbb{J}_i M_i' \rangle$, and the final-state density matrix can be written as:

$$\begin{aligned}
\left\langle \alpha_f \mathbb{J}_f M_f,\; \mathbf{p}\, m_s \,|\, \rho_f \,|\, \alpha_f \mathbb{J}_f M_f',\; \mathbf{p}, m_s' \right\rangle \;=\; & \sum_{\lambda_1\,\lambda_1'\,\lambda_2\,\lambda_2'} \langle \mathbf{k}\,\lambda_1 \,|\, \rho_\gamma \,|\, \mathbf{k}\,\lambda_1' \rangle \; \langle \mathbf{k}\,\lambda_2 \,|\, \rho_\gamma \,|\, \mathbf{k}\,\lambda_2' \rangle \; \langle \alpha_i \mathbb{J}_i \, M_i \,|\, \rho_i \,|\, \alpha_i \mathbb{J}_i \, M_i' \rangle \\
& \times \sum\!\!\!\!\!\!\int_\nu \frac{\left\langle \alpha_f \mathbb{J}_f M_f,\; \mathbf{p} m_s \left| \sum_j \; \alpha_j \mathbf{u}_{\lambda_2 j}\, e^{i\mathbf{k}\cdot\mathbf{r}_j} \right| \alpha_\nu \mathbb{J}_\nu M_\nu \right\rangle \left\langle \alpha_\nu \mathbb{J}_\nu M_\nu \left| \sum_n \alpha_n \mathbf{u}_{\lambda_1 j}\, e^{i\mathbf{k}\cdot\mathbf{r}_j} \right| \alpha_i J_i M_i \right\rangle}{E_{\alpha_i \mathbb{J}_i} + \omega \; - \; E_{\alpha_\nu \mathbb{J}_\nu}} \\
& \times \sum\!\!\!\!\!\!\int_\nu \frac{\left\langle \alpha_f J_f M_f',\; \mathbf{p} m_s' \left| \sum_j : \alpha_n \mathbf{u}_{\lambda_2' j}\, e^{i\mathbf{k}\cdot\mathbf{r}_j} \right| \alpha_\nu' \mathbb{J}_\nu' M_\nu' \right\rangle \left\langle \alpha_\nu' \mathbb{J}_\nu' M_\nu' \left| \sum_n \alpha_n \mathbf{u}_{\lambda_1' j}\, e^{i\mathbf{k}\cdot\mathbf{r}_j} \right| \alpha_i J_i M_i' \right\rangle}{E_{\alpha_i \mathbb{J}_i} \; + \; \omega - E_{\alpha_\nu' \mathbb{J}_\nu'}} .
\end{aligned}$$

➢ Total two-photon ionization cross sections for initially unpolarized atoms For initially unpolarized atoms and equally-polarized plane-wave photons with wave vector $\mathbf{k} \,||\, \mathbf{e}_z$ and Stokes parameters P_1, P_2, P_3 , the total two-photon ionization cross sections for the transition

$|\alpha_i J_i\rangle \to |\alpha_f J_f\rangle$ is given by:

$$\sigma(\alpha_i J_i \to \alpha_f J_f) \;=\; \frac{32\pi^5\,\alpha^2}{\omega^2\,[J_i]} \sum_{M_i} \sum_{\lambda_1\lambda_1'\,\lambda_2\lambda_2'} \langle \mathbf{k}\,\lambda_1 \,|\, \rho_{\,\gamma} |\, \mathbf{k}\,\lambda_1'\rangle\; \langle \mathbf{k}\,\lambda_2 \,|\, \rho_{\,\gamma} |\, \mathbf{k}\,\lambda_2'\rangle \sum_{J_t M_t \kappa} \mathcal{M}^{\lambda_1\lambda_2}_{\kappa \mathbb{J}_t M_t}\, \mathcal{M}^{\lambda_1'\lambda_2'*}_{\kappa \mathbb{J}_t M_t}$$

$$\mathcal{M}^{\lambda_1\,\lambda_2}_{\kappa \mathbb{J} M} \;=\; \sum_{\mathbb{M}_1\,\mathbb{M}_2} \sum\!\!\!\!\!\!\int_{\mathbb{J}_\nu M_\nu} i^{L_1+L_2}\; \frac{[L_1,\,L_2]^{1/2}}{[J_\nu,\,J]^{1/2}}\; (i\lambda_1)^{p_1}\; (i\lambda_2)^{p_2}\; \langle J_i M_i,\, L_1\lambda_1 \,|\, J_\nu M_\nu\rangle\; \langle J_\nu M_\nu,\, L_2\lambda_2 \,|\, JM\rangle$$

$$\times\; \frac{\big\langle (\alpha_f \mathbb{J}_f,\, \varepsilon\kappa)\mathbb{J} \,\big\|\, \mathbb{O}^{\,(\mathbb{M}_1,\,\text{photoionization})} \,\big\|\, \alpha_\nu J_\nu \big\rangle\; \big\langle \alpha_\nu \mathbb{J}_\nu \,\big\|\, \mathbb{O}^{\,(\mathbb{M}_2,\,\text{absorption})} \big\|\, \alpha_i \mathbb{J}_i \big\rangle}{E_{\alpha_i \mathbb{J}_i} \;+\; \omega \;-\; E_{\alpha_\nu \mathbb{J}_\nu}}.$$

➢ Total two-photon ionization cross sections for initially unpolarized atoms and unpolarized light: For initially unpolarized atoms and unpolarized plane-wave photons with wave vector $\mathbf{k} \,||\, \mathbf{e}_z$, the total two-photon ionization cross sections for the transition $|\alpha_i J_i\rangle \to |\alpha_f J_f\rangle$ is given by:

$$\sigma(\alpha_i J_i \to \alpha_f J_f) \;=\; \ldots$$

8.2.d. Coulomb excitation (CoulombExcitation)

Process, notations & application:

- Coulomb excitation of an atom or ion by fast, heavy ions: $A + Z_p \longrightarrow A^* + Z_p$ (projectile remains unaffected)
- Formal quantum notation: $|\alpha_i \mathbb{J}_i\rangle + Z_p(\beta_p) \longrightarrow |\alpha_f \mathbb{J}_f\rangle\,, \qquad \beta_p = \frac{v_p}{c}$
- Using JAC: Perform an `Atomic.Computation(.., process=CoulExc, processSettings=CoulombExcitation.Settings(..), ..)` or call directly functions from the module `CoulombExcitation`.

Motivation

- In Coulomb excitation processes, one often assumes that a single electron from a (fast-moving) projectile ion with relative velocity $\beta_p = v_p/c$ (with regard to the target) is excited by a target nucleus at rest.
- Of course, an analogue process occurs also when we consider the excitation of the target that may occur due to a fast-moving (bare) projectile ion, and in which case the role of the projectile and target need simply to be interchanged in all formulas below.
- The Coulomb excitation or ionization of the projectile (ion) will be affected, in addition, also by the target electrons (or, *vice versa,* the projectile electrons) but such rather small effects are often not considered in detail.
- The Coulomb excitation of few-electron ions in fast ion-atom collisions leads to the formation of excited ionic states. In typical ion-atom collision experiments, a *prefared* direction is hereby defined for the overall systems, both at storage rings and the EBIT, and this typically results in an *alignment* of the excited ions along this distinct direction.
- The first step in calculating energy- and angle-differential as well as total Coulomb excitation cross sections usually refers to determining the impact-parameter dependence of the excitation probability $P(b)$. The weighted K-shell Coulomb excitation probability $2\pi\, b\, P(b)$ is known to have a maximum in the vincinity of the K-shell radius. This is quite similar as for the Coulomb ionization probabilities.
- In JAC, the partial and total Coulomb excitation cross sections are calculated and tabulated by default for all selected pairs of initial and final levels.

Coulomb excitation amplitude of few-electron projectile ions in position space

➢ Coulomb (excitation) amplitude for the excitation of a (single) projectile electron: If a one-electron projectile moves at a trajectory with impact parameter b, the amplitude for an excitation from level $i \to f$ is given by Eichler & Meyerhof (1995, Eq. 6.2)

$$\mathcal{M}_{fi}^{(\mathrm{Coulex})}(b) = i\,\frac{\gamma\,Z_t\,e^2}{\hbar}\int dt\,\exp\left(\frac{i}{\hbar}\,(E_f-E_i)\,t\right)\int d^3r\,\psi_f^\dagger(\mathbf{r})\,\frac{(1-\beta_p\,\alpha_z)}{r'(t)}\;\psi_i(\mathbf{r}),$$

$$r'(t) = \sqrt{(x-b)^2+y^2+\gamma^2\,(z-v\,t)^2}, \qquad \beta_p = \frac{v_p}{c},$$

where $\mathbf{r}$ is the coordinate of the projectile electron, $r'(t)$ its (time-dependent) distance from the target nucleus, and where $\psi_f(\mathbf{r})$ and $\psi_i(\mathbf{r})$ denote the final- and initial-state eigenfunctions of the projectile electron with energies E_f and E_i.

➢ Coulomb (excitation) amplitude for the excitation of a many-electron projectile (ion): For an Coulomb excitation of a many-electron projectile from the sublevel $|\alpha_i\,\mathbb{J}_i M_i\rangle \to |\alpha_f\,\mathbb{J}_f M_f\rangle$, the excitation amplitude for given impact parameter b can then be written in first-order perturbation theory and natural units ($\hbar = m_\mathrm{e} = c = 1$) as:

$$\mathcal{M}_{fi}^{(\mathrm{Coulex})}(b;\,\alpha_f\,\mathbb{J}_f M_f,\,\alpha_i\,\mathbb{J}_i M_i) = i\,\gamma\,\alpha\,Z_t\int dt\;e^{i\,(E_f-E_i)t}\left\langle \alpha_f\mathbb{J}_f M_f\left|\sum_{k=1}^{N}\frac{1-\beta_p\,\hat{\alpha}_z(k)}{r'_k(t)}\right|\alpha_i\mathbb{J}_i M_i\right\rangle.$$

➢ From this transition amplitude, the cross section for an excitation of the projectile from (sub-) level $|\alpha_i\,\mathbb{J}_i\rangle \to |\alpha_f\mathbb{J}_f M_f\rangle$ can be obtained by integrating over all the impact parameters b and by taking the average over the initial magnetic sublevels M_i.

➢ In Jac, we do not use the Coulomb excitation amplitude in position space but make use of a representation of this amplitude in momentum space instead, see below.

Coulomb excitation amplitude of few-electron projectile ions in momentum space:

➢ Coulomb (excitation) amplitude for the excitation of a (single) projectile electron: To evaluate Coulomb excitation cross sections for one- and many-electron atoms, it is often more convinient to work in momentum space and to express all properties in terms of the

Fourier transform of the Coulomb excitation amplitude in position space. If we make use of the momentum transfer $\mathbf{q} = (\mathbf{q}_b, q_z)$, the time-integration in this Coulomb (excitation) amplitude can be carried out explicitly (Eichler & Meyerhof 1995, Eq. 6.4)

$$\mathcal{M}_{fi}^{(\mathrm{Coulex})}(b) = \frac{i\,\nu_p}{\pi}\int \frac{d^2\,q_b}{q_b^2+(1-\beta^2)\,q_0^2}\; e^{-i\,\mathbf{q}_0\cdot\mathbf{b}}\,\mathcal{K}_{fi}^{(\mathrm{Coulex})}(\mathbf{q})\,; \qquad \mathcal{K}_{fi}^{(\mathrm{Coulex})}(\mathbf{q}) = \left\langle \psi_f(\mathbf{r})\left|(1-\beta\,\alpha_z)\,e^{i\,\mathbf{q}\cdot\mathbf{r}}\right|\psi_i(\mathbf{r})\right\rangle .$$

This formula removes the complicated time dependence in $r'(t)$ and replaces it instead by an explicit wave number (momentum transfer) dependence.

➢ Note, that in momentum space, the (momentum-space) Coulomb excitation amplitude $\mathcal{K}_{fi}^{(\mathrm{Coulex})}(\mathbf{q})$ does no longer depend on the impact parameter b but now simply contains an integration over the momentum transfer $\mathbf{q}$, and which starts from the minimum momentum transfer for the excitation of the initial ion from level $|i\rangle \rightarrow |f\rangle$: $q_0 = (E_f - E_i)/v_p$.

➢ In momentum space, indeed, most Coulomb excitation cross sections can be expressed directly in terms of the momentum-space Coulomb excitation amplitude $\mathcal{K}_{fi}^{(\mathrm{Coulex})}(\mathbf{q})$.

➢ (Momentum-space) Coulomb excitation amplitude for many-electron projectiles: This amplitude can be further simplified by using the Wigner-Eckert theorem (Surzhykov and Fritzsche, 2008)

$$\mathcal{K}_{fi}^{(\mathrm{Coulex})}(\mathbf{q};\,\alpha_f\,\mathbb{J}_f M_f,\,\alpha_i\,\mathbb{J}_i M_i) \;=\; \left\langle \alpha_f\,\mathbb{J}_f M_f \left| \sum_k^N (1-\beta\,\alpha_z(k))\; e^{i\,\mathbf{q}\cdot\mathbf{r}_k} \right| \alpha_i\,\mathbb{J}_i M_i \right\rangle$$

$$= \sum_{LM} i^L\, Y^*_{LM}(\arccos(q_0/q),0)\, \left\langle \alpha_f \mathbb{J}_f M_f \left| \sum_{k=1}^N (1-\beta_p\,\hat{\alpha}_z(k))\; j_L(q\,r_k)\; Y_{LM}(\vartheta_k,\varphi_k) \right| \alpha_i \mathbb{J}_i M_i \right\rangle ,$$

$$= \sum_t \frac{1}{\sqrt{2J_f+1}}\, \langle J_i M_i,\, t\,(M_f-M_i) \,|\, J_f M_f\rangle \sum_L i^L\, Y^*_{L,\,M_f-M_i}(\arccos(q_0/q),0)\, \left\langle \alpha_f \mathbb{J}_f \left\| H_{tL}^{(\mathrm{Coulex})}(q) \right\| \alpha_i \mathbb{J}_i \right\rangle$$

$$= \sum_t \frac{1}{\sqrt{2J_f+1}}\, \langle J_i M_i,\, t\,(M_f-M_i) \,|\, J_f M_f\rangle \sum_L i^L\, Y^*_{L,\,M_f-M_i}(\arccos(q_0/q),0)$$

$$\times\; \left(\delta_{t\,L}\, \left\langle \alpha_f \mathbb{J}_f \left\| \mathbb{K}^{(\mathrm{L,\,Coulex,\,jY})} \right\| \alpha_i \mathbb{J}_i \right\rangle \;-\; \beta_p\, \langle LM,\,10\,|\,tM\rangle\, \left\langle \alpha_f \mathbb{J}_f \left\| \mathbb{K}^{(\mathrm{t,\,Coulex,\,jT})} \right\| \alpha_i \mathbb{J}_i \right\rangle\right)$$

➢ In Jac, these (momentum-space) Coulomb excitation amplitudes $\mathcal{K}_{fi}^{(\mathrm{Coulex})}(\mathbf{q};\,\alpha_f\,\mathbb{J}_f M_f,\,\alpha_i\,\mathbb{J}_i M_i)$ are implemented explicitly and the integration over q is typically performed by a Gauß-Legendre integration.

Coulomb excitation operators and interaction strength:

➢ Coulomb excitation (interaction) strength: The (full) Coulomb excitation amplitude in momentum space above combines two kinds of reduced (many-electron) matrix elements due to the two interaction operators: $\sum_{k=1}^N j_L(q\,r_k) Y_L(\vartheta_k,\varphi_k)$ of rank L as well as $\sum_{k=1}^N j_L(q\,r_k)\,\hat{\boldsymbol{\alpha}}(k)\cdot \mathrm{T}_{tL}(\vartheta_k,\varphi_k)$ of rank t, respectively. These two reduced matrix elements are the actual building blocks that are needed in order to represent and to explore the properties of the target or projectile excitation process.

➢ Coulomb excitation (interaction) strength: The building blocks for the computation of the Coulomb excitation and ionization amplitudes

are given by the reduced matrix elements

$$\left\langle \alpha_f \mathbb{J}_f \left\| \mathbb{K}^{(\mathrm{L,\,Coulex,\,jY})} \right\| \alpha_i \mathbb{J}_i \right\rangle = \left\langle \alpha_f \mathbb{J}_f \left\| \sum_{k=1}^{N} j_L(q\, r_k)\, Y_L(\vartheta_k, \varphi_k) \right\| \alpha_i \mathbb{J}_i \right\rangle$$

$$\left\langle \alpha_f \mathbb{J}_f \left\| \mathbb{K}^{(\mathrm{t,\,Coulex,\,jT})} \right\| \alpha_i \mathbb{J}_i \right\rangle = \left\langle \alpha_f \mathbb{J}_f \left\| \sum_{k=1}^{N} j_L(q\, r_k)\, \hat{\boldsymbol{\alpha}}(k) \cdot \boldsymbol{T}_{tL}(\vartheta_k, \varphi_k) \right\| \alpha_i \mathbb{J}_i \right\rangle$$

Energie-differential, partial and total Coulomb excitation cross sections:

➢ Partial Coulomb excitation cross section: If the Fourier transformation from the position to momentum coordinates is performed, the integrals over the time t and the impact parameter b can be evaluated *analytically*. Then, the partial (excitation) cross section for the Coulomb excitation from (sub-) levels $|\alpha_i \mathbb{J}_i\rangle \to |\alpha_f \mathbb{J}_f M_f\rangle$ can be written as (Surzhykov and Fritzsche, 2008)

$$\sigma(\alpha_i \mathbb{J}_i \to \alpha_f \mathbb{J}_f M_f) = \frac{2\pi}{2J_i + 1} \sum_{M_i} \int_0^\infty \mathrm{d}b\, b \left| \mathcal{M}_{fi}^{(\mathrm{Coulex})}(b;\, \alpha_f\, \mathbb{J}_f M_f,\, \alpha_i\, \mathbb{J}_i M_i) \right|^2$$

$$= 2\pi \left(\frac{8\,\pi\, Z_t\, \alpha}{\beta_p} \right)^2 \frac{1}{2J_i + 1} \sum_{M_i} \int_{q_0}^\infty dq\, \frac{q}{\left(q^2 - q_0^2 \beta_p^2\right)^2} \left| \mathcal{K}_{fi}^{(\mathrm{Coulex})}(\mathbf{q};\, \alpha_f\, \mathbb{J}_f M_f,\, \alpha_i\, \mathbb{J}_i M_i) \right|^2 .$$

Alignment of Coulomb-excited ions:

➢ Alignment of Coulomb-excited ions in level $|\alpha_f \mathbb{J}_f\rangle$: For a well-defined ion-atom collision axis, a Coulomb-excited ion in level $|\alpha_f \mathbb{J}_f\rangle$ is generally aligned; this alignment depends on the partial Coulomb cross sections $\sigma(\alpha_f\, \mathbb{J}_f M_f)$ can be described in terms of one (or several)

parameters $\mathcal{A}_k(\alpha_f \mathbb{J}_f)$:

$$\mathcal{A}_k(\alpha_i \mathbb{J}_i \to \alpha_f \mathbb{J}_f) \;=\; \frac{\sqrt{2J_f+1}}{\sigma(\alpha_i \mathbb{J}_i \to \alpha_f \mathbb{J}_f)} \sum_{M_f} (-1)^{J_f - M_f} \, \langle J_f M_f \, J_f - M_f \,|\, k0 \rangle \;\; \sigma(\alpha_i \mathbb{J}_i \to \alpha_f \mathbb{J}_f M_f) \,,$$

8.2.e. Photoionization & fluorescence (PhotoIonizationFluor)

Process, notations & application:

- ➢ Photoionization of an atom or ion with subsequent fluorescence emission: $A + \hbar\omega \;\longrightarrow\; A^* + e_p^- \;\longrightarrow\; A^{(*)} + e_p^- + \hbar\omega'$
- ➢ Formal quantum notation: $|\alpha_i \mathbb{J}_i\rangle + \hbar\omega \;\longrightarrow\; |\alpha_e \mathbb{J}_e\rangle + |\varepsilon\kappa\rangle \;\longrightarrow\; |\alpha_f \mathbb{J}_f\rangle + |\varepsilon\kappa\rangle + \hbar\omega_f(\mathbb{M})$
- ➢ Apart from astrophysical interest, emphasis on the photoionization of inner-shell electrons from multiple and highly charged ions and its subsequent photon emission arises also from the diagnostics of various *laboratory* plasmas.

Density operator of the fluorescence photon $\hbar\omega_f(\mathbb{M})$:

- ➢ After the inner-shell photoionization, the photoion appears to be in an excited level $|\alpha_e \mathbb{J}_e\rangle$ that decays subsequently to some energetically lower level $|\alpha_f \mathbb{J}_f\rangle$ by the emission of a characteristic photon.
- ➢ Characteristic photon density matrix in the helicity representation: For this characteristic photon, the density matrix can be expressed in the form $\langle \mathbf{k}_0 \, \lambda \,|\, \rho_\gamma \,|\, \mathbf{k}_0 \, \lambda' \rangle$, in which $\mathbf{k}_0 \equiv (\vartheta_0, \varphi_0)$ denotes the wave vector along the propagation direction of the fluorescence photon and $\lambda = \pm 1$ its helicity. Note that the helicity representation of this density matrix also describes the photon polarization.

Stokes parameter of the fluorescence photon $\hbar\omega_f(\mathbb{M})$:

- ➢ The density matrix of the fluorescence photon $\hbar\omega_f(\mathbb{M})$ is usually parametrized in terms of the so-called Stokes parameters (Blum 1981; Balashov *et al.*, 2001)

$$\big\langle \mathbf{k}_0 \, \lambda \,\big|\, \rho_{\omega_f} \,\big|\, \mathbf{k}_0 \, \lambda' \big\rangle \;\equiv\; c_{\lambda,\lambda'} \;=\; \frac{1}{2} \begin{pmatrix} 1+P_3 & -P_1 + iP_2 \\ -P_1 - iP_2 & 1-P_3 \end{pmatrix} ,$$

and which are utilized to characterize both the degree of linear (P_1 and P_2) and circular (P_3) polarization of the light.

➢ Apart from the population of the excited sublevels $|\alpha_e \mathbb{J}_e M_e\rangle$ and the angle ϑ of the emitted photon, the degree of linear polarization of the characteristic x-ray radiation also depends on the total angular momenta of the excited level $|\alpha_e \mathbb{J}_e\rangle$ and the final level $|\alpha_f \mathbb{J}_f\rangle$ of the characteristic transition as well as on its *multipolarity*.

8.2.f. Photoionization & autoionization (PhotoIonizationAutoIon)

Process, notations & application:

➢ Photo ionization of an atom or ion with subsequent autoionization: $A + \hbar\omega \longrightarrow A^{+,*} + e_p^- \longrightarrow A^{(*)} + e_p^- + e_a^-$

➢ Formal quantum notation: $|\alpha_i \mathbb{J}_i\rangle + \hbar\omega(\mathbb{M}) \longrightarrow |\alpha_r \mathbb{J}_r\rangle + |\varepsilon_p \kappa_p\rangle \longrightarrow |\alpha_f \mathbb{J}_f\rangle + |\varepsilon_p \kappa_p\rangle + |\varepsilon_a \kappa_a\rangle$

Photo-Auger electron coincidence spectrometry:

➢ Photo-Auger electron coincidence spectrometry has been found a versatile tool for studying the structure and dynamics of atoms, molecules and solids. In atomic physics, for example, it has been utilized to realize a so-called complete experiment in the photoionization of atoms as well as for exploring small effects of coherence and post-collision interactions in photo-induced Auger processes.

➢ For a full analysis of the photoionization and subsequent autoionization process, both electrons should be detected in coincidence by measuring the energy and angular distributions, i.e. the photo-Auger electron correlation function.

➢ The photoionization and subsequent autoionization process differs from the direct double photoionization due to the formation of a (well-defined) intermediate ionic state and, thus, the emission of the two electrons can usually be considered within a two-step model.

➢ Investigations of the magnetic circular dichroism in the photoemission from solids have been found useful for studying the magnetic properties of solids.

Photo-Auger electron correlation function:

➢ Sequential ionization of polarized targets: There are three relevant directions that need to be distinguished in the sequential ionization of polarized targets: the direction of the photoelectron $\mathbf{n}_p = (\vartheta_p, \varphi_p)$, those of the Auger electron $\mathbf{n}_a = (\vartheta_a, \varphi_a)$ and the direction of the

target polarization $\mathbf{n}_t = (\vartheta_t, \varphi_t)$. Because of these three relevant but independent directions, the (triple-differential) cross sections can be expanded in terms of tripolar spherical harmonics

$$\left\{\mathbb{Y}_{k_0}(\mathbf{n}_t) \otimes \{\mathbb{Y}_{k_1}(\mathbf{n}_p) \otimes \mathbb{Y}_{k_2}(\mathbf{n}_a\right\}_k\Big\}_{k'q'} = \langle \dots | \dots \rangle \langle \dots | \dots \rangle Y_{k_0\,q_0}(\vartheta_t, \varphi_t)\, Y_{k_1\,q_1}(\vartheta_p, \varphi_p)\, Y_{k_2\,q_2}(\vartheta_a, \varphi_a)$$

8.2.g. Dielectronic recombination & fluorescence (DielectronicFluores)

Process, notations & application:

- Dielectronic recombination of an atom or ion with subsequent fluorescence:
  $A^{q+} + e_s^- \longrightarrow A^{(q-1)+\,*} \longrightarrow A^{(q-1)+\,(*)} + \hbar\omega \longrightarrow A^{(q-1)+\,(*)} + \hbar\omega + \hbar\omega'$
- Formal quantum notation: $|\alpha_i \mathbb{J}_i\rangle + |\varepsilon_s \kappa_s\rangle \longrightarrow |\alpha_r \mathbb{J}_r\rangle \longrightarrow |\alpha_d \mathbb{J}_d\rangle + \hbar\omega_d\,(\mathbb{M}_d) \longrightarrow |\alpha_f \mathbb{J}_f\rangle + \hbar\omega_d\,(\mathbb{M}) + \hbar\omega_f\,(\mathbb{M}_f)$

8.2.h. Electron-impact (de-) excitation (ImpactExcitation)

Process, notations & application:

- Electron-impact excitation of an atom or ion: $e_s^- + A \longrightarrow A^* + e_s^{-\prime}$
- Formal quantum notation: $|\alpha_i \mathbb{J}_i\rangle + |\varepsilon_i \kappa_i\rangle \longrightarrow |\alpha_f \mathbb{J}_f\rangle + |\varepsilon_f \kappa_f\rangle$ or $|\alpha_i \mathbb{J}_i\rangle + |\mathbf{p}_i\, m_i\rangle \longrightarrow |\alpha_f \mathbb{J}_f\rangle + |\mathbf{p}_f\, m_f\rangle$
- Electron-impact excitation is formally an inelastic scattering process in which a free incident electron $|\varepsilon_i \kappa_i\rangle$ is scattered at the atom and leaves as final electron $|\varepsilon_f \kappa_f\rangle$.
- Electron-impact ionization cross sections are required in different field, for example, for calculating level populations and spectral line intensities of non-local-thermodynamic-equilibrium (non-LTE) plasmas.

Computation of electron-impact processes:

➢ The electron-impact excitation of atoms is often described in first-order Born approximation, in which one can easily distinguish individual excitation channels. This approximation neglects however the coupling of the *continuum channels*, but which can later be incorperated perturbatively.

➢ Distorted-wave Born approximation (DWBA): We here make use of the DWBA that accounts for the distortion of the continuum orbitals due to (local) potential of the nucleus and all the electrons of the target. The DWBA typically gives better results than the *pure* Born or the Coulomb-Born approximation. The current implementation is similar to the codes by Zhang *et al.*(1989) as well as to the FAC code (Gu 2008).

➢ For a reliable evaluation of plasma parameters, such as temperature, density or level populations, the excitation cross sections need to be known quite accurately.

➢ Computational methods for electron-impact excitation & ionization: Three methods are commonly used in the literature to calculate electron-impact excitation and ionization cross sections: i) Coulomb-Born (CB) approximation, where the continuum orbital just represent a free electron in a Coulomb potential; ii) distorted-wave (DW) approximation that includes a more realistic potential for the continuum orbitals; iii) close-coupling (CC) approximation. In the first two approximations, all excitation channels are treated independently and give overall rise to a scattering matrix which is not necessarily unitary.

➢ Electron-impact excitation in plasma diagnostics: In plasma-diagnostics measurements, the population of the excited states, relevant for plasma diagnostics, is largely driven by the direct electron-impact excitation of the ground and low-lying metastable states, and followed by their radiative decay.

Collision strength and cross sections:

➢ Collision strength: The name *collision strength* was first suggested by Seaton (1953). For a given (atomic target) transition $\alpha_i \mathbb{J}_i \rightarrow \alpha_f \mathbb{J}_f$, the collision strength is related to the cross section Q by

$$\Omega(\alpha_i \mathbb{J}_i,\, \alpha_f \mathbb{J}_f) \;=\; \frac{4\pi\, g_i}{\lambda_i^2}\, Q(\alpha_i \mathbb{J}_i,\, \alpha_f \mathbb{J}_f),$$

if the continuum orbitals are normalized per unit energy. The statistical weight g_i of level $|\alpha_i \mathbb{J}_i\rangle$ ensures the detailed-balance relation $\Omega(\alpha_i \mathbb{J}_i,\, \alpha_f \mathbb{J}_f) \;=\; \Omega(\alpha_f \mathbb{J}_f,\, \alpha_i \mathbb{J}_i)$.

➢ Collision strength: If $|\varepsilon_i, \kappa_i\rangle$ and $|\varepsilon_f, \kappa_f\rangle$ denote the partial waves of the incident and scattered electrons, the collision strength is given by

$$\Omega_{if} \;=\; \sum_{\kappa_i,\,\kappa_f} \sum_{\mathbb{J}_t} [J_t] \; \left| \left\langle (\mathbb{J}_f,\; \epsilon_f, \kappa_f)\; \mathbb{J}_t M_t \,\middle|\, V^{\,(\mathrm{e-e})} \,\middle|\, (\mathbb{J}_i,\; \epsilon_i, \kappa_i)\; \mathbb{J}_t M_t \right\rangle \right|^2 .$$

➢ In the JAC program, the standard decomposition of the electron-electron interaction matrix elements is utilized to compute the collision strength.

➢ Normalization of continuum orbitals: A continuum orbital is said to be normalized per unit energy if it has an asymptotic amplitude $\sqrt{k/\varepsilon}$ (or, $\sqrt{2/k}$ in the non-relativistic limit) or, equivalently, if it fullfills, equivalently,

$$\int dr \; [P_\varepsilon(r)\; P_{\varepsilon'}(r) \;+\; Q_\varepsilon(r)\; Q_{\varepsilon'}(r)] \;=\; \pi\, \delta(\varepsilon \,-\, \varepsilon') \,.$$

➢ For electron-impact processes, the collision strength $\Omega(\alpha_i \mathbb{J}_i,\; \alpha_f \mathbb{J}_f)$ is typically of the order of unity, though still large variation may still occur owing to its dependence on the particular ion as well as the transition and impact energy. Therefore, it is usually not justified to assume $\Omega \,=\, 1$ as sometimes done in astrophysical codes.

➢ Simplification for heavy ions with open d- and f-shells: For heavy and ionized atoms with open d- and f-shells, the fine-structure of just (mixed) single initial- and final-state configurations may give rise to thousands of (fine-structure) transitions, for which the radial integrals often depend only weakly on the transition energy. For such transition arrays, the total cross section computations can be sipmplified considerably by either neglecting the weak dependence of the radial integrals or by some simple interpolation.

➢ Accurate calculations of electron-impact excitation of atom and ions are overall still a challenge for contempary electronic methods, such as convergent close-coupling, R-matrix close-coupling or time-dependent close-coupling scheme, and even by using the largest (parallel) computers.

Collisional-excitation rate coefficients:

➢ The rate coefficient of collisional excitation is given by

$$\alpha^{\,(\mathrm{impact:excitation})} \;=\; \int_{\Delta E}^{\infty} dv\; f(v)\; \sigma^{\,(\mathrm{impact-excitation})}(v)$$

where $f(v)$ is velocity distribution of electrons which is typically assumed to have a Maxwellian distribution with electron temperature T_e, $\sigma^{(\text{impact}-\text{excitation})}(\alpha_i \mathbb{J}_i, \alpha_f \mathbb{J}_f)$ is the electron-impact excitation cross-section from level $i \to f$ at velocity v, and $\Delta E = E_f - E_i$ is the excitation energy.

➢ For a given energy of the incident electrons, the collisional-excitation rate coefficient can be expressed also as

$$\alpha^{(\text{impact}-\text{excitation})} = \sqrt{\frac{\pi}{E}} \int_{\Delta E}^{\infty} dE\, E\, \sigma^{(\text{impact}-\text{excitation})}(E)\, \exp\left(-\frac{E}{T_e}\right).$$

8.2.i. Electron-impact excitation & autoionization (ImpactExcitationAutoIon)

Process, notations & application:

➢ Electron-impact excitation with subsequet autoionization of an atom or ion: $A + e_s^- \longrightarrow A^* + e_s^{-\prime} \longrightarrow A^{+(*)} + e_s^{-\prime} + e_a^-$

➢ Formal quantum notation: $|\alpha_i \mathbb{J}_i\rangle + |\varepsilon_i \kappa_i\rangle \longrightarrow |\alpha_r \mathbb{J}_r\rangle + |\varepsilon_r \kappa_r\rangle \longrightarrow |\alpha_f \mathbb{J}_f\rangle + |\varepsilon_r \kappa_r\rangle + |\varepsilon_a \kappa_a\rangle$

➢ Electron-impact excitation with subsequet autoionization occurs frequently in plasma and has been utilized to study the autoionization of atoms and ions.

8.2.j. Radiative-Auger decay (RadiativeAuger)

Process, notations & application:

➢ Radiative-Auger (autoionization) of an atom or ion: $A^{q+*} \longrightarrow A^{(q+1)+,(*)} + (e_a^- + \hbar\omega)$

➢ Formal quantum notation: $|\alpha_i \mathbb{J}_i\rangle \longrightarrow |\alpha_f \mathbb{J}_f\rangle + \hbar\omega\,(\mathbb{M}) + |\varepsilon_a\, \kappa_a\rangle$

➢ The radiative Auger process results in the simultaneous emission of an electron and photon, and mainly occurs for inner-shell excited atoms and ions. There are no characteristic electron or photon lines associated with this process, since the transition energy is shared between the photon and the electron.

8.2.k. Multi-photon double ionization (MultiPhotonDoubleIon)

Process, notations & application:

➢ Multi-photon double ionization: of an atom or ion: $A + n\,\hbar\omega \longrightarrow A^{(*)} + e^-_{p_1} + e^-_{p_1}$

➢ Formal quantum notation: $|\alpha_i \mathbb{J}_i\rangle + \hbar\omega_1\,(\mathbb{M}_1) + \hbar\omega_2\,(\mathbb{M}_2) + ... + \hbar\omega_n\,(\mathbb{M}_n) \longrightarrow |\alpha_f \mathbb{J}_f\rangle + |\varepsilon_1\,\kappa_1\rangle + |\varepsilon_2\,\kappa_2\rangle$

➢ The energy of several photons together can also lead to the emission of two electrons: This emission can occur either sequential, direct (non-sequential) or via some given resonances of the atom.

➢ In this section, we only consider the direct (non-sequential) multi-photon double ionization in which the energy of all photons is contineously shared by the two emitted electrons: $n\,\hbar\omega = E_f - E_i + \varepsilon_1 + \varepsilon_2$.

8.2.l. Internal conversion (InternalConversion)

Process, notations & application:

➢ Internal conversion of an atom or ion: $A^{q+} + \text{nucleus}^* \longrightarrow A^{(q+1)+*} + e^-_c$

➢ Formal quantum notation: $|\alpha_i \mathbb{J}_i\rangle + \text{nucleus}^*\,(\{\mathbb{M}\}, \mathcal{E}) \longrightarrow |\alpha_f \mathbb{J}_f\rangle + e^-_c(\mathbf{p}, m_s)$ or
$|\alpha_i \mathbb{J}_i\rangle + \text{nucleus}^*\,(\{\mathbb{M}\}, \mathcal{E}) \longrightarrow |\alpha_f \mathbb{J}_f\rangle + |\varepsilon\,\kappa\rangle\,,$ $\varepsilon = \mathcal{E} - (E_i - E_f)$

➢ Here, the excited nucleus decays under the release of the energy $\mathcal{E}$ by (several) multipoles $\{\mathbb{M}\}$ and , leading to an emitted electron with well-defined kinetic energy ε .

➢ Internal conversion: formally refers to the decay an excited nucleus to its ground or some lower-lying level, and where the excitation energy is given to a (bound) electron, leading to an ionization of the atom or ion. In general, the internal (energy) conversion competes with the gamma-ray emission as well as the formation of a electron-positron pair for nucear excitation energies above 1.022 MeV.

➢ Often, the continuum wave of the outgoing electron has been calculated in the (final-state) atomic potential with a vacancy in the inner shell. Sometimes, however, this hole has been disregarded, leading to differences in the internal conversion coefficients as large as ~ 15 % for low kinetic energies $\varepsilon \sim 1$ keV and $L = 5$ transitions.

Nuclear decay by internal conversion:

- The internal conversion is more than a simple photoionization process, in which an emitted γ photon leads to the emission of electrons, but refers to an alternative de-excitation of excited nuclei.
- Electron conversion coefficient: In the internal conversion process, an atomic electron is ejected from one of the atomic shells. The electron conversion coefficient is defined as the probability ratio for emitting an atomic electrons from shell x to the emission of a γ-ray, $a_x = P_x \,/\, P_\gamma$.
- The kinetic energy of the emitted electron $\varepsilon = \Delta E_{\rm nuc} - E_b$ can be deduced from the nuclear transition energy, the binding energy of the atomic electron and the recoil energy of the emitting atom, which is typically very small.Transitions involving conversion electrons are only possible if $\varepsilon > 0$.
- The internal conversion process (ICP) has been found a versatile tool for studying nuclear structure. In particular, the measurement and analysis of conversion electron spectra reveal possible transitions between nuclear levels. From the comparison of these spectra with calculated internal conversion coefficients, it is often possible to assign a unique multipolarity to the nuclear gamma radiation and, hence, a total angular momentum and parity to the excited nuclear states.
- The internal conversion coefficients can provide detailed information about the atomic nucleus if theoretical and experimental values are compared for transitions of different multipolarity and mixing ratios. A detailed knowledge of these coefficients is needed, for instance, for deriving absolute transition rates and for the normalization of decay schemes, for Mössbauer spectrocopy, for nuclear reaction computations as well as for the calculation of the decay heat of the fuell cells of nuclear reactors.
- The internal conversion process is largely independent of the nuclear structure, although a non-zero probability requires a finite nuclear size and a finite probability of the electron to be found inside of the nucleus. For highly supressed transitions, this finite-size effect can become quite significant. For these transitions, Pauli developed formulae to correct the theoretical conversion coefficient for both, the electric and magnetic multipolarities.

General theory:

- The internal conversion can be described as QED process by the retarded interaction of charges.
- In particular, the internal conversion is a second-order quantum-electrodynamical process in which a virtual photon is exchanged between the nucleus (proton) and an electron.

➢ Internal conversion amplitude: The (single-electron) matrix element of the conversion transition can be written in terms of the Hamiltonian (Listengarten 1961; Band *et al.*, 2002)

$$\left\langle f \left| \, \mathbb{h}^{\,(\mathrm{conversion})} \, \right| i \right\rangle \;=\; -e \int d^3\mathbf{r}\; \psi_f^*(\mathbf{r}) \;\; [\, \Phi(\mathbf{r}) \,+\, \boldsymbol{\alpha} \cdot \mathbf{A}(\mathbf{r}) \,] \;\; \psi_i(\mathbf{r}),$$

where $\Phi(\mathbf{r})$ and $\mathbf{A}(\mathbf{r})$ are the time-independent parts of the scalar and vector potentials of the electro-magnetic field that arise due to the nuclear transition charges and currents, and by including the retardation of these interactions.

➢ The retarded potentials in the internal conversion amplitude above are

$$\Phi(\mathbf{r},t) \;=\; e^{-i\,\omega\,t}\,\Phi(\mathbf{r}), \qquad \Phi(\mathbf{r}) \;=\; \int d^3\mathbf{R}\;\frac{\rho(\mathbf{R})}{|\mathbf{r}\,-\,\mathbf{R}|}\;e^{i\,k\,|\mathbf{R}\,-\,\mathbf{R}|} \;=\; \sum_{LQ} \Phi_{LQ}(\mathbf{r})$$

$$\mathbf{A}(\mathbf{r},t) \;=\; e^{-i\,\omega\,t}\,\mathbf{A}(\mathbf{r}), \qquad \mathbf{A}(\mathbf{r}) \;=\; \frac{1}{c}\int d^3\mathbf{R}\;\frac{\mathbf{J}(\mathbf{r})}{|\mathbf{R}\,-\,\mathbf{R}|}\;e^{i\,k\,|\mathbf{R}\,-\,\mathbf{R}|} \;=\; \sum_{LQ} \mathbf{A}_{LQ}(\mathbf{r})$$

with the wavenumber $k \,=\, \omega/c \,=\, \mathcal{E}/\hbar\,c$, and where $\mathbf{r} \,=\, (r,\vartheta,\varphi)$ and $\mathbf{R}$ are the coordinates of the electron and nucleus (proton), respectively.

➢ Here, we shall not go into further details for the representation of these potentials but just note that these interaction potentials can be written as a sum over multipole contributions as well as in terms of the nuclear charge density $\rho(\mathbf{R})$ and current density $\mathbf{J}(\mathbf{r})$ of the bound electrons, respectively.

Internal conversion coefficients:

➢ Internal conversion coefficient: The internal conversion coefficient is defined as the ratio of the number of electrons N_e ejected from the atomic shell $(n\ell)$ to the number of gamma quanta N_γ leaving the atom during the same time:

$$\alpha^{\,(\mathrm{conversion})}(n\ell) \;=\; \frac{N_e}{N_\gamma}, \qquad\qquad \alpha^{\,(\mathrm{conversion})}(\alpha_i \mathbb{J}_i) \;=\; \sum_f \alpha^{\,(\mathrm{conversion})}(n\ell)$$

The total internal conversion coefficient of a given (initial) level $\alpha^{\,(\mathrm{conversion})}(n\ell)$ of the nucleus is the sum of partial conversion coefficient associated with all possible ionization channels (lines) of the atom or ion.

- Internal conversion coefficients have been tabulated in a larger number of tables and compilations; in these tabulations, the screening of the nuclear electric field by the atomic electrons was often treated in the framework of either some statistical Thomas-Fermi-Dirac or Dirac-Fock-Slater models.
- For different x_α pre-factors in the Dirac-Fock-Slater (type) potentials, the differences in the calculated conversion coefficients are typically small ~ 1 % for K-shell electrons but may increase to ~ 70 % for outer electrons or even larger for low kinetic energies of the conversion electron ($\leq$ 1 keV). The question of whether the electronic hole should be taken into account into the atomic potential has been explored previously but seem to have a minor role only.
- A new internal conversion coefficient database BrIcc has been developed that includes various tabulations of internal electron conversion (IECC), internal electron-positron pair conversion coefficients (IPCC) as well as the *electronic* factors Ω(E0) .
- Theoretical conversion coefficients $\alpha^{(\mathrm{internal-conversion})}$ are associated with two kinds of uncertainties: (i) due to the physics model that is used in the computations and (ii) due to the spline interpolation that is frequently used in order to generate the tabulations. The physics model is typical based on assumtions about the atomic nucleus and the electron density.

8.2.m. Electron capture with nuclear decay

Process, notations & application:

- Electron capture of an atom or ion by nuclear decay: $A(Z+1) + e^- \longrightarrow A(Z) + \nu_e$
- Formal quantum notation: $E_\nu = Q^+ - E_f - E_b > 0$
- Here, the nucleus decays by capturing an atomic electron (often from the K-shell), and under the emission of an electron neutrino. Here, Q^+ is the energy difference due to the rest masses of the parent and daughter nucleus, E_f the energy of the final nuclear state of the daughter nucleus and E_b the binding energy of the captured electron. The release energy E_ν will be shared between the emitted neutrino and, possible, some bremsstrahlungs photon or the shake-up/shake-off of a valence electron.
- For allowed nuclear transitions, nearly all vacancies occur in the ns shells of the atoms or ions, i.e. in the K, L_1 , M_1, ... shells.

8.3. Further processes, not yet considered in JAC

8.3.a. Coulomb ionization (CoulombIonization)

Process, notations & application:

- Coulomb ionization by fast, heavy ions: $A^{(q+1)+} + Z_p \longrightarrow A^{(q+1)+(*)} + e^- + Z'_p$
- Formal quantum notation: $|\alpha_i \mathbb{J}_i\rangle + Z_p(...) \longrightarrow |\alpha_f \mathbb{J}_f\rangle + e^-$
- The Coulomb ionization of projectile ions by target atoms leads to a different charge state of the ions and often determines their lifetime in storage rings.
- If one of the projectile electrons is ionized, the ion is lost from the ring since it will be misbent by subsequent steering magnets.

Perturbative calculation of ionization cross sections:

- Semi-relativistic treatment of the Coulomb ionization: In their semi-relativistic treatment, Anholt and Becker (1987) distingiush three contributions to the ionization cross sections due to Coulomb ionization, transverse ionization, and the ionization due to the spin-flip of the ionized electron. These three contributions have different asymptotic behaviour in ultra-relativistic collisions. — In this approach, the Coulomb ionization cross section is the same as in the plane-wave Born approximation for nonrelativistic projectiles.
- The Coulomb part is dominant at nonrelativistic energies, while the transverse part mainly arise from the magnetic interactions at large impact parameters.
- The cross section for the (projectile) ionization of a $1s$ electron increases as $\ln \gamma$ due to the transverse interaction for high projectile energies and if the target screening is neglected. This transverse interaction is however screened and reduced if the charge of the projectile is smaller than those of the target, $Z_p < Z_t$.
- For fast collisions and for impact parameters b comparable with, or larger than the ionic K-shell radius, the perturbation of the target atom by the projectile can be treated in first-order time-dependent perturbation theory, even for high-Z projectiles.
- Perturbation theory breaks generally down for high-Z projectiles (or high-Z targets). For these high-Z projectiles, an approximate scaling rule for the ionization probability at high relativistic energies ($\gamma > 5$) and fixed impact parameters has been established by numerical calculations. For $b = 0$, for example, the ionization probability $P(b = 0) = 1.8 \times 10^{-4}\, Z_p^2$ is independent of the target charge within about ± 10 % up to the heaviest elements.

8.3.b. Bremsstrahlung (BremsStrahlung)

Process, notations & application:

- Bremsstrahlung emitted by an electron in the field of an atom or ions $A^{q+} + e_i^- \longrightarrow A^{(q)+*} + e_f^- + \hbar\omega$
- Formal quantum notation: $|\alpha_i \mathbb{J}_i\rangle + |\varepsilon_i \kappa_i\rangle \longrightarrow |\alpha_f \mathbb{J}_f\rangle + |\varepsilon_f \kappa_f\rangle + \hbar\omega\,(\mathbb{M})$
- Bremsstrahlung arises generally if a charged particle is decelerated or deflected by another charged particle, often an electron or nucleus, and if parts of its kinetic energy is converted into radiation.
- More generally speaking, bremsstrahlung or braking radiation refers to any radiation that arises due to the deceleration of charged particle, including synchrotron radiation from relativistic particles or cyclotron radiation from non-relativistic particles.
- In atomic physics, bremsstrahlung often refers to the radiation from electrons that are slowed down in matter.
- Atomic bremsstrahlung: This term sometimes refers also to the polarized radiation that arise from the Coulomb field of the incident charged particle.
- Bremsstrahlung has a continuous spectrum and a peak intensity that shifts toward higher frequencies with an increasing energy transfer from the decelerated particles.

8.3.c. Inverse bremsstrahlung

Process, notations & application:

- Inverse bremsstrahlung of a charged particle in the field of an atom or ions $\hbar\omega + A^{q+} + e_i^- \longrightarrow A^{(q)+} + e_f^-$
- Formal quantum notation: $\hbar\omega(\mathbb{M}) + |\alpha_i \mathbb{J}_i\rangle + |\varepsilon_i \kappa_i\rangle \longrightarrow |\alpha_f \mathbb{J}_f\rangle + |\varepsilon_f \kappa_f\rangle$
- In the inverse bremsstrahlung process, a free electron gains kinetic energy due to the absorption of a photon.

8.3.d. Radiative recombination & fluorescence

Process, notations & application:

➢ Radiative recombination & fluorescence of an ion: $A^{q+} + e_s^- \longrightarrow A^{(q-1)+,*} + \hbar\,\omega_r \longrightarrow A^{(q-1)+} + \hbar\,\omega_r + \hbar\,\omega_f$

➢ Formal quantum notation: $|\alpha_i \mathbb{J}_i\rangle + |\varepsilon_i \kappa_i\rangle \longrightarrow |\alpha_r \mathbb{J}_r\rangle + \hbar\omega_r(\mathbb{M}_r) \longrightarrow |\alpha_f \mathbb{J}_f\rangle + \hbar\omega_r(\mathbb{M}_r) + \hbar\omega_f(\mathbb{M}_f)$

➢ In the photorecombination & fluorescence process, also known radiative recombination (RR) or radiative electron capture (REC), an electron is captured by the ion into an excited state that subsequently decay under fluorescence emission.

8.3.e. Resonant two-color (two-photon, single-electron) ionization

Process, notations & application:

➢ Resonant two-color (two-photon, single-electron) ionization of an ion: $A + \hbar\,\omega + \hbar\,\omega' \longrightarrow A^* + \hbar\,\omega' \longrightarrow A^{+*} + e_p^-$

➢ Formal quantum notation: $|\alpha_i \mathbb{J}_i\rangle + \hbar\omega\,(\mathbb{M}) + \hbar\omega'\,(\mathbb{M}') \longrightarrow |\alpha_r \mathbb{J}_r\rangle + \hbar\omega'\,(\mathbb{M}') \longrightarrow |\alpha_f \mathbb{J}_f\rangle + |\varepsilon\kappa\rangle$

➢ In the resonant two-color photoionization, an atom or ion is resonantly excited by one photon and subsequently ionized by a second photon of the same or some different frequency.

8.3.f. Interference of multi-photon ionization channels `(MultiPhotonInterference)`

Process, notations & application:

➢ Interference of *non-resonant* one-photon (2ω) and *resonant* two-photon (ω) ionization of an atom or ion:

$$A + \begin{bmatrix} \hbar\,(2\omega) \\ \hbar\,\omega + \hbar\,\omega \end{bmatrix} \longrightarrow A^+(*) + e_p^-$$

➢ Formal quantum notation: $|\alpha_i \mathbb{J}_i\rangle \; + \; \begin{bmatrix} \hbar\,(2\omega) \\ \hbar\,\omega \; + \; \hbar\,\omega \end{bmatrix} \quad \longrightarrow \quad |\alpha_i \mathbb{J}_i\rangle \; + \; |\varepsilon\kappa\rangle$

➢ The two-pathway quantum interference has been explored in order to better understand the quantum control of atoms and ions.

➢ Such quantum control studies were initially stimulated by the small fraction of the second harmonic that typically arise at XFEL and that cannot so easily be filtered out, though it may strongly influence the experimental from two-photon ionization experiments. Despite of the rather small intensity of the second harmonic, the ionization by photons with frequency $2\,\omega$ (second harmonic, first-order process) can readily compete with, or even dominate, the two-photon ionization by photons with frequency ω.

Interference of non-res. one-photon (2ω) and resonant two-photon (ω) ionization:

➢ Experimental signals: For a linearly-polarized bichromatic beam, the interference due to different quantum paths manifests itself in an asymmetry of the photoelectron angular distributions (PAD) with respect to the plane that is perpendicular to the electric field of the incident radiation; cf. Grum-Grzhimailo *et al.*(2015).

➢ Photoelectron angular distribution (PAD): In the dipole approximation and for an isotropic target, this angular distribution must be axially symmetric with regard to the polarization direction

$$\frac{dW}{d\Omega} \;=\; \frac{W_o}{4\pi}\left[1 \,+\, \sum_{k=1}^{K} \beta_k \, P_k(\cos\vartheta)\right]$$

where ϑ is the angle of the photoelectron with regard to the polarization direction (**E**-field) and β_k the corresponding anisotropy parameters, which can expressed in terms of the photoionization amplitudes.

➢ For the interference of one-photon and two-photon ionization paths, all terms with $k \,=\, 1, 2, 3, 4$ must be taken into account in the PAD above. The odd polynomials arises from the photoelectron partial waves with opposite parities due to the innteraction of the atom with the fundamental and second harmonic of the radiation.

➢ The quantum interference of absorption amplitudes with an even and odd number of photons, such as $(\omega \,+\, 2\,\omega)$ photoionization, does not modify the total yield but only affect the angle-resolved observations. The interference between an even or odd number of photons lead to photoelectron partial waves with opposite parities.

➢ Interference in photoionization: Many photoionization experiments have been performed in order to better understand the concept of quantum-mechanical interference. Interference in photoionization occurs since the phase of the incident photons is eventually imprinted upon

the wave of the emitted electron. Apart from cross sections, this phase imprint enables one to extract the phases from the measurements, and which could not be derived for classical particles.

➢ Interference in photoionization: Using a seeded free-electron laser, first coherent optical experiments have been performed also at short wavelengths; in these experiments, high xuv harmonics have been utilized to coherently control the outcome of experiments by controlling the electron beam in the accelerator. Such a control requires to precisely know both, the amplitude and phase of each harmonic.

➢ Time-dependent electric field in two-color experiments: In two-color experiments, the field is often approximated by (DiFraia *et al.*, 2019)

$$\mathcal{E}(t) \;=\; \sqrt{I_\omega(t)}\,\cos\omega t \;+\; \sqrt{I_{2\omega}(t)}\,\cos\left(2\,\omega\,t \;-\; \phi\right), \qquad\qquad \boldsymbol{\mathcal{E}}(t) \;=\; \mathcal{E}(t)\,\mathbf{e}_z,$$

and where $I_\omega(t)$, $I_{2\omega}(t)$ are the envelopes of the two pulses and ϕ the relative phase between the $\omega - 2\,\omega$ pulses. In this definition, the larger ϕ as more the $2\,\omega$ pulse is delayed.

8.3.g. Two-color multi-photon interference ionization (TwoColorInterferenceIon)

Process, notations & application:

➢ Two-color multi-photon interference ionization of an ion: $A \;+\; m\,\hbar\,\omega \;+\; n\,\hbar\,\omega' \;\longrightarrow\; A^{+*} \;+\; e_p^-$

➢ Formal quantum notation: $|\alpha_i \mathbb{J}_i\rangle \;+\; m\,\hbar\omega\,(\mathbb{M}) \;+\; n\,\hbar\omega'\,(\mathbb{M}') \;\longrightarrow\; |\alpha_f \mathbb{J}_f\rangle \;+\; |\varepsilon\kappa\rangle$

➢ In the two-color multi-photon interference ionization, an atom or ion emits an electon whose angular distribution is affected by the interference of different ionization pathes.

8.3.h. Two-photon above-threshold ionization (ATI) (TwoColorInterferenceIon)

Process, notations & application:

➢ Two-photon above-threshold ionization of an ion:

➢ Formal quantum notation:

➢ Petrov *et al.* (2019) considered the two-photon $3p$ ionization of argon: Ar $3p^6 + 2\gamma \longrightarrow 3p^5\,\varepsilon\kappa$ with $\varepsilon > \hbar\,\omega$.

8.3.i. Double photoionization (DoublePhotoIonization)

Process, notations & application:

➢ Simultaneous double photoionization of an atom or ion: $A^{q+*} + \hbar\,\omega \longrightarrow A^{(q+2)+(*)} + (e^-_{p_1} + e^-_{p_2})$

➢ Formal quantum notation: $|\alpha_i \mathbb{J}_i\rangle + \hbar\,\omega\,(\mathbb{M}) \longrightarrow |\alpha_f \mathbb{J}_f\rangle + |\varepsilon_1\,\kappa_1\rangle + |\varepsilon_2\,\kappa_2\rangle$

➢ The (direct) double photoionization of atoms has attracted much interest during the last decades as the emission of a second electron is caused by the electron-electron interaction.

➢ The recent advancements of free electron lasers (FEL) has lead to intense short pulses with rather high photon energies, and which may help investigate the (direct) double photoionization process for multiply charged ions.

Cross sections:

➢ Triple-differential cross section for the double ionization of polarized atoms: If one expresses the cross section in terms of the solid angles $\Omega_{1,2}$ of the two electrons as well as the energy E_1 of one of the emitted electrons, this (five-fold differential) cross section can be written as trace over the final-state density matrix ρ_f

$$\frac{d^3\,\sigma}{d\,\Omega_1\,d\,\Omega_2\,d\,E_1} = c\,\mathrm{Tr}\,\rho_f = c\,\mathrm{Tr}\,(R\,\rho_i\,R^+) = c\,\mathrm{Tr}\,(D\,\rho^\gamma\,\rho_i\,R^+),$$

where ρ^γ is the photon density matrix and c just a kinematically determined normalization constant. Usually, this expression is evaluated in a basis with well-defined symmetry $\mathbb{J}$.

➢ Within the density matrix and the statistical tensor formalism, the triply differential cross section for single-photon double ionization from above can be written as (Berakdar and Kabachnik, 2005)

$$\frac{d^3\,\sigma}{d\,\Omega_1\,d\,\Omega_2\,d\,E_1} = c \sum_{\alpha\alpha'\,\mathbb{J}\mathbb{J}'\,kq} \rho^f_{kq}(\alpha\mathbb{J},\,\alpha'\mathbb{J}')\,\epsilon^*_{kq}(\alpha\mathbb{J},\,\alpha'\mathbb{J}')$$

where $\rho^f_{kq}(\alpha\mathbb{J},\ \alpha'\mathbb{J}')$ is the final-state statistical tensor of the "ion + two electrons" with symmetries $\mathbb{J}$ and $\mathbb{J}'$ and where $\epsilon_{kq}(\alpha\mathbb{J},\ \alpha'\mathbb{J}')$ denotes the efficiency tensor of the detector system to record these final states. Here, the summation over α, α' refers to all other quantum numbers which remain unobserved.

➢ Final-state density matrix: The final-state density matrix of the "photoion + two free electrons" can be expressed in terms of the statistical tensors of the total initial state "atom + photon" as well as the reduced electron-photon (photoionization) amplitudes (Berakdar and Kabachnik, 2005)

$$\rho^f_{kq}(\alpha\mathbb{J},\ \alpha'\mathbb{J}') = \sum_{k_o q_o\, k_\gamma q_\gamma} [k_o, k_\gamma]^{1/2}\ \langle k_o q_o,\ k_\gamma q_\gamma \,|\, kq\rangle \begin{Bmatrix} J_o & 1 & J \\ J_o & 1 & J' \\ k_o & k_\gamma & k \end{Bmatrix} \rho_{k_o q_o}(\alpha_o \mathbb{J}_o)\ \rho^\gamma(P_1, P_2, P_3)$$
$$\times\ \left\langle \alpha\mathbb{J} \left\| \mathbb{O}^{\,(\text{photoionization})} \right\| \alpha_o \mathbb{J}_o \right\rangle \left\langle \alpha'\mathbb{J}' \left\| \mathbb{O}^{\,(\text{photoionization})} \right\| \alpha_o \mathbb{J}_o \right\rangle^* .$$

➢ Although such expressions for the (triple-differential) cross sections appear to be rather complex, they can be handle quite easily in Jac.

Single-photon multiple ionization:

➢ Single-photon multiple ionization: The direct multiple ionization of atoms and ions by single photons is perhaps the simplest many-body process. Such a simultaneous release of two or more electrons is caused by interelectronic correlations and is very different from the (typical) inner-shell excitation or ionization of atoms and the subsequent autoionization. Therefore, the direct double (multiple) ionization is sensitive to details of the electron-electron interaction, and this applies especially for negative ions.

➢ Direct multiple ionization: While a direct multiple photoionization has been observed for both, positive and negative ions, a clear separation of the direct and sequential ionization processes is often difficult.

8.3.j. Double-Auger decay (DoubleAuger)

Process, notations & application:

➢ Simultaneous double Auger electron emission (autoionization) of an atom or ion: $A^{q+*} \longrightarrow A^{(q+2)+(*)} + (e^-_{a_1} + e^-_{a_2})$

➢ Formal quantum notation: $|\alpha_i \mathbb{J}_i\rangle \longrightarrow |\alpha_f \mathbb{J}_f\rangle + |\varepsilon_1\, \kappa_1\rangle + |\varepsilon_2\, \kappa_2\rangle$

➢ An autoionization of an atom may occur also via the simultaneous emission of two electrons which share the overall excess energy.

➢ The (direct) double Auger (DA) emission is an important second-order processes in which two electrons are ejected simultaneously from an inner-shell excited atom. A first evidence of the direct DA was found in K-shell photoionization experiments of neon with photon energies between 867 and 913 eV by Krause and coworkers (1965) as well as for argon.

➢ For the decay of a Ne 1s-hole, already Carlson and Krause (1965) found an about 8 % portion of Ne^{3+} ions due to the simultaneous double Auger decay. This portion occurs in contrast to the $\lesssim$ 1 % prediction from a simple shake-off model.

8.3.k. Positron-annihilation-induced autoionization

Process, notations & application:

➢ Positron-annihilation-induced autoionization of an ion: ...

➢ Formal quantum notation:

➢ Positron-annihilation-induced Auger electron spectroscopy (PAES): This positron-induced autoionization help explore surface structures and the observation of segregation processes. The time-dependent PAES has been utilized as a novel technique for the selective investigation of, e.g. heterogeneous catalysis, corrosion, or surface alloying.

➢ Mayer *et al.* (2010) applied the time-resolved PAES for the first time in order to determine the time constant for segregation as well as the final segregated configuration at the surface. For Cu-Pd alloys, for example, the amount of Cu atoms and their exact position was found to strongly affect the mechanical stability and the catalytic properties of Pd membranes. These authors also investigated the stability and dynamics of thin Cu layers on the surface of poly-crystalline Pd. When compared with the electron-induced Auger electron spectroscopy, the PAES appears intrinsically to be sensitive to the topmost atomic layer of a sample. These experiments were performed by means of the high intensity neutron-induced positron source Munich (NEPOMUC) which delivers about 10^9 monoenergetic positrons per seccond.

➢ Positron affinity: PAES is a highly selective technique for selecting specific atoms at surfaces because of the quite different positron affinities of the surface atoms. If more than a single element is present at some surface, the positrons are attracted to and annihilated with those atoms that have a higher relative positron affinity. Because of the high positron affinities of Pd, the positron will likely annihilate with electrons from Pd atoms in a Cu-Pd alloy, if such atoms are within the diffusion length of the positron at the surface.

8.3.l. Resonant excitation with sequential double autoionization (RESDA):

Process, notations & application:

➢ Resonant excitation with sequential double autoionization (RESDA) of an ion: ...

$$A^{q+} + e_s^- \longrightarrow A^{(q-1)+,*} \longrightarrow A^{q+,*} + e_{a_1}^- \longrightarrow A^{(q+1)+} + e_{a_1}^- + e_{a_2}^-$$

➢ Formal quantum notation: $|\alpha_i \mathbb{J}_i\rangle + |\varepsilon_i \kappa_i\rangle \longrightarrow |\alpha_m \mathbb{J}_m\rangle \longrightarrow |\alpha_n \mathbb{J}_n\rangle + |\varepsilon_1 \kappa_1\rangle \longrightarrow |\alpha_f \mathbb{J}_f\rangle + |\varepsilon_1 \kappa_1\rangle + |\varepsilon_2 \kappa_2\rangle$

➢ Lithium-like ions are perhaps the simplest ions in whicha RESDA can occur. This process can be observed by measuring the ratio of the numbers of trapped ions of two neighbouring charge states as a function of electron energy within an electron beam ion trap.

8.3.m. Resonant excitation with direct double autoionization (REDDA):

Process, notations & application:

➢ Resonant excitation with direct double autoionization (REDDA): of an ion: ...

$$A^{q+} + e_s^- \longrightarrow A^{(q-1)+*} \longrightarrow A^{(q+1)+} + (e_{a_1}^- + e_{a_2}^-)$$

➢ Formal quantum notation: $|\alpha_i \mathbb{J}_i\rangle + |\varepsilon_i \kappa_i\rangle \longrightarrow |\alpha_m \mathbb{J}_m\rangle \longrightarrow |\alpha_f \mathbb{J}_f\rangle + |\varepsilon_1 \kappa_1\rangle + |\varepsilon_2 \kappa_2\rangle$

➢ In the REDDA process, an electron is resonantly captured into a (doubly) excited level that subsequently decays by the simultaneous emission of two electrons, a so-called double autoionization, and where the two electrons share the overall excess energy.

8.3.n. Radiative double electron capture

Process, notations & application:

➢ Radiative double electron capture (RDEC) of an ion: $A^{q+*} + e_1^- + e_2^- \longrightarrow A^{(q-2)+} + \hbar\omega$

➢ Formal quantum notation: $|\alpha_i \mathbb{J}_i\rangle + |\varepsilon_1 \kappa_1\rangle + |\varepsilon_2 \kappa_2\rangle \longrightarrow |\alpha_f \mathbb{J}_f\rangle + \hbar\omega\,(\mathbb{M})$

➢ The radiative double electron capture (RDEC) is the time-reversed process of the single-electron direct double photoionization; it includes the transfer of two target electrons into a bound state of the projectile under the simultaneous emission of a single photon. Indeed, RDEC can be considered as the simplest and (almost) background-free tool for studying electron-electron correlations in high-Z ions.

➢ Experimental evidence: Simon *et al.* (2010) have presented experimental evidence of radiative double electron capture in the collision of 38 MeV O^{8+} with a carbon foil. When compared to theoretical cross sections, the experiments suggest a 5 times larger cross sections. This discrepancy may arise from the fact that no capture into excited states were included into the computations and that the electrons were considered as quasi-free in all computations.

➢ The (non-resonant) radiative electron capture is known to be dominant for fast collisions of heavy ions with light target atoms and shows a rather weak dependence on the inter-electron interaction between the projectile and target ions. The RDEC is a single-step process where the energy of two correlated captured electrons are converted into the energy and momentum of one emitted photon (Chernovskaya *et al.*, 2011).

➢ The RDEC can be described as the inverse process to double photoionization. Indeed, RDEC can be seen as a prominent tool for investigating the role of interelectronic interactions in the process of ion-atom collisions.

8.3.o. Generalized osciallator strengths (GOS)

Process, notations & application:

➢ Inelastic scattering of high-energetic photons or electrons The generalized oscillator strengths has been utilized to describe the inelastic scattering of high-energetic photons or fast electrons at atoms. This inelastic scattering has been discussed quite early by Bethe (1931) but has received less attention afterwards.

➢ Inelastic scattering of a fast electron by an atom or ion: $A^{q+} + e_s^- \longrightarrow A^{r+} + e_s^{-\prime}$ with $r \geq q$.

➢ The notion of GOS has been introduced if only the effective scattering cross section (strength) is of interest and if all the other released electrons are neglected from the theoretical treatment.

GOS expressions:

➢ Fast electron impact: The GOS for an excitation of the atom by fast electrons has been expressed as (Zhu *et al.*, 2006)

$$f(E,K) \;=\; \frac{E}{2}\,\frac{p_i}{p_f}\,K^2\,\frac{d\sigma}{d\Omega} \;=\; \frac{2\,E}{K^2}\,\left|\langle\alpha_f \mathbb{J}_f M_f\,|T_1(\mathbf{K})|\,\alpha_i \mathbb{J}_i M_i\rangle\right|^2 ,$$

where E is the excitation energy, K the momentum transfer, p_i, p_f the incident and scattered electron momenta, while $\frac{d\sigma}{d\Omega}$ refers to the differential scattering cross section of the incident electron.

8.3.p. Electron-impact ionization (ImpactIonization)

Process, notations & application:

➢ Electron-impact ionization of an atom or ion: $e_s^- \;+\; A \;\longrightarrow\; A^* \;+\; e_s^{-\prime} \;+\; e^-$

➢ Formal quantum notation: $|\alpha_i \mathbb{J}_i\rangle + |\varepsilon_i\,\kappa_i\rangle \;\longrightarrow\; |\alpha_f \mathbb{J}_f\rangle + |\varepsilon_f\,\kappa_f\rangle + |\varepsilon_c\,\kappa_c\rangle$ where $|\varepsilon_c\,\kappa_c\rangle$ is the initially bound *atomic* electron.

➢ The electron-impact ionization process is important in all (high-temperature) plasma, both in astro and plasma physics, and elsewhere. It is the inverse process to the three-body recombination, $A \;+\; e^- \;\longleftrightarrow\; A^+ \;+\; e_1^- \;+\; e_2^-$.

➢ We refer to the three *free* electrons, that are involved in this process, as incident, (final-) scattered and additional (-ly released) electron, and with the corresponding indices above.

Cross sections:

➢ Electron-impact ionization cross section: These cross sections are obtained rather similarly as the electron-impact excitation cross sections but by allowing an ionizing transition between fine-structure levels $\alpha_i \mathbb{J}_i(N) \;\to\; \alpha_f \mathbb{J}_f(N-1)$ (Fontes *et al.* 2015)

$$\sigma^{\,(\mathrm{ionization})}(\alpha_i \mathbb{J}_i, \alpha_f \mathbb{J}_f) \;=\; \frac{8}{k_i^2\,g_i}\sum_{\mathbb{J}_c,\,\mathbb{J}_t}(2J_s+1)\sum_{\kappa_i\,\kappa_f\,\kappa_e}\int_0^{\varepsilon_i\,-\,I_p}\varepsilon'\left|\left\langle\left((\alpha_f \mathbb{J}_f,\,\epsilon_c\kappa_c)\,\mathbb{J}_c\right),\,\epsilon_f\kappa_f\right)\,\mathbb{J}_t\,\middle\|\,\mathbb{V}^{(\mathrm{e-e})}\,\middle\|\,(\alpha_i \mathbb{J}_i,\,\epsilon_i\kappa_i)\,\mathbb{J}_t\right\rangle\right|^2$$

➢ This cross section contains a summation over all possible values $\mathbb{J}_t$ of the initial ion and the (incoming) incident electron in the partial wave $|\varepsilon_i\kappa_i\rangle$.

8.3.q. Electron-impact multiple ionization

Process, notations & application:

- Electron-impact multiple ionization of an atom or ion: $e_s^- + A \longrightarrow A^* + e_s^{-'} + e_a^- + e_b^- + ...$
- Formal quantum notation: $|\alpha_i \mathbb{J}_i\rangle + |\varepsilon_i\, \kappa_i\rangle \longrightarrow |\alpha_f \mathbb{J}_f\rangle + |\varepsilon_f\, \kappa_f\rangle + |\varepsilon_a\, \kappa_a\rangle + |\varepsilon_b\, \kappa_b\rangle + ...$
  where $|\varepsilon_a\, \kappa_a\rangle$, $|\varepsilon_b\, \kappa_b\rangle$, ... refer to the initially bound *atomic* electrons.
- To describe the multiple ionization in electron-impact processes, one needs to consider the (electron-impact) excitation, ionization as well as several resonant excitation processes. This is usually done in the isolated resonance approximation, in which all the processes are treated independently. The multiple ionization is then obtained from a proper summation over individual decay pathways and branching ratios.
- Charge state distribution (CSD) in plasma: Electron-impact double and multiple ionization plays a central role upon the charge state distribution of a plasma if the electron temperature changes rapidly either in time or space.
- For a plasma in a collisional-ionization equilibrium, the CSD is determined by the balance between electron-ion recombination and electron-impact – single and multiple – ionization. Therefore, accurate electron-impact excitation and ionization cross sections are important for plasma diagostics over a wide range of plasma (electron) temperatures, electron densities and elemental abundancies.

8.3.r. Three-body recombination

Process, notations & application:

- Three-body recombination of an ion: $A^{q+} + e_i^- + e_c^- \longrightarrow A^{(q-1)+} + e_f^-$
- Formal quantum notation: $|\alpha_i \mathbb{J}_i\rangle + |\varepsilon_i\, \kappa_i\rangle + |\varepsilon_c\, \kappa_c\rangle \longrightarrow |\alpha_f \mathbb{J}_f\rangle + |\varepsilon_f\, \kappa_f\rangle$
- The three-body recombination of an ion is the inverse process of the electron-impact ionization.
- The three-body recombination combination of an electron results in the capture of an electron by an positive ion due to energy and momentum transfer of the (captured) free electron to another free electron in the neighborhood of the atom or ion.
- Three-body recombination: For low-temperature afterglow and recombination-laser plasmas, the three-body collisional recombination to higher levels and deexcitation between higher levels are often dominant.

8.3.s. Elastic scattering of electrons and ions

Process, notations & application:

➢ Elastic scattering of electrons and positrons by atoms and ions of an ion: $A^{q+} + e_i^- \longrightarrow A^{q+} + e_f^-$

➢ Formal quantum notation: $|\alpha_i \mathbb{J}_i\rangle + |\varepsilon_i \kappa_i\rangle \longrightarrow |\alpha_f \mathbb{J}_f\rangle + |\varepsilon_f \kappa_f\rangle^+$

➢ Potential scattering of relativistic electrons and positrons: The scattering of relativistic electrons or positrons by a – real or complex – central-field $V(r)$ is completely described by the direct scattering amplitude $f(\vartheta)$ and the spin-flip scattering amplitude $g(\vartheta)$, which are both complex functions of the polar scattering angle ϑ.

➢ These scattering amplitudes are derived from the asymptotic behaviour for $r \text{ø} \infty$ of the distorted plane-wave solutions of the Dirac equation *plus* an outgoing spherical wave.

Static scattering potentials:

➢ Static-field approximation: This approximation only includes the (electro-) static potential *plus* approximate local exchange potential for the interaction between the incoming or outgoing electron and the (target) ion. For electrons with kinetic energies $E_{\text{kin}} \lesssim 10$ keV, moreover, one often includes optionally a semi-empirical correlation-polarization potential in order to account for the dynamically induced polarization of the target.

➢ Local exchange potential: For electron scattering processes, three simple analytical approximations for a local exchange potential refer to the Thomas-Fermi, Furness-McCarthy as well as the Riley-Truhlar potential (Salvat *et al.*, 2005).

➢ Absorption potential: For the calculation of elastic scattering cross sections, it is sometimes helpful to optionally include an imaginary (absorptive) part into the static potential in order to account for the coupling with inelastic channels.

➢ Exchange potential: For in- and/or outgoing electrons, a possible exchange with a bound electron need to be taken into account as it occurs naturally if all electrons are treated together by an (antisymmetrize) Slater determinant. In general, however, these exchange terms in the Dirac-Hartree-Fock equations are difficult to deal with and are often approximated in some suitable form.

Scattering amplitudes and cross sections:

➢ Partial-wave expansion of the scattering amplitudes: For a projectile with wave number $k = \hbar/p$ and kinetic energy E, the direct and spin-flip scattering amplitudes are given by

$$f(\vartheta) = \frac{1}{2\,ik}\sum_{\ell=0}^{\infty}\{\,(\ell+1)\,[\exp(2i\,\delta_{\kappa=-\ell-1}) - 1] + \ell\,[\exp(2i\,\delta_{\kappa=\ell}) - 1]\}\,P_\ell(\cos\vartheta)$$

$$g(\vartheta) = \frac{1}{2\,ik}\sum_{\ell=0}^{\infty}[\exp(2i\,\delta_{\kappa=\ell}) - \exp(2i\,\delta_{\kappa=-\ell-1})]\,P_\ell^1(\cos\vartheta), \qquad (c\hbar\,k)^2 = E\,(E + 2mc^2),$$

and where $P_\ell^1(x)$ is an associated Legendre function. The scattering amplitudes above apply for both, electrons and positrons if the sign of their charges is taken into account, and which turns an attractive potential into a respulsive potential and *vice versa*.

➢ Analogue to non-relativistic theory, attractive potentials are generally associated with positive phase shifts and repulsive potentials with negative phase shifts.

➢ Elastic differential and total CS: (Salvat *et al.*, 2005)

$$\frac{d\sigma^{\,(\mathrm{elastic})}}{d\Omega} = |\,f(\vartheta)\,|^2 + |\,g(\vartheta)\,|^2, \qquad \sigma^{\,(\mathrm{elastic})} = \int d\Omega\,\frac{d\sigma^{\,(\mathrm{elastic})}}{d\Omega} = 2\pi\int_0^\pi d\vartheta\,\sin\vartheta\,\frac{d\sigma^{\,(\mathrm{elastic})}}{d\Omega}\,.$$

Spin-polarization of elastically scattered electrons:

➢ Sherman function: This function describes the degree of spin polarization of electrons or positrons as function of the scattering angle ϑ for an initally unpolarized beam

$$S(\vartheta) \equiv i\,\frac{f(\vartheta)\,g^*(\vartheta) - f^*(\vartheta)\,g(\vartheta)}{|\,f(\vartheta)\,|^2 + |\,g(\vartheta)\,|^2}.$$

Applications of elastic scattering:

➢ Application of differential elastic cross sections $\frac{d\sigma^{\,(\mathrm{elastic})}}{d\Omega}$: Accurate differential cross sections (DCS) for the elastic scattering of electrons and positrons by atoms and molecules are required in surface science, electron microscopy, electron-probe microanalysis, the design of radiation detectors, radiation protection, radiation-therapy planning and at several places elsewhere (Salvat *et al.*, 2005). Moreover, DCS for the elastic scattering by positive ions are needed also in order to describe the electron transport in plasmas.

8.3.t. Negative-continuum dielectronic recombination

Process, notations & application:

➢ Negative-continuum dielectronic recombination of an ion: $A^{q+} + e_s^- \longrightarrow A^{(q-2)+\,*} + e^+$

➢ Formal quantum notation: $|\alpha_i \mathbb{J}_i\rangle + |\varepsilon_i\, \kappa_i\rangle \longrightarrow |\alpha_f \mathbb{J}_f\rangle + |\varepsilon_f\, \kappa_f\rangle^+$

➢ The capture of an electron by a bare heavy nucleus may occur non-resonantly via the creation of a free-positron-bound-electron pair. This process is refered to as negative-continuum dielectronic recombination since it leads to the capture of (two) electrons into a bound state while a positron is relased.

8.3.u. Nonradiative electron capture (NRC)

Process, notations & application:

➢ Non-radiative electron capture of an ion: ... $A^{q+} + e^- + Z_t \longrightarrow A^{(q-1)+,\,(*)} + Z_t'$

➢ Formal quantum notation: $|\alpha_i \mathbb{J}_i\rangle + |\varepsilon_f\, \kappa_f\rangle \longrightarrow |\alpha_f \mathbb{J}_f\rangle$

➢ The nonradiative electron capture of a quasi-free electron by a projectile ion mainly occurs if the electron and ion velocities match to each other.

➢ The nonradiative capture is often described within the eikonal approximation, which enables one to estimate the capture from any filled shell of the target to any shell of the projectile.

➢ In high-Z targets, the nonradiative electron capture into excited states of the projectile is dominant, as predicted by the eikonal calculations and confirmed by measurements.

Nonrelativistic capture cross sections:

➢ In the nonrelativistic theory, the (nonradiative electron capture) cross section of a stationary bare nucleus to capture an electron with energy $E = \frac{m}{2} v^2$ is given by (Spitzer, 1956)

$$\sigma^{(\mathrm{NRC,\,non-rel})}(E) \;=\; A \sum_{n=1}^{\infty} \frac{\varepsilon_g}{\hbar\,\omega_n\,E\,n^3}\,g_n,$$

where $A = 32\pi/\sqrt{27}\,\hbar e^2/(m^2c^3) \approx 2.11 \times 10^{-22}$ cm^2, ε_g is the ground-state binding energy of the hydrogenic projectile and $\hbar\,\omega_n = E - \varepsilon_n$ the emitted photon energy for capture into level n. The factor $g_n \approx 1$ is a correction factor which is typically not specified in detail for most computations.

➢ For $g_n = 1$, this cross section can be written

$$\sigma^{(\mathrm{NRC,\,non-rel})}(E) \;=\; A\left(\frac{\varepsilon_g}{E}\right) \sum_{n=1}^{\infty} \frac{1}{n\,(n^2 + \frac{\varepsilon_g}{E})} \;=\; \frac{A\varepsilon_g}{2\,E}\left\{\psi\left(1 + i\sqrt{\frac{\varepsilon_g}{E}}\right) + \psi\left(1 - i\sqrt{\frac{\varepsilon_g}{E}}\right) + 2\,\gamma_E\right\}$$

where $\psi(z) = \frac{1}{\Gamma(z)}\frac{d}{dz}\Gamma(z)$ is the digamma function and $\gamma_E \approx 0.57772$ is Euler's constant.

➢ Using the asymptotic form of $\psi(z)$, the cross sections can then be approximated as

$$\sigma^{(\mathrm{NRC,\,non-rel})}(E) \;=\; A\left(\frac{\varepsilon_g}{E}\right)\left[\gamma_E + \ln\sqrt{\frac{\varepsilon_g}{E}}\right] .$$

Velocity distributions:

➢ Two velocity distributions have been frequently applied to study nonradiative electron capture processes at proton and heavy-ion storage rings.

➢ Maxwell distribution: $f(E) = \frac{1}{(2\pi kT/m)^{3/2}} \exp\left(-\frac{E}{kT}\right).$

➢ 'Flattened' Maxwell distribution: $f(E) = \frac{1}{(2\pi kT/m)} \exp\left(-\frac{E}{kT}\right) \delta(v_{\rm ex})$

which is obtained by suppressing one of the components of velocity.

➢ Nonradiative electron-capture rates: By using the asymptotic form of the digamma function in the nonradiative electron capture cross section above but different velocities distributions for the electrons to capture, various approximations for the capture rates can be derived. From the capture cross section $\sigma^{\rm (NRC,\,non-rel)}(E)$, the averaged coefficient α_r can be evaluated analytically for different velocity distributions

$$\alpha_r^{\rm (NRC,\,non-rel)}\,({\rm Maxwell}) = \frac{\sqrt{2}\,A\varepsilon_g}{\sqrt{m,kT}}\,\frac{2}{\sqrt{\pi}}\left\{\gamma_1 + \frac{\gamma_E}{2} + \Gamma\left(\frac{4}{3}\right)\,\gamma_2\,\left(\frac{kT}{\varepsilon_1}\right)^{1/3} + \ln\sqrt{\frac{\varepsilon_1}{kT}}\right\}$$

$$\alpha_r^{\rm (NRC,\,non-rel)}\,({\rm flattened}) = \frac{\sqrt{2}\,A\varepsilon_g}{\sqrt{m\,kT}}\,\sqrt{\pi}\left\{\gamma_1 + \frac{\gamma_E}{2} + \Gamma\left(\frac{5}{6}\right)\,\frac{\gamma_2}{\sqrt{\pi}}\,\left(\frac{kT}{\varepsilon_g}\right)^{1/3} + \ln\left(2\sqrt{\frac{\varepsilon_1}{kT}}\right)\right\}.$$

Semi-relativistic capture cross sections:

➢ Cross section calculations for nonradiative electron capture in relativistic heavy-ion collisions are often based on an eikonal approximation. Anholt (1985) adapted some prior form of the assymmetric eikonal theory in order to calculate total nonradiative electron capture cross sections from any filled target shell to any projectile shell by just scaling the nuclear charges Z_t and Z_p by the principal quantum numbers n_t and n_p. In general, this approximation was found to become better for high-energetic ions and can be applied confidentely also for ultra-relativistic collisions.

8.3.v. Vacuum-electron capture

Process, notations & application:

- Vacuum electron capture of an ion: ... $A^{q+} + Z_t + e^- + e^+ \longrightarrow A^{(q-1)+,(*)} + Z_t' + e^+$
- Formal quantum notation: $|\alpha_i \mathbb{J}_i\rangle + |\varepsilon_- \kappa_-\rangle + |\varepsilon_+ \kappa_+\rangle \longrightarrow |\alpha_f \mathbb{J}_f\rangle + |\varepsilon_+ \kappa_+\rangle$
- The vacuum electron capture process refers to the capture of an electron by fast projectiles due to the creation of an electron-positron pair and under the emission of the positron.
- In the vacuum electron capture, the target is considered to act as an perturbing potential that help create an electron-positron pair in the field of the projectile nucleus. While the electron is captured in one of the bound states (predominantly into $1s$), the positron is emitted.
- The creation of an electron-positron pair from the vacuum is similar to the Coulomb ionization process of the projectile ion, except that the relative momentum of the ion is impartet into the vacuum instead of exciting an electron into a higher state of the projectile.

Semi-relativistic capture cross sections:

- Due to the high value of momentum transfer, which is needed to excite an electron-positron pair from the vacuum, vacuum-electron capture takes place predominantly at small impact parameters, where the screening of the target nucleus by the target electrons is unimportant.
- Vacuum-capture cross sections The vacuum-capture process involves a momentum transfer from the target nucleus to the vacuum followed by an electron capture into the projectile K-shell. Therefore, the vacuum capture cross section is $\sim Z_t^2$, similar to most momentum transfer processes like excitation and ionization, and also $\sim Z_p^5$ as typical for projectile electron capture processes. For large γ, the cross sections increases as $\ln \gamma$ by they vanish for $v \ll c$ unlike for projectile ionization.
- Anholt and Becker (1987, table I) provide (reduced) vacuum capture cross sections for any combination of target-projectile and for $\gamma \geq 10$. For these large values of γ, the cross section is approximately

$$\sigma^{(\mathrm{VAC})} = Z_p^5 \, Z_t^2 \, a \, \ln\left(\frac{\gamma}{\gamma_0}\right) \qquad (\gamma > \gamma_0)$$

where $a\,(Z_p)$ is a slowly varying function between 0.4 and 2.7 and γ_0 is an offset. As the capture into higher shells than the K-shell varies as n^{-3}, the cross section for $1s$ has been multiplied by 1.2 by Anholt and Becker to provide an estimate for the total capture. For $\gamma > 10$, these cross sections are expected to be accurate within approximately 20 %.

➢ The capture of an electron into the $1s$ shell of the projectile under the simultaneous emission of a positron has been calculated by Becker *et al.* (1987) and by Bertulani and Bauer (unpublished).

8.3.w. Positron-bound-electron pair annihilation with single-photon emission (PairAnnihilation1Photon)

Process, notations & application:

➢ Positron-bound-electron pair annihilation with single-photon emission from an atom or ion: $A^{q+} + e^+ \longrightarrow A^{(q+1)+*} + \hbar\omega$

➢ Formal quantum notation: $|\alpha_i \mathbb{J}_i\rangle + |\varepsilon\,\kappa\rangle^+ \longrightarrow |\alpha_f \mathbb{J}_f\rangle + \hbar\omega\,(\mathbb{M})$

➢ A positron can annihilate with a bound electron from an atom or ion under the emission of one, two or more photons. Here, we consider the emission of a single photons which is possible only due to the presence of the atom.

8.3.x. Positron-bound-electron pair annihilation with two-photon emission (PairAnnihilation2Photon)

Process, notations & application:

➢ Positron-bound-electron pair annihilation with two-photon emission from an atom or ion: $A^{q+} + e^+ \longrightarrow A^{(q+1)+*} + \hbar\omega_1 + \hbar\omega_2$

➢ Formal quantum notation: $|\alpha_i \mathbb{J}_i\rangle + |\varepsilon\,\kappa\rangle^+ \longrightarrow |\alpha_f \mathbb{J}_f\rangle + \hbar\omega_1\,(\mathbb{M}_1) + \hbar\omega_2\,(\mathbb{M}_2)$

➢ A positron can annihilate with a bound electron from an atom or ion under the emission of one, two or more photons. Here, we consider the emission of two photons.

➢ Positron-emission tomography: A detailed understanding of the angular distribution of photon pairs from the (e^-, e^+) annihilation determines the spatial resolution of tomography and the defect analysis of tissue and materials. A good quantitative understanding of this emission is relevant also for upcoming positron facilities, e.g. at the Lawrence Livermore National Laboratory.

Cross section for positron-bound-electron annihilation:

➢ Differential cross section for positron-bound-electron annihilation: The differential cross section for the annihilation of a positron with energy ε_i and velocity v_i by a bound electron with energy ε_a via the simultaneous emission of a photon pair is given (in relativistic units) by (Zaytsev *et al.*, 2019)

$$\frac{d^2\sigma}{d\mathbf{k}_1\, d\mathbf{k}_2} = 4\,\alpha^2\,\frac{(2\pi)^6}{v_i}\,|\mathcal{M}|^2\,\delta(\varepsilon_a + \varepsilon_i - \omega_1 - \omega_2)$$

$$\mathcal{M} = -\sum_n \left(\frac{\langle(-p_i\mu_i)\,|\,\boldsymbol{\alpha}\cdot\boldsymbol{A}^*_{\mathbf{k}_2\lambda_2}\,|\,n\rangle\,\langle n\,|\,\boldsymbol{\alpha}\cdot\boldsymbol{A}^*_{\mathbf{k}_1\lambda_1}\,|\,a\rangle}{\varepsilon_a - \omega_1 - \varepsilon_n\,(1-i\,0)} + \frac{\langle(-p_i\mu_i)\,|\,\boldsymbol{\alpha}\cdot\boldsymbol{A}^*_{\mathbf{k}_1\lambda_1}\,|\,n\rangle\,\langle n\,|\,\boldsymbol{\alpha}\cdot\boldsymbol{A}^*_{\mathbf{k}_2\lambda_2}\,|\,a\rangle}{\varepsilon_a - \omega_2 - \varepsilon_n\,(1-i\,0)} \right)$$

Here, $\sum_n$ implies the summation over the complete spectrum of the single electron, including the summation over the positive and negative parts of the continuum. μ_i is the helicity of the incident positron. Both, the double-differential cross section and the amplitude follow standard lines from the QED formalism.

➢ Differential cross section for positron-bound-electron annihilation: In practice, one typically needs to consider only the double differential angular cross section

$$\frac{d^2\sigma}{d\Omega_1\, d\Omega_2} = \int d\omega_1\, d\omega_2\, \omega_1^2\, \omega_2^2\, \frac{d^2\sigma}{d\mathbf{k}_1\, d\mathbf{k}_2},$$

and which needs to be further averaged over the angular momentum and spin projections of the bound electron and positron as well as (to be summed over) the polarization of the emitted photons.

:

➢

8.3.y. Positron-bound-electron pair production by a photon (PairProduction)

Process, notations & application:

➢ Positron-bound-electron pair production by a (single) photon of an atom or ion: $A^{q+} + \hbar\omega \longrightarrow A^{(q-1)+*} + e^+$

➢ Formal quantum notation: $|\alpha_i \mathbb{J}_i\rangle + \hbar\omega(\mathbb{M}) \longrightarrow |\alpha_f \mathbb{J}_f\rangle + |\varepsilon\, \kappa\rangle^+$

➢ At high photon energies, the electron-photon interaction can lead to the creation of an electron-positron from which the electron is eventually bound by a multiply or highly-charged ion.

8.4. Other topics closely related to atomic processes

8.4.a. Atomic database from the literature

CHIANTI: A database for emission lines:

- CHIANTI is a database of assessed atomic parameters and transition rates that are needed for the simulation of line and continuum emission spectra from optically thin and collisionally-dominated plasma.
- CHIANTI was first released in 1996 and, since then, several new releases have been made available in order to expand the database and improve the quality of the data. Emphasis in developing this database has been given especially to the line identification and improvement of the reference wavelengths.
- For several ions, the wavelengths and identifications are different from and considered to be more accurate than those of the NIST database. Therefore, CHIANTI is now often applied as a reference atomic database for ions and has been included into several other atomic codes and packages.
- In its last version (Del Zanna *et al.*, 2015), the CHIANTI database includes a large amount of new data which improve simulations for the soft x-ray, extreme UV (EUV) as well as UV spectral regions. These regions are currently covered by several space missions.

DREAM: A database for lanthanide spectra:

- DREAM database The Mons group (Biemont and coworkers) have calculated various neutral and near-neutral lanthanide spectra; these data are kept within the DREAM database. In these computations, they employed the least-squares fitting procedure in the Cowan code (Cowan 1981) together with a core-polarization potential in order to obtain spectroscopic quality radiative rates.

NIST-XCOM:

- The XCOM database provides photon scattering data and attenuation coefficients between 1 keV and 100 GeV for all the elements of the periodic table. It also lists total cross sections, attenuation coefficients and partial interaction coefficients for selected processes, such as Compton and Rayleigh scattering, photoelectric absorption as well as pair production (Amako *et al.*, 2005).

NIST-ESTAR:

➢ The ESTAR database provides (electron) stopping powers and ranges for incident electrons with energies between 10 keV and 1 GeV, and as derived from the so-called ICRU Report (Amako *et al.*, 2005).

NIST-PSTAR:

➢ The PSTAR and ASTAR databases provide (proton) stopping powers and ranges for incident protons with energies between 1 keV – 10 GeV, and as derived from the so-called ICRU Report 49.

8.4.b. Codes that require atomic data input

Codes from astro and plasma physics:

➢ The main reason for differences in the output of different codes are typically the different sources of atomic data.

➢ Radiative-Collisional code based on FAC, RCF: This code has been used to simulate steady-state plasmas under non-local thermodynamic equilibrium condition, and especially for photoinization-dominated plasmas. RCF takes almost all of the radiative and collisional atomic processes into account by rate equations in order to interpret the plasmas systematically. The Flexible Atomic Code (FAC) supplies all the atomic data that are needed for RCF in order to ensures completeness and consistency of the atomic data.

➢ RCF is a steady-state, collisionalradiative, optically thin model. Its rate-equation

$$\frac{dN_{i,j}}{dt} = \text{populating processes} - \text{depopulating processes} = 0$$

where $N_{i,j}$ is the density of the j-th level in the i-th charge state. RCF includes ionization and recombination between neighboring charge states as well as the excitation and de-excitation within the same charge state. Moreover, the inverse processes are typically taken into account by the detailed-balance principle.

➢ GALAXY employs an average-of-configuration approximation for the electronic states as well as screened hydrogenic wave functions for both, the collisional and radiative processes. This code also employes Hartree-Dirac-Slater or Kramers cross-sections for photoionization.

- ➢ FLYCHK uses a hydrogenic approximation in order to calculate energy levels and level populations. However, the results of GALAXY and FLYCHK largely deviate from measured ones.
- ➢ In PHICRE, the energy levels and spontaneous decay rates are taken from the NIST database, and other rate coefficients are calculated by widely used formulas.
- ➢ ATOMDB calculates the x-ray/UV spectrum of a hot, collisionally-dominated optically-thin plasma, based on knowledge of the atomic transition rates and energies of the involved ions. This code also help analyse the interplay between the different rates. The line and continuum results of ATOMDB (`http://www.atomdb.org`) apply to an optically-thin thermal plasma with astronomical abundances; cf. Anders and Grevesse (1989).
- ➢ XSTAR is a command-driven, interactive, computer program for calculating the physical conditions and emission spectra of photoionized gases; cf. `http://ascl.net/9910.008`. It may be applied in a wide variety of astrophysical contexts. In particular, XSTAR computes the reradiated light when the gas of a star absorbs energy. The user typically need to supply the shape and strength of the incident continuum, the elemental abundances in the gas as well as the density or pressure, and the thickness of the gas layer.
- ➢ MOOG code: This code generates synthetic absorption spectra of photospheres in cool stars by assuming a local thermodynamic equilibrium. It requires an (externally given) model atmosphere in order to derive the temperature, gas pressure and electron density at different layers of the surface gas. The code also requires an atomic line list that comprises all data about the absorption transitions (at rest), oscillator strength as well as excitation (ionization) energies of the lower levels for the element or ion of interest.
- ➢ In the MOOG code, the strengths of the observed absorption features are obtained by solving the radiative transfer equations with a plane-like parallel treatment of the atmosphere, and where the velocity distribution of the ions is assumed to be Maxwellian. Moreover, the excitation and ionization processes of the ions in selective charge states are described by the Boltzmann and Saha equations.
- ➢ The MOOG code basically follows some prior code developments by Kurucz (http://kurucz.harvard.edu/); for contact use: chris@verdi.as.utexas.edu.
- ➢ The MOOG code has been applied with Kurucz' model atmosphere and with data from the NIST data base.

8.4.c. Radiative opacities

Radiative opacity computations:

- Radiative opacity of a plasma: The radiative opacity of a plasma is of great significance for various research fields, such as inertial confinement fusion, stellar physics as well as the development of x-ray lasers. The (so-called) Opacity Project calculated the atomic data for most astrophysically abundant elements and also generated a database of opacities.
- Opacity computations generally imply the accurate knowledge of different atomic data, such as level energies, oscillator strength, photoionization cross sections for all ionic species in the plasma. They also require simulations over a wide range of temperatures and densities, an adequate equation of state for determining the ionization fractions and level populations and information about line broadening mechanisms.
- Knowing the opacity of a plasma, the fraction of transmitted radiation with regard to some incident radiation of given intensity can be expressed as:

$$F(h\nu) \;=\; \exp\left(-\rho\,\eta'\,L\right), \qquad\qquad \eta' \;=\; \eta'(h\nu)$$

  where L is the path length of the light travelling through the plasma, ρ the mass density and $\eta'(h\nu)$ the radiative opacity. The fraction of transmitted radiation can be readily determined experimentally and can be obtained theoretically by taking the integral over a Gaussian function, if the full width corresponds to the spectrometer resolution.
- Radiative opacity of iron plasma: The radiative opacity of iron plasmas at high temperatures has been found important in astrophysics and, therefore, various experiments have been carried out to accurately measure their radiative opacity during recent decades.
- Although the fraction of iron is typically quite small in most stellar environments, especially when compared with the high abundance of hydrogen and helium, the opacity of iron plays an important role for understanding the radiative transfer in astrophysical plasmas, such as the Sun.
- Opacity computation can provide valuable information about a plasma, including the fractional distribution of the different ion stages and whether the plasma is in a local thermodynamic equilibrium (or not) as well as about the temperature gradient in plasma.
- Radiative opacity are often analysed and displayed either as isothermal sequences for different mass densities and as isodensity sequences for different temperatures.
- Barnes and Kasen (2013) applied the line data from the VALD database in order to study the opacityy of the lanthanides and to demonstrate that these heavy elements may exhibit a much larger opacity. At present, however, the limitations of VALD does not allow to compute reliable r-process opacities over the wavelength and temperature range as required by realistic transport calculation. In particular, VALD contains almost no lines with wavelengths greater than $1\,\mu$m and, hence, cannot be applied to compute sensible infrared opacities or emissivities of the neutron-star merger.

- A detailed modelling of the radiative properties of the high-Z ions will be a long-term endeavor because of the number of electrons and the shell structure of the lanthanides as well as most elements beyond.
- The atomic properties of the light elements ($Z < 30$) are known reasonably well from experiment and many previous computations. In particular, Kurucz (1993) and Kurucz and Bell (1995) provide an extensive list of lines (with about 42 million lines and 500,000 line shifts), which is dominated by the lines from the iron group elements. These lists were generated by using the CATS code (Cowan 1981) and by tuning the theoretical energies semi-empirically in order to reproduce the extensive observed experimental level energies.

Definition of detailed and mean radiative opacities:

➢ Radiative opacity $\eta(\hbar\omega)$: For a plasma in a local thermodynamic equilibirum at temperature T and mass density ρ, the radiative opacity $\eta(\hbar\omega)$ is given by (Cheng and Jiaolong, 2008)

$$\rho\,\eta(\hbar\omega) \;=\; \left[\mu^{\,(\text{bound}-\text{bound})}(\hbar\omega) \,+\, \mu^{\,(\text{bound}-\text{free})}(\hbar\omega) \,+\, \mu^{\,(\text{free}-\text{free})}(\hbar\omega)\right] \,\left(1 \,-\, \exp\left(\frac{\hbar\omega}{k_B\,T}\right)\right) \,+\, \mu^{\,(\text{scattering})}(\hbar\omega)$$

where $\mu^{\,(\text{bound}-\text{bound})}$, $\mu^{\,(\text{bound}-\text{free})}$, $\mu^{\,(\text{free}-\text{free})}$ and $\mu^{\,(\text{scattering})}$ are the absorption coefficients due to bound-boud, bound-free, free-free and well as scattering processes, respectively.

➢ Rosseland mean opacity: Radiative transfer is mainly controlled by the Rosseland mean opacity and is often expressed in terms of the reduced photon energy u

$$\frac{1}{\kappa_R} \;=\; \left[\frac{dB}{dT}\right]^{-1} \,\left[\int_0^\infty d\nu\,\frac{1}{\kappa_\nu}\,\frac{\partial B_\nu}{\partial T}\,\right] \;=\; \int_0^\infty du\,\frac{1}{\kappa_u}\,\times\,g(u), \qquad g(u) \;=\; \frac{15}{4\pi^4}\,u^4\,\frac{\exp(-u)}{\left[1\,-\,\exp(-u)\right]^2}, \qquad u \;=\; \frac{h\nu}{kT}\,.$$

➢ Rosseland mean opacity: The Rosseland opacity is defined by

$$\frac{1}{K^{\,(\text{Rosseland})}} \;=\; \int_0^\infty du\,\frac{W^{\,(\text{Rosseland})}}{\eta(u)}\,, \qquad W^{\,(\text{Rosseland})} \;=\; \frac{15}{4\,\pi^4}\,\frac{u^4\,e^{-u}}{(1\,-\,e^{-u})^2}, \qquad u \;=\; \frac{\hbar\omega}{k_B\,T}.$$

➢ Planck mean opacity:

$$\frac{1}{K^{\,(\text{Planck})}} \;=\; \int_0^\infty du\,W^{\,(\text{Planck})}\,\left[\eta(u)\,-\,\eta^{\,(\text{scattering})}(u)\right]; \qquad W^{\,(\text{Planck})} \;=\; \frac{15}{\pi^4}\,\frac{u^3\,e^{-u}}{(1\,-\,e^{-u})}, \qquad u \;=\; \frac{\hbar\omega}{k_B\,T}.$$

➢ Rosseland and Planck mean opacities: The spectrally-resolved Rosseland and Planck mean opacities for iron plasmas at different temperatures from a few eV to a few hundred eV have been found useful important in studying the evolution of stars, such as the Sun. These studies range from the stellar envelopes to their interiors.

➢ The Rosseland and Planck mean opacities are required for many practical applications such as radiative transfer.

➢ Gray opacity: The gray opacity value just results from the Thomson-scattering opacity, $\kappa^{\,(\text{Thomson})} \,=\, 0.4(\bar{Z}/A)\ \text{cm}^2/\text{g}$ and if one assumes a (fully) ionized material (medium) with $\bar{Z} \,=\, Z$. Here, A is atomic weight and one often applies $\bar{Z}/A \,\approx\, 1/2$ for most elements.

Spectral intensity and energy density:

➢ Spectral intensity I_λ: The (specific) light intensity describes the amount of electromagnetic radiation with wavelengths between $\lambda \,...\, \lambda+d\lambda$ that passes in the time dt through the area dA and into the solid angle $d\Omega = \sin\vartheta\, d\vartheta\, d\varphi$ (Pettini 2018)

$$W_\lambda\, d\lambda \;=\; I_\lambda(\vartheta,\varphi)\, d\lambda\, dt\, dA\, \cos\vartheta\, \sin\vartheta\, d\vartheta\, d\varphi$$

In astrophysics, the intensity is often measured in units: erg s^{-1} cm^{-2} $Å^{-1}$ sr^{-1}.

➢ Spectral and total energy density u_λ: The specific energy density refers to the energy per unit volume that is contained in the radiation field with wavelengths between $\lambda \,...\, \lambda + d\lambda$, and from which the total energy density is easily obtained

$$u_\lambda\, d\lambda \;=\; \frac{d\lambda}{c} \int d\Omega\, I_\lambda(\vartheta,\varphi) \;=\; \frac{4\pi}{c}\, J_\lambda\, d\lambda \qquad \Longrightarrow \qquad u \;=\; \int_0^\infty d\lambda\, u_\lambda$$

8.4.d. Opacities for astrophysical matter clouds

Astrophysical opacities models:

➢ Opacity: The opacity of a (plasma) medium characterizes the transport of radiation through matter. Opacity computations generally require atomic data for a large number of processes involving the absorption and scattering of radiation (Seaton 1987).

➢ A new astrophysical opacity model (called OPAL) has been developed at the Lawrence Livermore National Laboratory (LLNL) with which it was shown that $\Delta n = 0$ transitions results in many overlapping lines. This overlap significantly increase the opacity of the iron component of the mixtures and which was suggested also to apply for their observation of stellar pulsations.

➢ Need of opacities: Opacities are frequently applied in various research fields, such as the standard solar model (SSM), helio and astero-seismology, non-LTE 3D hydrodynamic photospheric modeling, nuclear reaction rates, solar neutrino observations, computational atomic physics as well as in plasma experiments (Mendoza 2018).

➢ Typically opacity computations have considered a total of up to 10^8 radiative lines. Since these computations cannot so easily be extended towards high-Z elements, the average-atom description has been applied as an alternative approach.

➢ Local Thermodynamic Equilibrium (LTE): Despite the complexity of (and complications with) astrophysical plasma, one makes often use of the LTE approximation as long as the mean free path of the photons and particles is small compared to the scale over which the temperature changes significantly. This applies for instance to many stellar interiors because of the high density and temperature and, hence, quite small mean distances between collisions.

➢ Expansion opacity: Most atomic computations are based on the formalism by Karp *et al.* (1977):

$$\kappa^{\,(\mathrm{expansion,bb})} \;=\; \frac{1}{\rho\, ct} \sum_{\ell} \frac{\lambda_\ell}{\Delta\lambda} \left(1 \,-\, e^{-\,\tau_\ell}\right), \qquad\qquad \tau_\ell \;=\; \frac{\pi\, e^2}{m\, c}\, f_\ell\, n_\ell\, \lambda_\ell\, t \;=\; \frac{\pi\, e^2}{m\, c} \left(\frac{n\, \lambda_\ell\, t}{g_o}\right) g_\ell\, f_\ell\, e^{-E_\ell/kT}.$$

In this expansion opacity, ρ and t refers to the density and time after the merger, while the summation runs over all lines ℓ in the chosen wavelength bin ($\Delta\lambda$), and where λ_ℓ is the transition wavelength and τ_ℓ the (so-called) Sobolev optical line depth. Here, moreover, g_ℓ, E_ℓ, f_ℓ are the statistical weight and the energy of the lower level as well as the oscillator strength of the transition.

➢ Number density n_ℓ: For the number density n_ℓ of levels at the energy of the lower levels, a Boltzmann distribution $n_\ell = \frac{g_\ell}{g_o}\, n\, \exp(-\,E_\ell/kt)$ is assumed, and where g_o refers to the statistical weight of the ground level. In the formulation by Karp *et al.* (1977), moreover, the number density n is calculated from the Saha equations by assuming an LTE.

Opacity calculations:

➢ Radiative opacities are required for the modeling of astrophysically relevant plasmas under local thermodynamic equilibrium (LTE) conditions. For the computation of these opacities, the atomic structure calculations should be carried out for all fine-structure levels and by including electronic correlations.

➢ Early opacity computations have often used data obtained from simple atomic models. However, already Simon (1982) suggested that such simple estimates are too small by factor of 2-3 for all elements heavier than helium.

➢ Three typical example applications for opacity calculations are: (i) The iron opacities at conditions of the solar convection zone, (ii) nickel opacities for modeling various stellar envelopes and (iii) the samarium opacities for the modeling of light curves as produced by neutron star mergers.

➢ In some recent work, the frequency-dependent LTE opacity of iron has been studied for the conditions of the solar convection zone. These studies revealed rather large (30-400%) differences between experiment and theory for the monochromatic opacity of an neon-like iron plasma (or nearby charge states). Until the present, the source of this not yet fully understood and remains an active area of research.

➢ Opacity calculations for lanthanides or actinides: In the previous opacity computations of the lanthanides or actinides, rather large uncertainties arose from the – experimentally and theoretically – unknown atomic states and line strengths of these complex elements. Indeed, these high-Z atoms still represent a major challenge for accurate atomic calculations and often requires the use of statistical models, and which need to be calibrated to experimental data.

➢ Opacities for ejecta from NS mergers: At the near-IR/optical frequencies, the dominant source of opacity arises from many bound-bound transitions between the low-lying levels of the atoms and ions. For this *continuum* of lines, the opacity is determined by the strength and wavelength density of the lines, and which depend sensitively on the composition of the ejecta.

➢ Opacities for ejecta from NS mergers: The opacity of the ejecta from NS mergers can significantly rise if they just contain a modest fraction of elements with a partially-filled f-shell, such as the elements from the lanthanide and actinide groups.

➢ Iron opacity: When compared to previous estimations, OPAL iron monochromatic opacities at density $\rho = 6.82 \times 10^{-5}$ g cm^{-3} and temperature $T = 20$ eV indicated large enhancements at photon energies around 60 eV, which may arise from $\Delta n = 0$ unresolved transition arrays in Fe, and which is supported by laboratory photoabsorption measurements.

➢ Bound-bound opacity: For nearly-neutral ions and neutral atoms, the bound-bound opacity depend sensitively on the level density just above of the ground state. This density increases with the electron occupation until a shell is half-filled, and this density may become quite sizeable for several open shells. Moreover, a large level density occurs for open d- and f-shell elements, i.e. the $3d$ and $4d$ transition elements and lanthanides. In general, the energy-level density is slightly shifted towards higher energies (above of the ground level) if the number of electrons increase in a given shell.

Opacity measurements for homogeneous plasma with uniform density:

➢ Uniform plasma density: For a uniform density, the transmisison of the sample

$$T(\omega) = \frac{I(\omega)}{I_o} = \exp\left(-\rho\, L\, \kappa(\omega)\right)$$

is measured where $I(\omega)$ is the attenuated intensity of the probe (backlighter) radiation and I_o the reference intensity. This transmission is related also to opacity by the Beer-Lambert law if the reabsorption can be neglected in the homogeneous plasma. Here, ρ is the density of the material and L its thickness.

➢ Iron opacity: Bailey *et al.* (2015) measured iron opacities at electron temperatures between $1.9 - 2.3$ million kelvin and electron densities between $(0.7 - 4.0) \times 10^{22}$cm^{-3} at the Z facility. In these measurements, the observed optical absorptions was found about $\sim 30 - 400$ % higher than those predicted by currently applied opacity models.

Neutron star mergers:

- Neutron stars: These stars have been postulated already short after the discovery of the neutron as the ultimate fate of massive stars, that end in a supernova. The existence of neutron stars was later shown in the 1960s following the observation of the first pulsars.
- Today, the equation of state and the distribution of neutron star masses are believed to be known reasonably well.
- The mass of the ejecta from neutron star mergers are predicted to be rather high and to reach from $10^{-3} \,..\, 10^{-2}\, M_\odot$ for the overall r-process matter.
- Modern simulations of neutron star mergers take into account both, the (elemental) composition of the ejecta as well as the neutrino wind along the poles.
- Material ejected from neutron-star mergers: The material that is ejected during or immediately after the merger of two neutron stars may produce considerable amounts of heavy elements through the r-process. The subsequent radioactive decay of these (neutron-rich) nuclei can power transient electromagnetic emission similar to, but significantly dimmer than, an ordinary supernova (Kasen *et al.*, 2013). One goal of future observations of the electro-magnetic transients in gravitational-wave astronomy is to better understand this r-process and, hence, the astrophysical sources of gravitational waves.
- Material ejected from neutron-star mergers: A key in studying the matter outside of the remnant of the neutron-star merger is the release of neutron rich-matter and a cascade of nuclear reactions. These reaction gives then rise to kilonova which can be observed on the time scale of hours, days and even months due to the radioactive decay of freshly synthesized, neutron-rich elements in the ejected matter.
- Light curves from neutron-star mergers: Since very little is known about the optical properties of the heavy r-process elements, most previous light-curve models have adopted the opacities from the iron group elements. Barnes and Kasen (2013) considered first the opacities of lanthanides and concluded, that the opacity of the ejecta material from neutron-star mergers might be larger by several orders of magnitude. In further detail, Barnes and Kasen included these opacities into time-dependent, multi-wavelength radiative transport calculations in order to predict the broadband light curves for a range of masses and velocities of the ejecta.
- Light curves of NS mergers: For heavy atoms and ions, such as the lanthanides and all heavier elements, the opacities of the r-process material are expected to be order of magnitude higher that those of the iron group elements. This increase of the opacity is not only caused by the complex shell structure of the heavy atoms and ions but also by the number and diversity of available atomic species. Such an enhanced opacity then results in (predicted) light curves that are longer, dimmer, and redder than previously thought. These light curves are not sharply peaked $t \sim 1$ day may lead to bolometric light curves $\sim$ week(s), cf. Barnes and Kasen (2013). Indeed, simulation suggest pseudo-blackbody spectra with some broad absorption features and some peak in the infrared (1 μm).

➢ Light curves from NS mergers: Tanvir *et al.* (2017) report the observation of optical and near-infrared spectra of the transient state of the ejecta from the NS merger (AT2017gfo). In particular, they have analyzed the broadband spectral energy distribution of AT2017gfo in a galaxy at $\sim$ 40 Mpc over the first 12 days, which shows a remarkable color change from blue to red. In more detail, the observed light curves exhibit both, a rapidly evolving blue and more slowly evolving red components.

➢ Ligh curves from NS mergers: The rise and decay of the (optical) light curves can be used together with the velocity of the ejecta in order to estimate its mass in terms of the opacity κ

$$M \;\sim\; 5 \times 10^{-3}\, M_\odot \left(\frac{0.1\ \mathrm{g\ cm^{-2}}}{\kappa} \;\; \frac{\nu}{0.1\, c} \right).$$

This estimate suggests, however, that only a fraction 10^{-3} of the totally released energy contributes to the kinetic energy of the ejecta.

➢ Light curves: In neutron-star mergers, the light curves usually decline rapidly in the *optical* region, while they evolve more slowly in the *near-infrared* (NIR) region. Moreover, a high expansion velocity is generally expected if featureless spectra are observed.

➢ Evolution of light curves: The evolution of the light from the transient state of the NS merger has been found consistent with predictions of kilonovae which are powered by the radioactive decay of massive neutron-rich nuclides due to the r-process nucleosynthesis in the neutron-star ejecta.

➢ Light curves from NS mergers: The analysis by Tanvir *et al.* (2017) of the multi-band light curves indicates the presence of at least two emission components: one with high opacity, and a second with low opacity. The high-opacity component arised due to the *tidal part* of the dynamical ejecta with a low electron fraction $Y_e \leq 0.25$.

Gravitational-wave astronomy:

➢ The discovery of gravitational waves (GW) from the inspiral and coalescence of binary black holes (BH) and/or neutron stars (NS) by the Laser Interferometer Gravitational Wave Observatory (LIGO) has opened a new window on the cosmos.

➢ The discovery of electromagnetic signals in coincidence with a chirp at the graviational-wave detectors leads to a better location and a much richer picture about the merger process. This may allow to extract directly information on the binary formation channels, the age of the stellar population as well as the dynamics of binary mergers.

➢ In general, the merger of BH binaries is not expected to produce luminous electro-magnetic emission because there is not enough baryonic matter in these systems.

- Gravitational-wave (GW) astronomy: The direct detection of GW opened a new era of (GW) astronomy. To further understand the astrophysical nature of GW sources, the identification of their electromagnetic (EM) counterparts is crucial, since the GW detectors are generally not accurate enough to pin down the position of these GW sources.
- Despite of a rather large number of expected BH-BH mergers during the next few years, a better synthesis and analysis of gravitational wave and the associated electro-magnetic signals will probably come from NS-NS or BH-NS mergers, i.e. if neutron stars are involved.
- Sources of graviational waves (GW): While most detected GW sources are nowadays believed to arise from black-hole binaries, neutron star mergers are another major source of gravitational waves. For thise NS mergers, an electro-magnetic signal is expected to arise in two forms: gamma-ray bursts (GRB) or from kilonovae (Metzger *et al.*, 2010). The GRB are expected to be short-lived with a jet-type signal, while the kilonovae are predicted to generate relatively isotropic signals.
- Sources of graviational waves: In practice, it is not easy to precisely locate the sky position of GW sources since they need to be determined by triangulating the arrival times of the GW signals from different detectors. At present, the uncertainties in this triangulation are quite large, although these uncertainties will be reduced to $\approx 10 - 100$ deg^2 , once Virgo in Italy and, eventually, KAGRA in Japan and LIGO-India will join the network (Metzger 2017). Initially, these uncertainties were ≈ 850 deg^2 for GW15091 and with a later improvement to ≈ 250 deg^2), though
- Even an localisation of the GW signals within $10 - 100$ deg^2 greatly exceeds however the fields of view of most radio, optical and x-ray telescopes, and in particular the field of view of those telescopes that are sensitive enough to detect the electro-magnetic counterparts of NS-NS and BH-NS mergers.
- Short γ-ray bursts (GRB): Although these short GRB are bright and high-energetic events, only a subset of these bursts will be observed since the most intense emission from a given merger will typically not intersect the line of sight from the Earth.
- γ-ray bursts (GRB): Short GRB are commonly believed to be powered by the accretion of a massive remnant disk, following some BH and/or NS mergers. These GRB are typically expected to occur already within seconds of the GW chirp, providing an unambiguous temporal signature to the GW signal. Although such short GRB are likely the cleanest electro-magnetic counterparts to the GW signals, their measured rate will remain low within the Advanced LIGO detection volume. This rate will probably be less than one observable event per year if the GW signal arises from NS-NS mergers since the γ-ray emission is beamed into a narrow solid angle not seen from Earth (Metzger 2017).
- NS-NS and BH-NS mergers are also predicted to be accompanied by a more isotropic counterpart, commonly known as kilonovae. These kilonovae provide both a robust electro-magnetic counterpart to the GW chirp, and which is expected to accompany a good fraction of BH-NS mergers and essentially all NS-NS mergers (Metzger 2017).

- The single NS-NS merger event (GW170817, GRB170817A, AT2017gfo) made a big qualitative step for gravitational-wave astronomy since it showed that these mergers can be observed and are directly linked to gravitational waves, gamma-ray bursts, kilonovae as well as the generation of heavy elements (nucleosynthesis).
- Role of neutrinos for neutron-star mergers: The absorption of neutrinos can make the ejected material from neutron-star mergers less neutron-rich and can increase the so-called electron fraction Y_e, e.g. the number of protons per nucleon.
- Simulation of NS mergers: While different (relativistic) simulations of NS mergers have predicted a wide ranges of electron fractions $Y_e = 0.05, ..., 0.45$, although a detailed understanding of the electron distribution depends on the nuclear equations of state as well as the masses and mass ratio of the neutron stars. For the sake of simplicity, a flat mass distribution and an electron fraction $Y_e = 0.1, ..., 0.4$ are assumed to represent dynamical ejecta.
- Spectra from AT2017gfo: A series of spectra have been observed from this merger has enabled one to analyze the evolution of the kilonovas primary electromagnetic output from 1.5 days until 10 days after the event (Watson *et al.*, 2019). It is expected from rather simple estimates that a large number of moderate-to-weak lanthanide lines with unknown oscillator strengths dominate the observed spectra. For a spherically expanding ejecta, the line broadening should be then comparable to the expansion velocity of the gas. However, a more detailed analysis will require also additional knowledge about the geometry of the gas cloud and the wavelength-dependent opacities over a wide range of elements.

Kilonovae:

- Kilonova: Kilonovae are day to week-long thermal, supernova-like transients which are powered by the radioactive decay of heavy, neutron-rich elements synthesized in the expanding ejecta of NS-NS or NS-BH mergers. The radioactive decay of such unstable neutron-rich nuclei powers a rapid evolution of a supernova-like transition of stellar matter that is known as kilonova or macronova in the literature. These kilonovae can be understood also as roughly isotropic electromagnetic counterpart to the GW signal and, thus, provide a unique and direct probe of such r-process sites (Metzger 2017).
- Kilonovae refer to optical transients that are powered by the radioactive decay of material ejected in the neutron-star merger. Simulations suggest an ejected mass of $10^{-4} ... 10^{-1}\, M_\odot$ due to a tidal stripping during the merger process itself or by a subsequent disk wind in course of the evolution of a post-merger remnant.
- Kilonovae: Kilonovaes are powered by the radioactive decay of it excited nuclear matter. These kilonovaes will emit more isotropically (compared to the accregation disk of the merger event) and will peak later than short-GRB afterglows. Kilonovaes are the best candidates for the electromagnetic counterparts of the GW detection.

- ➢ Photon emission from kilonovae: A detailed understanding of the photon emission from kilonovae require (detailed) information and simulations on the composition, velocity structure and the opacity of the ejecta as well as on the transport of radiation through the ejecta.
- ➢ Key observables of kilonovae: Three main ingredients need to be understood to quantify the key observables of a kilonovae, namely its peak time scale, the luminosity and the effective temperature. These ingredients are: (i) The mass and velocity of the ejecta from NS-NS or BH-NS mergers; (ii) the opacity κ of the expanding neutron-rich matter; and (iii) the variety of sources which contribute to the heat of the ejecta $Q(t)$. This ingredients are important especially on the time scale of $t^{(\mathrm{peak})}$, when the ejecta is first becoming transparent.
- ➢ Kilonovae: This term refers to an optical/infrared transient that has been observed a few days after the merger of two neutron stars. These transient spectra may allow to observe spectral signatures of newly created neutron-capture elements. For example, Watson *et al.* (2019) reported the identification of the neutron-capture element strontium from a detailed re-analysis of the observed transient spectra. The identification may prove that neutron stars are made of neutron-rich matter, although the discussion by Watson *et al.* seem not to be very stringent.

r-process:

- ➢ Burbidge *et al.* (1957) and Cameron (1957) realized already more than 60 years ago that approximately half of the elements heavier than iron are synthesized via the capture of neutrons by light seed nuclei, such as iron, in a dense neutron-rich environment, in which the time scale for neutron capture is shorter than the lifetimes for β-decay.
- ➢ Opacities of the *r*-process Barnes and Kasen (2013) showed that more realistic opacities of the *r*-process material may have a dramatic effect upon the predicted light curves of a kilonovae. In these simulations, they applied improved estimates of the radiative opacities of heavy elements as derived from *ab-initio* atomic-structure computations. The enhanced opacities of the lanthanides strongly affect the radioactive powered light curves from the ejecta of the neutron-star merger.
- ➢ Production of heavy elements: In all the suggested scenarios, the r-process nuclei are produced in two steps. (i) An initial explosion burns at high temperatures until the electrons and ions freeze-out during expansion of the ejecta but still with a high neutron-to-seed ratio, and which is followed by (ii) the rapid capture of neutrons by the seed nuclei, leading eventually to heavy nuclei.
- ➢ Production of heavy elements: Despite of intense research, little is known so far about the neutron-rich and in the *r*-process produced heavy elements. Indeed, the nuclei beyond the iron group elements (with mass numbers $A \sim 90\,..\,100$) need to be formed via successive neutron capture owing to the high Coulomb barriers for other nuclear reactions with charged particles.

r-process environments:

- r-process: The rapid neutron capture or (so-called) r-process is considered to be responsible for about half of the elements heavier than iron, although this process was previously attributed to core-collapse supernovae. However, recent studies of the r-process have disfavored supernovae because their conditions are not suitable to produce the heavy elements near to the *platinum peak* around $A \propto 195$. Instead, neutron-star mergers have received a lot of recent interest as a major r-process production site (Tanvir *et al.*, 2017).
- r-process environment: A current question in astrophysics is whether the mergers of neutron stars gives rise to a robust r-process environment that lead to heavy neutron-rich isotopes with mass $A \geq 130$, and in proportions similar to solar abundancies (Thielemann *et al.*, 2017).
- r-process environment: Various astrophysical sites have been suggested for the r-process of the nucleosynthesis. Apart from regular supernovas, the r-process has been associated especially with neutrino-induced processes in the outer shells of massive stars, the ejecta from compact binary mergers as well as from so-called magneto-hydrodynamic (MHD) jet supernovae which exhibit high magnetic fields and neutron-rich jet ejecta along the poles.
- In the neutron-rich ejecta from neutron star (NS-NS) and BH-NS binaries, in particular, the so-called r-process nucleosynthesis (rapid neutron capture) is expected to proceed rapidly, leading to many heavy elements like gold, platinum and many others.
- r-process environment: In astrophysical environments, the theory of the r-process was worked out 60 years ago and made it clear that an enormous neutron flux is required in order to explain the observed abundances of the elements. Because of this enormous flux, the details and necessary conditions of the r-rpocess is still under debate in astrophysics. New interest in this topic arose from the neutron-star mergers as a very probable r-process site, and the discovery of freshly synthesized r-process elements will stimulate this discussion.

8.4.e. Absorption and emission spectra of distinct astrophysical objects

Identification of absorption spectra

- Sako *et al.* (2001) present first results from high-resolution x-ray observation of IRAS 13349+2438 with the XMM-NEWTON observatory. The observed spectrum was obtained with the Reflection Grating Spectrometer (RGS) and shows a wealth of discrete spectral features, including the (first) astrophysical detection of an unresolved transition array (UTA) due to the $2p - 3d$ inner-shell excitations of M-shell iron ions. These spectral features could have been easily misidentified as an O VII edge, when observed with only moderate resolution spectrometers.
- Other prominent features in the spectra of Sako *et al.* (2001) were K-shell absorption lines of hydrogen- and helium-like carbon, nitrogen, oxygen and neon, and L-shell lines of Fe XVII-XX.

x-ray spectra from astrophysical missions:

- x-ray spectra from Chandra and XMM-Newton: In x-ray astronomy, the satellites Chandra and XMM-Newton provided (x-ray) spectra from many different astronomical objects, including K-shell transitions of carbon, nitrogen, oxygen, neon, silicon and sulphur as well as K-shell transitions from the iron-group elements with wavelength between 5–45 Å. These spectra help understand extreme environments in active galactic nuclei, x-ray binary systems, Wolf-Rayet Stars as well as from interstellar media (ISM; SantAnna *et al.*, 2011). A detailed analysis of spectra from XMM-Newton enables one to characterize ISM if the absorption cross sections near to K-edge are known.
- Atmosphere of the Earth: In planetary science, the photoabsorption due to inner-shell excitations of nitrogen is known to affect the transmission through the upper atmosphere of the Earth as well as the temperature in the thermosphere due to production of nitric oxide.

8.4.f. Radiation transport in astrophysical and hydrodynamical environments

Energy transport in plasma:

- Energy transport in plasma: In many astrophysical environments, the energy transport by radiation or relativistic particles is ubiquitous and need to be modelled by hydrodynamical simulations. Examples of such environments range from the formation of planets to the evolution of cosmic structures, and up to core collapse supernova or gamma-ray bursts.

➢ Energy transport in plasma: Often, the energy transport simulations in plasma are limited by the (approximate) treatment of the radiation transport and the relativistic particles. These limitations also hinder our understanding of the complex astrophysical Universe as well as the star and galaxy formation. Many requirements for an improved understanding arise similarly at short time scales and for large astrophysical environments.

➢ Energy transport in plasma: Energy transport simulations in plasma is a very complex or even formadible task for various reasons: (1) There occurs a large number of processes at the atomic scale, including, e.g., emission, absorption, scattering; (2) the vast majority of astrophysical scenarios are intrinsically three-dimensional (Reed *et al.*, 2018).

➢ Radiation and neutrino transport (RT/NT) codes: Most of the presently available codes apply very approximate algorithms and can be utilized only for a limited range of parameters and conditions, e.g. a single radiative source with an optically thin diffuse gas. This limitation is quite in contrast to the typically large dynamical structures in astrophysics and, hence, to the large effective range of the optical depth that occur in such environments.

➢ Role of radiation and neutrino transport: Radiation transport plays a key role for the dynamics of many astrophysical processes; the radiation feedback from stars and black holes plays a essential role for the rate of gas accretion for the formation of stars within galaxies. The star formation rate determines the observable properties from galaxies, such as stellar luminosity, color, and age.

➢ DIAPHANE library: This library provides various radiation and neutrino transport (RT/NT) routines for a wide range of astrophysics simulations Reed *et al.* (2018). These routines can be utilized directly in simulations, although it remains rather unclear from this write-up which hierarchy of models apply and how they need to be adapted for certain physical environments. In this library, the opacity $\kappa(\rho, T)$ is simply interpolated from a table of Rosseland mean opacities.

8.4.g. Ionization equilibria in astrophysical sources

Astrophysical observation of EUV spectra:

➢ High-quality EUV spectra: The Solar EUV Rocket Telescope and Spectrograph (SERTS, 1992) and the Extreme Ultraviolet Explorer (EUVE, 1990) spectrometers provided high-quality EUV spectra and helped improve the diagnostics of high-temperature plasmas in astrophyscial objects.

➢ The ability to resolve a large number of individual emission lines and to measure the accurate intensities over a wide wavelength range have allowed to analyze the temperatures, densities and abundances of elements in a variety of astrophysical sources (Brickhouse *et al.*, 1995).

➢ The fine structure of (line) multiplets nowadays allow to solve the full rate equations for several atoms in the plasma, including collisions among all levels and cascades. This enables one to calculate also the emissivities of weak lines that were previously omitted from the investigation.

➢ X-ray emission from astrophysical objects: From the analysis of line intensities in exotic dense-plasma environments, several key properties of astrophysical objects may be derived that are not attainable through other observational windows.

➢ Temperature of stars: This can be defined in various different ways (Pettini 2018):

1. Effective temperature: as defined in terms of the luminosity of the star and its radius;
2. Excitation temperature: as given by the relative population of different excited levels of an atom or ion in the plasma, and by using Boltzmann's equation;
3. Ionization temperature: as defined by the relative population of different ionisation stages of an atom, and by using Saha's equation;
4. Kinetic temperature: as defined by the Maxwell-Botzmann distribution:

$$n_v\,dv \;=\; n\,\left(\frac{m}{2\pi\,kT}\right)^{3/2}\,e^{-m\,v^2/2kT}\,4\pi\,v^2\,dv$$

with the number density n_ν (number of particles per unit volume) of particles with speeds between v ... $v+dv$ and the total number density n of all particles with mass m;

5. Color temperature: as the temperature of the blackbody whose spectral energy distribution resembles most closely that of the given star.

8.4.h. Photoionized, steady-state plasma

Ion distributions:

➢ All plasmas, that are produced in the laboratory, are generally quite far from local thermodynamic equilibrium (LTE). Therefore, the ion distribution of such laboratory plasma cannot be described by the usual Saha-Boltzmanm equations, neither for selected ions nor for dealing with different charge states of the ions.

➢ Z-pinch experiments: In the laboratory, one often has a steady-state plasma, far from equilibrium, that is formed by x-ray radiation from a Z-pinch. In such plasma, the ambient radiation field is important in addition to the electron-collisional processes in order to determine the the excitation and ionization dynamics. Such photoionized plasmas are believed to occur also in many astrophysical situations; in fact, Z-pinch experiment allow for the first time to compare numerical models of photoionized plasmas with experiment (Rose *et al.*, 2004).

➢ The standard method for calculating the ion distribution in a non-LTE system is to solve the rate equations for all the important ionic states and by including different excitation and ionization channels due to the incident radiation. From the solutions of these rate equations, a time history of the electron temperature and density as well as the time evolution of the different charge states in the plasma can be evaluated. The steady-state solution is then obtained by following the time evolution until the populations do no longer change with time.

➢ For ion-distribution calculations in non-LTE plasma, a major simplification is achieved if only the shell populations, averaged over the dsitribution of the ionic states, is taken into account within the average-atom model. This approach reduces the number of differential equations significantly, when compared to a detailed treatment of all charge states though the shell occupancies are non-integers then.

8.4.i. Plasma light sources for nanolithography

Development of EUV light sources:

➢ Ions with several open shells: The (correlated) electronic structure of medium and heavvy ions with several open shells is both, tedious and difficult to calculate, and their complex level structure often hampers a straightforward experimental assignment.

➢ EUV light sources at 13.5-nm wavelength: In order to generate extreme ultraviolet (EUV) light at 13.5-nm wavelength by laser-produced plasmas, the emission of multiply-charged tin ions have been found promising for nanolithographic applications. For these ions, the EUV light is generated by thousands of transitions that form so-called unresolved transition arrays (UTA), and with rather little dependence on the particular charge state of the tin ions (Winderberger *et al.*, 2016).

➢ For multiply charged tin ions with a [Kr] $4d^m$ $m = 6 \ldots 0$ configuration, the upper configurations for an EUV emission are [Kr]$(4p^6 4d^{m-1} 4f + 4p^6 4d^{m-1} 5p + 4p^5 4d^{m+1})$ (Winderberger *et al.*, 2016).

➢ Apart from application for EUV light sources, the optical transitions in medium and heavy ions with multiple open shells, such as Sn^{11+}–Sn^{14+}, also represent a stringent test for *ab-initio* atomic structure calculations of complex (many-electron) spectra with non-negligible Breit contributions.

8.4.j. Universal shape function for charged-particle impact ionization

Universal shape functions:

➢ Universal shape function for charged-particle impact ionization cross sections: A universal shape function can be formulated for the cross sections of single and multiple impact ionization by charged particles. If we refer to the position and the height of the cross section maximum by E_M and σ_M, and if E refers to the *excess* energy of the particle impact, this parametrization is given by (Pattard, 2002)

$$\sigma(E) \;=\; \sigma_M \, x^\alpha \left(\frac{\alpha \,+\, 1}{\alpha \, x \,+\, 1} \right)^{\alpha+1}, \qquad\qquad x \;=\; E/E_M.$$

Here, α is the Wannier exponent that is characteristic for the given process and which follows from Wannier theory. Note that the *excess* energy E is not the projectile (kinetic) energy but the energy that is left to all collision partners after ionization.

➢ Universal shape function for charged-particle impact ionization cross sections: The parametrization above describes indeed the particle-impact ionization cross sections quite well as long as no excitation-autoionization processes occur at these impact energies. Apart from the position and height of the *cross section maximum*, the formula is free of further parameters and can be readily applied for fittings (Pattard, 2002).

➢ Universal shape function for charged-particle impact ionization cross sections: The reason that the impact ionization by different particles, such as electrons, positrons, protons or even antiprotons, all follow the same parametrization is given by the inclusion of the correct power law behaviour (which is of course different for the different projectiles) near to the ionization threshold. The derivation and use of such threshold laws has been found useful also for parametrizing few-body Coulomb break-up processes.

➢ Universal shape function for single-photon multiple-ionization cross sections: The shape function by Pattard (2002) provides an excellent parametrization of photoionization cross sections if *all* electrons are ionized simultaneously, e.g. for helium. It help parametrize multiple-ionization cross sections whose *ab-initio* calculations is highly non-triveal, especially if three or more electrons are involved.

➢ For photon impact, a universal shape function can therefore be derived only for multiple, at least double, (photo-) ionization.

➢ Universal shape function for single-photon multiple-ionization cross sections: For single-photon multiple-ionization, Pattard (2002) suggest the parametrization

$$\sigma(E) \;=\; \sigma_M \, x^\alpha \left(\frac{\alpha \,+\, 7/2}{\alpha \, x \,+\, 7/2} \right)^{\alpha+7/2}, \qquad\qquad x \;=\; E/E_M,$$

and which obeys the correct limits at low and high photon energies. This is in contrast to the parametrization for charged-particle impact, for which the $\ln E/E$ was neglected for the sake of simplicity.

8.4.k. Laser-induced fluorescence spectroscopy (LIFS) in flames

Laser-induced fluorescence & applications:

- Laser-induced fluorescence describes the spontaneous emission from atoms or molecules following the prior excitation by laser radiation. In multi-level atoms or molecules, the laser is usually tuned to one of the absorbing transitions. From the so excited level, the atoms then decay either to some lower lying state or are re-populated by collisions to adjacent states. In LIFS, therefore, a fluorescence spectrum is observed that contains individual transition of the excited level as well as from levels nearby (Daily 1997).
- The laser-induced fluorescence signal after laser excitation can be exploited in various ways: (i) The observed spectrum provides a measure for the population of the initially excited states; (ii) it allows to extract the total number density of different species in the probe, if a clear relationship can be established between the number density of all involved quantum states; (iii) the observed spectrum (may) help deduce the ground-state distribution function and, hence, the temperature of the probe. Morever, (iv) the pressure, temperature and velocity may be deduced from the observed line shapes under suitable circumstances.

Combustion processes:

- Combustion: Combustion is the primary propulsion technology and is very frequently applied for the generation of electricity, the heating of buildings and at many places elsewhere. Combustion is applied also for the synthesis of new materials and for chemical processing (Daily 1997). In nature, combustion is a frequent source when natural areas are changed by fire.
- Combustion systems: Flames and combustion systems vary widely in their size, fuel type and purpose. They range from small mm-to-cm systems, such as furnace and stove pilot flames, gas stove burners or small laboratory burners to medium-size motors and heating systems, and up to pulverized coal fire boilers, marine diesels and forest fires, each with length scales on the order of several meters (Daily 1997).
- Performance evaluation of combustion processes: Combustion processes are often analyzed with regard to their energy conversion efficiency, material synthesis yield, material purity and/or pollutant emissions. This analysis is often made by measuring the exhaust and without that the combustion zone is affected directly.

8.4.I. Synthetic spectra for laser-induced breakdown spectroscopy (LIBS)

Laser-induced breakdown spectroscopy:

- The laser-induced breakdown spectroscopy (LIBS) has been found a versatile analytical tool with various applications.
- In this technique, a high-power laser beam is typically focused onto the surface of a sample that need to be analyzed. If the laser power exceeds a certain threshold, an optical breakdown occurs due to the formation of a laser-induced plasma. In practice, the breakdown threshold depends on the wavelength and duration of the laser pulses as well as on the analyzed media.
- For a nanosecond laser ablation, for example, the threshold varies from $1.9 \cdot 10^8\,\mathrm{W\,cm^{-2}}$ for copper up to $10^{10} \ldots 10^{11}\,\mathrm{W\,cm^{-2}}$ for aqueous solutions (Yaroshchyk *et al.* 2006).
- During the breakdown, a plasma of highly-ionized atoms is formed with an electron density of $10^{16} \ldots 10^{20}\,\mathrm{cm^{-3}}$ for typical Nd:YAG laser-induced plasmas.

Computation of LIBS spectra:

- Ciucci *et al.* (1999) first estimated with limited accuracy the composition of a laser-induced plasma by using computational methods instead of the (standard) calibration standards. Their computation were based on the assumption that the plasma and sample compositions are the same and that the plasma is optically thin and in local thermal equilibrium (LTE) during the observation.
- Yaroshchyk *et al.* (2006) describe some software for synthesizing laser-induced breakdown spectroscopy emission spectra and to predict sample composition by using a proposed calibration-free algorithm. This code applies a database of atomic emission lines in order to create a theoretical emission spectrum for selected elements using defined plasma parameters.
- The code by Yaroshchyk *et al.* (2006) is also based on the assumption of a LTE and a well-defined plasma temperature and electron density; it takes a number of characteristics atomic emission lines as input to create a synthesized theoretical emission spectrum of selected elements which are compared to the spectra of four separate compact spectrometers covering the spectral region 185–950 nm.
- Until the present, all heavy elements are typically represented in LIBS plasmas by their neutral atoms and their singly- and doubly-charged ions that emit radiation at characteristic wavelengths. From the intensity of individual wavelength, the composition of the samples are then estimated both, qualitatively and quantitatively.

8.4.m. X-ray absorption of solid-state materials

Near-edge spectroscopy of solid-state samples:

- X-ray near-edge absorption (XANES): XANES as well as other related spectroscopies, such as the resonant x-ray scattering spectroscopy (RXS) and x-ray magnetic circular dichroism (XMCD), are powerful spectroscopic techniques for probing the electronic structure around the absorbing atom in a fluid or solid-state probe sequences (Bunau and Joly, 2009).
- In the near-edge region, one is very sensitive to the surroundings of the absorbing atom. This makes absorption spectroscopies a very useful tool to investigate the geometric and electronic structure of the samples.
- In x-ray absorption spectroscopy, there has been a great need for codes that help reproduce the near-edge structure within a reasonable calculation time.
- These codes can be classified into two major categories:
  i) multi-electronic but monoatomic codes which are based on some multiplet theory and which give rise to a proper parametrized description of the localized electronic state. In these codes, however, while the delocalized states can often not be decribed correctly.
  ii) multi-atomic but mono-electronic codes which provide correct description of the extended states but fail to account for the highly correlated state that interact with the core hole. This applies, for example, for the calculation of the L2 and L3 edges of the $3d$ elements.
- X-ray absorption spectroscopy (XAS): This technique is widely used at synchrotron radiation facilities for determining the local geometric and/or electronic structure of matter, such as gases, solutions, or solids.
- X-ray absorption spectroscopy (XAS): The absorption of x-ray photons result in a core-excited initial state with a well-defined symmetry, and which determines also the final states in the continuum due to selection rules. While the most intense features arise of course from electric-dipole allowed transitions, mixtures of multipole components also occur. The most intense features at a K-edge are typically due to $1s \rightarrow np$ core excitations, and those at the L_3-edge due to $2p \rightarrow nd$ excitations.

8.4.n. X-ray quantum optics

Phenomena in x-ray quantum optics:

- X-ray quantum optics has evolved rapidly during the last year owing to the development of novel x-ray light sources and x-ray optics.
- A few important phenomena from x-ray quantum optics include: i) x-ray parametric down conversion; ii) nuclear γ-ray superradiance, and others. Indeed, various concepts form conventional (near-visible) quantum optics have been suggested to study also at higher photon energies. These concepts include photon correlations and entanglement, squeezing, and others.
- There are important differences between the interaction of x-rays and optical photons because of the inner-shell atomic energy levels, nuclear resonances, or quite large energy shifts in Compton scattering as the photon energies approach the electron rest mass.

8.4.o. Coherent x-ray scattering at high intensities

X-ray radiation sources:

- In 2009, the Linac Coherent Light Source (LCLS) at the SLAC National Accelerator Laboratory was the first x-ray FEL in operation with photon energies up to 8.3 keV, up to 2×10^{12} photons per pulse, and with a pulse length of just a few femtoseconds.
- Nowadays, further x-ray FEL include the SPring-8 Compact SASE Source (SCSS, Japan) and the European x-ray FEL (XFEL) at DESY. This XFEL can deliver photon energy up to 14 keV and has a 50-500 times higher average brightness than the (early) LCLS.

Single-shot imaging:

- Single-shot imaging: One central goal and applications of the European XFEL is single-shot imaging of individual macromolecules by means of coherent x-ray scattering. Such an imaging should help determine the atomically resolved structure of noncrystallized nanoparticles and biomolecules. Single-shot imaging might become possible for a sufficiently high-fluence and well-focused FEL pulse in order to generate a sufficiently large number of scattered photons from each (single-molecule) sample.
- Radiation damage: One of the key problems in single-shot imaging is the radation damage in course of the irradation of the sample. Typically, a much higher flux is required than the conventional radiation damage limit of about 200 photons/Å^2, and this may seriously degrade the scattering patterns and, hence, the possibility of determining the atomic positions within the target molecule (Son *et al.*, 2011).

Single-shot imaging therefore requires a sufficiently short pulse duration of less than 10 fs in order to keep the atomic position effectively frozen during the irradiation by the pulse.

➢ Single-shot imaging: Even if the atomic positions are nearly frozen, the single-shot imaging will be affected however by changes in the electron density of the target. This makes it necessary to understand also the detailed ionization and relaxation dynamics in individual parts of the molecules under ultrashort and ultraintense x-ray pulses (Son *et al.*, 2011). This dynamics can be simulated by means of time-dependent rate equations in order to explore the formation and relaxation of the inner-shell vacancies.

Ionization dynamics in short light pulses:

➢ Rate equations for configuration-averaged population dynamics: The transitions among all possible electronic configurations c of a given atom are described by a set of coupled rate equations of the form,

$$\frac{d\,P_c(t)}{dt} \;=\; \sum_{c' \neq c} \left(\Gamma_{c' \to c}\; P_{c'}(t) \;-\; \Gamma_{c \to c'}\; P_c(t) \right)$$

where P_c is the (relative) population of the c-th configuration, $\Gamma_{c' \to c}$ is the rate for generating the configuration c from c' and $\Gamma_{c \to c'}$ the rate for all decay transitions from configuration c to configuration c'. In a simplified dynamical model, Γ can be either a (configuration-averaged) time-independent Auger or fluorescence rate, or a time-dependent photoionization rate given by $\sigma_p\, J(t)$ with the photon flux $J(t)$ of the x-ray pulse at some given time t.

➢ For unpolarized and linearly-polarized x-rays, the differential cross section for coherent scattering is given by (Son *et al.*, 2011)

$$\frac{d\sigma^{(\mathrm{unpolarized})}}{d\Omega} \;=\; \alpha^4\, |f^{(0)}(Q)|^2\; \frac{1 \,+\, \cos^2\vartheta}{2}, \qquad\qquad \frac{d\sigma^{(\mathrm{lin-polarized})}}{d\Omega} \;=\; \alpha^4\, |f^{(0)}(Q)|^2\; \left(1 \,-\, \cos^2\varphi\, \sin^2\vartheta\right),$$

where φ is the azimuthal angle of the scattered photon momentum with respect to the x-ray propagation and polarization axes. This differential cross section gives distributions of the scattered x-ray emission if one restricts the model to fixed electronic configurations. From measurement of the x-ray distribution, one can retrieve information about the electronic density. If an atomic cloud is exposed to an ultraintense x-ray pulse, the atomic electron density is dynamically modified. This may require to introduce a suitably averaged, time-dependent differential scattering cross section,

$$\frac{d\sigma^{(\mathrm{averaged})}}{d\Omega}(t) \;=\; \sum_{c}^{\mathrm{all\ configs}} P_c(t)\, \frac{d\sigma^{(\mathrm{c})}}{d\Omega}$$

where $P_c(t)$ is the population of the c-th configuration as obtained from the rate equations above. The differential scattering cross section for the c-th configuration is evaluated from the form factor for the charge density $\rho(r)$ of the c-configuration.

8.4.p. Decay of medical radioactive isotopes

Radioactive isotopes used in clinical therapy:

- Linear energy transfer (LET): Most radioactive isotopes, that are used in clinical therapy, emit β particles as ionizing radiation. The biological effect of this radiation is often characterized by the so-called linear energy transfer (LET) and measured in units of [keV/μm] for the deposited energy along the particle track.
- The LET for most therapeutic α emitters ranges from 25 to 230 [keV/μm].
- A new class of radioactive nuclides refer to the α emitters ^{149}Tb, ^{213}Bi, ^{211}Po, ^{211}A, ^{223}Ra, ^{225}Ac, ^{227}Ac, ^{226}Th and ^{230}U and have been considered for therapy.
- The electrons and positrons emitted in the nuclear β decay and the internal conversion processes often have kinetic energies from tens of keV to several MeV, while their LET $\sim$0.2 [keV/μm] is much lower than for α emitters.

8.4.q. Configuration-averaged energies and cross sections

Configuration averages:

➢ For various applications, it is desirable to use and readily access configuration-averaged energies, rates and cross sections.

➢ Configuration-averaged energies Cowan (1981)provides a non-relativistic expression for the configuration-averaged energy as it often occurs in the computation of radiative and collisional rates (Peyrusse, 1999)

$$E_c \;=\; \sum_a N_a\,\langle a\rangle \;+\; \sum_{ab} N_a\,(N_b \;-\; \delta_{ab})\;\langle a,b\rangle$$

$$\langle a\rangle \;=\; \varepsilon_a \;+\; \left\langle a\left|\, -V^{\,(\mathrm{SCF})}(r) \;-\; \frac{2\,Z}{r}\,\right|a\right\rangle, \qquad\qquad \langle a,b\rangle \;=\; \frac{1}{2}\,\frac{g_a}{g_a \;-\; \delta_{ab}}\left[R^{(0)}(ab,ab) \;-\; \frac{1}{2}\sum_k \begin{pmatrix}\ell_a & k & \ell_b\\ 0 & 0 & 0\end{pmatrix}^2 R^{(k)}(ab,ba)\right].$$

Here, $g_a \;=\; 2(2\ell_a+1)$ is the degeneracy of subshell a, $V^{\,(\mathrm{SCF})}(r))$ is the self-consistent atomic potential and R is the non-relativistic Slater integral.

8.4.r. Mass attenuation coefficients

Attenuation coefficients:

➢ The photon mass-attenuation coefficient μ/ρ is calculated from the density ρ of the target material and the thickness d of the material in the direction of the incident photons as

$$\frac{\mu}{\rho} \;=\; -\,\frac{1}{\rho\,d}\,\ln\left(\frac{N}{N_o}\right),$$

and where N_o, N are the numbers of incident and transversing photons, respectively.

9. Atomic cascades

9.1. Cascade approaches and cascade simulations

Cascade approaches:

➢ Atomic cascades (may) often require an enormous amount of computational effort in order to generate, simulate and interprete all data as required for a given experiment. It therefore appears necessary and highly desirable to distinguish a number of sfmopredefined cascade approaches which define a hierachy of possible approximations for a given scenario.

➢ Here, we briefly summarize these (predefined) approaches which can be further refined by choosing proper parameters for the given computation.

➢ Decay cascade: Such a cascade usually starts from a given set of initial levels (and together with their relative population) that may decay by various atomic processes, such as autoionization, photon emission and others, until a given number of electrons is released and/or the ions cannot further decay.

i) Average singe-configuration approach (AverageSCA): In this approach, only one common set of orbitals is applied for all ionization stages of the atom. Moreover, all electron configurations in the cascade are treated in terms of single-CSF levels, i.e. without any configuration mixing.

➢ In practice, the AverageSCA approach should be realistic for (almost) all atoms and ions from the periodic table, independent of how well this approach describes the underlying physics of a given autoionization cascade.

ii) Singe-configuration approach (SCA): This approach applies a common set of orbitals for electron configuration (cascade block) in the given cascade. stage of the atom.

iii) Multiple-configuration approach (MCA): In this approach, we intent to incorporate further electron-electron correlations by configuration mixing contributions with closeby-lying configurations; the program attempts to *group* different configurations together by using physical insight into the cascade process.

➢ For each of these (cascade) approaches above, the mean computational effort should increase by (at least) one order of magnitude, perhaps also by several orders.

➢ Although the overall computational effort is quite difficult to estimate and formalize for general atomic systems, the various cascade approaches should be clearly discernible from each other and the 'costs' of any simpler approach (than the currently chosen one) should be typically negligible. In general, however, not all of these approaches will be feasible for a given cascade computation.

Implementation of cascade computations:

➢ Formally, a cascade computation is separated into several steps which are treated independently: (i) A list of electron configurations is generated as they may occur during the decay of levels from one or several initial (hole-state) configurations; (ii) From the configurations, a list of *cascade blocks* (groups of configurations) is formed and a common SCF field and Hamiltonian matrix calculated for each of these blocks; (iii) For each pair of cascade blocks, all fine-structure transitions are calculated for all selected decay processes; (iv) A (common) list of radiative lines, Auger lines, etc. is compiled and forms the basis for all subsequent cascade simulations.

Cascade simulations:

➢ Cascade simulation: A cascade simulation makes use of the calculated (many-electron) amplitudes, rates and cross sections in order to derive different distributions and spectra which can be compared with experiment. Cascade computations and cascade simulations are always handled independently.

9.2. In JAC implemented cascade approaches

9.2.a. Average single-configuration approach (AverageSCA), using a common set of orbitals `(Cascade)`

Cascade, notations & application:

➢ AverageSCA approach: This approach applies a common set of orbitals for all steps of the cascade. Moreover, each single configuration forms an independent multiplet (cascade block) and all configuration interactions are omitted in this simple approach. Generally, the orbitals of the initial configurations/levels are utilized also in order to compute the cross sections and rates for all subsequent steps of the

cascade. This single-CSF representation of all atomic levels is assumed to rather equivalent to the use of *configuration-averaged rates and cross sections*, although this equivalence is far from being obvious for complex configurations.

➢ General restrictions: (a) Only electric-dipole (E1) transitions are included for all radiative decays; (b) continuum orbitals are generated at an configuration-averaged transition energy and only for partial waves with $|\kappa| \leq 4$.

Computational steps of the AveragedSCA and SCA approaches:

➢ The following steps are carried out separately in these two approaches:

1) Cascade blocks: Determine all single configurations that are energetically allowed in photon emission and autoionization processes from the initially chosen configurations/levels, and until a given maximum number of electrons are released. These electron configurations form a list of (so-called) cascade blocks from which the decay cascade is then built by calculating all requested decay lines for each pair of blocks.

2) Radial orbitals: Bound radial orbitals are calculated only only for the first (and uppermost) block in the cascade, i.e. the initial hole configuration with the energetically highest-lying energy levels. These bound orbitals are then applied in order to set the `basis::Basis` of all other blocks.

3) Level representation: An individual level multiplet is calculated for each single non-relativistic electron configuration (cascade block) but without any CI, i.e. without configuration mixing. Therefore, the levels in all cascade blocks are given by a single CSF, and no explicit diagonalization of the Hamiltonian matrix is needed in this approach.

4) Decay processes & cascade steps: The requested radiative and non-radiative decay processes are considered between each configuration pair. This is achieved by performing standard atomic computations with the corresponding submodules, such as `AutoIonization` or `PhotoEmission`. The following restrictions are applied throughout the computations: (a) Only electric-dipole (E1) transitions are included for all radiative decays; (b) continuum orbitals are generated at an configuration-averaged transition energy and only for partial waves with $|\kappa| \leq 4$. – This step gives rise to a list of `lines` but without that all details are printed to screen.

5) Decay lines: For each pair of cascade blocks, the calculated decay lines are appended to common lists `linesR, linesA, ...` as finally returned by an instance of `Cascade.Data`.

9.2.b. Single-configuration approach (SCA) with individual sets of orbitals (Cascade)

Cascade, notations & application:

- SCA approach: This approach applies an individual set of orbitals for all steps of the cascade, while each individual electron configuration in the decay tree still forms an independent cascade block, i.e. level multiplet. For each of these blocks, an independent SCF is generated and the configuration mixing included by diagonalizing the corresponding Hamiltonian matrix. The single-configuration approach (SCA) is expected to already provide a quite reasonable description of all strong decay pathes.
- General restrictions: (a) Multipoles of the radiative transitions can be defined by the given `Settings`; (b) continuum orbitals are generated in a slightly simplified Dirac-Fock-Slater potential of the corresponding (final-level) configuration but for energies of the individual fine-structure transitions. (c) No orbital relaxation is incorporated into the amplitudes apart from the separate orbital representation (SCF) of the inital and final levels.
- See subsection 9.2.a for the individual steps of the cascade computation.

9.3. In JAC partly-implemented cascade approaches

9.3.a. User-grouped multi-configuration approach (UserMCA; Cascade)

Cascade, notations & application:

- UserSCA approach: This approach applies an individual set of orbitals for all steps of the cascade, which can be compiled by the user. For this, the program first provides a list of (single electron) configurations that can be either combined interactively or by some explicit calls (code) in the function .... For each of these user-specified cascade blocks, an independent SCF is generated and the configuration mixing included by diagonalizing the corresponding Hamiltonian matrix. The UserMCA enables one to include further physical insight about strong configuration mixing into the computation of the cascade.
- General restrictions: (a) Multipoles of the radiative transitions can be defined by the given `Settings` or directly in the code; (b) continuum orbitals are still generated in a simplified Dirac-Fock-Slater potential of the corresponding (final-level) configuration but for energies of the individual fine-structure transitions. (c) No orbital relaxation is incorporated into the amplitudes apart from the separate orbital representation (SCF) of the inital and final levels.

➢ See subsection 9.2.a for the major steps of the cascade computation.

9.3.b. Multi-configuration approach with shake transitions (ShakedMCA; `Cascade`)

Cascade, notations & application:

➢ ShakedMCA approach: This approach applies an individual set of orbitals for all steps of the cascade. However, these steps do include not only the nominal electron configurations as they obviously occur in the cascade but also configurations with the *replacement of additional electrons*, and which refer to shake-up or shake-down transition. The generation of these additional configurations are done via a *maximal number of electron replacements* that are considered in addition to the standard configurations.

➢ These shake configurations can be treated as indidivual groups of configurations or together with other configurations of the decay cascade.

➢ Similar as in the UserMCA, the program first provides a list of (single electron) configurations that can be either combined interactively or by some explicit calls (code) in the function .... For each of these user-specified cascade blocks, again, an independent SCF is then generated and the configuration mixing included by diagonalizing the corresponding Hamiltonian matrix.

➢ Although the UserMCA and ShakedMCA are quite similar in spirit, the incorporation of shake-up or shake-down configurations typically enlarges the effort enormously and need to be handled with great care. The ShakedMCA enables one to include further physical insight about strong shake processes and configuration mixing into the computation of the cascade.

➢ General restrictions: (a) Multipoles of the radiative transitions can be defined by the given `Settings` or directly in the code; (b) continuum orbitals are still generated in a simplified Dirac-Fock-Slater potential of the corresponding (final-level) configuration but for energies of the individual fine-structure transitions. (c) No orbital relaxation is incorporated into the amplitudes apart from the separate orbital representation (SCF) of the inital and final levels.

9.4. Further cascade approaches not yet considered in JAC

Light pulses: shape and intensities

➢

Rate equations

➢

9.5. In JAC implemented cascade simulations

9.5.a. Ion distribution (...; `Cascade`)

Distribution, notations & application:

➢

9.6. In JAC partly-implemented cascade simulations

9.6.a. Electron intensity spectrum (...; `Cascade`)

Spectrum, notations & application:

➢

9.6.b. Photon intensity spectrum (...; `Cascade`)

Spectrum, notations & application:

➢

10. Collision- and field-induced atomic responses

10.1. Interaction with external particles and fields. Notations

10.1.a. Atoms interacting with external particles

Ion-atom collisions:

- Coupled-channel calculations: In particular, coupled-channel calculations within an independent-electron model has been found capable to predict the single-electron capture in slow collisions with helium.
- Application of ion-atom collision data: A detailed understanding of the ionization and charge-exchange phenomena in ion-atom collisions is essential for different fields of physics, such a astrophysics, plasma physics or hadron therapy
- First Born approximation (FBA): This approximation has often been applied to high-energy ion-atom collisions for which the coupling between different excitation or ionization channels is expected to be negligible. There exist several versions of the FBA approximation to calculate, for instance, electron-capture cross sections in the p-He collisions. For example, a FBA with corrected boundary conditions were developed and utilized at intermediate-to-high energies collision energies, usually based in some independent-particle model. However, the FBA and other perturbative approaches become unreliable whenever the speed of the projectiles is comparable or smaller than the velocity of the target (valence) electrons. For such collisions, a semi-classical close-coupling approach is a useful alternative, although these approaches are expensive and often appear quite sensitive to the choice of basis functions as well as to a proper *completeness* of the basis.

10.1.b. Atoms in time-harmonic (Floquet) fields

Floquet formalism:

➢ Floquet formalism: Many physical systems are time-periodic to a good approximation. For these systems, the (time) evolution can be solved either directly by numerical integration of the (time-dependent) SE or by making use of the Floquet ansatz to separate out parts of the (time-dependent) Hamiltonian.

➢ Floquet formalism: For a periodic evolution, any time-dependent problem can be transformed also quite easily into a time-independent problem by applying the Floquet formalism. Such a transformation may simplify the solution considerably since time-independent problems can often be solved more efficiently.

10.1.c. Atoms in intense radiation fields

Few-cycle intense laser pulses:

➢ Intense laser pulses: Nowadays, few-cycle femtosecond laser pulses can be routinely produced both, in the visible as well as mid-infrared regimes. If these few-cycle pulses are focused properly, ultra-intense electric fields can be generated with peak-field strengths which are comparable to the (static field) in the atom.

➢ Carrier-envelope phase (CEP): Light pulses with a well-defind absolute or carrier-envelope phase (CEP) are crucial for extracting information about the electron dynamics in strong-field physics. A good control of the CEP is particularly important if the HH are generated by pulses with just one or a few optical cycles, since the CEP phase then directly determines the relevant electron trajectories and whether a single or multiple attosecond bursts of radiation is emitted.

Electron dynamics & processes in intense radiation fields:

➢ Simple man's model: This three-step model for the electron dynamics in intense radiation fields provides an intuitive basis for both, the (analytical) strong-field approximation (SFA) as well as for interpretions of the (numerical) solutions of the time-dependent Schrödinger equation. In particular, this model help explain different strong-field phenomena, such as high-harmonic generation (HHG), above-threshold ionization (ATI), the non-sequential multi-electron ionization (NSMI), and several others.

➢ Keldysh parameter γ: The ionization regimes of strong-field processes are often classified by means of the Keldysh parameter

$$\gamma \;=\; \sqrt{\frac{I_p}{2\,U_p}}, \qquad\qquad U_p \;=\; \frac{e^2\,\mathcal{E}_o^2}{4\,m_e\,\omega_o^2} \;=\; \frac{I_o^2\,e^2\,\lambda_o^2}{8\pi^2\,m_e\,\epsilon_o\,c^3} \;=\; 9.337\cdot 10^{-20}\;I_o\,\lambda_o^2\;\frac{\text{eV}}{\text{W cm}^{-2}\,\text{nm}^2}\,.$$

Here, $\mathcal{E}_o$ is the electric-field amplitude, m_e the mass of the electron, and ω_o, λ_o, I_o refer to the central frequency, wavelength and, respectively, the intensity of the incident laser radiation. As usual, moreover, ϵ_o is the vacuum permittivity and c the speed of light.

➢ Ionization regimes: Different operational conditions for strong-field ionization processes are often distinguished in the literature due to the photon energy ω, ionization potential I_p of the atomic targets as well as the ponderomotive energy of the laser field U_p. This table has been adapted from Amini *et al.* (2019).

Ionization regime	Conditions
Single-photon ionization (SPI)	$\hbar\omega > I_p \gg U_p$
Multi-photon ionization (MPI)	$I_p > \hbar\omega \gg U_p$
Above-threshold ionization (ATI)	$I_p > U_p > \hbar\omega$
Tunnel ionization (TI)	$U_p > I_p > \hbar\omega$

➢ Above-threshold ionization (ATI) is a natural extension of multi-photon ionization but where one or several photons *more* are absorbed of which are needed in order to surpass the ionization potential I_p of the atom. In general, ATI processes are often governed by the coexistence of perturbative and non-perturbative distortions of the electron dynamics.

➢ High-order ATI (HATI): In the high-energy region of the photoelectron spectrum at $2\,U_p \leq \varepsilon_p \leq 10\,U_p$, the electron dynamics is strongly governed by recollisions and the interplay between elastic and inelastic scattering processes.

➢ Frustrated tunnel ionization: Frustrated tunnel ionization is one of the dominant channels in strong-field ionization that results in the excitation of atoms. Theory predicts that the excitation efficiency increases with the pulse duration and decreases when going to a few-cycle regime.

Strong-field spectroscopy:

➢ Laser-induced electron diffraction (LIED) refers to a spectroscopic technique in which structural information about the atomic target is derived by measuring the doubly-differential elastic scattering cross-sections in the re-collision of electrons with the target atoms. Obviously, however, a very detailed theoretical understanding of the ATI and HHG processes is hereby needed in order to extract useful information from (time-resolved) LIED and HHG spectrum. In the simple man's model, contributions to the LIED spectrum arise especially from highly-energetic returning electrons with $2\,U_p \leq \varepsilon_p \leq 10\,U_p$ that collide elastically with their parent ion and that lead to a very characteristic momentum transfer and momentum distributions of the released electrons.

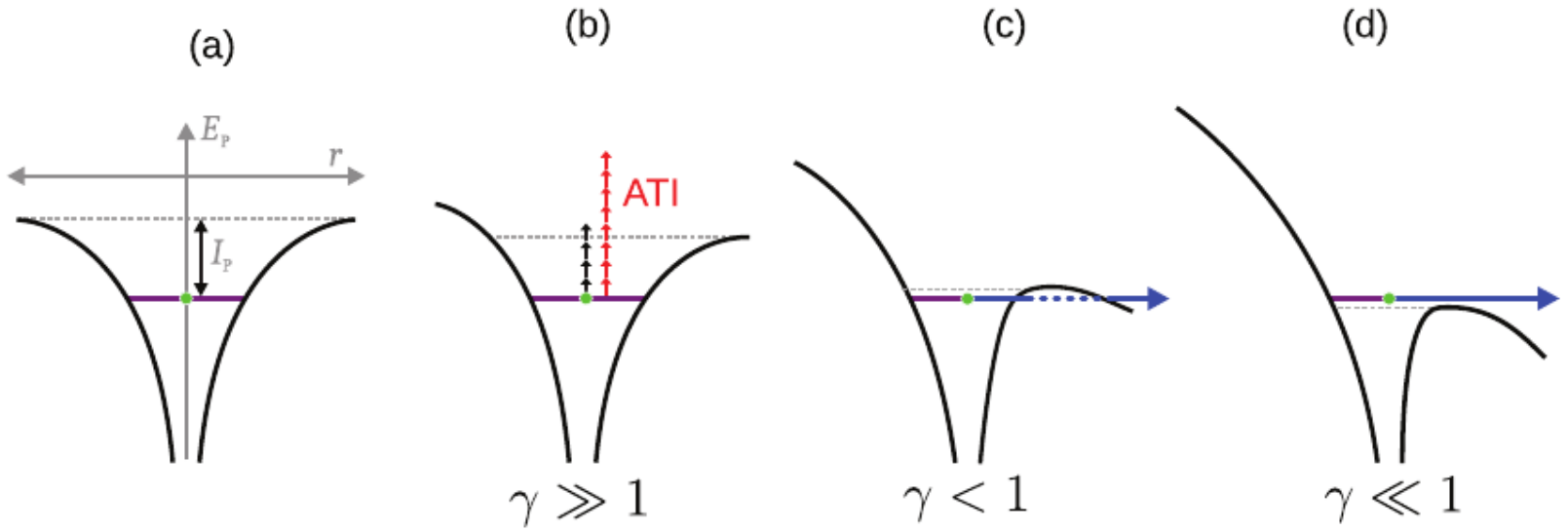

Figure 10.1.: Atomic potential in the presencs of an intense laser field: (a) without the laser; (b) ATI absorbes more photons than required for the release of an electron; (c) tunnel ionization, and (d) over-the-barrier ionization. Taken from Amini *et al.* (2019, Fig. 1).

➢ Above-threshold ionization (ATI) spectroscopy: Since both, the bound-free and the rescattering continuum-continuum transitions are CEP sensitive, the ATI photoelectron distribution can be utilized also in order to extract information about the electronic structure of the target atoms.

➢ Subcycle tracing of ionization enabled by infrared (STIER) pulses: STIER pulses refers to a streak camera that temporally resolves strong-field ionization caused by a linearly-polarized few-cycle pulse. STIER provides insight into the sub-cycle dynamics of strong-field ionization. STIER samples the photoelectrons produced by a few-cycle laser pulse in the near-visible spectral range, for example at 735 nm (Kübel *et al.*, 2017).

➢ STIER: This method enables one to separate the electron wave packets generated at different half-cycle maxima of the visible pulse. The best separation occurs, when the visible pulse is centered around a field maximum of the IR pulse, i.e. when the signal in the STIER trace is centered around $p_z = 0$. In this case, the observed momentum distribution directly reflects the ionization dynamics during a single half-cycle.

Atto-second pulse trains:

➢ Attosecond pulse trains: The high-harmonic process can be applied to generate attosecond pulses with excellent coherence in the extreme ultraviolet or even in the soft x-ray regime; here, an unprecented time structure of these trains can arise quite readily since the ionization of the electrons occurs just close to the maxima of the electric field and, hence, the electrons always return *in time*, namely, when the laser field is just *zero*.

➢ Attosecond pulse trains: Such pulse trains are generated by means of multi-cycle femto-second laser pulse, while a single broadbanded attosecond pulse can be produced from a single-cycle continuous broadband spectrum.

➢ Circulary-polarized attosecond pulse trains (APT): Because of the spatial separation of the left- and right-circularly polarized harmonics at the detector, twisted APT with well-defined circular polarization can be generated. For example, one obtains a right-circularly polarized APT for low angles of divergence $\beta \approx 1$ mrad, and right-circularly polarized APT for $\beta \approx 2$ mrad.

➢ Attosecond pulses: The generation of structured high-frequency pulses with well-defined torus-knot angular momentum also results in bright xuv radiation with customized polarization and OAM. These pulses may enable one to explore the spin-orbit coupling at the nanoscale or to study subtle changes in the photoionization dynamics of single atoms or molecules.

10.1.d. Atoms forming local plasma

None.

10.2. In JAC considered ion-atom collisional responses

10.2.a. Semi-classical ion-atom collisions [theoretical background]

Semi-classical approximation for ion-atom collisions:

➢ Semi-classical approximation (SCA) for ion-atom collisions: In the semi-classical approximation, the target is often assumed to be fixed (for instance, at the origin of the coordinates), while the projectile moves with constant speed v_p along a straight line with impact parameter b: $\mathbf{R}(t) = (b, 0, v_p\, t)$.

➢ Goals of the SCA: The goal is to solve an effective single-electron TDSE for initially occupied target electrons; in general, the *key* in using the SCA is to find a proper potential to be included into the single-electron TDSE.

$$i\,\frac{\partial \phi_k(\mathbf{r},t)}{\partial t} \;=\; h(t)\,\phi_k(\mathbf{r},t), \qquad\qquad k \;=\; 1,\,...,\,N\,.$$

Applications of ion-atom collisions:

➢ Proton-atom collisions & ionization: Chuluunbaatar *et al.* (2019) presents fully differential single-ionization cross sections for the impact of 1 MeV protons on helium. Both, ultra-high resolved experimental and theroetical cross sections in Born approximation are provided and agree reasonably well within the *kinematic* regime close to the (so-called) Bethe ridge. Further away from this region, however, the binary peak is clearly shifted with regard to the observations.

➢ Measurement of ion-atom collision cross sections: The cold-target recoil ion momentum spectroscopy (COLTRIMS) has been found a versatile tool for measuring and analyzing ion-atom ionization processes since it help determine the three-dimensional angular distribution of electrons at given values of energy and momentum transfer. Moreover, COLTRIMS has reached an unprecedented precision.

➢ Application of ion-atom collisions: Studies of ion-impact ionization processes are of fundamental and applied interest in order to understand, for instance, the penetration of swift ions through matter. Moreover, ion-atom collisions find their application in radiation material science and ion therapy.

➢ Measurement of ion-atom collision cross sectionss: In COLTRIMS measurement, the following fully-differential cross sections (FDCS) have been recorded for proton-helium collisions with regard to the energy E_e and solid angle Ω_e of the electron as well as the solid angles of the scattered proton Ω_p :

$$\text{FDCS} := \frac{d^5\sigma}{dE_e\, d\Omega_e\, d\Omega_p} = \frac{k_e\, m_p^2}{(2\pi)^5}\, |T_{if}|^2; \qquad \text{FDCS} := \frac{d^5\sigma}{dE_e\, d\vartheta_e\, d\varphi_e\, dq\, d\varphi_q} = |\sin\vartheta_e|\, \frac{k_e\, q}{(2\pi)^5\, v_p^2}\, |T_{fi}|^2,$$

and where (ϑ_e, φ_e) are the angles of the emitted electrons with regard to the axis of the incident proton beam and φ_q the azimuthal angle of the momentum transfer.

➢ Fully-differential cross sections: The upper form of the FDCS is used especially for studying the binary and recoil peaks in the electron angular distribution and how these peaks are shifted with regard to those from a simple Born approximation. In contrast, the second form can hardly be compared with experiment but has been applied in order to analyze various kinks in the cross sections as well as the asymmetry of the FDCS in forward and backward directions.

➢ Kinematic region for ion-atom collisions: For proton-helium collisions, most previous computations were done so far for the kinematic regime of small momentum transfer (0.75 a.u.) and low ejected-electron energy (6 eV).

Single-electron capture and subsequent x-ray emission in ion-atom collisions:

- Leung *et al.* (2015) studied the x-ray spectra following the single-electron capture in collisions of 4.54 keV/amu bare Ne^{10+} ions with helium, neon and argon gas targets. In this work, the single-particle capture probabilities were calculated by using the two-center basis generator method, based on independent electrons. Moreover, the response of the target on the capture cross sections and x-ray spectra was modeled by means of an time-dependent screening potential.
- Using COLTRIMS techniques, a triple-coincidence measurement on 4.54 keV/amu Ne^{10+} ion collisions with helium, neon and argon gas targets were carried out by Ali *et al.* (2010) who obtained (relative) shell-selective capture cross sections and x-ray spectra. In these measurements, the x-ray spectra from single-electron capture were separated from those from a multiple-electron capture due to coincidences with hydrogenic Ne^{9+} ions.
- Several groups have studied charge-exchange collisions in the laboratory in order to measure capture cross sections and the subsequent x-ray emission. For example, the Lyman-*alpha* emission was recorded for C^{6+}-Kr and O^{8+}-Kr collisions at low and intermediate collision energies. In these studies, emphasis was placed especially to estimate reliable single-electron capture cross sections.
- Classical overbarrier model (OBM): This model suggests that hydrogen and krypton should have (very) similar shell-selective capture cross sections because of the similar ionization potentials of 13.6 eV and 14.0 eV, respectively. However, a comparison of experimental data shows a rather different subshell selectivity, i.e. with regard to the electron capture rate into $(n\ell)$ subshells.
- To model the single-electron capture cross sections from a krypton target, an effective ground-state potential was obtained from the optimized-potential method by Talman and coworkers which includes the electron-nucleus interaction as well as terms due to screening and exchange (Leung *et al.*, 2018)).

10.3. In JAC considered high harmonic (HH) responses

10.3.a. High-harmonic generation HHG [phenomenology]

Basics of HHG:

- HHG: High-order harmonic generation is a non-linear (optical) up-conversion process for which the conservation of energy, linear momentum as well as spin and orbital angular momentum of individual harmonics can often be expressed by means of simple selection rules. This non-linear process is mediated by a laser-driven recollision mechanism of electrons, and which may lead to high harmonics with photon energies hundreds or even thousands times larger than the driving laser frequency.

➢ High-harmonic generation: When an *intense* laser ($I \sim 10^{14}$ W cm^{-2}) irradiates an (atomic) gas target, coherent radiation at multiples of the fundamental laser frequency is emitted. This process is called high-harmonic generation (HHG).

➢ HHG *versus* multi-photon emission: In comparison to HHG, most multi-photon emission and ionization processes have a rather limited complexity and can be described perturbatively.

➢ Maximum harmonic order: In a classical model, the electron can gain in a field with ponderomotive potential $U_p = I/4\omega^2 = \mathcal{E}_o^2/4\omega^2$ a maximum of 3.17 U_p kinetic energy and, hence, the (so-called) *cut-off* energy for the harmonics is $3.17\ U_p + I_p$. In the saddle-point approximation, in contrast, one finds solutions where the electron returns with a kinetic energy $\gtrsim 4\ U_p$ and which correspond to orbits with no *classical* counterpart.

➢ Plateau auf HH: If the high harmonics arise from the excitation with low-frequency lasers, the (HH) spectrum exhibits a characteristic behaviour, namely, a rapid decrease of the yield for the first few harmonics, and which is followed then by a plateau and a rather abrupt cut-off.

➢ HHG is known as a unique source of coherent and collimated xuv femto- and attosecond pulses. However, the efficiency of HHG is notoriously low, although it might be (moderately) enhanced if the resonances of the atomic or molecular targets are properly exploited. Indeed, the *free* one-dimensional motion of the electrons in the laser field is very essential for HHG as seen from the rapid decrease of the harmonic yield for an incident elliptical laser.

➢ Efficiency of HHG: Great efforts have been undertaken in order to increase the efficiency and photon flux in HHG. This efficiency is strongly influenced also by collective effects, such as the propagation and phase matching of the HH emitted from individual atomic targets, and where the maximum efficiency is affected by the absorption of the harmonics in the surrounding gas.

➢ Absorption-limited conversion efficiency of HHG: Constant *et al.* (1999) found that the maximum conversion efficiency of HHG is ultimately limited by reabsorption of the generated HH photons within the (generating atomic) medium itself. In particular, this so-called absorption-limited conversion efficiency is proportional to the absorption cross section $\sigma(q\,\omega)$ at the frequency $q\,\omega$ of the q-th harmonic. Therefore, the efficiency can be enhanced only if the emission cross section can be enhanced independent of the absorption.

➢ HHG: High-order harmonics, i.e. highly-energetic photons at multiples of the (fundamental) laser frequency, can be produced by focusing either a high-frequency (excimer) laser or some low-frequency laser (Nd:glass, Ti:sapphire) into an atomic gas.

➢ HH spectra: The properties of high-harmonic spectra have been intensively explored with regard to the energy, linear momentum as well as the orbital and spin angular momenta of the individual harmonics.

➢ Role of the atomic target for HHG: For atoms, only the valence electrons (orbital) are considered to be relevant for HHG and, hence, a direct link between HHG and valence-shell photoionization might exists and might be observed in the spectra. For example, the HHG spectrum

is known to show a lower intensity at the Cooper minimum in the photoionization cross section of argon atoms. Such a correspondence between the HHG and photoionization exist also for resonances in the photoionization cross sections and might help enhance the low efficiency of the HHG process. For the resonances in the photoionization cross sections, indeed, a large number of case studies exist in the literature and helped establish relations to the autoionization or to the shape and giant resonances of atoms.

➢ HHG with linear *versus* circularly-polarized beams: All harmonics that are generated by means of linearly-polarized beams are generally also linearly polarized, while HHG with (single) circularly-polarized beams is strongly suppressed, since the classical trajectories of the electrons will not come back so easily to the parent ion (Lorentz force) and since the (same) helicity of several photons *cannot* be add up to a well-defined helicity of the HH.

➢ HHG with bicircularly-polarized beams: HHG becomes possible for superposition of a circularly-polarized beam with its counter rotating second (or higher) harmonic. For such a superposition of two counter-rotating fields, the electric field of a bicircular field exhibits a Lissajous (-type) figure, and this obviously help return the electron back to the parent ion.

➢ High-gain harmonic-generation at free-electron lasers: Such a high-gain HHG@FEL has been demonstrated experimentally by means of laser-seeding in order to produce amplified, longitudinally coherent and Fourier transform-limited output at a certain harmonic of the seed laser. For example, a seed carbon dioxide laser with 10.6 micrometers help produce saturated and amplified second-harmonic wavelength at 5.3 micrometers. These experiments helped verify the technique and paved the way for its application in the vacuum ultraviolet region of the spectrum, and perhaps to even provide intense and highly-coherent hard x-rays in the future.

➢ High-gain harmonic-generation at free-electron laser: Single-pass FEL bunches provide the intensity and spatial coherence of SASE but with high temporal coherence. In the HHG@FEL, a seed laser imposes a small energy modulation of the electron beam while passing through a short undulator (the modulator). This energy modulation is then converted into a coherent spatial density modulation as the electron beam traverses a dispersion magnet (a three-dipole chicane). If a second undulator (the radiator) is tuned to a higher harmonic of the seed frequency ω, a microbunched electron beam emits coherent radiation at the harmonic frequency $n\,\omega$. These HH have a single phase that is determined by the seed laser and spectral bandwidth that is limited by the Fourier transform. The HHG@FEL may result in a high degree of stability and control of the central wavelength, bandwidth, energy, and duration of the output pulse.

➢ Fermi FEL: Fermi is located at the Elettra laboratory in Trieste; it covers the VUV to soft x-ray photon energy range with two FEL that are both based on High-Gain Harmonic Generation (HGHG) seeded mode.

➢ Rates for HHG: Explicit formulas for the HHG rate within the three-step model are provided, for instance, by the Lewenstein model and include a *factor* from the field-free photorecombination cross section (third step). While the derivation of these formulas are made in the single active-electron approximation, the proportionality of the HHG rate to the field-free photorecombination cross section already indicates quite strong multi-electron effects upon the HHG rate for most atoms, since the photorecombination cross section are know to be

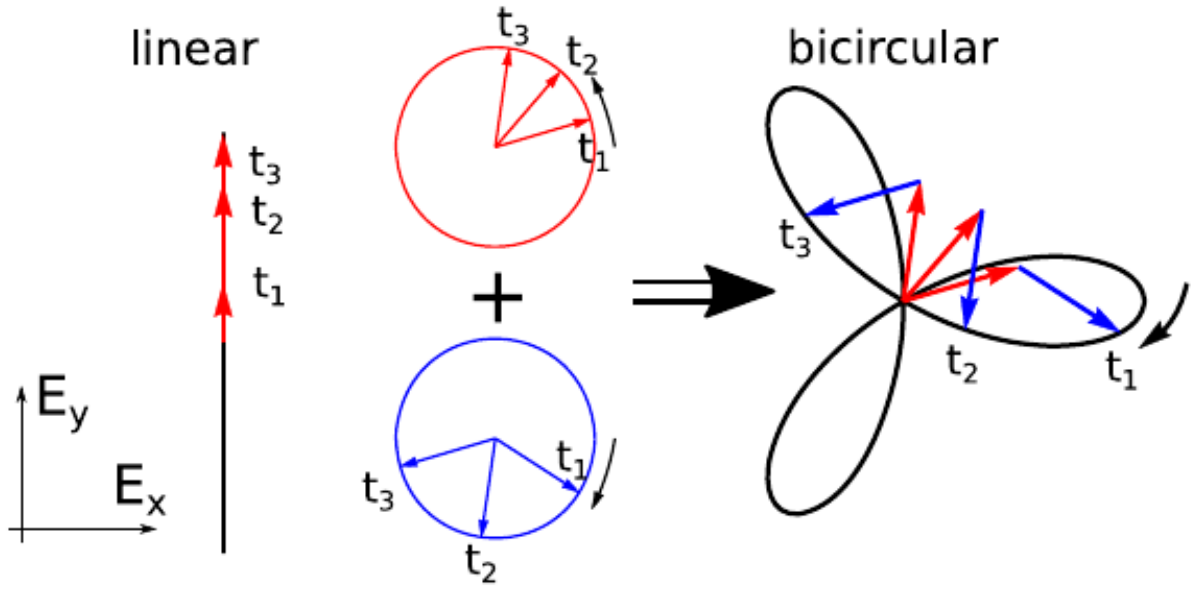

Figure 10.2.: Parametric plots of the electric field vectors at different times t_1, t_2, ... (Left) The electric field vector in a linearly-polarized beam just oscillates in one dimension. The red arrows indicate the electric field vectors at three different times. (Middle) Circularly-polarized field (red) and its counter-rotating second harmonic (blue). The arrows indicate the electric field vectors at the same times as for the linearly-polarized field. (Right) Bicircular field as a superposition of a circularly-polarized beam and its counter-rotating second harmonic, which gives rise to a Lissajous figure for the electric field. From Paufler *et al.* (2019, Fig. 5)

sensitive to the description of the many-electron wave functions. Although the role of such electron correlations upon the HHG spectra has been discussed *qualitatively* in the literature, not many detailed computations have been carried out so far.

➢ Resonant electron capture in HHG: If the relative phase of different capture processes is neglected, the dielectronic resonance strength $S(i \to d \to f) \propto \frac{2\pi^2\hbar}{k_i^2} A_r$ determines entirely the behaviour of the resonance. For low- and medium-Z elements, therefore, no significant enhancement in the HHG spectrum is expected even if the capture (Auger) rate for the formation of the doubly-excited states is quite large.

Phase matching of HHG spectra:

- Phase matching of HHG: Usually, rather dense atomic targets of $\sim 10^{17}$ atoms/cm^{-3} are needed in order to generate high-order harmonics. Apart from the microscopic interaction of individual atoms, however, one has also to consider also the macroscopic target distribution in order to analyze the superposition of all individual responses.
- Phase matching of HHG: A (phase matching) analysis of the HH spectrum may help improve the conversion efficiency and provides information about the cutoff of the harmonics. It also aims to find conditions so that the radiation from most atoms to a given harmonic add up constructively at the detector.
- Size of atomic targets for HHG: For the HHG with Gaussian beams, a sufficient intensity often occurs only within a thin cylinder of $\simeq 7$ mm length and a radius of $\simeq 730$ μm, and with about 1000 atoms within this tiny volume. Even for such a rather small volume, however, the radiation emitted from different atoms is not in phase. Phase-matching aims to find areas in the interaction regions, for which an intense signal with good phase is obtained at the detector.
- Phase of the emitted radiation: For target atoms at different positions, two contributions crucially determine the phase of the q-th harmonic, namely, (i) the dipole phase owing to the response of a single atom to the local intensity of the beam as well as (ii) the intrinsic beam phase as it naturally arise from focusing the laser beam.
- Phase matching on axis: For Gaussian beams, this just refers to a simplified 1-dimensional model, and which can be adapted also to Laguerre-Gaussian beams.

High-harmonic generation (HHG) with twisted light beams:

- High harmonics with well-defined OAM: Circularly-polarized HH with well-defined OAM can be generated with bicircular LG beams. Moreover, these HH may form also circularly-polarized (twisted) attosecond pulse trains if the intensity ratio of the bicircular driving fields has been tailored properly.
- Microscopic & macroscopic interplay of HHG with twisted beams: For driving beams with helical phase fronts, in particular, both the (microscopic) interaction of the individual target atoms as well as the (macroscopic) superposition of the emitted radiation in the far-field plays a crucial role for the generation and detection of HH. The interplay of these two components to the recorded spectra determines eventually the OAM as well as divergence of the emitted high harmonics.
- HHG with OAM: The OAM of the HH can be controlled, or even explicitly *selected*, by tuning the polarization, intensity (ratio) and OAM of the driving laser fields.
- Selection rules for the q-th harmonic: For an (incident) linearly-polarized twisted light beam with frequency ω and orbital angular

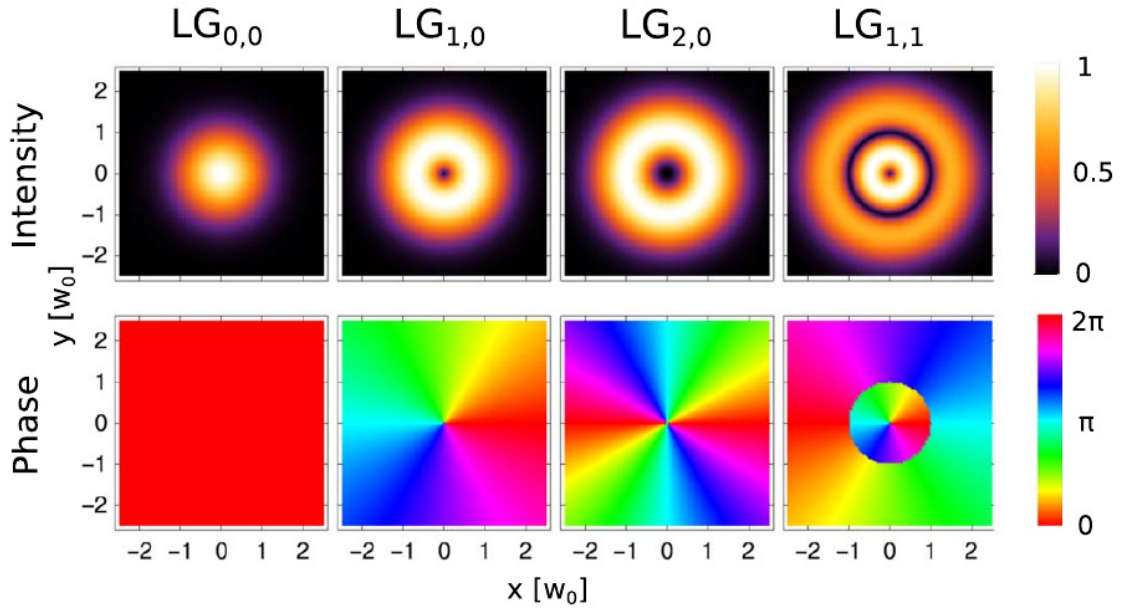

Figure 10.3.: Intensity (upper panel) and phase profiles (lower panel) of different LG beams at the focal plane ($z = 0$). Left column: A Gaussian beam has its intensity maximum at the beam axis and a constant phase profile because of its *zero* OAM. Middle columns: $\mathrm{LG}_{\ell,p}$ beams with angular momentum ℓ, in contrast, have zero intensity at the beam axis and a $2\pi\,\ell$ phase change in going once around the beam axis. Right column: $\mathrm{LG}_{\ell,p}$ beams with $p > 0$ exhibit $p+1$ rings in the intensity profile and a corresponding phase profile with a p-dependent phase and a phase change $2\pi\,\ell$. From Paufler *et al.* (2019, Fig. 1).

momentum ℓ, the q-th harmonic obeys the selections rules:

$$\mathrm{HHG}\ @\quad \mathrm{LG}_{\ell,p}^{\omega\leftrightarrow} \longrightarrow \begin{cases} \omega_q = q\cdot\omega \\ \ell_q = q\cdot\ell \\ \mathrm{linearly-polarized} \end{cases} .$$

➢ Selection rules for the q-th harmonic: For (a co-linear superpositon of) two bicircular light beam with frequencies (ω, 2ω) and orbital

angular momenta (ℓ_1, ℓ_2), both the SAM and OAM are conserved simultaneously, and the q-th harmonic obeys the selections rules:

$$\text{HHG @} \quad \text{LG}_{\ell_1,0}^{\omega\circlearrowleft} \oplus \text{LG}_{\ell_2,0}^{2\omega\circlearrowleft} \longrightarrow \begin{cases} \omega_q = q\,\omega = m\,\omega + n\,2\omega \\ \ell_q = m\,\ell_1 + n\,\ell_2 \\ m - n = \pm 1 \end{cases} .$$

For this particular HHG scheme with bicircular $(\omega, 2\omega)$ beams, every *third* harmonic is suppressed, while the other two contributing harmonics exhibit alternating helicities due to $m = n \pm 1$. This can be seen also from the photon-coupling diagram for each harmonic and, hence, the OAM of the generated harmonics can be tailored explicitly for a proper combination ℓ_1, ℓ_2 of the bicircular beam, cf. Fig. 10.3.a. In addition, it is possible that all generated harmonics carry the same modulus of OAM if the incident beams have the OAM $\ell_1 = -\ell_2$.

High-harmonic generation (HHG) with linearly-polarized LG beams:

➢ HHG with two (non-) colinear but linearly-polarized LG beams: The OAM of the generated harmonics can be controlled by using superpositions (so-called mode mixing) of two or more twisted beams; cf. Figure 10.3.b.

(1) For two co-linear and linearly-polarized LG beams with the same frequency but different OAM, let us simply write

$$\text{HHG @} \quad \text{LG}_{1,0}^{\omega\leftrightarrow} \oplus \text{LG}_{2,0}^{\omega\leftrightarrow} \Rightarrow .$$

For such mixed beams, different photon pathes contribute to the q-th harmonic; cf. the photocoupling diagrams in Fig. 10.3.b. Obviously, however, if the electron absorbs n photons from the first beam, it must emit $q - n$ from the second beam (and where $n > q$ is also possible, though much less likely). Quite generally, the HHG probability decreases with the (total) number of photons that are involved in the process, and with a rather sharp cut-off criterion.

(2) For two non-colinear but linearly-polarized LG beams with the same frequency and different OAM, we write instead

$$\text{HHG @} \quad \text{LG}_{0,0}^{\omega\leftrightarrow} \oplus \text{LG}_{1,0}^{\omega\leftrightarrow}, \angle .$$

For such a superposition, the high harmonics will not have a well-defined OAM here but their wave vectors still need to fullfil $\mathbf{k}_q = n_1\,\mathbf{k}_1 + n_2\,\mathbf{k}_2$, $n_1 + n_2 = q$. Therefore, the harmonics generated by different pairs of photon numbers (n_1, n_2) will eventually be spatially separated at the detector.

(3) For two non-colinear but linearly-polarized LG beams with different frequencies and different OAM, we write

$$\text{HHG @} \quad \text{LG}_{0,0}^{\omega\leftrightarrow} \oplus \text{LG}_{1,0}^{2\omega\leftrightarrow}, \angle .$$

10.3.b. High-harmonic generation in the strong-field approximation [theoretical background]

High-harmonic theory:

➢ Lewenstein's model for HHG: This model describes the interaction of a single (-electron) atom with a plane-wave laser within the dipole approximation (homogeneous electric field). In this approximation, the time-dependent SE can be solved analytically if the following three assumptions are made: (i) only the ground state and the continuum states of the electron contribute to the overall time-evolution of the state of the atom; (ii) the electron always moves as *free* particle within the continuum, independent of the remaining potential $V(r)$ of the parent ion; and (iii) the time evolution of the electronic state does not lead to a depletion of the ground state.

➢ Lewenstein's model for HHG with twisted beams: This model, and especially the dipole approximation, is still justified to describe the HHG with twisted light beams, if the azimuthal phase dependence due to the OAM ℓ is properly taken into account. In particular, the dipole approximation remains valid here in the optical and infra-red regions since the released electron in the HHG process typically just travels 1-2 nm away from its target atom and, hence, does not feel (much of) the spatial structure of the twisted light field.

➢ Lewenstein's model of HHG is therefore expected to be valid for low-frequency and rather intense lasers, i.e. the basic assumptions of SFA. The long-wavelength limit for λ_o (when compared with the Bohr radius $a_o = 5.29 \cdot 10^{-11}$ m) ensures a spatially homogeneous electric field over the extent of the atom (dipole approximation),

$$\mathbf{E}(t) \;=\; \mathcal{E}_o \, f(t) \, \sin(\omega_o t + \phi_o) \, \mathbf{e}_z .$$

➢ HHG power spectrum: From the time-dependent dipole amplitude $d(t)$, the HHG power spectrum is obtained as the time-integrated Fourier transform

$$d(\omega, \omega^{(\text{laser})}) \;=\; \frac{i}{\omega T} \int_{-T}^{T} dt \; e^{-i\omega t} \; d(t), \qquad\qquad \mathcal{P}(\omega, \omega^{(\text{laser})}) \;=\; |d(\omega, \omega^{(\text{laser})})|^2 .$$

High-harmomic amplitudes in the near- and far-field:

➢ Far-field HH spectra from twisted beams: To predict (and explain) the HH spectra in the far-field at the detector, one needs to sum over all the single-atom responses due to the interaction of these atomic centers with the twisted beam. Obviously, this summation affects the overall phase and intensity profile as well as the OAM of the observed HH radiation in the far-field.

➢ Fraunhofer diffraction formula: This formula can be applied in order to calculate the phase and intensity profile of the far-field for the different orders of the HH. To make use of this formula, the contributions of the individual target atoms to the HH amplitude need to be model properly, for instance by assuming a thin layer of (target) atoms, and which might be displaced with regard to the focus plane.

➢ Complex amplitude of q-th harmonic: Using Frauenhofer's diffraction formula, the spatically-dependent (complex) light field, averaged over time, can be written in terms of the wavelength $\lambda_q = \lambda/q$ and the (complex) near-field amplitude $A_q^{(\mathrm{near-field})}(\rho', \varphi', z')$ of the q-th harmonic

$$A_q^{(\mathrm{far-field})}(\beta, \varphi) \;=\; \int_0^\infty d\rho'\, \rho' \int_0^{2\pi} d\varphi\, A_q^{(\mathrm{near-field})}(\rho', \varphi', z') \;\exp\left(-\frac{2\pi\, i}{\lambda_q}\, q'\, \tan\,\beta\, \cos(\varphi - \varphi')\right),$$

and where β refers to the polar angle (angle of divergence) with regard to the incident beam.

➢ Near-field amplitude of the q-th harmonic & for an incident twisted beam: In Lewenstein's model, the near-field amplitude of the q-th harmonic can be expressed as $A_q^{(\mathrm{near-field})}(\rho', \varphi') = f(\rho')\, e^{i\,\ell_q\,\varphi'}$, and where $f(\rho')$ includes all the radial dependence.

➢ Complex amplitude of q-th harmonic: For this simple expression of the near-field amplitude from Lewenstein's model, the integration over the azimuthal angle φ' in the complex far-field amplitude above can be carried out analytically

$$A_q^{(\mathrm{far-field})}(\beta, \varphi) \;=\; 2\pi\, i^{\,\ell_q}\, e^{i\,\ell_q\,\varphi} \int_0^\infty d\rho'\, \rho'\; J_{\ell_q}\left(\frac{2\pi}{\lambda_q}\,\beta\,\rho'\right).$$

Here, $J_k(x)$ refers to a Bessel function of the first kind. The polar angle $\beta_{\max}$, for which the (modulus of the) far-field amplitude reaches its maximum, is a simple measure for the divergence of each harmonic order. Apparently, this divergence increases with the OAM $\ell_q \propto q \cdot \ell$ but decreases with the harmonic order q. Therefore, all harmonics are emitted with quite similar divergence.

Phase of target atoms to the far-field amplitude:

➢ Effective dipole phase: Different terms contribute to the effective dipole phase of an atomic target atom:

(i) The focal phase arises from the phase-front ratio $R(z) = z\,(1 + z_r^2/z^2)$ due to the non-zero Rayleigh range $z_r = k\,W_o^2/2$ and the finite beam waist W_o. For LG beams, the focal phase is $k\,r^2\,/\,2\,R(z)$ and, hence, independent of the OAM of the beam.

(ii) The intrinsic phase owing to the Gouy phase as well as the OAM of the beam.

➢ Coherence length of HHG: This length characterizes the (changes in the) total phase of the HH amplitude and is simply given by:

$$L_q^{(\mathrm{coherence-length})}(r,z) \;=\; \frac{\pi}{|\,\nabla\phi_q(r,z)\,|}\,.$$

This expression shows immediately that a zero phase-mismatch results in perfectly matched harmonics $L_q^{(\mathrm{coherence-length})} \to \infty$. In practice, a coherence length $\sim$ 1 mm already refers to quite good experimental conditions.

Phase matching in HHG with twisted light:

➢ Phase matching on maximum: For an incident Gaussian beam, HH are dominantly emitted *along* the (beam) axis since these harmonics mainly arise near to the intensity maxima in the cross section perpendicular to the direction of the beam. In the phase-matching analysis, it is therefore often sufficient to consider the target distribution just *on axis*, a simplification known as phase matching on axis. A similar simplification can be made also for LG beams if this 'fictious axis' is either shifted to the first intensity maximum of the beam or if one just considers the target distribution along the 'ring' as defined by the first intensity maximum. We here refer to this approximation as phase matching on maximum.

➢ Intensity maximum of LG beams: For an $\mathrm{LG}_{\ell,0}$ beam, the first intensity maximum can be written is found in terms of the beam waist W_o and the Rayleigh length z_r ; it is given by the radius

$$r_\ell^{(\max)}(z) \;=\; \sqrt{\frac{|\ell|}{2}}\,W(z) \;=\; \sqrt{\frac{|\ell|}{2}}\,W_o\,\sqrt{1+\frac{z^2}{z_r^2}}\,.$$

10.3.c. High harmonic spectra from localized target clouds [partly-implemented in Jac]

Use & notations:

➢ Using Jac: Perform an `HighHarmonic.Computation(.., observable=[UniColorSpectrum, BiColorSpectrum, ..], configs=[..], hhgSettings=HighHarmonics.Settings(..), ..)` or call directly functions from the module `HighHarmonic`.

10.3.d. Phase matching in high-harmonic generation from extended target clouds [partly-implemented]

Use & notations:

➢ Using Jac: Perform an `HighHarmonic.Computation(.., observable=[UniColorSpectrum, BiColorSpectrum, ..], configs=[..], hhgSettings=HighHarmonics.Settings(..), ..)` or call directly functions from the module `HighHarmonic`.

10.3.e. Far-field phase distributions [not yet implemented]

None.

10.3.f. Far-field intensity distributions [not yet implemented]

None.

10.4. In JAC considered above-threshold ionization (ATI) processes

10.4.a. ATI in the strong-field approximation [phenomenology]

Above-threshold ionization (ATI):

- Above-Threshold Ionization refers to the absorption by an atomic electron of more photons than are required for ionization. ATI was discovered in 1979 and is a rather universal phenomenon. This process occurs in light pulses that are short and strong enough to eliminate the influence of collisions.
- ATI in strong fields: In this multi-photon ionization regime (with Keldysh parameter $\gamma > 1$), the atom absorbs more photons than required for the release of one of its bound electrons. This multi-photon absorption leads to the characteristic above-threshold ionization (ATI) peaks in the photoelectron spectra that are separated by the energy of the laser photons. Moreover, the overall spectrum is shifted by the ponderomotive potential with regard to a perturbative treatment of the binding and photon energies.

10.4.b. ATI in the strong-field approximation [theoretical background]

...:

-

10.5. In JAC considered non-sequential double ionization (NSDI) processes

10.5.a. NSDI in the strong-field approximation [phenomenology]

Non-sequential double ionization (NSDI):

➢ Non-sequential double ionization (NSDI): This (non-linear) strong-field process has been studied for more than 30 years but still attracts good attention for its sensitivity with regard to (a proper many-electon description of) the correlated motion of the two emitted electrons. The observed (and characteristic) *knee* structure provides clear evidence for NSDI since the double-ionization yield strongly increases at the 'knee' by one or several orders of magnitude. Indeed, this increase is much larger than predicted for a subsequent emission of two electrons from the same atom.

➢ Rescattering picture of NSDI: In the rescattering picture of strong-field physics, NSDI is simply attributed to the inelastic scattering of the returning electron in the (static) potential of the parent ion. Already this quite simplified pictur requirese however to take different ionization mechanisms into account: the recollision direct ionization (RDI) and the recollision excitation with subsequent ionization (RESI); cf. Chen *et al.* (2020).

➢ NSDI: This (non-linear) process depends crucially on the laser intensity as seen, for instance, from recoil-ion momentum measurements. In these measurements, a single peak in the momentum distribution becomes a double-hump structure as the intensity increases near to or beyond the threshold intensity. Moreover, the electron-electron (momentum) correlation function then displays a clear transition from an (angle-) correlated into a anti-correlated emission if the laser intensity decreases below of the threshold intensity. In particular, prominent finger-like structures in the PEMD have been observed at the relatively low intensity of the laser field. These features show the correlated many-electron features of NSDI.

10.5.b. NSDI in the strong-field approximation [theoretical background]

...:

➢ Theoretical models for NSDI: The NSDI process has been explored by various models, including a semi-classical quasi-static model, the quantitative rescattering (QRS) model or the explicit solution of some (simplified) time-dependent Schrödinger equation. All these models confirmed, or at least indicate, that the finger-like structures in the PEMD at low laser intensity arises from the Coulomb interaction among the emitted electrons. However, different mechanisms are emphasized in most of these models, such as the *shake-off* of the second electron

by the nonadiabatic change of the atomic potential if the first electron is released, some $(e, 2e)$ collision due to the ionized electron if driven back by the laser, or other mechanisms. Today, the role of laser-induced recollisional excitation and ionization model as the major mechanism is widely accepted, and the number of (sub-) mechanisms has been further refined for the NSDI (Chen *et al.*, 2020): (1) The interaction of the laser field with both electrons; (2) Coulomb interaction of the residual photoion and the two electrons; (3) the interaction among the electrons. Obviously, all these interactions can be easily read-off the (many-electron) Hamiltonian and should be treated on similar footings, if possible.

➢ Quantitative rescattering (QRS) model for NSDI: The QRS model was originally developed for high-order above-threshold ionization (HATI) as well as HHG but has been further improved over the years. This model nowadays incorporates different mechanisms, such as the lowering of the threshold potential due to the electric field at the time of recollision. This model is based on the S-matrix theory and strong-field approximation, and it has been applied to simulate the total double ionization yield, the cross section ratio for double-to-single ionization as well as correlated two-electron momentum distributions. In practice, the QRS model is conceptual much simpler than the explicit solution of the time-dependent Schrödinger equation or even the time-dependent Newton equations of the two electrons. The QRS model basically *factorizes* the electron dynamics of the two electrons into a returning wave packet for the initially ionized electron as well as the differential cross sections for its inelastic scattering with a second electron in the potential of the parent ion (Chen *et al.*, 2019).

10.6. In JAC considered collisional-radiative (CR) models

10.6.a. Simple CR models [phenomenology]

Role and applications of CR models:

➢ Collisional-radiative (CR) models: These zero-dimensional plasma models are typically applied in order to compute atomic charge-state distributions for – (ionic) mixtures of – one or several elements, and in particular as function of particle densities and temperatures.

➢ Different CR models have been found useful for the interpretation of experimental observations, for instance in order to derive the electron density and temperature in plasma. In addition, CR models can be applied to determine effective ionization and recombination rates as well as the effective emissivity of plasma as function of its electron temperature and density.

➢ Atomic level population densities: CR models help determine atomic level population densities of atoms in different plasma environments. Calculations are typically based on the CR recombination and ionization rate coefficients, radiative energy losses as well as on various individual rate coefficients.

➢ Classification of CR models: Different CR models can be distinguished due to the – analytical or numerical – treatment of the rate coefficients as well as due to the number and type of processes, for which such (effective) rate coefficients are taken into account.

➢ Effectice rates: CR models can be applied to calculate the effective emissivity or the effective ionization and recombination rates as function of electron temperature and density. In particular, these rates can later be utilized in plasma transport model in order to determine local ionization, recombination and radiation effects.

Frequent assumptions of CR models:

➢ Collisional radiative models are sometimes called also zero-dimensional plasma models. In these models, one often assumes that the radiative absorption and emission as well as electron-collision processes dominate the plasma and that all other (ion-atom, three-atom, ...) processes are negligible.

➢ In most CR models, the plasmas just consist out of a single atomic species but with various excited states in between the ground state of some charge state A^{q+} of the ion and the ground state of the next higher charge state $A^{(q+1)+}$. A further typical restriction of such models is that the density of the excited states is assumed to be small, when compared to the (two) ground state densities.

10.6.b. CR models [theoretical background]

Time-evolution of level densities:

➢ Level densities $n(p)$: CR models are typically built on the level densities $n(p)$, $p = p_1, p_2, ..., p_N$ of a serious of levels whose temporal and spatial distribution is related to each other by the diffusion equation

$$\left(\frac{\partial\, n(p)}{\partial t}\right)_{\rm CR} \;=\; \frac{\partial\, n(p)}{\partial t} \;+\; \boldsymbol{\nabla}\cdot\left(n(p)\,\boldsymbol{\omega}(p)\right).$$

➢ Dominance of radiative and collisional (de-) excitation processes: If changes in the level density are dominated by radiative and collisional (de-) excitation processes, most CR models simply assume

$$\left(\frac{\partial\, n(p)}{\partial t}\right)_{\rm CR} \;=\; 0 \;=\; P(p) \;-\; n(p)\,D(p)$$

and just solve a (single) matrix equation. Here, $P(p)$ is the collisional and radiative production rate, and $D(p)$ the (so-called) *destructive* factor. The two functions $P(p)$, $D(p)$ can be written in terms of different rate coefficients for electron-impact excitation, ionization as well as for radiative and three-body recombination.

10.7. Atomic responses not yet considered in JAC

10.7.a. Floquet theory [theoretical background]

Time-dependent SE and master equations:

➢ Time-dependent single-electron Schrödinger equation: In quasi-harmonic light fields (and elsewhere), the single-electron SE can be written as

$$i\,\hbar\,\frac{\partial}{\partial t}\,\Psi(\mathrm{r},t) \;=\; H(\mathrm{r},t)\,\Psi(\mathrm{r},t) \;=\; \left(\frac{1}{2m}\,[-i\hbar\,\boldsymbol{\nabla}\,+\,e\,\mathbf{A}(t)]^2\,+\,V^{\,(\mathrm{atom})}\right)\,\Psi(\mathrm{r},t)\,,$$

$$i\,\hbar\,\frac{\partial}{\partial t}\,\Psi(\mathrm{r},t) \;=\; \left(\frac{\hbar^2}{2m}\,\boldsymbol{\nabla}^2\,-\,\frac{i\,e\,\hbar}{m}\,\mathbf{A}(t)\cdot\boldsymbol{\nabla}\,+\,V^{\,(\mathrm{atom})}\right)\,\Psi(\mathrm{r},t) \qquad \text{... velocity gauge}$$

$$i\,\hbar\,\frac{\partial}{\partial t}\,\Psi(\mathrm{r},t) \;=\; \left(\frac{\hbar^2}{2m}\,\boldsymbol{\nabla}^2\,+\,e\,\mathbf{E}(t)\cdot\mathrm{r}\,+\,V^{\,(\mathrm{atom})}\right)\,\Psi(\mathrm{r},t) \qquad \text{... length gauge ,}$$

and where the atomic potential $V^{\,(\mathrm{atom})}$ is often modeled by a Yukawa and a long-range Coulomic potential.

➢ Relation between the wave functions (solutions) in length and velocity gauge:

$$\exp\left[-i\,\frac{e^2}{2m\,\hbar}\,\int dt\;\mathbf{A}^2(t)\right]\;\Psi^{\,(\mathrm{velocity})}(\mathrm{r},t) \;=\; \exp\left[-i\,\frac{e}{\hbar}\,\mathbf{A}(t)\cdot\mathbf{r}\right]\;\Psi^{\,(\mathrm{length})}(\mathrm{r},t) \;\equiv\; \Psi(\mathrm{r},t).$$

Floquet ansatz:

➢ Floquet ansatz: With this ansatz, the time-dependent SE in a stationary incident field can be simplified to a set of time-independent coupled differential equations. This set of equations need to be solved by imposing (so-called) Siegert boundary conditions on the wave function and by expanding it, for instance, upon a complex basis set.

➢ Generalized Floquet ansatz: For the interaction with two laser fields with frequencies ω_1, ω_2 , the Floquet ansatz can be written

$$\Psi^{\,(\text{velocity},\,\text{length})}(\mathrm{r},t) \;=\; e^{-i\,E\,t/\hbar}\sum_{N_1\,N_2} e^{\,-i\,(N_1\,\omega_1\,+\,N_2\,\omega_2)}\;F_{N_1\,N_2}(\mathrm{r})\,.$$

In this ansatz, the Floquet components $F_{N_1\,N_2}(\mathrm{r}) \;\equiv\; F^{(\text{velocity},\,\text{length})}_{N_1\,N_2}$ and energies $E \;\equiv\; E^{\,(\text{velocity},\,\text{length})}$ satisfy a system of time-independent equations that are equivalent to the time-dependent Schrödinger equation, cf. Potvliege (1998).

➢ Floquet ansatz for the wave function:

$$\psi(t) \;=\; \exp(-i\,Et)\sum_{n=-\infty}^{\infty}\exp(-i\,n\,\omega t)\;\psi_n\,, \qquad\qquad E \;=\; \Re(E)\;-\;i\Gamma/2\,,$$

where the functions ψ_n are often called the harmonic components, while E is the complex quasi-energy of the Siegert state $\psi(t)$ and Γ the total ionization rate of this state.

Applications of Floquet theory to HHG:

➢ Induced electric-dipole moment: The induced electric-dipole moment from the theory of high harmonics can be expressed within the Floquet theory in the form (Gebarowski *et al.* 1997)

$$\mathbf{D}(t) \;=\; \exp(-\,\Gamma\,t)\;\left[\mathbf{D}_o\;+\;2\sum_{q=1}^{\infty}\Re\left[\mathbf{D}_q\;\exp(-\,iq\,\omega\,t)\right]\right], \qquad\qquad \mathbf{D}_q \;=\; \sum_{n=-\infty}^{\infty}\;-\,\langle\psi_{n-q}\,|\,\mathbf{R}_N\,|\,\psi_n\rangle\;.$$

➢ Emission rate for photons with frequency $\omega_q = q\,\omega$ and polarization $\boldsymbol{\lambda}$: The rate for emission of photons into a given solid angle $d\Omega$ is then obtained by summing over all polarizations of the emitted radiation

$$\frac{dR(\omega_H, \boldsymbol{\lambda})}{d\Omega} = \frac{\omega_H^3}{2\pi\, c^3} \left|\boldsymbol{\lambda}^* \cdot \mathbf{d}_q\right|^2 ,$$

and the total emission rate by an integrating over all directions.

10.7.b. Two-color sideband formation in atomic photoionization [theoretical background]

Processes & notations:

➢ Photoionization by a long twisted pulse and a long NIR pulse:

$$\hbar\,\omega^{(\text{long, twist})} + A + \hbar\,\omega^{(\text{String NIR})} \longrightarrow A^+ + e_p^- \,(E_p, \text{sidebands})$$

➢ In this strong-field ionization process, the photoelectron moves after its ionization in a Volkov state with the NIR field, and this gives rise to well-defined sidebands in the photoionization probability $W(E_p; m, \Lambda_X, \Lambda_L)$.

10.7.c. Phase control of atomic photoionization in multi-color fields [theoretical background]

Processes & notations:

➢ Coherent-control schemes: While various quantum coherent-control schemes have been developed and utilized already within the optical and IR regions, their use at high frequencies has been hampered by the lack of sufficient coherent xuv sources. An important step ahead was made by seeded FEL beams, for instance at FERMI, which provide high longitudinal coherence. This coherence of the light beams enables one to observe interference of two- and one-photon pathways in the photoelectron angular distributions following the xuv irradiation.

➢ Application of phase control: The phase control of photoprocesses has attracted much recent interest and has found promising applications, such as the control of chemical reactions, the study of biological changes, ultrafast and nonlinear optics as well as four-dimensional (4D) ultrafast electron microscopy.

➢ Differential ionization probability: In second-order perturbation theory, the angle-differential ionization probability for the emission of a photoelectron and for a transition $i \rightarrow f$ of the photoion can be expressed as

$$\frac{dW}{d\Omega} = \frac{1}{2\,J_i + 1} \sum_{M_i, M_f \mu} \left| \eta\, U^{(1,2\omega)}_{M_i, M_f \mu} + U^{(2,\omega)}_{M_i, M_f \mu} \right|^2$$

where $U^{(1,2\omega)}_{M_i, M_f \mu}$ is the first-order amplitude for ionization by the second harmonic and $U^{(2,\omega)}_{M_i, M_f \mu}$ the second-order amplitude for two-photon ionization by the fundamental frequency. Here, the magnetic quantum numbers refer to the initial atomic state state $|\mathbb{J}_i M_i\rangle$, the residual ion $|\mathbb{J}_i M_i\rangle$ as well as the photoelectron $|\mathbf{p}\,\mu\rangle$.

➢ Electric dipole approximation:

$$U^{(1,2\omega)}_{M_i, M_f \mu} = -i \left\langle \alpha_f \mathbb{J}_f M_f,\, \mathbf{p}\mu^{(-)} \,|\, e\,\mathbb{D}\,|\, \alpha_i \mathbb{J}_i M_i \right\rangle\, T^{(1)}$$

$$U^{(2,\omega)}_{M_i, M_f \mu} = \sum_{\nu} \int \left\langle \alpha_f \mathbb{J}_f M_f,\, \mathbf{p}\mu^{(-)} \,|\, e\,\mathbb{D}|\, \alpha_\nu \mathbb{J}_\nu M_\nu \right\rangle \left\langle \alpha_\nu \mathbb{J}_\nu M_\nu \,|\, e\,\mathbb{D}|\, \alpha_i \mathbb{J}_i M_i \right\rangle\, T^{(2)}_{E_\nu}.$$

Here α_ν specifies the quantum numbers of the intermediate states ν, while $\sum_\nu \int$ denotes the infinite summation over all discrete and continuum states. The minus sign in the outgoing electron wave indicates the proper asymptotic form of the continuum wave function, E_ν is the energy of the intermediate virtual atomic state. The time-dependent $T^{(1)}$ and $T^{(2)}_{E_\nu}$ were described elsewhere in the literature (Gryzlova *et al.*, 2018).

10.8. Theoretical background to atomic responses considered above

Theoretical methods:

➢ Time-dependent CI singles (TDCIS): This one-electron formulation for describing strong-field ionization is guided mainly by the first step in all strong-field processes, in which an electron is pulled away from the parent ion by the laser field. The use of the single-active electron (SAE) approximation has been shown to be sufficient to predict the single-ionization production, the cutoff in the HHG spectrum as well as the ATI photoelectron spectra in different atoms.

➢ TDCIS: This is an approximate one-electron approach that goes beyond the SAE treatment. In this *ab-initio* electronic-structure method, the time-dependent wave function is restricted to spin-singlets which conserve single-particle excitations from the ground-state determinant.

10.8.a. Strong-field approximation (SFA) [background]

Elements of SFA:

➢ Applications of SFA: This theory help explain multi-photon ionization (MPI), above-threshold ionization (ATI), tunnel ionization (TI) as well as over-the-barrier (OTB) ionization. In the strong-field regime, the forces of the laser field are comparable to those of the Coulomb force between the nucleus and electrons so that neither one can be described (only) perturbatively. Such a distortion of the Coulomb potential often also leads to a lowering of the ionization barrier.

➢ Angular-dependent PEMD: The angular-dependent PEMD of an electron with asymptotic momentum is

$$\frac{d^3\,\mathcal{P}^{(\mathrm{SFA})}}{dp_x\,dp_y\,dp_z} \;=\; |\{^{(SFA)}(\mathbf{p})|^2.$$

For a linearly- or circularly-polarized laser field, the angular-dependent PEMD has cylindrical symmetry and, hence, a 2-dimensional PEMD can be defined by

$$\frac{d^2\,\mathcal{P}^{(\mathrm{SFA})}}{dp_\perp\,dp_z} \;=\; 2\pi\,p\,\sin\vartheta_p\;|\{^{(SFA)}(\mathbf{p})|^2, \qquad\qquad p_\perp \;=\; \sqrt{p_x^2\,+\,p_y^2}\,,$$

and where ϑ_p is the angle between the polarization axis $\boldsymbol{\mathcal{E}} \,||\, \mathbf{e}_z$ and the direction of the emitted photoelectron (linear polarization) or the polar angle between the photoelectron and the propagation axis of the laser $\mathbf{k} \,||\, \mathbf{e}_z$ (circular polarization), respectively. In both cases, the integration over the azimuthal angle φ_p can be carried out explicitly.

➢ Energy-dependent PEMD: The energy-dependent distribution is obtained from the SFA amplitude by

$$\frac{d\,\mathcal{P}^{\,(\mathrm{SFA})}}{d\,E} \;=\; 2\pi\,\sqrt{2\,E}\;\int_{-1}^{1} d\,(\cos\vartheta_p)\;\;|\{^{\,(SFA)}(\mathbf{p})|^2 .$$

Vector potentials and fields in dipole approximation:

➢ Electric field: For a linearly-polarized laser field, the electric field is often taken as:

$$\mathbf{E}(t) \;=\; \mathbf{E}_o\,\cos(\omega\,t)\,\mathbf{e}_x, \qquad\qquad \mathbf{A}(t) \;=\; -\,\frac{\mathbf{E}_o}{\omega}\,\sin(\omega\,t)\,\mathbf{e}_x\,.$$

➢ Vector potential: $\mathbf{E}(t) \;=\; \frac{\partial\,\mathbf{E}(t)}{\partial t}$.

Time-dependent dipole amplitudes:

➢ Continuum orbital of free electrons with asymptotic momentum $\mathbf{p}$, $|\mathbf{p}\rangle \;=\; e^{-i\,\mathbf{p}\cdot\mathbf{r}}$: Free electrons are described by (continuum solutions of the) Hamiltonian

$$H_o\;|\mathbf{p}\rangle \;=\; \frac{p^2}{2}\;|\mathbf{p}\rangle\,.$$

➢ Time-dependent dipole amplitude: If the electron is initially in the bound-state $|\phi_o\rangle$ of the atom, the time-dependent dipole amplitude is given by

$$\mathbf{d}(\mathbf{p}) \;=\; \langle\mathbf{p}\,|\,\mathbf{r}\,|\,\phi_o\rangle\,.$$

➢ Time-dependent dipole amplitude for non-relativistic hydrogenic $1s$ orbitals: If the bound electron is initially in the $1s$ orbital, the dipole amplitude is given by

$$\mathbf{d}(\mathbf{p}) \;=\; -i\,2^{7/2}\,\alpha^{5/4}\,\frac{\mathbf{p}}{\pi\,(p^2\,+\,\alpha)^3}\,.$$

Approximations to the Volkov phase:

➢ Kinetic *versus* canonical momentum of a particle in an em field: The (dressed) kinetic momentum $\pi(\mathbf{p},t) = \mathbf{p} + \mathbf{A}(\mathbf{r},t)$ of a particle with charge e differs from its canonical momentum $\mathbf{p}$ by the (coupling of the local) vector potential and, hence, the dressing of the em field. Often, one considers the motion of electrons in either a linearly- or circularly-polarized field.

➢ Volkov phase: The classically accumulated action of the electron, if it propagates in a laser field, reflects the dressing of the particle by the field; in the SFA, this action appears in the (so-called) Volkov phase

$$S(\mathbf{p},t,t') \;=\; \int_{t'}^{t} dt''\,\frac{[\mathbf{p}\,+\,\mathbf{A}(\mathbf{r},t)\,]^2}{2}\,+\,I_p$$

➢ Saddle point of the time-dependent momemtum: The saddle point fulfills the equation $\boldsymbol{\nabla}_{\mathbf{p}}\,S(\mathbf{p},t,t') = 0$

$$\mathbf{p}^{\,(\text{saddlepoint})} \;=\; -\,\frac{1}{t\,-\,t'}\int_{t'}^{t} d\tau\,\mathbf{A}(\tau).$$

➢ Saddle-point approximation to the Volkov phase: This approximation leads for the q-th harmonic to three equations for the canonical momentum $\mathbf{p}_s$ at the saddle point

$$\mathbf{p}_s(t,t') \;=\; \frac{1}{t\,-\,t'}\int_{t'}^{t} dt''\,\mathbf{A}(t''),\qquad \frac{[\mathbf{p}\,+\,\mathbf{A}(t')\,]^2}{2} \;=\; -\,I_p,\qquad \frac{[\mathbf{p}\,+\,\mathbf{A}(t)\,]^2}{2} \;=\; q\,\omega\,-\,I_p\,.$$

The last two relations simply reflect the conservation of energy, namely, for the *release* of the electron into the continuum at the *ionization* time t' and for its recombination with the parent ion at the *(recombination)* time t. Both of these times are generally complex because $I_p > 0$.

Time-dependent dipole moment $\mathbf{D}(t)$:

➢ Time-dependent dipole moment:

$$\mathbf{D}(t) \;=\; \int_{\infty}^{t} dt' \int d^3\mathbf{p}\;\; \mathbf{d}^*(\mathbf{p} + \mathbf{A}(t))\, \mathbf{E}(t')\, \mathbf{d}(\mathbf{p} + \mathbf{A}(t'))\, e^{-i\, S(\mathbf{p},t,t')} \;+\; \text{c.c.}$$

➢ Time-dependent dipole moment in saddle-point approximation: In the saddle-point approximation, the dipole moment with $\mathbf{p}^{(\text{sp})} \equiv \mathbf{p}^{(\text{saddle-point})}$ to:

$$\mathbf{D}^{(\text{saddle-point approx})}(t) \;=\; \int_{\infty}^{t} dt' \left(\frac{2\pi\, i}{(t \,-\, t' \,-\, i\,\epsilon)}\right) \mathbf{d}^*(\mathbf{p}^{(\text{sp})} + \mathbf{A}(t))\, \mathbf{E}(t')\, \mathbf{d}(\mathbf{p}^{(\text{sp})} + \mathbf{A}(t'))\, e^{-i\, S(\mathbf{p}^{(\text{sp})},t,t')} \;+\; \text{c.c.}\,,$$

and where ϵ is ...

Frequency-dependent power spectrum $\mathbf{D}(q\,\omega)$:

➢ Frequency-dependent dipole moment in saddle-point approximation: For the q-th order of the high-harmonic, the dipole moment in saddle-point approximation is given with $\mathbf{p}^{(\mathrm{sp})} \equiv \mathbf{p}^{(\mathrm{saddle-point})}$ by

$$\mathbf{D}^{(\mathrm{saddle-point\ approx})}(q\,\omega) \;=\; i \int_{\infty}^{\infty} dt \int_{\infty}^{t} dt' \left(\frac{2\pi\, i}{(t \,-\, t' \,-\, i\,\epsilon)} \right) \mathbf{d}^{*}(\mathbf{p}^{(\mathrm{sp})} \,+\, \mathbf{A}(t))\, \mathbf{E}(t')\, \mathbf{d}(\mathbf{p}^{(\mathrm{sp})} \,+\, \mathbf{A}(t'))\, e^{iq\,\omega t \,-\, i\,S(\mathbf{p}^{(\mathrm{sp})},t,t')} \,+\, \mathrm{c.c.}$$

➢ Frequency-dependent dipole moment in saddle-point approximation: In this approximation, the frequency-dependent dipole moment of the q-th harmonic can be expressed as a sum of products *[field* $\times$ *dipole amplitude]*, and which just need to be evaluated at the saddle points:

$$\mathbf{D}(q\,\omega) \;=\; i \sum_{s} \frac{2\pi}{\sqrt{\det(S'')}} \left(\frac{2\pi}{t_s \,-\, t'_s} \right) \mathbf{d}^{*}(\mathbf{p}_s \,+\, \mathbf{A}(t_s))\; \mathbf{E}(t'_s)\; \mathbf{d}^{*}(\mathbf{p}_s \,+\, \mathbf{A}(t'_s))\; \exp[-i\,S(\mathbf{p}_s, t_s, t'_s) \,+\, iq\,\omega\, t_s]\,.$$

Here $S'' \;=\; \frac{\partial S(\mathbf{p},t,t')}{\partial t\, \partial t'}\,|_{(\mathbf{p}_s,t_s,t'_s)}$ denotes the Hessian matrix of the action at the saddle point. The saddle-point approximation is closely related to the classically allowed trajectories of a free electron in a strong laser field.

➢ Power spectrum of high harmonics, $\mathbf{D}(q\,\omega)$: The (so-called) power spectrum of the emitted harmonic radiation is obtained from the Fourier transform of the dipole acceleration $\frac{\partial^2\,\mathbf{D}(t)}{\partial t}$.

Semi-classical trajectories of electrons in Lewenstein's model:

➢ Harmonics of well-defined order: In practice, only a very small fraction of the released electrons find their way back to the parent ion and will recombine eventually. Obviously, the harmonic order is determined by the (dressed) kinetic momentum $\mathbf{p} + \mathbf{A}(t)$ at the recombination time.

➢ *Long* and *short* trajectories: There are exactly two trajectories per half cycle which return the electron, and with the same energy, to the parent ion. Both trajectories will therefore contribute to the same harmonic order, though they are often referred to as *long* and *short* trajectories because of the different travel time of the electron along these trajectories.

➢ Dipole phase of the short and long tranjectories: For the harmonics at the plateau, the dipole phases of the short and long tranjectories clearly differ from each other because of the different travel times along these orbits, while the phases approach each other towards the cut-off [cf. Paufler *et al.* (2019), Fig. 1]. Moreover, the dipole phase generally depends linear on the intensity of the incident beam.

10.8.b. Guo-Aberg-Crasemann (GAC) theory [background]

Differential GAC ionization cross sections:

- Lowest-order perturbation theory typically fails to explain the the shape of the envelope of the individual ATI photoelectron peaks. Perturbation theory also fails to predict the dependence of the strength of the ATI peaks on the intensity of the laser light, if the laser intensity exceeds 1 TW cm^{-1}.
- Differential transition-rate formula: Within the GAC theory, the lowest-order transition matrix element can be utilized together with the (integer) constraint $z = m - n$, in order to obtain a differential transition-rate formula for the ionization of electron that have absorbed $q = lm$ photons (Guo *et al.*, 1989)

$$\frac{d\omega}{d\Omega} = \frac{(2\,m^3\,\omega^5)^{1/2}}{4\pi^2}\;|\Phi_i(\mathbf{p} - q\,\mathbf{k})|^2\;q^2\left(q - \frac{E_b}{\omega}\right)^{1/2}\;|\mathcal{J}_{q+z}|^2\;|\mathcal{J}_z|^2,$$

  where $\Phi_i(\mathbf{p} - q\,\mathbf{k})$ is the Fourier transform of the initial-state wave function with binding energy E_b. The angular and polarization dependences of this differential transition-rate formula are determined by $\mathbf{p} - q\,\mathbf{k}$ in Φ_i as well as by the arguments of the two elliptically polarized Bessel functions $\mathcal{J}_t$.
- In the nonrelativistic limit and for a large photon-number, the final state can be reduced to a single but modified Volkov state, if the ponderomotive energy is an integer multiple of the photon energy. Therefore, the scattering amplitude strinctly exists only in the integer case, where it becomes a product of the original KFR amplitude and the overlap between the final plane-wave state and the Volkov state, and vanishes otherwise.

10.8.c. Twisted light beams [background]

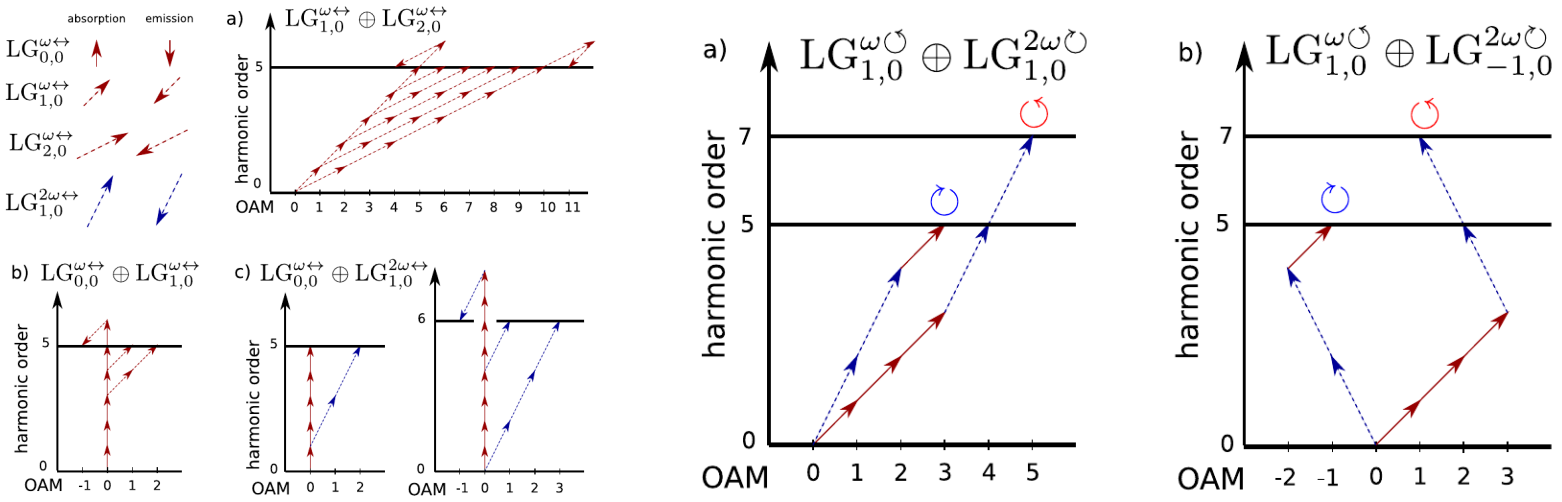

Figure 10.4.: Photon-coupling diagrams in HHG. (Left) Three different scenarios of HHG with superpositions of two linearly-polarized (Laguerre-) Gaussian beams are shown and can be utilized in order to control and manipulate the OAM of the generated harmonics. Different arrows from the left-upper corner here represent the absorption and emission of photons from different beams. (a) Superposition of two linearly-polarized LG beams with the same photon energy but different OAM. This scheme gives rise to multiple couplings for the generation of each harmonic order and, hence, each harmonic may carry different values of OAM. (b) Non-collinear superposition of a strong Gaussian beam with a weaker LG beam gives rise to the spatially separated xuv-vortices with a well defined OAM. (c) Non-collinear superposition of a strong Gaussian with its second harmonic. Similar to (b), we get spatially separated xuv-vortices, each with well-defined that carry a well-defined OAM as well. (Right) Photon-coupling diagrams of HHG with with bicircular twisted beams. (a) Superposition of two LG beams with the same OAM. For each harmonic order, there is only *one* possible diagram which gives rise to xuv vortices with well-defined OAM. Each of these harmonic is circularly-polarized. (b) Superpositions of two LG beams with opposite OAM. Since the number of photons absorbed from the ω-beam always differs by one from the number of photons absorbed from the $2\,\omega$ beam, the modulus of the OAM of each xuv vortex is $|\ell| = 1$.

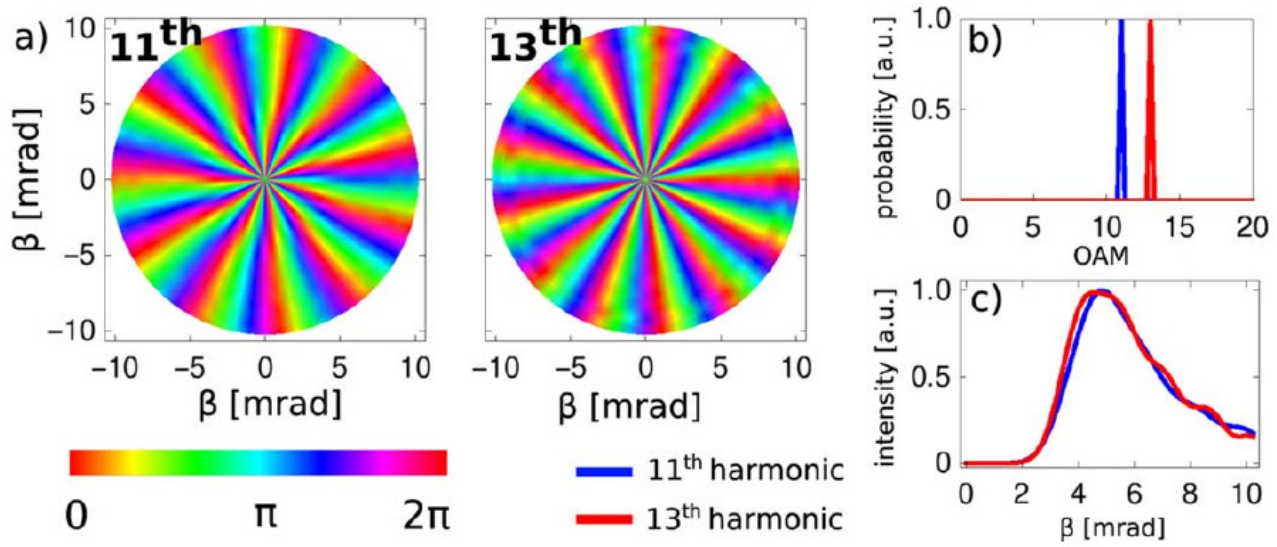

Figure 10.5.: Phase profile and spectrum of HH, generated with a linearly-polarized LG beam: (a) Phase profiles of the 11th and 13th harmonic at the detector, and where the OAM (number of phase canges of π) is equal to the harmonic order. (b) OAM of the 11th (blue) and 13th (red) harmonic as obtained by a Fourier transform along the azimuthal coordinate. (c) Intensity distributions of the 11th (blue) and 13th (red) harmonic in the far-field. From Paufler *et al.* (2019, Fig. 3).

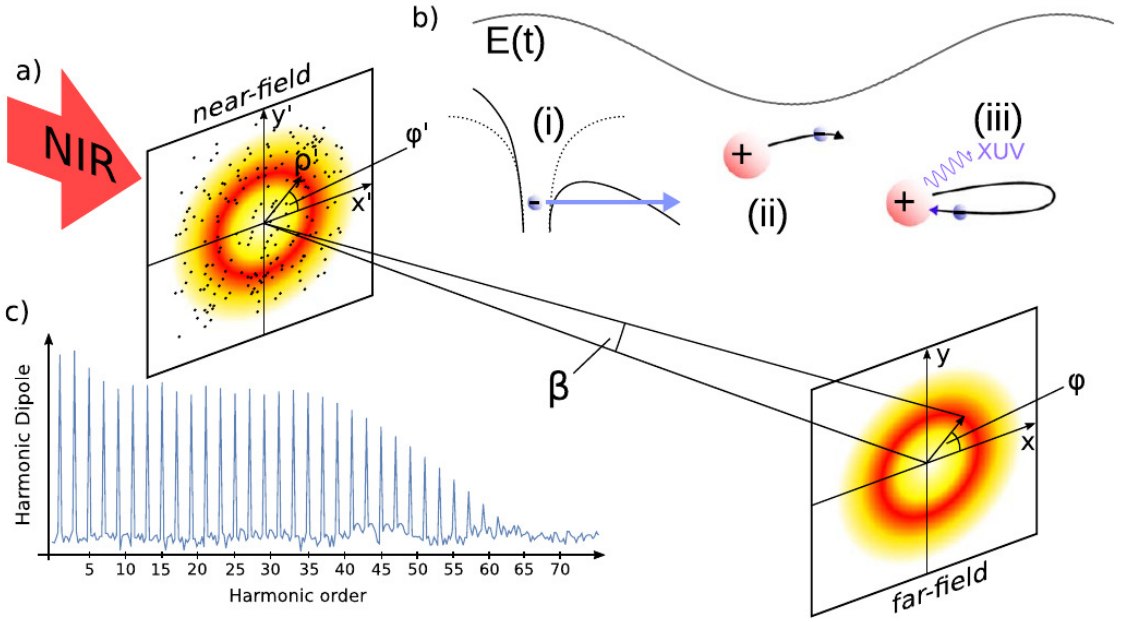

Figure 10.6.: HHG in the near- and far-field. (a) Superposition of the far-field due to locally generated HH in the near field and as described by the Fraunhofer diffraction formula. (b) Illustration of the simple man's three step model: (i) release of the electron by tunnel ionization, (ii) propagation and acceleration of the *free* electron in the strong laser field and (iii) recombination of the electron with the parent ion under the emission of a high-energetic photon at multiple laser frequency. (c) Typical high-harmonic spectrum as generated with a linearly-polarized laser field, and where only odd harmonic orders contribute to the spectrum. From Paufler *et al.* (2019, Fig. 2).

11. Time-evoluation of many-electron atomic state functions and density matrices

11.1. Time-dependent approximations of many-electron states

Time-dependent methods:

- Time-dependent theory: The response of multi-electron atoms to strong laser fields with intensity $\sim 10^{14}$ W/cm^2 can be typically described only by explicitly time-dependent approaches. For short and intense light pulses, for example, the ionization rate is known to change rapidly during the pulse, and this makes the use of just a monochromatic field incorrect in the theoretical description. For laser intensities $\gtrsim 10^{16}$ W/cm^2, moreover, the electric field becomes even stronger than the inter-atomic fields, leading to a breakdown of perturbation theory. Then, the time-dependent Schrödinger equation need to be integrated explicitly in order to properly deal with the shape and intensity of the light pulses, although the *limits* of perturbation theory are not yet well understood in this time and intensity domain.
- Light sources for studying electron dynamics in atoms: New light sources and technologies facilitate nowadays various experiments with intense attosecond extreme-ultraviolet (XUV) pulses in order to resolve in time the ejection of electrons from the atomic target.
- New coherent light sources: Recently developed light sources include attosecond lasers, high-order-harmonic generation (HHG) sources or free-electron lasers. These novel light will pave the way for studying the interaction of matter with intense femtosecond or even sub-femtosecond radiation pulses in the visible and XUV regime.
- New light sources: Recent advances in the generation of ultra-short and extreme ultraviolet (XUV) pulses at free-electron lasers (FEL), attosecond high harmonic pulses or few-cycle optical laser pulses have pave the way for imaging and controlling the electronic and nuclear dynamics in molecules, and with many exciting applications in physics, chemistry and elsewhere. In particular, table-top HHG sources of femtosecond and sub-femtosecond XUV pulses enable one to observe the dynamics at the attosecond time scale.

➢ X-ray free-electron lasers (XFEL): Various XFEL's worldwide have recently extended the range of nonlinear processes due to intense ionizing radiation ($> 10^{15}$ PW/cm^2) .

➢ FEL *versus* synchrotron sources: Although both are based on accelerator technology, FEL (may) emit *coherently* because of its multi-electron coherence, while synchrotron radiation is always emitted incoherently due to its independently radiating electrons. Therefore, FEL are able to combine the intensity and coherence of an (optical) laser with the broad spectral coverage of synchrotrons.

➢ Third-generation synchrotrons: Modern synchrotron facilites support ionization studies of atoms and molecules across a wide energy range, using quite stationary conditions, and with much higher resolution than ever before. Moreover, these spectroscopic studies are often combined with synchronized laser pulses.

➢ The development of sub-femtosecond radiation pulses enables one to explore the electron dynamics in atoms *or* the (combined) electron and nuclei dynamics in molecules with a high degree of temporal and spatial resolution.

➢ Femto-slicing: Ultra-short x-ray pulses are nowadays an indispensable tool for visualizing ultra-fast processes in molecules, liquids and solids. Such ultra-short pulses can be generated by femto-slicing, i.e. if the relativistic electrons in an undulator are accompanied by some ultra-short and co-propoagating laser pulse. This technique enforces x-ray pulses with just 100 fs duration and at a time-scale that is comparable to atomic ordering phenomena in solids.

➢ Femto-slicing: This technique was first proposed by Zholents and Zoloterev in 1996 in order to generate ultra-short x-ray pulses at synchrotron facilities, and it was later demonstrated experimentally at the Advanced Light Source (ALS) in Berkeley. A first undulator-baser femto-slicing source was completed at BESSY II in Berlin in 2004. This techique has been further advanced during recent year in high-flux beamline and by using novel Zone Plate Monochromator (ZPM).

➢ Short-pulse, short-wavelength radiation: There are several approaches known for achieving ultra-short and high-energetic photon pulses:

- The conversion of fs laser pulses to higher photon energy by (i) HHG, (ii) by plasma generation with intense laser pulses, and which then emits x-rays, or (iii) by relativistic Thomson scattering.
- The time structure of electron bunches can be changed in a storage ring, for instance, if the (so-called) momentum-compaction factor is changed or if the laser-induced energy modulation is modified (femto-slicing), or by further compression of electron bunches in linear accelerators and especially at free-electron laser (FEL). In this regime, however, only laser-based techniques (femto-slicing and seeded FELs) facilitate a natural synchronization between the laser and the x-ray pulses for pump-probe experiments.

➢ Need for new time-dependent theoretical models: To support modern experiments with intense atto-second pulses, new time-dependent models and methods need to be develope beyond the current standard schemes, such as the single-active-electron approximation.

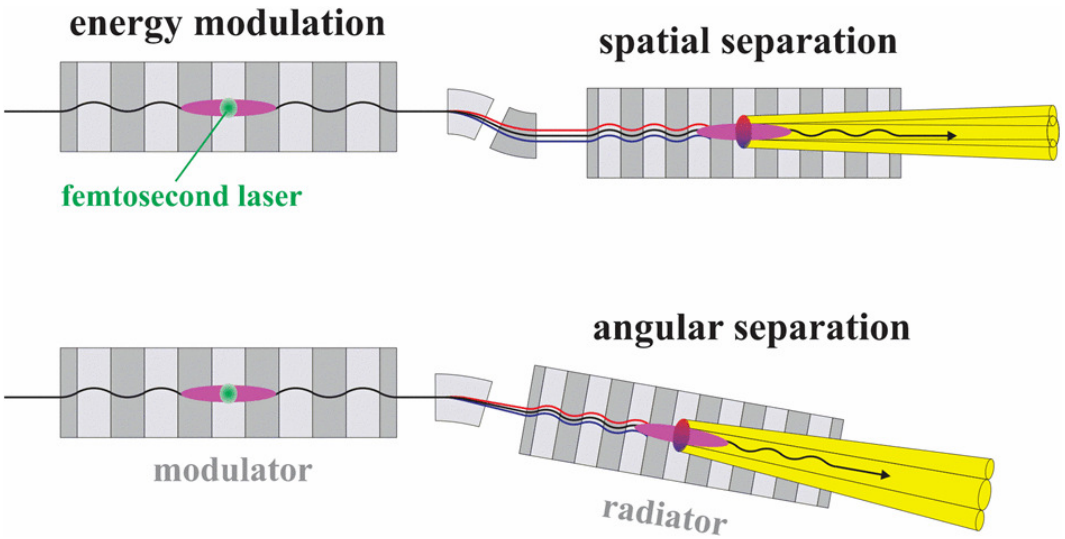

Figure 11.1.: Generation of short x-ray pulses by laser-induced energy modulation of electrons and subsequent spatial (top) and angular (bottom) separation. From Ref. DOI: 10.1109/PAC.2005.1590500.

➢ Time-dependent Hartree-Fock (TDHF) method: In this method, the time evolution of the electronic orbitals is accounted for during the interaction with an external field or collision partner by following the (time-dependent) mean field of the total electron density in the given potential. This method therefore properly treats the nuclear interaction and the *mean field* of the electrons but averages over all electronic correlations. In practice, such a mean-field approximation significantly reduces the dimension of the N-particle quantum system from $3\,N$ spatial coordinates to just three coordinates for the *mean* density. The TDHF method is an initial value problem that typically starts from the wave function of the static ground state of the system.

➢ Time-dependent RAS method with space partition: In this method, the wave functions are expanded in terms of Slater determinants with explicitly time-dependent CI coefficients. The Slater determinants are usually based on two type of time-independent orbitals: (i) Orbitals that are just defined in an inner region close to the atomic nucleus and (ii) orbitals in an outer region with zero-contribution to the inner region (Miyagi and Madsen, 2017).

➢ Space partition methods: A partitioning of space has been widely utilized for describing atom-electron collisions since the very first advent of the R-matrix theory. In all these models, a configuration-interaction (CI) expansion of the many-electron wave function is typically made in some inner region in order to deal with electronic correlations. In the outer region, in contrast, the electrons are supposed to move

independently of each other in just a long-range effective potential, and without that further exchange and correlation contributions are taken into accout. This piecewise definition of the wave function then requires to make sure that it remains continuously differentiable across the surface between the two regions.

➢ Time-dependent MCHF (TD-MCHF) method: This method is presently seen as the most accurate and widely used technique in order to describe the many-electron dynamics in explicitly time-dependent potentials, such as the laser-induced dynamics of N-electron atoms. When compared to the space-partition methods, the TD-MCHF method has the great advantage that, for a sufficiently large (radial) domain of the orbitals, all single- and multi-electron interactions (continua) can be taken into account, at least in principle.

➢ Time-evolution with separable (atomic) potentials (TESP): Galstyan *et al.* (2018) describe a new and computationally inexpensive method for studying the interaction of complex atoms or molecules with intense ultrashort laser pulses within the single active electron approximation. With this method, they have analyzed the photoionization of water molecules from the highest occupied molecular orbital and calculated, in particular, the ionisation yield for different orientations of the molecule with regard to the polarization of the incident pulse.

➢ TESP method: This method is an approximation since the exact solution would require to incorporate an infinite number of separable potentials in the representation of the kernel. This method is therefore especially useful for pulses with high frequency where only the lowest (few) levels play a crucial role for the ionization of the system.

➢ Central idea of the TESP method: The main idea of this method is to work in momentum space and to replace the kernel of the Coulomb potential by a sum of N symmetric separable potentials which each support just a single bound state of the system. The use of separable potentials enables one to reduce the N-dimensional time-dependent Schr"odinger equation (TDSE) to a system of N one-dimensional Volterra integral equations which only depend on time. This method is known also by Separable Potentials for Atoms and Molecules (SPAM).

➢ Weaknesses of the TESP method: The separable potential is not necessarely unique and does usually not represent the correct asymptotic behaviour of the potential. Moreover, the method is not gauge invariant and the question about proper gauges will need to be explored in further detail.

Time-evolution of ASF:

➢ A reliable description of the time-dependent (TD) many-electron dynamics has attracted recent interest in order to theoretically support a real-time analysis and control of the ultrafast electronic and nuclear dynamics of atoms and molecules in intense laser pulses.

➢ A computational and conceptual simple approach to the many-electron dynamics is the TD configuration-interaction singles (TD-CIS) method in which only singly excited configurations, relative to the Hartree-Fock ground state, are taken into account in the configuration interaction expansion.

➢ Miyagi and Madsen (2013) make use of the TD-CIS method by performing an optimization of the orbitals as well as the expansion coefficients at each time step in the evolution. This separate optimization makes it possible to construct a reasonable accurate wave function with just a relatively small number of electronic configurations. For the optimization, Miyagi and Madsen (2013) utilized the Dirac-Frenkel-McLachlan TD variational principle.

11.2. Time-dependent statistical tensors

Motivation:

➢ In physics, Liouville's theorem is known from classical statistical and Hamiltonian mechanics, and it asserts that the phase-space distribution function is constant along the trajectory of the system.

➢ Similarly, the quantum-mechanical analog of Liouville equation describes the time evolution of a mixed state. The quantum form can be obtained by the standard replacements of classical variables with quantum operators and Poisson brackets with commutators.

➢ The Liouville equation for the atomic density matrix ρ reads

$$\frac{\partial \rho}{\partial t} \;=\; -\frac{i}{\hbar}\,[\mathbb{H},\,\rho\,] \;-\; \Gamma\,\rho, \qquad\qquad \mathbb{H} \;=\; \mathbb{H}^{(\mathrm{atom})} \;+\; \mathbb{H}^{(e-\gamma)}$$

where the first term in the Hamiltonian describes the (inner-) atomic and the atom-photon interactions, and the second term the relaxation matrix Γ. This relaxation matrix accounts for the atomic spontaneous decay due to either radiative or nonradiative (Auger) processes of the atom.

11.3. Time-integration of statistical tensors

Motivation:

➢ Various methods can be applies to solve the coupled first-order odg's for the time-evolution of the statistical tensors. Apart from those methods which solve the equations with given accuracy (but typically require the evaluation of the rhs at any given time t), we are mainly interested in *shooting* or *predictor-corrector* methods which makes only use of previous solutions of ρ and $d\rho/dt = f$ on a equidistant time grid.

Numerical methods:

➢ If we use a step-size h and define $\rho(t_j) = \rho_j$, $\frac{d\rho}{dt}(t_j) = f_j$, the following integration formulas can be applied.

➢ Euler's methods:

$$\rho_{j+1} = \rho_j + h\, f_j$$

➢ Adams-Bashford methods:

$$\rho_{j+1} = \rho_j + h\left[\frac{3}{2} f_j - \frac{1}{2} f_{j-1}\right]$$

$$\rho_{j+1} = \rho_j + h\left[\frac{23}{12} f_j - \frac{16}{12} f_{j-1} + \frac{5}{12} f_{j-2}\right]$$

$$\rho_{j+1} = \rho_j + h\left[\frac{55}{24} f_j - \frac{59}{24} f_{j-1} + \frac{37}{24} f_{j-2} - \frac{9}{24} f_{j-3}\right]$$

11.4. Time evolution of statistical tensors. Formalism

11.4.a. Liouville equation for the atomic density matrix

Vector potential and state multipoles:

- In the electron-photon interaction, the vector potential of the electromagnetic field is typically chosen to fulfill $\mathrm{div}\mathbf{A}(\mathbf{r}_i, t) = 0$.
- When the electron-photon interaction Hamiltonian $\mathbb{H}^{(e-\gamma)}$ is applied upon the density operator ρ, we shall consider only processes with one photon.
- Moreover, we assume a vector potential for a monochromatio field with frequency ω and wave vector $\mathbf{k} = (\vartheta_k, \varphi_k)$ $(|\mathbf{k}| = \frac{\omega}{c})$ with regard to the coordinates in the laboratory system.
- Envelope of the vector potential: For a pulse with (real) envelope $f(t)$, the vector potential then includes two terms

$$\mathbf{A}(\boldsymbol{r}, t) \;=\; \mathbf{A}(\mathbf{r})\, f(t)\, e^{-i\omega t} \;+\; \mathbf{A}^*(\mathbf{r})\, f^*(t)\, e^{i\omega t}.$$

Liouville equation in the representation of well-defined angular momenta:

- Liouville equation: In an atomic basis with well-defined total angular momenta and parity, the Liouville equation can be re-written as

$$\frac{\partial}{\partial t}\, \langle \alpha \mathbb{J}_\alpha M_\alpha \,|\, \rho \,|\, \beta \mathbb{J}_\beta M_\beta \rangle \;=\; -\frac{i}{\hbar}\, (E_\alpha \,-\, E_\beta)\, \langle \alpha \mathbb{J}_\alpha M_\alpha \,|\, \rho \,|\, \beta \mathbb{J}_\beta M_\beta \rangle$$

$$-\,\frac{i}{\hbar} \sum_{\nu \mathbb{J}_\nu M_\nu} \Big(\big\langle \alpha \mathbb{J}_\alpha M_\alpha \,\big|\, \mathbb{H}^{(\mathrm{e}-\gamma)} \,\big|\, \nu \mathbb{J}_\nu M_\nu \big\rangle\, \langle \nu \mathbb{J}_\nu M_\nu \,|\, \rho \,|\, \beta \mathbb{J}_\beta M_\beta \rangle \;-\; \langle \alpha \mathbb{J}_\alpha M_\alpha \,|\, \rho \,|\, \nu \mathbb{J}_\nu M_\nu \rangle \big\langle \nu \mathbb{J}_\nu M_\nu \,\big|\, \mathbb{H}^{(\mathrm{e}-\gamma)} \,\big|\, \beta \mathbb{J}_\beta M_\beta \big\rangle \Big)$$

$$-\sum_{\gamma \mathbb{J}_\gamma M_\gamma} \langle \alpha \mathbb{J}_\alpha M_\alpha \,|\, \Gamma \,|\, \gamma \mathbb{J}_\gamma M_\gamma \rangle\, \langle \gamma \mathbb{J}_\gamma M_\gamma \,|\, \rho \,|\, \beta \mathbb{J}_\beta M_\beta \rangle$$

11.4.b. Time-dependent statistical tensors of atomic lines

Time-dependent statistical tensors:

➢ Statistical tensors: With the substitutions of the statistical tensors from above and the notations $[ab...c] \equiv (2a+1)(2b+1)...(2c+1)$, the Liouville equation can be written as Grum-Grzhimailo, 2012)

$$
\begin{aligned}
i\hbar\dot{\tilde{\rho}}_{kq}(\alpha\mathbb{J}_\alpha,\beta\mathbb{J}_\beta) \;=\; & -2\pi\sqrt{\frac{\hbar}{c\,k}}\sum_{\nu\mathbb{J}_\nu\,KQ}\\
& \Big[f(t)\,e^{-i(\omega-\omega_{\alpha\nu})t}\sum_{LM\lambda} g_\lambda(-1)^{J_\alpha+J_\beta+K+L}[LK]^{1/2}\,\langle KQ,\,LM\,|\,kq\rangle \begin{Bmatrix} J_\alpha & J_\beta & k\\ K & L & J_\nu\end{Bmatrix} D^{L}_{M\lambda}(\varphi_k,\vartheta_k,0)\,\Big(\Big\langle\alpha\mathbb{J}_\alpha\Big\|\,\mathbb{T}^{(m)}_L\,\Big\|\nu\mathbb{J}_\nu\Big\rangle + i\lambda\,\Big\langle\alpha\mathbb{J}_\alpha\Big\|\,\mathbb{T}^{(e)}_L\,\Big\|\nu\mathbb{J}_\nu\Big\rangle\Big)\,\tilde{\rho}_{KQ}(\nu\mathbb{J}_\nu,\beta\mathbb{J}_\beta)\\
& - f^*(t)\,e^{i(\omega-\omega_{\nu\alpha})t}\sum_{LM\lambda} g^*_\lambda(-1)^{J_\beta+k+J_\nu+L}[Lk]^{1/2}\,\langle kq,\,LM\,|\,KQ\rangle \begin{Bmatrix} J_\alpha & J_\beta & k\\ K & L & J_\nu\end{Bmatrix} D^{L*}_{M\lambda}(\varphi_k,\vartheta_k,0)\,\Big(\Big\langle\nu\mathbb{J}_\nu\Big\|\,\mathbb{T}^{(m)}_L\,\Big\|\alpha\mathbb{J}_\alpha\Big\rangle - i\lambda\,\Big\langle\nu\mathbb{J}_\nu\Big\|\,\mathbb{T}^{(e)}_L\,\Big\|\alpha\mathbb{J}_\alpha\Big\rangle\Big)\,\tilde{\rho}_{KQ}(\nu\mathbb{J}_\nu,\beta\mathbb{J}_\beta)\\
& + f(t)\,e^{-i(\omega-\omega_{\nu\beta})t}\sum_{LM\lambda} g_\lambda(-1)^{J_\alpha+J_\beta+K}[LK]^{1/2}\,\langle KQ,\,LM\,|\,kq\rangle \begin{Bmatrix} J_\alpha & J\_beta & k\\ L & K & J_\nu\end{Bmatrix} D^{L}_{M\lambda}(\varphi_k,\vartheta_k,0)\,\Big(\Big\langle\nu\mathbb{J}_\nu\Big\|\,\mathbb{T}^{(m)}_L\,\Big\|\beta\mathbb{J}_\beta\Big\rangle + i\lambda\,\Big\langle\nu\mathbb{J}_\nu\Big\|\,\mathbb{T}^{(e)}_L\,\Big\|\beta\mathbb{J}_\beta\Big\rangle\Big)\,\tilde{\rho}_{KQ}(\alpha\mathbb{J}_\alpha\,\nu\mathbb{J}_\nu)\\
& - f^*(t)\,e^{i(\omega-\omega_{\beta\nu})t}\sum_{LM\lambda} g^*_\lambda(-1)^{J_\alpha+K+J_\nu}[Lk]^{1/2}\,\langle kq,\,LM\,|\,KQ\rangle \begin{Bmatrix} J_\alpha & J_\beta & k\\ L & K & J_\nu\end{Bmatrix} D^{L*}_{M\lambda}(\varphi_k,\vartheta_k,0)\,\Big(\Big\langle\beta\mathbb{J}_\beta\Big\|\,\mathbb{T}^{(m)}_L\,\Big\|\nu\mathbb{J}_\nu\Big\rangle - i\lambda\,\Big\langle\beta\mathbb{J}_\beta\Big\|\,\mathbb{T}^{(e)}_L\,\Big\|\nu\mathbb{J}_\nu\Big\rangle\Big)\,\tilde{\rho}_{KQ}(\alpha\mathbb{J}_\alpha,\nu\mathbb{J}_\nu)\Big]\\
& - i\hbar\sum_{\gamma\mathbb{J}_\gamma} G^{KQ}_{kq}(\alpha\mathbb{J}_\alpha,\beta\mathbb{J}_\beta,\gamma\mathbb{J}_\gamma)\,e^{i\omega_{\alpha\gamma}t}\,\tilde{\rho}_{KQ}(\gamma\mathbb{J}\gamma,\beta\mathbb{J}_\beta)
\end{aligned}
$$

11.5. Observables to be derived from time-dependent statistical tensors

Motivation:

➢ If we solve the set of time-dependent (Liouville) equations for the state multipoles, we can obtain the atomic statistical tensors for
(a) discrete atomic states $\rho_{kq}(\alpha\mathbb{J}_\alpha;\beta\mathbb{J}_\beta)$ (b) for atomic states with one electron in continuum $\rho_{kq}(\alpha_f\mathbb{J}_f,\varepsilon\kappa:\alpha\mathbb{J}_\alpha,\alpha'_f\mathbb{J}'_f,\varepsilon'\kappa':\alpha\mathbb{J}_\alpha)$,
(c) *nondiagonal* elements $\rho_{kq}(\alpha_f\mathbb{J}_f,\varepsilon\kappa:\alpha\mathbb{J}_\alpha,\,\beta\mathbb{J}_\beta)$ and $\rho_{kq}(\alpha_f\mathbb{J}_f,\varepsilon\kappa:\alpha\mathbb{J}_\alpha,\alpha'_f\mathbb{J}'_f,\varepsilon'\kappa':\beta\mathbb{J}_\beta)$.

12. Atomic descriptors

Machine learning. Basic concepts, goals & notations:

- Machine learning (ML): Methods in ML basically apply statistical algorithms whose performance improve with training, similar as in daily life. ML approaches are therefore able to learn the rules that underlie a given dataset. These approaches access some available portion of data and *build* automatically a model to make predictions for so-far unknown systems.
- Machine learning (ML) in quantum chemistry and material science: ML methods circumvent the task of solving the SE explicitly by using instead the data from a finite subset of well-known solutions in order to estimate solutions for (yet) unknown systems and materials. Since, more generally, many reserach fields require a frequent solution of the SE, ML methods may enable one to explore quantum behavior in much larger spaces, such as the (so-called) chemical compound space in material science.
- Goals of machine learning: The goal of ML is to automatically derive a function (or relation) that, for a specific set of input data, is able to predict the desired output values to an acceptable degree of fidelity.
- Machine learning algorithms: These algorithms generally establish a nonlinear map between input data (descriptors) and the specific property that need to be predicted; their efficiency mainly depend on how well the input data are represented by the various descriptors.
- Artificial-intelligence methods: The emergence of contemporary artificial-intelligence methods has substantially altered and enhanced the role of computers in science and engineering during the past years (Butler *et al.*, 2018).
- Fourth paradigm of science: The combination of artificial-intelligence methods with large data sets has been termed in the public discussion as fourth paradigm of science or fourth industrial revolution. This new paradigm includes in particular a rapidly increasing number of applications in chemistry and material science. This paradigm is also quite different from most traditional computations, where computers simply acts as 'calculator' and just employ some hard-coded algorithm as provided by some human expert (Butler *et al.*, 2018).
- Inverse design: This new paradigm in designing molecules and materials start from the functionality and then searches for some (ideal) molecular structure, for which this functionality is realized. In contrast to quantum-chemical methods, here the input is the desired property, while the outout is a corresponding (geometrical) structure and composition of the molecule. Typically, however, a give function does not

map uniquely to just *one* molecular structure but to a distribution of *probable or nearby* geometrical structures (Sanchez-Lengeling and Aspuru-Guzik, 2018).

➢ Deep learning algorithms aim for generating data distributions by training with large data sets. The loss function is hereby a measure how the empirically observed and the generated distribution differ from each other.

➢ High-throughput calculations of atomic level representations (state vectors) and processes is usually highly time-consuming. This suggests to make use of ML approaches in order to predict atomic data as they are needed, for instance, in astro and plasma physics. Once a ML model has been trained on an atomic (training) set, ML based computations are expected to be very fast.

➢ High-throughput virtual screening (HTVS): This simulation method has its roots in the pharmaceutical industry for drug discovery in order to screen a (very) large number of synthesized or potentially useful molecules. While HTVS appears in spirit quite similar to inverse material design, it differs in philosophy since HTVS also includes automation and time-critical performance with the goal to identify 'promising candidates', and which are later further processed by more expensive methods.

Feature selection and engineering in atomic physics:

➢ Feature engineering: Like in (human) learning, a machine-learning algorithm might learn more effectively by using one *particular* format rather than other formats (Butler *et al.*, 2018). Therefore, the raw input data need to be converted into a more suitable form for a given algorithm, a process that is known as featurization or feature engineering. In practice, however, it is by far not obvious which particular descriptor will eventually give rise to the best performance of an machine-learning algorithm, and special intuition and experience are typically required for each particular field of application.

➢ Feature engineering: The selection and transformation of (given) input data into proper descriptors is a highly non-trivial task and requires special insight into a particular research field. In practice, this transformation has to be based more on intuition than a systematic treatment, since descriptors need to be computed frequently and easily.

➢ Role of descriptors: Machine learning typically starts with a rather silent and unspectacular task, namely the choice of proper descriptors, i.e. the choice of useful parameters that connects available data sets with some learning method. If the choice of descriptors in inappropriate, it remains usually unclear of what can be learned from the (given) descriptor-property relations.

➢ Descriptors or (so-called) features generally define (vector) variables owing to some particular parametrization of data, suitable for ML. In this parametrization, domain knowledge is very important in order to obtain a *best* set of descriptors. Moreover, these descriptors should be independent of each other. Different ML methods help identifying more (and less) relevant descriptors, although some ambiguity in choosing these descriptors usually remains.

➢ Atomic descriptors: The definition of proper (atomic) descriptors is central for building models for machine learning and for predicting the physical properties and behaviour of atomic systems. These descriptors are also known also as feature transformations in the literature.

➢ Descriptors for atomic (or molecular) states: In electronic structure theory, the (electronic) state of an atom or molecule need to be transformed into a (more or less) simple vector representation, called descriptor. A set of such descriptors are then utilized as input for training a machine learning model on one or a few selected properties, and as associated with one or several atomic states.

➢ Atomic descriptors: A fast ML scan are often faster by a few (2-3) orders of magnitude, when compared with full quantum-mechanical computations, and may be applied as a preliminary step before detailed computations are made for selected structures and processes.

➢ Data parallelism: Since the descriptors of a *given* atomic system are usually independent from those of other systems, the computation of descriptors can easily be parallelized. Any useful implementation of such feature transformations should therefore consider a parallel descriptor creation for multiple samples.

➢ Property-labelled atomic fragments: Since not all atomic properties can likely be derived from a single set of descriptors, it is desirable to construct so-called property-labelled atomic fragments in order to simplify the feature selection process.

➢ Property-Labelled Atomic Fragments (PLAF): Following ideas from material science, it might be desirable to represent atomic (many-electron) states by graphs and to associate fragement descriptors to certain parts of these graphs. However, not much work has been done in this direction so far.

➢ Fragement descriptors: For each atomic property $q(r)$, such as electron densities, density convolutions, etc., one may also consider the minimum [min(q)], maximum [max(q)], total sum [$\sum q$], average [avg(q)] as well as the standard deviation [std(q)] of property q as potential descriptors in order to encode an atomic level or the underlying electron configuration.

➢ Primary features of an atom or ion:

- ionization potential (IP) and electro-negativity (EA);
- energies of the highest-occupied and lowest-unoccupied shell;
- radii of maximum charge distribution of all individual shells, calculated in a rather simplified shell model.

12.1. In JAC implemented atomic descriptors

None.

12.2. In JAC partly-implemented atomic descriptors

12.2.a. Descriptors for electronic densities (Descriptor)

Feature transformations:

➢ A feature transformation of the electron density is often applied in material science and will likely help also to characterize atomic (shell) structures and levels.

Use & notations:

➢ Using JAC: Perform an `Atomic.Descriptor(feature::AbstractFeature, ..., Descriptor.Settings(..)` or call directly functions from the module `Descriptor`.

➢ In JAC, we shall provide a list of features to which an approximate electron density can be transformed to.

4D surfaces of spatial densities:

➢ Use of a 4-dimensional unit sphere: Bartok *et al.* (2010) projected the electron densities of all atoms (in some given unit cell) upon the surface of a four-dimensional unit sphere. This can be achieved by a very similar transformation as applied for constructing the Riemann sphere

$$(\varphi, \vartheta, \vartheta_o) \;=\; \big[\tan^{-1}(y/x),\, \cos^{-1}(z/|\mathbf{r}|),\, |\mathbf{r}|/r_o\,\big]\,, \qquad\qquad r_o \;>\; r_{\rm cut}/\pi$$

➢ The use of this transformation has the advantage that all the information from the 3D spherical region inside the cutoff is now encoded by three angles of the 4D surface, and including the radial dependence of the (electron) density.

➢ 4D spherical harmonics $U^{(j)}_{mm'}$: For such a four-dimensional unit sphere, the 4D spherical harmonics $U^{(j)}_{mm'}$, also known as the Wigner matrices, provide a natural complete basis for the interior of the 3D sphere and without the need for radial basis functions. An approximate projection of the atomic density upon the 4D sphere is then obtained by just using a subset of expansion coefficients $c^{(j)}_{mm'} = \left\langle U^{(j)}_{mm'} \,|\, \rho \right\rangle$.

Bispectra of electronic densities:

➢ Bispectrum of an atomic density: A descriptor of the electron density can be formed also by means of the bispectrum of the projection coefficients $(c^{(j)}_{mm'})$ of some atomic or shell density upon a 4D sphere as well as the standard Clebsch-Gordan coefficients

$$B_{j_1,j_2,j} \;=\; \sum_{m_1,m_1'=-j_1}^{j_1} \sum_{m_2,m_2'=-j_2}^{j_2} \sum_{m,m=-j}^{j} (c^{(j)}_{m'm})^* \;\langle j_1 m_1,\, j_2 m_2 \,|\, jm\rangle \;\langle j_1 m_1',\, j_2 m_2' \,|\, jm'\rangle \;c^{(j_1)}_{m_1' m_1} \;\; c^{(j_2)}_{m_2' m_2}.$$

➢ Bispectrum of an atomic density: The elements of the three-index array $\mathbf{b} = (B_{j_1,j_2,j})$ from above are invariant with respect to rotations of the 4D space, and hence also to rotations of the 3D space. In practice, one can easily limit the spatial resolution in describing the atomic density by truncating the summation to $j,\, j_1,\, j_2 \;\leq\; J_{\max}$.

Partial radial distribution functions (PRDF):

➢ Partial radial distribution function (PRDF): These functions have been widely applied in the analysis of x-ray powder diffraction patterns in crystallography as well as for text mining in computer science. In physics, the PRDF representation may encode the distribution of pairwise distances d_{ab} between two (given) atoms or atomic levels of type a and b.

➢ PRDF: In molecular physics and material science, the PRDF can be seen as the density of atom-type b in a shell of radius r that is centered around atom a. If averaged over all atoms of a given type, the discrete PRDF representation is given by (Schütt *et al.*, 2014)

$$g_{ab}(r) \;=\; \frac{1}{N_a\, V_r} \sum_{i=1}^{N_a} \sum_{j=1}^{N_b} \Theta(d_{a_i\, b_j} \;-\; r)\; \Theta(r \;+\; dr \;-\; d_{a_i\, b_j}),$$

where N_a, N_b are the (total) number of atoms of type a, b, and V_r is the volume of the sphere. In solid-state physics, one usually considers the atoms in the unit cell. The PRDF representation has the advantage that it is not fixed to a certain number of atoms in the unit cell of the training materials and, hence, can be used also in order to predict the properties of other (related) systems.

12.2.b. Descriptors for pairs of atomic levels

Feature transformations:

- Descriptors for a single atomic level might include: various radii, one-electron binding energies, bispectrum of atomic density; effective atomic charges for shells/subshells.
- Descriptors for pairs of atomic levels: overlap integrals of valence electrons.
- Shell-coupling labeled atomic fragments: It still need to be worked out how the coupling information of atomic levels can be transformed into useful features.
- Cocatenation of descriptors: All fragment-based atomic descriptors can be concatenated quite easily in order to represent a particular level uniquely. From this concatenated vector descriptor, one then has to filter out low-variance as well as highly-correlated features in order to ensure a stable learning process.

12.3. Methods of machine learning

Machine learning. A short overview:

- Machine learning (ML): Frankly speaking, ML methods can be understood as a collection of computational methods which make use of data to predict yet unknown, though helpful new information. ML is closely related to data mining which applies machine learning and other methods to unveil information that is already within the data but did not (yet) become apparent so far.
- Machine learning (ML): The widespread use of ML methods in engineering sciences, social sciences, financial sciences, statistics, marketing, etc., has lead to many new methods and techniques which are independent of the research field they were developed originally.
- Machine learning includes several generic tasks, rather independent of the particular application: (i) Modelling of existing data by means of probability distributions; (ii) clustering and classification of data; (iii) regression analysis; and (iv) feature reduction. Different – formal and numerical – techniques have been developed and applied in order to deal with each of these tasks.
- Mathematics behind ML methods: These methods usually return a statistics-based model for some given data set, and which is then utelized in order to interpolate between the known data. A high accuracy in fitting the available data (low bias) often results in a rather high variance *between* these data points. Therefore, the accuracy of the fitting need to be tested by some cross-validation with test data or with experiment.

➢ Branches of machine learning: Three branches (classes) of ML methods are often distinguished: (i) Supervised learning; (ii) unsupervised learning as well as (iii) reinforcement learning (RL).

➢ Supervised learning: This approach is the most mature and powerful learning approach and, hence, has been applied in a large number of machine-learning studies in the physical and natural sciences, such as in the mapping of chemical compositions to some property of interest, picture recognition and elsewhere.

➢ Supervised learning aims for learning some conditional distribution $P(\mathbf{y}|\mathbf{x})$, and by assigning labels $\mathbf{y}$ to the classification data $\mathbf{x}$ based on training data from the distribution $P(\mathbf{y}, \mathbf{x})$. For example, supervised learning may aim to 'learn' a function $y = f(x)$ from a given data set.

➢ Unsupervised learning aims to identify certain structures within a given distribution $P(\mathbf{x})$, such as some clustering of data.

➢ Reinforcement learning tries to learn some correct behavior due to (so-called) reinforcement signals-rewards or punishments. The agent's goal is to obtain rewards with a high probability (Dunjko *et al.*, 2016).

➢ Generative models for machine learning: While there are various ways for building generative models, the main three approaches are: (i) variational autoencoders (VAEs); (ii) reinforcement learning (RL); and (iii) generative adversarial networks (GAN).

➢ Quantum machine learning: Analogue to quantum computing, this field aims to devise and implement explicit quantum algorithms (software) for machine learning that are faster than any known algorithms on some classical computers. Although a number of quantum algorithms are meanwhile well established, there are still many hardware and software challenges to be solved (Biamonte *et al.*, 2016). The use of quantum instead of classical algorithms is also known as quantum speedup. Quantum software makes in particular use of quantum algorithms to process information.

12.3.a. Supervised learning methods

Concepts & notations:

➢ Supervised learning models: These models can be used to predict output values from either a discrete set (e.g. classification of materials) or a continuous set of date (e.g. polarizability). To make predictions from a discrete set requires classification, while regression is needed to forcast continuous data.

➢ Kernel-based learning methods: These methods are based on the mapping of (atomic or molecular) data upon a high-dimensional feature space. This mapping is made implicitly by using a kernel function, e.g., a Gaussian kernel $k(x, y) = exp(xy/\sigma^2)$ or some Laplacian kernel $k(x, y) = exp(xy/\sigma)$. Here, the kernel can be interpreted as a measure to characterize the similarity between the given and predicted data. The predicted property is then computed as a linear combination of kernel functions that depend on the material of interest and the training materials (Schütt *et al.*, 2014).

Advantages & limitations:

➢ Since the regression coefficients $\{c_i\}$ arise from a nonlinear model, i.e. due to a nonlinear transformation of the training data, such a kernel-based ML model is specific to some selected property and cannot be applied to any other properties or regions of compound space.

Kernel ridge regression (KRR) method:

➢ Regression model based on the Coulomb matrix: Rupp *et al.* (2012) apply a ML model, in which the energy of a molecule is expressed as a sum over weighted Gaussians

$$E^{(\text{estimate})}(\mathbf{M}) = \sum_i^N c_i \exp\left[-\frac{d(\mathbf{M}, \mathbf{M}_i)^2}{2\,\sigma^2}\right]$$

where i runs over all molecules $\{\mathbf{M}_i\}$ from the training set. The training on the available reference data $\{\mathbf{M}_i, E_i^{(\text{reference})}\}$ then results in a set of regression coefficients $\{c_i\}$ as well as the length-scale parameter σ . In such a regression model, each molecule i from the training set contributes not only by its distance but also due to its regression coefficient c_i.

➢ Kernel ridge regression: In this regularized model, the norm of regression coefficients $\{c_i\}$ is restricted to ensure the transferability of some model towards some unexplored species. For a given length-scale parameter σ and regularization parameter λ, the regression coefficients

are obtained by determining the minimum of the function (Rupp *et al.*, 2012)

$$\min_{\{c_i\}} \sum_i \left(E^{(\text{estimate})}(\mathbf{M}_i) - E_i^{(\text{reference})} \right)^2 + \lambda \sum_i c_i^2 \qquad \Longrightarrow \qquad \mathbf{c} = \frac{\mathbf{E}^{(\text{reference})}}{(\mathbf{K} + \lambda \mathbf{I})}, \qquad K_{ij} = \exp\left[- \frac{d(\mathbf{M}_i, \mathbf{M}_j)}{2\,\sigma} \right].$$

$\mathbf{K}$ is called the Kernel matrix of all training molecules, while $\mathbf{I}$ here denotes the identity matrix.

➢ Locality of the kernel ridge regression: The locality of this model is measured by the length scale σ ; this parameters determines a range outside of which any training molecule $\mathbf{M}_i$ only contributes with (a rather) negligible weight to the selected property. Usually, the length scale σ is determined by some ML method and becomes smaller as the size of the training set increases, i.e. a model is said to become more *local* as more training data are available.

12.3.b. Neural network (NN) methods

Concepts & notations:

➢ Deep neural network (DNN) model: In these model, atomic or molecular representations are transformed first by a linear and later nonlinear function across several stages (layers) of the network. For a given task and associated loss function, the parameters for each layer (weights) are then optimized via the backpropagation algorithm.

➢ Deep learning: Since the DNN architecture transforms the original data into some other representation, more suitable for tasks like classification or generation, deep learning is often characterized as representation learning.

12.3.c. autoencoder methods

Concepts & notations:

➢ Autoencoder (AE) model: Such model includes two steps, namely, the encoding of descriptors into some lower-dimensional (latent) space, and the mapping of the latent vector back to the original representation. These AE models often work better if the latent vector are generated by means of probability distribution so that a (single) descriptor is no longer represented as single point but rather as probability distribution in the latent space.

- In AE models, systems and properties are represented as continuous and differentiable vectors from some probabilistic manifold (Sanchez-Lengeling and Aspuru-Guzik, 2018).
- Latent vector spaces: These are continuous vector space and, hence, enable one to apply direct gradient-based optimization procedures. Nevertheless, the manifold of (atomic or molecular) data may lead to many local minima, so that other optimization approaches are also necessary.
- Multilevel variational AE: These AE refer to structured architectures and are presently promising research directions in ML, including so-called reinforcemen learning (RL) methods.

12.3.d. Other methods

Concepts & notations:

- Active learning approaches attempt to provides guidance to optimize a particular property for some large and unexplored class of systems. So far, however, very little is known how some available or possible experimetal set-ups should be sampled in order to obtain optimal output. Here, active learning techniques aim to predict optimal future experiments that enable one to better understand a given problem. In particular, such active machine-learning approaches may help directly select future experiments, a feature that has been discussed, for instance, in crystallography.

12.4. Feature transformations & applications of machine learning

12.4.a. Feature transformation and engineering

Requirements & notations:

- The recent boom in ML applications in molecular physics and material science has led to a plethora of (atomistic) descriptors that are — more or less — suitable for ML algorithms. However, a proper software implementation of these descriptors is either not accessible so easily for the users or is widely scattered across different programs and libraries.

➢ Least absolute shrinkage and selection operator (LASSO): In the selection of proper features, it is usually desirable to determine a small set of parameters that is able to keep all relevant information about the given data.

➢ Feature selection: This term comprises a rather widespread set of techniques that are used in statistical analysis in different fields, and the least absolute shrinkage and selection operator (LASSO) is just one of them.

➢ Feature selection: To reduce the size of the feature space, one often defines rules for linear and non-linear combinations of the primary features. This then usually gives rise to a very large number of candidate descriptors.

Properties of good descriptors:

➢ In material science, the properties of good (molecular) descriptors have been summarized at various places in the literature; cf. Himanen *et al.* (2019). In particular, such descriptors should be:

(a) invariant with regard to a spatial translation of the coordinate system;

(b) invariant with regard to a rotation of coordinates;

(c) unique, i.e. there should be a single way to construct a descriptor from the (atomic) structure and occupation of the unit cell, and the descriptor itself just refers to a single property of the material;

(d) continuous, i.e. small changes in the atomistic structure of the unit cell should translate into small changes in the descriptor;

(e) computationally cheap since the computation of descriptor should be significantly faster than any direct computation of the property of interest.

➢ Properties of useful descriptors: The following properties are considered to be important if not even necessary (Ghiringhelli *et al.*, 2015) but are very similar to the criteria above:

(a) A vector descriptor $\mathbf{d}_i$ should uniquely characterizes the system or process of interest.

(b) Different (similar) systems or processes should be characterized by different (similar) vector descriptors.

(c) The computation of the vector descriptor should be (much) cheaper than the property of inerest.

(d) The vector dimension Ω of the descriptor should be as low as possible (for a certain request of accuracy).

12.4.b. Applications in molecular physics

Special concepts & notations of ML in molecular physics:

- Molecular graphs: Molecular systems can be quite readily described by graphs in which vertices represent the atoms and edges the chemical bonds. In such a representation, fragment descriptors characterize subgraphs of the full 3D molecular network. From this perspective, different materials can be considered as coloured graphs, where different colors represent different atoms and interatomic interactions. Such a graphical perspective also enables one to represent the individual parts of a molecular graph by linear combinations of fragment descriptors and, hence, to simplify the computation, storage and interpretation of the different descriptors.
- Molecular graphs: Following semi-empirical rules from bond theory, every molecule can be easily expressed as an undirected graph where each atom is a node and the bonds are the edges. In these graphs, all hydrogen atoms are usually treated implicitly in order to keep the size of the graphs moderate.
- Molecular graphs: SMILES strings form an established standard for molecular graphs; these strings follow the typical text encoding of the standard chemical notation (e.g., H2O or C2H5OH). Other and more advanced representation use weighted graphs with various vector features in order to assign bonding type, aromaticity, charge, and distance to the edges and nodes of the graph (Sanchez-Lengeling and Aspuru-Guzik, 2018).
- Molecular graphs: Since there is generally no unique translation between the molecular structure and some corresponding graph, the use of different such 'translations' can either appear to be advantageous (e.g., for further data augmentation) or disadvantageous, if different graphs cause noise in the ML process.
- Chemical space project: The chemical space formally comprises the set of all possible molecular and solid-state compounds which, obviously, still contains huge unexplored regions. For pharmacologically relevant small molecules, the number of structures is estimated to be on the order of 10^{60} (Sanchez-Lengeling and Aspuru-Guzik, 2018). In the chemical space project, a total of 166.4×10^9 billion molecules with at most 17 heavy atoms have been (formally) summarized.
- Compound space in quantum chemistry: ML models are often based on measuring distances in compound space in order to extract useful information about the stoichiometry and the configurational variation of different molecules. This requires of course a measure measure of molecular (dis)similarity that should be invariant with regard to translations, rotations and the particular ordering of atoms.
- Gaussian approximate potentials (GAP): Even for rather small systems, the GAP model for molecular potential energy surface is orders of magnitude faster than standard plane-wave DFT codes, although significantly more expensive and accurate than simple analytical potentials (Bartok *et al.*, 2010).

Molecular descriptors:

➢ Molecular descriptor: A better representation of data requires less computational resources in order to *learn* the underlying patterns. For example, a representation that can span all of chemical space would need to capture all the symmetries of the Schrödinger equation, such as the permutational, rotational, reflectional as well as translational invariance for particles of the same type.

➢ Molecular descriptor: The Coulomb matrix and other descriptors often refer in counting atoms to their nuclear charge, although other criteria, such as the electron configuration of number of valence electrons could be used as well.

➢ Molecular descriptor: The finding of good molecular representations is presently an open research area. While there are various representations available, no *single* representation seems to work for all properties of interest. More general, those representations that encode the relevant physics will result in a better learning process.

➢ Types of molecular descriptors: Three such types are often distinguished, namely, discrete (e.g., text), continuous (e.g., vectors and tensors) or weighted graphs. Although each graphs can be re-expressed also as sparse matrices, graphs are quite different of how they are processed within the models of machine learning (Sanchez-Lengeling and Aspuru-Guzik, 2018).

➢ Mulliken electro-negativity of an atom: $E^{(\mathrm{MN})} = -(IP + EA)/2$; it is simply formed from the ionization potential (IP) and the electro-negativity (EA) of the atom or ion.

➢ Coulomb matrix: This matrix representation encodes the Coulombic forces between the nuclear charges of each atom.

➢ Coulomb matrix: This molecular descriptor has not always been found useful in ML and this applies, in particular, to periodic solids.

➢ Coulomb matrix: For single molecules with nuclear charges $\{Z_i\}$ and positions $\{\mathbf{r}_i\}$ of all atoms, the Coulomb matrix has been found a good (molecular) descriptor

$$C_{ij}^{(\mathrm{molecule})} = \begin{cases} 0.5\, Z_i^{2.4} & \text{for} \quad i = j \\ \frac{Z_i\, Z_j}{|\mathbf{r}_i - \mathbf{r}_j|} & \text{for} \quad i \neq j. \end{cases}$$

The Coulomb matrix is invariant under rotation and translation but cannot be applied so easily to infinite periodic crystals.

➢ Galvez matrix of molecular graphs: The construction of descriptors can be inspired also by (so-called) topological charge indices or Kier-Hall electro-topological state indices. In this construction scheme, a Galvez matrix $M = A \cdot D$ is formed by multiplying the adjacency matrix A of the graph by the reciprocal square distance matrix ($D_{ij} = (1/r_{ij}^2)$. Obviously, this is a $n \times n$ quadratic matrix with n being

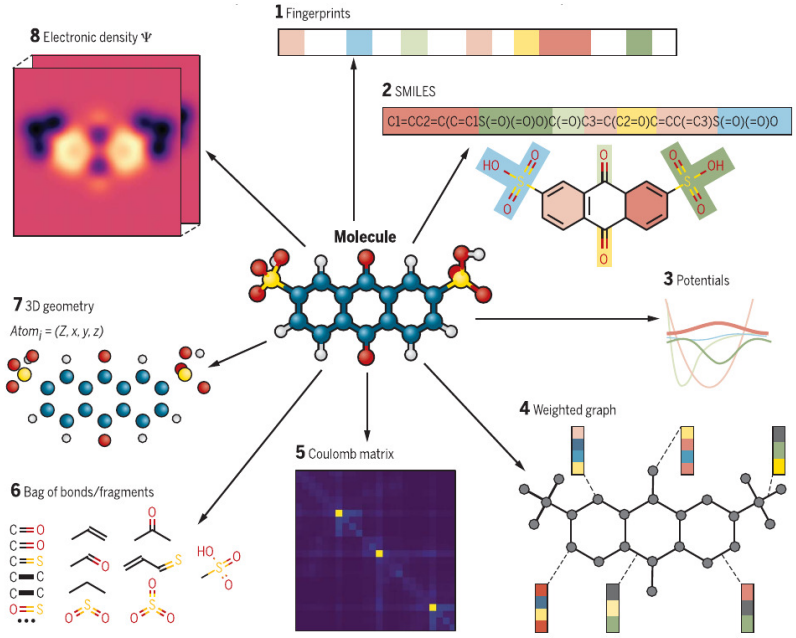

Figure 12.1.: Different types of molecular descriptors that can be applied to some molecule: (1) A fingerprint vector that quantifies the presence or absence of certain molecular environments; (2) SMILES for simple text encoding of the chemical species; (3) various potential energy functions that model the interactions and symmetries of the molecule; (4) a graph with atoms and bond weights; (5) Coulomb matrix; (6) a bag of bonds and fragments; (7) 3D geometry with associated atomic charges; and (8) encoding of the electronic density; taken from: Sanchez-Lengeling and Aspuru-Guzik (2018).

the number of atoms in the unit cell. From the Galvez matrix, various descriptors of some reference property $\mathbf{q}$ can be calculated by (Isayev *et al.*, 2017):

$$T = \sum_{i=1}^{n-1} \sum_{j=i+1}^{n} |q_i - q_j| \, M_{ij}, \qquad T_{\text{bond}} = \sum_{i,j \in \text{bonds}} |q_i - q_j| \, M_{ij} \, .$$

➢ Feature matrix $(X_{ij,n}) = g_{ab}(r_n)$: Matrix of the PRDF of all pairs of atoms (a, b) , evaluated for some cut-off radius r_n. The distance

of two molecules or crystals is then defined by the Frobenius norm between these those matrices; these distances can be directly used also for some of the kernels of ML methods. The feature matrix is a global descriptor for the similarity of molecules, which is invariant under translation, rotation, and the particular choice of the unit cell (Schütt *et al.*, 2014).

Applications:

➢ Potential energy surface (PES): ML approaches has been used to predict the Born-Oppenheimer potential energy surface (PES) for a set of atoms without explicit molecular computations. For example, Bartok *et al.* (2010) modeled the bulk phases of carbon, silicon, germanium, iron and gallium nitride, based on a unified framework in forming atomistic descriptors. These authors also developed a framework for automatically generating finite range interatomic potential models from quantum-mechanically calculated atomic forces and energies.

12.4.c. Applications in solid-state physics and material science

Special concepts & notations of ML in material science:

➢ Machine learning in material science: ML methods will likely augment or even supplant in the (near) future the time consuming and often intuition-based, trial-and-error experimentation for the design and discovery of new materials.

➢ Machine learning in material science: Methods in ML may help optimize several properties simultaneously with the best trade-off, for example, by maximizing one property, while keeping another property bound near to some required value. In a Pareto plot with axis due to these properties, this means to identify the boundary for one given property, which the materials cannot cross without deteriorating the value of some other properties.

➢ Machine learning in crystallography: Computationally efficient ML models have been applied during recent year in order to predict molecular properties of many crystals with similar accuracy as obtained from DFT. These models are especially useful to systematically screen millions of crystals with only milliseconds per single prediction (Faber *et al.*, 2016).

➢ Material Genome Initiative (MGI): In 2011, Obama announced this initiative to mainten the US manufacturing competitiveness by halving the time it takes to discover new materials. Since then, this initiative has been supported and sustained by various US agencies. New materials are sought in order to reduce the costs and environmental friendliness, with special focus upon Kevlar and Li-based batteries and their potential replacements.

- Inverse material design: Since it appears intractable to explore the huge space of (different classes of) materials, neither computationally nor experimentally, the inverse design aims to discover tailored materials by starting directly from some desired functionality and to combine available databases with methods from machine learning.
- Inverse material design: Various approaches to inverse material design has been proposed and benefitted from recent developments in machine learning. In particular, deep generative models have been applied to numerous classes of materials including the rational design of prospective drugs, synthetic routes to organic compounds as well as a further optimization of photovoltaics and redox flow batteries (Sanchez-Lengeling and Aspuru-Guzik, 2018).
- Structure maps: Originally, these maps refer to simple scatter plots that display two physical properties *versus* each other for a number of compounds or materials, such as ionization potentials, valences, ionic radii, etc. These structure plots have been frequently used in material science in order to identify class of systems whose physical properties come already close to some desired behaviour. In particular, the Periodic Table is a particular structure map that establishes trends in the chemical properties of all atoms, if one moves along its rows or columns.
- Structure maps: Various well-known structure maps in chemistry and material science are based on symmetric combinations, e.g., sums or differences, of ionic radii which are computed by means of pseudopotential. Since the use of coordinates do not require extra computation nor measurements, they can be easily applied in structure maps for clustering physical properties other than crystal structure or melting temperatures, etc.
- Structure maps: ML methods can extent traditional structure maps towards three or more dimensions and, hence, remove the subjectivity or ambiguity in the decisions of where to draw the boundaries for clusters and to replace simple boundaries by more sophisticated and flexible manifolds (Gubernatis and Lookman, 2018).
- Ashby plot: Historically, an Ashby plot displayed the Youngs modulus *versus* the density of some material in order to show overlays of metals, polymers, ceramics, foams, etc. This structure map has been applied in material engineering in order to select the most appropriate material for a particular application.
- Molecular fragments: This concept from molecular physics has been adopted in material science during the last years to design crystalline materials and has helped improve the molecular nomenclature and representation.
- Property-Labelled Material Fragments (PLMF): Fragments or (vector) desriptors that are just associated with a certain parts of a molecular or material graph.

Descriptors for solid-state physics and material science:

- Descriptors for material science: Coulomb matrix, Ewald sum matrix, sine matrix, Many-body Tensor Representation (MBTR), Atom-centered Symmetry Functions (ACSF) and Smooth Overlap of Atomic Positions (SOAP); cf. Himanen *et al.* (2019).
- Descriptors for material science: To encode the atomistic structure of some molecule or material, the descriptor either depicts a local atomic environment or the structure as a whole. Global descriptors encode information about the whole atomistic structure, such as the size, temperature variation, etc.
- Voronoi cells: A Voronoi tessellation is a partitioning of space into regions based on some predefined subset of points, called seeds, sites, or generators. For each of these seeds, there is a region consisting of all points closer to that seed than to any other one; these regions are called Voronoi cells. The Voronoi cells of a crystal coincide with the so-called Wigner-Seitz cells of each atom, if the atomic sites are taken as seeds. The tessellation of a crystall is unique and insensitive to the particular choice of unit cell.

Applications:

- Formation energy of elpasolites: Faber *et al.* (2016) introduced a newly developed ML model to investigate and predict the formation energies of all 2×10^6 elpasolites that can be (formally) constructed from all main-group elements up to Bi. These predictions helped identify a new elemental order of descending elpasolite formation energy, including crystals with quite peculiar atomic charges.
- Formation enthalpy of binary compounds: Curtarolo *et al.* (2003) built a ML model for predicting the formation enthalpy of binary compounds, and which was based on the formation enthalpies of the same elements but in other chemical and solid-state structures.
- High-throughput density functional theory (HT-DFT) calculations: In materials science, large data bases have been generated by HT-DFT calculations and in a few cases by high throughput experiments.

12.4.d. Other applications

ML in text mining:

- Text mining: Because of the rapid increase of information, available to researchers via the web and scientific literature, navigation has become more and more difficult. Here, text mining became a popular approach to identifying and extracting information from unstructured text sources.
- Text mining aims for extracting facts and relationships in a structured form in order to create specialized databases, to transfer knowledge between domains or, more generally, to support decision-making (Butler *et al.*, 2018).

13. Semiempirical estimates

13.1. In JAC implemented estimates for atomic properties and data

13.1.a. Data from the periodic table of elements (PeriodicTable)

Symbols, atomic mass and ionization potentials:

- In JAC, the (mean) atomic masses of all elements are obtained from a call of `[PeriodicTable.]get(Z::Int64)` or `[PeriodicTable.]get(sy::Symbol)`, if `sy` refers to a valid element symbol.
- In JAC, the first ionization potential of a given element with nuclear charge Z or symbol `Sy` is obtained from a call of `[PeriodicTable.]get("", Z::Int64)` or ...
- Atomic mass:

13.1.b. Isotope data (PeriodicTable)

:

- Detailed isotope data are required, for instance, to calculate hyperfine A, B parameters, isotope-shift parameters, and at various places elsewhere.
- The isotope data need to be specified for the nuclear model `nm::Nuclear.Model`, if such properties are to be calculated.
- In JAC, a few selected isotope-specific data can be obtained by a call to `[PeriodicTable.]getIsotope(" ", ... ,Z::Int64)`. However, no attempt is made to provide data for all isotopes and elements; instead we encourage the user to add further data as the need arises in specific applications.

13.1.c. Binding energies of inner- and valance-shell electrons (PeriodicTable)

Binding energies:

➢ In Jac, an estimate for the binding energy of an $n\ell$-electron in the neutral atom can be obtained from `[PeriodicTable.]get("ionization potential: inner-shell", shell::Shell, Z::Int64)`.

13.1.d. Atomic radii, susceptibilities and polarizibilities (PeriodicTable)

Atomic polarizibilities:

➢ In Jac, ... can be obtained from `[PeriodicTable.]get( )`.

➢ Further details

Atomic radii:

➢ In Jac, ... can be obtained from `[PeriodicTable.]get( )`.

➢ Atomic radii: The concept of atomic and ionic radii has been found helpful for understanding, explaining or even predicting various physico-chemical properties of atoms, ions and molecules. However, this is quite different to the use of such radii in crystal chemistry where they are used in order to estimate and to explain the binding lengthes in crystal lattices.

➢ Atomic radii: Ghosh (2002) applied computed theoretical radii in order to estimate a number of size-dependent physical properties of isolated atoms: (1) the diamagnetic part of the magnetic susceptibility $\chi^{(\text{diamagnetic})}$ for all elements up to xenon, (2) the atomic polarizability α and (3) the global hardness η for all elements of the periodic table.

13.2. In JAC partly-implemented estimates for atomic properties and data

13.2.a. Weak-field ionization of effective one-electron atoms

Property & notations:

- Field ionization: by a quasi-static external field: $A^{(*)} + F\,\mathbf{e}_z \longrightarrow A^+ * e^-$.
- Formal quantum notation: $|\alpha \mathbb{J}\rangle \longrightarrow$ ...
- Not yet implemented.
- In JAC, all estimates on the field-ionization rates of atoms are always based on a non-relativistic, single-electron approach. No attempt has (yet) been made to generalize this approximation towards real many-electron atoms and ions with their fine-structure.

Motivation:

- Ionization of atoms by an external electric field is a fundamental atomic process that plays an important role, for instance, in the formation of charge-state distributions in (dilute) plasma under strong fields.
- Vice versa: The observations of temporal variations in the line intensities of ions, that are produced by field ionization, can help determine spectroscopically the macroscopic-field distribution in plasma.
- Since the field-ionization probability grows (very) rapidly with the electric field strength F, the field strength can be derived from accurate measurements of the ionization probabilities.

Further information:

- Ionization probabilities are often calculated within the WKB approximation, i.e. in the weak-field limit. In general, field ionization probability depends critically on the projection of the total orbital angular momentum upon the direction of the field.

➢ In most field-ionization probability computations, a quasi-static and homogeneous electric field is assumed as it occurs, for example, for macroscopic-scale fields in plasma. This assumption is in contrast to many local fields that may occur at the atomic scale.

➢ For the case of a single electron with binding energy E in the valence shell $(n\,\ell)$ and outside of closed shells otherwise, the quasi-classical escape rate is given by (Fisher *et al.*, 1998)

$$\Gamma(E,\ell,m) \;=\; B_{n\ell}^2\,\frac{(2\ell+1)\,(\ell+m)!}{2^{m+1}\,k^m\,m!\,(\ell-m)!}\,\left(\frac{2\,k^2}{F}\right)^{2Z/k\,-\,m\,-\,1}\,\exp\left(-\frac{2\,k^3}{3\,F}\right)$$

where Z is the charge of the parent ion as seen by the electron are large r, $k = \sqrt{2\,|E|}$ is the modulus of the (electron's) wave vector and $B_{n\ell}$ is the amplitude that characterizes the outgoing electron wave.

13.2.b. Tunnel ionization rates

Tunnel ionization rates:

➢ ADK rate for tunnel ionization: The first step in the strong-field photoionization by a linearly-polarized laser field (with $\gamma < 1$) is often modeled by means of the Ammosov-Delone-Kainov (ADK) rate for the tunnel ionization of an atom in an oscillating electric field. This rate is given by (Chen *et al.*, 2019)

$$W^{\,(\mathrm{ADK})}(\,|\boldsymbol{\mathcal{E}}(t)|\,) \;=\; |c_{n^*\ell^*}|^2\,f(\ell,m)\,I_p\,\left(\frac{2\,\kappa}{|\boldsymbol{\mathcal{E}}(t)|}\right)^{2n^*\,-\,|m|\,-\,1}\,\exp\left(-\frac{2\,\kappa}{3\,|\boldsymbol{\mathcal{E}}(t)|}\right),\qquad n^* \;=\; \frac{Z^{\,(\mathrm{ion})}}{\sqrt{2\,I_p}},\qquad \ell^* \;=\; n^*\,-\,1$$

$$|c_{n^*\ell^*}|^2 \;=\; \frac{2^{\,2n^*}}{n^*\,\Gamma(n^*\,+\,\ell^*\,+\,1)\,\Gamma(n^*\,-\,\ell^*)},\qquad f(\ell,m) \;=\; \frac{(2\ell+1)\,(\ell\,+\,|m|)!}{2^{|m|}\,|m|!\,(\ell\,-\,|m|)!},\qquad \kappa \;=\; (2\,I_p)^{\,3/2}.$$

In this notation, $(n^*,\,\ell^*)$ are effective quantum numbers, while $(\ell,\,m)$ are the orbital and magnetic quantum numbers of the (single-active) valence electron, and $Z^{\,(\mathrm{ion})}$ is the charge of the residual ion.

➢ ADK rate for tunnel ionization: Tong and Lin (2005) found that the ADK rates significantly overestimate the (static) ionization rate if calculated numerically in an barrier-suppressing electric field. In the near- and over-the-barrier regimes, these authors suggested instead

the modified ADK rate

$$W^{(\text{modified ADK})}(\,|\boldsymbol{\mathcal{E}}(t)|\,) \;=\; W^{(\text{ADK})}(\,|\boldsymbol{\mathcal{E}}(t)|\,)\;\exp\left(-\,\mu\,\frac{[Z^{(\text{ion})}]^2}{I_p}\;\frac{|\boldsymbol{\mathcal{E}}(t)|}{\kappa}\right), \qquad 6 \,<\, \mu \,<\, 10 \qquad \text{... fitting parameter.}$$

For a few atoms and ions, the fitting parameters μ is given by Tong and Lin (2005).

➢ PPT rate for tunnel ionization: The ADK rate for tunnel ionization is the limes of an extremely strong laser field ($\gamma \,\to\, 0$) of a more general model by Perelomov, Popov, and Terentev (PPT) from (1967) which was originally derived for arbitary values of the Keldysh parameter γ. In this PPT model, the ionization rate is given by

$$W^{(\text{PPT})}(\,|\boldsymbol{\mathcal{E}}(t)|,\,\omega) \;=\; |c_{n^*\ell^*}|^2\; f(\ell,m)\; I_p\;\left(\frac{2\,\kappa}{|\boldsymbol{\mathcal{E}}(t)|}\right)^{2n^*\,-\,|m|\,-\,1}\;(1\,+\,\gamma^2)^{\,|m|/2\,+\,3/4}\;A_m(\omega,\gamma)\;\exp\left(-\,\frac{2\,\kappa}{3\,|\boldsymbol{\mathcal{E}}(t)|}\,g(\gamma)\right)$$

$$g(\gamma) \;=\; \frac{3}{2\,\gamma}\left[\left(1\,+\,\frac{1}{2\,\gamma^2}\right)\,\sinh^{-1}\gamma\;-\;\frac{\sqrt{1\,+\,\gamma^2}}{2\,\gamma}\right], \qquad A_m(\omega,\gamma) \;\ldots\; \text{see literature,}$$

while all other entities are the same as in the ADK rate above.

➢ Total ionization probability from tunnel ionization rate: For a given laser pulse $\boldsymbol{\mathcal{E}}(t)$, the total ionization probability is given by

$$\mathcal{P}^{(\text{tunnel rate})} \;=\; 1\;-\;\exp\left(\int_{-\infty}^{\infty} dt\; W^{(\text{tunnel rate})}(\,|\boldsymbol{\mathcal{E}}(t)|,\,\ldots)\right),$$

and where $W^{(\text{tunnel rate})}$ refers to one of the tunnel ionization rates from above.

13.2.c. Electron-impact ionization. Cross sections

Semi-empirical electron-impact excitation and ionization cross sections:

➢ Temperature dependence of cross sections and rate coefficients: Vriens and Smeets (1980) analyzed how the electron-impact excitation, ionization and de-excitation cross sections and rate coefficients depend on the electron energy and temperature as well a few other parameters. They cover a rather wide range of electron-impact energies from *sudden* up to *adiabatic* collisions. In particular, Vriens and Smeets (1980)

constructed a set of simple analytical formulas for the electron-impact cross sections and rate coefficients as well as for the total depopulation and three-body recombination, although it appears rather difficult to follow this paper in detail, and especially to which entities the given formulas refer and when they are valid.

➢ Electron-impact cross sections for CR simulations: CR models have been applied in the literature in order to simulate different nonequilibrium plasmas; these models typically require the cross sections or rates for all major electronic transfer processes. While different approximate cross-section and rate formulas are available from the literature, these formulas often have a limited range of validity, and there occur serious discrepancies among the different approximations. Vriens and Smeets (1980) here provide practical formulas that are accurate over a resonable wide range of primary energies and which are applicable for different transitions.

➢ Two characteristic energies of electron-impact processes refer to the binding energy $E^{(\text{binding})}$ of the (least-bound) valence electron and to the kinetic energy of the incident electrons $E^{(\text{impact})}$.

➢ Two regimes for electron-impact processes: (i) In the sudden regime of rather high impact energies, $E \gtrsim 4\,E^{(\text{binding})}$, there is generally good agreement between the binary-encounter and the Bethe-Born approximation. (ii) For low collision energies $E^{(\text{binding})} \lesssim E \lesssim 4\,E^{(\text{binding})}$ the binary-encounter cross sections are larger (up to $\sim$ 40 %) than the classical three-body as obtained by Monte-Carlo trajectory calculations.

Kolbenstvedt model for the electron-impact ionization:

➢ Haque and coworkers (2010) explored a so-called Kolbenstvedt model for the electron-impact ionization of the K-, L- and M-shells of neutral atoms and ions.

13.3. Further estimates on atomic properties, not yet considered in JAC

13.3.a. Electron and positron stopping powers (StoppingPower)

Property & notations:

➢ Stopping power: due to the penetration of electrons and positrons through matter: $A^{(*)}$ .. .

Motivation:

➢ Stopping powers of matter for electrons are important for many applications involving energy deposition. In radiation physics, chemistry, biology and medicine, it is important to have simple but accurate estimates about the stopping power of energetic electrons in various media for (Gümüs, 2005).

➢ Until the present, no simple and practical model exists for the stopping power of electrons with energies below 10 keV.

Approximate stopping power formulas:

➢ The stopping power of materials arise from two types of processes, namely collisional and radiative processes. The collisions of the incident particles with the target material is most important and mainly arises from collisions between the incident particles and the atomic electrons.

$$\frac{dE}{dx} = \left(\frac{dE}{dx}\right)^{(\text{collision})} + \left(\frac{dE}{dx}\right)^{(\text{radiative})}$$

➢ For incoming electrons, a modified collisional stopping power formula for incoming electrons can be written as given by Sugiyama (1985) or Rohrlich and Carlson (1954)

➢ Full Bethe-Bloch formula:

$$-\frac{dE}{dx} = \left(\frac{e^2}{4\pi\,\epsilon_o}\right) \frac{4\pi\,z^2\,N_A\,Z\,\rho}{mc^2\,\beta^2\,A} \left[\ln\left(\frac{2mc^2\,\beta^2}{I}\right) - \ln(1-\beta^2) - \beta^2\right]$$

13.3.b. Stopping power of multiply-charged ions

Motivation:

➢ Stopping power of multiply-charged ions: The energy loss and the range of penetration of multiply-charged ions in matter is relevant for different fields, from radiation damage and dosimetry to radiation chemistry and biology, to nuclear and health physics, and at several places in science and technology (Ziegler and Manoyan, 1988).

➢ Stopping power of multiply-charged ions: The stopping power pf medium and heavy ions generally depends on the charge and velocity of the incident ions. In particular, the velocity need to be compared with the (so-called) Bohr velocity $\mathbf{v}^{(\mathrm{Bohr})} \approx 25$ keV/amu, i.e. the velocity of electrons in the conduction band of a solid. While ions with $\mathbf{v} < \mathbf{v}^{(\mathrm{Bohr})}$ undergo adiabatic collisions with the target electrons and, hence, experience only a small stopping power in the material, the stopping power increases for ions with nuclear charge Z with the velocity for $\mathbf{v} > \mathbf{v}^{(\mathrm{Bohr})}$ until a peak occurs at about $\mathbf{v}^{(\mathrm{peak})} \approx 3\,\mathbf{v}^{(\mathrm{Bohr})}\,Z^{2/3}$. For velocities $\mathbf{v} > \mathbf{v}^{(\mathrm{peak})}$, the interaction of the ions with the target electrons become less relevant owing to the shorter effective interation time and, thus, the stopping power decreases with increasing velocity of the ions (Ziegler and Manoyan, 1988).

➢ SRIM code: This code estimates stopping powers and ranges for different ions and target materials. Since an earlier version from 1985, a few major upgrades have been published about every six years, and with good number of citations ($\sim$ 700) every year. In the SRIM-2010 version, a number of major improvements have been made (Ziegler *et al.*, 2010): (1) Further experimental stopping powers were added to the database and now contains a total of about 28,000 stopping powers; (2) improved corrections were made for the stopping power of ions in various compounds; (3) a number of additional computations of stopping powers have been carried out for heavy ions and now lead to more accurate predictions; (4) the development of a self-contained SRIM module for the stopping powers and range values of ions that can be invoked by other software tools; (5) incorporation of interatomic potentials for selective ion-atom collisions.

Empirical rules:

➢ Stopping power of ions in different target materials: Apart from the charge and velocity of the incident ions, the stopping power also depends on the target materials. For a hydrocarbon target gas, the stopping power can be derived approximately from the stopping powers of pure carbon and hydrogen targets by following Braggs empirical rule. A number of earlier works discussed the possibility of finding the stopping power for other targets by using the results of hydrocarbon target gases.

➢ Empirical Bragg rule for stopping powers: This rule tells that the stopping power of a compound target can be estimated by using a linear combination of the stopping powers of the individual elements. While this rule has been found reasonably accurate within about 20 %, all further improvements of this rule failed since the stopping power depend of course also on the detailed electronic structure and the excitation energies in the target.

➢ Sigmund's theory of stopping power (1982): This theory allows for rather arbitrary electronic configurations of the target, and it also takes the detailed internal motion of the electrons into account. This theory has been applied by Sabin and coworkers to evaluate stopping

powers for both, individual elements and for the stopping of protons in hydrocarbons. This theory often predicts stopping powers which agree with experiment by a few percent.

➢ Brandt-Kitagawa rules: Ziegler and Manoyan (1988) apply the (so-called) Brandt-Kitagawa rules in order to apply the known stopping powers *one* ion to other ions. In practice, these rules scale the proton stopping powers to those of other ions at the same velocity by making a few simple assumptions: (i) The heavy ions will loose all electrons that are slower than the velocity of the incident ion relative to the target material; (ii) the size of the ions thrinks due to the electron loss to the size of hydrogenic ions of charge $Z^{(\mathrm{eff})}$. – However, the presentation and notation by Ziegler and Manoyan (1988) is quite cumbersome, although the parametrizations look overall rather simple. Moreover, all the write-ups by Ziegler (1988) and by Ziegler and coworkers (1999, 2010) are rather sophisticated and do not make use of standard atomic notations.

➢ Stopping power at high ion velocities: Two assumptions are often made for light ions with incident velocities much higher than those of the projectile electrons: (i) All electrons are stripped off the ions; (ii) even light and medium-heavy ions are much heavier than the target electrons. These assumptions apply for light ions with incident energies between 1 MeV/u and 10 GeV/u.

Empirical theories:

➢ Bohr's model for the stopping power of ions in matter: Following Bohr, the energy loss of ions, passing through matter, can be divided into two contributions: (i) a nuclear contribution due to the (positive) charge of the ions in the material and (ii) due to the (quasi-) free electrons of the material, and which is often dominant. Bohr's considerations are mainly based on the relative masses and the abundances of the target electrons and ionic cores. For incident ions with nuclear charge Z and valence electron with orbital frequency ω, a simple model gives rise to the energy loss that can be extended towards relativistic energies ($\gamma = 1/\sqrt{1 - v^2/c^2}$) (Ziegler 1999)

$$\frac{dE}{dx}^{(\mathrm{non-relativistic})} = 4\pi\, Z^{(\mathrm{target})}\, \frac{Z^2\, e^4}{m\, v^2}\, \ln\left(\frac{m\, v^3}{Z\, e\, \omega}\right) \qquad \Longrightarrow \qquad \frac{dE}{dx}^{(\mathrm{relativistic})} = 4\pi\, Z^{(\mathrm{target})}\, \frac{Z^2\, e^4}{m\, v^2}\, \ln\left(\frac{\gamma^2\, m\, v^3}{Z\, e\, \omega}\right)$$

13.3.c. Stark broadening of spectral lines in plasma

Motivation:

➢ Stark broadening of spectral lines: This broadening has been found very important in (so-called) DA and DB white dwarf atmospheres.

➢ Apart from white dwarfs, Stark broadening of spectra is also an important pressure-broadening mechanism for arious types of other stars.

➢ Various semi-empirical calculations of the Stark widths and shifts have been performed in the impact approximation by using Griems (1968) formula.

➢ For selected lines, it was shown that Stark broadening can change the observed widths by 10-45 %.

Semi-empirical approximations:

➢ Lorentzian profile of isolated lines: For isolated lines $|\alpha_i \mathbb{J}_i\rangle \rightarrow |\alpha_f \mathbb{J}_f\rangle$ with level energies E_i and E_f, the line profile is often assumed to be Lorentzian, shifted by the energy d and with the (total) line widths Γ due to the (plasma) Stark broadening.

$$F(\omega) \;=\; \frac{(\Gamma/2\pi)}{(\omega \,-\, \omega_{if} \,-\, d)^2 \,+\, (\Gamma/2)^2}, \qquad\qquad \omega_{if} \;=\; \frac{E_i \,-\, E_f}{\hbar} \,.$$

where

➢ Energy shift and (total) widths of the Stard-broadened line: Both, the energy shift d as well as the (total) widths Γ can be expressed in terms of the velocity distribution $f(v)$ of the electrons in the plasma, its density $N^{\,(\mathrm{elec})}$, the impact parameter b of the incident electrons as well as the elastic and inelastic (electron-impact excitation) cross sections for excitations of the initial and final levels to neighboured levels.

$$\Gamma \;=\; N^{\,(\mathrm{elec})} \int dv\, v\, f(v) \;\left(\sigma^{\,(\mathrm{elastic}} \,+\, \sigma^{\,(\mathrm{inelastic}}\right); \qquad\qquad d \;=\; N^{\,(\mathrm{elec})} \int dv\, v\, f(v) \;\int_{R_1}^{R_{\mathrm{Debye}}} db\, 2\pi\, b\, \sin(\phi_p)$$

and where ϕ_p is a plasma-specific phase shift. Further details on the Stark broadening of spectral lines are given by Dimitrijevich and Sahel-Brechot (1996).

➢ In 1968, Griem suggested simple semiempirical formulas for the Stark line shift and widths in impact approximation which is based on some original formular by Baranger (1958) as well as an effective Gaunt factor by Seaton (1962) and Regemorter (1962). With these formulas,

the Stark linewidths and Stark line shifts can be obtained by:

$$\frac{\Gamma}{[a.u.]} = 8 \left(\frac{\pi}{3}\right)^{3/2} \frac{\hbar}{m\, a_o} N_e \left(\frac{E_H}{k\, T}\right)^{1/2} \left[\sum_{i'} |\, \langle i' |\mathrm{r}| i \rangle\, |^2\, g_{se} \left(\frac{E}{\Delta\, E_{i'i}}\right) + \sum_{f'} |\, \langle f' |\mathrm{r}| f \rangle\, |^2\, g_{se} \left(\frac{E}{\Delta\, E_{f'f}}\right)\right]$$

$$\frac{d}{[a.u.]} = -8 \left(\frac{\pi}{3}\right)^{3/2} \frac{\hbar}{m\, a_o} N_e \left(\frac{E_H}{k\, T}\right)^{1/2} \left[\sum_{i'} \left(\frac{\Delta\, E_{i'i}}{|\Delta\, E_{i'i}|}\right) |\, \langle i' |\mathrm{r}| i \rangle\, |^2\, g_{sh} \left(\frac{E}{\Delta\, E_{i'i}}\right) + \sum_{f'} \left(\frac{\Delta\, E_{f'f}}{|\Delta\, E_{f'f}|}\right) |\, \langle f' |\mathrm{r}| f \rangle\, |^2\, g_{sh} \left(\frac{E}{\Delta\, E_{f'f}}\right)\right]$$

In these formulae, E_H is the hydrogen ionization energy, N_e is the free-electron density of the perturber levels, T is the electron temperature, $E = 3/2\, kT$ the mean energy of the perturbing electron and g_{se}, g_{sh} are the effective Gaunt factors which are calculated and tabulated by Griem. These Gaunt factors are slowly varying functions of $x_{j'j}$ where $x_{j'j} = E/\Delta\, E_{j'j}$ is the energy difference between a perturbing level j' and the perturbed initial/upper (final/lower) level j.

➢ The atomic matrix elements need often to be obtained from *ab-initio* Hartree-Dirac-Fock computations, and the summation over the levels is obtained by making use of the table by Moore (1958).

13.3.d. Atomic electron-momentum densities

Definition & notations:

➢ For a given atomic level $|\alpha\mathbb{J}\rangle$, the (radial electron) momentum density $I(p;\,\alpha\mathbb{J})$ and the one-electron momentum density $\Pi_{n\kappa}(p;\,\alpha\mathbb{J})$ and is given by (Koga and Thakkar, 1996)

$$I(p;\,\alpha\mathbb{J}) \;=\; 4\pi\,p^2\,\Pi(p;\,\alpha\mathbb{J}), \qquad\qquad \Pi(p;\,\alpha\mathbb{J}) \;=\; \frac{1}{4\pi\,p^2}\,\sum_{i=1}^{N}\,\langle\psi_\alpha\,|\,\delta(p\,-\,p_i|\,\psi_\alpha\rangle\,.$$

➢ The radial one-electron momentum density I is used to calculate the corresponding moments of the momentum density

$$\langle p^k\rangle \;=\; \int_0^\infty dp\,p^k\,I(p;\,\alpha\mathbb{J}), \qquad\qquad -2\;\leq\;k\;\leq\;4$$

➢ These moments are often applied in:

- density functional theory: since $\langle p\rangle\,/\,\pi$ is close to the Dirac-Slater exchange energy;
- x-ray cristallography: since $\langle p^3\rangle$ is roughly proportional to the initial value of the so-called Patterson function
- Compton profiles: since $J(q) \;=\; \frac{1}{2}\,\int_{|q|}^\infty dp\,p^{-1}\,I(p)$ is twice the peak height of the isotropic Compton profile.

14. Beams of light and particles

14.1. Helmholtz wave equation

Propagation of light in free space:

➢ Helmholtz wave equation: If we consider the propagation of light in free space, the Maxwell equations simplify and the spatial structure of their solution satisfy the well-known Helmholtz wave equation, an elliptic partial differential equation

$$\nabla^2 u(\mathbf{r}) \; + \; k^2 \, u(\mathbf{r}) \;\; = \;\; 0 \, .$$

This equation follows from the (full) time-dependent wave equations due to the separation of variables.

➢ Harmonic solution of the Helmholtz equation:

$$u(\mathbf{r}) \;\; = \;\; C_1 \, e^{i \, \mathbf{k} \cdot \mathbf{r}} \; + \; C_2 \, e^{-i \, \mathbf{k} \cdot \mathbf{r}}, \qquad\qquad k \;\; = \;\; |\mathbf{k}| \;\; = \;\; \frac{\omega}{c} \, .$$

➢ The solution in time is a linear combination of sine and cosine functions with angular frequency ω, while the form of the spatial solution of the Helmholtz equation depends rather sensitively on the given boundary conditions.

➢ Vector potential of optical beams: There exist various expressions to represent the vector potential of optical beams of different kind and spatial structure, and which are solutions of the Helmholtz equation. These vector potentials represent different spatial structures and phases.

➢ Below, several of these solution are provided for different beams in terms of the (scalar) amplitudes of the corresponding light fields.

➢ Synonym notions of vortex beams: helically phased light beams; optical vortex beams with a field dependence $e^{im\varphi}$, ...

Paraxial approximation to the Helmholtz equation:

➢ Paraxial approximation: The Helmholtz equation still represents a complicated partial differential equation; in the science of optics, one often has well-defined paraboloidal waves or Gaussian beams in which the field change along the propagation direction is small compared to the change in perpendicular direction; $\partial u/\partial z \ll \partial u/\partial x$, $\partial u/\partial y$.

➢ For these conditions, the Helmholtz equation simplifies to

$$\nabla_\perp^2 \, u(\mathbf{r}) \; + \; 2ik \, \frac{\partial u}{\partial z}(\mathbf{r}) \;\; = \;\; 0 \, .$$

➢ Conditions for the paraxial approximation: The restrictions upon the variation of the amplitude function u is often also written in the form

$$\left| \frac{\partial u}{\partial z} \right| \ll |k \, u| \qquad \text{and} \qquad \left| \frac{\partial^2 u}{\partial z^2} \right| \ll |k^2 \, u| \, .$$

➢ The paraxial approximation is obtained if the ansatz $\psi(\mathbf{r}) \; = \; u(\mathbf{r}) \; e^{ikz}$ is used in the Helmholtz equation and if the term $\sim \frac{\partial^2 u}{\partial^2 z}$ is neglected, when compared with $\sim \frac{\partial \psi}{\partial z}$.

14.2. Symmetries of light beams

14.2.a. Orbital and spin angular momentum

Angular momentum of photons:

➢ Angular momentum of photons: Following Maxwell's theory, the angular momentum quantum numbers of the photon are integers [in units of the Planck constant $\hbar$] in the usual three-dimensional settings. For the propagation of light in reduced dimensions, in contrast, photons can also have some half-integer total angular momentum. Such an half-integer quantization of the total angular momentum is known from the quantum Hall effect and can be measured by using noise measurements. Therefore, new forms of quantization arises for photons in a beam, similar as known for electrons in reduced dimensions, .

➢ Applications of the angular momentum of photons: The angular momentum of photons may cause various optomechanical effects in optical trapping as well as with the manipulation of – microscopic and mesoscopic – particles. This angular momentum can be utilized also to remotely detect rotations of light in astronomy at radio-frequencies. In QIP, the angular momentum of light is utilized in order to create high-dimensional entanglement, quantum dense coding or for the identification of different objects.

➢ Jones vector: For a paraxial beam, the two-component complex vector field $\boldsymbol{\mathcal{E}}(t)$ generally describes the amplitudes of both polarizations ($\boldsymbol{\mathcal{E}}$-field) in the plane perpendicular to the beam axis. For a helicity basis and the use of polar coordinate (ρ, φ) in this plane, the angular momentum (AM) operators can generate only rotations of the field around the beam axis. For a paraxial beam, this AM operator includes the 3×3 Pauli matrix $s_z = \hbar \sigma_z$, which rotates the polarization direction homogeneously across the beam, and the projection of the orbital angular momentum $l_z = -i\hbar \frac{d}{d\varphi}$, which rotates the spatial beam profile but leaves the polarization unchanged otherwise. Both of these rotations keep the light field ($\boldsymbol{\mathcal{E}}$-field) transverse to the beam propagation so that the projections of the spin and orbital angular momenta are conserved independently.

➢ Photon propagation in 3 dimensions: The free (3-dimensional) propagation of photons follows Maxwells equations and, hence, only the total angular momentum $\mathbf{j} = \mathbf{l} + \mathbf{s}$ and its projection upon the quantization axis $j_z = l_z + s_z$ is conserved owing to the rotational invariance of the equations.

➢ Measurement of the photon's angular momentum: The angular momenta of photons can be measured, for instance, by means of a Mach-Zehnder interferometer, quite independent of whether the AM is of type spin, orbital or total angular momentum. For this, the eigenstates of the light field, associated with the given AM operator, must pick up a phase factor by passing through the interferometer. This technique can be generalized also for half-integer and even rational eigenvalues of the AM operator if proper wave plates and prism are applied, such that the spatial and spin components of the light field rotates properly (Ballantine *et al.*, 2016). For example, a half-wave plate reverses the sign of the spin quantum number $\lambda = \pm 1$ but does not affect the orbital angular momentum and, hence, results in a torque of $2\hbar\lambda$ per photon. In contrast, an ideal polarization-preserving Dove prism leads to an inversion of orbital angular momentum and results in a torque of $2\hbar\ell$ per photon (Ballantine *et al.*, 2016).

Beams with well-defined OAM:

➢ Photons from twisted (OAM) beams: For a beam with well-defined (projection of the) orbital angular momentum, the relevant quantum numbers are the eigenvalues [in units of $\hbar$] of the spin and orbital angular momentum operators, l_z and s_z, respectively. While the spin quantum number $\lambda = \pm 1$ characterizes the circular polarization of the beam, the orbital quantum number $\ell = 0, \pm 1, \pm 2, \ldots$ typically characterizes the phase $e^{i\ell\varphi}$ of the spatial part of the light field. For paraxial beams, then, the conservation of the (projection of the) total angular momentum, $j_z = l_z + s_z$ still ensures integer eigenvalues (Ballantine *et al.*, 2016).

➢ The conservation of the total angular momentum $j_z = l_z + s_z$ follows from the rotational symmetry of the Maxwell equations. Since this symmetry is no longer fulfilled for a light beam with a given propagation direction, only the angular momentum (operator) as associated with the propagation of photons in the 2-dimensional cross section of the beam will be conserved owing to the Noether theorem. This angular momentum operator then just generates rotations of the beam around the propagation direction. Moreover, this *restricted* symmetry leads to a new form of total angular momentum with either half-integer or even rational eigenvalues. This quantization of the light field of optical beams can be verified also experimentally by analyzing the noise in the total angular momentum current (Ballantine *et al.*, 2016).

➢ Photons from twisted (OAM) beams: The total angular momentum operator j_z generates simultaneous rotations of the polarization *and* the spatial part of the light field, although generally through different angles. However, this projection of the total angular momentum is only conserved, e.g. a good quantum number, if the field can be (completely) expanded into eigenfunctions of j_z and if these eigenfunctions are, up to a phase factor, invariant under the associated rotations. For a monochromatic beam, the solutions must then fulfill the eigenvalue equations

$$(l_z + \gamma\, s_z)\, \boldsymbol{\mathcal{E}} = j_z^{(\gamma)}\, \boldsymbol{\mathcal{E}}, \qquad \boldsymbol{\mathcal{E}} = c_1\, e^{i\,\ell_1\,\varphi}\, \mathbf{e}_1 + c_{-1}\, e^{i\,\ell_2\,\varphi}\, \mathbf{e}_{-1}$$

where $\mathbf{e}_1$ $\mathbf{e}_{-1}$ are the polarization (unit) vectors in the helicity basis. Moreover, the radial dependence of these eigenmodes is *irrelevant* and omitted from the notation. Since the $\boldsymbol{\mathcal{E}}$ should be unchanged by a complete rotation $(2n\,\pi)$, both ℓ_1, ℓ_2 must be integer. Since all modes are simply superpositions of two states with definite spin and orbital angular momenta, the gyroscopic factor γ and the eigenvalue of the total angular momentum operators are given by

$$\gamma = \frac{\ell_2 - \ell_1}{2}, \qquad j^{(\gamma)} = \frac{\ell_2 + \ell_1}{2}$$

14.2.b. Torus-knot angular momentum

Coordinated rotations (CR) of light fields:

➢ Coordinated rotations (CR) of light fields: These rotations describe symmetry transformations in which the spatial component of the light field is rotated by some azimuthal angle ϕ_o around the beam axis (z axis), while the electric-field vector (polarization) is rotated by the angle $\gamma\,\phi_o$. Here γ is generally referred to as gyroscopic factor or coordination parameter.

➢ Coordinated rotations (CR) of light fields: These symmetry operations are generated by the linear combination of the OAM and SAM projection operators, $j_z^{(\gamma)} = l_z + \gamma\, s_z$, and whose (eigen-) values are independently conserved only within the paraxial regime. For paraxial beams, therefore, not only the eigenvalues ℓ and λ are good quantum numbers but also the torus-knot angular momentum $j^{(\gamma)}$, although these values need no longer to be integer. The coordinated rotations are sometimes said to induce Möbius-stripe topologies.

➢ Gyroscopic factor: For monochromatic light, the gyroscopic factor γ can take only integer or half-integer values and can be mathematically related to the topology of a Möbius strip. For bichromatic fields, in contrast, the gyroscopic factor γ can take all rational values, at least in principle.

➢ Monochromatic bicircular fields: For monochromatic light, the gyroscopic factor γ for a coordinated rotation of the light field must be either integer or a half-integer, since the polarization ellipse of the overall beam coincides with itself only for a rotation of $n\,\pi$ after each half-cycle, $\gamma \propto n/2$. However, this restriction does not apply to general electromagnetic fields. For bicricular fields, of course, only bichromatic superpositions need to be considered in order to analyze all the possible coordinated rotations for counter-rotating bicircular fields.

➢ Symmetries of the electric-field: Even for a monochromatic beam, the real-valued electric field $\boldsymbol{\mathcal{E}}(\mathbf{r},t) = \Re\,(\boldsymbol{\mathcal{E}}^{\,(\text{complex})}\, e^{-i\,\omega\,t})$ is generally not an eigenstate of the torus-know angular momentum operator (symmetry operator). A well-defined TKAM can only be assigned if the optical field fullfills the combined symmetry and time-translation operation of a coordinated rotation (Pisanty *et al.*, 2019)

$$R\,(\gamma\alpha)\;\boldsymbol{\mathcal{E}}(R^{-1}\,(\alpha)\,\mathbf{r},t) \;\;=\;\; \boldsymbol{\mathcal{E}}(\mathbf{r},\,t+\tau\alpha),$$

and where τ [time] is a constant and $R\,(\alpha)$ a 2×2 rotation matrix for a rotation by the angle α of the coordinates perpendicular to the beam axis.

Beams with well-defined torus-knot angular momentum:

➢ Beams with well-defined torus-knot angular momentum: Pisanty *et al.* (2019) showed that the eigenvalues $j^{\,(\gamma)}$ of the torus-knot angular momentum, known also as the torus-knot topological charge, are conserved for beams with a properly defined gyroscopic factor $\gamma \in \mathbb{Q}$. This topological can help classify the high-harmonics as generated from such bichromatic and bicircular beams. Since TKAM beams are invariant under coordinated rotations for the associated coordination factor $\gamma \in \mathbb{Q}$, the non-linear HHG process will preserve also the torus-knot topological charge, in addition to the conserved charges of the OAM and SAM.

➢ Beams with well-defined TKAM: These beams are not only invariant under coordinated rotations but also associated with a *combined* angular momentum operator $j_z^{(\gamma)} = l_z + \gamma\, s_z$ of the (projections of the) orbital l_z and spin s_z angular momentum operators with regard to the beam axis. In the paraxial approximation, both the OAM and SAM (projections) are conserved and can be measured independently.

➢ Symmetry classification of torus knots & Lissajous figures: These knots can be characterized by two indices, namely the symmetry order m of the (polarization) Lissajous figure itself as well as the spatial rotation number n, how often this Lissajous figure rotates if one goes once around the beam axis within the cross section of the beam. For each symmetry order m, the spatial rotation number n characterizes the spatial topology of the optical field (beam).

➢ Construction of the torus: From the Ferris-wheel diagram, the topology of a torus can be immediately read off if one follows the tips of the tre-foild and fold this together after going once around the beam axis. This twists the m tips of the tre-foil n times around and can be understood as m lines (symmetry order) on a torus that crosses its – inner – equatorial plane at n torus knots (spatial rotations). A similar analysis can be made for the eigenvalues of the torus-know angular momentum operator.

➢ Torus-knot angular momentum: Because of the algebraic identification of beam topology and the operator for a coordinates rotation, we can refer to the subgroup generator $j^{(\gamma)}$ as the torus-knot angular momentum (TKAM). The name of this (formal) angular momentum is derived from the close relation of the generated coordinated rotation and the topology of the torus.

➢ Concept of torus knot: This concept appears in different optical situations, for instance, for generating special optical vortices (or so-called C-lines) and field lines. However, neither the torus nor the knots with its equatorial plane does exist as real-space $3D$ object for a given beams, although this concept help characterize the topology of beams with regard to their properties such a as paraxial, the possible Lissajous-type figures and others.

$\omega - 2\omega$ bichromatic bicircular beams:

➢ $\omega - 2\omega$ bichromatic bicircular fields: These bichromatic fields with counter-rotating right- (↻) and left-handed circular (↺) polarizations can be characterited by their *two* (well-defined) orbital angular momenta, ℓ_1 and ℓ_2, or by just *one* torus-knot angular momentum $j^{(\gamma)} = j^{(\gamma)}(\ell_1, \ell_2)$. Indeed, the particular combination of (ℓ_1, ℓ_2) OAM uniquely determines the allowed gyroscopic factor γ for which the overall bicircular beam is invariant with regard to a coordinated rotation of the spatial and spin-components of the light beam.

➢ TKAM charges of bichromatic beams: For a bichromatic beam, the two (monchromatic) driving fields must have different TKAM charges in order to fullfill the overall dynamic symmetry of a coordinated rotation as the local phases of the light field depend on the frequencies.

➢ $\omega - 2\omega$ bichromatic bicircular fields: The two frequency components of a $\omega - 2\omega$ bichromatic and bicircular beam with well-defined OAM have the TKAM quantum numbers $j_1^{(\gamma)} = \ell_1 + \gamma$ and $j_2^{(\gamma)} = \ell_2 - \gamma$. For the q-t harmonic, this gives rise to the TKAM value

$j_q^{(\gamma)} = q\, j_1^{(\gamma)}$, i.e. in a linear increase of the TKAM with the order q of the harmonic. Of course, the orbital angular momenta ℓ_q can be obtained directly from the torus-knot angular momentum $j_q^{(\gamma)}$, and if the assigned (right- and left-handed) polarization of the $\omega - 2\omega$ incident beam, e.g. $\mathrm{LG}^{\omega\circlearrowleft}_{\ell_1,p_1} \oplus \mathrm{LG}^{2\omega\circlearrowleft}_{\ell_2,p_2}$, is taken into account.

➢ $\omega - 2\omega$ bichromatic bicircular fields with $\ell_1 = \ell_2 = 1$: For $\mathrm{LG}^{\omega\circlearrowleft}_{\ell_1,p_1} \oplus \mathrm{LG}^{2\omega\circlearrowleft}_{\ell_2,p_2}$ bicircular beam, one finds: $j_1^{(\gamma)} = 2/3$, $j_q^{(\gamma)} = 2/3\, q$.

➢ $\omega - 2\omega$ bichromatic bicircular fields: Counter-rotating circularly polarized beams at different frequencies help construct beams of light that are invariant under coordinated rotations for quite arbitrary rational gyroscopic factors γ. This additional freedom of bichromatic field for choosing a well-defined TKAM arise from the higher internal symmetry of these bichromatic superpositions. It was shown that these beams can be classified by means of the topology of a torus knot and, more specifically, by the eigenvalues $j^{(\gamma)}$ of a (so-called) torus-knot angular momentum (operator) $j_z^{(\gamma)} = l_z + \gamma\, s_z$.

➢ $\omega - 2\omega$ bichromatic bicircular fields: These beams forms so-called bicircular trefoil-shaped Lissajous figures.

➢ $\omega - 2\omega$ Bichromatic bicircular fields: The tre-foil polarization figure of these beams rotates smoothly when one goes once around the beam axis (in the plane perpendicular to it). This can be read off immediately from a so-called Ferris-wheel diagram which display the Lissajous figure at different angles φ in the cross section of the beam. From such figures, it can be seen also that the internal rotation of the Lissajous figure induces a Möbius-strip topology to the polarization.

➢ $\omega - 2\omega$ bichromatic bicircular fields: The concept of monochromatic bicircular fields can be generalized towards bichromatic bicircular fields which posess a high symmetry order m in their (polarization) Lissajous figures. For a $\omega - 2\omega$ bichromatic bicircular beam with a right-circularly polarized beam component at fundamental frequency ω and a left-circularly polarized second harmonic, for example, the fundamental component rotates counterclockwise by 120^o, while the 2ω component rotates clockwise by 240^o. Therefore the polarization (electric-field vector) at all spatial points in the beam is symmetric with regard to a rotation by $2\pi/3 = 120^o$.

➢ $r\,\omega - s\,\omega$ bichromatic bicircular fields: A $r\,\omega - s\,\omega$, bichromatic beam with coprime numbers r, s generally has a $(r+s)$-fold symmetric Lissajous figure.

➢ $r\,\omega - s\,\omega$ bichromatic bicircular fields: For such a bichromatic beam with orbital angular momenta ℓ_r and ℓ_s of the right- and left-circularly polarized field components, the winded tips still confine to the surface of a torus, from which the two characteristic symmetry numbers can be read off: (1) the symmetry number $m = r + s$ as number of points that appear with fixed angle φ_o in the cross each cross section of the torus and that is equal to the lobes of the Lissajous figure; (2) a signed (spatial) number $n = r\,\ell_r - s\,\ell_s$ for the spatial symmetry. While $|n|$ denotes the number of crossings in the – inner – equatorial plane of the torus, the characerizes the phase changes of the right- and left-circularly polarized beam components.

14.3. Light beams

Light beams:

➢ Characterization and properties of beams: In studying light-matter interactions, light beams play a major practical role and, hence, their characterization and properties are very important in order to understand the details of the interaction.

➢ Beams from applications: Light beams are usually formed when the em field from a given source is projected by filters and blends into a beam. In some lighting devices, lamps or parabolic reflector are used to produce an artificially light beam with a more or less large divergence (for example, car headlights, spotlights, ect.).

➢ Experimental beam parameters: The geometry and behavior of a Gaussian beam are governed by a set of beam parameters which are defined slightly different for different kinds of beams but which are often used to characterize the beams. These beam parameters include:

- Beam width: There are over five definitions of beam width.
- Beam quality: Quantified by the beam quality parameter, M2.
- Beam divergence: This is a measure of how the beam spreads with distance with regard to the focus plane.
- Beam profile: A beam profile is the 2D intensity plot of a beam at a given location along the beam path. A Gaussian or flat-top profile is often desired for many applications. The beam profile indicates nuisance due to high-order spatial modes in a laser cavity as well as hot spots in the beam.
- Beam astigmatism: A beam is called astigmatic when the vertical and horizontal focus of the beam is placed at different locations along the beam path.
- Beam wander or jitter: The amount by which the centroid or peak value of the beam profile moves with time.

Twisted (vortex) light beams:

➢ Charles Darwin (1932; 1887-1962) was one of the first who worked on light with a spatial structure of the phase.

➢ For circularly-polarized plane-wave light, the photons carry a projection of the angular momentum $\Delta L_z = \pm\hbar$ upon the propagation direction.

➢ Polarization state of a light beam: In 1892, Poincare showed that the state of polarization of a light beam can be described as a point on the surface of a unit sphere now known as the Poincare sphere.

14.3.a. Gaussian beams

Characerization and use:

➢ Gaussian beam: In optics, a Gaussian beam is a beam of electromagnetic radiation whose transverse electric field amplitude and, hence, its intensity distributions are approximately described by some Gaussian distribution.

➢ Both, planes waves and Gaussian beams are solutions of the Maxwell equation *and* the homogenous wave equation they both generally possess a **polarization** but can be readily described in terms of complex amplitudes.

➢ Complex-valued electric field amplitude $u(\mathbf{r})$: In a Gaussian beam, the electric field amplitude

$$u(\rho, z) \;=\; u_0 \frac{w_0}{w(z)} \exp\left(\frac{-\rho^2}{w^2(z)}\right) \exp\left(-ikz \,-\, ik\frac{\rho^2}{2R(z)} \,+\, i\zeta(z)\right)$$

obeys the paraxial Helmholtz equation. This amplitude is sufficient in order to describe the properties of the beam since the electric field and magnetic field propagate together and obey the same wave equation.

➢ Characteristic parameters: In the definition of the electric-field amplitude above, we have

- ρ ... radial distance from the center axis of the beam;
- z ... the axial distance from the beam's narrowest point (the beam waist),
- $k = \frac{2\pi}{\lambda}$ ... the wave number (in radians per meter), $E0 = |E(0,0)|$
- $w_0 = w(0)$ ... the waist size,
- $w(z)$ ... the radius at which the field amplitude drop to $1/e$ and, hence, the intensity to $1/e^2$ at axis with regard to $w_0 = w(0)$,
- $R(z)$ ... the radius of curvature of the beam's wavefronts,
- $\zeta(z)$ ... the Gouy phase shift, an extra contribution to the phase that is seen in Gaussian beams.

➢ In fact, many laser emit beams with roughly a Gaussian profile; these beams are often called the TEM_{00} fundamental modes of the laser's optical resonator. Gaussian beams form a widespread model in laser physics.

14.3.b. Vortex beams. Characterization and properties

General remarks:

➢ The recent years have seen a tremendous effort in generating and manipulating vortex beams together with a good number of new or promising applications, including the capture, manipulation and transport of nanoscopic particles (optical tweezer), high-resolution microsocopy or for data transmission.

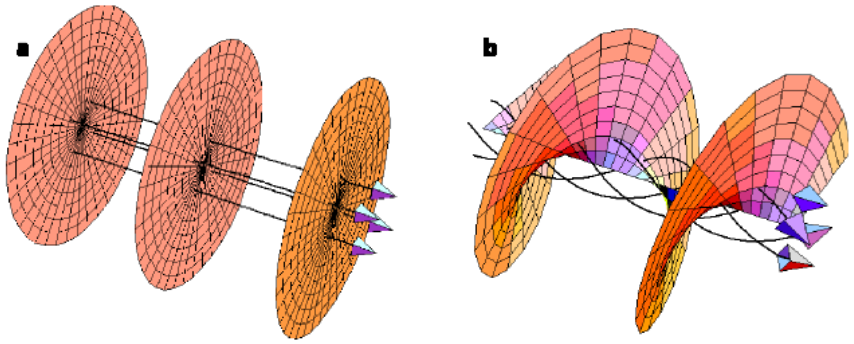

Figure 14.1.: Laser beams usually have planar wavefronts with wavevectors parallel to the beam axis. Beams with helical wavefronts have wavevectors which spiral around the beam axis and give rise to an orbital angular momentum; from Padgett and Allen (2000).

➢ Twisted photons carry both, spin angular momentum (SAM) as well as orbital angular momentum (OAM) along their propagation direction.

➢ Topological charge The z-projection of the OAM, m, is often called the topological charge or the winding number of the beam. This charge describes the number of the 2π windings of the helical phase around the vortex in one wavelength.

➢ Synonym notions of vortex beams: helically phased light beams; optical vortices with a field dependence $e^{im\varphi}$.

➢ Optical vortex beams are well-known and have been routinely used for the last 20 years; a first demonstration dates back to Durnin *et al.* (1987).

➢ For optical vortices, charge values of $m \leq 5000$ have been realized (Shen *et al.*, 2013).

➢ Reviews on optical vortex beams are given by Allen *et al.* (1999); Franke-Arnold *et al.* (2008), Zhan (2009) and Yao and Padgett (2011).

Characterization of vortex beams:

- A vortex state of light carries a well-defined projection of the orbital angular momentum (OAM) with respect to the beam axis.
- Wave functions: $\sim e^{im\varphi}$ are eigenfunctions of $\ell_z = \frac{\partial}{\partial \varphi}$.
- Photon field: For a quantized radiation field, each particle also carries a projection $m\hbar$ of the OAM, that is part of the total angular momentum. In general, the spin and orbital angular momentum cannot be separated.
- In the paraxial approximation, the spin and OAM longitudinal components of the vortex state can be separated from each other. Beyond the paraxial limit, however, the spin-orbit interaction does not allow a simple separation of the spin and orbital angular momentum.

Properties of vortex beams:

- For all points in the beam, the ratio between the azimuthal and z-components of the momentum is found to be ℓ/kr .
- The linear momentum of each photon is given by $\hbar k$; since the azimuthal component of the wavevector is m/r and is independent of the wavelength, the orbital angular momentum per photon is

$$p = \hbar k \quad \longrightarrow \quad p_\varphi = \hbar k \phi \quad \longrightarrow \quad \ell = r \times p_\varphi = r \times \frac{\ddot{\cdot}}{r} = m\hbar$$

- However, OAM $\neq$ SAM, despite the rather similar illustrations in the literatur; in particular, there exist also vortex states for spin-less waves, such as acoustic vortex waves.

14.3.c. Vortex beams. Generation

Generation of vortex beams with different photon energies:

- For intense, short-wavelength FEL radiation, optical methods can often not be applied due to strong limitations and difficulties in the fabrications of optical surfaces (Terhalle *et al.* 2011, Peele *et al.* 2002).
- Twisted EUV beams: Ribic and coworkers (2014) proposed an efficient scheme in order to generate intense coherent and twisted OAM beams in the EUV region. These beams can be realized by means of a seeded FEL, i.e. by using a (seeding) laser pulse with a transverse, staircaselike phase. For this phase pattern, in particular, the diffraction and mode selection drive the radiation profile towards a dominant OAM mode at saturation.
- Twisted x-ray beams: Hemsing an coworkers proposed two clever approaches for generating FEL vortex beams within the x-ray region:
  (i) By using the interaction of an electron beam with a seeded laser within a helical undulator (Hemsing *et al.*, 2011);
  (ii) by using a so-called echo-enabled harmonic generation (EEHG) scheme, in which two seed lasers and two magnetic chicanes are utilized in order to produce harmonic microbunches of an electron beam with a corkscrew distribution.

Generation of vortex beams by pitch-fork holograms:

- The superposition of a regular phase profile with some proper grating already results in a fork hologram that help generate vortex beams.
- Fork-like or pitch-fork holograms are known to diffract the light and to generate beams with OAM. Such holograms can be generated also dynamically by using a spatial light modulator and readily controlled by a computer.
- A pitchfork hologram is obtained adding a twisting and an oblique phase. The width of six 2π phase ramps is highlighted.

Generation of vortex beams by spiral phase plates:

- A (plane-wave) light beam can acquire a non-zero OAM by crossing a spiral phase plate with an inhomogeneous thickness.
- Spiral phase plates (SPP): Such a SPP is a transparent dielectric plate with a thickness that varies as a smooth ramp; this variation in the thickness adds a phase shift to an incident field that increases linear with the azimuthal angle φ.
- Light field: If a SPP is placed into the waist of a Laguerre-Gaussian beam with well-defined quantum numbers, $u_{\ell p}^{\mathrm{LG}}$, the complex light amplitude just behind the plate can be described by means of a phase-plate operator $S(m_s, \alpha)$

$$\langle r, \varphi \,|S(m_s, \alpha = 0)|\, l, p\rangle \;\; = \;\; u_{lp}^{\mathrm{LG}}(r, \varphi)\; e^{i m_s \varphi},$$

and where m_s is the phase shift per unit angle of the given SPP.

➢ SPP help explore high-dimensional entanglement with just two detector, while 6 detectors are required by other popular methods in order to prove the entanglement of the OAM degree of freedom for two entangled photons (Oemrawsingh *et al.*, 2004).

➢ The figure below shows the transformation of a TEM_{00} mode into a helical beam.

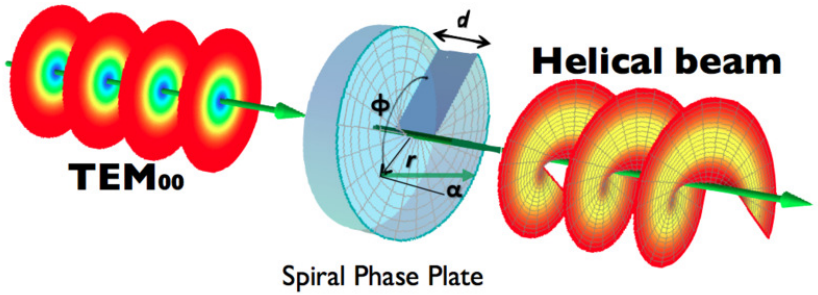

Figure 14.2.: Experimental scheme for generating light orbital angular momentum with spiral phase plates. Taken from Beijersbergen *et al.* (1994).

Generation of vortex beams by q-plates:

➢ q-plate: A (so-called) q-plate is a device that is realized by means of liquid crystals, polymers or sub-wavelength gratings; this device exploits a change of sign if the polarization of the incoming light is modified.

Generation of vortex beams by spatial light modulators:

➢ xxxxx A spatial light modulator (SLM) is an object that imposes some form of spatially varying modulation on a beam of light. A simple example is an overhead projector transparency. Usually when the phrase SLM is used, it means that the transparency can be controlled by a computer. In the 1980s, large SLMs were placed on overhead projectors to project computer monitor contents to the screen. Since then more modern projectors have been developed where the SLM is built inside the projector. These are commonly used in meetings of all kinds for presentations.

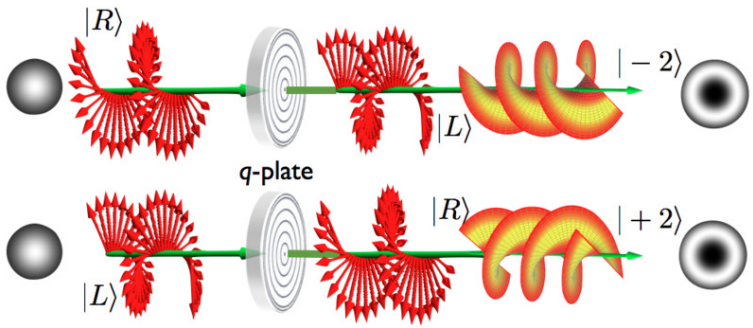

Figure 14.3.: The q-plate effect for left and right-hand circular polarizations.

Generation of vortex beams by cylcindrical mode converters:

➢ A Hermite-Gaussian beam can be converted into a Laguerre-Gaussian beam with well-defined OAM by using an astigmatic system with two well-aligned cylindrical lenses. In this scheme, these lenses are placed at some specific distance in order to introduce a well-defined relative phase between the horizontal and the vertical Hermite-Gaussian beams.

Generation of vortex beams by helical undulators:

➢ X-ray vortex beams with photon energies $\hbar\omega \approx 100$ eV have been generated in a helical undulator by Bahrdt *et al.* (2013) and Hemsing *et al.* (2013).

➢ Another interesting approach has been suggested by Ribic and coworkers (2014). These authors proposed to modify he phase mask and to manipulate directly the seeding laser in order to change the transverse properties of the FEL light.

14.3.d. Hermite-Gaussian beams

Characterization and use:

➢ Hermite-Gaussian modes HG_{mn} : have a rectangular symmetry and are described by means of two mode indices m and n; these mode indices give the number of nodes in the x and y directions respectively.

➢ Hermite-Gaussian modes: These modes are a convenient description for the output of lasers whose cavity design is not radially symmetric but asymmetric in horizontal and vertical directions.

14.3.e. Laguere-Gauss beams

Characterization and use:

➢ The Laguerre-Gaussian (LG) beams carry an intrinsic OAM like the intrinsic SAM for beams with a circular polarization (Allen *et al.* 1992, 2003). This appeared originally rather surprising as the OAM of LG beams arise from the helical phase distribution about the beam axis, and which coincides also with a phase singularity (Nye and Berry, 1974).

➢ Laguerre-Gaussian modes $u_{\ell p}^{\mathrm{LG}}$: For a Laguerre-Gaussian beam with well-defined magnetic and radial quantum numbers (m, p) , the complex amplitude of the light field in the waist of the beam is defined as in the polar represenation

$$u_{\ell p}^{\mathrm{LG}}(r,\varphi) \;=\; \langle r,\varphi \,|\, m,p\rangle \;=\; R_{mp}(r)\,\Phi_m(\varphi) \qquad \text{with} \qquad \Phi_m(\varphi) \;=\; \frac{e^{im\,\varphi}}{\sqrt{2\pi}}$$

➢ Laguerre-Gaussian modes $u_{\ell p}^{\mathrm{LG}}$: If the problem is cylindrically symmetric, these modes are the natural solution of the paraxial wave equation. They are often written in cylindrical coordinates by using Laguerre polynomials.

14.3.f. Bessel beams

Characterization and use:

➢ Bessel beams: A Bessel beam refers generally to an electromagnetic field whose amplitude is given by a Bessel function of the first kind. 5

➢ Although these beams are an idealization, true Bessel beam are monochromatic and non-diffractive and, hence, do not not diffract and spread out when they propagate. This behaviour is quite in contrast to other typical optical (or sound) waves if they are focused at some spot.

➢ Bessel beams are known to be self-healing if they are obstructed at some point, i.e. they reform to a Bessel beam again further down the beam axis.

➢ Pure Bessel modes generally carry a well-defined OAM; in particular, they typically include three components of the topological charge since only the (projection of the) total angular momentum is conserved for these beams. For this reason, the z-projections of the orbital and spin angular momentum are not defined independently.

➢ Bessel modes $|\kappa, m\rangle$: Bessel beams can be written also as a superposition over plane waves with well-defined (fixed) transverse momentum , longitudinal momentum as well as circular polarization

$$\psi(\mathbf{r}) \;=\; e^{-i\,\omega t\,+\,i\,k_z\,z}\;|\kappa, m\rangle\;, \qquad\qquad |\kappa, m\rangle \;\propto\; e^{i\,m\varphi}\;J_m(\kappa\,\rho)$$

➢ Vector potential: The vector potential of the Bessel beams is often written as Fourierintegral over Bessel states of different projections of the orbital angular momentum $a_{\kappa\,m}(\mathbf{k}_\perp)$,

$$\mathbf{A} \;=\; e^{-i\,\omega t}\,\frac{1}{(2\pi)^2}\int d\mathbf{k}_\perp\,e^{-i\,\mathbf{k}\cdot\mathbf{r}}\;a_{\kappa\,m}(\mathbf{k}_\perp)\,\mathbf{e}_{\mathbf{k},\lambda}, \qquad\qquad a_{\kappa\,m}(\mathbf{k}_\perp) \;=\; \sqrt{\frac{2\pi}{\kappa}}\,(-i)^m\,e^{-i\,m\,\varphi_{\mathbf{k}}}\;\delta(k_\perp\;-\;\kappa)$$

$$\mathbf{e}_{\mathbf{k},\lambda} \;=\; \frac{1}{\sqrt{2}}\begin{pmatrix}\cos\vartheta_k\,\cos\varphi_k\;-\;i\lambda\,\sin\varphi_k\\ \cos\vartheta_k\,\sin\varphi_k\;+\;i\lambda\,\cos\varphi_k\\ -\,\sin\vartheta_k\end{pmatrix} \qquad\qquad \tan\vartheta_k \;=\; \frac{\kappa}{k_z}$$

and where $\mathbf{e}_{\mathbf{k},\lambda}$ are known as polarization (unit) vector and ϑ_k as the opening angle of the Bessel beam.

➢ Plane-wave expansion: Of course, every monochromatic plane-waves can be expanded also in terms of Bessel waves as they are both just two different bases in order to describe wave packets

$$e^{i\,(\mathbf{k}\cdot\mathbf{r}\,-\,\omega t)} \;=\; \sum_{m=-\infty}^{\infty}\;e^{-i\,\omega t\,+\,i\,k_z\,z}\;i^m\;e^{-i\,m\,\varphi_{\mathbf{k}}}\;|\kappa,\,m\rangle$$

➢ Electron-photon interaction operator for Bessel beams: For (a Bessel beam of) twisted photons, the transition operator reads as:

$$V^{\,(\mathrm{tw})} \;=\; \alpha\,\mathbf{A}_{\varkappa m_\gamma k_z\lambda}(\mathbf{r})\,\mathbf{p}\,.$$

$$\mathbf{A}_{\varkappa m_\gamma k_z\lambda}(\mathbf{r}) \;=\; \int \mathbf{e}_{\mathbf{k}\lambda}\,e^{i\mathbf{k}\mathbf{r}}\;a_{\varkappa m_\gamma}(\mathbf{k}_\perp)\,e^{-i\mathbf{k}_\perp\mathbf{b}}\,\frac{d^2k_\perp}{(2\pi)^2}, \qquad\qquad a_{\varkappa m_\gamma}(\mathbf{k}_\perp) \;=\; (-i)^{m_\gamma}\,e^{im_\gamma\varphi_k}\,\sqrt{\frac{2\pi}{k_\perp}}\,\delta(k_\perp-\varkappa)\,.$$

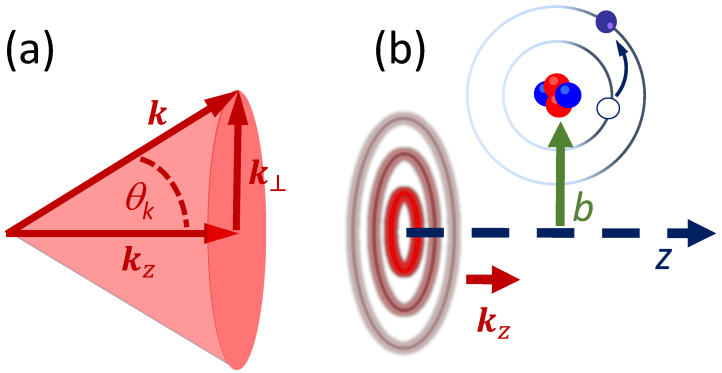

Figure 14.4.: (a) In momentum representation, the twisted light can be seen as a coherent superposition of plane waves. These plane waves with wavevectors $\mathbf{k}$ are all lying on a cone with (polar) opening angle $\vartheta_k = \arctan(|\mathbf{k}_\perp|/k_z)$ and with polarization vectors $\mathbf{e}_{\mathbf{k},\lambda}$ which are perpendicular to $\mathbf{k}$. (b) For a given atom, the absorption amplitude depends on the position of the atom in a plane perpendicular to the propagation direction. The position of the target atom with regard to the beam axis is specified by the impact parameter (vector) $\mathbf{b}$ (c-05-photobeam-interaction.eps).

In this expression, the factor $e^{-i\mathbf{k}_\perp \mathbf{b}}$ specifies the position of a target atom within the incident wave-front, and which refers to the complex spatial structure of the Bessel beam.

14.3.g. Airy beams

Characterization and use:

- Airy beams: Similar to Bessel beams, the cross section of an ideal Airy beam has an area of principal intensity and with a series of adjacent, less luminous areas up to infinity. Airy beams can be derived from the Airy integral that was first developed by George Biddell Airy in the 180s in order to explain the optical caustics in a rainbow and elsewhere.
- An Airy beam preserves its shape of intensity during propagation and forms a parabolic curve, quite analogue to the trajectory of a free projectile as seen in a plane perpendicular to the propagation.
- Airy beam are freely accelerating, i.e. they bend to form a parabolic arc as they propagate (Berry and Balazs, 1979; Siviloglou *et al.*, 2007), although the linear momentum remains conserved for these beams since the intensity centroid of an Airy beam forms a straight line.

➢ Airy beam do also not diffract, i.e. they do not spread out after focussing.

14.3.h. Necklace ring beams

Characterization and use:

➢ Necklace ring beams: These beams refer to optical vector solitons that consist of incoherently coupled self-trapped 'necklace' beams; these beams can carry zero, integer or even some fractional angular momentum.

➢ Necklace ring beams exhibit a self-stabilizing mutual attraction between different beam components and a quasistable propagation for much larger distances than the corresponding scalar vortex solitons

14.3.i. Light beams with non-integer OAM

Characterization and use:

➢ Beams with non-integer OAM: These beams refer to structurally propagation invariant light beams carrying non-integer orbital angular momentum (OAM) using Hermite-Laguerre-Gaussian (HLG) modes.

14.3.j. Vector beams

Characterization and use:

➢ Vector beams: The vector beams need to be described in the product space of the optical SAM and OAM subspaces and are characterized by higher-order Stokes parameters.

➢ Vector beams exhibit a spatially variant polarization.

➢ Cylindrical vector beams are axially symmetric solution to the full electromagnetic (vector) wave equation.

➢ Generation of vector beams: These beams can be generated via different active and passive methods.

14.3.k. Traktor beams

Characterization and use:

- Tractor beam: These beams refer to optical fields that help attract one object to another from a distance.
- The concept of tractor beams originates from the novel Spacehounds of IPC by E. E. Smith (1931) and by re-coining an earlier 'attractor beam', in contrast to other, 'repulser beams'.
- Tractor beam are defined to use (a negative) nonconservative radiation pressure, that differs from a gradient force, and which is directed towards the source. This generally requires a continuous redirection of momentum flux (Sukhov and Dogariu, 2010, 2011; Chen *et al.* 2011).
- Traktor beams are based on the maximization of forward scattering of light due to interference of different radiation multipoles. It was shown especially that an simultaneous excitation of multipoles is necessary in the particle in order to realize a negative (pulling) optical force.

14.3.l. Polarization radiation

Characterization and use:

- In electrodynamics, one generally distinguishes two classes of emitted radiation: bremsstrahlung and polarization radiation. While bremsstrahlung is produced by accelerated charges, polarization radiation can be emitted by a uniformly moving charge, although only in the presence of a medium.
- In dependence on the given medium or target geometry, one distinguishes various forms of polarization radiation: Cherenkov radiation, transition radiation, diffraction radiation as well as Smith-Purcell radiation.
- Polarization radiation: Electromagnetic radiation can be emitted not only by accelerated charges but also due to the motion of magnetic moments and higher multipoles. Until the present, however, this (so-called) polarization radiation has never been verified experimentally for any frequency of light.
- The main experimental difficulty for approving this radiation refers to the (very) small current of a magnetic moment that is suppressed by $\sim 10^{-5}$ w.r.t. a corresponding charge current.
- A pure quasi-classical treatment of the polarization radiation is inconsistent since quantum corrections are of the same order for this type of radiation phenomena.

14.3.m. Manipulation of optical beams

Optical elements:

- Dove prism: This is a (type of) reflective prism that can be used to invert a given image. These prisms are often shaped from a truncated right-angle prism.
- If a beam enters the prims at one of the sloped faces and parallel to the longitudinal axis, it undergoes total internal reflection at the inside of the longest (bottom) face, and then leaves the prism at the opposite sloped face. Therefore, any image that passes through the prism is flipped (mirrored) and also also inverted but not laterally transposed.
- Hologram: A holgram usually refers to a three-dimensional image of an object that is created by holography, i.e. an optical technique for recording and reconstructing the amplitude and phase distributions of a coherent wave. Holography is often used to produce three-dimensional images or holograms.
- Half-wave plate: A wave plate, sometimes known as a retarder, designates an optical device that alters the polarization state of a light wave. While a half-wave plate shifts the polarization direction of linearly polarized light, a quarter-wave plate converts linearly-polarized light into circularly-polarized light and vice versa. Quarter-wave plate can be used also in order to produce elliptically-polarized light.

Mach-Zehnder interferometers:

- These interferometers make use of two separate beam splitters in order to split and recombine an input beam but from which the beam can emerge and detected at two outputs. The optical path lengths in the two arms of the interferometer may be nearly identical or may be different in order to introduce an extra delay path.
- If a beam is sent through the interferometer, the optical powers at the two outputs depends on in practice sensitively on the the precise difference in optical arm lengths as well as on the wavelength of the light.
- The Mach-Zehnder interferometer was first developed by Ludwig Mach and Ludwig Zehnder.

14.3.n. Optical forces of vortex beams

Optical forces:

➢ :

➢ A positive radiation force is relatively intuitive and occurs in the backscattering or absorption of the forward-directed momentum of a beam; it was first reported already by Nichols and Hull (1903).

14.3.o. Application of optical (vortex) beams

Remarks:

➢ Different applications of optical vortex beams and the angular momentum of light have been envisaged and are currently explored in research laboratories, although no real commercial application are yet known.

➢ Fields of applications: Cold atoms, trapped nanoparticles, micro manipulation and detection of spinning objects, remote measurement of the rotation of mesoscopic particles, entanglement and quantum information, optical data transmission, interaction with matter, microscopy and astrophysics.

➢ X-ray magnetic circular dichromism By using different OAM states in the measurements, the dipole and quadrupole contributions to the circular dichroism signal can be separated from each other.

Optical tweezer:

➢ Optical tweezer: These tweezers usually refer to single-beam gradient force trap that are realized by some highly focused laser beam. These focused beams provide an attractive or repulsive force on nano- or mesoscopic dielectric objects.

➢ Optical tweezers have been utilized to manipulate the orientation of particles or particle aggregates.

➢ In optical tweezers, the forces are typically on the order of piconewtons; they depends on the refractive index of the object.

Optical phasors:

➢ Phasor: A complex constant in complex wave notation that encapsulates the amplitude; sometimes known also as sinor or complexor.

Applications in quantum information theory:

➢ The orbital-angular momentum (OAM) of light has recently emerged as a promising candidate for quantum and classical information systems.

➢ In OAM beams, the spatial degrees of freedom provide a high-dimensional alphabet to quantum information processing which enables one to use qunits instead of qubits.

➢ Quantum information encoding, Higher-dimensional quantum information encoding has been discussed in the literature for possible future applications in quantum cryptography or quantum computations. The discrete, unbounded state-space of OAM promises in particular vastly enhanced data rates as well as an increased tolerance to eavesdropping in quantum communication.

14.4. Electron beams

Electron beams:

➢ Electron beams are quite frequently applied in physics; such beams may refer, for instance, to some stream of electrons as obtained from a betatron. Electron beams are generally generated either by heat (thermionic emission), bombardment of surfaces with charged atoms or particles (secondary electron emission), or by means of strong electric fields (field emission).

➢ Electrons may be collimated by holes and slits. Because they are electrically charged, they can also be deflected, focused or accelerated by electric and magnetic fields.

Twisted electron beams:

➢ Apart from twisted (vortex) solutions of the Dirac equation, a quais-relativistic wave equation for twisted relativistic electron in arbitrary electric and magnetic fields can be derived by using a Foldy-Wouthuysen transformation.

➢ The interaction of twisted (vortex) electrons with electric and magnetic fields can be described quite readily, based on Lorentz transformations.

14.4.a. Gaussian electron beams

Characterization and use:

➢ It has been demonstrated experimentally that a Gaussian-profile model better describes the (equilibrium) electron beam than a beam with a uniform-profile model.

14.4.b. Vortex electron beams

General remarks:

➢ Electron vortex beams were first realized experimentally by Uchida and Tonomura (2010), Verbeeck, Tian and Schattschneider (2010) and McMorran *et al.* (2011). Uchida and Tonomura, in particular, generated an electron vortex beams with (electron) energy $E = 300$ keV, a projection of the OAM with $m \lesssim 100$ and by focusing the electron beam to a spot size of 1.2 Å.

➢ Vortex electrons can generally carry a rather large intrinsic projection of the orbital angular momentum (OAM) $m \sim 100$ with respect to their propagation direction. Therefore, the magnetic moment of vortex electrons $\mu \approx m\,\mu_B$ is similarly large, when compared with the Bohr magneton μ_B due to the spin motion of the electron.

➢ The magnetic moment of twisted electrons due to their OAM comes in addition to the known magnetic moment due to the spin motion.

➢ Since Vortex electrons are sensitive to external magnetic fields, they can be utilized to probe atomic magnetism and, thus, open novel opportunities for electron microscopy.

➢ While vortex photon beams have been created and routinely used for several decades already, the vortex states of electrons and charged particles is a presently emerging field.

14.4.c. Generation of vortex electron beams

Generation of vortex electron beams with different energies:

➢ Indeed, several new ideas were proposed in the literature in order to create electron vortex beams experimentally.

Generation of vortex electron beams by undulators:

➢ Electrons in a helical modulator: cf. Figure 14.4.c

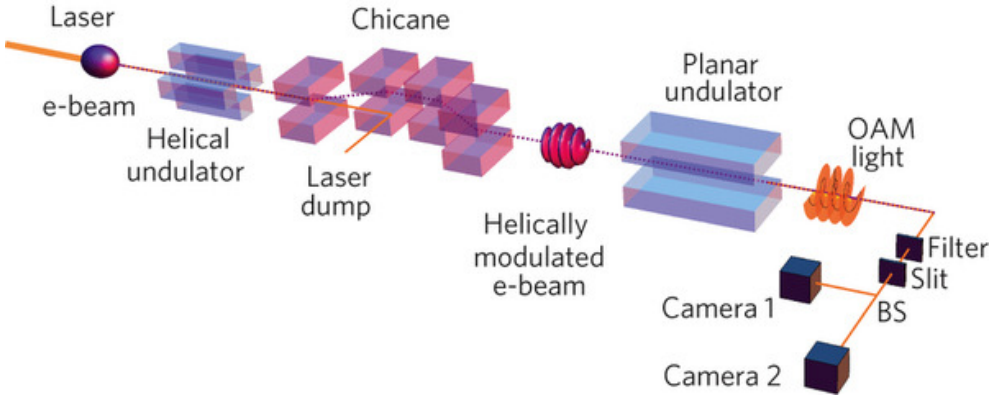

Figure 14.5.: An unmodulated relativistic electron beam interacts with a linearly polarized laser in a helical undulator, which gives the electrons an energy kick that depends on their position in the focused laser beam.

Generation of vortex electron beams by transmission electron microscopes:

➢ Voloch-Bloch *et al.* (2013) generated Airy electron beams by using a holographic technique within a transmission electron microscope. Both, self-bending and self-healing features were observed in the experiments if the beam was obstructed by a small object during its propagation.

Generation of vortex electron beams by holograms:

➢ Grillo *et al.* (2014) generated an electron Bessel beam by the diffraction of electrons at a nanoscale phase hologram. This hologram imposed a conical phase structure upon the electron wave-packet. The so obtained beams propagated for 0.6 m without measurable spreading and could reconstruct also its intensity distributions, if these beams where partly obstructed by an obstacle.

14.4.d. Bessel electron beams

Characterization and use:

➢ Quasi-Bessel beams can be obtained within a good approximation, while it is not possible to generate an ideal Bessel beam because they are not normalizable in their total intensity,

➢ Wave function of a Bessel electron: In cylindrical coordinates r, φ, z, the wave function of electrons in a Bessel beam is given by

$$\psi(r,\varphi,z;t) \;=\; J_m(\kappa\, r)\, e^{i\, m\varphi}\, e^{-i\,(\omega t - k_z z)},$$

where $J_m(x)$ is the m-th order Bessel function of the first kind and κ and k_z denote the transverse and longitudinal components of the wave vector, respectively.

➢ Probability-density distribution of Bessel electron beams: This wave function give rise to a probability-density distribution $\mathcal{P} \;=\; \psi\,\psi^{+}$ that is independent of z and t:

$$\mathcal{P}(r,\varphi,z;\,t) \;=\; \mathcal{P}(r,\varphi,0;0) \;=\; [\,J_m(\kappa\, r)\,]^2\,.$$

➢ This shows that the probability-density distribution is stationary in the transverse plane and independent of where this plane is taken.

➢ The energy of the electron $E \;=\; \hbar\,\omega$ defines the de Broglie wave length and the modulus of the wave vector by

$$k^2 \;=\; k_r^2 \,+\, k_z^2 \;=\; \frac{2m\omega}{\hbar} \;=\; \left(\frac{2\pi}{\lambda_{dB}}\right)^2\,.$$

- For Bessel beams with a nonzero m value, the electrons possess a non-uniform helical phase front with m dislocations in the phase, and where the handedness of the phase front is defined by the sign of m.
- Current density of electron Bessel beam: This current density circulates azimuthally in the transverse plane and introduces an (projection of the total) orbital angular momentum of $m\hbar$ per electron.
- An Bessel electron beam with a nonzero m value possess exhibit a shape with multiple rings and with a null probability density at the origin.
- Bessel electron beams can be represented also as a coherent superposition of conical plane waves along a closed ring (circle).

14.4.e. Airy electron beams

Characterization and use:

- Airy electron beams can be generated by diffraction of electrons through a nanoscale hologram, which imprints a cubic phase modulation on wavefunction of the electrons in the transverse plane.

14.4.f. Application of twisted electron beams

Remarks:

- The scattering of twisted electrons can provide insights into the magnetic structure of the target materials.
- Beams with non-zero OAM helped explore the vacuum Faraday effect as well as Larmor and Gouy rotations.
- Bessel electron beams have been used in electron microscopy.

15. Symbolic evaluation of expressions from Racah's algebra

15.1. Racah's algebra in atomic and many-body physics

15.1.a. Advantages of using Racah's algebra

Goals and use of Racah's algebra:

- The theories of angular momentum and spherical tensor operators play a significantly role in atomic and nuclear physics, and at several places elsewhere. These two theories lead to algebraic expressions which are usually written in terms of generalized Clebsch-Gordan coefficients and/or Wigner $3n$–j symbols as well as the Wigner rotation matrices and spherical harmonics. Although the evaluation and simplification of such expressions is in principle a straigthforward task, it can become extremely cumbersome, if more complex systems or physical scenarios are considered.
- Indeed, the study of open-shell atoms and nuclei quickly raises the question how the rotational symmetry of (closed) systems, i.e. the conservation of angular momentum, can efficiently be exploited in understanding many-particle systems. After the pioneering work by Wigner in the late thirties, Racah (1941, 1942, 1943) developed a powerful machinery, known as Racah algebra, to deal with such systems, and which is one of the fundamental concepts in the (quantitative) treatment of many-particle systems.
- In many-particle physics, an explicit re-coupling of the angular momenta is often required due to the use and sequence of different coupling schemes. In general, such recoupling transformations are written in terms of recoupling coefficients that need to be evaluated over and over again.
- Spin-angular integration of many-particle matrix elements In atomic and nuclear structure theory, the evaluation and spin-angular integration of many-particle matrix elements is typically based on standard quantities like the matrix elements of the unit tensor, the (reduced) coefficients of fractional parentage as well as a number of other reduced matrix elements for different products of creation and annihilation operators. These quantities arise rather frequently in both, configuration interaction approaches and in the derivation of perturbation expansions for many-particle systems by using symmetry-adapted configuration state functions.

➢ Theory of angular momentum In the treatment of quantum many–particle systems, the theory of angular momentum offers two crucial advantages: (i) The reduction of complicated many-electron matrix elements to a rather small number of *standard quantities* and (ii) an elegant and very powerful calculus which help simplify and evaluate sophisticated expressions.

➢ Racah algebra techniques: Owing to these advantages, the techniques from the theory of angular momentum, shortly known also as Racah algebra techniques (Racah 1941, 1942, 1943), have been utilized in a large number of applications and in quite different field of many-particle physics (Wigner 1959, Varshalovich *et al.* 1988).

➢ Racah expressions: With the symbolic evaluation of expressions from Racah's algebra, we wish to focus on the algebraic transformation of (Racah) expressions such as:

$$\text{Racahexpr} := \sum_{j_1,j_2,l_1,\ldots} (-1)^{2j_1-j_2+\ldots}\; j_1^{3/2}\; [j_2]\ldots \begin{pmatrix} \cdot & \cdot & j_1 \\ \cdot & \cdot & \cdot \end{pmatrix} \begin{pmatrix} j_1 & j_2 & \cdot \\ \cdot & \cdot & \cdot \end{pmatrix} \begin{Bmatrix} \cdot & j_3 & \cdot \\ j_1 & \cdot & \cdot \\ J & \cdot & j_2 \end{Bmatrix} \ldots$$

$$\times \int d\Omega_1\, Y_{\ell_1 m_1}(\Omega_1)\, Y_{\ell_2 m_2}(\Omega_2) \int d\beta\; d^{j_3}_{p_3 q_3}(\beta)\; d^{j_4}_{p_4 q_4}(\beta') \;\ldots.$$

Here, the Clebsch-Gordan coefficients need not to shown explictly in this expression since, apart from an additional phase, they are equivalent to the Wigner $3-j$ symbols. Up to the present, we (must) also drop the rotation matrices and spherical harmonics which are not (yet) supported in Jac. We introduce this notation of Racahexr with the intention for providing an (internal) data type which facilitates automatic manipulations and which is flexible enough to support a wide range of applications.

➢ Racah expressions: Such expressions may generally include any number of Wigner n–j symbols of different kind as well as (various integrals over) the spherical harmonics and Kronecker and triangular deltas. Of course, the complexity of such Racah expressions increases rapidly as more Wigner symbols are involved in the product terms.

➢ The symbolic evaluation of typical expressions from Racah's algebra is naturally based on the knowledge of a large set of sum rules that may include rules with a (multiple) summations over dummy indices (Varshalovich *et al.* 1988). For complex and lengthy Racah expressions, moreover, the algebraic simplification can often be considerably accelerated if the graphical rules due to Yutsis *et al.* (1962) are taken into account.

➢ Sum and orthogonality rules: To obtain a simplification for complex Racah expressions, a large variety of sum and orthogonality rules have been implemented from the monograph by Varshalovich *et al.*(1988).

➢ In the past decades, various techniques in simplifying expressions from Racah's algebra have been developed, based either on graphical methods or on the explicit knowledge of special values and sum rules, as they can be found in some standard form in the literature. The direct application of these rules is however often laborious due to a large number of symmetric forms of the Wigner and related symbols.

➢ Graphical loop rules: These loop rules are typically used in order to find out about and to simplify those parts in a recoupling coefficient (or generally in any Racah expression) that belong together. The implementation of graphical rules even allows to easily simplify recoupling coefficients which include several ten angular momenta to an (completely equivalent) sum of products of Wigner 6–j and/or 9–j symbols, multiplied by proper weights.

➢ Algebraic simplifications: The simplification of expressions from Racah's algebra critically depends how easily all equivalent symmetric forms of these expression are recognized internally. Obviously, the symmetry of a Racah expression as a whole is closely related to the symmetries of all the Wigner $3n$–j symbols which are involved in the expression.

➢ Classical symmetries of the Wigner symbols: Apart from the classical symmetries of the Wigner symbols, there is an extended range of symmetries due to Regge (1958); these symmetries are however of minor practical importance.

➢ Although the mathematical background of angular momentum theory is today quite well understood, the treatment and simplification of typical expansions as they naturally arise by using Racah's algebra, is often very laborious.

➢ In Jac, we shall facilitate the symbolic evaluation of expressions from Racah's algebra and, is particular, for (complex) expressions for which the known algebraic and graphical methods start to become tedious and prone to making errors.

15.1.b. Frequently applied symbols and functions from Racah's algebra

Table of symbols and functions from the theory of angular momentum:

➢ The following symbols and functions from the theories of angular momentum and irreducible tensor operators occur very frequently in the computation and analysis of atomic and many-body systems

Symbol	Designation	Calls in Jac
$\begin{pmatrix} a & b & c \\ m_a & m_b & m_c \end{pmatrix}$	Wigner 3–j symbol	`Wigner_3j()`
$\begin{Bmatrix} a & b & c \\ d & e & f \end{Bmatrix}$	Wigner 6–j symbol	`Wigner_6j()`
$\begin{Bmatrix} a & b & c \\ d & e & f \\ g & h & i \end{Bmatrix}$	Wigner 9–j symbol	`Wigner_9j()`
$\left\{ \begin{array}{cccc\|c} a & b & c & d & \\ e & f & g & h & s \\ i & j & k & l & \end{array} \right\}$	Wigner 12–j symbol of kind $s = 1, 2$	Not implemented.
$\begin{Bmatrix} - & a_2 & a_3 & a_4 \\ b_1 & - & b_3 & b_4 \\ c_1 & c_2 & - & c_4 \\ d_1 & d_2 & d_3 & - \end{Bmatrix}$	Sharp's symbol (Sharp 1955)	Not implemented.
$\langle a\ m_a,\ b\ m_b \mid c\ m_c \rangle$	Clebsch–Gordan coefficient	`ClebschGordan()`
$W(abcd; ef)$	Racah's W coefficient	Not implemented.

Symbol	Designation	Calls in JAC
$d^j_{mm'}(\beta)$	Wigner $d^j_{mm'}(\beta)$ rotation matrix	`Wigner_d()`
$D^j_{mm'}(\alpha,\beta,\gamma)$	Wigner's $D-$function	Not implemented.
$U^j_{mm'}(\omega;\Theta,\Phi)$	Rotation matrix $U(\omega)$	Not implemented.
$Y_{\ell m}(\vartheta,\varphi)$	Spherical harmonic	Not implemented.
$\{\mathbf{Y}_{l_1}(\vartheta_1,\varphi_1)\otimes\mathbf{Y}_{l_2}(\vartheta_2,\varphi_2)\}_{LM}$	Bipolar spherical harmonic	Not implemented.
$\big\{\mathbf{Y}_{l_1}(\vartheta_1,\varphi_1)\otimes\{\mathbf{Y}_{l_2}(\vartheta_2,\varphi_2)\otimes\mathbf{Y}_{l_3}(\vartheta_3,\varphi_3)\}_{l_{23}}\big\}_{LM}$	Tripolar spherical harmonic	Not implemented.
$\mathbf{Y}^l_{jm}(\vartheta,\varphi)$	Vector spherical harmonic	Not implemented.
$\Omega^l_{jm}(\vartheta,\varphi)$	Spinor spherical harmonic	Not implemented.
$Y^{ls}_{jm}(\vartheta,\varphi)$	Tensor spherical harmonic	Not implemented.

Brief explanation of symbols and functions:

➢ Wigner $3n$–j symbols (n = 1, 2, and 3): The Wigner $3n$–j symbols are all related to the (re-) coupling) of angular momenta between different coupling schemes. For n = 1, 2, and 3, these symbols form the basic data types in the symbolic evaluation of expressions from Racah's algebra. Indeed, the Wigner $3n$–j symbols frequently arise in (almost) all applications of the theory of angular momentum.

➢ 12–j symbols of first and second type. Sharp's symbol: Wigner $3n$–j symbols of higher order ($n \geq 4$) are rarely used in applications as their complexity increases rapidly with n and as several *kinds* of these symbols need to be distinguished (Varshalovich *et al.* 1988). In particular, there are two kinds of 12–j symbols, called the *first* and *second* kind or 12–$j(1)$ and 12–$j(2)$ symbols, respectively. These symbols are often written as

$$\left\{ \begin{array}{cccc|c} a_1 & a_2 & a_3 & a_4 & \\ b_1 & b_2 & b_3 & b_4 & s \\ c_1 & c_2 & c_3 & c_4 & \end{array} \right\},$$

where $s = 1, 2$ selects the *kind*. Instead of the 12–$j(2)$ symbol of *second* kind, *Sharp's symbol* (Sharp 1955) is sometimes used that exhibits a slighly higher symmmetry. For $n \geq 4$, the properties of the $3n$–j symbols are still a research topic in modern group theory.

➢ Clebsch-Gordan coefficients: The Clebsch-Gordan or vector coupling coefficients appear naturally as Fourier coefficients in the *re-coupling* of angular momenta; they are closely related to the Wigner 3–j symbols. In JAC, we make use of the Condon-Shortley phase convention (Condon and Shortley 1935)

$$\langle j_1 m_1,\, j_2 m_2 \,|\, j_3 m_3 \rangle \;=\; (-1)^{j_1 - j_2 + m_3}\, [j_3]^{\,1/2} \begin{pmatrix} j_1 & j_2 & j_3 \\ m_1 & m_2 & -m_3 \end{pmatrix} .$$

➢ Racah's W coefficients: The Racah W coefficients, $W(abed; cf) = (-1)^{a+b+d+e} \begin{Bmatrix} a & b & c \\ d & e & f \end{Bmatrix}$, are basically equivalent to the Wigner 6–j symbols and were mainly applied in the earlier literature on the recoupling of angular momenta. In the JAC program, we only use the Wigner 6–j symbols in all symbolic evaluations.

➢ Wigner's D-function $D^j_{mm'}(\alpha, \beta, \gamma)$: The D-functions are often required for the transformation of wave functions, if either the system or the coordinates are rotated

$$|\Psi_{jm'}(\vartheta', \varphi', \sigma')\rangle \;=\; \sum_m \,|\, \Psi_{jm}(\vartheta, \varphi, \sigma)\rangle \; D^j_{mm'}(\alpha, \beta, \gamma).$$

Here ϑ, φ and ϑ', φ' are the polar angles in the initial and the rotated system, while $\sigma(\sigma')$ denote the corresponding spin variables. More general, these functions occur in the transformation of any irreducible spherical tensor of rank j. Therefore, the D-functions occur very frequently in the treatment of scattering processes from elementary particles up to molecules and clusters, and by including capture, transfer, and emission processes. The Wigner D-functions also fullfill a large number of symmetry properties (Varshalovich *et al.* 1988) and are expressed most readily in terms of the Euler angles and the (so-called) Wigner rotation matrix $d^j_{mm'}(\beta)$, see below.

➢ Rotation matrix $d^j_{mm'}(\beta)$: This (real) matrix describes the rotation of any spherical tensor by the angle β around a given axis, say, the quantization axis of the system. Several explicit representations of this real function exist in terms of $\sin(\beta/2)$ or $\cos(\beta/2)$, the hypergeometric function, or various other polynomials. In JAC, the rotation matrix $d^j_{mm'}(\beta)$ is one of the basic data structures in the algebraic manipulation of expressions from Racah's algebra.

➢ Spherical harmonics: The spherical harmonics are applied in many fields of physics. In quantum mechanics, they form an important basis for classifying the one- and many-particle states since they are known to be simultaneous eigenfunctions of one component and of the square of the orbital angular momentum operator $-i\mathbf{r} \times \nabla$. In many-particle physics, the properties of these functions (completeness, orthogonality, ...) are frequently utilized to represent and evaluate the spin-angular part of the corresponding matrix elements analytically.

➢ Spherical harmonics $Y_{\ell m}(\theta,\phi)$: These functions form a complete and orthonormal set on the unit sphere, and are therefore widely used in classical and quantum physics. The spherical harmonics frequently appear in the representation of wave functions for a wide range of physical systems, in the evaluation of the corresponding (quantum) matrix elements, and at many places elsewhere. In JAC, these functions are also one of the basic data structures in the algebraic manipulation of expressions from Racah's algebra.

15.1.c. Symmetries of the Wigner $3n$–j symbols, rotation matrices and spherical harmonics

Symmetries of the Wigner $3n$–j symbols:

➢ Symmetries of the Wigner 3–j symbols: This symbol has the following symmetries with regard to a permutation of columns and with regard to a change of signs in the projections of all angular momenta

$$\begin{pmatrix} j_1 & j_2 & j_3 \\ m_1 & m_2 & m_3 \end{pmatrix} = \begin{pmatrix} j_2 & j_3 & j_1 \\ m_2 & m_3 & m_1 \end{pmatrix} = \begin{pmatrix} j_3 & j_1 & j_2 \\ m_3 & m_1 & m_2 \end{pmatrix} = (-1)^{j_1+j_2+j_3} \begin{pmatrix} j_1 & j_3 & j_2 \\ m_1 & m_3 & m_2 \end{pmatrix}$$

$$= (-1)^{j_1+j_2+j_3} \begin{pmatrix} j_2 & j_1 & j_3 \\ m_2 & m_1 & m_3 \end{pmatrix} = (-1)^{j_1+j_2+j_3} \begin{pmatrix} j_3 & j_2 & j_1 \\ m_3 & m_2 & m_1 \end{pmatrix}$$

$$\begin{pmatrix} j_1 & j_2 & j_3 \\ m_1 & m_2 & m_3 \end{pmatrix} = (-1)^{j_1+j_2+j_3} \begin{pmatrix} j_1 & j_2 & j_3 \\ -m_1 & -m_2 & -m_3 \end{pmatrix}$$

➢ Classical symmetries: When combined, these symmetry relations give rise to 12 formally different 3–j symbols with the same absolute value. There are additional symmetries known due to Regge (1958) which are most easily explained in terms of Regge symbols (Varshalovich *et al.* 1988).

➢ A similiar distinction between classical symmetries and additional symmetric forms due to Regge can be made also for the 6–j symbols.

➢ Number of symmetries of the Wigner $3n$–j symbols: The table below lists the number of classical symmetries vs. the overall number of symmetric forms known for the Wigner symbols. In order to simplify Racah algebra expressions, it is crucial to exploit these symmetries; they are therefore all incorporated in the program as it is explained below.

➢ For practical purposes, however, the classical symmetries are much more important and the distinction is therefore kept. In our notation, the classical symmetries are a subset of the Regge symmetries.

➢ Number of classical symmetries of Wigner 3–j symbols vs. the symmetries known due to Regge (1958)

3–j symbol	classical symmetries	Regge symmetries (Regge 1958)
3–j	12	72
6–j	24	144
9–j	72	—

Definition and symmetries of the Wigner $D-$functions and rotation matrices:

➢ Wigner D-functions $D^j_{pq}(\alpha,\beta,\gamma)$: The Wigner D-functions are defined as the matrix elements of the rotation operator $\hat{R}(\alpha,\beta,\gamma)$ in $\mathcal{R}^3$ and are often parametrized in terms of the three Euler angles α, β, and γ. In particular, these functions arise not only in the transformation of tensor components under the rotation of the coordinates but also as the eigenfunctions of the spherical top.

➢ Definition of the $D^j_{pq}(\alpha,\beta,\gamma)$ and $d^j_{pq}(\beta)$ rotation matrices: The Wigner D-function is defined as a product of three functions that each depend on just a single Euler angle and with the so-called Wigner rotation matrix $d^j_{pq}(\beta)$:

$$D^j_{pq}(\alpha,\beta,\gamma) \;=\; e^{-ip\,\alpha}\, d^j_{pq}(\beta)\, e^{-iq\,\gamma}\,.$$

➢ Euler angles (α,β,γ) : These angle can be utilized to characterize all possible rotations of a given (coordinate) system if the following range of values are considered:

$$0 \le \alpha \le 2\pi, \qquad 0 \le \beta \le \pi, \qquad 0 \le \gamma \le 2\pi\,.$$

➢ Symmetries of the D^j_{pq} functions and Wigner rotation matrices d^j_{pq}: The Wigner rotation matrix $d^j_{pq}(\beta)$ satisfies the following basic symmetries (Varshalovich *et al.*, 1988, eq. 4.4.1):

$$\begin{aligned}
d^j_{pq}(\beta) &= (-1)^{p-q}\, d^j_{-p-q}(\beta) = (-1)^{p-q}\, d^j_{qp}(\beta) = d^j_{-q-p}(\beta) \\
&= d^j_{qp}(-\beta) = (-1)^{q-p}\, d^j_{qp}(\beta) = (-1)^{-j-p}\, d^j_{-pq}(\beta-\pi) = (-1)^{-j-2p-q}\, d^j_{p-q}(\beta-\pi) \\
&= (-1)^{-2j}\, d^j_{pq}(\beta+2\pi) = (-1)^{-2j}\, d^j_{pq}(\beta-2\pi) = (-1)^{j-q}\, d^j_{p-q}(\beta+\pi) = (-1)^{j-2q-p}\, d^j_{-pq}(\beta+\pi)\,.
\end{aligned}$$

The symmetry properties of the Wigner D-function are listed by Varshalovich *et al.* (1988, Eq. 4.2.2) and are taken into account since the D-function are internally handled in terms of the Wigner rotation matrix.

Symmetries of the spherical harmonics:

➢ Symmetries: The spherical harmonics satisfy the following basic symmetries:

$$\begin{aligned} Y_{\ell m}(\vartheta,\varphi) &= (-1)^m\, e^{2im\varphi}\, Y_{\ell,-m}(\vartheta,\varphi) = (-1)^m\, Y_{\ell m}(-\vartheta,\varphi) = e^{2im\varphi}\, Y_{\ell,-m}(-\vartheta,\varphi) = (-1)^m\, Y_{\ell,-m}(\vartheta,-\varphi) \\ &= e^{2im\varphi}\, Y_{\ell m}(\vartheta,-\varphi) = Y_{\ell,-m}(-\vartheta,-\varphi) = (-1)^m\, e^{2im\varphi}\, Y_{\ell m}(-\vartheta,-\varphi)\,. \end{aligned}$$

15.1.d. Expansions of the Wigner $3n$–j symbols, rotation matrices and spherical harmonics

Explicit formulas for the computation of the Wigner $3n$–j symbols:

➢ Δ symbol:

$$\Delta(a,b,c) = \left[\frac{(a+b-c)!\,(a-b+c)!\,(-a+b+c)!}{(a+b+c+1)!}\right]^{1/2}.$$

➢ Wigner 3–j symbol: The numerical value of a Wigner 3–j symbol can be calculated by the expression (Racah, 1942) and has a non-zero value only if the arguments of all factorials are non-negative integers

$$\begin{aligned} \begin{pmatrix} j_1 & j_2 & j_3 \\ m_1 & m_2 & m_3 \end{pmatrix} &= \delta_{m_1+m_2+m_3,0}\,(-1)^{j_1-j_2-m_3}\,\Delta(j_1,j_2,j_3)\,[(j_1-m_1)!\,(j_1+m_1)!\,(j_2-m_2)!\,(j_2+m_2)!\,(j_3-m_3)!\,(j_3+m_3)!]^{1/2} \\ &\times \sum_l \left[\frac{(-1)^l}{l!\,(j_1+j_2-j_3-l)!\,(j_1-m_1-l)!\,(j_2+m_2-l)!\,(j_3-j_2+m_1+l)!\,(j_3-j_1-m_2+l)!}\right]. \end{aligned}$$

➢ Wigner 6–j symbol: Edmonds (1957) displays the following epxression for the computation of a Wigner 6–j symbol

$$\begin{Bmatrix} j_1 & j_2 & j_3 \\ l_1 & l_2 & l_3 \end{Bmatrix} = \Delta(j_1,j_2,j_3)\,\Delta(j_1,l_2,l_3)\,\Delta(l_1,j_2,l_3)\,\Delta(l_1,l_2,j_3)\sum_l \left[\frac{(-1)^l\,(\ell+1)!}{(l-j_1-j_2-j_3)!\,(l-j_1-l_2-l_3)!}\right.$$

$$\left. \times \frac{1}{(l-l_1-j_2-l_3)!\,(l-l_1-l_2-j_3)!(j_1+j_2+l_1+l_2-l)!\,(j_2+j_3+l_2+l_3-l)!\,(j_3+j_1+l_3+l_1-l)!}\right] .$$

➢ Wigner 9–j symbol: The Wigner 9–j symbol with numeric arguments is usually calculated by the known sum rule over three Wigner 6–j symbols and is zero unless the arguments in each row and column satisfy the triangular relation

$$\begin{Bmatrix} j_{11} & j_{12} & j_{13} \\ j_{21} & j_{22} & j_{23} \\ j_{31} & j_{32} & j_{33} \end{Bmatrix} = \sum_j (-1)^{2j} \begin{Bmatrix} j_{11} & j_{21} & j_{31} \\ j_{32} & j_{33} & j \end{Bmatrix} \begin{Bmatrix} j_{12} & j_{22} & j_{32} \\ j_{21} & j & j_{23} \end{Bmatrix} \begin{Bmatrix} j_{13} & j_{23} & j_{33} \\ j & j_{11} & j_{12} \end{Bmatrix} .$$

Explicit formulas and expansions of the Wigner rotation matrices $d^j_{pq}(\beta)$:

➢ Below, we display six explicit expansions of the Wigner rotation matrices in alphabetical order.

➢ Asymptotic expansion of d^j_{pq} for $j \gg 1$: There are three asymptotics expansion of Wigner rotation matrices as displayed by Varshalovich *et al.* (1988, Eqs. 4.18.1–4). For $j \gg 1$, for instance, the Wigner rotation matrix can be written as

$$d^j_{p\,q}(\beta) \approx \xi_{p\,q}\sqrt{\frac{s!(s+\mu+\nu)!}{(s+\mu)!(s+\nu)!}}\sqrt{\frac{2}{\pi s}}\,\frac{\cos\left[\left(s+\frac{\mu+\nu+1}{2}\right)\beta - \frac{\pi}{4}(2\mu+1)\right]}{\sqrt{\sin\beta}} + O\left(\frac{1}{J^{\frac{3}{2}}}\right) ,$$

and where μ, ν, and s are related to p, q, and j as follows

$$\mu = |p-q|, \qquad \nu = |p+q|, \qquad s = j - \frac{1}{2}(\mu+\nu), \qquad \xi_{pq} = \begin{cases} 1 & \text{if } q \geq p, \\ (-1)^{q-p} & \text{if } q < p. \end{cases}$$

➢ Asymptotic expansion of d^j_{pq} for $J \to \infty$ and $\beta \to 0$: A second expansion for $j\,\beta < \infty$ is given in terms of the Bessel functions $J_n(x)$ by

$$d^j_{p\,q}(\beta) \approx J_{p-q}(j\beta)$$

➢ Asymptotic expansion of d^{j}_{pq} for small variations of the rotation axis:

$$d^{j}_{p\,q}(\beta) \;\approx\; \frac{\xi_{p\,q}}{\mu!}\sqrt{\frac{(s+\mu+\nu)!(s+\mu)!}{s!(s+\nu)!}}\left(\frac{\beta}{2}\right)^{\mu}\left\{1-\frac{2s(s+\mu+\nu+1)+\nu(\mu+1)}{2(\mu+1)}\left(\frac{\beta}{2}\right)^{2}+\ldots\right\}, \qquad \beta \;\to\; 0$$

$$d^{j}_{p\,q}(\beta) \;\approx\; \frac{(-1)^{s}\xi_{p\,q}}{\nu!}\sqrt{\frac{(s+\mu+\nu)!(s+\nu)!}{s!(s+\nu)!}}\left(\frac{\pi-\beta}{2}\right)^{\mu}\left\{1-\frac{2s(s+\mu+\nu+1)+\mu(\nu+1)}{2(\nu+1)}\left(\frac{\pi-\beta}{2}\right)^{2}+\ldots\right\}, \qquad \beta-\pi \;\to\; 0$$

➢ Clebsch-Gordan series expansion of products of two $d^{j}_{pq}(\beta)$ with equal arguments: Products of two Wigner rotation matrices with equal angular arguments can be expanded in terms of their uncoupled and coupled representations, i.e. by means of the Clebsch-Gordan coefficient. When expressed in terms of the Wigner 3–j symbols, the product of two Wigner rotation matices (with equal angular arguments) are given by

$$d^{j_1}_{p_1\,q_1}(\beta)\,d^{j_2}_{p_2\,q_2}(\beta) \;=\; \sum_{J\,P\,Q}(-1)^{-2J+2j_2-p_2-q_2}\,(2j_2+1)\begin{pmatrix} J & j_2 & j_2 \\ P & p_2 & -p_2\end{pmatrix}\begin{pmatrix} J & j_2 & j_2 \\ Q & q_2 & -q_2\end{pmatrix} d^{J}_{PQ}(\beta)$$

in terms of two Wigner 3-j symbols and one Wigner rotation matix $d^{J}_{PQ}(\beta)$. For $\beta = \frac{\pi}{2}$, in particular, the magnetic quantum numbers can be replaced by $j_1 = j_2 = j$, $p_1 = p_2 = p$ and $q_1 = q_2 = q$, and this gives rise to the expansion

$$\left(d^{j}_{p\,q}(\frac{\pi}{2})\right)^{2} \;=\; \sum_{J=0,2,4,\ldots}(-1)^{J+2j+2p}\,(2j+1)\,\frac{(J-1)!!}{J!!}\begin{pmatrix} J & j & j \\ 0 & p & p\end{pmatrix}\begin{pmatrix} J & j & j \\ 0 & q & q\end{pmatrix}.$$

Such expansion relates the Wigner rotation matrices to the Wigner n–j symbols. These two expansions are displayed in Varshalovich *et al.* (1988, Eq. 4.6.1 and Eq. 4.16.9), although expressed in terms of Clebsch-Gordan coefficients.

Expansions of the spherical harmonics:

➢ Varshalovich *et al.* (1988, section 5.2) shows several explicit formulas for computing the spherical harmonicfor $Y_{\ell m}(\vartheta,\varphi)$ with given integers ℓ and m, and where the summation runs over all terms with non-negative factorials.

➢ Expansion of $Y_{\ell m}(\vartheta,\varphi)$ in terms of $\sin\vartheta$: Varshalovich *et al.* (1988, Eq. 5.2.17)

$$Y_{\ell m}(\vartheta,\varphi) = e^{im\varphi}\sqrt{\frac{2\ell+1}{4\pi\,(\ell+m)!\,(\ell-m)!}}\begin{cases}\sum_{s=|m|,|m|+2,\ldots}^{\ell}(-1)^{\frac{s+m}{2}}\frac{(\ell+s)!}{(s+m)!!\,(s-m)!!}\cdot\frac{(\ell+m)!!\,(\ell-m)!!}{(\ell+s)!!\,(\ell-s)!!}(\sin\vartheta)^s & \text{if } \ell-m \text{ is even,}\\ \cos\vartheta\sum_{s=|m|,|m|+2,\ldots}^{\ell-1}(-1)^{\frac{s+m}{2}}\frac{(\ell+s)!}{(s+m)!!\,(s-m)!!}\cdot\frac{(\ell+m-1)!!\,(\ell-m-1)!!}{(\ell+s-1)!!\,(\ell-s-1)!!}(\sin\vartheta)^s & \text{if } \ell-m \text{ is odd.}\end{cases}$$

➢ Expansion of $Y_{\ell m}(\vartheta,\varphi)$ in terms of $\sin\vartheta$ and $\cos\vartheta$: Cf. Varshalovich *et al.* (1988, Eq. 5.2.19) with a polynomial in $\cos\vartheta$

$$Y_{\ell m}(\vartheta,\varphi) = e^{im\varphi}\sqrt{\frac{2\ell+1}{4\pi}\frac{(\ell-m)!}{(\ell+m)!}}(\sin\vartheta)^m \sum_{\substack{s\\ \ell+m-s \text{ even}}}(-1)^{\frac{\ell+m-s}{2}}\frac{(\ell+m+s-1)!!}{(\ell-m-s)!!}\frac{(\cos\vartheta)^s}{s!}$$

15.2. In JAC implemented symbolic evaluations of Racah algebra expressions

15.2.a. Strategies in the symbolic evaluation of expressions from Racah's algebra

Strategies for simplification:

➢ For the successful simplification of expressions from Racah's algebra, one need often to exploit the orthogonality relations as well as a variety of important sum rules. The literature about Racah's algebra is therefore devoted to a large extent in order to find and to prove proper relations among the Wigner symbols and/or to compile them in some applicable form.

➢ Standard presentation of orthogonality and sum rules: The standard presentation of the different orthogonality and sum rules, as they are diaplayed below, gives a first impression how complex expressions can be rewritten in a simpler form. In practice, however, these standard forms are often not of great help since one first need to recognize the equivalence of some part of a Racah algebra expression, for instance with one side of a given sum rule, before this special rule can be applied.

➢ A numerical evaluation of a Racah expression is of couse not possible as long as the input angular momentum quantum numbers are specified numerically. On the other hand, the main strength of using the techniques of Racah's algebra techniques is that such expressions can often be simplified considerably by algebraic transformations.

➢ Understanding the symmetries and properties of Wigner symbols, three different strategies for the simplification can be derived quite easily:

(i) Use of known special values. This replaces a Wigner $3n$–$j$symbol by a (much) simpler expression that, in particular, does not contain any implicit summation. For this strategy, each Wigner $3n$–j symbol can be analysed and perhaps replaced independently by some special-value rules.

(ii) Use of orthogonality properties.

(iii) Use of sum rules.

➢ The main obstacle in applying the strategies (ii) and (iii) is that these strategies require a careful analysis of the Racah expression as a whole. Since all orthogonality relations and sum rules include summations over formal quantum numbers, all summation variables not only have to be in the correct position in the Wigner $3n$–j-symbols, but they must also contribute to a correct phase and weight of the overall expression. Moreover, the same variables may not occur in other Wigner symbols of the Racah expression which are not part of the selected rule.

➢ These difficulties in the simplification process are further enhanced by the large number of equivalent forms of the total Racah expression due to the symmetries of the Wigner $3n$–j symbols. Therefore, in order to simplify a Racah expression by a given sum rule, in practice one has to start with a certain part of the expression and then try to identify equivalence with some relation by means of the various symmetries of the $3n$–j symbols.

➢ Once the equivalence has been proven, this part of the Racah expression can be replaced by a corresponding simpler term. In this context, simplification of a Racah expression always means to 'reduce' the number of summation indices and/or the number of Wigner $3n$–j symbols.

➢ Aim of symbolic transformations: The aim of these symbolic transformation is to obtain an *optimum* summation formula in the sense of a minimal number of Wigner 6–j symbols and/or summation variables.

➢ Results of the simplification process: The results of the simplification process will be provided as Racah expressions and may thus immediatly be used for further derivations and calculations within the theory of angular momentum.

➢ This rather cumbersome procedure of running through all symmetric forms of a Racah expression and of identifying algebraic equivalent parts makes the simplification of such expressions very suitable for symbolic evaluations. An efficient scheme to perform simplifications of Racah expressions by means of the steps (i-iii) is aimed to be realized by the symbolic evaluations of the JAC tools.

➢ A major difficulty for the simplification of general Racah expressions arise from the large number of symmetric forms of the total expression which is the direct result of the symmetries of the Wigner $3n$–j symbols. Apart from the so-called classical symmetries of the Wigner $n-j$ symbols, there are additional symmetries known due to Regge for the 3–j and 6–j symbols; cf. section 15.1.c. These symmetries need to be exploited in order to simplify general Racah algebra expressions. In JAC, we shall keep the distinction between the classical symmetries

and those due to Regge since the classical ones are by far more important for all practical purposes; as mentioned above, we onsider the classical symmetries to be a subset of the Regge symmetries.

15.3. In JAC partly-implemented symbolic evaluations of Racah algebra expressions

15.3.a. Recursive relations for the Wigner $3n$–j symbols and rotation matrices

Recursion relations of the Wigner 3–j symbols:

➢ Four recursion relations of the Wigner 3–j symbols are listed by Rotenberg *et al.* (1959, Eqs. 1.45–1.48), and where we use $J = j_1 + j_2 + j_3$.

➢ Half-integer recursion: This recursion relation decreases two j-values by 1/2

$$[(J+1)(J-2j_1)]^{1/2} \begin{pmatrix} j_1 & j_2 & j_3 \\ m_1 & m_2 & m_3 \end{pmatrix}$$

$$= [(j_2+m_2)(j_3-m_3)]^{1/2} \begin{pmatrix} j_1 & j_2-1/2 & j_3-1/2 \\ m_1 & m_2-1/2 & m_3+1/2 \end{pmatrix} - [(j_2-m_2)(j_3+m_3)]^{1/2} \begin{pmatrix} j_1 & j_2-1/2 & j_3-1/2 \\ m_1 & m_2+1/2 & m_3-1/2 \end{pmatrix}.$$

➢ Louck's (1958) half-integer recursion:

$$(j_2+m_2)^{1/2}\,(2j_3+1) \begin{pmatrix} j_1 & j_2 & j_3 \\ m_2-m_3 & -m_2 & m_3 \end{pmatrix} = - [(J-2j_1)(J+1)(j_3+m_3)]^{1/2} \begin{pmatrix} j_1 & j_2-1/2 & j_3-1/2 \\ m_2-m_3 & -m_2+1/2 & m_3-1/2 \end{pmatrix}$$

$$- [(J-2j_3)(J-2j_2+1)(J+1)(j_3-m_3+1)]^{1/2} \begin{pmatrix} j_1 & j_2-1/2 & j_3+1/2 \\ m_2-m_3 & -m_2+1/2 & m_3-1/2 \end{pmatrix}.$$

➢ Integer recursion: A decrease of a single j-values by 1 is made with

$$[(J+1)(J-2j_1)(J-2j_2)(J-2j_3+1)]^{1/2} \begin{pmatrix} j_1 & j_2 & j_3 \\ m_1 & m_2 & m_3 \end{pmatrix}$$

$$= [(j_2-m_2)(j_2+m_2+1)(j_3+m_3)(j_3+m_3-1)]^{1/2} \begin{pmatrix} j_1 & j_2 & j_3-1 \\ m_1 & m_2+1 & m_3-1 \end{pmatrix} - 2m_2 [(j_3+m_3)(j_3-m_3)]^{1/2} \begin{pmatrix} j_1 & j_2 & j_3-1 \\ m_1 & m_2 & m_3 \end{pmatrix}$$

$$- [(j_2+m_2)(j_2-m_2+1)(j_3-m_3)(j_3-m_3-1)]^{1/2} \begin{pmatrix} j_1 & j_2 & j_3-1 \\ m_1 & m_2-1 & m_3+1 \end{pmatrix}.$$

➢ Magnetic recursion: A recursion relation with regard to the magnetic quantum numbers reads:

$$- [(j_3+m_1+m_2+1)(j_3-m_1-m_2)]^{1/2} \begin{pmatrix} j_1 & j_2 & j_3 \\ m_1 & m_2 & -m_3+1 \end{pmatrix}$$

$$= [(j_1+m_1+1)(j_1-m_1)]^{1/2} \begin{pmatrix} j_1 & j_2 & j_3 \\ m_1 & m_2+1 & -m_3 \end{pmatrix} + [(j_2+m_2+1)(j_2-m_2)]^{1/2} \begin{pmatrix} j_1 & j_2 & j_3 \\ m_1+1 & m_2 & -m_3 \end{pmatrix}.$$

Recursion relations of the Wigner 6–j symbols:

➢ No explicit recurrance relation has yet been considered for the Wigner 6–j symbols.

Recursion relations of the Wigner 9–j symbols:

➢ A single recursion relation among the Wigner 9–j symbols is shown by Rotenberg *et al.* (1959, Eq. 3.24).

$$\begin{Bmatrix} s & s & 1 \\ l_1 & l_2 & L \\ j_1 & j_2 & L \end{Bmatrix} = \frac{l_1(l_1+1)+j_2(j_2+1)-j_1(j_1+1)-l_2(l_2+1)}{2\,[s(s+1)(2s+1)L(L+1)(2L+1)]^{1/2}} \begin{Bmatrix} s & s & 0 \\ l_1 & l_2 & L \\ j_1 & j_2 & L \end{Bmatrix}.$$

Recursion relations of the spherical harmonics:

➢ Recursion relations: Cf. Varshalovich *et al.* (1988, Eqs. 5.7.1–2)

$$\cos\vartheta\, Y_{\ell m}(\vartheta,\varphi) = \sqrt{\frac{(\ell-m+1)\,(\ell+m+1)}{(2\ell+1)\,(2\ell+3)}}\, Y_{\ell+1,m}(\vartheta,\varphi) + \sqrt{\frac{(\ell-m)\,(\ell+m)}{(2\ell-1)\,(2\ell+1)}}\, Y_{\ell-1,m}(\vartheta,\varphi)$$

$$-2m\,\cos\vartheta\, Y_{\ell m}(\vartheta,\varphi) = \sqrt{l\,(\ell+1)-m\,(m+1)}\, e^{-i\varphi}\, Y_{\ell,m+1}(\vartheta,\varphi) + \sqrt{l\,(\ell+1)-m\,(m-1)}\, e^{i\varphi}\, Y_{\ell,m-1}(\vartheta,\varphi)\,.$$

15.3.b. Special values of the Wigner $3n$–j symbols and rotation matrices

Special values of the Wigner 3–j symbols:

➢ Edmonds (1957, appendix 2) lists the following 20 special values for 3–j symbols

$$\begin{pmatrix} j_1 & j_2 & j_3 \\ 0 & 0 & 0 \end{pmatrix} = (-1)^{J/2} \left[\frac{(j_1+j_2-j_3)!(j_1+j_3-j_2)!(j_2+j_3-j_1)!}{(j_1+j_2+j_3+1)!} \right]^{1/2} \frac{(J/2)!}{(J/2-j_1)!\,(J/2-j_2)!\,(J/2-j_3)!}$$

$$\begin{pmatrix} j_1 & j_2 & j_3 \\ 0 & 0 & 0 \end{pmatrix} = 0 \qquad \begin{cases} \text{if} \quad J = j_1+j_2+j_3 & \text{is even} \\ \text{if} \quad J = j_1+j_2+j_3 & \text{is odd} \end{cases}$$

$$\begin{pmatrix} J+1/2 & J & 1/2 \\ M & -M-1/2 & 1/2 \end{pmatrix} = (-1)^{J-M-1/2} \left[\frac{J-M+1/2}{(2J+2)(2J+1)} \right]^{1/2}$$

$$\begin{pmatrix} J+1 & J & 1 \\ M & -M-1 & 1 \end{pmatrix} = (-1)^{J-M-1} \left[\frac{(J-M)(J-M+1)}{(2J+3)(2J+2)(2J+1)} \right]^{1/2}$$

$$\begin{pmatrix} J+1 & J & 1 \\ M & -M & 0 \end{pmatrix} = (-1)^{J-M-1} \left[\frac{2(J+M+1)(J-M+1)}{(2J+3)(2J+2)(2J+1)} \right]^{1/2}$$

$$\begin{pmatrix} J & J & 1 \\ M & -M-1 & 1 \end{pmatrix} = (-1)^{J-M} \left[\frac{2(J-M)(J+M+1)}{(2J+2)(2J+1)(2J)} \right]^{1/2}$$

$$\begin{pmatrix} J & J & 1 \\ M & -M & 0 \end{pmatrix} = (-1)^{J-M} \frac{M}{[(2J+1)(J+1)J]^{1/2}}$$

$$\begin{pmatrix} J+3/2 & J & 3/2 \\ M & -M-3/2 & 3/2 \end{pmatrix} = (-1)^{J-M+1/2} \left[\frac{(J-M-1/2)(J-M+1/2)(J-M+3/2)}{(2J+4)(2J+3)(2J+2)(2J+1)} \right]^{1/2}$$

$$\begin{pmatrix} J+3/2 & J & 3/2 \\ M & -M-1/2 & 1/2 \end{pmatrix} = (-1)^{J-M+1/2} \left[\frac{3(J-M+1/2)(J-M+3/2)(J+M+3/2)}{(2J+4)(2J+3)(2J+2)(2J+1)} \right]^{1/2}$$

$$\begin{pmatrix} J+1/2 & J & 3/2 \\ M & -M-3/2 & 3/2 \end{pmatrix} = (-1)^{J-M-1/2} \left[\frac{3(J-M-1/2)(J-M+1/2)(J+M+3/2)}{(2J+3)(2J+2)(2J+1)(2J)}\right]^{1/2}$$

$$\begin{pmatrix} J+1/2 & J & 3/2 \\ M & -M-1/2 & 1/2 \end{pmatrix} = (-1)^{J-M-1/2} \left[\frac{(J-M+1/2)}{(2J+3)(2J+2)(2J+1)(2J)}\right]^{1/2} (J+3M+3/2)$$

$$\begin{pmatrix} J+2 & J & 2 \\ M & -M-2 & 2 \end{pmatrix} = (-1)^{J-M} \left[\frac{(J-M-1)(J-M)(J-M+1)(J-M+2)}{(2J+5)(2J+4)(2J+3)(2J+2)(2J+1)}\right]^{1/2}$$

$$\begin{pmatrix} J+2 & J & 2 \\ M & -M-1 & 1 \end{pmatrix} = (-1)^{J-M}\, 2 \left[\frac{(J+M+2)(J-M+2)(J-M+1)(J-M)}{(2J+5)(2J+4)(2J+3)(2J+2)(2J+1)}\right]^{1/2}$$

$$\begin{pmatrix} J+2 & J & 2 \\ M & -M & 0 \end{pmatrix} = (-1)^{J-M} \left[\frac{6(J+M+2)(J+M+1)(J-M+2)(J-M+1)}{(2J+5)(2J+4)(2J+3)(2J+2)(2J+1)}\right]^{1/2}$$

$$\begin{pmatrix} J+1 & J & 2 \\ M & -M-2 & 2 \end{pmatrix} = (-1)^{J-M+1}\, 2 \left[\frac{(J-M-1)(J-M)(J-M+1)(J+M+2)}{(2J+4)(2J+3)(2J+2)(2J+1)(2J)}\right]^{1/2}$$

$$\begin{pmatrix} J+1 & J & 2 \\ M & -M-1 & 1 \end{pmatrix} = (-1)^{J-M+1}\, 2\,(J+2M+2) \left[\frac{(J-M+1)(J-M)}{(2J+4)(2J+3)(2J+2)(2J+1)(2J)}\right]^{1/2}$$

$$\begin{pmatrix} J+1 & J & 2 \\ M & -M & 0 \end{pmatrix} = (-1)^{J-M+1}\, 2M \left[\frac{6(J+M+1)(J-M+1)}{(2J+4)(2J+3)(2J+2)(2J+1)(2J)}\right]^{1/2}$$

$$\begin{pmatrix} J & J & 2 \\ M & -M-2 & 2 \end{pmatrix} = (-1)^{J-M} \left[\frac{6(J-M-1)(J-M)(J+M+1)(J+M+2)}{(2J+3)(2J+2)(2J+1)(2J)(2J-1)}\right]^{1/2}$$

$$\begin{pmatrix} J & J & 2 \\ M & -M-1 & 1 \end{pmatrix} = (-1)^{J-M}\,(1+2M) \left[\frac{6(J+M+1)(J-M)}{(2J+3)(2J+2)(2J+1)(2J)(2J-1)}\right]^{1/2}$$

$$\begin{pmatrix} J & J & 2 \\ M & -M & 0 \end{pmatrix} = (-1)^{J-M}\, \frac{2\left[3M^2 - J(J+1)\right]}{\left[(2J+3)(2J+2)(2J+1)(2J)(2J-1)\right]^{1/2}}$$

Special values of the Wigner 6–j symbols:

➢ Edmonds (1957, appendix 2, table 5) displays the following 19 special values for 6–j symbols; in this list, moreover, we use $s = a + b + c$.

$$\begin{Bmatrix} a & b & c \\ 1 & c-1 & b-1 \end{Bmatrix} = (-1)^s \left[\frac{s(s+1)(s-2a-1)(s-2a)}{(2b-1)2b(2b+1)(2c-1)2c(2c+1)} \right]^{1/2}$$

$$\begin{Bmatrix} a & b & c \\ 1 & c-1 & b \end{Bmatrix} = (-1)^s \left[\frac{2(s+1)(s-2a)(s-2b)(s-2c+1)}{2b(2b+1)(2b+2)(2c-1)2c(2c+1)} \right]^{1/2}$$

$$\begin{Bmatrix} a & b & c \\ 1 & c-1 & b+1 \end{Bmatrix} = (-1)^s \left[\frac{(s-2b-1)(s-2b)(s-2c+1)(s-2c+2)}{(2b+1)(2b+2)(2b+3)(2c-1)2c(2c+1)} \right]^{1/2}$$

$$\begin{Bmatrix} a & b & c \\ 1 & c & b \end{Bmatrix} = (-1)^{s+1} \frac{2\left[b(b+1)+c(c+1)-a(a+1)\right]}{\left[2b(2b+1)(2b+2)2c(2c+1)(2c+2)\right]^{1/2}}$$

$$\begin{Bmatrix} a & b & c \\ 3/2 & c-3/2 & b-3/2 \end{Bmatrix} = (-1)^s \left[\frac{(s-1)s(s+1)(s-2a-2)(s-2a-1)(s-2a)}{(2b-2)(2b-1)2b(2b+1)(2c-2)(2c-1)2c(2c+1)} \right]^{1/2}$$

$$\begin{Bmatrix} a & b & c \\ 3/2 & c-3/2 & b-1/2 \end{Bmatrix} = (-1)^s \left[\frac{3s(s+1)(s-2a-1)(s-2a)(s-2b)(s-2c+1)}{(2b-1)2b(2b+1)(2b+2)(2c-2)(2c-1)2c(2c+1)} \right]^{1/2}$$

$$\begin{Bmatrix} a & b & c \\ 3/2 & c-3/2 & b+1/2 \end{Bmatrix} = (-1)^s \left[\frac{3(s+1)(s-2a)(s-2b-1)(s-2b)}{2b(2b+1)(2b+2)(2b+3)} \right]^{1/2} \left[\frac{(s-2c+1)(s-2c+2)}{(2c-2)(2c-1)2c(2c+1)} \right]^{1/2}$$

$$\begin{Bmatrix} a & b & c \\ 3/2 & c-3/2 & b+3/2 \end{Bmatrix} = (-1)^s \left[\frac{(s-2b-2)(s-2b-1)(s-2b)}{(2b+1)(2b+2)(2b+3)(2b+4)} \right]^{1/2} \left[\frac{(s-2c+1)(s-2c+2)(s-2c+3)}{(2c-2)(2c-1)2c(2c+1)} \right]^{1/2}$$

$$\begin{Bmatrix} a & b & c \\ 3/2 & c-1/2 & b-1/2 \end{Bmatrix} = (-1)^s \frac{\left[2(s-2b)(s-2c)-(s+2)(s-2a-1)\right]\ \left[(s+1)(s-2a)\right]^{1/2}}{\left[(2b-1)(2b)(2b+1)(2b+2)(2c-1)2c(2c+1)(2c+2)\right]^{1/2}}$$

$$\begin{Bmatrix} a & b & c \\ 3/2 & c-1/2 & b+1/2 \end{Bmatrix} = (-1)^s \frac{[(s-2b-1)(s-2c)-2(s+2)(s-2a)]}{[2b(2b+1)(2b+2)(2b+3)]^{1/2}} \frac{[(s-2b)(s-2c+1)]^{1/2}}{[2c(2c+1)(2c+2)(2c-1)]^{1/2}}$$

$$\begin{Bmatrix} a & b & c \\ 2 & c-2 & b-2 \end{Bmatrix} = (-1)^s \left[\frac{(s-2)(s-1)s(s+1)(s-2a-3)}{(2b-3)(2b-2)(2b-1)2b(2b+1)}\right]^{1/2} \left[\frac{(s-2a-2)(s-2a-1)(s-2a)}{(2c-3)(2c-2)(2c-1)2c(2c+1)}\right]^{1/2}$$

$$\begin{Bmatrix} a & b & c \\ 2 & c-2 & b-1 \end{Bmatrix} = (-1)^s\, 2 \left[\frac{(s-1)s(s+1)(s-2a-2)(s-2a-1)}{(2b-2)(2b-1)2b(2b+1)(2b+2)}\right]^{1/2} \left[\frac{(s-2a)(s-2b)(s-2c+1)}{(2c-3)(2c-2)(2c-1)2c(2c+1)}\right]^{1/2}$$

$$\begin{Bmatrix} a & b & c \\ 2 & c-2 & b \end{Bmatrix} = (-1)^s \left[\frac{6s(s+1)(s-2a-1)(s-2b-1)(s-2a)(s-2b)}{(2b-1)2b(2b+1)(2b+2)(2b+3)}\right]^{1/2} \left[\frac{(s-2c+1)(s-2c+2)}{(2c-3)(2c-2)(2c-1)2c(2c+1)}\right]^{1/2}$$

$$\begin{Bmatrix} a & b & c \\ 2 & c-2 & b+1 \end{Bmatrix} = (-1)^s\, 2 \left[\frac{(s+1)(s-2a)(s-2b-2)(s-2b-1)(s-2b)}{2b(2b+1)(2b+2)(2b+3)(2b+4)}\right]^{1/2} \left[\frac{(s-2c+1)(s-2c+2)(s-2c+3)}{(2c-3)(2c-2)(2c-1)2c(2c+1)}\right]^{1/2}$$

$$\begin{Bmatrix} a & b & c \\ 2 & c-2 & b+2 \end{Bmatrix} = (-1)^s \left[\frac{(s-2b-3)(s-2b-2)(s-2b-1)(s-2b)}{(2b+1)(2b+2)(2b+3)(2b+4)(2b+5)}\right]^{1/2} \left[\frac{(s-2c+1)(s-2c+2)(s-2c+3)(s-2c+4)}{(2c-3)(2c-2)(2c-1)2c(2c+1)}\right]^{1/2}$$

$$\begin{Bmatrix} a & b & c \\ 2 & c-1 & b-1 \end{Bmatrix} = (-1)^s\, 4 \frac{[(a+b)(a-b+1)-(c-1)(c-b+1)]}{[(2b-2)(2b-1)2b(2b+1)(2b+2)]^{1/2}} \left[\frac{s(s+1)(s-2a-1)(s-2a)}{(2c-2)(2c-1)2c(2c+1)(2c+2)}\right]^{1/2}$$

$$\begin{Bmatrix} a & b & c \\ 2 & c-1 & b \end{Bmatrix} = (-1)^s\, 2 \frac{\left[(a+b+1)(a-b)-c^2+1\right]}{[(2b-1)2b(2b+1)(2b+2)(2b+3)]^{1/2}} \left[\frac{6(s+1)(s-2a)(s-2b)(s-2c+1)}{(2c-2)(2c-1)2c(2c+1)(2c+2)}\right]^{1/2}$$

$$\begin{Bmatrix} a & b & c \\ 2 & c-1 & b+1 \end{Bmatrix} = (-1)^s\, 4 \frac{[(a+b+2)(a-b-1)-(c-1)(b+c+2)]}{[2b(2b+1)(2b+2)(2b+3)(2b+4)]^{1/2}} \left[\frac{(s-2b-1)(s-2b)(s-2c+1)(s-2c+2)}{(2c-2)(2c-1)2c(2c+1)(2c+2)}\right]^{1/2}$$

$$\begin{Bmatrix} a & b & c \\ 2 & c & b \end{Bmatrix} = (-1)^s \frac{2}{[(2b-1)2b(2b+1)(2b+2)(2b+3)]^{1/2}} \frac{[3X(X-1)-4b(b+1)c(c+1)]}{[(2c-1)2c(2c+1)(2c+2)(2c+3)]^{1/2}}$$

and where we use $s = a+b+c$ and $X = b(b+1)+c(c+1)-a(a+1)$ in the last relation.

Special values of the Wigner 9–j symbols:

➢ One special value for a Wigner 9–j symbol reads as

$$\begin{Bmatrix} a & b & 0 \\ c & d & 0 \\ e & f & 0 \end{Bmatrix} = \delta_{ab}\,\delta_{cd}\,\delta_{ef}\frac{\delta(a,c,e)}{[a,c,e]^{1/2}}\,.$$

➢ Another special value for the Wigner 9–j symbols is given by Varshalovich *et al.* (1988, Eq. 10.9.1)

$$\begin{Bmatrix} a & b & c \\ d & e & f \\ g & h & 0 \end{Bmatrix} = \delta_{cf}\,\delta_{gh}\frac{(-1)^{b+c+e+f}}{[c,g]^{1/2}}\begin{Bmatrix} a & b & c \\ e & d & g \end{Bmatrix}\,.$$

15.3.c. Orthogonality and sum rules of the Wigner $3n$–j symbols

Remarks:

➢ A rather comprehensive set of sum rules for the Wigner n–j symbols is given by Varshalovich *et al.* (1988, chapter 12). These rules are most easily be ordered by the number of Wigner n–j symbols that contribute to a given rule. For the case of an equal numbers of such symbols, we further classify these rules by the type of the Wigner symbols.

➢ Orthogonality relations: The Wigner n–j symbols fulfill a variety of orthogonality relations. Two such relations are known for the Wigner 3–j symbols as well as one orthogonality relation for each, the Wigner 6–j and 9–j symbols. Because these orthogonalities have formally the same structure like all other sum rules of the Wigner n–j symbols, they are all treated together in the JAC program.

Sum rules with one Wigner 3–j, 6–j or 9–j symbol:

➢ Sum rules with one 3–j symbol: Varshalovich *et al.* (1988, Eq. 12.1.2) shows one sum rule with one 3–j symbol

$$\sum_m (-1)^{j-m} \begin{pmatrix} j & j & j' \\ m & -m & m' \end{pmatrix} = [j]^{1/2}\ \delta_{m'0}\,\delta_{j'0}\,.$$

➢ Sum rules with one 6–j symbol: Rotenberg *et al.* (1959, Eqs. 2.9–10) show sum rules with one 6–j symbol. A more general form is given by Varshalovich *et al.* (1988, Eqs. 12.2.3–4)

$$\sum_X [X] \begin{Bmatrix} a & b & X \\ a & b & c \end{Bmatrix} = (-1)^{2c}\,\delta(a,b,c)$$

$$\sum_X (-1)^{a+b+X}\ [X] \begin{Bmatrix} a & b & X \\ b & a & c \end{Bmatrix} = [a,b]^{1/2}\ \delta_{c0}\,.$$

➢ Sum rules with one 9–j symbol: Varshalovich *et al.* (1988, Eqs. 12.2.5–6) give two sum rules with one 9–j symbol

$$\sum_X [X] \begin{Bmatrix} a & b & e \\ c & d & f \\ e & f & X \end{Bmatrix} = \frac{\delta_{bc}}{[b]}\ \delta(a,b,e)\,\delta(b,d,f)$$

$$\sum_X (-1)^{a+b+c+d-X}\ [X] \begin{Bmatrix} a & b & e \\ c & d & f \\ f & e & X \end{Bmatrix} = \frac{\delta_{ad}}{[a]}\ \delta(d,b,e)\,\delta(a,c,f)\,.$$

Sum rules with two 3–j, 6–j and/or 9–j symbols:

➢ Orthogonality of two 3–j symbols: Two orthogonality relations for 3–j symbols are given by Rotenberg *et al.* (1959, Eqs. 1.13–14) as well as by Varshalovich *et al.* (1988, Eqs. 12.1.3–4)

$$\sum_{j_3 m_3} (2j_3+1) \begin{pmatrix} j_1 & j_2 & j_3 \\ m_1 & m_2 & m_3 \end{pmatrix} \begin{pmatrix} j_1 & j_2 & j_3 \\ m_1' & m_2' & m_3 \end{pmatrix} = \delta(m_1, m_1')\, \delta(m_2, m_2')$$

$$\sum_{m_1 m_2} \begin{pmatrix} j_1 & j_2 & j_3 \\ m_1 & m_2 & m_3 \end{pmatrix} \begin{pmatrix} j_1 & j_2 & j_3' \\ m_1 & m_2 & m_3' \end{pmatrix} = \frac{\delta(j_3, j_3')\, \delta(m_3, m_3')}{(2j_3+1)}\, \delta(j_1, j_2, j_3)\,.$$

➢ Orthogonality of two 6–j symbols: An orthogonality relation for the Wigner 6–j symbols is given by Rotenberg *et al.* (1959, Eq. 2.6) as well as by Varshalovich *et al.* (1988, Eq. 12.2.7)

$$\sum_X [X] \begin{Bmatrix} a & b & X \\ c & d & p \end{Bmatrix} \begin{Bmatrix} c & d & X \\ a & b & q \end{Bmatrix} = \frac{\delta_{pq}}{[p]}\, \delta(a,d,p)\, \delta(b,c,p)\,.$$

➢ Sum rules with two 6–j symbols: Rotenberg *et al.* (1959, Eq. 2.7) as well as Varshalovich *et al.* (1988, Eq. 12.2.8) gives a sum rule for two 6–j symbols

$$\sum_X (-1)^{p+q+X}\, [X] \begin{Bmatrix} a & b & X \\ c & d & p \end{Bmatrix} \begin{Bmatrix} c & d & X \\ b & a & q \end{Bmatrix} = \begin{Bmatrix} c & a & q \\ d & b & p \end{Bmatrix}.$$

➢ Sum rules with two 6–j symbols: Varshalovich *et al.* (1988, Eq. 12.2.15) show a sum rule including a triple summation over a 6–j symbol

$$\sum_{XYZ} [X,Y,Z] \begin{Bmatrix} X & Y & Z \\ a & b & c \end{Bmatrix} \begin{Bmatrix} X & Y & Z \\ a & b & c \end{Bmatrix} = [a,b,c]\,.$$

➢ Sum rules with one 6–j and one 9–j symbol: Varshalovich *et al.* (1988, Eqs. 12.2.9–10) show two sum rules for one 6–j symbol and one

9–j symbol, and with $R = a+b+c+d+e+f+p+q$

$$\sum_X [X] \begin{Bmatrix} a & f & X \\ d & q & e \\ p & c & b \end{Bmatrix} \begin{Bmatrix} a & f & X \\ e & b & s \end{Bmatrix} = (-1)^{2s} \begin{Bmatrix} a & b & s \\ c & d & p \end{Bmatrix} \begin{Bmatrix} c & d & s \\ e & f & q \end{Bmatrix}$$

$$\sum_X (-1)^{R+X} [X] \begin{Bmatrix} a & f & X \\ d & q & e \\ p & c & b \end{Bmatrix} \begin{Bmatrix} a & f & X \\ b & e & s \end{Bmatrix} = (-1)^{2s} \begin{Bmatrix} p & q & s \\ e & a & d \end{Bmatrix} \begin{Bmatrix} p & q & s \\ f & b & c \end{Bmatrix}.$$

Sum rules for three Wigner 3–j, 6–j and/or 9–j symbols:

➢ Sum rules with three 3–j symbols: One such rule is given by Rotenberg *et al.* (1959, Eq. 2.20) as well as by Varshalovich *et al.* (1988, Eq. 2.1.6), and with $S = l_1+l_2+l_3+n_1+n_2+n_3$

$$\sum_{n_1 n_2 n_3} (-1)^S \begin{pmatrix} j_1 & l_2 & l_3 \\ m_1 & n_2 & -n_3 \end{pmatrix} \begin{pmatrix} l_1 & j_2 & l_3 \\ -n_1 & m_2 & n_3 \end{pmatrix} \begin{pmatrix} l_1 & l_2 & j_3 \\ n_1 & -n_2 & m_3 \end{pmatrix} = \begin{pmatrix} j_1 & j_2 & j_3 \\ m_1 & m_2 & m_3 \end{pmatrix} \begin{Bmatrix} j_1 & j_2 & j_3 \\ l_1 & l_2 & l_3 \end{Bmatrix}.$$

➢ Sum rules with two 3–j symbols and one 6–j symbol: One such rule is given by Rotenberg *et al.* (1959, Eq. 2.19) as well as by Varshalovich *et al.* (1988, Eq. 12.1.5)

$$\sum_{l_3 n_3} (-1)^{j_3+l_3+m_1+n_1} [l_3] \begin{Bmatrix} j_1 & j_2 & j_3 \\ l_1 & l_2 & l_3 \end{Bmatrix} \begin{pmatrix} l_1 & j_2 & l_3 \\ n_1 & m_2 & n_3 \end{pmatrix} \begin{pmatrix} j_1 & l_2 & l_3 \\ m_1 & n_2 & -n_3 \end{pmatrix} = \sum_{m_3} \begin{pmatrix} j_1 & j_2 & j_3 \\ m_1 & m_2 & m_3 \end{pmatrix} \begin{pmatrix} l_1 & l_2 & j_3 \\ n_1 & n_2 & -m_3 \end{pmatrix}.$$

➢ Sum rules with three 6–j symbols: There is a sum rule for three 6–j symbols from Biedenharn and Elliot; see also Rotenberg *et al.* (1959, Eq. 2.8) or Varshalovich *et al.* (1988, Eq. 12.2.18), and with $R = a+b+c+d+e+f+p+q+r$

$$\sum_X (-1)^{R+X} [X] \begin{Bmatrix} a & b & X \\ c & d & p \end{Bmatrix} \begin{Bmatrix} c & d & X \\ e & f & q \end{Bmatrix} \begin{Bmatrix} e & f & X \\ b & a & r \end{Bmatrix} = \begin{Bmatrix} p & q & r \\ e & a & d \end{Bmatrix} \begin{Bmatrix} p & q & r \\ f & b & c \end{Bmatrix}.$$

➢ Sum rules with three 6–j symbols: Another sum rules corresponds to the representation of the 9–j symbol in terms of 6–j symbols; see Rotenberg *et al.* (1959, Eq. 3.1) and Varshalovich *et al.* (1988, Eq. 12.2.19)

$$\sum_X (-1)^{2X}\ [X] \begin{Bmatrix} a & b & X \\ c & d & p \end{Bmatrix} \begin{Bmatrix} c & d & X \\ e & f & q \end{Bmatrix} \begin{Bmatrix} e & f & X \\ a & b & r \end{Bmatrix} = \begin{Bmatrix} a & f & r \\ d & q & e \\ p & c & b \end{Bmatrix}.$$

Sum rules with four Wigner 3–j, 6–j and/or 9–j symbols:

➢ Sum rules with three 3–j symbols: Rotenberg *et al.* (1959, Eq. 2.18) as well as Varshalovich *et al.* (1988, Eq. 12.1.8) display the representation of a 6–j symbol in terms of four 3–j symbols, and with $S = l_1 + l_2 + l_3 + n_1 + n_2 + n_3$

$$\begin{Bmatrix} j_1 & j_2 & j_3 \\ l_1 & l_2 & l_3 \end{Bmatrix} = \sum_{m_1 m_2 m_3\, n_1 n_2 n_3} (-1)^S \begin{pmatrix} j_1 & j_2 & j_3 \\ m_1 & m_2 & m_3 \end{pmatrix} \begin{pmatrix} j_1 & l_2 & l_3 \\ m_1 & n_2 & -n_3 \end{pmatrix} \begin{pmatrix} l_1 & j_2 & l_3 \\ -n_1 & m_2 & n_3 \end{pmatrix} \begin{pmatrix} l_1 & l_2 & j_3 \\ n_1 & -n_2 & m_3 \end{pmatrix}$$

$$= \sum_{m_1 m_2\, n_1 n_2 n_3} (-1)^S\ [j_3] \begin{pmatrix} j_1 & j_2 & j_3 \\ m_1 & m_2 & m_3 \end{pmatrix} \begin{pmatrix} j_1 & l_2 & l_3 \\ m_1 & n_2 & -n_3 \end{pmatrix} \begin{pmatrix} l_1 & j_2 & l_3 \\ -n_1 & m_2 & n_3 \end{pmatrix} \begin{pmatrix} l_1 & l_2 & j_3 \\ n_1 & -n_2 & m_3 \end{pmatrix}.$$

➢ Another sum rule for four 3–j symbols is given by Varshalovich *et al.* (1988, Eq. 12.1.9).

$$\sum_{n_r n_p n_q n_s} (-1)^{p-n_p+q-n_q+r-n_r+s-n_s} \begin{pmatrix} p & a & q \\ n_p & n_a & -n_q \end{pmatrix} \begin{pmatrix} q & b & r \\ n_q & n_b & -n_r \end{pmatrix} \begin{pmatrix} r & s & p \\ n_r & n_s & -n_p \end{pmatrix} \begin{pmatrix} s & c & d \\ -n_s & n_c & n_d \end{pmatrix}$$

$$= \begin{Bmatrix} a & b & s \\ r & p & q \end{Bmatrix} \sum_{n_s} \begin{pmatrix} a & s & b \\ n_a & n_s & n_b \end{pmatrix} \begin{pmatrix} d & s & c \\ n_d & -n_s & n_c \end{pmatrix}.$$

➢ A useful relation between 3–j and 9–j symbols is due to de-Shalit; cf. Rotenberg *et al.* (1959, Eq. 3.21) as well as Varshalovich *et al.* (1988, Eq. 12.1.11)

$$\sum_{MNRS} \begin{pmatrix} a & e & g \\ n_a & M & N \end{pmatrix} \begin{pmatrix} b & f & h \\ n_b & R & S \end{pmatrix} \begin{pmatrix} e & f & c \\ M & R & n_e \end{pmatrix} \begin{pmatrix} g & h & d \\ N & S & n_x \end{pmatrix} = \sum_{XY} [X] \begin{pmatrix} a & b & X \\ n_a & n_b & Y \end{pmatrix} \begin{pmatrix} X & c & d \\ Y & n_e & n_x \end{pmatrix} \begin{Bmatrix} a & b & X \\ e & f & c \\ g & h & d \end{Bmatrix}.$$

Only this (last) sum rule for four Wigner 3–j symbols need to be implemented explicitly because the other two above can be simplified in a two-step evaluation using other sum rules.

Sum rules with five Wigner 3–j, 6–j and/or 9–j symbols:

➢ Sum rules with five 3–j symbols: Varshalovich *et al.* (1988, Eqs. 12.1.12–14) give three sum rules involving products of five 3–j symbols.

$$\sum_{n_p n_q n_r n_s n_t n_u n_v} (-1)^{p-n_p+q-n_q+r-n_r+s-n_s+t-n_t+u-n_u+v-n_v} \begin{pmatrix} r & t & q \\ n_r & n_t & -n_q \end{pmatrix} \begin{pmatrix} q & p & u \\ n_q & n_p & -n_u \end{pmatrix} \begin{pmatrix} u & a & v \\ n_u & n_a & -n_v \end{pmatrix} \begin{pmatrix} v & s & r \\ n_v & n_s & -n_r \end{pmatrix} \begin{pmatrix} s & p & t \\ -n_s & -n_p & -n_t \end{pmatrix}$$

$$= (-1)^{2u} \frac{\delta_{uv}\,\delta_{a0}\,\delta_{n_a 0}}{[u]^{1/2}} \begin{Bmatrix} q & p & u \\ s & r & t \end{Bmatrix}$$

$$\sum_{n_p n_q n_r n_s n_t n_u} (-1)^{p-n_p+q-n_q+r-n_r+s-n_s+t-n_t+u-n_u} \begin{pmatrix} p & a & q \\ n_p & n_a & -n_q \end{pmatrix} \begin{pmatrix} q & r & t \\ n_q & n_r & -n_t \end{pmatrix} \begin{pmatrix} t & s & p \\ n_t & -n_s & -n_p \end{pmatrix} \begin{pmatrix} s & c & u \\ n_s & n_c & -n_u \end{pmatrix} \begin{pmatrix} u & b & r \\ n_u & n_b & -n_r \end{pmatrix}$$

$$= \begin{pmatrix} a & b & c \\ n_a & n_b & n_c \end{pmatrix} \begin{Bmatrix} a & b & c \\ u & s & r \end{Bmatrix} \begin{Bmatrix} a & p & q \\ t & r & s \end{Bmatrix}$$

$$\sum_{n_p n_q n_r n_s n_t n_u} (-1)^{p-n_p+q-n_q+r-n_r+s-n_s+t-n_t+u-n_u} \begin{pmatrix} p & a & q \\ n_p & n_a & n_q \end{pmatrix} \begin{pmatrix} p & a & q \\ n_p & n_a & n_q \end{pmatrix} \begin{pmatrix} q & t & r \\ -n_q & -n_t & -n_r \end{pmatrix} \begin{pmatrix} r & b & s \\ n_r & n_b & n_s \end{pmatrix}$$

$$\times \begin{pmatrix} s & p & u \\ -n_s & -n_p & -n_u \end{pmatrix} \begin{pmatrix} u & c & t \\ n_u & n_c & n_t \end{pmatrix} = (-1)^{r+b+s} \begin{pmatrix} a & b & c \\ -n_a & -n_b & -n_c \end{pmatrix} \begin{Bmatrix} a & b & c \\ p & s & u \\ q & r & t \end{Bmatrix}$$

Sum rules with six Wigner 3–j, 6–j and/or 9–j symbols:

➢ Sum rules with six 3–j symbols: A sum rule corresponds to the representation of the 9–j symbol in terms of six 3–j symbols; see Rotenberg *et al.* (1959, Eq. 3.1).

$$\begin{Bmatrix} a & b & c \\ d & e & f \\ g & h & j \end{Bmatrix} = \sum_{ABCDEFGHJ} \begin{pmatrix} a & b & c \\ A & B & C \end{pmatrix} \begin{pmatrix} d & e & f \\ D & E & F \end{pmatrix} \begin{pmatrix} g & h & j \\ G & H & J \end{pmatrix} \begin{pmatrix} a & d & g \\ A & D & G \end{pmatrix} \begin{pmatrix} b & e & h \\ B & E & H \end{pmatrix} \begin{pmatrix} c & f & j \\ C & F & J \end{pmatrix} .$$

Graphical loop rules for the Wigner 3–j symbols:

➢ Loop rules for one Wigner 3–j symbol: Several loop rules ($n-$loops) can be implemented separately for algebraic evaluations. A loop for one Wigner 3–j symbol is given by Varshalovich *et al.* (1988, Eq. 12.1.2)

$$\sum_m (-1)^m \begin{pmatrix} j & j & J \\ m & -m & M \end{pmatrix} = (-1)^j [j]\, \delta_{J0}\, \delta_{M0} .$$

➢ Loop rules for two Wigner 3–j symbol: Varshalovich *et al.* (1988, Eq. 12.1.3) also displays a loop for two Wigner 3–j symbols

$$\sum_{m_1,m_2} \begin{pmatrix} j_1 & j_2 & j_3 \\ m_1 & m_2 & m_3 \end{pmatrix} \begin{pmatrix} j_1 & j_2 & j_3' \\ m_1 & m_2 & m_3' \end{pmatrix} = \frac{1}{2j_3+1}\, \delta_{j_3,j_3'}\, \delta_{m_3,m_3'}\, \delta(j_1,j_2,j_3) .$$

➢ Loop rules for three Wigner 3–j symbol: Varshalovich *et al.* (1988, Eq. 12.1.6) also displays a loop for three Wigner 3–j symbols.

$$\sum_{m_1,m_2,m_3} (-1)^{-m_1-m_2-m_3} \begin{pmatrix} j_1 & j_4 & j_2 \\ m_1 & m_4 & -m_2 \end{pmatrix} \begin{pmatrix} j_2 & j_5 & j_3 \\ m_2 & m_5 & -m_3 \end{pmatrix} \begin{pmatrix} j_3 & j_6 & j_1 \\ m_3 & m_6 & -m_1 \end{pmatrix}$$

$$= (-1)^{-j_1-j_2-j_3+j_4+j_5+j_6} \begin{pmatrix} j_4 & j_5 & j_6 \\ m_4 & m_5 & m_6 \end{pmatrix} \begin{Bmatrix} j_4 & j_5 & j_6 \\ j_3 & j_1 & j_2 \end{Bmatrix} .$$

15.4. Symbolic evaluations of Racah algebra expressions not yet considered in JAC

15.4.a. Orthogonality, completeness and integral representation of the Wigner rotation matrices:

Unitarity and completeness of the rotation matrices:

➢ Unitarity condition: This condition for the Wigner rotation matrices can be written either in terms of the Wigner D-function (Varshalovich *et al.*, 1988, Eqs. 4.1.6) or, equivalently, by means of the Wigner rotation matrices

$$\sum_{p=-j}^{j} d^j_{pq}(\beta)\, d^j_{pr}(\beta) \;=\; \delta_{qr}, \qquad\qquad \sum_{q=-j}^{j} d^j_{pq}(\beta)\, d^j_{rq}(\beta) \;=\; \delta_{pr}\ .$$

➢ Orthogonality and normalization condition for the rotation matrices: The orthogonality and normalization condition in terms of $d^j_{pq}(\beta)$ is shown by Varshalovich *et al.* (1988, Eqs. 4.10.6 and 4.11.7)

$$\int_0^{2\pi} d\beta\ \sin\beta\ d^j_{pq}(\beta) d^k_{pq}(\beta) \;=\; \frac{2}{2j+1}\delta_{jk}$$

$$\int_0^{2\pi} d\alpha\, e^{-i(p_1-p_2)\alpha} \int_0^{2\pi} d\gamma\, e^{-i(q_1-q_2)\gamma} \int_0^{\pi} d\beta\, \sin\beta\, d^{j_1}_{p_1\,q_1}(\beta)\, d^{j_2}_{p_2\,q_2}(\beta) \;=\; \frac{8\pi^2}{2j_2+1}\,\delta_{j_1 j_2}\,\delta_{p_1 p_2}\,\delta_{q_1 q_2}\ .$$

➢ Completeness condition of the rotation matrices: cf. Varshalovich *et al.* (1988, Eq. 4.10.7) with double domain proportional to $16\pi^2$

$$\sum_{j=0,\frac{1}{2},1,\ldots}^{\infty} \sum_{p=-j}^{+j} \sum_{q=-j}^{+j} (2j+1)\, e^{+i[(\alpha_1-\alpha_2)p+(\gamma_1-\gamma_2)q]}\ d^j_{p\,q}(\beta_1)\, d^j_{p\,q}(\beta_2) \;=\; 16\pi^2\,\delta(\alpha_1-\alpha_2)\,\delta(\cos\beta_1-\cos\beta_2)\,\delta(\gamma_1-\gamma_2)\ .$$

Integrals involving Wigner D^j_{pq} functions or rotation matrices d^j_{pq}:

➢ The Wigner rotation matrices fulfill various integration rules as well as integration with invariant summation rules, and where some of these integrals involve products of more than one Wigner D-function. Whenever possible, we express the Clebsch-Gordan series as a product of two Wigner 3-j symbols. Most of the following integration rules require solid angle integration either over the standard domain

$$\int d\Omega \;\equiv\; \int_0^{2\pi} d\alpha \int_0^{2\pi} d\gamma \int_0^{\pi} d\beta \;\sin(\beta)$$

or over an extended domain with

$$\int d\Omega \;\equiv\; \int_0^{4\pi} d\alpha \int_0^{2\pi} d\gamma \int_0^{\pi} d\beta \;\sin(\beta) \qquad \text{or} \qquad \int d\Omega \;\equiv\; \int_0^{2\pi} d\alpha \int_0^{4\pi} d\gamma \int_0^{\pi} d\beta \;\sin(\beta)\;.$$

$$0 \le \alpha \le 4\pi, \quad 0 \le \beta \le \pi, \quad 0 \le \gamma \le 2\pi, \qquad \text{or} \qquad 0 \le \alpha \le 2\pi, \quad 0 \le \beta \le \pi, \quad 0 \le \gamma \le 4\pi,$$

For this redefinition of the domain of integration, the factors $8\,\pi^2$ must typically be replaced by $16\,\pi^2$.

➢ Integrals with *one* $D^j_{pq}(\alpha,\beta,\gamma)$: Varshalovich *et al.* (1988, Eqs. 4.11.1 and 4.11.6) displays the following normalization integral as well as the corresponding special case for $\alpha = \gamma = 0$ and/or $p = q = 0$

$$\int d\Omega\; D^j_{p\,q}(\alpha,\beta,\gamma) \;=\; \int d\Omega\; e^{-i(p\alpha+q\gamma)}\; d^j_{p\,q}(\beta) \;=\; 8\pi^2\,\delta_{j0}\,\delta_{p0}\,\delta_{q0}, \qquad \text{if} \quad j \text{ is integer}$$

$$\int_0^{\pi} d\beta\; \sin\beta\; d^j_{00}(\beta) \;=\; 2\,\delta_{j0}.$$

15.4.b. Sum rules for spherical harmonics

Products of two and more spherical harmonics:

➢ Sum rules for two spherical harmonics:

$$\sum_{m=-\ell}^{\ell} (-1)^m \, Y_{\ell m}(\vartheta,\varphi) \, Y_{\ell,-m}(\vartheta,\varphi) \;=\; \sum_{m=-\ell}^{\ell} |Y_{\ell m}(\vartheta,\varphi)|^2 \;=\; \frac{2\ell+1}{4\pi}$$

$$\sum_{l=0}^{\infty} \sum_{m=-\ell}^{\ell} (-1)^m \, m \, Y_{\ell,-m}(\vartheta,\varphi) \, Y_{\ell m}(\vartheta,\varphi) \;=\; 0$$

$$\sum_{l=0}^{\infty} \sum_{m=-\ell}^{\ell} (-1)^m \, m^2 \, Y_{\ell,-m}(\vartheta,\varphi) \, Y_{\ell m}(\vartheta,\varphi) \;=\; \frac{l\,(\ell+1)\,(2\ell+1)}{8\pi} \, \sin^2\vartheta$$

$$\sum_{l=0}^{\infty} \sum_{m=-\ell}^{\ell} (-1)^m \, Y_{\ell,-m}(\vartheta,\varphi) \, Y_{\ell m}(\vartheta',\varphi') \;=\; \delta(\varphi-\varphi') \, \delta(\cos\vartheta - \cos\vartheta') \;=\; \delta(\varphi-\varphi') \, \frac{\delta(\vartheta-\vartheta')}{|\sin\vartheta|} \; .$$

➢ The Clebsch-Gordan expansion of two spherical harmonics: A product of two spherical harmonics with the same angles can be written as shown by Varshalovich *et al.* (1988, Eq. 5.6.9)

$$Y_{\ell_1 m_1}(\vartheta,\varphi) \, Y_{\ell_2 m_2}(\vartheta,\varphi) \;=\; \sum_{L,M} \left[\frac{(2\ell_1+1)\,(2\ell_2+1)}{4\pi\,(2L+1)} \right]^{1/2} \langle \ell_1 0, \, \ell_2 0 \,|\, L 0 \rangle \; \langle \ell_1 m_1, \, \ell_2 m_2 \,|\, L M \rangle \; Y_{LM}(\vartheta,\varphi)$$

➢ The Clebsch-Gordan expansion of n spherical harmonics: Using this relation $n-1$ times, one can easily derive a more general expression

$$\prod_{i=1}^{n} Y_{\ell_i m_i}(\vartheta,\varphi) \;=\; \sum_{L_n} B_{L_n} \, Y_{L_n M_n}(\vartheta,\varphi)$$

$$B_{L_n} \;=\; \frac{1}{\sqrt{(4\pi)^{n-1}(2L_n+1)}} \sum_{\substack{L_1,L_2,\ldots,L_n \\ M_1,M_2,\ldots,M_n}} \prod_{i=1}^{n} \sqrt{2l_i+1} \; \langle L_{i-1} 0, \, l_i 0 \,|\, L_i 0 \rangle \; \langle L_{i-1} M_{i-1}, \, l_i m_i \,|\, L_i M_i \rangle \; .$$

➢ Irreducible tensor product of two spherical harmonics: An irreducible tensor product of two spherical harmonics with the same angules can be written as (Varshalovich *et al.* 1988, Eq. 5.6.14)

$$\{Y_{\ell_1}(\vartheta,\varphi) \otimes Y_{\ell_2}(\vartheta,\varphi)\}_{LM} = \left[\frac{(2\ell_1+1)\,(2\ell_2+1)}{4\pi\,(2L+1)}\right]^{1/2} \langle \ell_1 0,\, \ell_2 0 \,|\, L0\rangle \; Y_{LM}(\vartheta,\varphi)$$

➢ Irreducible tensor product of n spherical harmonics: Using this relation $n-1$ times, one finds a more general expression (Varshalovich *et al.* 1988, Eq. 5.6.16):

$$\Big\{ \cdot \, \big\{ \{Y_{\ell_1}(\vartheta,\varphi) \otimes Y_{\ell_2}(\vartheta,\varphi)\}_{L_2} \otimes Y_{\ell_3}(\vartheta,\varphi)\big\}_{L_3} \cdot \otimes Y_{\ell_n}(\vartheta,\varphi)\Big\}_{L_n M_n} = \frac{1}{\sqrt{(4\pi)^{n-1}(2L_n+1)}} \prod_{i=1}^{n} \Big[\sqrt{2\ell_i+1}\;\langle L_{i-1}0,\, \ell_i 0 \,|\, L_i 0\rangle\Big]\; Y_{L_n M_n}(\vartheta,\varphi)\,.$$

➢ Multipole expansions by using spherical harmonics: The spherical harmonics are not only orthonormal to each other but they also form a complete set of functions for the expansion of any function $f(\Theta,\Phi)$ that satisfies the given condition:

$$\int_0^{2\pi} d\Phi \int_0^{\pi} d\Theta\, \sin\Theta\, |f(\Theta,\Phi)|^2 < \infty : \qquad f(\Theta,\Phi) = \sum_{l=0}^{\infty} \sum_{m=-\ell}^{\ell} \tilde{f}_{lm}\, Y_{\ell m}(\Theta,\Phi), \qquad \tilde{f}_{lm} \equiv \int_0^{2\pi} d\varphi \int_0^{\pi} d\vartheta\, \sin\vartheta\, Y^*_{\ell m}(\vartheta,\varphi)\, f(\vartheta,\varphi)\,.$$

15.4.c. Integrals involving spherical harmonics

Integrals involving spherical harmonics:

➢ Orthonormality of the spherical harmonics:

$$\int_0^{2\pi} d\varphi \int_0^{\pi} d\vartheta\, \sin\vartheta\, Y^*_{\ell m}(\vartheta,\varphi)\, Y_{\ell' m'}(\vartheta,\varphi) = \delta_{\ell\ell'}\,\delta_{mm'}\,.$$

➢ Further integrals over 4π: Cf. Varshalovich *et al.* (1988, Eqs. 5.9.1 and 5.9.5):

$$\int_0^{2\pi} d\varphi \int_0^{\pi} d\vartheta \, \sin\vartheta \, Y_{\ell m}(\vartheta,\varphi) \;=\; \sqrt{4\pi}\,\delta_{\ell 0}\,\delta_{m 0}$$

$$\int_0^{2\pi} d\varphi \int_0^{\pi} d\vartheta \, \sin\vartheta \, Y_{\ell_1 m_1}(\vartheta,\varphi)\, Y_{\ell_2 m_2}(\vartheta,\varphi)\, Y_{\ell_3 m_3}(\vartheta,\varphi) \;=\; \sqrt{\frac{(2\ell_1+1)\,(2\ell_2+1)\,(2\ell_3+1)}{4\pi}} \begin{pmatrix} \ell_1 & \ell_2 & \ell_3 \\ 0 & 0 & 0 \end{pmatrix} \begin{pmatrix} \ell_1 & \ell_2 & \ell_3 \\ m_1 & m_2 & m_3 \end{pmatrix} .$$

Derivatives of spherical harmonics:

➢ Derivatives of spherical harmonics: Cf. Varshalovich *et al.* (1988, Eq. 5.8.5) and with the associated Legendre polynomials $P_l^m(\cos\vartheta)$

$$\frac{d}{dx} \int_{g(x)}^{h(x)} dy \, f(y) \;=\; \frac{dh(x)}{dx}\, f(h(x)) \;-\; \frac{dg(x)}{dx}\, f(g(x)) \qquad \text{chain rule}$$

$$\frac{d}{d\vartheta}\, Y_{\ell m}(\vartheta,\varphi) \;=\; \frac{1}{2}\sqrt{\ell\,(\ell+1) - m\,(m+1)}\, Y_{\ell,m+1}(\vartheta,\varphi)\, e^{-i\varphi} \;-\; \frac{1}{2}\sqrt{\ell\,(\ell+1) - m\,(m-1)}\, Y_{\ell,m-1}(\vartheta,\varphi)\, e^{i\varphi} .$$

$$\frac{d}{d\varphi}\, Y_{\ell m}(\vartheta,\varphi) \;=\; i\,m\, Y_{\ell m}(\vartheta,\varphi) .$$

16. References

1992 *Phys. Rev.*

Åberg T and Howat G 1982 in *Corpuscles and Radiation in Matter I*, ed Mehlhorn W (in: Encyclopedia of Physics, vol XXXI; Springer, Berlin, p 469) *Theory of the Auger Effect*

Agostinelli S and Geant 4 collaboration 2003 *Nuc. Instr. Meth.* **A506** 250 *Geant 4 – A simulation toolkit*

Allen L, Beijersbergen M W, Spreeuw R J C and Woerdman J P 1992 *Phys. Rev.* **A45** 8185 *Orbital angular momentum of light and the transformation of Laguerre-Gaussian laser modes*

Allen L, Barnett S M and Padgett M J 2003 *Optical Angular Momentum* (Institute of Physics Publishing, Bristol)

Allen L, Padgett M J and Babiker M 1999 *Progress in Optics* **39** 291 *The orbital angular momentum of light*

Amini K, Biegert J, Calegari F, Chacon A, Ciappina M F, Dauphin A, Efimov D K, de Morisson Faria C F, Giergiel K, Gniewek P et al. 2019 *Rep. Prog. Phys.* **82** 116001 *Symphony on strong field approximation*

Ashkin A, Dziedzic J M, Bjorkholm J E and Chu S 1986 *Opt. Lett.* **11** 288 *Observation of a single-beam gradient force optical trap for dielectric particles*

Astapenko V 2013 in: Springer Series on Atomic, Optical, and Plasma Physics **72** *Polarization Bremsstrahlung on Atoms, Plasmas, Nanostructures and Solids*

Astropy Collaboration 2013 *Astronomy & Astrophys.* **558** A33 *Astropy: A community Python package for astronomy*

Avgoustoglou E, Johnson W R, Plante D R, Sapirstein J, Sheinerman S and Blundell S A 1992 *Phys. Rev.* **A46** 5478 *Many-body perturbation theory formulas for the energy levels of excited states of closed-shell atoms*

Avgoustoglou E, Johnson W R, Liu Z W und Sapirstein J 1995 *Phys. Rev.* **A51** 1196 *Relativistic many-body calculations of* $[\,2p^5 3s\,]$ *excited state energy levels for neon-like ions*

Badnell N R 2011 *Comp. Phys. Commun.* **182** 1528 *A Breit-Pauli distorted wave implementation for* AUTOSTRUCTURE

Bahrdt J, Holldack K, Kuske P, Müller R, Scheer M and Schmid P 2013 *Phys. Rev. Lett.* **111** 034801 *First observation of photons carrying orbital angular momentum in undulator radiation*

Balashov V V, Grum-Grzhimailo A N and Kabachnik N M 2000 *Polarization and Correlation Phenomena in Atomic Collisions* (Kluwer Academic Plenum Publishers, New York)

Ballantine K E, Donegan J F and Eastham P R 2016 *Sci. Adv.* **2** e1501748 *There are many ways to spin a photon: Half-quantization of a total*

optical angular momentum

Band I M, Trzhaskovskaya M B, Nestor Jr N W, Tikkanen P O and Raman S 2002 *Atom. Data Nucl. Data Tables* **81** 1 *DiracFock internal conversion coefficients*

Bazhenov V Y, Vasnetsov M V and Soskin M S 1990 *JETP Lett.* **52** 429 *Laser-beams with screw dislocations in their wave-fronts*

Becke A D and Edgecombe K E 1990 *J. Chem. Phys.* **92** 5397 *A simple measure of electron localization in atomic and molecular systems*

Beijersbergen M W, Coerwinkel R P C, Kristensen M and Woerdman J P 1994 *Opt. Comm.* **12** 321 *Helical-wavefront laser beams produced with a spiral phase plate*

Berengut J C, Dzuba V A, Flambaum V V and Ong A 2012 *Phys. Rev.* **A86** 022517 *Highly charged ions with E1, M1, and E2 transitions within laser range*

Bethe H A and Salpeter E E 1957 *Quantum Mechanics of One- and Two-Electron Systems* (Springer-Verlag, Berlin, Gttingen, Heidelberg)

Bezanson J, Edelman A, Karpinski S and Shah V B 2017 *SIAM Review* **59** 65 *Julia: A fresh approach to numerical computing*

Bezanson J, Chen J, Chung B, Karpinski S, Shah V B, Vitek J and Zoubritzky J 2018 *Proceedings of the ACM on Programming Languages* **2** 120 *Julia: Dynamism and performance reconciled by design*

Bliokh K Y, Bliokh Y P, Savelev S and Bliokh F N 2007 *Phys. Rev. Lett.* **99** 190404 *Semiclassical dynamics of electron wave packet states with phase vortices*

Bliokh K Y, Dennis M R and Franco Nori 2011 *Phys. Rev. Lett.* **107** 174802 *Relativistic electron vortex beams: angular momentum and spin-orbit interaction*

Borgoo A, Scharf O, Gaigalas G and Godefroid M 2010 *Comp. Phys. Commun.* **181** 426 *Multiconfiguration electron density function for the ATSP2K-package*

Bozinovic N, Yue Y, Ren Y, Tur M, Kristensen P, Huang H, Willner A E, Ramachandran S 2013 *Science* **340** 1545 *Terabit-scale orbital angular momentum mode division multiplexing in fibers*

Butler K T, Davies D W, Cartwright H, Isayev O and Walsh A 2018 *Nature* **559** 547 *Machine learning for molecular and materials science*

Cai X, Wang J, Strain M J, Johnson-Morris B, Zhu J, Sorel M, O'Brien J L, Thompson M G, Yu S 2012 *Science* **338** 363 *Integrated compact optical vortex beam emitters*

Canton-Rogan S E, Wills A A, Gorczyca T W, Wiedenhoeft M, Nayandin O, Liu C-N and Berrah N 2000 *Phys. Rev. Lett.* **85** 3113 *Mirroring doubly excited resonances in argon*

Chen J, Ng J, Lin Z and Chan C T 2011 *Nat. Photonics* **5** 531 *Optical pulling force*

Chen Z, Liu F and Wen H 2019 *Chin. Phys.* **B28** 123401 *Quantitative rescattering theory for nonsequential double ionization*

Cheng G and Jiaolong Z 2008 *Phys. Rev.* **E78** 046407 *Spectrally resolved and Rosseland and Planck mean opacities of iron plasmas at temperatures above 100 eV: A systematic study*

Cowan R D 1981 *The Theory of Atomic Structure and Spectra* (University of California Press, 1981, 731 pages)

Da Pieve F, Fritzsche S, Stefani G and Kabachnik N M 2007 *J. Phys.* **B40** 329 *Linear magnetic and alignment dichroism in Auger-photoelectron*

coincidence spectroscopy

Darwin C G 1932 *Proc. R. Soc. Lond.* **A 136** 36 *Notes on the theory of radiation*

Delone N B and Krainov V P 1992 *Phys. Uspekhi.* **47** 669 *AC Stark shift of atomic energy levels*

Derevianko A, Johnson W R and Cheng K T 1999 *At. Data Nucl. Data Tables* **73** 153 *Non-dipole effects in photoelectron angular distributions for rare gas atoms*

Derevianko A, Johnson W R, Safronova M S and Babb J F 1999 Phys. Rev. Lett. **82** 3589 *High-precision calculations of dispersion coefficients, static dipole polarizabilities and atom-wall interaction constants for alkali-metal atoms*

Dzuba V R and Johnson W R 1998 *Phys. Rev.* **A57** 2459 *Calculation of the energy levels of barium using B splines and a combined configuration-interaction and many-body-perturbation-theory method*

Dzuba V A and Flambaum V V 2009 *Phys. Rev.* **A80** 062509 *Calculation of the (T , P)-odd electric dipole moment of thallium and cesium*

Dzuba V A, Flambaum V V and Ginges J S M 2000 *Phys. Rev.* **A61** 062509 *Calculation of parity and time invariance violation in the radium atom*

Dzuba V A, Flambaum V V and Porsev S G 2009 *Phys. Rev.* **80** 032120 *Calculation of* (P, T)*-odd electric dipole moments for the diamagnetic atoms* ^{129}Xe*,* ^{171}Yb*,* ^{199}Hg*,* ^{211}Rn*, and* ^{225}Ra

Edmonds A R 1957 *Angular Momentum in Quantum Mechanics* (Princeton University Press New York)

Eichler J and Meyerhof W 1995 *Relativistic Atomic Collisions* (Academic Press, San Diego)

Fano U 1965 *Phys. Rev.* **140** A67 *Interaction between configurations with several open shells*

Feiock F D and Johnson W R 1968 *Phys. Rev. Lett.* **21** 785 *Relativistic evaluation of internal diamagnetic fields for atoms and ions*

Feiock F D and Johnson W R 1969 *Phys. Rev.* **187** 39 *Atomic susceptibilities and shielding factors*

Fisher D, Maron Y and Pitaevskii L P 1998 *Phys. Rev.* **A58** 2214 *Ionization of many-electron atoms by a quasistatic electric field*

Flambaum V V and Ginges J S M 2005 *Phys. Rev.* **A72** 052115 *Radiative potential and calculations of QED radiative corrections to energy levels and electromagnetic amplitudes in many-electron atoms*

Fontes C J, Zhang H L, Abdallah Jr J, Clark R E H, Kilcrease D P, Colgan J, Cunningham R T, Hakel P, Magee N H and Sherrill M E 2015 *J. Phys.* **B48** 144014 *The Los Alamos suite of relativistic atomic physics codes*

Franke-Arnold S, Allen L, Padgett M J 2008 *Laser and Photonics Reviews* **2** 299 *Advances in optical angular momentum*

Freiburghaus C, Rosswog S and Thielemann F-K 1999 *Astrophys. J.* **525** L121 *r-Process in neutron star mergers*

Fritzsche S 1997 *Comp. Phys. Commun.* **103** 51 *Maple procedures for the coupling of angular momenta. I. Data structures and numerical evaluation*

Fritzsche S 2001 *J. Electron Spectrosc. Relat. Phenom.* **114-116** 1155 *A toolbox for studying the properties of openshell atoms and ions*

Fritzsche S 2002 *Phys. Scr.* **T100** 37 *Largescale accurate structure calculations for openshell atoms and ions*

Fritzsche S, Nikkinen J, Huttula S-M, Aksela H, Huttula M and Aksela S 2007 *Phys. Rev.* **A75** 012501 *Interferences in the* $3p^4nl$ *satellite emission following the excitation of argon across the* $2p^5_{1/2}4s$ *and* $2p^5_{3/2}3d$ $J = 1$ *resonances*

Fritzsche S, Fricke B and Sepp W-D 1992 *Phys. Rev.* **A45** 1465 *Reduced* L_1 *level-width and Coster-Kronig yields by relaxation and continuum interactions in atomic zinc*

Froese Fischer C, Godefroid M, Brage T, Jönsson P and Gaigalas G 2016 *J. Phys.* **B49** 182004 *Advanced multiconfiguration methods for complex atoms: I. Energies and wave functions*

Furukawa H and Nishihara K 1992 *Phys. Rev.* **A46** 6596 *Fermi-degeneracy and discrete-ion effects in the spherical-cell model and electron-electron correlation effects in hot dense plasma*

Gaidamauskas E, Naze C, Rynkun P, Gaigalas G, Jönsson P and Godefroid M 2011 *J. Phys.* **B44** 175003 *Tensorial form and matrix elements of the relativistic nuclear recoil operator*

Gaigalas G, Froese Fischer C, Rynkun P and Jönsson P 2017 *atoms* **5** 6 *JJ2LSJ: Transformation and unique Labeling for energy levels*

Gaigalas G, Zalandauskas T and Fritzsche S 2004 *Comp. Phys. Commun.* **157** 239 *Spectroscopic LSJ notation for atomic levels obtained from relativistic calculations*

Galstyan A, Popov Y V, Janssens N, Mota-Furtado F, OMahony P F, Decleva P, Quadri N, Chuluunbaatar O and Piraux B 2018 *Chem. Phys.* **504** 22 *Ionisation of H_2O by a strong ultrashort XUV pulse: A model within the single active electron approximation*

Gaunt 1929 *Proc. R. Soc.* **A122** 513 *IV. The triplets of helium*

Ghiringhelli L M, Vybiral J, Levchenko S V, Draxl C and Scheffler M 2015 *Phys. Rev. Lett.* **114** 105503 *Big data of materials science: Critical role of the descriptor*

Ginzburg V L and Tsytovich V N 1979 *Phys. Rep.* **49** 1 *Transition radiation and transition scattering*

Goldman S P and Drake G W F 1992 *Phys. Rev. Lett.* **68** 1683 *Asymptotic Lamb shifts for helium Rydberg states*

Gordon R G and Kim Y S 1972 *J. Chem. Phys.* **56** 3122 *Theory for the forces between closed-shell atoms and molecules*

Grant I P 1988 *in: Methods in Computational Chemistry* ed Wilson S, vol 2 (Plenum, New York, p 1) *Relativistic effects in atoms and molecules*

Grant I P and Pyper N C 1976 *J. Phys.* **B9** 761 *Breit interaction in multiconfiguration relativistic atomic calculations*

Grant I P and Quiney H M 1988 *in: Advances in Atomic and Molecular Physics* **23** eds D Bates and B Bederson (Academic, New York, p 37) *Foundation of Relativistic Theory of Atomic and Molecular Structure*

Griem H 1974 *Spectral Line Broadening by Plasmas* (Academic Press, New York, London)

Grier D G 2003 *Nature* **424** 810 *A revolution in optical manipulation*

Grillo V, Gazzadi G-C, Mafakheri E, Frabboni S, Karimi E and Boyd R W 2015 *Phys. Rev. Lett.* **114** 034801 *Holographic generation of highly twisted electron beams*

Grum-Grzhimailo A N, Gryzlova E V, Staroselskaya E I, Venzke J and Bartschat K 2015 *Phys. Rev.* **A91** 063418 *Interfering one-photon and two-photon ionization by femtosecond VUV pulses in the region of an intermediate resonance*

Gu M F 2008 *Can. J. Phys.* **86** 675 *The flexible atomic code*

Guo D-S, Åberg T and Crasemann B 1989 *Phys. Rev* **A40** 4997 *Scattering theory of multiphoton ionization in strong fields*

Guo D-S and Drake G W F 1992 *Phys. Rev* **A45** 6622 *Multiphoton ionization in circularly polarized standing waves*

Haque A K F, Shahjahan M, Uddin M A, Patoary M A R, Basak A K, Saha B C and Malik F B 2010 *Phys. Scr.* **81** 045301 *Generalized Kolbenstvedt model for electron impact ionization of the K-, L- and M-shell ions*

Hartgers A, van Dijk J, Jonkers J, van der Mullen J A M 2001 *Comp. Phys. Commun.* **135** 199 *CR-Model: A general collisional radiative modeling code*

He H, Friese M E J, Heckenberg N R and Rubinsztein-Dunlop H 1995 *Phys. Rev. Lett.* **75** 826 *Direct observation of transfer of angular momentum to absorptive particles from a laser beam with a phase singularity*

Hemsing E, Marinelli A Rosenzweig J B 2011 *Phys. Rev. Lett.* **106** 164803 *Generating optical orbital angular momentum in a high-gain free-electron laser at the first harmonic*

Hemsing E and Marinelli A 2012 *Phys. Rev. Lett.* **109** 224801 *Echo-enabled x-ray vortex generation*

Hemsing E, Knyazik A, Dunning M, Xiang D, Marinelli A, Hast D and Rosenzweig J B 2013 *Nature Phys.* **9** 549 *Coherent optical vortices from relativistic electron beams*

Hubbell J H, Veigele W J, Briggs E A, Brown R T, Cromer D T and Howerton R J 1992 *J. Phys. Chem. Ref. Data* **4** 471 *Atomic form factors, incoherent scattering functions, and photon scattering cross sections*

Huntemann N, Sanner C, Lipphardt B, Tamm C and Peik E 2016 *Phys. Rev. Lett.* **116** 063001 *Single-ion atomic clock with* 3×10^{18} *systematic uncertainty*

Inal M K, Surzhykov A and Fritzsche S 2005 *Phys. Rev.* **A72** 042720 *Linear polarization of the* $2p^5 3s \rightarrow 2p^6$ *lines following the inner-shell photoionization of sodiumlike ions*

Inhester L, Burmeister C F, Groenhof G and Grubmüller H 1992 *J. Chem. Phys.* **136** 144304 *Auger spectrum of a water molecule after single and double core ionization*

Isinger M, Squibb R J, Busto D, Zhong S, Harth A, Kroon D, Nandi S, Arnold C L, Miranda M, Dahlström J M, Lindroth E et al. 2017 *Science* **358** 893 *Photoionization in the time and frequency domain*

Ivanov I P and Karlovets D V 2013 *Phys. Rev. Lett.* **110** 264801 *Detecting transition radiation from a magnetic moment*

Jaganathen Y, Id Betan R M, Michel N, Nazarewicz W and Ploszajczak M 2017 *Phys. Rev.* **C96** 054316 *Quantified Gamow shell model interaction for psd-shell nuclei*

Jahrsetz T, Fritzsche S and Surzhykov A 2015 *Phys. Rev.* **A89** 042501 *Inelastic Raman scattering of light by hydrogenlike ions*

Jia C-S, Diao Y-F, LiuX-J, Wang P-Q, Liu J-Y and Zhang G-D 2012 *J. Chem. Phys.* **137** 014101 *Equivalence of the Wei potential model and Tietz potential model for diatomic molecules*

Jiao L G, Zan L R, Zhu L, Ma J and Ho Y K 2019 *Comp. Phys. Commun.* **244** 217 *Accurate computation of screened Coulomb potential integrals in numerical Hartree-Fock programs*

Johnson W R 1995 *in: Physics with Multiply Charged Ions* ed D Liesen (NATO ASI Series 348, Plenum Press, New York London, p 1 *Correlation and QED for highly-charged ions*

Johnson W R 2007 *Atomic Structure Theory: Lectures on Atomic Physics* (Springer)

Johnson W R and Feiock F D 1968 *Phys. Rev.* **168** 22 *Rayleigh scattering and the electromagnetic susceptibility of atoms*

Johnson W R, Guo D S, Idrees M and Sapirstein J 1985 *Phys. Rev.* **A32** 2093 *Weak-interaction effects in heavy atomic systems*

Jönsson P, Gaigalas G, Bieron J, Froese Fischer C and Grant I P 2013 *Comp. Phys. Commun.* **184** 2197 *New version: Grasp2K relativistic atomic structure package*

Judd B R 1963 *Operator Techniques in Atomic Spectroscopy* (McGraw-Hill New York)

Kabachnik N M 1981 *J. Phys.* **B14** L337

Kabachnik N M, Fritzsche S, Grum-Grzhimailo A N, Meyer M and Ueda K 2007 *Phys. Rep.* **451** 155 *Coherence and correlations in photoinduced Auger and fluorescence cascades in atoms*

Kassimi N E and Thakkar A J 1994 *Phys. Rev.* **A50** 2948 *Static hyperpolarixability of atomic lithium*

Kibeedia T, Burrows T W, Trzhaskovskayac M B, Davidsona P M and Nestor Jr C W 2008 *Nucl. Instr. Meth.* **A589** 202 *Evaluation of theoretical conversion coefficients using BrIcc*

Killoran N, Izaac J, Quesada N, Bergholm V, Amy M and Weedbrook C 2019 *Quantum* **3** 129 *Strawberry Fields: A Software Platform for Photonic Quantum Computing*

Kim Y S and Gordon R G 1974 *Phys. Rev.* **B9** 3548 *Theory of binding of ionic crystals: Application to alkali-halide and alkane-earth-dihalide crystals*

Klar H 1980 *J. Phys.* **B13** 4741

Kien F L, Schneeweiss P and Rauschenbeutel A 2013 *Eur. Phys. J.* **D67** 92 *Dynamical polarizability of atoms in arbitrary light fields: General theory and application to cesium*

Krause M O 1979 *J. Phys. Chem. Ref. Data* **8** 329 *Atomic radiative and radiationless yields for K and L shells*

Koga T and Thakkar A J 1996 J. Phys. **B 29** 2973 *Moments and expansion coefficients of atomic electron momentum densities: numerical Hartree-Fock calculations for hydrogen to lawrencium*

Leung A C K and Kirchner T 2015 *Phys. Rev.* **A92** 032712 *Independent-electron analysis of the x-ray spectra from single-electron capture in Ne^{10+} collisions with He, Ne, and Ar atoms*

Li W, Grumer J, Brage T and Jönsson P 2020 *Comp. Phys. Commun.* **xxx** xxx HFSZEEMAN95 – *A program for computing weak and intermediate magnetic-field- and hyperfine-induced transition rates*

Libermann D A 1979 *Phys. Rev.* **B20** 4981 *Self-consistent field model for condensed matter*

Lindgren I and Rosen A 1974 *Case Studies in Atomic Physics* **5** *Relativistic self-consistent-field calculations with application to atomic hyperfine interaction. Part I: Relativistic self-consistent fields*

Lindgren I and Morrison J 1986 *Atomic Many-Body Theory*, 2nd ed (Springer Berlin)

Liu C-N and Starace A F 1999 *Phys. Rev. A* **59** 1731(R) *Mirroring behavior of partial photodetachment and photoionization cross sections in the neighborhood of a resonance*

Liu P F, Liu Y P, Zeng J L and Yuan J M 2014 *Phys. Rev.* **A89** 042704 *Electron-impact excitation and single- and multiple-ionization cross sections of heavy ions: Sn^{13+} as an example*

Liu Z, Lee H, Xiong Y, Sun C and Zhang X 2007 *Science* **315** 1686 *Far-field optical hyper lens magnifying sub-diffraction-limited objects*

Marxer H 1991 *Phys. Rev. A* **44** 1543 *Exact correspondence relationship for the expectation values of r^{-k} for hydrogenlike states*

Marxer H 1995 *J. Phys.* **B28** 341 *Off-diagonal matrix elements* $\langle n\ell \,|\, r^k \,|\, n\ell' \rangle$ *for hydrogen-like states: an exact correspondence relationship in terms of orthogonal polynomials and the WKB approximation*

Matula O, Hayrapetyan A G, Serbo V G, Surzhykov A and Fritzsche S 2013 *J. Phys.* **B46** 205002 *Atomic ionization of hydrogen-like ions by twisted photons: angular distribution of emitted electrons*

Matula O, Hayrapetyan A G, Serbo V G, Surzhykov A and Fritzsche S 2014 *New J. Phys.* **16** 053016 *Radiative capture of twisted electrons by bare ions*

Mazevet S and Abdallah Jr J 2006 *J. Phys.* **B39** 3419 *Mixed UTA and detailed line treatment for mid-Z opacity and spectral calculations*

McClean J R, Sung K J, Kivlichan I D, Cao Y, Dai C, Fried S E, Gidney C, Gimby B, Gokhale P et al. 2019 *Phys. Rev.* **A** in print *OpenFermion: The electronic structure package for quantum computers*

McGloin D and Dholakia K 2005 *Contemp. Phys.* **64** 15 *Bessel Beams: Diffraction in a New Light*

McMorran B J, Agrawal A, Anderson I M, Herzing A A, Lezec H J, McClelland J J and Unguris J 2011 *Science* **331** 192 *Electron vortex beams with high quanta of orbital angular momentum*

Mendoza C 2018 *atoms* **6** 28 *Computation of Atomic Astrophysical Opacities*

Metzger B D 2017 *Living Rev. Relativ.* **20** 3 *Kilonovae*

Milione G, Sztul H I, Nolan D A and Alfano R R 2011 *Phys. Rev. Lett.* **107** 053601 *Higher-order Poincare sphere, Stokes parameters and the angular momentum of light*

Mitroy J, Safronova M S and Clark C W 2010 *J. Phys.* **B43** 202001 *Theory and applications of atomic and ionic polarizabilities*

Müller A, Lindroth E, Bari S, Borovik Jr A, Hillenbrand P-M, Holste K, Indelicato P, Kilcoyne A L D, Klumpp S, Martins M, Viefhaus J, Wilhelm P and Schipp 2018 *Phys. Rev.* **A98** 033416 *Photoionization of metastable heliumlike* C^{4+} $(1s2s\ {}^3S_1)$ *ions: Precision study of intermediate doubly excited states*

Müller A, Borovik Jr A, Bari S, Buhr T, Holste K, Martins M, Perry-Samannshausen A, Phaneuf R A, Reinwardt S, Ricz S, Schubert K and Schippers S 2018 *Phys. Rev. Lett.* **120** 133202 *Near-K-edge double and triple detachment of the F negative ion: Observation of direct two-electron ejection by a single photon*

Nye J F and Berry M V 1974 *Proc. R. Soc. London Ser.* **A336** 165 *Dislocations in wave trains*

Oemrawsingh S S R, Aiello A, Eliel E R, Nienhuis G and Woerdman J P 2014 *Phys. Rev. Lett.* **92** 217901 *How to observe high-dimensional two-photon entanglement with only two detectors*

Ong W and Russek A 1978 *Phys. Rev.* **A17** 120 *Simple asymptotic wave function for a continuum Dirac electron*

Pan L, Taylor K T and Clark C W 1988 *Phys. Rev. Lett.* **61** 2673 *Computation of the ac Stark effect in the ground state of atomic hydrogen*

Parpia F, Froese Fischer C and Grant I P 1996 *Comput. Phys. Commun.* **94** 249 *GRASP92: A package for large-scale relativistic atomic structure calculations*

Pattard T 2002 *J. Phys.* **B35** L207 *A shape function for single-photon multiple ionization cross sections*

Paufler W, Birger Böning B and Fritzsche S 2019 *J. Opt.* **21** 094001 *High harmonic generation with Laguerre-Gaussian beams*

Paufler W, Birger Böning B and Fritzsche S 2019 *Phys. Rev.* **A100** 013422 *Coherence control in high-order harmonic generation with Laguerre-*

Gaussian beams

Peele A G, McMahon P J, Paterson D, Tran C Q, Mancuso A P, Nugent K A, Hayes J P, Harvey E, Lai B and McNulty I 2002 *Opt. Lett.* **27** 1752 *Observation of an x-ray vortex*

Picon A, Mompart J, Vaizquez de Aldana J A, Plaja L, Calvo G F and Roso L 2007 *Opt. Express* **18** 3660 *Photoionization with orbital angular momentum beams*

Pisanty E, Machado G J, Vicuna-Hernandez V, Celi A, Torres J P and Lewenstein M 2019 *Nat. Phot.* **13** 569 *Knotting fractional-order knots with the polarization state of light*

Porsev S G, Kozlov M G and Reimers D 2009 *Phys. Rev.* **A79** 032519 *Transition frequency shifts with fine-structure constant variation for Fe I and isotope-shift calculations in Fe I and Fe II*

Porsev S G and Derevianko A 2006 *J. Exp. Theo. Phys.* **102** 195 *High-accuracy calculations of dipole, quadrupole and octupole electric-dynamic polarizabilities and van-der-Waals coefficients C_6, C_8 and C_{10} for alkaline-earth dimers*

Porsev S G, Rakhlina Y G and Kozlov M G 1999 *Phys. Rev.* **A60** 2781 *Electric-dipole amplitudes, lifetimes, and polarizabilities of the low-lying levels of atomic ytterbium*

Post D E and Kendall R P 2004 *Int. J. HPC Applications* **18** 399 *Software project management and quality engineering practices for complex, coupled ...*

Potvliege R M 1998 *Comput. Phys. Commun.* **114** 42 *STRFLO: A program for time-independent calculations of multiphoton processes in one-electron atomic systems: I. Quasi-energy spectra and angular distributions*

Poynting J H 1909 *Proc. R. Soc.* **A82** 560 *The wave motion of a revolving shaft, and asuggestion as to the angular momentum in abeam of circularly polarised light*

Radice D, Perego A, Hotokezaka K, Fromm S A, Bernuzzi S and Roberts L F 1992 *Astrophys. J.* **869** 130 *Binary neutron star mergers: mass ejection, electromagnetic counterparts, and nucleosynthesis*

Radtke T, Fritzsche S and Surzhykov A 2006 *Phys. Rev. A* **74** 032709 *Density-matrix formalism for the photoion-electron entanglement in atomic photoionization*

Ribic P R, Guathier D and De Ninno G 2014 *Phys. Rev. Lett.* **112** 203602 *Generation of coherent extreme-ultraviolet radiation carrying orbital angular momentum*

Roberts B M, Dzuba V A and Flambaum V V 2014 *Phys. Rev.* **89** 042509 *Strongly enhanced atomic parity violation due to close levels of opposite parity*

Rohrlich F and Carlson B C 1954 *Phys. Rev.* **93** 38 *Positron-electron differences in energy loss and multiple scattering*

Rothhardt J, Hädrich S, Demmler S, Krebs M, Fritzsche S, Limpert J and Tünnermann A 2014 *Phys. Rev. Lett.* **112** 233002 *Enhancing the macroscopic yield of narrow-band high-order harmonic generation by Fano resonances*

Rose S J, van Hoof P M M, Jonauskas V, Keenan F P, Kisielius R, Ramsbottom C, Foord M E, Heeter R F and Springer P T 1992 *J. Phys.* **37** L337 *Calculation of photoionized plasmas with an average-atom model*

Rotenberg M, Bivins R, Metrapolis N, and Wooten J K jr 1959 *The 3–j and 6–j symbols* (The Technology Press Cambridge Massachusetts)

Rudzikas Z 1997 *Theoretical Atomic Spectroscopy* (Cambrige University Press, Cambrige)
Safronova M S, Porsev S G, Sanner C and Ye J 2018 *Phys. Rev. Lett.* **120** 173001 *Two clock transitions in neutral Yb for the highest sensitivity to variations of the fine-structure constant*
Saha B and Fritzsche S 2006 *Phys. Rev. E***73** 036405 *Be I isoelectronic ions embedded in hot plasma*
Saha B and Fritzsche S 2007 *J. Phys. B***40** 259 *Influence of dense plasma on the low-lying transitions in Be-like ions: relativistic multiconfiguration DiracFock calculation*
Salvat F, Jablonski A and Powell C J 2005 *Comp. Phys. Commun.* **165** 157 ELSEPA – *Dirac partial-wave calculation of elastic scattering of electrons and positrons by atoms, positive ions and molecules*
Sanchez-Lengeling B and Aspuru-Guzik A 2018 *Science* **361** 360 *Inverse molecular design using machine learning: Generative models for matter engineering*
Sapirstein 1987 *Phys. Scr.* **36** 801 *Quantum-electrodynamics of many-electron atoms*
Sasaki S and McNulty I 2008 *Phys. Rev. Lett.* **100** 124801 *Proposal for generating brilliant x-ray beams carrying orbital angular momentum*
Schollwöck U 2011 *Ann. Phys.* **326** 96 *The density-matrix renormalization group in the age of matrix product states*
Scholz-Marggraf H M, Fritzsche S, Serbo V G, Afanasev A and Surzhykov A 2014 *Phys. Rev.* **A90** 013425 *Absorption of twisted light by hydrogen-like atoms*
Schütt K T, GlaweH, Brockherde F, Sanna A, Muüller K R and Gross E K U 2014 *Phys. Rev.* **B89** 205118 *How to represent crystal structures for machine learning: Towards fast prediction of electronic properties*
Shabaev V M, Tupitsyn I I, Yerokhin V A, Plunien G and Soff G 2004 *Phys. Rev. Lett.* **93** 130405 *Dual kinetic balance approach to basis-set expansions for the Dirac equation*
Shabaev V M, Tupitsyn I I and Yerokhin V A 2013 *Phys. Rev.* **A88** 012513 *Model operator approach to the Lamb shift calculations in relativistic many-electron atoms*
Sharma L, Surzhykov A, Inal M K and Fritzsche S 2010 *Phys. Rev.* **A81** 023419 *Polarization transfer in the innershell photoionization of sodiumlike ions*
Shen Y, Campbell G T, Hage B, Zou H, Buchler B C and Shen P K L et al. 2013 *J. Opt.* **15** 044005 *Generation and interferometric analysis of high charge optical vortices*
Simon A, Warczak A, ElKafrawy T and Tanis J A 2010 *Phys. Rev. Lett.* **104** 123001 *Radiative double electron capture in collisions of O^{8+} ions with carbon*
Smith D Y 1987 *Phys. Rev.* **A35** 3381 *Anomalous x-ray scattering: Relativistic effects in x-ray dispersion analysis*
Stone N J 2005 *Atomic Data and Nuclear Data Tables* **90** 175 *Table of nuclear magnetic dipole and electric quadrupole moments*
Sukhov S and Dogariu A 2010 *Opt. Lett.* **35** 3847 *On the concept of tractor beams*
Sukhov S and Dogariu A 2011 *Phys. Rev. Lett.* **107** 203602 *Negative nonconservative forces: optical tractor beams for arbitrary objects*
Surzhykov A, Radtke T, Indelicato P and Fritzsche S 2009 *Eur. J. Phys. Spec. Topics* **169** 129 *Photon polarization in the two-photon decay of heavy*

hydrogenlike ions

Surzhykov A, Volotka A, Fratini F, Santos J P, Indelicato P, Plunien G, Stoöhlker and Fritzsche S 2008 *Phys. Rev.* **A81** 042510 *Angular correlations in the twophoton decay of heliumlike heavy ions*

Surzhykov A, Jentschura U D, Stöhlker T and Fritzsche S 2006 *Phys. Rev.* **A73** 032716 *Radiative electron capture into high-Z few-electron ions: Alignment of the excited ionic states*

Tanaka M, Kato D, Gaigalas G, Rynkun P, Radziute L, Wanajo S, Sekiguchi Y, Nakamura N, Tanuma H, Murakami I and Sakaue H A 2018 *Astrophys. J.* **852** 109 *Properties of kilonovae from dynamical and post-merger ejecta of neutron star mergers*

Tanaka M, Kato D, Gaigalas G and Kawaguchi K 2020 *Astrophys. J.* **??** xxx *Systematic Opacity Calculations for Kilonovae*

Tchang-Brillet W L, Wyart J-F, Meftah A and Mammar S A 2018 *atoms* **6** 52 *Parametric calculations of radiative decay rates for magnetic dipole and electric quadrupole transitions in Tm IV, Yb V, and Er IV*

Torres and Torner (eds) 2011 *Twisted photons* (Wiley-VCH, Weinheim)

Tupitsyn I I, Shabaev V M, Lopez-Urrutia J R C, Draganic I, Orts R S and Ullrich J 2003 *Phys. Rev.* **A68** 022511 *Relativistic calculations of isotope shifts in highly charged ions*

Tupitsyn I I, Kozlov M G, Safronova M S, Shabaev V M and Dzuba V A 2016 *Phys. Rev. Lett.* **117** 253001 *Quantum electro-dynamical shifts in multivalent heavy ions*

Uchida M and Tonomura A 2010 *Nature* **467** 737 *Generation of electron beams carrying orbital angular momentum*

van Veenendaal M and McNulty I 2007 *Phys. Rev. Lett.* **98** 157401 *Prediction of strong dichroism induced by x rays carrying orbital momentum*

Varshalovich D A, Moskalev A N, Khersonskii V K 1988 *Quantum Theory of Angular Momentum* (World Scientific Singapore a.o.)

Verbeeck J, Tian H and Schattschneider P 2010 *Nature* **467** 301 *Production and application of electron vortex beams*

Voloch-Bloch N, Lereah Y, Lilach Y, Gover A and Arie A 2013 *Nature* **494** 331 *Generation of Electron Airy Beams*

Volotka A V, Bilal M, Beerwerth R, Ma X, Stöhlker T and Fritzsche S 2019 *Phys. Rev.* **A100** 010502(R) *QED radiative corrections to the* $^2P_{1/2} - ^2P_{3/2}$ *fine structure in fluorinelike ions*

Volotka A V, Yerokhin V A, Surzhykov A, Stöhlker T and Fritzsche S 2016 *Phys. Rev.* **A93** 023418 *Many-electron effects on x-ray Rayleigh scattering by highly charged He-like ions*

von der Wense, Seiferle B, Stellmer S, Weitenberg J, Kazakov G, Palffy A and Thirolf P G 2017 *Phys. Rev. Lett.* **119** 132503 *A laser excitation scheme for* ^{229m} *Th*

Vriens L and Smeets A H M 1980 *Phys. Rev.* **A22** 940 *Cross-section and rate formulas for electron-impact ionization, excitation, deexcitation and total depopulation of excited atoms*

Wouters S and Van Neck D 2014 *Eur. Phys. J.* **68** 272 *The density matrix renormalization group for ab initio quantum chemistry*

Yao A M and Padgett M J 2011 *Adv. Opt. Photon.* **3** 161 *Orbital angular momentum: origins, behavior and applications*

Yudin V Y, Taichenachev A V and Derevianko A 2014 *Phys. Rev. Lett.* **113** 233003 *Magnetic-dipole transitions in highly charged ions as a basis of ultraprecise optical clocks*

Yutsis A P, Levinson I B und Vanagas V V 1962 *Mathematical apparatus of the theory of angular momentum.* Israel Program for Scientific Translation, Jerusalem 1962

Zaitsevskii A V und Heully J-L 1992 *J. Phys.* **B25** 603 *Rayleigh-Schrödinger QDPT for hermitian intermediate Hamiltonians by the shift technique*

Zambrini R and Barnett S 2006 *Phys. Rev. Lett.* **96** 113901 *Quasi-intrinsic angular momentum and the measurement of its spectrum*

Zarrabian S, Laidig W D und Bartlett R J 1990 *Phys. Rev.* **A41** 4711 *Convergence properties of multireference many-body perturbation theory*

Zaytsev V A, Volotka A V, Yu D, Fritzsche S, Ma X, Hu H and Shabaev V M 2019 *Phys. Rev. Lett.* **123** 093401 *Ab initio QED treatment of the two-photon annihilation of positrons with bound electrons*

Zhan Q W 2009 *Adv. Opt. Photon.* **1** 1 *Cylindrical vector beams: from mathematical concepts to applications*

Zhu X-M and Pu Y-K 2010 *J. Phys.* **D43** 015204 *A simple collisionalradiative model for low-temperature argon discharges with pressure ranging from 1 Pa to atmospheric pressure: kinetics of Paschen* $1s$ *and* $2p$ *levels*

Ziegler J F 1999 *J. Appl. Phys.* **85** 1249 *Stopping of energetic light ions in elemental matter*

Index